OPTIMIZING WOODCHIP BIOCHAR FOR ADSORPTION OF INORGANIC METAL ION CONTAMINANTS

By

Ify Leonard Ugbomeh MSc, BSc (Hons)
A thesis submitted to the University of Birmingham for the degree of DOCTOR OF PHILOSOPHY (Ph.D.)

Division of Environmental Health and Risk Management College of Life and Environmental Sciences School of Geography, Earth and Environmental Sciences, The University of Birmingham, Edgbaston, B15 2TT, United Kingdom.

October 2023

UNIVERSITY OF
BIRMINGHAM

University of Birmingham Research Archive

e-theses repository

This unpublished thesis/dissertation is copyright of the author and/or third parties. The intellectual property rights of the author or third parties in respect of this work are as defined by The Copyright Designs and Patents Act 1988 or as modified by any successor legislation.

Any use made of information contained in this thesis/dissertation must be in accordance with that legislation and must be properly acknowledged. Further distribution or reproduction in any format is prohibited without the permission of the copyright holder.

ABSTRACT

Affordable, reliable, and low-cost methods for removal of oil-associated heavy metal contaminants (Ni^{2+} and Pb^{2+}) from the environment are urgently needed. The use of adsorbent's produced from organic biomass which is a renewable feedstock has gained attention recently. In this work, seven woodchip biomass samples (Ash, Apple, Alder, Beech, Birch, Cherry and Oak) were characterized in terms of their surface area, pore size, pore volume , elemental composition (Carbon, Nitrogen, Hydrogen, Oxygen), moisture, volatile substances, heat content , and metal ion concentrations (Mg, Mn, P, Ca, Co, Cu, Cr, Fe, Ni, Cd, Pb) and statistically compared using Pairwise non-parametric Kruskal-Wallis one-way ANOVA) to identity a subset based on significantly (<0.05) different parameters for conversion to biochar. Based on this analysis, four biomass samples were selected (Ash, Apple, Beech, and Birch) and subjected to pyrolysis at 550°C for 5 hrs to produce its derived biochar (Bc-Ash, Bc-Apple, Bc-Beech, and Bc-Birch). The Biochar samples had large surface areas: 307.3 ± 7.31m^2/g, 314.2 ± 7.31m^2/g, 305.1 ± 7.28m^2/g and 287.3 ± 6.77m^2/g for Bc-Ash, Bc-Apple, Bc-Beech, and Bc-Birch, respectively and were evaluated in terms of their efficacy for sorption of Ni^{2+} and Pb^{2+}. Sorption results for Ni^{2+} (0.7977 - 0.8124 mg/g biochar) and Pb^{2+} (0.7958 – 0.8073 mg/g biochar) were slightly below expectation with hydrogen bonding/ electrostatic being the only binding mechanism identified for all 4 biochar types. To improve sorption capacity and possibly introduce an additional sorption mechanism, the Bc-Beech was functionalised with nanoscale materials to create hybrid biochar. Three functionalization routes were explored: Hydroxyapatite-Biochar (HA-Bc), Magnetic-Biochar (MBc), and Magnetic-Hydroxyapatite-Biochar (MHA-Bc). These hybrid Biochar samples were characterised and found to have surface areas of 141.1 ± 1.95 m^2/g (HA-Bc), 190.64 ± 4.11 m^2/g (MBc) and 104.5 ± 0.11 m^2/g (MHA-Bc) and interacted effectively in both

mono (Ni^{2+}or Pb^{2+}) and binary ($Ni^{2+}$and Pb^{2+}) exposure modes with the target pollutants. MBc (0.25 mg/g) had better affinity for Ni^{2+} than HA-BC (0.24 mg/g), MHA-Bc (0.24 mg/g) had the highest affinity for Pb^{2+}, while in the binary system the total amount of pollutants bound decreased in the order MBc (0.49 mg/g) > MHA-Bc (0.49 mg/g) HABc> (0.49 mg/g). Nanomaterial functionalization of biochar reduced the number of active sites for sorption but added a new attachment mechanism (complexation) to the existing one (precipitation), thereby enhancing the overall adsorption efficiencies.

DEDICATION

I dedicate this work to God Almighty and my beloved parents, the late Professor G.M.M. Ugbomeh and Mrs. A.N. Ugbomeh, for their unwavering support and prayers throughout my journey. Your tireless efforts to ensure a better life for me, along with your unwavering optimism, will forever hold a special place in my heart. Dad, I dearly wish you were here to share in this moment with me and bask in the glory it brings.

ACKNOWLEDGMENTS

My Gratitude goes to God Almighty for the gift of life and good health and to my Parents (the late Prof GMM Ugbomeh and Mrs Teena. N. Ugbomeh) for their love and endless support. I equally want to appreciate my sponsor (Delta state University) for the opportunity given to study and to build impactful Academic relationships. Words cannot explain how grateful I am to my lead supervisor and supervisory team (Prof Iseult Lynch, Dr. Lesley Batty and Dr. Tassos Papadiamantis) for their patience, time, encouragement and advise - truly you guys are the best. Also, I want to appreciate the WG1 and WG3 lab staff, nano group, friends, and colleagues who stood tall with me when it was rough and hard. Indeed, I am blessed to have you all in my life. I am hugely appreciative of the thorough, thoughtful, and supportive suggestions for improvement of the thesis made by the internal and external examiners also – Prof. Sami Ullah (University of Birmingham) and Dr. Tom Sizman (University of Reading) - I have learned a lot from you both.

CONTENTS

ABSTRACT 2

DEDICATION 4

ACKNOWLEDGMENTS 5

CHAPTER 1 25

INTRODUCTION AND LITERATURE REVIEW 25

1.1 Environmental pollution 25

1.2 Cation Exchange capacity (CEC) 27

1.3 Biochar Introduction 32

1.4 Primary Constituents of a Typical Lignocellulosic Biomass 34

1.4.1 Cellulose 34

1.4.2 Hemicellulose 35

1.4.3 Lignin 35

1.5 Biochar Characterization: Key Concepts 36

1.5.1 Atomic Ratios 36

1.5.2 Aromaticity 37

1.5.3 Temperature 38

1.5.4 Surface Area 39

1.5.5 Functional Groups 40

1.5.6 Zeta Potential 41

1.5.7 Pore Volume and Size Distribution 42

1.5.8 Density and Porosity 43

1.6 Biochar and Inorganic Pollutant Removal 43

1.6.1 Precipitation 44

1.6.2 Surface Complexation 45

1.6.3 Ion Exchange 45

1.7 Introduction to Adsorption 46

1.7.1 Adsorption Process 49

1.7.2 Adsorption Mechanism and Equilibrium 50

1.7.3 Role of Time: Adsorption Kinetics 52

1.7.4 Pseudo-First-Order Kinetics Model (PFO) 53

1.7.5 Pseudo-Second-Order Kinetics Model 54

1.7.6 Elovich Equation 55

1.7.7 Intraparticle Diffusion Model 56

1.7.8 Role of Absorbant/Adsorbate Concentration: Adsorption Isotherms 56

1.7.9 Langmuir Isotherm 57

1.7.10 Freundlich Isotherm 58

1.7.11 Temkin Isotherm 59

1.8 Biochar and Pyrolysis Temperature Classification 60

1.8.1 Hydrophilic Biochar 61

1.8.2 Hydrophobic Biochar 62

1.9 Adsorption Mechanism 62

1.9.1 Organic Pollutant 64

1.9.2 Inorganic Pollutants 65

1.10 Functionalization of Biochar 66
1.10.1 Steam Activation Functionalization 68
1.10.2 Acidic Modification Functionalization 68
1.10.3 Alkaline Modification Functionalization 69
1.10.4 Impregnation Method Functionalization 69
1.10.5 Nano material Functionalization 70
1.11 Aims and Objectives of the Research 76
1.11.1: Hypothesis of the Research 76
1.12 Chapter Summary 77
CHAPTER 2 79
INSTRUMENTATION 79
2.1 Introduction 79
2.2 Theoretical Basis of the Methods Applied for Biomass and Biochar Characterization 79
2.2.1 Scanning Electron Microscopy (SEM) 79
2.2.2 Elemental Analysis 82
2.2.3 Fourier Transform infrared Spectroscopy coupled to thermogravimetric Analysis (FTIR-TGA) 83
2.2.4 Brunauer-Emmett-Teller (BET) analysis of surface area and pore volume 87
2.2.5 Centrifuge 89
2.2.6 Bomb Calorimetry 90
2.3 Summary 93
CHAPTER 3 95
SELECTION AND CHARACTERIZATION OF WOODCHIP BIOMASS AND ITS DERIVED BIOCHAR 95

3.0 Introduction 95

3.1 Sample Preparation, Methodology and Expectation Overview 97

3.1.1 Pyrolysis of woodchip biomass to produce Biochar. 98

3.1.2 Biomass and Biochar Characterisation 99

3.1.3 Sample Digestion (Biomass and Biochar) for Analysis of the Metal Content 103

3.1.4 Statistical Analysis of Biomass Samples Characteristics 104

3.2 Results and Discussion 107

3.2.1 Analysis of the surface functional groups on the biomass and biochar samples 144

3.2.2 Morphological features of the biomass and biochar 148

Birch 149

Beech 149

3.2.3 Surface area and porosity of the biomass and biochar samples 151

3.3 Biochar Stability 152

3.4 Conclusion 155

CHAPTER 4 156

SORPTION OF HEAVY METALS ON WOODCHIPS BIOMASS AND DERIVED BIOCHAR-ANALYSIS OF THE DRIVERS AND MECHANISM 156

4.0 Introduction 156

4.1 Methodology: Preparation of Calibration Curves and Samples for Sorption 158

4.2.1 Biochar Sorption of Ni^{2+} and Pb^{2+} 162

4.2.2 Sorption Kinetics 175

5.3 Conclusion 179

CHAPTER 5 181

CHARACTERIZATION OF SORPTION OF HEAVY METALS BY HYBRID DERIVED-BIOCHAR IN A MONO AND BINARY SYSTEM. 181

5.1 Introduction 181

5.2 Biochar Hybridization Selection 183

5.3 Method: Preparation of Hybrid Biochar 184

5.3.1 Hydroxyapatite and Hydroxyapatite Biochar (Ha-Bc) 184

5.3.2 Magnetic Biochar preparation (M-Bc) 186

5.3.3 Magnetic Hydroxyapatite-Biochar preparation (MHa-Bc) 187

5.4 Characterization of Functionalized Hybrid Biochar 188

5.4.1 Effect of functionalisation on the biochar physico-chemical characteristics 191

5.4.2 Sorption mechanisms of the Functionalized Biochar 199

5.5 Conclusion 201

CHAPTER 6 203

OVERALL CONCLUSION AND RECOMMENDATIONS 204

6.1 Future Work and What I Would Do Differently 211

7.1.1 What Was Learnt/Contribution to Knowledge. 213

REFERENCES ..... **Error! Bookmark not defined.**

APPENDIX 251

FUNCTIONAL GROUP 252

APPENDIX B 258

CALIBRATION 258

APPENDIX C 261

BET SAMPLES ANALYSIS 261

APPLE SUMMARY REPORT 262

Surface Area 262

Pore Volume 262

Pore Size 262

Langmuir Report 272

Ash Summary Report 290

Pore Volume 290

Pore Size 291

BET Report 291

Table C 2.0: Bc-Ash Isotherm Tabular Report 292

Figure C-2.3: Bc-Ash BET Isotherm Log Plot 298

Figure C-2.5: Bc-Ash BET Surface Area Plot 301

Langmuir Report 302

Figure C-2.6: Langmuir Surface Area Plot 305

Table C 2.3: Bc-Ash BJH Adsorption Pore Distribution Report 306

Figure C-2.9: BJH Adsorption Cumulative Pore Area (Larger) (Halsey: Faas Correction 310

Figure.C-2.11: Bc-Ash BJH Adsorption dA/dlog(D) Pore Area 312

Table C 2.4: Bc-Ash BJH Desorption Pore Distribution Report 313

Figure C-2.15: Bc-Ash BJH Desorption cumulative pore area 317

BEECH SUMMARY REPORT 320

Pore Volume 320

Pore Size 320

BJH Desorption Pore Distribution Report 341

BIRCH SUMMARY REPORT 349

Summary Report Surface Area 349

Pore Volume 349

Pore Size 349

Faas Correction Halsey 372

FUNCTIONALIZE SAMPLES 381

MAGNETIC HYDROXYAPPETITE BIOCHARA-(MHA-BC) SUMMARY REPORT ... 382

HYDROXYAPPATIE -BIOCHAR (HA-Bc) SUMMARY REPORT 397

HYDROXY APPATITE (HA) SUMMARY REPORT 422

MAGNETIC BIOCHAR (MBC) SUMMARY REPORT 437

1.1: Discussion 458

LIST OF FIGURES

Figure 1.2: Typical Lignocellulosic biomass undergoing thermal degradation in the absence of oxygen, which results in the biomass losing its primary and secondary components to produce secondary products (bio-oil/gas) leading to the production of a carbon rich solid material (biochar)..... 33

Biochar applications have not been restricted to remediation of contaminated soils, as its potentials has been harnessed in (1) Agriculture where it has been use for soil amendment, (2) Carbon sequestration which aims to control the amount of carbon emitted into the atmosphere, and (3) In waste management where biochar is used to treat wastewater and sludge to produce a reasonable discharge or re-useable form of effluent (Liu et al., 2018)..... 34

Figure 1.3: Reproduced van Krevelen diagram of natural carbonation of coal and biochar, showing how atomic ratios, aromaticity and polarity reduce with increase in temperature leading to a more stable biochar (Weber et al., 2018; Jafri et al., 2018; Aller, Bakshi et al., 2017;Manyà et al., 2014)..... 37

Figure 1.4: Illustration of the increase in Carbon yield (big black circles) as pyrolysis temperature increases, and corresponding reduction in Hydrogen (small black circles), Oxygen (Green-circles) and Nitrogen (yellowish brown circles) (Weber and Quicker, 2018; Jafri *et al.*, 2018). Increasing temperature reduces H, O and N but increases the yield of carbon (thus inducing a high stability)..... 39

Figure 1.5: Stability of a Particle as a function of its Zeta Potential. The isoelectric point is the point at which the surface has zero charge and is therefore unstable as there are no electrostatic repulsive forces (Tarafdar & Adhikari, 2015)..... 42

Figure 1.6: Schematic illustration of the two potential Biochar sorption mechanisms responsible for the removal of inorganic contaminants (Pb^{2+} and Ni^{2+}) from the environment to the active sites of the biomass-derived biochar. 46

Figure 1.7: Schematic illustration of the classification of sorption phenomena into Adsorption and Absorption focusing on its mode of contaminants attachment as a key factor that differentiates them from each other. 48

Figure 1.8: Schematic illustration of Temperature Based Characterization of Biochar for removal of contaminants based on the biochar fluid content, surface area, stability, pH and surface functional groups and categorisation into hydrophobic versus hydrophilic Biochar. 61

Figure 1.9: Adsorption mechanisms for organic and inorganic pollutants removal showing sorption mechanisms as it relates to surface active groups or the entire bulk of the adsorbent (Oliveira et al., 2017; Harris, 2009; Lu et al., 2012; Ahmad et al., 2014; Teixidó et al., 2011; Oliveira et al., 2017; Xie et al., 2015). 66

Figure 2.1: Elemental Analyser (FLASH 2000 Combustion) for Quantification of C, H, N, S, O in a sample. 83

Figure 2.2: TGA-FTIR-GCMS analyser plus a connected PC to view spectra and input suitable operational methods for surface functional groups analysis and TGA (University of Birmingham). 85

Figure 2.3: Brunauer – Emmett – Teller (BET) device (SA3100 WL Beckman Coulter, Inc) University of Birmingham. 88

Figure 2.5: Bomb Calorimeter (IKA® C200) University of Birmingham (Collaborative Teaching Laboratory). The analyser measures the heat content a of sample. This method was used on all 7 of the biomass samples (ash, apple, alder, beech, birch, cherry, and oak). 92

Figure 2.6: Summary of chapter 2 showing details of characterization methods (BET, FTIR, TGA, Calorimeter, Elemental Analyser and Zeta potential) and parameters characterised (Atomic ratio, HHv, Surface area and functional group, pore size/volume and SEM imaging) for each of the biomass / biochar samples and the modification techniques utilised to produce the hybrid Biochar samples and how these parameters and modifications could affect sorption of the heavy metal ions. 94

Figure 3.1: Seven different Wood chips (Ash, Apple, Alder, Beech, Birch, Cherry and Oak)) obtained from Amazon. 98

Figure 3.2a: Ground samples (left), and the essential components of the BET device (University of Birmingham). 102

Figure 3.2b: SEM images of biomass and its derived char showing the effect of pyrolysis (550 ^{o}C for 5 hours) on the morphological features, specifically the opening of blocked pores and the increased pore volume following pyrolysis. 102

Figure 3.3: Reflux digestion unit for biomass and derived biochar (University of Birmingham). 104

Figure 3.4: Schematic summary of the experimental work performed in Chapter 4, showing how the 7 biomass woodchip samples (Ash, Apple, Alder, Birch, Beech, Cherry, and Oak) were analysed (characterized via proximate and ultimate analysis, SEM, BET and elemental analysis) and statistically evaluated in order to select 4 (Ash, Apple, Birch and Beech) for pyrolysis and subsequent re-characterization of the biochar samples by the same methods prior to their use for sorption experiments in chapter 4. 106

Figure 3.5a: SEM images of selected biomasses showing morphological features such as blocked pores and low pore volume 149

Figure 3.5b: SEM images of selected wood-chip biomass samples and their derived biochar samples showing the effect of pyrolysis (550°C for 5 hour) on the morphological features, especially the opening of blocked pores and the increased pore volume following pyrolysis. 150

Figure 3.6: Schematic illustration of a van Krevelen Diagram showing biochar stability. These types of diagrams are used to plot the hydrogen: carbon atomic ratio (aromaticity) as a function of the oxygen: carbon atomic ratio, which in the original utilisation of these plots could be used as an indicator of the ability of a rock to produce oil during maturation. In the biochar context the ratio is used to confirm its stability during the conversion of biomass into biochar (Weber & Quicker, 2018; Jafri et al., 2018; Aller et al., 2017; Manyà et al., 2014). 154

Figure 4.1: Schematic of the sorption experiment setup (shaker, weighting pan, falcon tubes, Centrifuge, Reflux digestion system, ICP-OES) with selected biomass samples (having interpolated equivalent surface areas for each) to its derived biochar (Bc-Ash, Bc-Apple, Bc-Beech and Bc-Birch) in falcon tubes in triplicates in a shaker (collected at intervals) before centrifugation, reflux digestion, ICP-OES analysis and interpretation. 161

Figure 4.2a: PCA component plot in rotated space loading Ni^{2+} adsorption to Biochar. Scree plot showing Eigen Values > 1 representing number of components (loaded characterization parameters) that is required to account for the variance in the data. . 167

Figure 4.3 (a): Bar chart showing the standard error of derived biochar (Bc-Ash, Bc-Apple, Bc-Beech, and Bc-Birch) average adsorption values ± Standard deviation (n = 4) of Pb^{2+} of Ni^{2+} (mg/g) at 1.5g dosage biochar in an incubation time frame of 12 hours (1,3,5,8 and 12). At a constant concentration of Ni (500 ppm) to monitor the sorption

rate in relation to time and biochar mass and to infer the most effective biochar in terms of Ni^{2+} sorption. 173

Figure 4.3 (b): Bar chart showing the derived biochar (Bc-Ash, Bc- Apple, Bc-Beech, and Bc-Birch) average adsorption values ± Standard deviation (n=4) of Pb^{2+} (mg/g) at the dosage of 1.5 g in an incubation time frame of 12 hours (1, 3, 5, 8 and 12 hours). A constant concentration of Pb^{2+} (500 ppm) was used, to monitor the sorption rate in relation to time and biochar mass and to infer the most effective biochar in terms of Pb^{2+} sorption. 174

Figure 4.4: Plots showing the adsorption isotherms of derived biochar for (a) Ni^{2+} and (b) Pb^{2+} sorption to 0.3 g biochar over time (from 60 to 720 mins) and the recorded concentration q_e (mg/g) bound to biochar. 176

Figure 4.5: Plot of the adsorption isotherm for 0.5 g derived biochar for (a) Ni^{2+} and (b) Pb^{2+} sorption over time (from 60 to 720 mins) and the adsorbed concentration q_e (mg/g). 177

Figure 4.6: Plot of the adsorption isotherm at 1.5 g dosage of derived biochar for (a) Ni^{2+} and (b) Pb^{2+} sorption over time (from 60 to 720 mins) and the absorbed concentration q_e (mg/g). 177

Figure 5.1: Schematic illustration of the process for functionalization of biochar with Hydroxyapatite or Iron (III) nitrate nonahydrate to produce the hybrid biochars Hydroxyapatite-Biochar and Magnetic Biochar, and the combination of both approaches to produce a super-hybrid (combination of hybrids) biochar, namely the Magnetic Hydroxyapatite-Biochar. 183

Figure 5.3 Schematic illustration of the synthesis of the Magnetic biochar preparation through heating for approximately 6 hours followed by then centrifugation at 3000 rpm at 25 ^{o}C and freeze dried for 72 hours. 186

Figure 5.4: Schematic illustration of Magnetic Hydroxyapatite-biochar preparation in details (20g of biochar in 100ml DI water containing Fe $(NO_3)_3$ 0.076M + Ca1.75M 41.5g stirred for proper mixing, with NH4OH used to regulate the pH ≥ 10, then heated for 90^oC for approximately 6hours) then centrifuged at 3000 rpm and 25 ^oC and freeze dried over 72 hours. 187

Figure 5.5a: Characterization of the hybrid biochar samples in terms of their morphology and surface area: SEM images and BET summary data for surface area, pore size/volume. compared to the original Beech-biochar. From Left to Right: Hydroxyapetite (alone, no biochar); hydroxyapatite modified Beech biochar (Ha-Bc), Beech Biochar, Magnetic biochar (M-Bc) and magnetic hydroxyapatite biochar (MHa-Bc). 189

Figure 5.5b: FTIR spectral of (a) Hydroxyapatite (HA), (b) Hydroxyapatite Biochar (HABC), (c) Magnetic Biochar (MBC), (d) Magnetic Hydroxyapatite (MHA), (e) Magnetic Hydroxyapatite Biochar (MHABC) and (f) Beech Biochar (Beech-Bc) as the unmodified control. 190

Figure 5.6: Plots of average adsorption ± standard deviation (mg/g) (n=3) of Ni^{2+} (A), Pb^{2+} (B) and Ni^{2+}- Pb^{2+} (C) exposed singularly (mono system) and simultaneously (binary system) to functionalized magnetic-Hydroxyapatite Biochar (MHA-Bc), Hydroxyapatite Biochar (Ha-Bc), and Magnetic biochar (MBc). 198

Figure 6.1: A summary of the experimental journey for the initial seven (7) biomasses, reduced by statistical evaluation to four (4) that were pyrolyzed to generate biochar, and then selection of one (1) for functionalized to create the hybrid biochar samples. Beech biochar was hybrid with hydroxyapatite, magnetite or both to produce the hybrid biochar (HaBc, MBc, MHaBc, respectively). The four biochar and three hybrid biochar samples were then used for sorption experiments with Ni^{2+} and Pb^{2+} in a mono (biochar

and hybrid biochar) and binary (hybrid biochar samples only) system. Each adsorbent was ranked according to their sorption performance of Ni^{2+} or Pb^{2+} and Ni^{2+}+ Pb^{2+}). 207

Figure 6.2: Summary of the research performed in this thesis: a systematic approach from Biomass selection and characterization to thermal degradation (showing hypothesis 1), base-line sorption experiments utilising the biomass-derived biochar samples, through to functionalization of the Beech biochar to produce hybrid biochar samples (showing hypothesis 2), then sorption in a mono and binary system. 210

Figure E 1.0: (a,b,c): Pseudo first order of Ni^{2+} at 0.3 g adsorbent. b. Pseudo second order Ni^{2+} at 0.3 g adsorbent. c. Intraparticle diffusion of Ni^{2+} at 0.3 g adsorbent. 452

Figure E1.1: (a,b,c): Pseudo first order of Ni^{2+} at 0.5 g adsorbent. b. Pseudo second order Ni^{2+} at 0.5 g adsorbent. c. Intraparticle diffusion of Ni^{2+} at 0.5 g adsorbent. 453

Figure E 1.2 (a, b, c): Pseudo first order Ni^{2+} at 1.5 g adsorbent. b. Pseudo second order Ni^{2+} at 1.5 g adsorbent. 457

Figure E 1.3: (a, b, c): Pseudo first order of Pb^{2+} at 0.3 g adsorbent. b. Pseudo second order of Pb^{2+} at 0.3 g adsorbent. c. Intraparticle diffusion of Pb^{2+} at 0.3 g adsorbent . 461

Figure E 1.4: a, b, c:. Pseudo first order of Pb^{2+} at 0.5 g adsorbent. b. Pseudo second order of Pb^{2+} at 0.5 g adsorbent. c. Intraparticle diffusion of Pb^{2+} at 0.5 g adsorbent . 462

LIST OF TABLES

Table 1.1: Remediation techniques and applications 29

Table 1.2: Biochar Application for Organic and Inorganic Contaminants Removal at different pH, temperatures and feed stock showing removal mechanism and decontamination efficiency..... 72

Table 2.1: Operational modes in the SEM and their parameter (Turkulin, Holzer, Richter, & Sell, 2005)..... 81

Table 3.1: Mean values of Proximate and Ultimate analysis from biomass characterization..... 110

Table 3.2: Characterization parameters (10) compared across samples with their significance difference and the decision as to whether the pair (shows sufficient difference to accept or rejects the null hypothesis). 111

Table 3.3: Pairwise comparisons of the Moisture content of the biomass samples to determine any significance differences. Sample numbers 1 = Alder, 2 = Ash, 3 = Apple, 4 = Birch, 5 = Beech, 6 = Cherry and 7 = Oak..... 113

Table 3.4: Pairwise comparisons of the Volatile Matter content of the biomass samples to determine any significance differences. Sample numbers 1 = Alder, 2 = Ash, 3 = Apple, 4 = Birch, 5 = Beech, 6 = Cherry and 7 = Oak. 115

Table 3.5: Pairwise comparisons of the Fixed Carbon content of the biomass samples to determine any significance differences. Sample numbers 1 = Alder, 2 = Ash, 3 = Apple, 4 = Birch, 5 = Beech, 6 = Cherry and 7 = Oak..... 117

Table 3.6: Pairwise comparisons of the Calorific value-HHv content of the biomass samples to determine any significance differences. Sample numbers 1 = Alder, 2 = Ash, 3 = Apple, 4 = Birch, 5 = Beech, 6 = Cherry and 7 = Oak..... 119

Table 3.7: Pairwise comparisons of the Carbon content of the biomass samples to determine any significance differences. Sample numbers 1 = Alder, 2 = Ash, 3 = Apple, 4 = Birch, 5 = Beech, 6 = Cherry and 7 = Oak. 121

Table 3.8: Pairwise comparisons of the Hydrogen content of the biomass samples to determine any significance differences. Sample numbers 1 = Alder, 2 = Ash, 3 = Apple, 4 = Birch, 5 = Beech, 6 = Cherry and 7 = Oak. 123

Table 3.9: Pairwise comparisons of the Nitrogen content of the biomass samples to determine any significance differences. Sample numbers 1 = Alder, 2 = Ash, 3 = Apple, 4 = Birch, 5 = Beech, 6 = Cherry and 7 = Oak. 125

Table 3.10: Pairwise comparisons of the Oxygen content of the biomass samples to determine any significance differences. Sample numbers 1 = Alder, 2 = Ash, 3 = Apple, 4 = Birch, 5 = Beech, 6 = Cherry and 7 = Oak. 127

Table 3.11: Pairwise comparisons of the Magnesium content of the biomass samples to determine any significance differences. Sample numbers 1 = Alder, 2 = Ash, 3 = Apple, 4 = Birch, 5 = Beech, 6 = Cherry and 7 = Oak. 129

Table 3.12: Pairwise comparisons of the Phosphorous content of the biomass samples to determine any significance differences. Sample numbers 1 = Alder, 2 = Ash, 3 = Apple, 4 = Birch, 5 = Beech, 6 = Cherry and 7 = Oak. 131

Table 3.13: Pairwise comparisons of the Calcium content of the biomass samples to determine any significance differences. Sample numbers 1 = Alder, 2 = Ash, 3 = Apple, 4 = Birch, 5 = Beech, 6 = Cherry and 7 = Oak. 133

Table 3.14: Pairwise comparisons of the Chromium content of the biomass samples to determine any significance differences. Sample numbers 1 = Alder, 2 = Ash, 3 = Apple, 4 = Birch, 5 = Beech, 6 = Cherry and 7 = Oak. 135

Table 3.15: Pairwise comparisons of the Cobalt content of the biomass samples to determine any significance differences. Sample numbers 1 = Alder, 2 = Ash, 3 = Apple, 4 = Birch, 5 = Beech, 6 = Cherry and 7 = Oak. 137

Table 3.16: Pairwise comparisons of the Iron content of the biomass samples to determine any significance differences. Sample numbers 1 = Alder, 2 = Ash, 3 = Apple, 4 = Birch, 5 = Beech, 6 = Cherry and 7 = Oak. 139

Table 3.17: Pairwise comparisons of the Manganese content of the biomass samples to determine any significance differences. Sample numbers 1 = Alder, 2 = Ash, 3 = Apple, 4 = Birch, 5 = Beech, 6 = Cherry and 7 = Oak. 141

Table 3.18: Summary of the significantly different characteristics / parameters between the different woodchip biomass samples, where the null Hypothesis was rejected. The four woodchips highlighted in red text were the ones that are most significantly different from one another, based on the characteristics highlighted in the green boxes, and were selected for pyrolysis to generate their associated biochar. 143

Table 3.19a: Surface functional groups determined in the woodchip biomass samples via FTIR analysis. 145

Table 3.19b: Analysis of the functional groups present on the surface of the four selected biomass-derived biochar samples, determined from FTIR analysis. 146

Table 3.20: Summary of the characterization of the four biochar samples. Comparison with Table 3.1 indicates the morphological changes caused by pyrolysis temperature. 152

Table 4.1: PCA of characterization parameters for Nickel Sorption to Biochar, showing total variance (%) by Eigen values >1 with the corresponding components in order of hierarchy (highest to low). 169

Table 4.2: PCA of characterization parameters for Lead sorption to Biochar, showing the Total Variance (%) by Eigen values >1 with its corresponding components in order of hierarchy (highest to low). 170

Table 4.3a: Baseline sorption experiment of Ni^{2+} to biochar, in mg/g, to determine the sorption capacity of the different biochar samples with respect to time. A constant concentration of Ni (500 ppm) was used, and the incubation time was 12 hours, at different dosages (0.3g, 0.5g, 1g, 1.5g) of the respective derived biochar (Ash, Apple, Birch, Beech). 171

Table 4.3b: Baseline sorption experiment of Pb^{2+} to biochar, in mg/g, to determine the sorption capacity of the different biochar samples with respect to time. A constant concentration of Pb (500 ppm) was used, and the incubation time was 12 hours, at different dosages (0.3g, 0.5g, 1g, 1.5g) of the respective derived biochar (Ash, Apple, Birch, Beech). 172

Table 5.1: Sorption results in mg/g of metal ions bound to the functionalized Biochar (Hydroxyapatite biochar (HABc), Magnetic Biochar (MBc) and Magnetic Hydroxyapatite Biochar) following incubation with Nickel and Lead in a mono and binary system over 12 hours. 195

Table E 1.0: Kinetic parameters for the biosorption of Ni^{2+} onto 0.3 g adsorbents showing q_e k_1 and R^2 values insinuating sorption mechanism. 454

Table E1.1: Kinetic parameters for the biosorption of Ni^{2+} onto 0.5 g adsorbents showing q_e k_1 and R^2 values insinuating sorption mechanism. 455

Table E 1.2: Kinetic parameters for the biosorption of Ni^{2+} onto 1.5 g adsorbents showing q_e k_1 and R^2 values insinuating sorption mechanism. 456

Table E 1.3: Kinetic parameters for the biosorption of Pb^{2+} onto 0.3 g (a.) and 0.5 g (b.) adsorbents showing q_e k_1 and R^2 values insinuating sorption mechanism. 459

Table E1.4: Kinetic parameters for the biosorption of Pb^{2+} onto 0.5 g adsorbents showing q_e k_1 and R^2 values insinuating sorption mechanism. 460

CHAPTER 1

INTRODUCTION AND LITERATURE REVIEW

1.1 Environmental pollution

The release of contaminants (organic and inorganic) into the environment has increased the need for development of efficient remediation approaches and exploration of what technique is most suitable for sorption of these unwanted pollutants. To accomplish this, carbon rich materials from renewable sources such as biomass have been prioritized based on their large surface area, active surface functional groups and well distributed pore size/volume. Other carbon-based materials such as graphene or activated carbon also possess these properties but are quite expensive and unsustainable on industrial scale for environmental applications, while biomass and its pyrolysis product, biochar (Bc) are relatively cost-effective.

Woodchips (ash, alder, apple, birch, beech, cherry, and oak) are an easily accessible biomass source and were selected for this work. Based on analysis of their physico-chemical properties, four of the biomasses were selected for conversion into biochar (Bc-ash, Bc-apple, Bc-Birch, and Bc-Beech) and from these, one was further functionalised with nanomaterials to generate hybrid biochar - Hydroxyapatite biochar (HA-Bc), Magnetic biochar (MBc) and Magnetic Hydroxyapatite Biochar (MHa-Bc). The choice of wood chips was based on the high lignin content of its biomass, which can potentially confer functional groups on the surface when used for generation of biochar, which is hypothesized would make them suitable for sorption of inorganic pollutants such as lead (Pb^{2+}) and nickel (Ni^{2+}).

In this thesis the mechanism(s) of heavy metal ion removal, and their equilibrium maximum adsorption isotherms were studied in singular (one metal at a time) and binary (both metals presented to the biochar at the same time) exposures.

Water, air, and soil are essential components of the environment needed for everyday survival by human beings and other living things (bacteria, plants, and animals) (Azhar et al., 2022a). The evolution towards an increasingly urbanized environment has encouraged environmentally damaging activities such as industrialization, mining, and exploitation of natural resources (Yadav et al., 2021). These activities generate substantial waste which poses urgent environmental challenges as the resulting waste, if mis-managed, results in pollution of air, water and soil and degradation of the environment. These concerns can be viewed in terms of waste disposal / management, contamination of surface and subsurface ground water (endangering aquatic life), pollution of soil with organic and inorganic contaminants (affecting plant-growth and soil health) and reduction in clean air quality (respiration diseases in humans) (Lim & Foo, 2021; Rasheed, 2022; Yadav et al., 2021).

Thus, exploitation of natural resources (such as crude oil), industrialization and mining activities have introduced a wide range of organic (e.g., Poly aromatic hydrocarbons (PAHs)) and inorganic (e.g., heavy metals) pollutants into the environment (water, air, and soil). Heavy metals such as lead (Pb^{2+}) and nickel (Ni^{2+}) are also introduced into the environment by anthropogenic means including industrialization, mining, and poor waste disposal. Ni^{2+} can also be introduced to the environment through natural means such as weathering and volcanic eruptions. Both Pb^{2+} and Ni^{2+} induce adverse health effects, and the environmental (soil, water, and air) implications and potential for plant bioaccumulation have inspired extensive research and efforts to remediate heavy metal contaminated soils. Nickel is present as Ni^{2+} in most biological and environmental

systems but exist in various oxidation states (-1 to +4). It is the 28th element in the Periodic Table, it is hard, ductile, silvery-white transition metal (Genchi et al., 2020). Nickel in combination with oxygen and sulphur is naturally present in the earth as oxides and sulphides. Its physical and chemical properties drive its relevance for metallurgies (alloy production, electroplating, nickel-cadmium battery production) and in turn serve as means of re-introducing it into the environment as a pollutant due to lack of proper waste management and poor process handling (S. Ding et al., 2022; Genchi et al., 2020; Khaleeq et al., 2022; Mitra et al., 2022).

On the other hand, lead (Pb^{2+}) is one of the most widely known pollutants in the environment; it exists as oxides, sulphates and carbonates when exposed to air and its introduction is basically by anthropogenic means (mining, use of fertilizers and pesticides). Its presence in soils trigger signals of immediate threat to human health (especially children) due to its highly toxic nature. When Pb^{2+} uptake into the food chain (phytotoxicity) causes indigestion of contaminated food, and impacts on the health of children, leading to neurotoxicity, cancer, kidney diseases and learning difficulties (Abbaszade et al., 2022; Beatrice et al., 2022; Collin et al., 2022; Yadav et al., 2021). The occurrences of these contaminants (organic and inorganic) in the environment have serious effect on the soil cation exchange capacity (CEC), plant growth/yield and human health.

1.2 Cation Exchange capacity (CEC)

Cation exchange capacity (CEC) is one of the soil physicochemical properties that measured the ability of the soil to bind or hold exchangeable cations (Olorunfemi *et al.*,

2016). In other words, it is a measure of the number of negatively charged binding sites in soil (Rashidi and Seilsepour, 2008). The cation exchange capacity of a soil represents the total amount of exchangeable cations that a soil can retain. Cation exchange capacity helps characterize the soil type under consideration. It is worth noting that CEC is a key parameter in many soil processes, such as nutrient retention, soil water retention capacity and soil pollution management, it is measured in milliequivalent (meq)/100g or centimol (cmolc/kg) positive charge per kg of soil) (Emamgholizadeh et al., 2022; Enang et al., 2022). Thus, CEC influences the soil stability and structure by helping to express amounts of negatively charged sites present in the soil and capable of attracting a positive ion, that is, it measures the soils' ability to hold nutrients (Emamgholizadeh et al., 2022). It was observed that soil contamination with some metals reduce the soil CEC value to < 10meq/100g which is typical for low CEC or poor-quality soils, which leads to increased acidity of the soil (Emamgholizadeh et al., 2022; Enang et al., 2022). Low CEC values resulting from increasing soil contamination by pollutants such as PAHs, Pb^{2+} and Ni^{2+} has driven the focussing of research towards development of a remediation technique to mitigate their adverse effects on the environment.

Remediation techniques to remove contaminants such as PAHs, Pb^{2+} and Ni^{2+} from soil, preserve soil cation exchange capacity (structural stability). Various techniques (vitrification, electrokinetic remediation, thermal desorption, soil for soil remediation, chemical remediation of soil, immobilization techniques, encapsulating technique, soil-washing, Chemical stabilization, and reversible surfactant) have been used to remediate contaminated (inorganic and organic) soil by isolating the pollutant and stabilizing the soil (Azhar et al., 2022b; Dai et al., 2022; Mitra et al., 2022; Yadav et al., 2021) (Table 1.1). These remediation techniques are effective to some extent in-terms of isolating the pollutants. However, the cost of their implementation is quite expensive because of

considerations such as the need for mobilization of equipment into and out of the site, the cost of chemicals involved, operational cost of equipment during the remediation period and hiring qualified personal to opera the equipment. These limitations of existing remediation techniques prompted an urgent need for development of a cost-effective technique, that is simple to understand, requires little expertise to operate and, most importantly, is efficient in removal/isolation of contaminants present in the environment. Carbon-rich materials satisfactory meet these sorption criteria, as presented in the next section.

Table 1.1: Remediation techniques and applications

Remediation techniques	Description of the techniques	Application medium	References
Vitrification	This occur through the heating the contaminated soil to high temperatures (1700–2000°C) while applying electric current, it is possible to restrict the movement of heavy metallic ions in the soil, which leads to the emergence of vitreous materials. Some metals may be volatilized under high temperatures during vitrification and are then composed for further treatment or dumping. Vitrification is not considered a conventional method for treating contaminated soil. In comparison to other	Soil-soil	(Alshawabkeh and Bricka, 2000; Azhar *et al.*, 2022)

	treatments, vitrification is the simplest to implement. This technique can easily treat organic and inorganics pollution.		
Electrokinetic	The electrokinetic treatment method works based on establishing an appropriate electric field gradient across the sides of an electrolytic container that comprises saturated contaminated soil. Removing heavy metallic ions by electrophoresis or electro-migration reduces pollution. This procedure entails applying low electrical currents to the contaminated surface in order to concentrate the contaminants to the electrode, where they may be collected later. Contaminants are eliminated, oxidized, and mobilized throughout the process.	Soil-soil	Yao *et al.*, 2012; Elicker *et al.*, 2014
	Thermal desorption remediates soil that has been polluted directly and indirectly by heating, and it separates contaminants depending on the low boiling point of the soil. Two steps are involved in this technology: volatilization of pollutants by		Azhar *et al.*, 2022

Thermal desorption	heating the contaminated soil and gas treatment. *In-situ* thermal desorption is commonly used in soil air extraction to recover gas from the ground. The pollutants volatilize during the thermal desorption stage and are transferred by the carrier gas to the flue gas treatment method. The volatility of the pollutants is a key factor for the thermal treatment. Pollutants that are under treatment are easily volatilized	Soil-soil	
Immobilization techniques	Various forms of immobilization methods for treating heavy metals have been discovered to decrease their concentration in contaminated soil. Soil immobilization involves injecting materials or reagents into contaminated soil to inhibit toxic metals solubility and mobility, avoiding the transfer of hazardous metals to other media as	Soil-soil	Azhar *et al.*, 2022; Tao *et al.*, 2017
	Mixing of the contaminated soil with lime, bitumen or concrete is known as encapsulation. Encapsulation makes the contaminated soil immovable thus	Soil-soil	Azhar *et al.*, 2022; Williams *et al.*, 2000.

Encapsulating technique	hindering the transfer of the contamination to the nearby areas. While making the solid chunks a number of encapsulating materials are available, but cement is proved to be the best one owing to its abundant nature, flexibility and cost-effectiveness.		
Soil washing	Separation and extraction of contaminants from soil	Soil-soil	Teng *et al.*, 2020
Chemical stabilization	Addition of chemical materials or chemical reagents. Chemical stabilization is adding chemical materials or reagents to the soil to deactivate heavy metals by complexation, adsorption processes, precipitation, limiting heavy metal mobility, and bioavailability	Chemical-soil	Teng *et al.*, 2020; Bower *et al.*, 2008; Zhao *et al.*, 2022

1.3 Biochar Introduction

Carbon-rich materials, originally derived from lignocellulose biomass, are defined by the USEPA as a non-fossilized and biodegradable organic material originating from plants, animals and/or micro-organisms that have been subjected to thermal dehydration or carbonation in the presence of little to no oxygen. This carbon rich material, formed by

pyrolysis, is called Biochar (Bc). According to the international biochar initiative (IBI) biochar is produced by thermal decomposition of organic material (biomass such as wood, manure, or leaves) under limited supply of oxygen (O_2), and at relatively low temperatures (<700 °C) (IBI, 2018). During the biochar production phase (pyrolysis) hemicellulose, cellulose, lignin, fat and starch in the biomass are thermally broken down into three major products; biochar (solid fraction), bio-oil (partly condensed volatile matter) and non-condensable gases as shown in Figure 1.2 (Ahmad et al., 2012; Suliman et al., 2016; Oliveira et al., 2017). Basically, for the purpose of sorption of pollutants, biochar can be produced in two main ways: slow pyrolysis and fast pyrolysis. Fast pyrolysis needs a high heating rate of the biomass (10-600 °C s^{-1}) and short residence time, which favours the production of bio-oil around 60-75%, whereas slow pyrolysis requires a slow heating rate (5-10 °C min^{-1}) coupled with a long residence time, which encourages a higher yield of biochar in the range of 30-40% (Dhyani & Bhaskar, 2019).

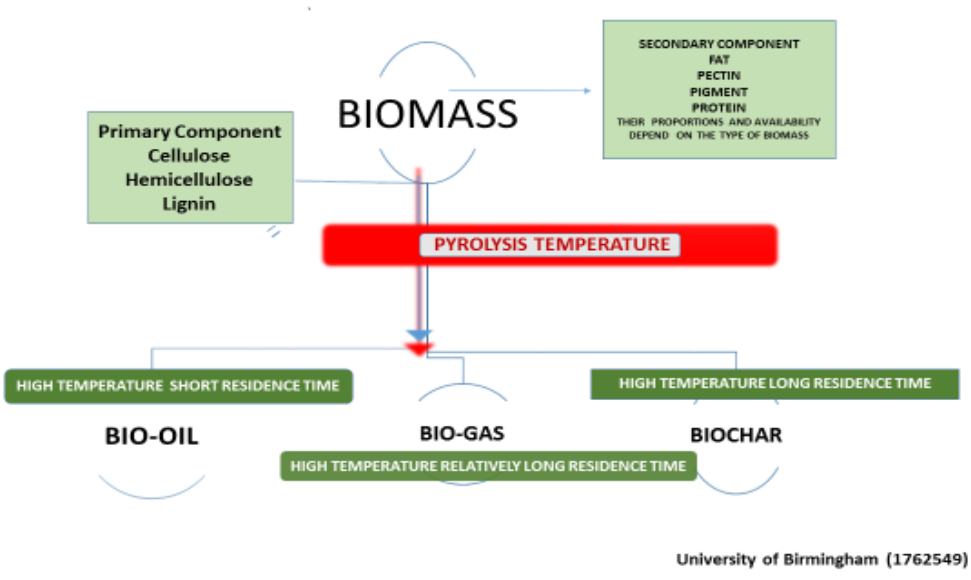


Figure 1.2: Typical Lignocellulosic biomass undergoing thermal degradation in the absence of oxygen, which results in the biomass losing its primary and secondary

components to produce secondary products (bio-oil/gas) leading to the production of a carbon rich solid material (biochar).

Biochar applications have not been restricted to remediation of contaminated soils, as its potentials has been harnessed in (1) Agriculture where it has been use for soil amendment, (2) Carbon sequestration which aims to control the amount of carbon emitted into the atmosphere, and (3) In waste management where biochar is used to treat wastewater and sludge to produce a reasonable discharge or re-useable form of effluent (Liu et al., 2018).

1.4 Primary Constituents of a Typical Lignocellulosic Biomass

1.4.1 Cellulose

Cellulose is the principal constituent of a typical plant cell wall, offering structural support and is equally abundant/present in the cell walls of microorganisms (fungi, bacteria, and algae) (Bajpai, 2016). It can exist in the form of a homopolymer, of beta-$_D$-glucopyranose moieties linked via beta-(1, 4) glucosides bonds with well conformed polymorphs (Den et al., 2018). The extent of cellulose polymerization ranges from 10,000 glucopyranose units in woody biomass to 15,000 in native lignocellulosic biomass. It has been reported that cellulose is stable at carbonization temperatures around 315 °C – 400 °C (Yang et al., 2007a). However, its thermal degradation is not fully understood despite it being the most abundant organic compound on earth (Weber and Quicker, 2018**;** Debiagi et al., 2018;Yang et al., 2007b).

1.4.2 Hemicellulose

Hemicellulose is a relatively abundant (20-50%) lignocellulosic biomass in nature. Its chemical morphology differs from that of cellulose in terms of homogeneity (more homogenous). It has several branches with short chains consisting of different monosaccharide sugars, i.e., pentoses (arabinose, xylose and rhamnose), hexoses (galactose, mannose, and glucose) and uronic acids (4-O methylglucuronic, D-glucuronic and D-galactouronic acids). Hemicellulose differs in composition from one biomass to another, as for example, hemicellulose from agricultural biomass (straw and grasses) is mainly composed of xylan while in biomass from soft wood the hemicellulose is glucomannan. Hemicellulose has the highest thermo-chemical sensitivity amongst all lignocellulosic primary components with thermal degradation at 220 ^{o}C- 315 ^{o}C (Den et al., 2018; Debiagi et al., 2018**;** Bajpai, 2016; Hendriks *et al.*, 2009; Yang et al., 2007b).

1.4.3 Lignin

Lignin polymer is abundant almost everywhere in nature; its complex structural morphology contains inter-woven polymers of phenolic monomers linked together by alkyl-aryl, alkyl-alkyl and aryl-aryl ester bonds. Lignin acts as a glue between biomass components that binds them together, thus making it insoluble in water. Its structural morphology provides a rigid support to plant cell walls, making them inaccessible (and thus resistant to) microbial attack and redox reaction attack (Hendriks and Zeeman, 2009; Bajpai, 2016).

The thermal degradation of lignin lies between 350 and 500 °C depending on the residence time and biomass (Weber & Quicker, 2018). Biomass with a higher proportion of

lignin to other primary components give a higher mass yield because of its high thermal stability (Weber & Quicker, 2018). In general, the composition of lignin depends on the biomass type, with herbaceous plants having the lowest amount of lignin while softwood biomass has the highest (Den *et al.*, 2018; (Bajpai, 2016). From biochar literature, the trend is that the greater the lignin content of a particular biomass the greater the carbon content (which affects the surface area and the pore sizes) of the resulting biochar (Nartey & Zhao, 2014). It is thus important to choose biomass (soft-hard woody) with high lignin content to produce biochar based on its guaranteed high carbon value.

1.5 Biochar Characterization: Key Concepts

1.5.1 Atomic Ratios

Chemical changes prevalent in the structure of a pyrolyzed biomass (biochar) compared to the nonpyritized form are mostly attributed to the detachment of functional groups**.** This applies to all forms of carbonization (biological, geochemical etc.), wherein the loss of functional groups (hydrogen and oxygen containing groups) brings about a decrease in their relative ratio with carbon. Carbonation progression rate can therefore be expressed in terms of atomic ratio. During natural carbonation process oxygen is expelled at twice the rate of hydrogen until hard coal is formed, which in turn is metamorphosed into anthracite characterized by a decrease in the hydrogen to carbon (H/C) ratio with a reduced oxygen content.

For a lignocellulosic biomass, as Figure 1.3 illustrates, an increase in temperature leads to the decrease of H/C and O/C ratios. The O/C ratio decreases at a higher rate than the H/C ratio, compared to the natural rate of carbonization of fossil fuel. It should be noted for raw biomass that the increase in the atomic ratios is constant almost to the point of

high temperature chars. It can be summarized that pyrolysis temperature and the nature of the feedstock to a large extent determines the type of surface functional group and most importantly the atomic ratios, H/C, O/C and N/C, of the resulting biochar. An increase in temperature decreases the atomic ratio (Li et al., 2017a). It should be noted that the temperature range of 250 °C to 350 °C brings about an optimum decrease in atomic ratio in woody biomass which affect the stability of the produced biochar (Weber and Quicker, 2018; Jafri et al., 2018).

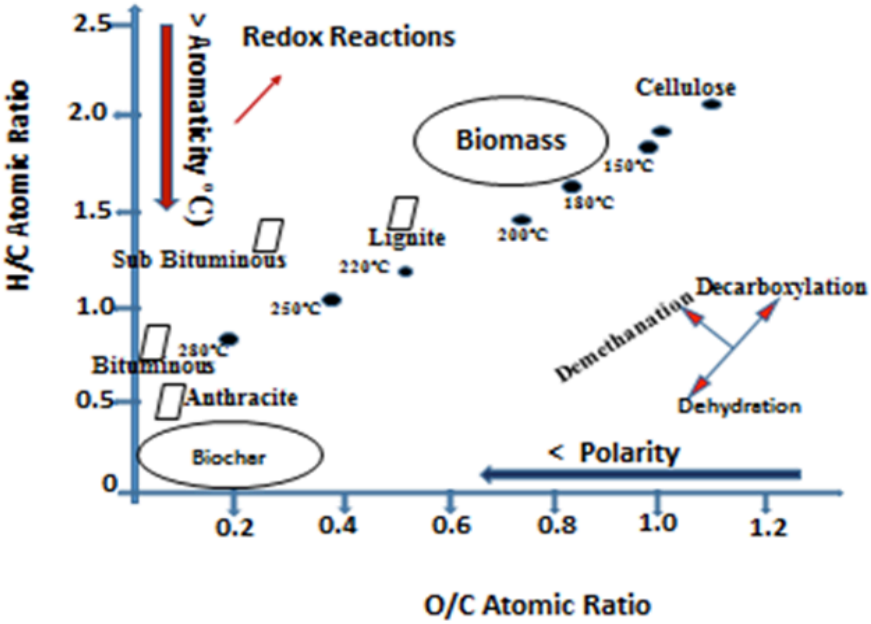


Figure 1.3: Reproduced van Krevelen diagram of natural carbonation of coal and biochar, showing how atomic ratios, aromaticity and polarity reduce with increase in temperature leading to a more stable biochar (Weber et al., 2018; Jafri et al., 2018; Aller, Bakshi et al., 2017;Manyà et al., 2014).

1.5.2 Aromaticity

The aromaticity of a biochar is described by the H/C ratio and the extent of carbon bonds quantitatively to structures (polycyclic aromatic ring). The fixed carbon in the biomass

that remains in the char during the pyrolysis process after devolatilization is called Biochar fixed carbon (BFC). BFC has a direct relationship with biochar aromaticity, and it is highly influenced by pyrolytic temperature as shown in Figure 1.3 (Aller et al, 2017; Manyà et al., 2014).

1.5.3 Temperature

Pyrolysis temperature plays one of the most important roles in converting lignocellulosic biomass into biochar. The aim of carbonization of a raw biomass is to induce an alteration in the chemical composition of the pyrolyzed biochar. All the changes in chemical composition are temperature dependant. An increase in pyrolytic temperature results in an increment in carbon content, surface area and porosity, and a consequent decrease in oxygen, hydrogen and nitrogen contents as seen in Figure 1.4. It is worth noting that the effect of temperature on nitrogen has not been fully understood (Weber and Quicker, 2018; Jafri et al., 2018).

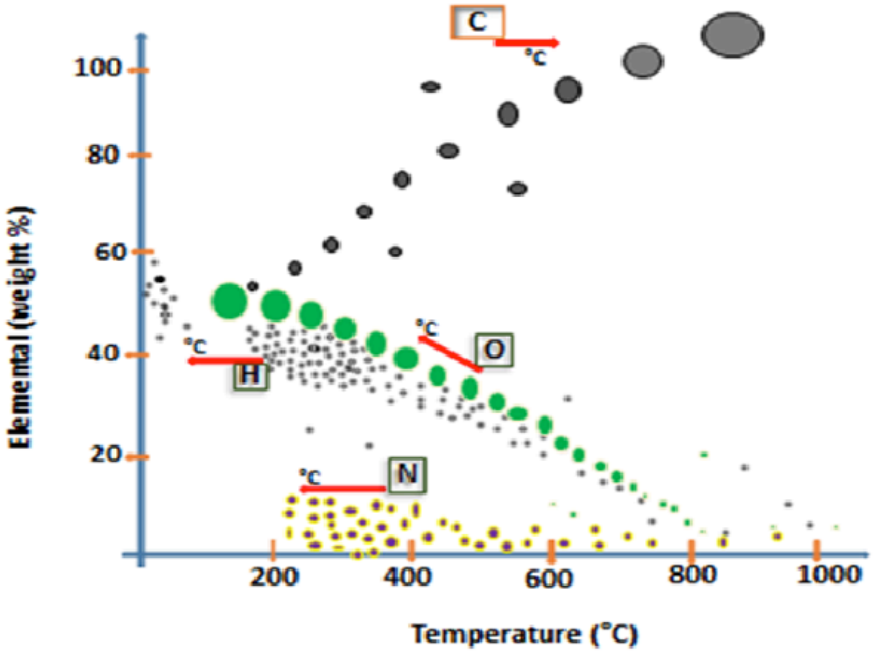


Figure 1.4: Illustration of the increase in Carbon yield (big black circles) as pyrolysis temperature increases, and corresponding reduction in Hydrogen (small black circles), Oxygen (Green-circles) and Nitrogen (yellowish brown circles) (Weber and Quicker, 2018; Jafri *et al.*, 2018). Increasing temperature reduces H, O and N but increases the yield of carbon (thus inducing a high stability).

1.5.4 Surface Area

Surface area contain active sites of biochar which determines the area available for binding of pollutants. Its value is measured in g/m^2, based on the BET (Brunauer, Emment and Teller) model equation, and it comprises of pores (micro–, meso- and macro-pores) which create a platform or interface for interaction between adsorbate (pollutant) and adsorbent (the biochar). This platform or interface is called the active sites for binding of pollutants. Depending on the nature of the feedstock (biomass) and pyrolysis temperature, surface functional groups are actively present at the active sites and may be responsible for the attachment mechanism (complexation) between adsorbate and adsorbent. In the absence of surface functional groups at the active sites, the adsorbate sticks to the negatively charged surface of biochar via a process called precipitation.

The surface area is an important characterization parameter in sorption of contaminants because several observations are drawn form it as to the attachment mechanism (surface or bulk phenomenon), prediction of estimated saturation time (low surface area suggests a short saturation time and vice-visa) and it provides the maximum possible sorption values (large surface area implies great sorption while a small surface area means low sorption) (Debiagi et al., 2018; Weber and Quicker, 2018). At higher pyrolysis

temperature pores are known to collapse and so there is limited active sites for sorption hence activation of the adsorbent might be necessary to increase surface area, for example, through treatment of the biochar with acid or steam treatment.

1.5.5 Functional Groups

Functional groups present on the surface of biochar help in the interaction process between the biochar and the adsorbent in the contaminated medium. These functional group are temperature dependant - they vary with pyrolysis temperature. A biochar produced at 350 °C will differ in surface functional groups from that produced at a pyrolysis temperature of 700 °C, because at a higher temperature biochar tends to gain more stability by losing some volatile matter and moisture content thus increasing the carbon content. The number of exchangeable ions a biochar surface can hold depends on the surface structure containing the functional groups. Biochar produced at relatively low pyrolytic temperatures (400 °C – 600 °C) exhibit the highest cation exchange capacity (Weber & Quicker, 2018).

Pyrolysis temperature and feedstock are key components controlling the amount and types of surface functional group on biochar (H. Li et al., 2017a). Surface functional groups and atomic ratio decrease with increasing pyrolysis temperature (300 °C – 700 °C), unlike surface area, porosity, pH and fixed carbon that increase with increasing pyrolysis temperature. Some of the identified functional groups on the surface of biochar include carboxylic, hydroxyl and amino (–COOH, -OH and R-CH-(NH_2)-COOH respectively), which are responsible for metal adsorption. It should be noted that surface functional groups on biochar vary from one biochar to another depending primarily on

the pyrolytic temperature and the biomass feedstock. The Fourier transform infrared spectroscopy (FTIR) technique is used for surface characterization of functional groups on biochar (H. Li et al., 2017a). It should be noted that these surface functional groups are key amongst other factors (surface area and porosity) for sorption of contaminates.

1.5.6 Zeta Potential

Zeta potential (also known as electro-kinetic potential) is the electric potential at the boundary of the double layer around a particle, or in a very simple terms are the charge a particle assumes when it is in a solution. A particle's zeta potential in dispersion helps predict its long-term stability (resistance to change in particle dispersion) as it provides an estimate of the degree of electrostatic repulsion between the biochar particles. Biochar's zeta potential can be influenced or altered in a medium by the pH, conductivity and ion concentration depending on the specificity of the application. Hence, pH is the key factor that influences zeta potential, and Figure 1.5 explains its role extensively. The range of zeta potential values are within +100 mV to -100 mV and stability is attained at either a very low pH or a high pH especially when the zeta potential value(mv) is with the range of -30 mV and below or +30 mV and above (Tarafdar & Adhikari, 2015).

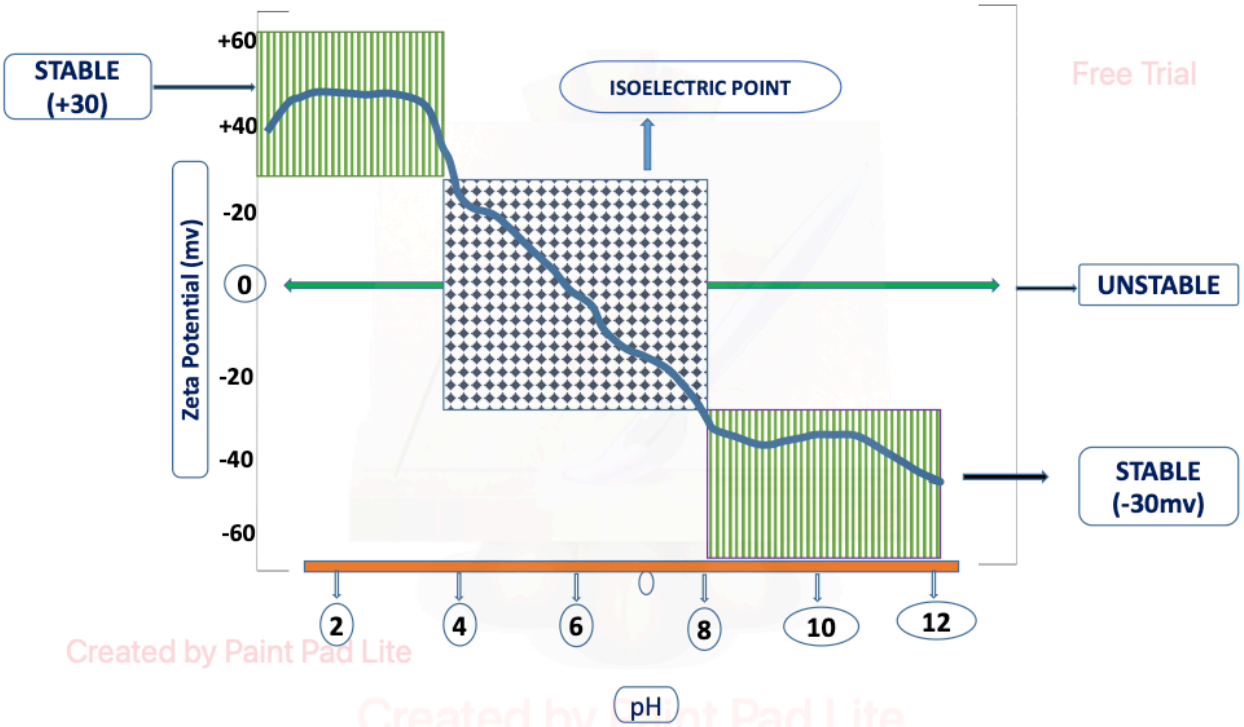


Figure 1.5: Stability of a Particle as a function of its Zeta Potential. The isoelectric point is the point at which the surface has zero charge and is therefore unstable as there are no electrostatic repulsive forces (Tarafdar & Adhikari, 2015).

1.5.7 Pore Volume and Size Distribution

An idea of the total surface area alone might not be sufficient for some applications of biochar. The diverse pore sizes found in biochar are as follows: micropores (0.05 - 0.0001 µm), mesopores (0.05 – 0.002 µm) and macropores (1000-0.05 µm) (Brewer *et al.*, 2014). Their proportion in the biochar contribute to the total surface area and pore volume. The adsorptive efficiency of biochar is dependent on the amount of surface area and most importantly on the diameter of the pores which make up the surface area. This is critical because prior to adsorption, the pore size distribution control the diffusion of pollutants through the pore mouths and channels to access the active sites.

1.5.8 Density and Porosity

Biochar weight and density increase with increasing pyrolysis temperature of carbonation energy, while the reverse is the case for the raw biomass. As gases (volatile mater) are given out during pyrolysis they create a porous vacuum in the biochar. The higher the porosity the lighter the biochar (Weber and Quicker, 2018).

1.6 Biochar and Inorganic Pollutant Removal

The unique features of Biochar, including its large surface area, surface functional groups, pore sizes and pore volume, have made it a potent and widely utilised approach for removal of inorganic contaminants ($Ni^{2+}$and Pb^{2+}) from the environment. The active sites present at the biochar surface, resulting from thermal dehydration, carry both charges (negative) and oxygen containing functional groups (-COOH and -OH) which help to initiate sorption plus are the mechanism responsible for pollution sorption, by providing a medium of interaction between adsorbate and adsorbent(Y. Liu et al., 2022).

Sorption of inorganic contaminants by biochar could be influenced by pH of the solution, biochar alkalinity helps in precipitating inorganic contaminants together (low pH leads to low sorption and vice versa), particle size (larger particle size implies lower number of active sites), absorbent dosage (higher dosage implies higher sorption), and temperature (high temperature increases the rate of reaction) (Barquilha & Braga, 2021; Y. Liu et al., 2022). The interactions observed between inorganic contaminants and biochar active sites are largely correlated with the prevailing adsorption mechanism. Sorption is an important

process in the fate of a contaminant (inorganic) as it diffuses, accumulates, and attaches itself to the active site of an adsorbent (Biochar) (Barquilha & Braga, 2021; Y. Liu et al., 2022). The extent of interaction of the inorganic molecules (contaminants) with active sites on the adsorbent (biochar) defines the nature and type of adsorption (Y. Liu et al., 2022). Basically, three (3) main mechanisms are responsible for adsorption of inorganic contaminants; they are the mechanisms of bonding to the biochar surface, which include physisorption (such as hydrogen-bond and electrostatic-interaction), and chemisorption, resulting in complexation. Physisorption can be explained as adsorption in which the responsible molecular interactions between the adsorbate and adsorbent are primarily van der Waals forces (Y. Liu et al., 2022). Chemisorption involves valence forces whereby adsorption takes place with the aid of a chemical bond (on the active site) between the adsorbate molecule and adsorbent (Y. Liu et al., 2022). It is important to note that physisorption is non-specific in nature and is generally regarded as a weak reversible process controlled by competitive adsorption and desorption at different rates on the active site of adsorbent (biochar).

1.6.1 Precipitation

Precipitation is one of the main mechanisms adopted by biochar for the removal of inorganic contaminants onto its active surface. Biochar as an adsorbent is very alkaline in nature. Thus, its addition into a medium or solution containing inorganic contaminants increases the pH (alkaline) and stimulates a clustering of contaminants which further precipitate together and get attached to the active sites of biochar with the aid of weak van der Waal forces such as hydrogen bonds, electrostatic interactions, and ion exchange (physisorption). Thus, biochar surface area acts as a platform where mineral precipitates

forms (see Figure 1.6) onto the biochar from solution (Y. Liu et al., 2018; Parmar et al., 2021; Reac, 2001).

1.6.2 Surface Complexation

The sorption of metal ions (Ni^{2+} and Pb^{2+}) is a surface phenomenon that involves the formation of complexes on the active sites of the biochar by coordination reaction in which the metal ion behaves like an electron pair acceptor and forms coordinates covalently bound to an electron pair donor (Barquilha et al., 2021; Azhar et al., 2022b). A complex is a molecule (polyatomic) with one or several central atoms ringed by attracted atoms or atomic group (ligands). The central atom exhibits vacant electron orbitals that enables chemical bonding as seen in Figure 1.6 with atoms plus their independent electrons (Chemisorption) (Barquilha et al., 2021). Hydrogen ion (H^+) and others might be released to establish bonds with existing functional groups on the carbonized biochar active site (Barquilha et al., 2021). It should be noted that this sorption mechanism is pH dependant as it involves the giving and receiving of H^+ (Barquilha et al., 2021).

1.6.3 Ion Exchange

Ion exchange is a known physisorption detachment mechanism for inorganic pollutant. It is best explained as a reversible exchange of ions between two phases, solid and liquid. The solid phase refers to the ion exchanger (cation or anion exchangers) which remains undissolved in the exchange medium (Barquilha & Braga, 2021). This physisorption mechanism displays binding preferences for different ions with respect to their chemical

structure and physical properties as shown in Figure 1.6 (H. Li et al., 2017b; A. K. Singh, 2022). In other words, if a receptive Anion A^- or cation X^+ biochar charge is placed in an aqueous medium of B^- and Y^+ ions respectively, an interchangeable reaction (ion exchange sorption mechanism) between A^-B^- and X^+Y^+ is likely to occur (Barquilha & Braga, 2021).

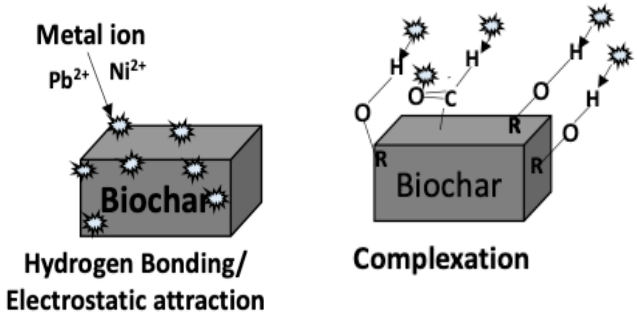


Figure 1.6: Schematic illustration of the two potential Biochar sorption mechanisms responsible for the removal of inorganic contaminants (Pb^{2+} and Ni^{2+}) from the environment to the active sites of the biomass-derived biochar.

1.7 Introduction to Adsorption

Sorption is the umbrella term that accommodates both absorption (absorbent material acts like a sponge thus the internal morphological structure of the sorbent is responsible for the sorption) and adsorption (wherein the surface morphological structure is responsible for sorption). Adsorption is the movement of substances from a fluid state (gas or liquid) to a solid interface, where it gets attached by physical and/or chemical interactions (Rajendran et al., 2022a). It is a mechanism where molecules move out of the solution

and, thereby get attached to the surface of the chemical through physical and chemical bonding (Petrovic et al., 2021).

Adsorption differs from absorption in that adsorption is based on surface whereas, absorption is based on volume. As the term "sorption' is used for both absorption and adsorption whereas desorption refers to the opposite of adsorption as displayed in Figure 2.0. Adsorption is thus a surface process where pollutants, mostly inorganic (e.g., heavy metals such as Pb^{2+} and Ni^{2+}) ions aqueous solution, transfer onto the active site of the solid adsorbent (J. Wang & Zhuang, 2018). The solids used to adsorb gases or dissolved substances are called adsorbents while the adsorbed molecules are usually referred to collectively as the adsorbate.

Adsorption is widely used in the environmental sector for pollution control and for, water and wastewater treatment (Guo and Wang, 2019). To understand the significance of adsorption in environmental applications, it is necessary to study the kinetics associated with the adsorption, which can be used to predict the pollutant removal rate, to establish the time dependence of the residual adsorbate in solution, and to reveal the mechanisms involved in the adsorption process (Zhuang *et al.,* 2021).

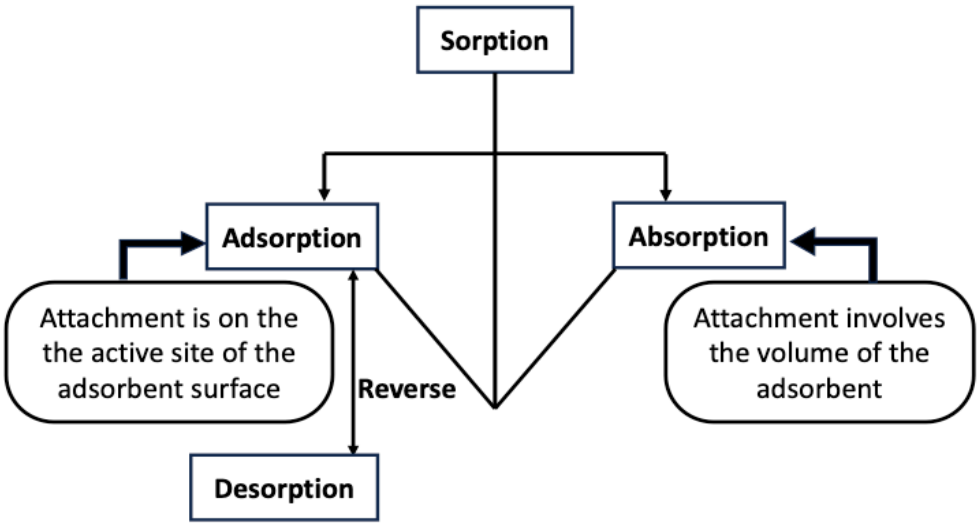


Figure 1.7: Schematic illustration of the classification of sorption phenomena into Adsorption and Absorption focusing on their modes of contaminants attachment as a key factor that differentiates them from one another.

Adsorption is mainly a consequence of surface energy interactions on the active site between the adsorbate and the adsorbent i.e., the mass transport of substances from either the gas or liquid state to a solid interface, whereupon the adsorbate gets attached by physical and/or chemical interactions to the adsorbent (Kalam et al., 2021).

The mechanism involves molecules moving out of the solution and, thereafter getting attached to the surface of the solid through physical and chemical bonding (Kalam et al., 2021). In a bulk material, bonding modes such as ionic, covalent or metallic are important for sorption process (Adigun et al, 2019; Liu et al., 2020). However, atoms on the surface, experience a bond deficiency, because they are not wholly surrounded by other atoms (Liu et al., 2020). Thus, it is energetically favourable for them to undergo bonding with available atoms from their surroundings (Liu et al., 2020). The exact nature of the bonding depends on the nature of the surface functional group species involved as adsorption is

either physisorption (physical adsorption) or chemisorption (chemical adsorption) (Sahmoune, 2019; Shrestha et al., 2021a)). Adsorption may also occur due to electrostatic attraction of oppositely charged entities ((Jawed et al., 2020; Krasucka et al., 2021; X. Li et al., 2020; Yi, Huang, et al., 2019).The nature of adsorption is dependent on the strengths of the interaction between the adsorbent and adsorbate (Sahmoune, 2019; Shrestha et al., 2021a).

In physisorption, the adsorbate is bound to the surface only through weak intermolecular van der Waals forces and is a reversible phenomenon, while in chemisorption a molecule binds or adheres to a surface through the formation of a covalent bond (Atif et al., 2022a; Mei et al., 2022). Chemisorption is thus an irreversible phenomenon, because it involves the formation of new chemical bonds at the adsorbent contact surface (active site) between the adsorbate and adsorbent (Krasucka et al., 2021). Furthermore, while chemisorption is essential for heterogeneous surface reactions, physisorption plays a major role during separation and enrichment processes at and near phase boundaries at the surface (Masebinu et al., 2019).

1.7.1 Adsorption Process

In recent times, adsorption has emerged as a reliable and innovative process for remediating/ long-term removal of contaminants (such as heavy metals) because of its effectiveness and efficiency in application plus its low cost makes it a viable economic approach (Atif et al., 2022b; Shrestha et al., 2021b). Adsorption is a widely used process today due to its flexibility in design and simplicity in operation and application (Chai et al., 2021;Wang and Zhuang, 2018). However, its primary application is for removing or capturing inorganic materials (e.g., heavy metals) that are present at reasonably low

concentrations. This singular adsorption feature enhances the application of adsorption as a universal practical treatment process (Shrestha et al., 2021a; L. Wang et al., 2019a).

The effectiveness of the adsorption process is mainly influenced by the nature of the solution in which the contaminants are dispersed, the molecular size and the polarity of the contaminant and the type of adsorbent (physiochemical properties) used (Krasucka et al., 2021; Rápó and Tonk, 2017a). Adsorptions occur due to the attractive interactions between a surface charges and functional groups and the species being adsorbed at the molecular level (Anastopoulos et al., 2019). The sorption process can be influenced by temperature, such that high physical adsorption occurs at a temperature close to the critical temperature of a given gas while chemical adsorption occurs at temperatures much higher than the critical temperature (Largitte & Pasquier, 2016). Under certain conditions, both processes (physisorption and chemisorption) can occur simultaneously or alternately.

1.7.2 Adsorption Mechanism and Equilibrium

Adsorption as a surface phenomenon has eluded the establishment of a specific mechanism responsible for attachment, however possible attachment mechanisms co-existing between the adsorbent surface (active site) and adsorbate (heavy metal ions) can be described with the use of adsorption isotherms, kinetics, and thermodynamics (T. Ahmad & Danish, 2022; Iftekhar et al., 2018; Nur et al., 2013). The adsorption models in single and binary component systems were extensively studied by several researchers (e.g., Atif et al., 2022;Azouaou et al., 2010). Nonetheless, adsorption isotherms describe the mechanism of adsorption as a function of the adsorbate and adsorbent concentrations. It

is important to analyse both the isotherm and kinetics data because they help to parameterise the equations developed to describe the results ratio of the adsorbent at a fixed temperature (Zhou et al., 2016; Saha et al., 2010). As a result, understanding adsorption kinetics is of great important in optimising the treatment of aqueous effluents as it provides valuable information on the reaction pathways and possibly reveals the responsible mechanism of adsorption and the reactions (Ai et al., 2019; Arampatzidou & Deliyanni, 2016).

The developed adsorption equation helps in the design and optimization of the process parameters. The frequently used isotherms for liquid/solid phase systems are the Langmuir and Freundlich Isotherms, while Pseudo first and second order kinetics equation are used to describe adsorption kinetics (Oninla et al., 2018; K. L. Tan & Hameed, 2017; L. Wang et al., 2019a). One reasons behind their widespread use is linked to their simplicity in terms of data acquisition and interpretation (Adebayo *et al.,* 2014).

The thermodynamics of metal ion sorption to a solid (such as biochar) can be explained based on thermodynamic parameters such as free energy (G°), enthalpy (H°) and entropy changes (S°) based on the endothermal and exothermal sorption processes(Aljeboree et al., 2017; Chang et al., 2016).

The goal of an adsorption system is the determination of the final amount of solute attached onto the active surface of the sorbent per unit of surface area, and the residual amount of the solute left in the liquid phase (Chang et al., 2016; Ghorbel-Abid & Trabelsi-Ayadi, 2015; Revellame et al., 2020). As sorption proceeds, desorption of solute from the active sites back into the liquid phase in parallel to adsorption, depending on the nature of the sorption process (Bujdák, 2020). When this happens, a steady state is reached whereby saturation (active sites filled up) takes place (equal amounts of solute adsorb and desorb simultaneously), then the system is said to be in an equilibrium state (Rajendran

et al., 2022b). Adsorption equilibrium primarily relates to the physiochemical statistics for evaluating the process parameters of the adsorption process for a specific adsorbent-adsorbate system in operation under predetermined reaction conditions (Rajendran et al., 2022b; Chang, Lai and Lee, 2016).

Adsorption of a solute from an aqueous phase (active site) proceeds by an adsorption isotherm, with specific kinetics, and thermodynamics investigation to evaluate events/activities occurring on the surface of the adsorbate (Anastopoulos et al., 2019). Eventually at equilibrium, there is no further adsorption as the active sites have been fully saturated. This distribution is depicted as the amount of solute or sorbate adsorbed per unit weight of adsorbent and is denoted by qe (mg/g). The remaining adsorbate left in the solution phase, or which failed to attach itself onto the surface of the sorbent is the residual equilibrium concentration and is denoted by Ce (mg/L) (Sahmoune, 2019).

1.7.3 Role of Time: Adsorption Kinetics

The kinetics quantifies the rate of adsorption (of the inorganic contaminants) with respect to time at a constant pressure and concentration (of both adsorbant and adsorbent) and is expected to determine the diffusion of adsorbate in the pores of the adsorbent (K. L. Tan & Hameed, 2017; Tong, McNamara, et al., 2019). It can be interpreted as the rate of adsorption and desorption, integrated with mathematical models that describe this behaviour (Akpomie et al., 2015; Rápó & Tonk, 2017b). Adsorption kinetics models are categorized into adsorption reaction models and adsorption diffusion models (Silva et al., 2021a). The adsorption reaction models are based on chemical reaction kinetic models and take the entire adsorption process as a whole and do not consider the different steps involved while the adsorption diffusion models are dependent on three different steps occurring during the adsorption process (Silva et al., 2021a; L. Wang et al., 2019a). The

three steps are the external or film diffusion, internal or intraparticle diffusion and mass action. The external diffusion is defined as the diffusion taking place across the fluid film surrounding the adsorbent particle, while the internal or intraparticle diffusion defines the diffusion taking place from the particle surface to the pellet interior via the pore openings and channels (Rees, 2014; Inglezakis, Fyrillas and Park, 2019; Silva et al., 2021b). Lastly, the mass action generally describes the adsorption and desorption occurring between the active sites and the adsorbate in aqueous solutions (Y. Zhang et al., 2019).

1.7.4 Pseudo-First-Order Kinetics Model (PFO)

The PFO process involves a rate-limiting step, the mechanism involves diffusion process, and the reaction rate does not depend on the concentrations of both reactants but only on the concentration of the adsorbate for a single adsorbate system, hence the kinetic model is controlled by physisorption (Largitte and Pasquier, 2016;Tan and Hameed, 2017). Therefore, when kinetics follows Lagergren pseudo–first-order rate equation, then it can be concluded that such adsorption occurs through diffusion at the interface which is best known as physisorption.

The Lagergren pseudo–first-order model can be described by the following linear form presented in Equation 1.0.

$$\frac{dq_t}{dt} = k_1(q_e - q_t) \qquad (1.0)$$

Integrating q=0 at t=0 and q=qt at t=t, yields (Equation 2.0)

$$\log(q_e - q_t) = \log q_e - \left(\frac{K_1}{2.303}\right) t \qquad (1.1)$$

The initial rate of sorption, h is determined by the following equation:

$$h = k_1 q_e^2 \qquad (1.3)$$

For an adsorption process that fits first-order kinetics, the intercept of log ($q_e - q_t$) versus t plot would be equal to the log of the experimentally determined value for q_e or adjusted to fit the experimental value where q_e and q_t are the amounts of adsorbate adsorbed (mg/g) at equilibrium and at time t (minute) respectively, h (mg/g-min) is the initial rate of sorption and k_1 (l/min.) is the adsorption rate constant.

1.7.5 Pseudo-Second-Order Kinetics Model

The pseudo–second-order kinetics model works on the assumption that the rate-limiting step is chemical sorption or chemisorption and helps to predict the behaviour over the whole range of adsorption. It is assumed that adsorption rate is dependent on adsorption capacity not on concentration of adsorbate (Revellame et al., 2020). One major advantage of this model over the Lagergren first order model is that the equilibrium adsorption capacity can be calculated from the model; therefore, there is theoretically no need to evaluate adsorption equilibrium capacity from experiment (Bujdák, 2020;Aljeboree, et al., 2017).

The pseudo-second-order equation based on equilibrium adsorption is expressed as shown in Equation 1.4 (Kushwaha et al., 2013; Revellame et al., 2020; Tong, McNamara, et al., 2019)

$$\frac{dq_t}{dt} = k_2(q_e - q_t)^2 \quad (1.4)$$

Separating the variables in Equation 1.4 gives the following Equation of 1.5.

$$\frac{dq_t}{(q_e - q_t)^2} = k_2 dt \quad (1.5)$$

Integrating Equation (1.5) with respect to boundary conditions q=0 at t=0 and q=qt, at t=t, yields Equation (1.6)

$$\frac{t}{q_t} = \left(\frac{1}{q_e}\right) t + \left(\frac{1}{k_2 q_e^2}\right) \quad (1.6)$$

$$h = k_2 q_e^2 \quad (1.7)$$

where, k_2 (g/mg h) is the rate constant of second-order adsorption and h (mg/g- min) is the initial rate of sorption. The linear plot of, versus t gives as the slope and as the intercept.

1.7.6 Elovich Equation

The Elovich kinetic model interpret the second-order kinetics assuming that the surface is energetically heterogeneous (Largitte & Pasquier, 2016). The Elovich equation is one of the most frequently used models for describing chemisorption t and is given in Equation 1.8 (Ozacar and Sengil, 2005).

$$\frac{dq_t}{dt} = \alpha e^{-\beta q_t} \quad (1.8)$$

where, a (mg/g h) is the initial sorption rate and b (g/mg) is related to the extent of surface coverage and activation energy for chemisorption.

The integration of the rate equation with the same boundary conditions as the pseudo first- and second-order equations gives the Elovich Equation 1.9.

$$q_t = \frac{1}{\beta} In(\alpha\beta) + \frac{1}{\beta} In\ t \quad (1.9)$$

The parameters (1/β) and (1/β) ln ($\alpha\beta$) can be obtained respectively from the slope and intercept of the linear plots of q_t versus *lnt*. The value of (1/β) is indicative of the number of sites available for adsorption while the (l/β) ln ($\alpha\beta$) is the adsorption quantity when *lnt* is equal to 0, i.e., the adsorption quantity when time t is 1. This value clarifies the adsorption behaviour of the first step (Inglezakis et al., 2019; Kushwaha et al., 2013; Tong, McNamara, et al., 2019; Wu and Tseng, 2006).

1.7.7 Intraparticle Diffusion Model

This model interprets the diffusion of absorbates involving the interior structures of the adsorbent. The experimental data is explained with the intra-particle diffusion equation to give answers and evaluate the role of diffusion as a rate controlling step in the sorption process (Silva et al., 2021a ;Rees, 2014). It is envisaged that sorption varies almost proportionally with the square root of time, rather than with the contact time t. Based on the theory proposed, the intraparticle diffusion model is defined by Equation 1.10 (Kushwaha et al., 2013):

$$q_t = k_1 t^{0.5} + C \qquad (1.10)$$

where, K_{id} (mg/g h) is, the intraparticle diffusion rate constant, and is obtained from the slope of the straight line of q_t versus, C gives an idea about the thickness of the boundary layer, i.e., the larger the intercept, the greater the boundary layer effect (Aljeboree et al., 2017). If intraparticle diffusion occurs, then q_t, versus will be linear. If the linear plot passes through the origin, then the rate limiting process is controlled by the intraparticle diffusion that is particle diffusion is involved in the rate controlling step. Previous researchers showed that the plot of q_t versus represents multi-linearity, which characterizes the two or more steps involved in the adsorption process (X. Liu & Lee, 2014).

1.7.8 Role of Absorbant /Adsorbate Concentration: Adsorption Isotherms

Adsorption isotherms are used to interpret the relationship between the amount adsorbed and the concentration. Adsorption equilibrium data are plotted in the form of an adsorption isotherm with the mass adsorbed on the y-axis and the mass remaining in the

fluid on the x-axis, at constant temperature (Rahmani et al., 2010; J. Wang et al., 2020). Adsorption isotherms are mathematical models that describe the distribution of the adsorbate species between the liquid and solid phases, based on a set of assumptions that are related to the heterogeneity/homogeneity of the solid surface, the type of coverage, and the possibility of interaction between the adsorbate specie (Wang et al., 2020; Shrestha et al., 2021). Additionally, adsorption isotherm helps in the understanding of attachment of adsorbate (fluid state) and adsorbate attached to the surface of the adsorbent at reaction equilibrium (constant temperature).

1.7.9 Langmuir Isotherm

This isotherm assumes that adsorbates are chemically adsorbed at a fixed number of active sites on the absorbent, that a monolayer of the adsorbate is formed over the surface of the adsorbent when it gets saturated, that each site can hold only one adsorbate species, that all sites are energetically equivalent, and that interactions between the adsorbate species do not exist (Jalees et al., 2019; Anastopoulos et al., 2019). The Langmuir model (Langmuir, 1918) is expressed as shown in Equation 1.11.

$$q_e = \frac{q_m K_L C_e}{1+K_L C_e} \tag{1.11}$$

Where the linear form of Langmuir isotherm is given by Equation 1.12.

$$\frac{C_e}{q_e} = \frac{1}{q_m} C_e + \frac{1}{K_L q_m} \tag{1.12}$$

where C_e is the equilibrium concentration of the adsorbate (mg/L), q_e is the amount of adsorbate adsorbed per unit mass of adsorbent (mg/g), qmax, (mg/g) and K_L (L/mg) are Langmuir constants related to maximum monolayer adsorption capacity and

rate of adsorption, respectively (Kushwaha et al., 2013). When C_e/q_e is plotted against C_e, a straight line with slope of $1/q_{max}\,K_L$ and intercept of $1/q_{max}K_L$ is determined.

This isotherm predicts that intermolecular forces decrease rapidly with the distance and consequently forecast the subsistence of monolayer of adsorbate at the outer surface of the adsorbent. It is implicit in this model that once the adsorbate attaches itself onto the site, no additional sorption can take place at that site (Y. Zhang et al., 2019).

1.7.10 Freundlich Isotherm

The Freundlich isotherm model is an exponential equation and assumes that the concentration of adsorbate on the adsorbent surface increases with any increase in the adsorbate concentration in solution. Theoretically, using this expression, an infinite amount of adsorption will occur (Ghorbel-Abid & Trabelsi-Ayadi, 2015). Similarly, the model assumes that the adsorption could occur via multiple layers instead of a single layer (Sahmoune, 2019). The equation has a wide application in describing the adsorption behaviour of heterogeneous systems (Ghorbel-Abid & Trabelsi-Ayadi, 2015).

The Freundlich isotherm is expressed as shown in Equation 1.13.

$$q_e = K_F C_e^{\frac{1}{n}} \qquad (1.13)$$

While the more well-known logarithmic form of Freundlich isotherm is given by the equation 1.14.

$$Inq_e = InK_F + \left(\frac{1}{n}\right) \qquad (1.14)$$

where C_e (mg/L) denotes the equilibrium concentration of the adsorbate, q_e (mg/g) is the amount of adsorbate adsorbed per unit mass of adsorbent, K_F and n are Freundlich constants with n giving an indication of how favourable the adsorption process is, and K_F

(mg/g (L/mg)) can be defined as the adsorption or distribution coefficient and represents the quantity of adsorbate adsorbed onto the adsorbent for a unit equilibrium concentration. The slope is the surface heterogeneity factor ranging between 0 and 1 and is a measure of adsorption intensity or surface heterogeneity, becoming more heterogeneous as its value gets closer to zero (Wang and Guo, 2020 ; Jalees et al., 2019). Steep slope that is value of close to 1 reflects high sorption capacity at high equilibrium concentration which diminishes rapidly at lower equilibrium concentration.

A flat slope with << 1 represents that the sorption capacity is slightly reduced at lower equilibrium concentration. A value for below one designates a normal Langmuir isotherm while above one reflects cooperative adsorption (J. Wang & Guo, 2020). The plot of log q_e versus log C_e gives a straight line with slope of and intercept of lnK_F.

1.7.11 Temkin Isotherm

The Temkin isotherm is based on a factor that describes the adsorbent- adsorbate interactions and which assumes that the heat of adsorption of all the molecules in the layer would decrease linearly with coverage (Akpomie, Dawodu and Adebowale, 2015; Raghav and Kumar, 2018; Jalees et al., 2019; Matouq et al., 2015). The adsorption is characterized by a standard distribution of binding energies, up to some maximum binding energy (Matouq et al., 2015). Equation 1.15 represents the Temkin model.

$$q_e = \left(\frac{RT}{b}\right) In(K_T C_e) \qquad (1.15)$$

The linear form of Temkin Isotherm is given by equation 1.16.

$$q_e = BInK_T + BInC_e \qquad (1.16)$$

where, K_T(L/g) and B are the Temkin isotherm constants. Whereas B is given by Equation 1.17.

$$B = \frac{RT}{b} \quad (1.17)$$

with R stands for gas constant (8.314 J/mol K), T the absolute temperature (K) and RT/b=B. Hence, a plot of q_e versus C_e yields a line with B as the slope and B (ln K_T) as the intercept.

1.8 Biochar and Pyrolysis Temperature Classification

The goal when applying biochar for pollution remediation is to attain optimum adsorption efficiency. Many authors have characterized biochar efficiency based on proximate and ultimate analysis. For example, (Mašek et al. 2018) performed proximate analysis of some standard biomass material with different pyrolysis instruments (fixed bed, screw reactor and rotary kiln) using their thermal history as a reference point. This characterization approach was deficient in itemizing and grouping each biochar properties to a nomenclature for a specific application(s).

Environmental application of biochar e.g., for remediation depends on its functional characteristics which are largely influenced by the most important pyrolysis component such as temperature. This is because pyrolysis temperature (along with residence time and feedstock) plays the most important role in biomass carbonization. Conversely, residence time and feedstock are equally significant, but their significance depends on the biomass treatment temperature. The pyrolysis temperature can be used to predict the optimum efficiency that a specific biochar application will attain. Based on the influence of pyrolysis temperature on optimum sorption capacity and target pollutant removal in

environmental applications, biochar can be classified as (1) hydrophilic biochar and (2) hydrophobic biochar as shown in Figure 1.8.

1.8.1 Hydrophilic Biochar

As the name implies Hydrophilic means substances or materials that have a high affinity for water. Hydrophilic biochars are those produced at pyrolysis temperature between 250 ^{o}C and 450 ^{o}C and are very efficient in the sorption of inorganic contaminants. These carbonated materials have the following properties: high surface functional group, stable zeta potential (surface charge), high volatile matter content, reasonable surface area, low atomic ratio (H/C and O/C), low aromaticity and low stability (see Figure 1.8).

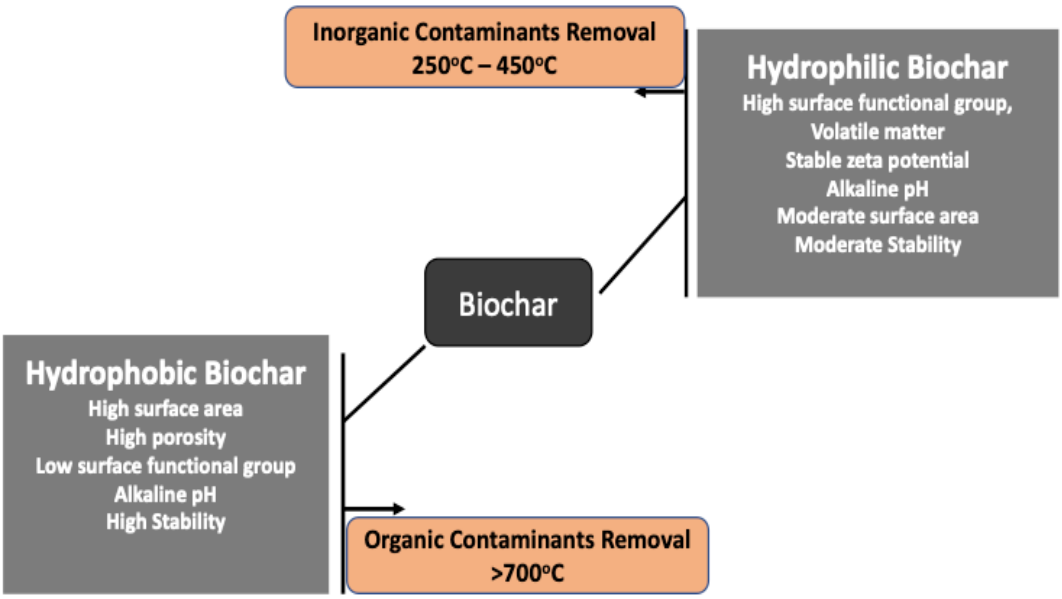


Figure 1.8: Schematic illustration of Temperature Based Characterization of Biochar for removal of contaminants based on the biochar fluid content, surface area, stability, pH and surface functional groups and categorisation into hydrophobic versus hydrophilic Biochar.

1.8.2 Hydrophobic Biochar

Hydrophobic biochar is highly carbonated biochar that has a relatively high resistance to water due to the high carbon content. It is produced through pyrolyzed biomass at >700^{o}C and is distinguished by its pure carbon content. Thus, hydrophobic biochar can serve as an economical approach for soil amendment, carbon sequestration for greenhouse gases, and removal of organic contaminants from soil. Hydrophobic biochar has the following properties: (a) high surface area, high aromaticity, lower atomic ratio, and high stability; and (b) relatively low surface functional group, high alkalinity, stable zeta potential and low volatile matter (Figure 1.8).

1.9 Adsorption Mechanisms of representative environmental pollutants

Pollutants introduced into the environment by anthropogenic means range in size and concentration, and the scale and duration of their effects in the environment depends on their persistence and the effectiveness of the remediation approach taken towards them (Zhu et al., 2017). Recently effort has been made towards optimization of methods for removal of series of targeted organic pollutants from the soil such, including antibiotics/ drugs (e.g., ibuprofen, tramadol, tylosine, sulfamethazine, famethoxazole, tetracycline etc.), agricultural chemicals (herbicides, insecticides, pesticides, fungicides) and industrial chemicals (petroleum, polyromantic hydrocarbon (PAHs), volatile organic gases (VOCs)) (Sharma, 2018;Chen et al., 2018; Zhang et al., 2013; Zhen et al., 2018; Cao *et al.* 2011; Zhou et al., 2013; Inyang and Dickenson, 2015;Mondal et al., 2016; Jung, Oh and Yoon, 2015;Xu et al., 2011). Inorganic (e.g., heavy metals) and organic (such as hydrocarbons, especially aliphatic and poly-aromatic hydrocarbons) pollutants are ubiquitous in the environment and have severe health effects (Zhang et al., 2014). These

contaminants pose a significant risk to public health and the environment. The USEPA, have prioritized 16 high concentration PAHs and several inorganic pollutants (including $Zn^{2+}Hg^{2+}$ $Ni^{2+}Pb^{2+}Cd^{2+}$ and Cu^{2+}) that have high toxicity and carcinogenic potentials (USEPA, 2000; Zhang et al., 2013; Uchimiya et al., 2011a; Uchimiya et al., 2011b). In recent times many authors have tried to monitor and understand the mechanism associated with adsorption of PAHs (as representative organic molecules) and heavy metals to biochar. PAHs exhibit high hydrophobicity and low solubility in water making absorption onto soil grains and hydrophobic biochar easy and degradation in soil difficult (Ping et al., 2007).

Biochar adsorptive abilities rely on its physiochemical properties, which can be manipulated, largely through the choice of pyrolysis temperature, to achieve high efficacy in application (Rajapaksha et al., 2016). For inorganic pollutants (e.g., heavy metal) removal, biochar pyrolyzed between 250 ^{o}C and 450 ^{o}C for 4 hrs is suitable, although this might vary a little based on biochar feedstock (Lam et al., 2018). Whereas for soil amendment, removal of organic contaminants (PAHs) and carbon sequestration (greenhouse gases) biochar derived from high lignin biomass and pyrolyzed at high temperature (>700 ^{o}C for 6 hrs) and thus forming a hydrophobic biochar is suitable as shown in Table 2.0 (Wang et al., 2018;Pace et al., 2018).

The choice of Pyrolysis temperature is thus dependant on the specific application of biochar (Figure 1.8) which, in-turn, affects biochar properties such as surface area, and the functional groups that are responsible for various adsorption mechanism see Figure 1.9. Biochar adsorption mechanism(s) are influenced or determined based on its physiochemical properties, including the amount of Volatile matter, moisture, fixed carbon content, elemental composition, and the amount and nature of the Functional groups. The nature of feedstock and residence time may play a secondary role in biochar

physiochemical properties. Its prerogative to know the Adsorption mechanism associated with organic and inorganic contaminates.

1.9.1 Organic Pollutants

Sorption of organic contaminants in the environment to the active sites of an adsorbent is influenced by the surface properties of the active sites, and the contaminants properties. For example, opposite charges attract (positive and negative) like charges repel, and hydrophobic contaminants seeks out hydrophobic surfaces to bind to (Jin et al., 2018; Tang et al., 2018; Tong, Mcnamara, et al., 2019). Sorption of organic pollutants by biochar is simply by chemical interaction mechanism (Oliveira et al., 2017). Primarily, sorption of degradable contaminants is by chemi-sorption (e.g., H-bonding, and redox-reaction) with active surface functional group (COOH, OH and R-OH)(Ahmad et al., 2014;Teixidó et al., 2011; Oliveira et al., 2017;Xie et al., 2015).

Moreover, degradation of organic pollutant by biochar maybe driven by polarity reduction (high aromaticity) and degradation stimulated by microorganisms present on the surface and in the pores of biochar (Kong et al., 2018; Oliveira et al., 2017; Ahmad et al., 2014; Xu, Cao and Zhao, 2013;Kong et al., 2011). For example, (L. Kong et al., 2018) attempted a study on the adsorptive mechanism of biochar (biomass from sawdust and wheat straw at 300 ^{o}C and 500 ^{o}C) on poly-aromatic hydrocarbon (PAH) for a period of 84 days. They concluded that instead of biochar adsorbing PAHs in the soil, rather it acted as a bio-stimulator for PAHs degrading bacteria for remediation (this might be because pyrolysis temperature was below 700 ^{o}C). In 2019, (Bao et al., 2019) reaffirms the same observation when the attempted remediating a PAHs contaminated soil with combined amendments (compost, mushroom residue, and corn straw) with biochar over

a 77-day period. Organic pollutant (e.g., antibiotics PAHs, and dye) removal by biochar can be obtained by chemisorption with the aid of surface functional group present on the active site of the absorbent. Notwithstanding, adsorption via chemisorption of organic pollutant is influenced by biochar dose, initial solution pH, reaction temperature, contact time, anion present, and initial pollutant concentration (L. Kong et al., 2018; Oliveira et al., 2017). The chemical interaction that pre-decides adsorption/removal of contaminants by biochar can be seen in Figure 1.9.

1.9.2 Inorganic Pollutants

Removal of inorganic pollutant from soil mainly driven by interactions with biochar surface has to do with biochar surface functional group via ion exchange and formation of complexes with active surface group, such as -OH, -COOH, R-OH, as shown schematically in Figure 1.9 (Harris, 2009; Lu et al., 2012). (Mahdi et al., 2018a) observed the effect of pyrolysis temperature (350 ^{o}C - 550 ^{o}C) on adsorption of copper and nickel ions by lignocellulose date-seed derived biochar; maximum sorption was at 550 ^{o}C at pH 6.0 with values of Cu^{2+} and Ni^{2+} adsorption of 0.421 and 0.333mmolg^{-1} respectively. The adsorption occurred mainly due to ion exchange mechanism and, complexation with surface functional groups (carboxyl and hydroxyl) equally contributed to adsorption (Zhou et al.) experimentally examined the effect of pyrolysis temperatures (300 ^{o}C – 600 ^{o}C) and pH (2.0 - 8.0) on the adsorption of chromium (IV) onto *Ramie* (crop biomass) biochar. The Cr (IV) sorption was fully pH dependant, at lower pyrolysis temperature (low aromaticity and high surface functional group content).

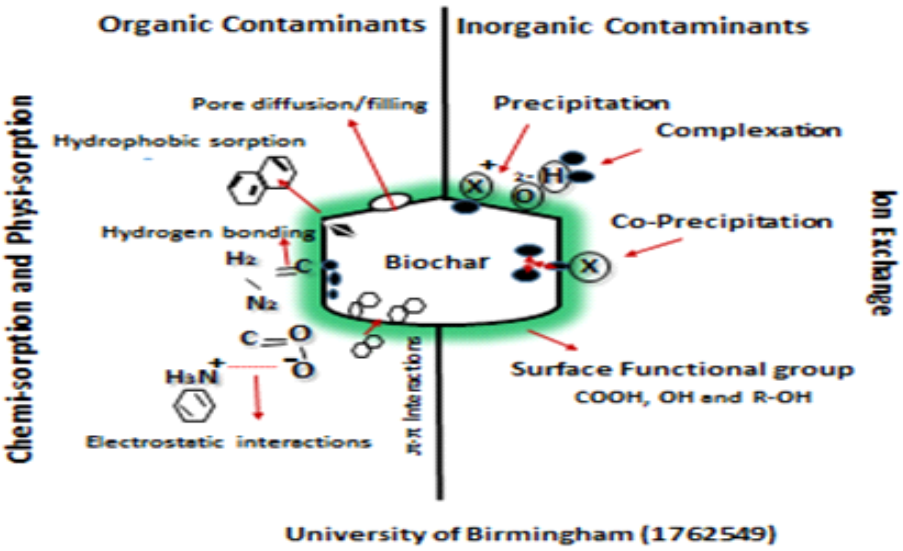


Figure 1.9: Adsorption mechanisms for organic and inorganic pollutants removal showing sorption mechanisms as they relate to surface active groups or the entire bulk of the adsorbent (Oliveira et al., 2017; Harris, 2009; Lu et al., 2012; Ahmad et al., 2014; Teixidó et al., 2011; Oliveira et al., 2017; Xie et al., 2015).

1.10 Functionalization of Biochar

The representative of heavy metal pollution studied in this thesis are lead (Pb) and nickel (Ni), which has attracted a lot of attention due to its impacts on aquatic life, agricultural production, soil fertility and human health (Zong et al., 2021). The concerns regarding these Ni^{2+} and Pb^{2+} pollutants are based on their persistence in the environment, their toxicity, and their bioaccumulation tendencies (Khan et al., 2020), as discussed in Section 1.1. Various carbon-based biomass sources (agricultural waste, woodchips, wastewater sludge) have been used as adsorbents for remediation of heavy metals, based on the biomass stability, range of surface functional groups and the high surface area that can be achieved via thermal degradation in an inert environment which commonly called pyrolysis (Sizmur et al., 2017). Notably, pyrolysis temperature plays a vital role in the

chemical and physical characteristic of the produced biochar (H. Li et al., 2017a). Modification of the physiochemical properties of biochar to achieve a specific goal (increasing sorption active sites, possibly introducing a new sorption mechanism and increase maximum adsorption capacity) can be achieved through different techniques depending on the targeted biochar property and biochar application (Ahmed et al., 2016).

The choice of biochar property to modify in order to optimise inorganic pollution remediation includes surface area and pore size / volume, as well as the composition of the biomass - the feedstock should have a good lignin content (Zhao & Lang, 2018). A study of the adsorption behaviour of functionalized (ferric-sulphate solution $(Fe_2SO_4)_3$) biochar (called magnetic reed biochar) and raw biochar (reed biochar) for the removal of an organic pollutant (florfenicol) found that the magnetic reed biochar had a greater surface area and pore volume of 254.6 m^2/g and 0.257 cm^3/g respectively, while the reed biochar had surface area and pore volume of 58.75 m^2/g and 0.119 cm^3/g respectively (H. Zhao & Lang, 2018). A higher surface area led to greater adsorption of florfenicol (9.29 mg/g and 6.14 mg/g respectively) by a hydrogen bonding mechanism. Different modification techniques are summarized below.

Experiments on magnetic biochar continued as four biomass (sugarcane bagasse (SMBC), rice straw (RMBC), peanut shell (PMBC) and herb residue (HMBC)) were functionalized using steel pickling waste liquor (serving as iron salt) for the adsorption of Cr (VI). SMBC gave the highest sorption of 43.1 mg/g which was 1.2 times, 3.2 times and 3.7 times higher than RMBC, PMBC and HMBC respectively (Yi, Tu, et al., 2019). Hydroxyapatite functionalized biochar (HAP-SSBC) derived from sewage sludge plus municipal solid waste was used to evaluate the sorption of Cu^{2+} and Cd^{2+}onto the surface of biochar. The observations show that HAP-SSBC had a higher maximum adsorption

than the raw sludge of 89.9 mg/g and 114.68 mg/g for Cu^{2+} and Cd^{2+} respectively, with the main mechanism being ion exchange (with Ca^{2+}) and complexation (-OH and -COOH)(Y. Chen et al., 2021). Table 2.0 shows different hybrid biochar's and their responsible removal mechanism for a range of organic and inorganic pollutants in the environment.

1.10.1 Steam Activation Functionalization

Steam functionalization is used to initiate and improve porous structures and oxygen – affiliated functional group (carboxylic, ether phenolic hydroxyl and carbonyl group) on biochar surface, thereby increasing the hydrophilicity of the biochar (Ahmed *et al.*, 2016). Steam activation is typically carried out at conditions such as (800ºC—900ºC for 30mins to 3hours with 2.21 to 5mLmin^{-1}) (Ippolito *et al.*, 2012; Rajapaksha *et al.*, 2015), in which it was found to alters biochar properties by releasing compounds resulting from incomplete combustion during pyrolysis and oxidizing to a stable carbon surface with H_2, CO and CO_2 (Ahmed *et al.*, 2016).

1.10.2 Acidic Modification Functionalization

A wild range of oxidant uses this modification to burst acidic property of sorbents by taken-off the mineral element thus increasing hydrophilicity in biochar (Shen et al., 2010). Functionalization with acid is carried out by immersing or suspending biochar in an acidic medium at a ratio of 1:10 biochar/acid (Zhou et al., 2013; Zhou et al., 2014). The biochar immersion period may take hours to days, followed by washing, drying and

pyrolysis (Ahmed *et al.*, 2016). Consequently, acidic (H_2SO_4) pre-treatment of corn stalk and rice hull biochar for the effective alleviation ammonia ($NH4^+$-N) in biogas engineering (anaerobic digestion) has been reported. The result showed that the modified biochar had 1.57 times higher adsorption capacity than the original biochar as a result of oxygen containing functional groups, resulting in an improved chemisorption mechanism (Chen et al., 2021).

1.10.3 Alkaline Modification Functionalization

Alkaline funtionalzation creates positve surfaces which helps in adsorbing negatively charged species. This functionalization process is caried out from room temperature to 100 ^oC by immersing or suspending biochar in different alkaine concentration within a time frame of 6-24 hours depending on the modification material to enhance its surface morphological properties (Surface charges and functional groups) (Fan et al., 2010;Jung et al., 2013; Li et al., 2014; Ma et al., 2014; Ahmed *et al.*, 2016). Biochar immersion period may take hours to days followed by washing, drying and pyrolysis (Ahmed *et al.*, 2016).

1.10.4 Impregnation Method Functionalization

The method of functionalization by impregnation involves the use of metal salts or oxides mixed precursors with biochar to increase the surface functional group potency in-terms of attachment and adsorption. This can be carried out before or after pyrolysis by immersing biomass (then pyrolysis follows) or biochar at different concentrations of salts

or oxides precursors at room temperature to 120°C with a steady stirring for 1-6 hours (C. Li et al., 2018). Examples of precursor solutions used in impregnation include ammonium chloride, carbonates, chitosan graphite CNT and hydrogen (B. Shen, Li, et al., 2015)[b,](B. Shen, Chen, et al., 2015)[a](Agrafioti et al., 2014) (Y. Zhou et al., 2013) (Y. Zhou et al., 2014). Li et al., 2017 reported the adsorption characteristic of Cadmium (11) on modified alkaline treatment BC-NaOH, $KMnO_4$ impregnation BC-MnO_x and ferric magnetic treatment BC-FeO_x rape straw biochar. The biochar displayed an increase in active sites (caused by the manganese oxide) plus formed complexes with a range of oxygen surface functional groups (C=O, C—O, -OH, Olefins, -CH_2, -CH_3, Aromatic rings) which were responsible for sorption of Cd (II). The findings showed that sorption results were 67.4mg/g, 81.1mg/g and 72.4mg/g respectively for BC-FeO_x , BC-MnO_x, and BC-NaOH, indicating that BC-MnO_x had the highest adsorption rate, while and the biochar had 32.7mg/g.

1.10.5 Nano material Functionalization

Biochar in recent times has been functionalized with a range of nanomaterials to improve its morphological structure and physiochemical properties for diverse environmental application. It has been reported that biochar loaded particles (Maghemite and EDTA functionalized layered double hydroxides) aimed for adsorption of Pb (II) (suspended 10hours in a mixture of distilled water and Fe^{2+}/ Fe^{3+} solution at room temperature, then filtered and washed with ethanol and kept at 80°C to dry) adsorbed 146.84mg/g Pb (11) compared to 37.40 mg/g from raw BC (C. Wang & Wang, 2018). The physiochemical properties and Electro-kinetic Stability of the functionalized biochar were determined using Dynamic Light Scattering (DLS), Fourier Transform infrared spectroscopy (FTIR),

Elemental Analyser, X-ray Diffraction (XRD) and Zeta Potential respectively (Song et al., 2019). The results prove that sorption on Nano-BC is achieved by increasing the adsorption sites, surface area, reaction adsorption mechanics and aromaticity (stability) of biochar insinuating a significant reduction in oxidation potential (L. Wang et al., 2019b). The mechanisms responsible for adsorption for metals are coordination and precipitation with minerals, ion-exchange and complexation (H. Li et al., 2017c). Nano-ZnO/ZnS-BC synthesized by slow pyrolysis of zinc contaminated corn stove was observed (C. Li et al., 2018) for the adsorption of Pb(II) Cu(II) and Cr(VI) had a surface area, porosity and sorption capacities (397.4m^2/g, TPV= 0.43cm^3/g and Pb(II) 135.8mg/g, Cu(II) 91.2 mg/g and Cr(VI) 24.5mg/g) better than the unloaded biochar (102.9m^2/g and TPV= 0.20cm^3/g Pb(II) 63.29mg/g, Cu(II) 27.05mg/g and Cr(VI)15.23mg/g). biochar (nano-hydroxyapatite) reported (Z. Li et al., 2020a) for the adsorption of antibiotics (Tylosin & sulfamethoxazole) and heavy metal (Cu (II)) in water body, had a surface area (566.056m^2/g), surface functional group, (-C=O, -OH and C-H) these properties aided adsorption in single, binary, and ternary system. BC modified Nanoscale zero-valent iron (NZVI) reported by (J. Chen et al., 2012) had a distinguished surface morphological characterization (surface area and functional groups) responsible for heavy metal (HM) adsorption by a reduction mechanism as described in Table 1.2.

Table 1.2: Biochar Application for Organic and Inorganic Contaminants Removal at different pH, temperatures and feed stock showing removal mechanism and decontamination efficiency.

Targeted pollutant	**Feed-stock**	**Functionalized Biochar**	**Pyrolysis Temp ^{o}C**	**Decontamination Efficiency (%)**	**pH**	**Surface Area (m^2/g)**	**Removal Mechanism**	**References**
Inorganic								
Cadmium	Corn-cob	Acrylonitrile	350	> 90	≥ 3	4.73	Ion exchange and adsorption complexation	(Luo et al., 2018)
Phosphate	Pineapple peels	Lanthanum(iii) Hydroxide	300	>96.04	3	84.89	Electrostatic interaction, precipitation, complexation and ligand exchange	(Liao et al., 2018)
Hexavalent Chromium	*Melia azedarach* wood	Iron (iii) Oxide	320	98.8	3	5.219	Adsorption – Reduction- and adsorption steps	(X. Zhang et al., 2018)

Florfenicol	Reed stalk	Ferric Sulphate	600	-	≤ 7	254.6	Hydrogen bonding, pore filling	(H. Zhao & Lang, 2018)
Lead (ii)	Palm fiber	Magnetite	400	89.9	6.5	103.87	Ion exchange, electrostatic interaction and complexation	(X. Zhou et al., 2018)
Lead Cadmium Nickel	*Prunus armeniaca* apricot stones	Phosphoric acid	500	95 50	6	1098.9	Chemisorption	(Turk Sekulić et al., 2018)
Organic								
Naproxen Chlorophenols				95 85				
Tetracycline	Sewage Sludge	Sodium-hydroxide Nitric Acid	800	>80	7	202.5	Strong stacking electron interaction and Pore Filling	(Tang et al., 2018)

		Acetic-Acid						
Atrazine	Wheat Straw	Zinc Chloride and phosphoric Acid	450	>81.2	6	1084 900.9	Chemisorption	(L. Zhao et al., 2018)
Formaldehyde Mercury	Pine-Corn	Copper oxide Manganese oxide	500	89 83	-	320.9	Ion exchange, electrostatic interaction and complexation	(Yi et al., 2018)
Pyridine Quinolone	Mango bark	Iron(iii)oxide	600	73 99	9	281.4	Electrostatic interaction and π-π interactions	(H. Xu et al., 2018)
Ammonium Nitrate Phosphate	Soya-beans straw	Magnesium Aluminium	500	-	>5.5	>280	Ion -exchange Electrostatic interaction and π-π interactions	(Q. Yin et al., 2018)

Organic compounds	Coco-nut fiber	Sodium-carbonate	700	>92		1130	Pore filling Hydrophobic interaction	(Bispo et al., 2018)
Safranine T	*Ramie bar* (plant)	Titanium dioxide	500	>81	>3	-	Electrostatic interaction/attraction, hydrogen bonding and π-π interactions	(Cai et al., 2018)
pyrene benzo[α]pyrene	Enteromorpha prolifera biomass	Hydrochloric + Hydrofluoric acid	500	> 75	-	205.32	Hydrophobic interactions	(Qiao et al., 2018)

1.11 Aims and Objectives of the Research

This research aims to achieve the following outcomes:

i. To Create Biochar from high lignin content woodchips and assess their effectiveness for remediation of inorganic pollutants (Ni^{2+} and Pb^{2+});

ii. To understand the binding / sorption mechanisms of Ni^{2+} and Pb^{2+} to the biochar and how binding efficiency can potentially be further optimised by functionalisation of the biochar with nanomaterials.

iii. To functionalize the most efficient biochar from the previous step in order to further increase its sorption efficiency for the inorganic contaminants by:

- Increasing the active sites – via functionalisation with hydroxyapatite nanoparticles.
- Adding an additional binding mechanism – via functionalisation with magnetite nanoparticles to facilitate complexation.
- Developing a hybrid functionalised biochar with both previous modifications to see if this further enhances the absorption capacity via an additive effect or if one functionalisation cancels out the other.

1.11.1: Hypothesis of the Research

- The first hypothesis was that the samples selected from the statistical analysis of the characterization parameters amongst the biomass samples (ash, alder, apple, birch, beech, cherry and oak) will produce Biochar with different sorption efficiencies and mechanisms.
- The second Hypothesis (only applicable if the first one is unsatisfactory) was that functionalisation of a selected biochar to increase the active sites on its surface

via decoration with nanomaterials, would increase sorption yield through increased surface area (active sites) and may initiate a new attachment mechanism and kinetics.

The remainder of the thesis is structured as follows: Chapters 2 summarises the methodologies and instrumentation used in the thesis, and then Chapters 3 – 5 present the results from the studies, with each chapter having a description of the experimental approaches utilised (its own methodology section). Chapter 3 presents the detailed biomass characterisation and selection of biomass for conversion to biochar (Elemental interpolation and statistical evaluation <0.005). Chapter 4 presents the detailed biochar characterisation resulting from the selected biomass samples and baseline adsorption, and Chapter 5 presents the functionalisation strategies and the results of the functionalisation on maximum adsorption efficiency and mechanisms involved. Chapter 6 pulls all the results together with some overarching conclusions and future work recommendations and a discussion of how the data and findings can be used to support soil remediation in Nigeria and elsewhere.

1.12 Chapter Summary

This chapter provides a better understanding on sorption (absorption and adsorption) of inorganic pollutants by biochar and describes their attachment mechanisms (bulk and surface phenomenon). It explains the factors (pyrolysis temperature and nature of feedstock) that influence the physiochemical composition of the derived adsorbent (biochar) and how the pyrolysis temperature results in classification of the resulting biochar as either hydrophobic (pyrolysis at > 700 ^{o}C) and hydrophilic (< 700 ^{o}C). The

chapter proceeds with the best biochar production technique (temperature) for specific environmental applications (pollutant remediation).

Moreover, organic, and inorganic pollutants were identified in this chapter and their possible removal techniques were clearly allocated to them as attachment mechanism. Organic and inorganic pollutant removal efficiency aligned hydrophobic and hydrophilic biochar respectively as the preferred sorbent for contaminants removal. This temperature classified adsorbent presented a possible attachment or removal mechanism as chemisorption, Electrostatic interaction, π-π interactions (organic) and precipitation complexation plus cation exchange (inorganic).

Furthermore, this chapter highlights various functionalization/modification techniques (acidic, alkaline, steam and impregnation) biochar can be subjected to with the aim to improve its application efficiencies. These improvements include the surface morphological properties (surface area, pore-size, pore volume, and surface functional group) and possibly induction of a new attachment mechanism for adsorption of contaminants. Lastly, the chapter presents the concept of isotherms (time and concentration) and kinetic models (Pseudo first, second order and Langmuir and Freundlich respectively) to help describe and explain maximum sorption capacity, attachment process/mechanism and provide useful data to generate equation (plus useful plots) to fit its kinetic models with respect to their R^2 value. These models explain adsorption as a surface phenomenon on a mono layer (pseudo first order) as solute uptake with time directly proportional to saturation concertation while for second order adsorption rate is dependent on adsorption capacity. While the Langmuir and Freundlich assumes that assumed that adsorbates are chemically attached to a fixed number of active sites on adsorbent and the other assumes adsorbate on the adsorbent surface increases with increase in the adsorbate concentration respectively.

CHAPTER 2

INSTRUMENTATION

2.1 Introduction

This chapter captures details and the bases for various instrumentation used on biomass samples (apple, ash, alder, birch beech, cherry and oak) from their selection/acquisition, storage, pre-treatment, characterization, reflux digestion, and quantitative analysis. The chapter also showcases a wide range of instrumentation and their importance towards sorption. The following instruments mentioned in these sub-sections were used to establish a theoretical basis for biomass and its derived biochar characterization. They include Scanning Electron Microscopy (SEM), Elemental Analyser, Fourier Transform infrared Spectroscopy and thermogravimetric Analyser (FTIR-TGA), Brunauer-Emmett-Teller (BET), Centrifuge, and Bomb calorimeter.

2.2 Theoretical Basis of the Methods Applied for Biomass and Biochar Characterization

2.2.1 Scanning Electron Microscopy (SEM)

Scanning electron microscopy (SEM) has been in existence for quite a long time, it has been wildly used for morphological characterization of a range of materials. It provides morphological information about a material such as particle size, porosity, matrix patterns, surface texture, etc. In the case of biochar, it provides a visual understanding of the effectiveness of the pyrolysis process and can be used to explore the impact of pyrolysis temperature on the resulting biochar structure (although this was not explored

in the current thesis) and the resulting insights into the biomass and biochar structures can used to understand the adsorbent effectiveness before biomass and after thermal degradation biochar.

In some cases, SEM image reveals that woodchips biomass surface morphology with blocked pores / pore-volume, insinuating that the biomass has little or no active sites for sorption to take place, whereas its derived-biochar possess good pore/volume distribution on the surface showing active sites ready for contaminants attachment. The technique uses electron beam rather than a beam of light, focused directly on the experimental sample. During analysis, a beam of highly concentrated electron is shot from an electron gun positioned at an elevated position in the instrument. SEM electron guns are of two types: field electron guns which operate by creating strong electrical fields that blot electrons away from their atoms, and thermionic guns which heat a filament until electrons stream away (Sponsors & News, 2015). The microscope (SEM) comprises sets of lenses enclosed in a vacuum chamber, that helps focus the electron beam onto the sample to optimize magnification efficiency.

When a beam released from an electron gun hits a sample (the incident beam), it releases energy in the form of x-rays and three kinds of electrons (primary backscatter electron, secondary electrons and Auger electrons) (Sponsors & News, 2015). The SEM uses the rebounded electrons (primary back scattered electrons and secondary electrons) on the electron recorder, and imprints onto a screen which allows for clear three-dimensional imaging. One major advantage of using the SEM is its ability to produces textural information. The technique is effective when samples are prepared properly; metallic samples do not require preparation (as they react with electrons beams) while non-metallic samples need preparation. Non-metallic samples such as biomass and biochar, need to be energized with a sputter coater (gold) to enable good morphological imaging.

The SEM working principle makes use of three environmental modes - high vacuum (HV), low vacuum (LV) and low vacuum short distance (LVSD), as well as a special operational mode for wet samples (Wet ESEM), each of which is distinguished by designated pressure ranges aligned with each setting, which influences the imaging conditions as presented in Table 2.1. These working modes align with a specific electron detector: for instance, HV and LV are mostly associated with secondary electrons (SE) and Backscattered Electrons (BSE), which make use of the Everhard-Thornley detector (which gives information about surface morphology) and the Backscattered electron Detector (which gives information about internal structural morphology) respectively. However, the physical state of the sample determines the operational mode for analyses, while the vapour pressure in the chamber in turn affects the imaging conditions. The physical state of a sample, the vapour pressure in the chamber and the imaging condition determines the efficiency of SEM analysis (Turkulin et al., 2005).

Table 2.1: Operational modes in the SEM and their parameter (Turkulin, Holzer, Richter, & Sell, 2005)

	Pressure range	**Electron detectors**
High Vacuum (HV)	10-6mbar/Torr	(Everhard-Thornley) SE- detector (BSE)
Low Vacuum (LV)	-0.8Torr	BSD (Backscattered electron Detector (Backscattered Electron)
Low Vacuum Short Distance (LVSD)	-1.8Torr	Large Field Detector with Environmental Scanning Electron Detector cap for short Beam Gas Path Length (Beam Gas Path Length)

Wet Environmental Scanning Electron Detector (ESEM)	>1 Torr	Environmental Scanning Electron Detector operates better at 1-3Torr
	Up to 10 Torr	Gaseous Secondary Electron Detector operates better at 3-6Torr

2.2.2 Elemental Analysis

An elemental analyser is a laboratory instrument that quantifies (as weight percent) an element in a compound of a given sample. These elemental analyser weight in percentages can be converted into atomic ratios of elements, such as hydrogen/carbon (H/C) and oxygen/carbon (O/C) which can be used to describe the maturity and stability (which relates to its aromaticity and the extent of carbonation) of biochar (in a ratio form) and maybe used to infer how surface functional groups are distributed across the active sites of biochar. The attachment mechanism for inorganic pollutants (heavy metal ion) onto adsorbents with high atomic ratio H/C (0.4 to 0.7) is likely to be induced by a surface functional group while for a low atomic ratio is likely to be attracted to the negative surface by precipitation.

The elemental analyser weights samples positioned in a furnace and subjects them to temperatures ≥1000^{o}C under stable conditions in a pure oxygen environment to ensure total combustion of degradable and non-degradable matter (Figure 2.1). The end products are carbon dioxide (CO_2), Nitrogen gas (N_2), oxides of nitrogen and water (H_2O), which pass through a reagent that screens out wanted materials (phosphorous halogens (salts) and sulphur) and are further passed through a scrubber (copper) to enable a proper redox reaction to take place and forwarded to a high precision thermal detector. The elements

of interest, including C, H, O, S, N are quantified with a standard calibration from known micro-analytical compounds. The different configurations are available depending on the application (Thompson, 2008).

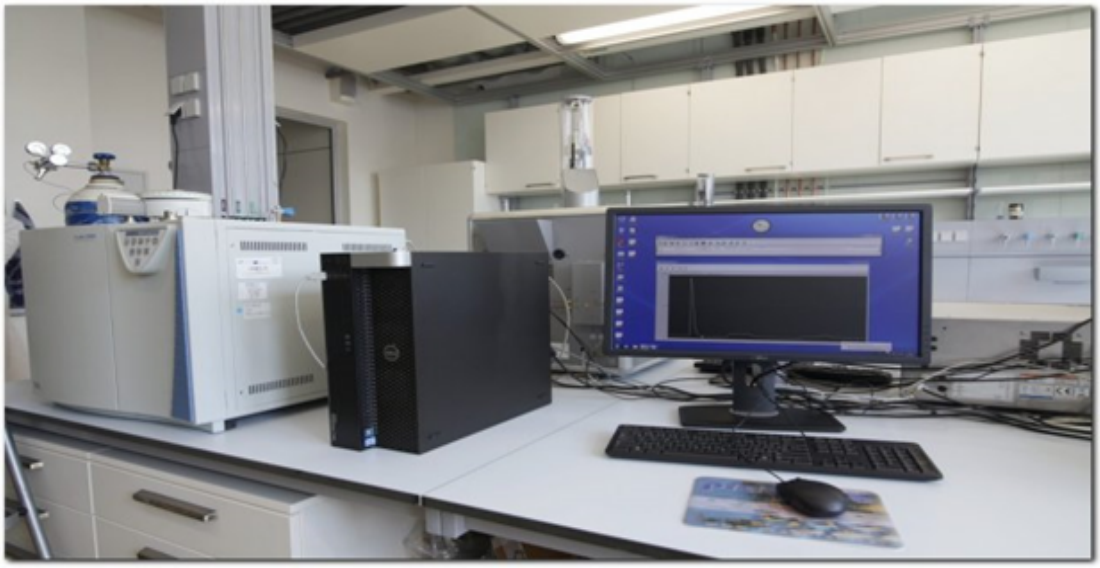


Figure 2.1: Elemental Analyser (FLASH 2000 Combustion) for Quantification of C, H, N, S, O in a sample.

2.2.3 Fourier Transform infrared Spectroscopy coupled to thermogravimetric Analysis (FTIR-TGA)

Fourier Transform Infrared Spectrometry (FTIR), shown in Figure 2.2, is efficiently specific in identifying functional groups, bonds between chemical compounds, and for classifying chemicals as organic or inorganic. The technique can be used to identify the different functional groups on the surface of the material responsible for initiating binding between the targeted pollutant and an adsorbent such as biomass or biochar. The surface groups present on the biochar surface are effective in removal of inorganic contaminants by exchange of ions or the formation of complexes. The spectrophotometer helps to

recognize vibrations linked with functional group and further interprets its molecular structure characteristics in relation to the functional groups present (Doyle, 2017) as shown in Figure 2.2. FTIR can be applied to a large range of samples (solid, liquids, and gases), and both qualitative and quantitative analysis can be done on a particular sample. It provides detailed information on molecular structures and co-existing chemical bonds present via the energy signal associated with bond vibrations and rotations (Dutta, 2017; Hasegawa, 2017). The spectra obtained from the FTIR expose a fingerprint of the peaks arising from a specific material that correlates to the frequencies of vibrations between the bonds and atoms in the material. Therefore, the infrared peaks enable the identification of functional groups at frequencies (qualitative analysis) and the size of the peak indicates the amount of the specific functional group present (quantitative analysis) (Dutta, 2017). The detection areas in the IR spectrum are subdivided into near – IR (400-10 cm^{-1}), mid – IR (4000- 400 cm^{-1}) and far –IR (1400- 400 cm^{-1}) regions.

The FTIR spectrophotometer vibrates molecular bonds of different elements at specific frequencies depending on the bond type. Each chemical bond vibrates at specific frequencies when in contact with infrared radiation, and these bonds absorb radiation at frequencies that corresponds to their vibration (Hasegawa, 2017; Dutta, 2017). A beam of IR irradiation is produced emitting energy from a black body source. The beam is encoded in an interferometer, various beams combine at different path lengths creating an interference (constructive and destructive) termed an interferogram. Samples adsorb energy at frequencies specific to their molecular bonds, and the detector measures the interferogram signal energy against time for all frequencies at same time.

The final spectrum obtained using the Fourier transformation software by subtracting the background spectrum from the sample spectrum. The functional group bonds appear as

single bonds associated with the functional groups Triple bond, Double bond and Fingerprint and these functional group (O-H, C-H, N-H), double bonds from the functional group (C=O, C=N, C=C, N=O), triple bonds from (C≡C, C≡N), functional group and fingerprints such as (C-Cl, C-O, C-N, C-C) (Dutta, 2017 ; Hasegawa, 2017). Thermogravimetric analysis is a method that measures the mass of a sample over time as the temperature changes. A thermogravimetric analyser, TGA (the right-most part of the hyphenated system shown in Figure 2.2) is used to profile a substance, which is subjected to a controlled temperature programme and atmosphere while assessing the mass loss or gain. The experiment requires a known sample mass to be heated using a specific heating profile of either increasing or decreasing with temperature over time. The TGA is made up of a sample pan, located in the furnace, supported by a well accurate balance. The mass of the sample is monitored during the experiment and the purge gas (inert) controls the environment of the sample (PerkinElmer, 2013; Netzsch, 2011).



Figure 2.2: TGA-FTIR-GCMS analyser plus a connected PC to view spectra and input suitable operational methods for surface functional groups analysis and TGA (University of Birmingham).

Thermogravimetric analysis accurately quantifies some parameters such as loss of water, loss of solvent, decarboxylation, pyrolysis, oxidation, decomposition, weight% filler, amount of metallic catalytic residue remaining on carbon nanotubes and weight % of ash. These measurable parameters are usually determined upon heating, which are controlled by PerkinElmer's proprietary thermal software, called Pyris software. The TGA displays a curve that show events of thermal degradation with respect to temperature and mass loss (%). This equipment has six (6) dependable operational variables that contributes to its reproducibility; they are (1) calibration, (2) sample atmosphere, (3) sample preparation, (4) temperature scanning rate, (5) furnace cleanliness, and (6) temperature range (PerkinElmer, 2013; Netzsch, 2011). The evolved gas analysis (EGA) during analysis can be used to determine/describe end products (gases) during a TGA experiment through a combination of techniques where two or more instruments are combined (hyphenated).

In this set-up, the volatile compounds given out by a sample undergoing TGA (the released gases) are collected and then transferred to the IR cell where it is analysed against a reference IR spectrum (PerkinElmer, 2013). At UoB, the TGA is hyphenated with a gas chromatography-mass spectrometry, where the evolved gas from the TGA is further analysed (first by the aforementioned FTIR) and then by GC-MS for better understanding and interpretation of the processes occurring. In this work a hyphenated TGA-FT-IR was used without the final step of GC-MS analysis (PerkinElmer, 2013; Netzsch, 2011). The combination of TGA and FT-IR is the most used EGA analysis system (PerkinElmer, 2013; Netzsch, 2011). Appendix A contains a reference table used in this work for identifying surface functional groups, absorption wave number (cm^{-1}), bond present and appearance on the surface of biomass and its derived chars.

2.2.4 Brunauer-Emmett-Teller (BET) analysis of surface area and pore volume

The Brunauer-Emmett-Teller (BET) method uses the BET equation for the determination of surface areas, pore sizes and pore volume distribution (reported in percentages) of dry solid materials. The resulting information on the adsorbent nature, obtained from BET analysis, helps in accessing the degree of carbonation of a material (if the adsorbent has been subjected to pyrolysis) and provides details of the surface embedded with active sites for sorption reactions to take place. The BET analytical theory is based the following assumptions: surface homogeneity, low molecular interactions, local equilibrium, infinite adsorption at saturation and kinetically limited process (Brame & Griggs, 2016).

The analysis is performed with the following materials: Liquid Nitrogen to cool the system and help generate the vacuum, Helium gas (99.9% pure) to provide an inert environment and purge any potential interferences and Nitrogen gas which is used in this work to probe the available surface area /porosity. The measurement is carried out under a vacuum system (10^{-4} Torr), and the instrument consist of a heating apparatus, sample holder, pressure gauge and precise laboratory balance for surface area analysis as shown in Figure 2.3 (Brame & Griggs, 2016).

The instrument has four analytical operational steps; sample mass measurement, outgassing of the sample, adsorption measurement and interpretation of analysed measurement (Brame & Griggs, 2016; Hassel et al., 2010). Further details (such as isothermal tabular report, log plots, linear plots, linear absolute plot, absolute log plots, isothermal pressure composition, Langmuir surface area plot, adsorption and desorption of pore area/volume plots) on all derived biochar samples and produced functionalized samples on BET analysis used in this work can be found in Appendix C and D.

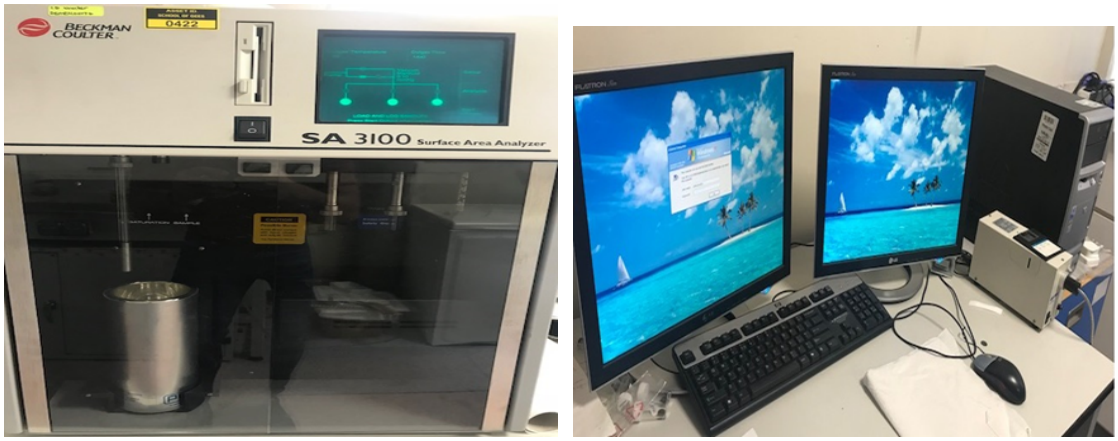


Figure 2.3: Brunauer – Emmett – Teller (BET) device (SA3100 WL Beckman Coulter, Inc) University of Birmingham.

The conversion of the N_2 adsorption to surface area and pore volume uses the BET equation presented in Equation 2.2.

$$q = \frac{a.p}{1+(a.p)} \quad (2.1)$$

$$\frac{1}{W\left(\left(\frac{P}{PO}\right)-1\right)} = \frac{1}{WmC} + \frac{C-1}{WmC}\left(\frac{P}{PO}\right) \quad (2.2)$$

$$Wm = \frac{1}{S+i} = \frac{C-1}{Cs+i} \quad (2.3)$$

$$S = \frac{WmLavAm}{Mv} \quad (2.4)$$

Where,

θ = the fractional cover of the surface,

P = the gas pressure

α = a constant

W = weight of adsorbed gas relative to pressure $P/P_{O,}$

Wm = weight of absorbate occupying a monolayer surface coverage

S_t = Total surface area be calculated with the following equation,

L_{av} = Avogadro's number,

A_m = Cross sectional area of the adsorbate and equals 0.162 nm^2 for an absorbed nitrogen molecule

M_v = molar volume and equals 22414 mL

C = BET constant, which is relatively proportional to the energy of adsorption in the first layer of adsorption, and whose value indicates the extent of interactions between adsorbent / adsorbate (Hassel et al., 2010).

2.2.5 Centrifugal separation of biochar prior to analysis of ion binding

Biomass and biochar samples (after adsorption incubation phase) were centrifuged in order separate the components of the mixture, enabling removal of a supernatant for analytical purpose. Sedimentation and gravitational force are the functioning principles underpinning centrifugal separation. The effect of centrifugal force generated by spinning imparts high gravity on the tube's, which are positioned such that their bottom sides face outwards when the tubes spun. The heavier components of a mixture are forced to the bottom of the tube while the lighter components settle on-top of it, allowing for solid components (such as biomass/biochar) to be separated from the surrounding liquid. The centrifuge is important for separating mixtures into its purest form for analysis purpose (before and after digestion) as shown in Figure 2.4.



Figure 2.4: Centrifuge (Eppendorf centrifuge 5804 R) University of Birmingham**.**

2.2.6 Bomb Calorimetry for determination of heat of adsorption of inorganic pollutants to biochar

Calorimeters are instruments used to measure/quantify the calorific value or higher heating value (HHV) of a substance. A calorimeter does this by measuring the amount of heat released or absorbed in a reaction (chemical or physical). To this end, heat is exchanged with a calibrated substance where readings are acquired (AZoSensors, 2015). The heating content or calorific value of a biomass is directly proportional with its lignin content. The carbon yield after pyrolysis (biochar) and lignin percentage of a biomass are also strongly correlated. Hypothetically, it is safe to assume that a biomass with high HHv will produce biochar with high carbon content (which means a high surface area and good pore/volume) with an excellent active site for sorption reaction (Demirbas, 2017; Telmo & Lousada, 2011). The calorific value of a substance (sample) can be defined as the amount of heat units given-off by a sample when burnt in an oxygen confined space (volume). The samples and oxygen are at the same temperature initially while the product of

combustion (water vapour condenses to liquid) is cooled at another temperature relative to the initial temperature. The heat of combustion (calorific value) quantified in the bomb calorimeter is the heat given-off by the combustion of the carbon and hydrogen base material (sample) in the presence of oxygen to produce carbon-dioxide and water plus heat given-off by other elements (sulphur) which may be present (Parr instrument company, 2007). Heat of combustion (calorific value) can be expressed in calories (cal), British thermal units (Btu) or Joules (J) using the international steam table calorie as the basic unit in the system. One calorie equals 4.1868 absolute joules, and it equates to the heat required to raise the temperature by one gram of water by one degree Celsius at 15 ^{o}C. The British thermal unit equates to 251.996 calories and is almost equivalent to the heat required to raise one pound of water one-degree Fahrenheit at 60 ^{o}F (Parr instrument company, 2007). The relationships between the different units of calorific energy are shown below.

1cal = 4.1868 Joules 1Btu/Ib = 2.326joules/gram

1Btu = 1056.06 joules 1.8Btu/Ib = 1.0 cal/ gram

1Btu = 251.996 calories

The bomb calorimeter (Figure 2.5) has four unique parts: (1) the vessel or bomb, (2) the cover box/container for holding the bomb in a measured quantity of water with a stirrer, (3) an insulating jacket to protect the calorimeter from heat loss during combustion, and (4) a thermometer or other device for measuring temperature changes (Parr instrument company, 2007). The bomb is a thick metal vessel, having a valve for oxygen filling under pressure and for expellant of by-products (CO_2 and other gases) after combustion. It allows for opening, to insert samples into a small fragile metallic hollow container and for cleaning after use. The electrodes carry the ignition to the thread connected to it and

to the sample in the hollow container. The bomb is designed to hold a high pressure(3000psig), while during combustion a pressure of about 1500psig is generated inside the bomb (Parr instrument company, 2007). The cover box is designed is to accommodate the bomb totally submerged in water, with an LCD to display the temperature. A stirrer is located at the bottom to ensure temperature equilibrium through rapid mixing, without the introduction of excess heat through mechanical energy (Parr instrument company, 2007).



Figure 2.5: Bomb Calorimeter (IKA® C200) University of Birmingham (Collaborative Teaching Laboratory). The analyser measures the heat content a of sample. This method was used on all 7 of the biomass samples (ash, apple, alder, beech, birch, cherry, and oak).

2.3 Summary

This chapter summarizes details of the biomass samples (apple, ash, alder, birch beech, cherry and oak) from its acquisition/storage to preparation, reflux digestion for analysis, detailed characterisation and statistical analysis and describes the final selection of which subset of biomass samples to take forward for pyrolysis. Furthermore, this chapter highlighted the theoretical basis of the various characterization methodologies plus their associated instrumentation. It focused on the working principles of these instruments and shows the interconnectivity amongst them in terms of providing detailed characterisation of the biomass and biochar samples (Figure 2.6) plus their precise location.

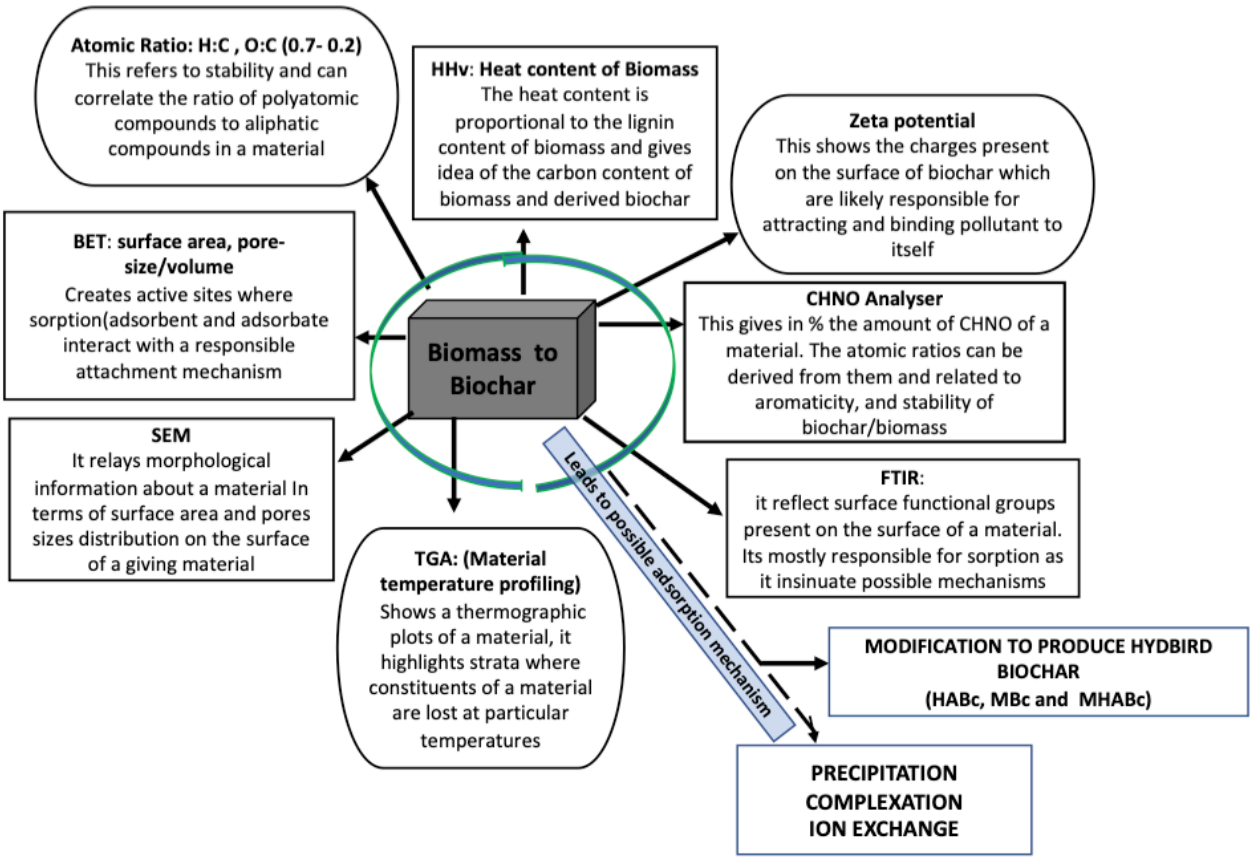


Figure 2.6: Summary of chapter 2 showing details of characterization methods (BET, FTIR, TGA, Calorimeter, Elemental Analyser and Zeta potential) and parameters characterised (Atomic ratio, HHv, Surface area and functional group, pore size/volume and SEM imaging) for each of the biomass / biochar samples and the modification techniques utilised to produce the hybrid Biochar samples and how these parameters and modifications could affect sorption of the heavy metal ions.

CHAPTER 3

SELECTION AND CHARACTERIZATION OF WOODCHIP BIOMASS AND ITS DERIVED BIOCHAR

3.0 Introduction

This chapter describes the biomass samples (apple, ash, alder, birch beech, cherry and oak) in terms of their selection/acquisition, storage, pre-treatment including reflux digestion, characterization statistical analysis and quantitative analysis, as well as the pyrolysis of the biomass to biochar and the characterization of the resulting biochar. The chapter also showcases the wide range of characterization techniques used on the samples (biomass and resulting biochar). The physiochemical characterisation and analytical methods deployed on biomass samples helped in identifying the most significantly different biomass samples (Ash, Apple, Birch, and Beech) which were selected for thermal dehydration (Pyrolysis). The chapter also presents the methodology utilised to determine the adsorption efficiency and adsorption mechanism of the representative heavy metal ions (Lead and Nickel), including the statistical approaches utilised. The biomass characterization was the basis upon which the experimental hypotheses for the thesis were established.

Biomass conversion into biochar has gained a lot of attention recently, based on their physiochemical properties which make them important scaffolds for a range of adsorption processes which is the basis of their effectiveness in environmental applications including environmental remediation and water purification. (Sharma, 2018). Biomass is rich in carbon and associated elements (hydrogen, oxygen and nitrogen) and when subjected to high temperatures in an inert environment produces biochar via pyrolysis (Luz et al.,

2018). There are various feedstock materials (biomass types) including wastewater sludge, agricultural waste, domestic waste, and forest waste can be converted to biochar because of the presences of carbon in them (Huang et al., 2017). However, the resulting biochar varies considerably in terms of adsorption abilities, hence the raw biomass should be well chosen depending on the desired interactions (Mirheidari et al., 2020). The physiochemical properties of the starting biomass, which are determined through proximate analysis which measures moisture content, volatile matter, and ash content and ultimate properties quantification of carbon, hydrogen, nitrogen and oxygen, the ratios of H/C and O/C, the calorific content (or higher heating content, HHC), surface area, pore size and pore volume as well as the pyrolysis temperature affect the properties of the resulting biochar, as well as its sorption efficacy, aromaticity, and stability. As a result, biochar has been applied in various sectors of the environment including for treatment of wastewater, for soil amendment in agriculture, for sorption of organic and inorganic contaminants and for carbon sequestration (Oliveira et al., 2017; Sharma, 2018).

When choosing a biomass for pyrolysis priority must be given to understanding the intended application of the derived biochar and if intended for use in environmental remediation of the nature of the target pollutant, in order to aid selection of the appropriate biomass with optimum characteristics for the specific application. The sorption mechanism of target pollutants (organic and inorganic) can be linked or correlated to the chemical and physical interaction mechanisms on the active sites of an adsorbent, which relates to its surface area, pore size-volume and surface functional groups (Oliveira et al., 2017). However, for organic pollutants such as pesticides and poly aromantic hydrocarbons it has been suggested that factors such as chemical transformations (of the pollutants) electrical conductivity, reductive reactions, polarity reduction, high aromaticity and possibly microorganism stimulated breakdown of the pollutant may

(individually or in combination) influence the sorption of organic pollutants by the biochar active sites (Kong et al., 2018; Oliveira et al., 2017; Ahmad et al., 2014). For inorganic pollutants such as nickel and lead, the removal mechanisms documented to date include hydrogen bonding/electrostatic attraction, and ion exchange by complexation with the active surface functional groups such as -OH, -COOH and R-OH (Mahdi et al., 2018a).

This chapter aims to fully characterize, the seven woodchip biomass samples Alder, Ash, Apple, Birch, Beech, cherry and Oak, in-terms of their atomic ratio, HHV, surface area and functional groups, pore size/volume and elemental composition (C, H, N, O) and based on a full evaluation of the statistically significant difference between the biomass samples, select the most significantly different samples for thermal dehydration (pyrolysis). The hypothesis underpinning the work in this chapter here is that (see also section 1.11.1) selecting the best biomasses which were statistically significantly different in terms of their physiochemical properties to be subjected to thermal dehydration (pyrolysis and conversion to biochar).

3.1 Sample Preparation, Methodology and Expectation Overview

Seven different woodchips were purchased form Amazon in their original state, such that the received chips were dry and untreated with any chemical. These woodchips, as shown in Figure 3.1, were not homogeneous in terms of word chip size per pack, thus they were placed in trays and larger sized woodchips were handpicked to sort out different size fractions from large to medium to small and finer ones. Each individual size class was then ground down, (with Kenwood blender 220 - 240 V, 350 W, 50/60 Hz, model BL23WG) to a very fine size (600 μm) and were then characterized in terms of their mean

values of surface area, morphology, surface chemistry, thermal properties and energy content (via BET, SEM, FTIR, TGA and calorific analysis, respectively), and used for experimental purposes to assess the biomass adsorption of the representative heavy metals, namely Pb^{2+} and Ni^{2+}. Based on the results of the biomass characterization, a subset of the woodchips were selected for thermal dehydration (pyrolysis) to produce their derived biochar aiming to achieve biochar with good surface area, well distributed pore-size/pore volume, and reasonable H:C and O:C ratios. Each of the woodchip (and resulting biochar) samples were well labelled, double wrapped and kept in transparent zip-lock bags to avoid mix-up and contamination.



Figure 3.1: Seven different Wood chips (Ash, Apple, Alder, Beech, Birch, Cherry and Oak)) obtained from Amazon.

3.1.1 Pyrolysis of woodchip biomass to produce Biochar.

Pyrolysis or thermal decomposition took place at temperature 550 ^{o}C for 5 hours for selected samples (Apple, Ash, Beech and Birch). The reactor (a locally made cylindrical shaped air lock device) allowed biomass loading in the middle with internal vent tubes

to create an inert environment (nitrogen gas), included also a thermometer that is visible outside (values on screen), calibrated collection containers (bio-oil) at opposite ends) and a heat chamber at the bottom (constructed to circulate head evenly across the reactor) that is monitored to ensure that the temperature increased at a rate of 10 ^{o}C min^{-1} until it approached the set temperature. The furnace was well padded and had a recyclable exhaust system such that the gaseous by-product (CH_4) is redirected into the furnace chamber as a secondary source of carbonating heat. The programme was set to 300 mins reaction time at a temperature of 550 ^{o}C. 550 g each of selected biomass samples (apple, ash, birch, and beech) were prepared separately in well labelled large crucibles and placed into the furnace for slow pyrolysis (which conforms with International Biochar Initiative (IBI) specifications for biochar) (Definition & Standards, 2015). From the initial 550.0 g of biomass added, the masses of biochar produced were 369.2 g, 340.3 g 395.1 g and 312.4 g leading to a yield of 67.1 %, 61.8 %, 71.8 % and 56.8 % for the Ash, Apple, Beech, and Birch biomass, respectively, which is in good agreement with the expectation for slow pyrolysis. The bio-oil was also collected and preserved but has not been characterised as part of this thesis. Upon cooling, the samples were stored in sealed Ziplock bags as described above for their parent biomass samples.

3.1.2 Biomass and Biochar Characterisation

Thermogravimetric analysis (TGA) was used to conduct Proximate Analysis of both the biomass and biochar samples, determining the Volatile Content, Moisture, Ash, and Fixed Carbon. The determination of these parameter was adopted from IBI and EBC who set out analytical temperatures for these variables (Minerals et al., 2014). The combination of TGA and FTIR is the most common in Evolved Gas Analysis System. For TGA 0.5g

of ground samples (biomass and biochar) were placed in triplicates in an oven carrier pan and subjected to temperature (25ºC to 900ºC) which then gives a thermal dehydration profile of sample (showing loss of moisture and volatile content, then fixed carbon and ash content in percentages in relation to increased temperature) on the connected computer monitor screen. The released volatile compounds were collected and transferred to the IR cell unit where the released volatile compounds are identified and characterized against the reference IR spectra (PerkinElmer, 2013). FTIR spectrometry was used in identifying surface functional groups on biomass and its derived char. The TGA-FTIR-GCMS instrument was left to run for a couple of minutes to reduce the effect of noise on the spectrum. Thus, the surface functional groups were observed between 2.5 μm to 25 μm and 4000 cm^{-1} to 400 cm^{-1} (wavelength and wave number, respectively) as described also by Shen et al. (2018). further details of the principle are discussed in section 2.3.3.

The ultimate analysis (C, H, N, O, S in percentages) was done using the elemental analyser (Thermo-Fisher Scientific Flash Smart 2018FLS0113) for both biomass and biochar samples. 0.4 g of the selected samples (in triplicate) was ground and placed separately in the desired elemental (C, N, H, O) column trays in the Elemental Analyser ready for analysis as shown in Figure 3.2a.

For SEM analysis samples 0.25 g of sample (the selected woodchips and derived char samples) was attached with double-sided sticky carbon tape to a circular aluminium pan. The tape and the pan were of almost equal circumference. The samples were placed in a Gold Sputtering Machine to create a thin layer of gold on the sample surface to facilitate electron interaction in the SEM. The samples were further transferred into the SEM for analysis, and the High Vacuum detection operational mode was used with image acquisition (NMUD7.3/7.4 x 1.0k/1.8k 100 μm / 50 μm, respectively) using an -SEM-

Hitachi TM3030-Desktop SEM (Engineering building, University of Birmingham) as seen in Figure 3.2b.

BET is used for surface area determination of samples (biomass and derived biochar) in solid state. Seven (7) different types of woodchip samples (Alder, Apple, Ash, Beech, Birch, Cherry, and Oak) were obtained from Amazon based on their high lignin contents. The samples (Figures 3.1 and 3.2a) were ground and then surface area analysis was performed using BET. The weight of the BET tubes was measured before and after the samples were placed inside. These samples were purified (moisture removal) by outgassing (at 70 ^{o}C for 55 minutes). Sample weight was taken to know the actual weight of sample after outgassing.

The Outgassed sample was then placed in the analyser column coupled with liquid nitrogen in the Dewar flask, and the programmed parameters were run. Each sample was run in triplicate in accordance with the ASTMD6556-14 procedure (Manufacturing, 2014), as shown in Figure 3.2a. Further details of the principles and equation used in BET and the specific instrumentation is given in section 2.3.4. The H/C and O/C ratios are used to interpret the maturity and stability of the biomass-derived biochar. The analytical values of these ratios serve as a reference point for better understanding and appreciation of the biochar pyrolysis process. The closer the values of aromaticity and stability are to 0.1 the better and the greater the confidence with which the derived char can be called biochar, although 0.7 is the maximum accepted value for the H/C and O/C ratios for biochar, according to the International Biochar Initiative (see Figure 3.3 and section 3.3).



Figure 3.2a: Ground samples (left), and the essential components of the BET device (University of Birmingham).

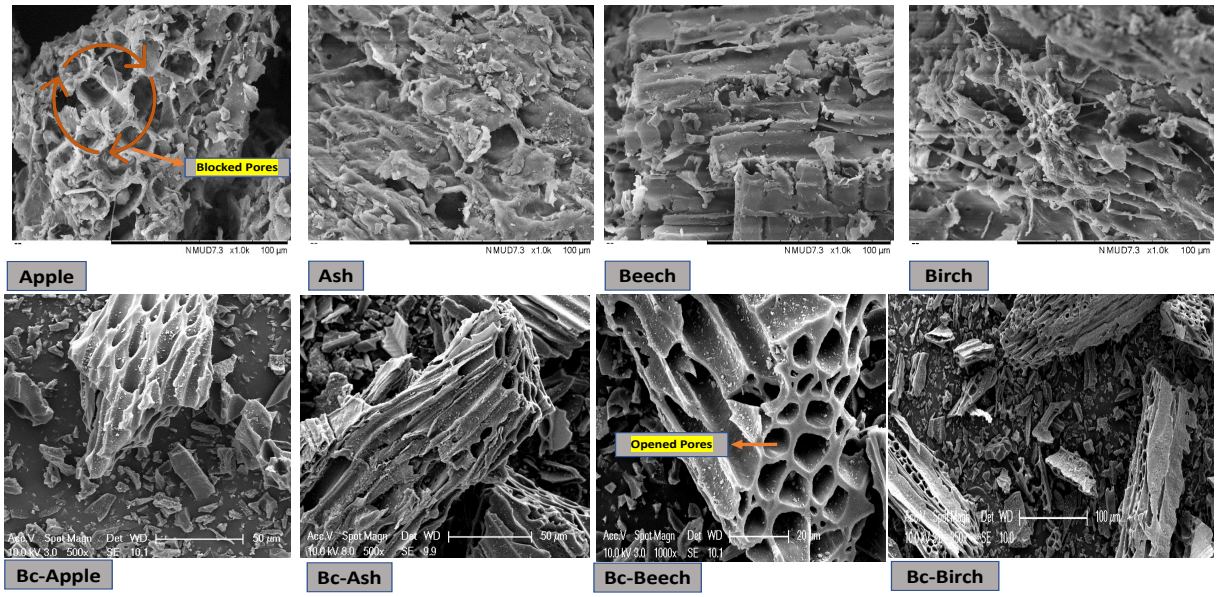


Figure 3.2b: SEM images of the various biomasses and their derived biochar showing the effect of pyrolysis (550 ºC for 5 hours) on the morphological features, specifically the opening of blocked pores and the increased pore volume following pyrolysis.

3.1.3 Sample Digestion (Biomass and Biochar) for Analysis of the Metal Content

Ground samples (woodchips and derived Biochar) were digested (in triplicate) to determine the distribution and quantify the amount of each element (Mg, P, Ca, Cr, Co, Fe, Cu, Mn, Ni, Cd and Pb) and targeted ions (Pb^{2+} and Ni^{2+}) in the samples, using procedures adopted and modified from the literature (Tafur-marinos et al., 2016), for woody biomass. The nitric acid (trace metal grade) used in this study was purchased from Fisher Scientific UK limited, while Hydrogen peroxide (ultra-trace analysis) was obtained from Sigma Aldrich. For biomass elemental digestion, 5 g of sample (biomass) was weighted into a 50 mL falcon tube and 25 mL of nitric acid (HNO_3) was added to it. The samples were left to digest overnight, before being heated to boiling for 6 hours in a reflux system (Figure 3.3). After the solution had cooled, 20 mL of hydrogen peroxide (H_2O_2) was added, and the solutions were reheated to boiling for a further 2 hours. Following cooling, syringe filters (0.45 μm) were used to filter the solutions before further dilution into 50 mL tubes ready for ICP-OES analysis (Perkin Elmer optima 8000). The calibration standards used were purchased from Sigma Aldrich (1000 ppm each). These standards were made as a cocktail in a 10 mL tube then serially diluted to concentrations of 10 ppm, 7.5 ppm, 5 ppm, 2.5 ppm, 1 ppm and 0 ppm in 50 mL tubes (See calibration curves in appendix B). The elements of interest had various detection limits (Mg 0.0075 mg/kg, P 5.7 mg/kg, Ca 0.015 mg/kg, Cr 0.525 mg/kg, Co 0.525 mg/kg, Fe 0.345mg/kg, Cu 0.375 mg/kg, Mn 0.105 mg/kg, Ni 0.75 mg/kg, Cd 0.2025 mg/kg and Pb 3.15 mg/kg).



Figure 3.3: Reflux digestion unit for biomass and derived biochar (University of Birmingham).

3.1.4 Statistical Analysis of Biomass Samples Characteristics

The nonparametric statistical analytical approach (Kruskal-Wallis one-way ANOVA) was used to help select the best samples for thermal dehydration. The test was used in a pairwise manner to explains the extent of significance each sample exhibits in respect to given characterization variables. For example, a characterization parameter (e.g., carbon content, moisture or surface area) is examined across all samples (Ash, Apple, Alder, Birch, Beech, Cherry and Oak) in random pairs (having different combinations) to accurately ascertain the samples with the greatest differences with respect to a particular characterization parameter. The observations from the pairwise Kruskal-Wallis one-way ANOVA on manifest variables identified four distinctive samples (Ash, Apple, Beech, and Birch) with a significance value <0.005, which is the basis for their selection for pyrolysis. This selection set the first Hypothesis (Chapter 1) into motion: that the

significantly different biomass samples, as obtained from the Kruskal-Wallis one-way ANOVA might lead to a significant difference in the characteristics of their derived biochar samples. As a consequence, the biochar samples may potentially exhibit different adsorption removal mechanisms for heavy metal ions. This statistical method helps to identify similarities and differences amongst the different samples in respect to the given characterization variable. This is helpful in inferring what samples are best for the subsequent experimental purposes by identifying those biomass samples that are the most different from one another. Figure 3.4 summarizes the experimental and analytical approaches the biomass samples were subjected to in this chapter, before proceeding to thermal dehydration (pyrolysis) process (in Chapter 4).

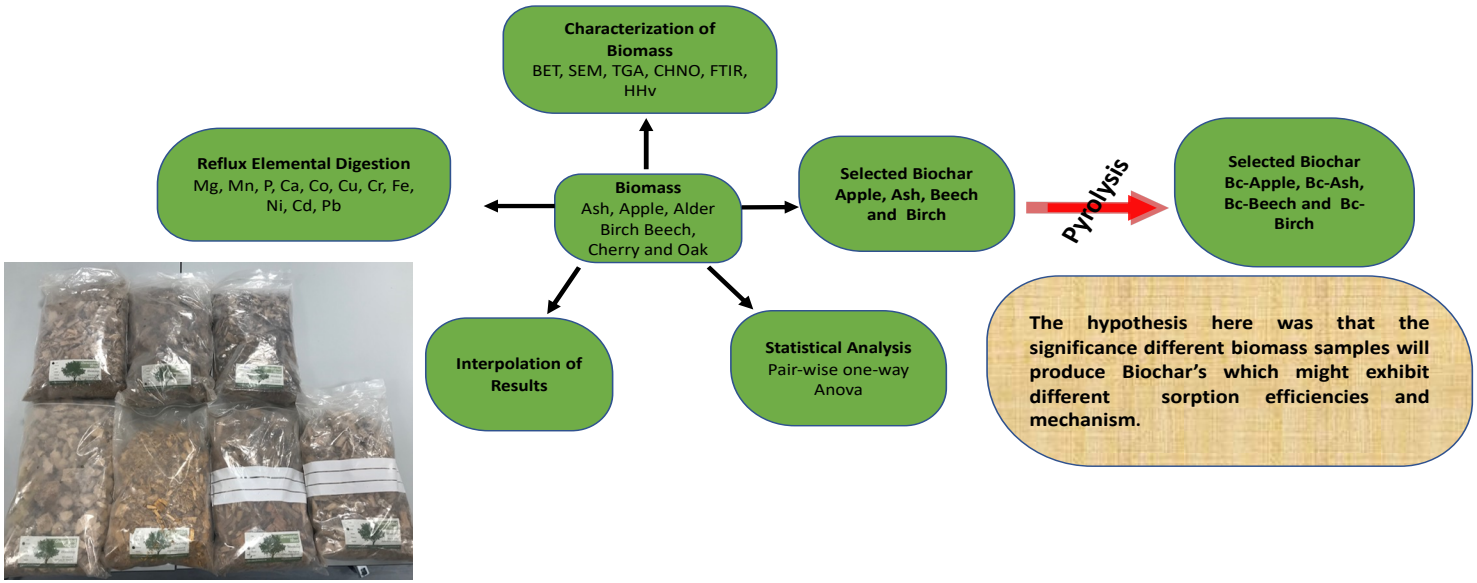


Figure 3.4: Schematic summary of the experimental work performed in Chapter 4, showing how the 7 woodchip biomass samples (Ash, Apple, Alder, Birch, Beech, Cherry, and Oak) were analysed (characterized via proximate and ultimate analysis, SEM, BET and elemental analysis) and statistically evaluated in order to select 4 (Ash, Apple, Birch and Beech) for pyrolysis and subsequent re-characterization of the biochar samples by the same methods prior to their use for sorption experiments in chapter 4.

3.2 Results and Discussion

The general characteristics of a biomass are explained by its proximate and ultimate analysis, shown as percentage (%) in Table 3.1. It explains the physiochemical properties of the biomass samples and gives a path for which hypotheses can be made by considering statistically how this characterisation parameters (10) varies individually across all biomass samples (in terms of their significant difference) and how each sample differ from each other in a pair wise manner to every distinct characterisation variable. From the observations obtained from the statistical analysis, significant samples were selected (Table 3.2) for pyrolysis with the hypotheses that the observed significance will be transferred to their derived biochar and in turn affect sorption mechanism.

Table 3.1 shows the weight (wt.) percentage (%) range of volatile matter (41 – 65%), fixed carbon (25-47%), and ash (9-13%) determined for the 7 woodchip biomass samples investigated here were in good agreement with obtained by Sahoo (Sahoo et al., 2021) and Singh (Y. D. Singh et al., 2017) for the bamboo and woody stem biomass respectively. The woodchip biomass was predominantly composed of carbon and oxygen with approximate values of 34.2 - 55% and 35 – 41 wt% respectively, which was similar to Singh's observation of woody stem biomass having 50% and 43% oxygen. The hydrogen contents of the woodchip biomasses were low, at just 5-6 wt%, while sulphur was not detected in the woodchip biomass samples.

Also, the H/C and O/C values ranged from 1.61 – 1.78 and 0.67 to 0.71, respectively (Table 3.2). The surface area of the biomass ranged between 1.2 – 7.6 g/m^2, indicating a low surface area and blocked pores as also seen from the SEM images (Figure 3.2a). The higher heating value (HHV or calorific value) ranged between 16800 – 18800 MJ/g,

which correlates highly with the elemental composition and high lignin content of biomass and indicates that feedstock is rich in carbon content and represents a good biomass for pyrolysis (Demirbaş, 2001; Demirbas, 2017; Telmo & Lousada, 2011). Statistical analysis of the biomass characterisation parameters including the elemental biomass digestion and compositional analysis by ICP-OES was performed using the non-parametric Krusal-Wallis pairwise one-way ANOVA test. The samples displayed significances difference <0.05 when compared across in a pair wise manner across the characterisation parameters (Tables 3.2 - 3.17).

Tables 3.1 – 3.18 present the analysis of the biomass sample in a pairwise manner, using the characterization parameter that rejected the null hypothesis. The null hypothesis statistically state that there is no significant difference observed amongst specified population i.e., biomass samples. This can be further interpreted in relation to characterization parameters of not having a significant different effect on biomass samples except proven otherwise as shown in Table 3.1 – 3.10. Several statistical differences were observed amongst samples in respect to individual characterization parameters and they were correlated with elemental digestion results (Table 3.11 - 3.18). Ash and Apple biomass gave significance difference in terms of their calcium, iron, Fixed - Carbon, carbon, and hydrogen content. Birch and Apple biomass were significantly different in terms of their moisture and nitrogen contents, while Beech and Apple had significance differences in Cobalt, volatile - matter and oxygen contents, while both Ash and Cherry biomasses were significantly different to oak in their carbon and manganese content. The analysed results showed that Ash, Apple, Birch, and Beech had the most significant differences in terms of their elemental distribution amongst the 7 samples (Table 3.18). The statistical analysis method helped to draw out significant differences amongst the samples in respect to the given characterization variables and thus helped in

inferring which biomass samples would be best for pyrolysis to produce biochar samples with the greatest differences in properties and thus in adsorption efficiencies. Four samples were chosen for thermal degradation (pyrolysis) in an inert environment at a fixed temperature. The resulting carbonated products were four wood-chip derived Biochar samples referred to as (Bc-Ash, Bc-Apple, Bc-Birch, and Bc-Beech). The aim is to identify and select significantly different samples for thermal degradation (pyrolysis) and hope that the peculiarity observed in these selected samples will be passed on to their derived char and possibly affect their contaminant attachment mechanism (which is the hypothesis for this chapter). It is important to note that samples were denoted by numbers in Tables 3.2 - 3.18, as follows 1 = Alder, 2= Ash, 3= Apple, 4 = Birch, 5=Beech, 6 = Cherry and 7= Oak for this pairwise comparisons.

Table 3.1: Mean values of Proximate and Ultimate analysis from biomass characterization.

Property	ALDER	ASH	APPLE	BEECH	BIRCH	CHERRY	OAK
Moisture (%)	9.91	8.44	6.45	8.78	16.4	12	6.36
Volatile Matter (%)	50.5	53.2	34.2	54.8	45.8	49.8	49
Fixed Carbon (%)	28.3	28.9	46.7	25.8	27.4	27.6	31.4
Ash (%)	11.3	9.43	12.6	10.7	10.5	10.7	13.3
C (%)	41	44.7	38.6	44.4	41.1	39.7	38.6
H (%)	5.67	6.17	5.28	5.97	6.01	5.79	5.73
N (%)	0.41	0.38	0.56	0.54	0.31	0.41	0.32
O (%)	36.9	40.1	35.4	41.4	38.8	36.7	35.4
H/C	1.66	1.65	1.63	1.61	1.76	1.75	1.78
O/C	0.67	0.67	0.69	0.7	0.71	0.69	0.69
Surface area (g/m^2)	3.48 ± 0.1061	1.29 ± 0.2380	2.64 ± 0.1512	3.38 ± 0.4210	1.96 ± 0.5743	6.74 ± 0.0750	7.60 ± 0.1903
Calorific Value (MJ/g)	17600 ± 0.0123	18200 ± 0.0092	16800 ± 0.0173	18700 ± 0.0300	17100 ± 0.0429	17500 ± 0.0169	17300 ± 0.0220

Table 3.2: Characterization parameters (10) compared across samples with their significance difference and the decision as to whether the pair (shows sufficient difference to accept or rejects the null hypothesis).

S/N	Null Hypothesis	Test	Sig.	Decision
1	Distribution of moisture is the same across categories.	Independent-Samples Kruskal-Wallis Test	0.004	Reject the null hypothesis.
2	Distribution of volatile matter is the same across categories of Treatment.	Independent-Samples Kruskal-Wallis Test	0.004	Reject the null hypothesis.
3	Distribution of fixed carbon is the same across treatment categories.	Independent-Samples Kruskal-Wallis Test	0.003	Reject the null hypothesis.
4	The distribution of ash content is the same across categories.	Independent-Samples Kruskal-Wallis Test	0.101	Retain the null hypothesis.
5	Distribution of surface area is the same across categories.	Independent-Samples Kruskal-Wallis Test	0.311	Retain the null hypothesis.
6	Distribution of HHV is the same across treatment categories.	Independent-Samples Kruskal-Wallis Test	0.01	Reject the null hypothesis.

7	The distribution of carbon is the same across treatment categories.	Independent-Samples Kruskal-Wallis Test	0.004	Reject the null hypothesis.
8	The distribution of hydrogen is the same across treatment categories.	Independent-Samples Kruskal-Wallis Test	0.005	Reject the null hypothesis.
9	The distribution of nitrogen is the same across treatment categories.	Independent-Samples Kruskal-Wallis Test	0.004	Reject the null hypothesis.
10	The distribution of oxygen is the same across treatment categories.	Independent-Samples Kruskal-Wallis Test	0.01	Reject the null hypothesis.
Asymptotic significances are displayed. The significance level is 0.05.				

Table 3.3: Pairwise comparisons of the Moisture content of the biomass samples to determine any significance differences. Sample numbers 1 = Alder, 2 = Ash, 3 = Apple, 4 = Birch, 5 = Beech, 6 = Cherry and 7 = Oak.

Sample 1-Sample 2	Test Statistic	Std. Error	Std. Test Statistic	Sig.	Adj. Sig.[a]
3-7	-3.000	5.066	-0.592	0.554	1.000
3-2	6.667	5.066	1.316	0.188	1.000
3-5	-9.000	5.066	-1.776	0.076	1.000
3-1	11.333	5.066	2.237	0.025	.531
3-6	-15.000	5.066	-2.961	0.003	.064
3-4	-18.000	5.066	-3.553	0.000	**0.008**
7-2	3.667	5.066	0.724	0.469	1.000
7-5	6.000	5.066	1.184	0.236	1.000
7-1	8.333	5.066	1.645	0.100	1.000
7-6	12.000	5.066	2.369	0.018	0.375
7-4	15.000	5.066	2.961	0.003	0.064
2-5	-2.333	5.066	-0.461	0.645	1.000
2-1	4.667	5.066	0.921	0.357	1.000
2-6	-8.333	5.066	-1.645	0.100	1.000
2-4	-11.333	5.066	-2.237	0.025	0.531
5-1	2.333	5.066	0.461	0.645	1.000
5-6	-6.000	5.066	-1.184	0.236	1.000
5-4	9.000	5.066	1.776	0.076	1.000
1-6	-3.667	5.066	-0.724	0.469	1.000

1-4	-6.667	5.066	-1.316	.188	1.000
6-4	3.000	5.066	.592	.554	1.000

Each row tests the null hypothesis that the selected Sample “1” and Sample “2” parameter is the same.

Asymptotic significances (2-sided tests) are displayed. The significance level is 0.05.

a. Significance values have been adjusted by the Bonferroni correction for multiple tests.

Table 3.4: Pairwise comparisons of the Volatile Matter content of the biomass samples to determine any significance differences. Sample numbers 1 = Alder, 2 = Ash, 3 = Apple, 4 = Birch, 5 = Beech, 6 = Cherry and 7 = Oak.

Sample 1-Sample 2	Test Statistic	Std. Error	Std. Test Statistic	Sig.	Adj. Sig.[a]
3-4	-3.000	5.066	-0.592	0.554	1.000
3-7	-6.667	5.066	-1.316	0.188	1.000
3-1	8.333	5.066	1.645	0.100	1.000
3-6	-12.000	5.066	-2.369	0.018	0.375
3-2	15.000	5.066	2.961	0.003	0.064
3-5	-18.000	5.066	-3.553	0.000	0**.008**
4-7	-3.667	5.066	-.724	0.469	1.000
4-1	5.333	5.066	1.053	0.292	1.000
4-6	-9.000	5.066	-1.776	0.076	1.000
4-2	12.000	5.066	2.369	0.018	0.375
4-5	-15.000	5.066	-2.961	0.003	0.064
7-1	1.667	5.066	.329	.742	1.000
7-6	5.333	5.066	1.053	.292	1.000
7-2	8.333	5.066	1.645	.100	1.000
7-5	11.333	5.066	2.237	.025	.531
1-6	-3.667	5.066	-.724	.469	1.000
1-2	-6.667	5.066	-1.316	.188	1.000
1-5	-9.667	5.066	-1.908	.056	1.000
6-2	3.000	5.066	.592	.554	1.000

6-5	6.000	5.066	1.184	.236	1.000
2-5	-3.000	5.066	-.592	.554	1.000
6-5	6.000	5.066	1.184	.236	1.000
2-5	-3.000	5.066	-.592	.554	1.000

Each row tests the null hypothesis that the Sample "1" and Sample "2" parameter is the same.

Asymptotic significances (2-sided tests) are displayed. The significance level is o.05.

Significance values have been adjusted by the Bonferroni correction for multiple tests.

Table 3.5: Pairwise comparisons of the Fixed Carbon content of the biomass samples to determine any significance differences. Sample numbers 1 = Alder, 2 = Ash, 3 = Apple, 4 = Birch, 5 = Beech, 6 = Cherry and 7 = Oak.

Sample 1-Sample 2	Test Statistic	Std. Error	Std. Test Statistic	Sig.	Adj. Sig.[a]
3-7	-3.000	5.066	-.592	.554	1.000
3-6	-6.000	5.066	-1.184	.236	1.000
3-1	9.000	5.066	1.776	0.076	1.000
3-5	-12.000	5.066	-2.369	0.018	0.375
3-4	-15.000	5.066	-2.961	0.003	0.064
3-2	18.000	5.066	3.553	0.000	0.008
7-6	3.000	5.066	.592	0.554	1.000
7-1	6.000	5.066	1.184	0.236	1.000
7-5	9.000	5.066	1.776	0.076	1.000
7-4	12.000	5.066	2.369	0.018	0.375
7-2	15.000	5.066	2.961	0.003	0.064
6-1	3.000	5.066	0.592	0.554	1.000
6-5	6.000	5.066	1.184	0.236	1.000
6-4	9.000	5.066	1.776	0.076	1.000
6-2	12.000	5.066	2.369	0.018	.375
1-5	-3.000	5.066	-0.592	0.554	1.000
1-4	-6.000	5.066	-1.184	0.236	1.000
1-2	-9.000	5.066	-1.776	0.076	1.000
5-4	3.000	5.066	0.592	0.554	1.000

5-2	6.000	5.066	1.184	0.236	1.000
4-2	3.000	5.066	0.592	0.554	1.000

Each row tests the null hypothesis that the Sample “1” and Sample “2” parameter is the same.

Asymptotic significances (2-sided tests) are displayed. The significance level is 0.05.

Significance values have been adjusted by the Bonferroni correction for multiple tests.

Table 3.6: Pairwise comparisons of the Calorific value-HHv content of the biomass samples to determine any significance differences. Sample numbers 1 = Alder, 2 = Ash, 3 = Apple, 4 = Birch, 5 = Beech, 6 = Cherry and 7 = Oak.

Sample 1-Sample 2	Test Statistic	Std. Error	Std. Test Statistic	Sig.	Adj. Sig.[a]
3-7	-6.000	5.066	-1.184	0.236	1.000
3-4	-6.333	5.066	-1.250	0.211	1.000
3-6	-8.667	5.066	-1.711	0.087	1.000
3-1	9.000	5.066	1.776	0.076	1.000
3-2	15.000	5.066	2.961	0.003	.064
3-5	-18.000	5.066	-3.553	0.000	.008
7-4	0.333	5.066	0.066	0.948	1.000
7-6	2.667	5.066	0.526	0.599	1.000
7-1	3.000	5.066	0.592	0.554	1.000
7-2	9.000	5.066	1.776	0.076	1.000
7-5	12.000	5.066	2.369	0.018	.375
4-6	-2.333	5.066	-0.461	0.645	1.000
4-1	2.667	5.066	0.526	0.599	1.000
4-2	8.667	5.066	1.711	0.087	1.000
4-5	-11.667	5.066	-2.303	0.021	.447
6-1	.333	5.066	0.066	0.948	1.000
6-2	6.333	5.066	1.250	0.211	1.000
6-5	9.333	5.066	1.842	0.065	1.000
1-2	-6.000	5.066	-1.184	0.236	1.000

1-5	-9.000	5.066	-1.776	0.076	1.000
2-5	-3.000	5.066	-0.592	0.554	1.000

Each row tests the null hypothesis that the Sample “1” and Sample “2” parameter is the same.

Asymptotic significances (2-sided tests) are displayed. The significance level is 0.05.

Significance values have been adjusted by the Bonferroni correction for multiple tests.

Table 3.7: Pairwise comparisons of the Carbon content of the biomass samples to determine any significance differences. Sample numbers 1 = Alder, 2 = Ash, 3 = Apple, 4 = Birch, 5 = Beech, 6 = Cherry and 7 = Oak.

Sample 1-Sample 2	Test Statistic	Std. Error	Std. Test Statistic	Sig.	Adj. Sig.[a]
3-7	-0.333	5.060	-0.066	0.947	1.000
3-6	-4.667	5.060	-0.922	0.356	1.000
3-1	7.667	5.060	1.515	0.130	1.000
3-4	-12.167	5.060	-2.405	0.016	0.340
3-5	-12.167	5.060	-2.405	0.016	0.340
3-2	16.667	5.060	3.294	0.001	0.021
7-6	4.333	5.060	0.856	0.392	1.000
7-1	7.333	5.060	1.449	0.147	1.000
7-4	11.833	5.060	2.339	0.019	0.406
7-5	11.833	5.060	2.339	0.019	0.406
7-2	16.333	5.060	3.228	0.001	0.026
6-1	3.000	5.060	0.593	0.553	1.000
6-4	7.500	5.060	1.482	0.138	1.000
6-5	7.500	5.060	1.482	0.138	1.000
6-2	12.000	5.060	2.372	0.018	0.372
1-4	-4.500	5.060	-0.889	0.374	1.000
1-5	-4.500	5.060	-0.889	0.374	1.000
1-2	-9.000	5.060	-1.779	0.075	1.000
4-2	4.500	5.060	0.889	0.374	1.000

5-2	4.500	5.060	0.889	0.374	1.000
4-5	0.000	5.060	0.000	1.000	1.000

Each row tests the null hypothesis that the Sample “1” and Sample “2” parameter is the same.

Asymptotic significances (2-sided tests) are displayed. The significance level is 0.05.

Significance values have been adjusted by the Bonferroni correction for multiple tests.

Table 3.8: Pairwise comparisons of the Hydrogen content of the biomass samples to determine any significance differences. Sample numbers 1 = Alder, 2 = Ash, 3 = Apple, 4 = Birch, 5 = Beech, 6 = Cherry and 7 = Oak.

Sample 1-Sample 2	Test Statistic	Std. Error	Std. Test Statistic	Sig.	Adj. Sig.[a]
3-1	4.000	5.061	0.790	0.429	1.000
3-7	-6.000	5.061	-1.185	0.236	1.000
3-6	-8.000	5.061	-1.581	0.114	1.000
3-4	-12.667	5.061	-2.503	0.012	0.259
3-5	-14.333	5.061	-2.832	0.005	0.097
3-2	18.000	5.061	3.556	0.000	0.008
1-7	-2.000	5.061	-0.395	0.693	1.000
1-6	-4.000	5.061	-0.790	0.429	1.000
1-4	-8.667	5.061	-1.712	0.087	1.000
1-5	-10.333	5.061	-2.042	0.041	0.865
1-2	-14.000	5.061	-2.766	0.006	0.119
7-6	2.000	5.061	0.395	0.693	1.000
7-4	6.667	5.061	1.317	0.188	1.000
7-5	8.333	5.061	1.646	0.100	1.000
7-2	12.000	5.061	2.371	0.018	0.373
6-4	4.667	5.061	0.922	0.357	1.000
6-5	6.333	5.061	1.251	0.211	1.000
6-2	10.000	5.061	1.976	0.048	1.000
4-5	-1.667	5.061	-0.329	0.742	1.000

4-2	5.333	5.061	1.054	0.292	1.000
5-2	3.667	5.061	0.724	0.469	1.000

Each row tests the null hypothesis that the Sample “1” and Sample “2” parameter is the same.

Asymptotic significances (2-sided tests) are displayed. The significance level is 0.05.

a. Significance values have been adjusted by the Bonferroni correction for multiple tests.

Table 3.9: Pairwise comparisons of the Nitrogen content of the biomass samples to determine any significance differences. Sample numbers 1 = Alder, 2 = Ash, 3 = Apple, 4 = Birch, 5 = Beech, 6 = Cherry and 7 = Oak.

Sample 1-Sample 2	Test Statistic	Std. Error	Std. Test Statistic	Sig.	Adj. Sig.[a]
4-7	-1.667	5.050	-0.330	0.741	1.000
4-2	5.333	5.050	1.056	0.291	1.000
4-6	-9.500	5.050	-1.881	0.060	1.000
4-1	10.167	5.050	2.013	0.044	0.926
4-5	-15.000	5.050	-2.970	0.003	0.062
4-3	16.667	5.050	3.300	0.001	0.020
7-2	3.667	5.050	0.726	0.468	1.000
7-6	7.833	5.050	1.551	0.121	1.000
7-1	8.500	5.050	1.683	0.092	1.000
7-5	13.333	5.050	2.640	0.008	0.174
7-3	15.000	5.050	2.970	0.003	0.062
2-6	-4.167	5.050	-0.825	0.409	1.000
2-1	4.833	5.050	0.957	0.338	1.000
2-5	-9.667	5.050	-1.914	0.056	1.000
2-3	-11.333	5.050	-2.244	0.025	0.521
6-1	0.667	5.050	0.132	0.895	1.000
6-5	5.500	5.050	1.089	0.276	1.000
6-3	7.167	5.050	1.419	0.156	1.000
1-5	-4.833	5.050	-0.957	0.338	1.000

1-3	-6.500	5.050	-1.287	0.198	1.000
5-3	1.667	5.050	0.330	0.741	1.000

Each row tests the null hypothesis that the Sample “1” and Sample “2” parameter is the same.

Asymptotic significances (2-sided tests) are displayed. The significance level is 0.05.

a. Significance values have been adjusted by the Bonferroni correction for multiple tests.

Table 3.10: Pairwise comparisons of the Oxygen content of the biomass samples to determine any significance differences. Sample numbers 1 = Alder, 2 = Ash, 3 = Apple, 4 = Birch, 5 = Beech, 6 = Cherry and 7 = Oak.

Sample 1-Sample 2	Test Statistic	Std. Error	Std. Test Statistic	Sig.	Adj. Sig.[a]
3-7	-2.667	5.066	-0.526	0.599	1.000
3-1	5.000	5.066	0.987	0.324	1.000
3-6	-5.000	5.066	-0.987	0.324	1.000
3-4	-11.333	5.066	-2.237	0.025	0.531
3-2	13.667	5.066	2.698	0.007	0.147
3-5	-16.000	5.066	-3.158	0.002	0.033
7-1	2.333	5.066	0.461	0.645	1.000
7-6	2.333	5.066	0.461	0.645	1.000
7-4	8.667	5.066	1.711	0.087	1.000
7-2	11.000	5.066	2.171	0.030	0.628
7-5	13.333	5.066	2.632	0.008	0.178
1-6	0.000	5.066	0.000	1.000	1.000
1-4	-6.333	5.066	-1.250	0.211	1.000
1-2	-8.667	5.066	-1.711	0.087	1.000
1-5	-11.000	5.066	-2.171	0.030	0.628
6-4	6.333	5.066	1.250	0.211	1.000
6-2	8.667	5.066	1.711	0.087	1.000
6-5	11.000	5.066	2.171	0.030	0.628

4-2	2.333	5.066	0.461	0.645	1.000
4-5	-4.667	5.066	-0.921	0.357	1.000
2-5	-2.333	5.066	-0.461	0.645	1.000

Each row tests the null hypothesis that the Sample “1” and Sample “2” parameter is the same.

Asymptotic significances (2-sided tests) are displayed. The significance level is 0.05.

Significance values have been adjusted by the Bonferroni correction for multiple tests.

Table 3.11: Pairwise comparisons of the Magnesium content of the biomass samples to determine any significance differences. Sample numbers 1 = Alder, 2 = Ash, 3 = Apple, 4 = Birch, 5 = Beech, 6 = Cherry and 7 = Oak.

Sample 1-Sample 2	Test Statistic	Std. Error	Std. Test Statistic	Sig.	Adj. Sig.[a]
7 - 1	3.333	5.066	0.658	0.511	1.000
7 - 2	7.000	5.066	1.382	0.167	1.000
7 - 5	9.00	5.066	1.776	0.076	1.000
7 - 6	10.000	5.066	1.974	0.048	1.000
7 - 4	13.667	5.066	2.698	0.007	0.147
7 - 3	17.667	5.066	3.487	0.000	**0.010**
1 - 2	-3.667	5.066	-0.724	0.469	1.000
1 - 5	-5.667	5.066	-1.119	0.269	1.000
1 - 6	-6.667	5.066	-1.316	0.188	1.000
1 - 4	-10.333	5.066	-2.040	0.041	0.869
1 - 3	-14.333	5.066	-2.829	0.005	0.098
2 - 5	-2.000	5.066	-0.395	0.693	1.000
2 – 6	-3.000	5.066	-0.592	0.554	1.000
2 – 4	-6.667	5.066	-1.316	0.188	1.000
2 – 3	-10.667	5.066	-2.105	0.035	0.740
5 - 6	-1.000	5.066	-0.197	0.844	1.000
5 – 4	4.667	5.066	0.921	0.357	1.000
5 - 3	8.667	5.066	1.711	0.087	1.000
6 – 4	3.667	5.066	0.724	0.469	1.000

6 -3	7.667	5.066	1.513	0.130	1.000
4 -3	4.000	5.066	0.790	0.430	1.000

Each row tests the null hypothesis that the Sample “1” and Sample “2” parameter is the same.

Asymptotic significances (2-sided tests) are displayed. The significance level is 0.05.

Significance values have been adjusted by the Bonferroni correction for multiple tests.

Table 3.12: Pairwise comparisons of the Phosphorous content of the biomass samples to determine any significance differences. Sample numbers 1 = Alder, 2 = Ash, 3 = Apple, 4 = Birch, 5 = Beech, 6 = Cherry and 7 = Oak.

Sample 1-Sample 2	Test Statistic	Std. Error	Std. Test Statistic	Sig.	Adj. Sig.[a]
7 - 4	1.667	5.066	0.329	0.742	1.000
7 - 6	5.667	5.066	1.119	0.263	1.000
7 - 2	7.667	5.066	1.513	0.130	1.000
7 - 1	8.333	5.066	1.645	0.100	1.000
7 - 3	13.667	5.066	2.698	0.007	0.147
7 - 5	16.667	5.066	3.290	0.001	**0.021**
4 - 6	-4.000	5.066	-0.790	0.430	1.000
4 - 2	6.000	5.066	1.184	0.236	1.000
4 - 1	6.667	5.066	1.316	0.188	1.000
4 - 3	12.000	5.066	2.369	0.018	0.375
4 - 5	-15.000	5.066	-2.961	0.003	0.64
6 - 2	2.000	5.066	0.395	0.693	1.000
6 - 1	2.667	5.066	0.526	0.599	1.000
6 - 3	8.000	5.066	1.579	0.114	1.000
6 - 5	11.000	5.066	2.171	0.030	0.628
2 - 1	0.667	5.066	0.132	0.895	1.000
2 - 3	-6.000	5.066	-1.184	0.236	1.000
2 - 5	-9.000	5.066	-1.776	0.076	1.000
1 - 3	-5.333	5.066	-1.053	0.292	1.000

1 - 5	-8.333	5.066	-1.645	0.100	1.000
3 –5	-3.000	5.066	-0.592	0.554	1.000

Each row tests the null hypothesis that the Sample 1 and Sample 2 parameter is the same.

Asymptotic significances (2-sided tests) are displayed. The significance level is 0.05.

Significance values have been adjusted by the Bonferroni correction for multiple tests.

Table 3.13: Pairwise comparisons of the Calcium content of the biomass samples to determine any significance differences. Sample numbers 1 = Alder, 2 = Ash, 3 = Apple, 4 = Birch, 5 = Beech, 6 = Cherry and 7 = Oak.

Sample 1-Sample 2	Test Statistic	Std. Error	Std. Test Statistic	Sig.	Adj. Sig.
1 – 4	-2.000	5.066	-0.395	0.693	1.000
1 – 6	-4.333	5.066	-0.855	0.392	1.000
1 – 5	-7.667	5.066	-1.513	0.130	1.000
1 – 7	-12.000	5.066	-2.369	0.018	0.375
1 – 2	-13.000	5.066	-2.566	0.010	0.216
1 – 3	-17.000	5.066	-3.356	0.001	**0.017**
4 – 6	-2.333	5.066	-0.461	0.645	1.000
4 – 5	-5.667	5.066	-1.119	0.263	1.000
4 – 7	-10.000	5.066	-1.974	0.048	1.000
4 – 2	11.000	5.066	2.171	0.030	0.628
4 – 3	15.000	5.066	2.961	0.003	0.064
6 – 5	3.333	5.066	0.658	0.511	1.000
6 – 7	-7.667	5.066	-1.513	0.130	1.000
6 – 2	8.667	5.066	1.711	0.087	1.000
6 – 3	12.667	5.066	2.500	0.012	0.261
5 – 7	-4.333	5.066	-0.855	0.392	1.000
5 – 2	5.333	5.066	1.053	0.292	1.000
5 – 3	9.333	5.066	1.842	0.065	1.000
7 – 2	1.000	5.066	0.197	0.844	1.000

7 – 3	5.000	5.066	0.987	0.324	1.000
7 – 3	-4.000	5.066	-0.790	0.430	1.000

Each row tests the null hypothesis that the Sample "1" and Sample "2" parameter is the same.

Asymptotic significances (2-sided tests) are displayed. The significance level is .05.

Significance values have been adjusted by the Bonferroni correction for multiple tests.

Table 3.14: Pairwise comparisons of the Chromium content of the biomass samples to determine any significance differences. Sample numbers 1 = Alder, 2 = Ash, 3 = Apple, 4 = Birch, 5 = Beech, 6 = Cherry and 7 = Oak.

Sample 1-Sample 2	Test Statistic	Std. Error	Std. Test Statistic	Sig.	Adj. Sig.
4 – 1	0.333	5.066	0.066	0.948	1.000
4 – 5	-4.667	5.066	-0.921	0.357	1.000
4 – 7	-8.667	5.066	-1.711	0.087	1.000
4 – 2	9.667	5.066	1.908	0.056	1.000
4 – 6	-15-000	5.066	-2.961	0.003	0.064
4 – 3	15.333	5.066	3.027	0.002	0.052
1 – 5	-4.333	5.066	-0.855	0.392	1.000
1 – 7	-8.333	5.066	-1.645	0.100	1.000
1 – 2	-9.333	5.066	-1.842	0.065	1.000
1 – 6	-14.667	5.066	-2.895	0.004	0.080
1 – 3	-15.000	5.066	-2.961	0.003	0.064
5 – 7	-4.000	5.066	-0.790	0.430	1.000
5 – 2	5.000	5.066	0.987	0.324	1.000
5 – 6	-10.333	5.066	-2.040	0.041	0.869
5 – 3	10.667	5.066	2.105	0.035	0.740
7 – 2	1.000	5.066	0.197	0.844	1.000
7 – 6	6.333	5.066	1.250	0.211	1.000
7 – 3	6.667	5.066	1.316	0.188	1.000
2 – 6	-5.333	5.066	-1.053	0.292	1.000

2 – 3	-5.667	5.066	-1.119	0.263	1.000
6 – 3	0.333	5.066	0.066	0.948	1.000

Each row tests the null hypothesis that the Sample "1" and Sample "2" parameter is the same.

Asymptotic significances (2-sided tests) are displayed. The significance level is 0.05.

Significance values have been adjusted by the Bonferroni correction for multiple tests.

Table 3.15: Pairwise comparisons of the Cobalt content of the biomass samples to determine any significance differences. Sample numbers 1 = Alder, 2 = Ash, 3 = Apple, 4 = Birch, 5 = Beech, 6 = Cherry and 7 = Oak.

Sample 1-Sample 2	Test Statistic	Std. Error	Std. Test Statistic	Sig.	Adj. Sig.
4 – 1	1.333	5.066	0.263	0.792	1.000
4 – 2	3.333	5.066	0.658	0.511	1.000
4 – 7	-7.667	5.066	-1.513	0.130	1.000
4 – 6	-8.000	5.066	-1.579	0.114	1.000
4 – 5	-12.667	5.066	-2.500	0.012	0.261
4 – 3	16.000	5.066	3.158	0.002	**0.033**
1 – 2	-2.000	5.066	-0.395	0.693	1.000
1 – 7	-6.333	5.066	-1.250	0.211	1.000
1- 6	-6.667	5.066	-1.316	0.188	1.000
1 – 5	-11.333	5.066	-2.237	0.025	0.531
1 – 3	-14.667	5.066	-2.895	0.004	0.080
2 – 7	-4.333	5.066	-0.855	0.392	1.000
2 – 6	-4.667	5.066	-0.921	0.357	1.000
2 – 5	-9.333	5.066	-1.842	0.065	1.000
2 – 3	-12.667	5.066	-2.500	0.012	0.261
7 – 6	0.333	5.066	0.066	0.948	1.000
7 – 5	5.000	5.066	0.987	0.324	1.000
7 – 3	8.333	5.066	1.645	0.100	1.000
6 – 5	4.667	5.066	0.921	0.357	1.000

6 – 3	8.000	5.066	1.579	0.114	1.000
5 – 3	3.333	5.066	0.658	0.511	1.000

Each row tests the null hypothesis that the Sample “1” and Sample “2” parameter is the same.

Asymptotic significances (2-sided tests) are displayed. The significance level is 0.05.

Significance values have been adjusted by the Bonferroni correction for multiple tests.

Table 3.16: Pairwise comparisons of the Iron content of the biomass samples to determine any significance differences. Sample numbers 1 = Alder, 2 = Ash, 3 = Apple, 4 = Birch, 5 = Beech, 6 = Cherry and 7 = Oak.

Sample 1-Sample 2	Test Statistic	Std. Error	Std. Test Statistic	Sig.	Adj. Sig.
1 - 4	-1.667	5.066	-0.329	0.742	1.000
1 – 5	-5.333	5.066	-1.053	0.292	1.000
1 – 2	-9.333	5.066	-1.842	0.065	1.000
1 – 7	-10.333	5.066	-2.040	0.041	0.869
1 – 3	-15.667	5.066	-3.092	0.002	**0.042**
1 – 6	-16.000	5.066	-3.158	0.002	**0.033**
4 – 5	-3.667	5.066	-0.724	0.469	1.000
4 – 2	7.667	5.066	1.513	0.130	1.000
4 – 7	-8.667	5.066	-1.711	0.087	1.000
4 – 3	14.000	5.066	2.763	0.006	0.120
4 – 6	-14.000	5.066	-2.829	0.005	0.098
5 – 2	4.000	5.066	0.790	0.430	1.000
5 - 7	-5.000	5.066	-0.987	0.324	1.000
5 – 3	10.333	5.066	2.040	0.041	0.869
5 – 6	-10.667	5.066	-2.105	0.35	0.740
2 – 7	-1.0000	5.066	-0.197	0.844	1.000
2 – 3	-6.333	5.066	-1.250	0.211	1.000
2 – 6	-6.667	5.066	-1.316	0.188	1.000
7 – 3	5.333	5.066	1.053	0.292	1.000

7 – 6	5.667	5.066	1.119	0.263	1.000
3 – 6	-0.333	5.066	-0.066	0.948	1.000

Each row tests the null hypothesis that the Sample "1" and Sample "2" parameter is the same.

Asymptotic significances (2-sided tests) are displayed. The significance level is 0.05.

Significance values have been adjusted by the Bonferroni correction for multiple tests.

Table 3.17: Pairwise comparisons of the Manganese content of the biomass samples to determine any significance differences. Sample numbers 1 = Alder, 2 = Ash, 3 = Apple, 4 = Birch, 5 = Beech, 6 = Cherry and 7 = Oak.

Sample 1-Sample 2	Test Statistic	Std. Error	Std. Test Statistic	Sig.	Adj. Sig.
1 – 2	-5.000	5.066	-987	0.324	1.000
1 – 3	-7.667	5.066	-1.513	0.130	1.000
1 – 6	-8.000	5.066	-1.579	0.114	1.000
1 – 4	-9.333	5.066	-1.842	0.065	1.000
1 – 5	-15.000	5.066	-2.961	0.003	0.064
1 – 7	-18.000	5.066	-3.553	0.000	**0.008**
2 – 3	-2.667	5.066	-0.526	0.599	1.000
2 – 6	-3.000	5.066	-0.592	0.554	1.000
2 – 4	-4.333	5.066	-0.855	0.392	1.000
2 – 5	-10.000	5.066	-1.974	0.048	1.000
2 – 7	-13.000	5.066	-2.566	0.010	0.216
3 – 6	-0.333	5.066	-0.066	0.948	1.000
3 – 4	-1.667	5.066	-0.329	0.742	1.000
3 - 5	-7.333	5.066	-1.447	0.148	1.000
3 – 7	-10.333	5.066	-2.040	0.041	0.869
6 – 4	1.333	5.066	0.263	0.792	1.000
6 – 5	7.000	5.066	1.382	0.167	1.000
6 – 7	-10.000	5.066	-1.974	0.048	1.000
4 – 5	-5.667	5.066	-1.119	0.263	1.000

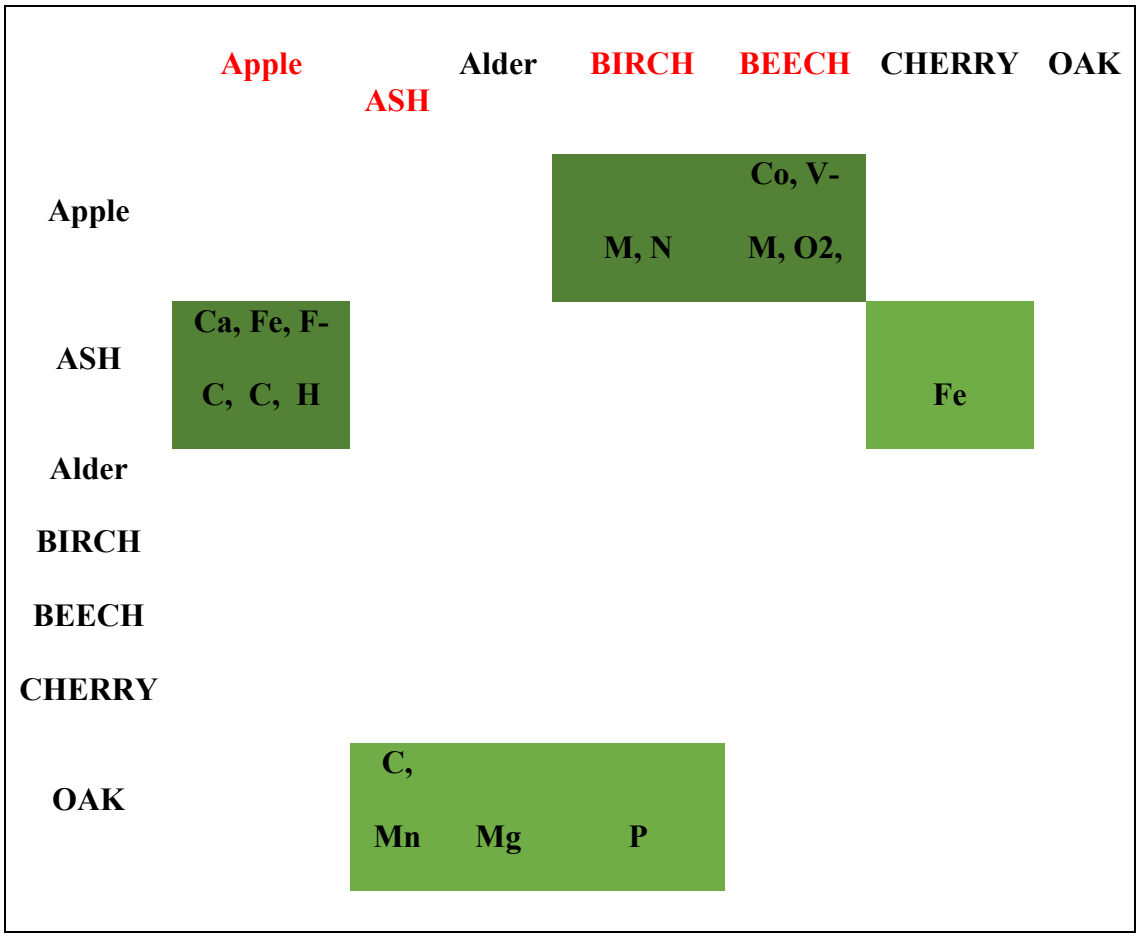
4 – 7	-8.667	5.066	-1.711	0.087	1.000
5 – 7	-3.000	5.066	-0.592	0.554	1.000

Each row tests the null hypothesis that the Sample “1” and Sample “2” parameter is the same.

Asymptotic significances (2-sided tests) are displayed. The significance level is 0.05.

Significance values have been adjusted by the Bonferroni correction for multiple tests.

Table 3.18: Summary of the significantly different characteristics / parameters between the different woodchip biomass samples, where the null Hypothesis was rejected. The four woodchips highlighted in red text were the ones that are most significantly different from one another, based on the characteristics highlighted in the green boxes, and were selected for pyrolysis to generate their associated biochar.



Key: H = hydrogen, **C** = carbon, **N** = nitrogen, **O_2** = oxygen, **V-M** = Volatile Matter, **M** = moisture, **F-C** = fixed-carbon, **Ca** = calcium, **Fe** = iron, **Co**=cobalt, **MN** = manganese, **Mg** = magnesium, **P =** phosphorus.

It is important to note that Table 3.18 was created from the non-parametric Krusal-Wallis pairwise one-way ANOVA test results of biomass characterization parameters (Table 3.1 to Table 3.17) and elemental reflux digested results (Mg, P, Ca, Co, Fe, Cu, Mn,) against the 7 Biomasses. The purpose of this was to corollate characterization parameters with biomass samples in a clearer visualisationing order to help pick out the most outstanding / significant samples (Apple, Ash, Birch, and Beech). These selected samples were chosen for thermal dehydration with the hypothesis mentioned in section 1.11 sub-section 1.11.1 in mind. The expectation here was that these different selected samples will give different sorption results and attachment mechanisms in the sorption experiments.

3.2.1 Analysis of the surface functional groups on the biomass and biochar samples

Several surface functional groups were observed at different frequencies on both the biomass (Table 3.19a) and biochar (Table 3.19b) samples. All seven of the biomass samples (Alder, Apple, Ash, Beech, Birch, Cherry and Oak) had hydrogen bonds with O-H stretching (O-H) (3500-3200 cm^{-1}), aliphatic hydrocarbons (CH_n) at 3000- 2840 cm^{-1}, carboxylic groups (1440-1395 cm^{-1}, 1720-17006 cm^{-1}), nitrogen bonds including N-O stretching (1550-1500 cm^{-1}) and N-H stretching (1650-1580 cm^{-1}), aldehyde (C=O) bonds (1740-1720cm^{-1}), and double-bonded hydrocarbons (benzene stretching C=C) at (1662-1626cm^{-1}) (Bardalai & Mahanta, 2018;Yang et al., 2007a). Pyrolysis has been reported to induce loss of surface functional groups in the biomass regions (cellulose hemicellulose and lignin) but to increase the overall carbon yield (Crombie et al., 2013) (Yang et al., 2007a), which was also observed here upon conversion of the 4 selected biomass samples to biochar (Table 3.19a,b).

Sahoo *et al.* observed when using different temperature (400, 500 and 600^{o}C) to produce biochar from bamboo and pigeon pea stalk (Sahoo et al., 2021), that as the pyrolysis

temperature increased functional groups seen at lower temperature disappeared, while the fixed carbon yield increased. Similar results were documented by Sakhiya et al. (2021) when slow pyrolysis at 500^{o}C of rice straw used to produce its derived biochar. After carbonation of the woodchip biomass samples to their derived biochar, most of the biomass surface functional groups were lost (Table 3.19b) because of thermal degradation. The loss of the aliphatic and hydroxyl groups, which are unstable functional groups brings about a decrease in the H/C ratios, with a subsequent decrease in the O:C ratio due to the effect of decarboxylation and dehydration as a result of the thermal degradation energy (Onorevoli et al., 2018).

Table 3.19a: Surface functional groups determined in the woodchip biomass samples via FTIR analysis.

Wavelength	**Band(s) Assigned**	**Biomass**						
		Alder (cm^{-1})	**Apple (cm^{-1})**	**Ash (cm^{-1})**	**Beech (cm^{-1})**	**Birch (cm^{-1})**	**Chery (cm^{-1})**	**Oak (cm^{-1})**
1300 - 1000	Alcohols, esters, ethers, anhydrides (C-O)	**C-O** 1031 1105 1156 1239	**C-O** 1031 1104 1156 1240	**C-O** 1030 1105 1156 1240	**C-O** 1032 1105 1157 1240	**C-O** 1034 1106 1157 1241	**C-O** 1034 1157 1241	**C-O** 1032 1107 1157 1239
1720-1706 1440-1395	carboxylic acid (O-H)	**O-H** 1422	**O-H** 1423	**O-H** 1422	**O-H** 1422	**O-H** 1423	**O-H** 1424	**O-H** 1422
1390 - 1310	Phenol (O-H)	**O-H** 1371 1324	**O-H** 1371	**O-H** 1373 1323	**O-H** 1370 1323	**O-H** 1326 1373	**O-H** 1371 1322	**O-H** 1326 1365
1550-1500	Nitro compound (N-O)	**N-O** 1504	**N-O** 1504	**N-O** 1505	**N-O** 1505	**N-O** 1504	**N-O** 1503	**N-O** 1506

1650-1580	Amines (N-H)	**N-H** 1594	**N-H** 1594	**N-H** 1593	**N-H** 1594	**N-H** 1594	**N-H**	**N-H** 1595 1624
1740 - 1720	Aldehyde (C=O)	**C=O** 1731	**C=O** 1732	**C=O** 1733	C=O	**C=O** 1731	**C=O 1731**	**C=O** 1729
3000 - 2840	Alkane (C-H)	**C-H** 2921	**C-H** 2895	**C-H** 2922	C-H 2921	**C-H** 2922	**C-H** 2921	**C-H 2921**
1662-1626	Alkene (C=C)	**C=C** 1633	**C=C 1637**	**C=C** 1636	**C=C** 1642	**C=C** 1643	**C=C** 1636	**C=C** -
3550 - 3200	Alcohol (O-H)	**O-H** 3344	**O-H** 3350	**O-H** 3342	**O-H** 3345	**O-H** 3348	**O-H** 3347	**O-H** 3342

Table 3.19b: Analysis of the functional groups present on the surface of the four selected biomass-derived biochar samples, determined from FTIR analysis.

Functional Group	**Bc-Apple (cm^{-1})**	**Bc-Ash (cm^{-1})**	**Bc- Beech (cm^{-1})**	**Bc-Birch (cm^{-1})**
$C\text{-}H_n$ Medium Aliphatic Aromantic	2348	-	-	-
Strong OH Bending	1411	-	-	-
C-H (Aromatic Hydrogen)	871	-	-	-
	784			
	670	603	670	604

Weak C-C Stretching	558	562	583	563

3.2.2 Morphological features of the biomass and biochar

A comparison of the scanning electron microscopy (SEM) images of both biomass and the associated wood-chip derived biochar, i.e., before and after pyrolysis, provided important insights into the morphological changes that occurred during pyrolysis. Figures 3.5a and 3.5b show a morphological metamorphosis of the biomass, triggered by the high temperature during the pyrolysis. SEM images of the biomass shows evidence of blocked pores in the biomass (Figure 3.5) it was difficult to physically see any open pores or large amounts of pore volume from the biomass SEM images. After being subjected to thermal degradation via pyrolysis for 5 hours at 550^{o}C the derived biochar exhibited some physical features that make them attractive for adsorption of inorganic pollutants such as large pores and an increased pore volume (Table 3.20 and Figure 3.2a). The visibility of the pores in the biochar was attributed to the removal of pore-blocking substances that clogged the pore spaces in the biomass via pyrolysis whereby the high temperature led to significant change in the morphology of the biomass derived biochar. These reports align with observations from previous literature (Guizani et al., 2017; Sahoo et al., 2021).

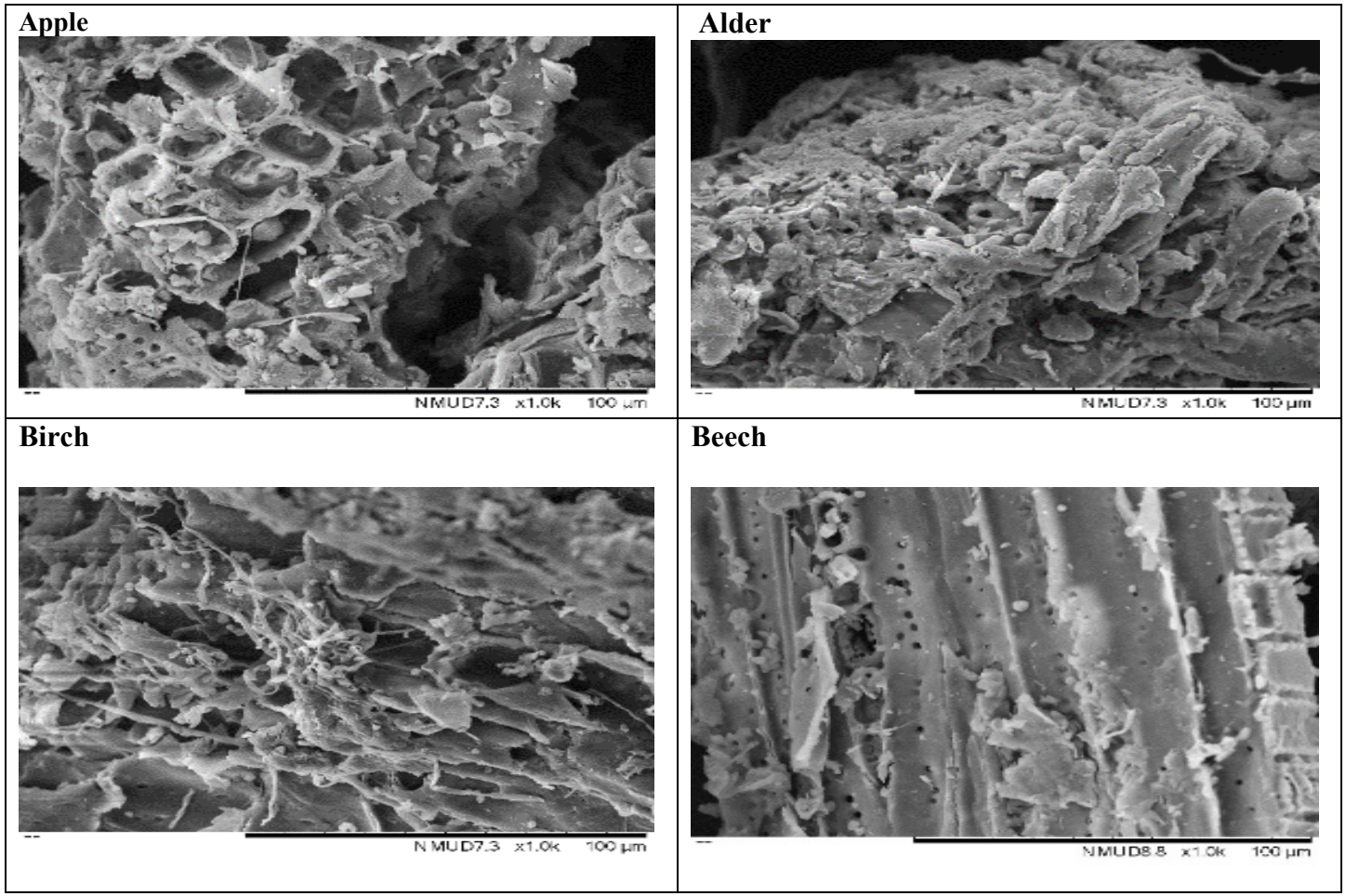


Figure 3.5a: SEM images of selected biomasses showing morphological features such as blocked pores and low pore volume

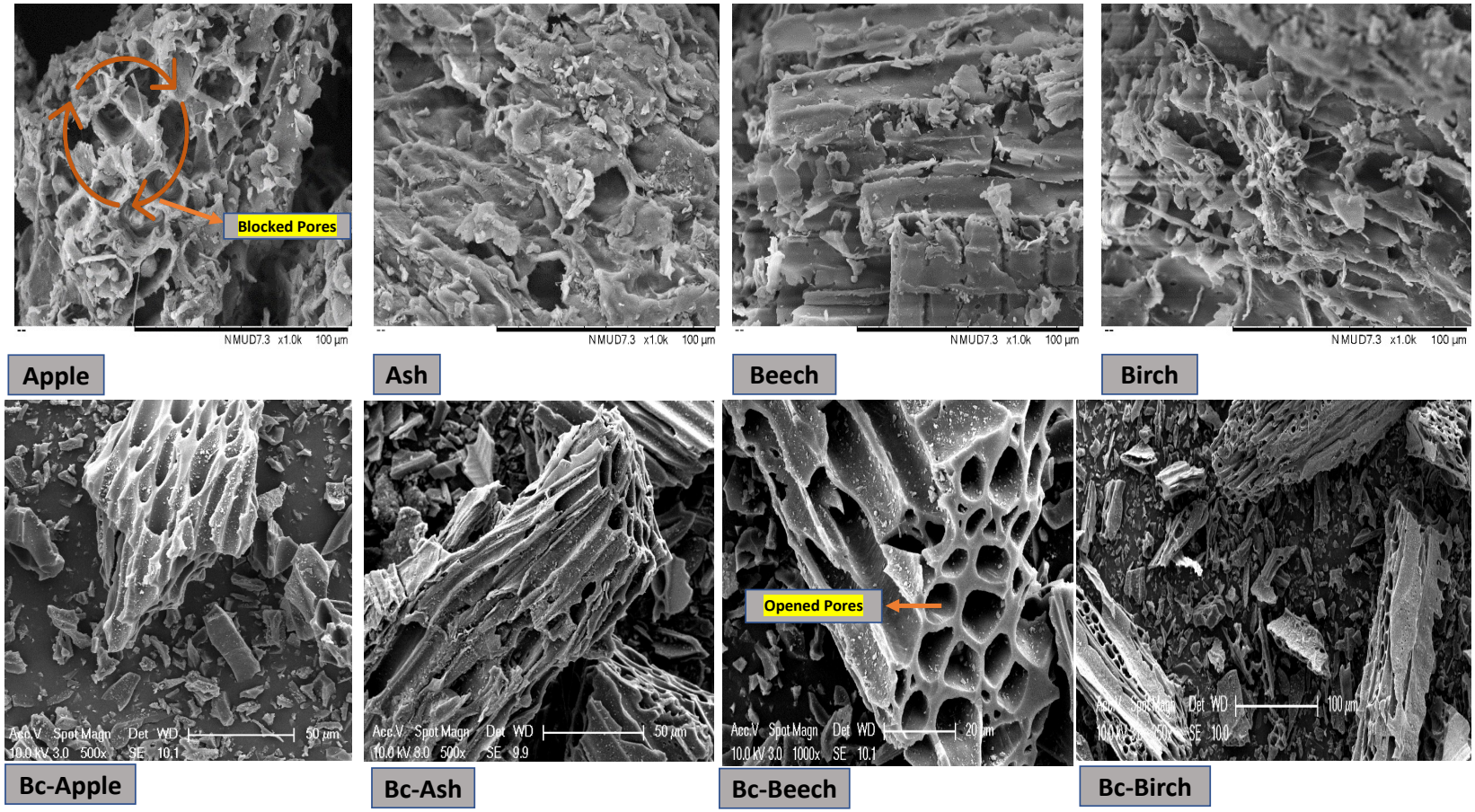


Figure 3.5b: SEM images of selected wood-chip biomass samples and their derived biochar samples showing the effect of pyrolysis (550°C for 5 hour) on the morphological features, especially the opening of blocked pores and the increased pore volume following pyrolysis.

3.2.3 Surface area and porosity of the biomass and biochar samples

The surface area, pore size and volume of the wood-chip derived biochar (Bc-Ash, Bc-Apple, Bc-Beech, and Bc-Birch) increased significantly after pyrolysis as a result of the altered morphological configuration described in section 3.2.2 above. The biomass samples (Ash, Apple, Beech, and Birch) exhibited a low surface area (1.29, 2.64, 3.38 and 1.96 g/m^2, respectively) until it was subjected to slow pyrolysis in an oxygen limited environment. The pyrolysis process led to a dramatic increase in surface area (307.3, 314.42, 305.07 and 287.3 g/m^2, respectively for the Bc-Ash, Bc-Apple, Bc-Beech, and Bc-Birch samples). The thermal degradation energy helps to expel trapped volatiles and other substances, thus creating room for the increase in pore size, pore volume and surface area in the biochar sample relative to their biomass precursors (Table 3.3).

Table 3.20: Summary of the characterization of the four biochar samples. Comparison with Table 3.1 indicates the morphological changes caused by pyrolysis temperature.

Properties	Bc-Ash	Bc-Apple	Bc-Beech	Bc-Birch
BET area (m^2/g)	307.31±7.3074	314.21±7.3119	305.07±7.275	287.32±6.768
Pore size (Å)	20.7	21.0	21.2	21.1
Pore volume (cm^3/g)	0.1	0.1	0.1	0.1
C %	67.7	93.9	85.6	86.1
H %	1.3	1.9	1.2	1.8
N %	0.3	0.3	0.2	0.2
O %	-	-	-	-
H/C_{org}	0.2	0.3	0.3	0.3
Zeta Potential (mV)	-22	-28.6	-24.0	-29.4

3.3 Biochar Stability

Biochar stability refers to the molecular morphology of carbon present in it. The carbon structure in biochar mainly comprises of polycyclic-aromatic compounds with little or nonaliphatic compounds. Various morphological indexes have been developed to help in predicting the stability of biochar produced from different biomass sources. These indexes include the polyromantic ring structures (polycyclic aromatic compounds e.g., benzene) indexes and biochemical stability determined based on elemental ratios i.e., O:C and H:C (Igalavithana et al., 2017), which is reasonable considering that biochar stability arises from its physical and chemical properties (the so-called proximate and ultimate characteristics). Ratios of Carbon to oxygen (O:C) and hydrogen (H:C), as proposed by Spokas and Budhai (Spokas, 2010; Budai et al., 2017), are useful in biochar stability

determination. Both researchers came up with maximum accepted values of 0.4 and 0.7 for O:C and H:C respectively. These values agree with the European Biochar Certificate (EBC) and International Biochar Initiative (IBI). The IBI believes that the H:C is more accurate in determining the stability of biochar based on the experimental challenges in the determination of the O content in the O:C ratio, which is through indirect calculations which may be exaggerated (H. Wang et al., 2021). Biochar's stability is correlated with the H:C ratio (aromaticity) and / or the O:C ratio (maturity) ratio, according to the IBI. Basically, the ratio of polycyclic aromatic compounds to that of aliphatic compounds determines the stability of biochar, which has been interpreted by its aromaticity / maturity (Wang *et al.*, 2021, 2022).

It can be observed that as the pyrolysis temperature increases, the formation of biochar through slow pyrolysis becomes better, although there are losses of surface morphological structures that bring about a corresponding increase in pore sizes, volume, and surface area (indicated as the red dots in Figure 3.6). The data generated herein and presented in Table 3.2 explains the effect of pyrolysis on the biomass properties leading to a highly carbonated biochar samples with high surface areas. It is important to state that biochar stability in this work was determined using the organic carbon fraction H:C_{org} which is in line with IBI recommendations and previous literature (H. Wang et al., 2021). Biochar H:C_{org} values (0.2, 0.3. 0.3 and 0.3 for Ash, Apple, Beech, and Birch, biochar respectively) were within the IBI and EBC accepted regions, as seen in Figure 3.6.

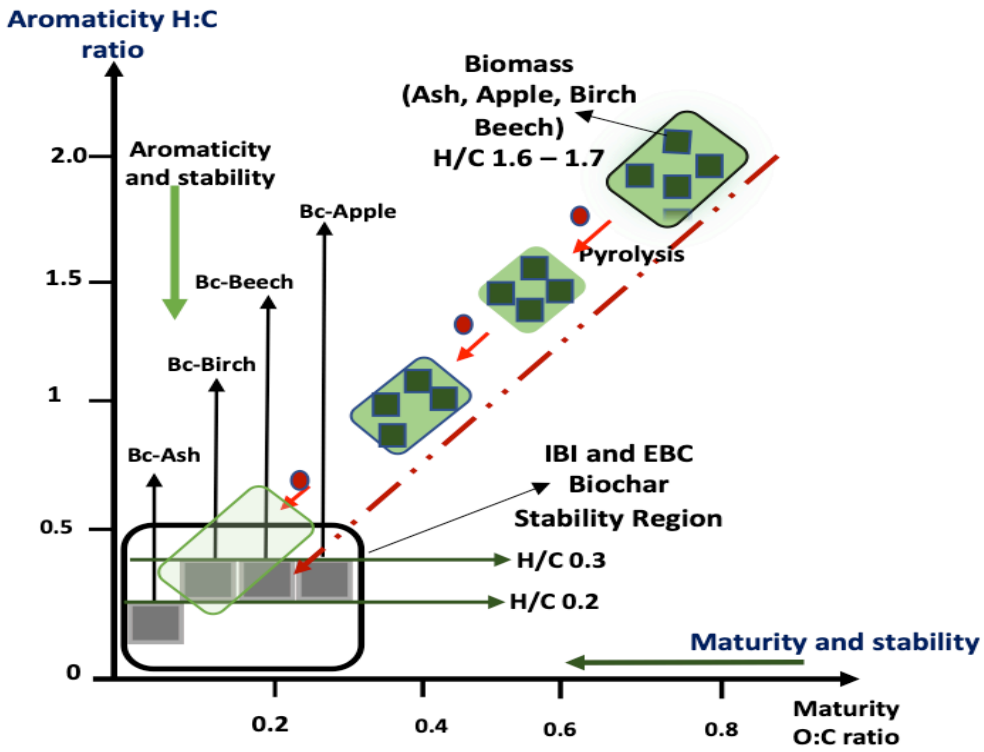


Figure 3.6: Schematic illustration of a van Krevelen Diagram showing biochar stability. These types of diagrams are used to plot the hydrogen: carbon atomic ratio (aromaticity) as a function of the oxygen: carbon atomic ratio, which in the original utilisation of these plots could be used as an indicator of the ability of a rock to produce oil during maturation. In the biochar context the ratio is used to confirm its stability during the conversion of biomass into biochar (Weber & Quicker, 2018; Jafri et al., 2018; Aller et al., 2017; Manyà et al., 2014).

3.4 Conclusion

Seven woodchip biomasses (Ash, Apple, Alder, Birch, Beech, Cherry, and Oak) were acquired, elementally digested, characterized for their ultimate/ proximate values and subjected to statistical analysis using one-way ANOVA in a pairwise manner, and shown schematically in Figure 3.1. The reason for the detailed characterisation of the biomass samples was to identify a sub-set of biomass samples that were significantly different from each other in terms of their physio-chemical characteristics and elemental compositions. Based on this characterisation and analysis, four biomass samples (Ash, Apple, Birch, and Beech) were chosen and thermally dehydrated to produce the derived biochar samples (Bc-Ash, Bc-Apple, Bc- Birch and Bc-Beech) which were then subjected to the same set of characterisation steps as the parent biomass samples. The next chapter (Chapter 4) explores the potential of woodchip biomass and the derived biochar for adsorption of Ni^{2+} & Pb^{2+} individually and in combination, with the working hypothesis that the different biomass / biochar properties would result in different sorption efficiencies and removal or attachment mechanism.

CHAPTER 4

SORPTION OF HEAVY METALS ON WOODCHIPS BIOMASS AND DERIVED BIOCHAR-ANALYSIS OF THE DRIVERS AND MECHANISM

4.0 Introduction

Biochar has been widely used in environmental applications either as an adsorbent in sorption experiments (Yi et al., 2021), or in agriculture for soil amendment (Canatoy et al., 2021). However, depending on the specific biochar application, its efficiency as an adsorbent depends on the effectiveness of the pyrolysis process coupled with its characterization parameters (Weber & Quicker, 2018). Assessment of different characterization parameters of wood-biomass and its derived biochar on the extent to which these characteristics affect or influence sorption is important in Biochar application, sorption studies, and for optimisation purposes when designing hybrid biochars with greater application efficiency.

During sorption, the main active parameters involved are those present on the surface (biochar active sites, surface functional groups and pore-size/volume) where interactions take place between adsorbent and adsorbate. Other parameters such as C, H, N, O, (atomic ratio of H:C_{org}, O/C) provide a measure of the maturity/stability of the biochar, plus the zeta potential or surface charge associated with the biochar surface, complement the features of biochar as an adsorbent and increase the prestige biochar has in environmental applications (as discussed in Chapter 1). Some of these parameters work independently (negative surface where attachment by precipitation takes place) during sorption experiments, while others act in synergy (active site plus surface functional group encouraging attachment by complexation) as shown in Figure 1.6. It is important to know

or infer which parameter(s) are responsible for certain sorption activities. For example, (Iamsaard et al., 2021) observed that the surface area acts together with the number of interconnected pores and / or the surface functional groups which are linked to the cation exchange capacity, and the interplay between these characteristics has been credited as the mechanism responsible for adsorption/absorption of Ni^{2+}, Zn^{2+} and Cu^{2+} onto Biochar in sorption experiments. Recent studies reported that adsorption or absorption (sorption) relates directly to surface area and morphology where different sorption types co- exist (Chemi-sorption, Physi-sorption, Surface Area, Pore Filling Hydrogen Bonding and Ion exchange precipitation, complexation) (P. Zhang et al., 2020;Schreiter et al., 2018;Oliveira et al., 2017).

Other studies focus on how biomass derived-biochar H/C and O/C ratios (which reflect the biochar maturity and stability) stand as fundamental properties in determining the efficacy of application in the environment`(M. Zhao et al., 2020; Z. Zhao et al., 2019). It is necessary to understand the relative importance of these different parameter(s) to the experimental objectives of using biochar for remediation of different pollutants, in order to identify the optimal combination of characteristics for specific applications. In this regard, different statistical approaches have been employed to correlate biochar characteristics and adsorption profiles, but the most common of them is principal component analysis (PCA).

PCA is a multivariate statistical technique that helps in retrieving information from greater dimensional correlated multivariate data by re-grouping them into a lower dimensional space (Li, Cheng, and Wu, 2016; Aidoo et al., 2021). Basically, it involves some mathematical procedures that streamline the dimensions of a given variable by rebuilding them into an uncorrelated combination (Q. Liu et al., 2021; F. C. Wu & Chyu, 2004), and collating variables that account for the highest amount of variance to form the

first principal component (PC1), then PC2 accounts for the next largest amount of variance and it progresses in that manner (Q. Liu et al., 2021; F. C. Wu & Chyu, 2004). PCA provides several gains for the user such as clarification of multivariate relationships, reduction of high-dimensional variables and identification of dependencies amongst a given set of variables (Aidoo et al., 2021;Liu et al., 2021;Wu and Management, 2004). PCA is applied to characterization parameters to re-group those parameters working together as component(s) to achieve optimum sorption of selected biomass and its derived biochar (Bc) ((Bc-Apple, Bc-Ash, Bc-Birch and Bc-Beech) for their baseline-sorption for Nickel and Lead (Ni^{2+} and Pb^{2+}) contaminants. Interactions amongst these parameters will be evaluated and conclusions will be drawn based on the aims and objectives of this chapter, namely, to identify the adsorption mechanisms of a range of wood chip derived biomass samples for metal pollutants. This chapter aims to subject biomass derived char to baseline analysis with the hypothesis that the significant difference observed amongst selected the inputs biomasses will be transferred to their derived biochar and possibly influence the binding/attachment mechanism of adsorbate to the adsorbent.

4.1 Methodology: Sorption experiments

Selected Woodchip samples (Ash, Apple, Beech, and Birch, see Table 3.2.17) showed the most variability in terms of elemental composition, proximate and ultimate characterisation parameters plus statistical (SPSS) evaluation as shown in Chapter 3, Sections 3.2.1 to 3.2.16. Biochar samples were weighed (1.5, 1, 0.5 and 0.3g) to assess the impact of biochar mass at constant pollutant dosage on adsorption efficiency, and samples were placed into 50 mL falcon tubes awaiting sorption experiments (see Figure 4.1 for the set-up).

Nickel (11) chloride hexahydrate ($NiCl_2.6H_20$) and Lead chloride ($PbCl_2$) were purchased from Sigma Aldrich with product codes 6136-100G and CHE2318 respectively. The percentages and concentrations of Ni & Pb were calculated as follows: $NiCl_2.6H_20$ equals 237.7g/mol (Ni 58.7 g/mol, Cl_2 70.9 g/mol, $6H_20$ 108 g/mol) and 1 g $NiCl_2.6H_20$ in 50 mL results in a Ni concentration of 4938 ppm which is % 24.7% of the entire compound ($NiCl_2.6H_20$). 500ppm of $Ni^{2+}$was then diluted out of stock solution (4938 ppm) into several 50 mL tubes ready for sorption experiments with biochar samples, while $PbCl_2$ equals 278.1 g/mol (Pb 207.2 g/mol, $Cl_2$70.9 g/mol, and 1g $PbCl_2$ in 50 mL is %Pb 207.2 g/mol is % 74.5 (14,900ppm). 500ppm of (Pb^{2+}) was calculated out of the stock (14,900ppm) into a 50 mL falcon tube for the preceding baseline experiments.

Sorption experiments were carried out in a shaker (Benchmark INCU-Shaker) with samples placed in a rack (to prevent falling). The shaker was programmed for 24 hours at 161 rpm at room temperature. 0.3g, 0.5g, 1g and 1.5g biochar were all placed into 50 mL falcon tubes (Figure 4.1). 10 mL of 500 ppm (Ni and Pb) was placed into these tubes singularly or as a binary mixture (i.e., one metal per tube and two metals per tube, respectively) and incubated / shaken for 12 hours. Samples were placed into these tubes in triplicate with a control (containing samples and deionized water). These biomass and derived biochar samples (50 mL falcon tubes in the shaker) were taken periodically in triplicate (1, 3, 5, 8 and 12 hours) for centrifugation (25 ^oC, 15 mins at 3500 rpm) following the extraction (10 mL pipette) of the supernatant (which was discarded) and reflux digestion.

ICP-OES Calibration Standards (CS) were purchased from Sigma Aldrich at 1000 ppm concentrations. CS of the metals of interest (Nickel and Lead) were prepared in 50 mL falcon tubes. Calibration Curves were prepared using ICP-OES (Perkin Elmer optima 8000) for metal identification and quantification and were fitted in a linear manner having

an R^2 value of 0.9997. These standards were made as a cocktail then serially diluted to different concentrations (10 ppm, 7.5 ppm, 5 ppm, 2.5 ppm, 1 ppm and 0 ppm) in 50 mL tubes. The internal standards used were Germanium (an element in group 14 of the periodic table, which can be used as an internal standard in ICP-OES/MS analysis to correct for variations in sensitivity and also to improve precision and accuracy) (Eickhorst & Seubert, 2004)) and Bismuth (element 83 in the periodic table, it has similar behaviour as lead and shares very close physiochemical properties) were spiked (50 µL) into all samples and standards (specifically for Nickel and Lead identification, respectively) to validate the ICP-OES analytical method (See Appendix B for the calibration curves). All biomass (Apple, Ash, Alder, Birch, Beech, cheery and Oak) and biochar samples (Apple Biochar, Ash biochar, Birch Biochar, and Beech Biochar) were analysed using ICP-OES.

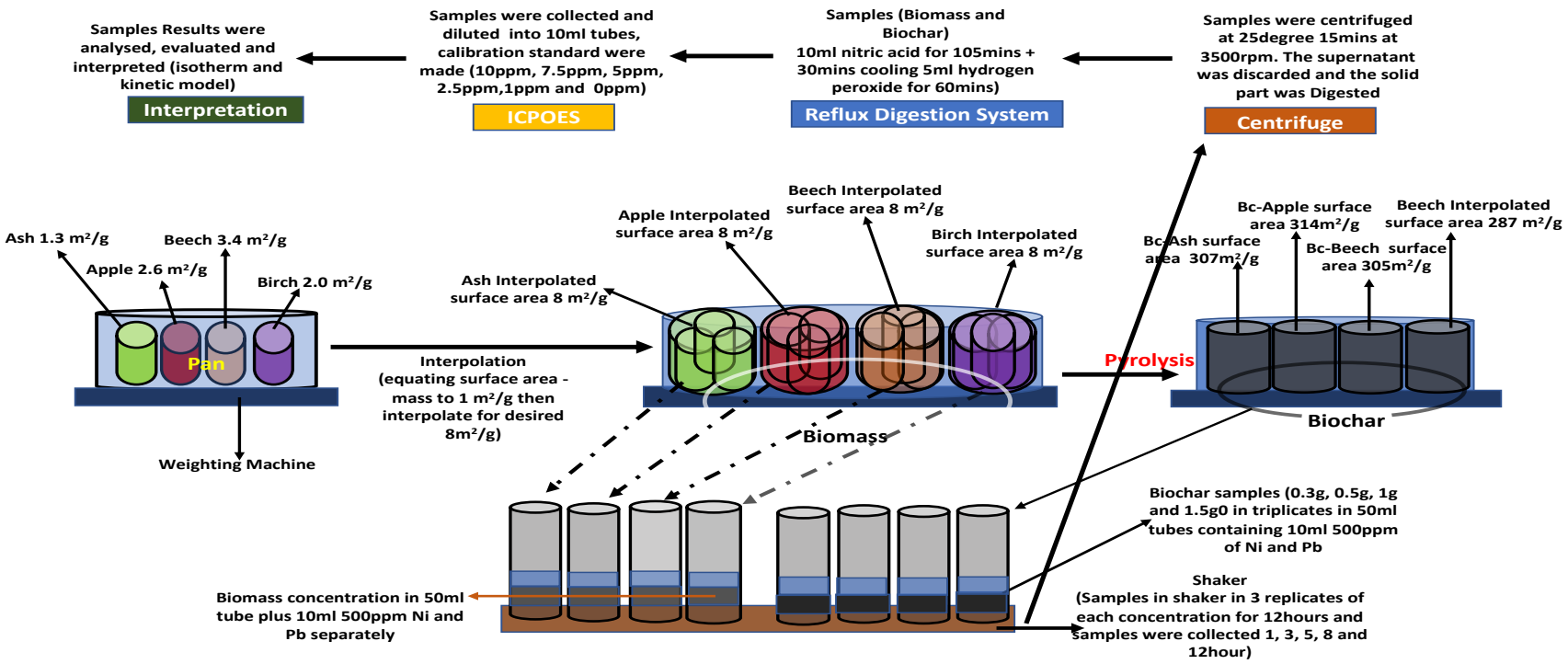


Figure 4.1: Schematic of the sorption experiment setup (shaker, weighting pan, falcon tubes, Centrifuge, Reflux digestion system, ICP-OES) with selected biomass samples (having interpolated equivalent surface areas for each) following conversion to its derived biochar (Bc-Ash, Bc-Apple, Bc-Beech and Bc-Birch) in falcon tubes in triplicate in a shaker (collected at intervals) before centrifugation, reflux digestion, ICP-OES analysis and interpretation.

4.2.1 Biochar Sorption of Ni^{2+} and Pb^{2+}

Principal component analysis (PCA) is a linear dimensionality reduction method that seeks to construct a meaningful representation of the dataset by linearly combining characteristics in the original high dimensional dataset. It was applied to provide insight into the similarity and patterns that exist in the biochar adsorption datasets based on the features of the different biochar samples. Based on their similarity, data can be clustered in a PCA plot. Thus, PCA plot explains variations and takes into consideration the various ways that the original features have been influenced based on the differences observed in the clusters. PCA analysis of the biochar adsorption results clearly identifies pyrolysis temperature and its resulting biochar characterization parameters as the driving force in actualization of the maximum sorption of Ni^{2+} and Pb^{2+} ions (Figure 4.2 and Table 4.1). Research has shown that the source of the biochar feedstock significantly affects its adsorption capacity (Higashikawa et al., 2016). A significant increase in the active sites on all derived biochar samples (Bc-Ash, Bc-Apple, Bc-Beech, and Bc-Birch) relative to their respective biomasses was observed, with the Bc surface morphology being active and ready to adsorb contaminants via hydrogen bonding/electrostatic interaction onto its charged surface. Additionally, it has been reported that the mechanism of metal adsorption could also include the exchange of metals with Ca^{2+}, Mg^{2+}, K^{+}, and Na^{+}, electrostatic attraction of the Ni^{2+} and Pb^{2+} cationic metals at sites of negative charge, and the surface complexation of metals with carboxyl and hydroxyl functional groups on biochar surfaces, in addition to hydrogen bonding (Higashikawa et al., 2016; Mahdi et al., 2018b).

The pyrolysis temperature greatly influenced the surface morphological features by unblocking pores/increasing pores/pore volume relative to the initial biomass (see Figure

3.2a,b and Table 3.2 and Table 4.2), reducing the amount of volatile matter present (loss of surface functional groups), reducing aromaticity/polarity (thereby increasing stability) and increasing the surface area (active sites where adsorption reactions take place) as seen in the comparison in Figure 3.2 and Table 3.3. It has been proven that when the pyrolysis temperature was increased from 400 °C to 900 °C, the surface area of the biochar enlarged and the capacity for Ni^{2+} and Pb^{2+} adsorption increased (Smoak & Schnoor, 2022). Biochar is produced by pyrolyzing biomass, and its physiochemical properties vary depending on several process factors such as residence time, gas atmosphere, and heat rate (Hart et al., 2023). The production conditions influence the adsorption capacity of the resulting biochar. Consequently, the surface characteristics and pore structure vary depending on the amount of carbon and functional groups present in the biochar. Whilst high pyrolysis temperature improves surface area, pore structure, and carbon content, it can affect the functional groups on the surface of the biochar, which provides the charges responsible for electrostatic attraction of contaminants (Hart et al., 2023).

Evaluation of the biochar adsorption results (Table 4.3) shows that the first hour was crucial for reactions (adsorption) happening on the active sites of biochar. A large proportion of interaction between adsorbate and adsorbent took place during the first hour and progressed towards equilibrium from the 3rd to the 12th hour for both $Ni^{2+}$and Pb^{2+}as seen in Figure 4.3a and b, respectively. The attachment mechanism responsible for binding adsorbate to adsorbent was mainly precipitation (Figure 1.6) as there were no observed functional groups after thermal dehydration. PCA analysis on the derived biochar(s) characterization parameters for Ni and Pb sorption produced three (3) components each, as shown in Tables 4.1 and 4.2 for Ni and Pb, respectively. These components differ from those realised from the biomass PCA (2 components as shown in appendix E confirming the effectiveness of the thermal degradation on the samples. The

components realised from the PCA (Tables 4.1 and 4.2 -dimension reduction) and shown in Figure 4.3a and b give insight into the biochar interactions with the metal ion pollutants and highlights its active sites via the key parameters loaded onto the different principal components at different loading values. The PCA analysis regroups characterization parameters in respect to how they affect the total variance in the samples, which then gives a better understanding of the mechanism of adsorption.

For Nickel sorption to biochar, the statistical dimension reduction (PCA) analysis gave 3 components which accounted for 99.5% of the variance. The first component (PC1) loaded four (4) characterization parameter (pore-size, Nitrogen, H/C_{org} and carbon content) which incorporated 49.40% of the variance and describes the physiochemical abilities of biochar as an adsorbent (well distributed pore sizes, good stability ratio and high carbon content). The results of an Analysis of Variance (ANOVA) showed that there was a statistically significant ($p < 0.01$) relationship between the temperature of pyrolysis and surface area (Smoak & Schnoor, 2022). Thus, for most biochar applications, larger surface area is preferred, hence higher pyrolysis temperatures could be ideal to produce characteristic features highlighted by the PC1. This is probably because volatile organic matters decomposes more thoroughly at higher temperatures, while the carbon content of the biochar increases. Consequently, the biochar pore network structure opens and the surface structure interconnectivity increases. The results agree with findings reported in the literature that the temperature at which biomass was pyrolyzed had a substantial impact on the biochar's characteristics (e.g., surface area, pore size, and carbon content) and can be critical to the adsorption process and capacity for sorption of Pb^{2+} and Ni^{2+} (W. Ding et al., 2014). The second component (PC2) accounted for 29.9% of the\variance and loaded three (3) biochar characterization parameters (Ni-adsorption, H content and

zeta potential). The third component (PC3) supports the first two by providing the medium/interface where absorption and adsorption took place.

It loaded two (2) characterization parameter (surface area and pore volume) and covered 20.7% of the variance. The pore volume and pore size go hand in hand with one another. The interconnectivity of the aligned pores increases the pore volume and brings about greater adsorption, while the surface area creates a platform for bonding and experimental reactions to take place. For adsorption to occur, there must be mass transfer of contaminants from a liquid phase to a solid phase biochar adsorbent. Thus, the intra-particle diffusion of contaminants, which depends on the pore size, plays a critical role in the adsorption process. Hence, if the pore size is too small, it would result in poor diffusion rates in the channels, thus the intraparticle diffusion limitation may increase relative to the size of the Ni^{2+} and Pb^{2+}. The larger the surface area, the more metal ions adsorbed, which implies higher adsorption capacity. The interaction between the contaminant and the biochar surface involves an exchange mechanism and its active sites. The biochar surfaces can interact with Ni^{2+} and Pb^{2+} ions in wastewater through the Van der Waals force, hydrogen bonding, ion exchange, and electrostatic attraction (Hart et al., 2023). The PCs for Lead-sorption to the biochar samples (dimension reduction) produced three (3) PCs, like that of Nickel, accounting for 99.8% of variance. five (5) characterization parameters (H/C_{org}, N, pore size, carbon, and zeta potential) were loaded in PC1 which captured 57% of the variance. This component is interpreted as describing bulk absorption based on its features (pore-interconnectivity, stability/maturity, and surface charges). PC2 accounts for 23% of the variance and holds two (2) biochar characterization parameters (pore volume and surface area). This component explains the platform for which sorption takes place (surface or bulk) either as a surface phenomenon (adsorption) or whole bulk (absorption). Based on results reported in the literature, the

temperature at which the biomass was pyrolysed and the surface area, pore volume, and pore size of the biochar are strongly connected with metal ion adsorption uptake (Mahdi et al., 2018). Hence, the results of the PCA are consistent with the literature in which increased adsorption capacity can be linked to the physiochemical properties of the biochar produced, such as surface area, pore volumes, pore size distribution, carbon content, and the accessibility of surface functional groups. It has also been reported that biochar with a large surface area and a mesoporous structure exhibited high adsorption capacity for Ni^{2+} (Vidhya et al., 2020).

PC3 (19% of the variance) has only one characteristic parameter (hydrogen), and it explains the most likely chemical bond on the surface of biochar and gives insights into the possibilities of an attachment mechanism triggered by surface charges and hydrogen bond. Published studies have proven that biochars with large surface area and more porous morphology such as high pore volumes and hierarchical pore structure are more effective in adsorbing heavy metals including nickel (Ni) and lead (Pb) on their surface via hydrogen bonding (Hidayat et al., 2018; Fahmi et al., 2018). This is because the hierarchical pore structure promotes mass transport by lowering pore diffusion restrictions of the contaminants and grants easy accessibility to the adsorbent active sites. In the literature, the hydrophilicity index of biochar is measured by the O/C ratio, which is indicative of biochar surface functional groups that include oxygen, such as the carboxyl group, while the H/C ratio is an indicator of biochar stability, with values less than 0.7 implying high stability (Fahmi et al., 2018). Thus, adsorption capacity and efficiency of biochar as an adsorbent for Ni^{2+} and Pb^{2+} can be improved by lowering the diffusion path length and exposing the inner pores and their functional groups through particle size reduction.

It possibly implies that hydrogen bonding or an associated bonding type may likely be the mechanism for adsorption aided by surface electrostatic interactions on the active sites interacting with charged atoms on the targeted pollutants. Polar surface area (regions of a molecular surfaces designated to oxygen, attached hydrogen and nitrogen) has been suggestive to be an index for measuring H-bonding capacity (X. F. Tan et al., 2021). The working hypothesis that the different selected samples will bring about differences in adsorption with their derived biochar samples and different removal mechanism was not found to be the case (the null hypothesis) was rejected as thermal dehydration removed the significant differences observed amongst the selected biomasses.

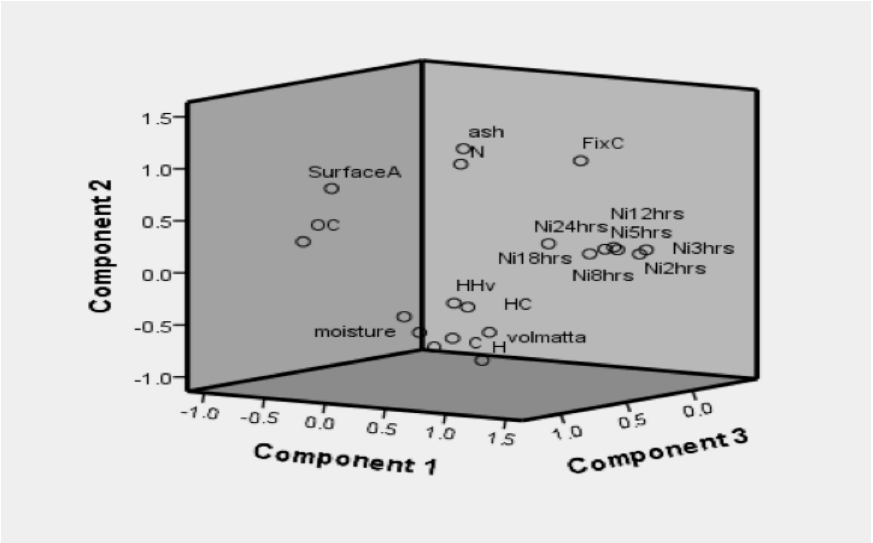


Figure 4.2a: PCA component plot in rotated space showing the loading of Ni^{2+} adsorption to Biochar. Scree plot showing Eigen Values > 1 representing the number of components (loaded characterization parameters) that is required to account for the variance in the data.

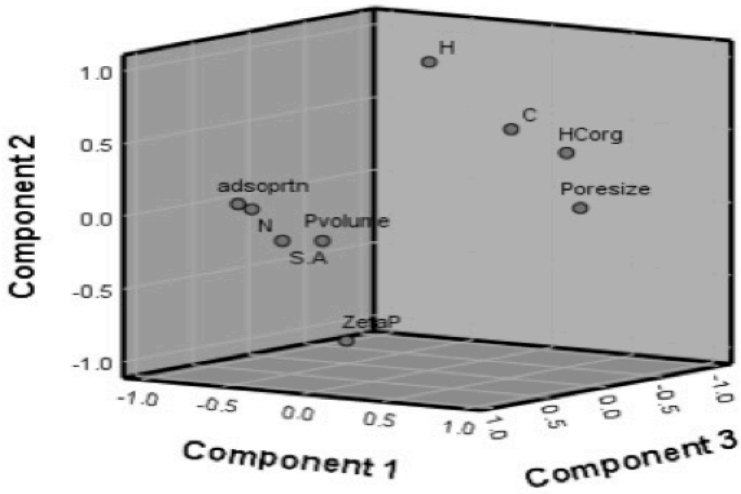


Figure 4.2b: PCA component loading of Pb^{2+} adsorption to Biochar. Scree plot showing Eigen Values > 1 representing the number of components (loaded characterization parameters) needed to account for the variance in the dataset.

Table 4.1: PCA of characterization parameters for Nickel Sorption to Biochar, showing total variance (%) by Eigen values >1 with the corresponding components in order of hierarchy (highest to low).

Total Variance Explained									
Component	**Initial Eigenvalues**			**Extraction Sums of Squared Loadings**			**Rotation Sums of Squared Loadings**		
	Total	**% of Variance**	**Cumulative %**	**Total**	**% of Variance**	**Cumulative %**	**Total**	**% of Variance**	**Cumulative %**
1	4.446	49.403	49.403	4.446	49.403	49.403	4.154	46.154	46.154
2	2.69	29.885	79.288	2.69	29.885	79.288	2.728	30.316	76.469
3	1.864	20.712	100	1.864	20.712	100	2.118	23.531	100
Extraction Method: Principal Component Analysis.									

Table 4.2: PCA of characterization parameters for Lead sorption to Biochar, showing the Total Variance (%) by Eigen values >1 with its corresponding components in order of hierarchy (highest to low).

Component	**Initial Eigenvalues**			**Extraction Sums of Squared Loadings**			**Rotation Sums of Squared Loadings**		
	Total	**% Of Variance**	**Cumulative %**	**Total**	**% Of Variance**	**Cumulative %**	**Total**	**% Of Variance**	**Cumulative %**
1	5.134	57.041	57.041	5.134	57.041	57.041	4.283	47.591	47.591
2	2.103	23.371	80.412	2.103	23.371	80.412	2.518	27.978	75.569
3	1.763	19.588	100	1.763	19.588	100	2.199	24.431	100

Extraction Method: Principal Component Analysis

Table 4.3a: Baseline sorption experiment of Ni^{2+} to biochar, in mg/g, to determine the sorption capacity of the different biochar samples with respect to time. A constant concentration of Ni (500 ppm) was used, and the incubation time was 12 hours, at different dosages (0.3g, 0.5g, 1g, 1.5g) of the respective derived biochar (Ash, Apple, Birch, Beech).

Sample	Time hours	0.3 mg/g	0.5 mg/g	1 mg/g	1.5 mg/g
Bc-Ash	**1**	0.83	0.82	0.82	0.81
	3	0.83	0.82	0.82	0.81
	5	0.83	0.82	0.82	0.81
	8	0.83	0.82	0.82	0.80
	12	0.83	0.82	0.82	0.81
Bc-Apple	**1**	0.83	0.82	0.82	0.81
	3	0.83	0.82	0.82	0.80
	5	0.83	0.82	0.82	0.81
	8	0.82	0.82	0.81	0.80
	12	0.82	0.82	0.81	0.81
Bc-Beech	**1**	0.82	0.81	0.80	0.79
	3	0.82	0.82	0.89	0.78
	5	0.82	0.81	0.78	0.78
	8	0.82	0.81	0.87	0.76
	12	0.82	0.81	0.80	0.77
Bc-Birch	**1**	0.83	0.82	0.80	0.81
	3	0.83	0.82	0.89	0.80
	5	0.83	0.82	0.80	0.81
	8	0.83	0.82	0.87	0.80
	12	0.82	0.82	0.80	0.79

Table 4.3b: Baseline sorption experiment of Pb^{2+} to biochar, in mg/g, to determine the sorption capacity of the different biochar samples with respect to time. A constant concentration of Pb (500 ppm) was used, and the incubation time was 12 hours, at different dosages (0.3g, 0.5g, 1g, 1.5g) of the respective derived biochar (Ash, Apple, Birch, Beech).

Sample	**Time**	**0.3 mg/g**	**0.5 mg/g**	**1 mg/g**	**1.5 mg/g**
Bc-Ash	1	0.81	0.80	0.79	0.79
	2	0.81	0.80	0.79	0.79
	3	0.81	0.80	0.79	0.81
	4	0.81	0.79	0.80	0.79
	5	0.80	0.78	0.81	0.79
Bc-Apple	1	0.79	0.79	0.79	0.81
	2	0.79	0.78	0.79	0.81
	3	0.807	0.78	0.80	0.80
	4	0.79	0.79	0.79	0.79
	5	0.79	0.79	0.80	0.79
Bc-Beech	1	0.803	0.79	0.79	0.79
	2	0.79	0.81	0.80	0.79
	3	0.79	0.79	0.80	0.80
	4	0.80	0.79	0.81	0.81
	5	0.80	0.80	0.81	0.81
Bc-Birch	1	0.80	0.80	0.79	0.80
	2	0.80	0.79	0.79	0.80
	3	0.79	0.79	0.78	0.80
	4	0.78	0.79	0.77	0.80
	5	0.79	0.79	0.77	0.79

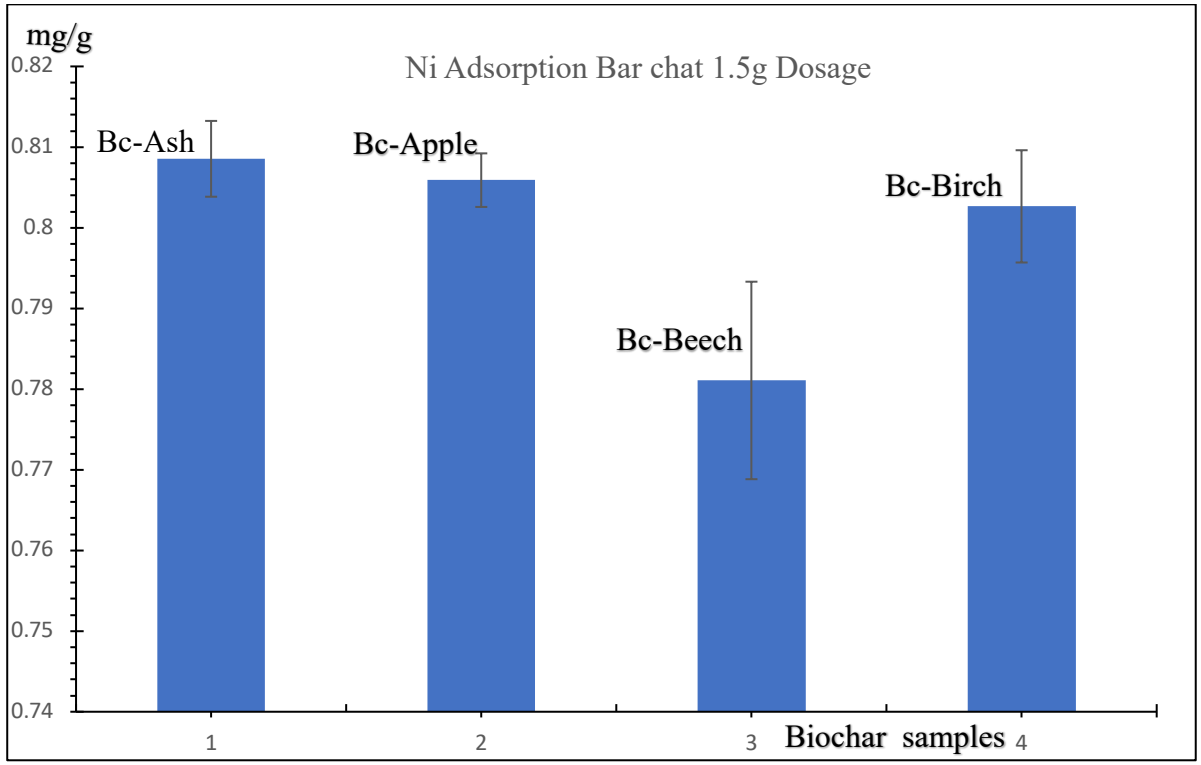


Figure 4.3 (a): Bar chart showing the standard error of derived biochar (Bc-Ash, Bc-Apple, Bc-Beech, and Bc-Birch) average adsorption values ± Standard deviation (n = 4) of Pb^{2+} of Ni^{2+} (mg/g) at 1.5g dosage biochar in an incubation time frame of 12 hours (1,3,5,8 and 12). At a constant concentration of Ni (500 ppm) to monitor the sorption rate in relation to time and biochar mass and to infer the most effective biochar in terms of Ni^{2+} sorption.

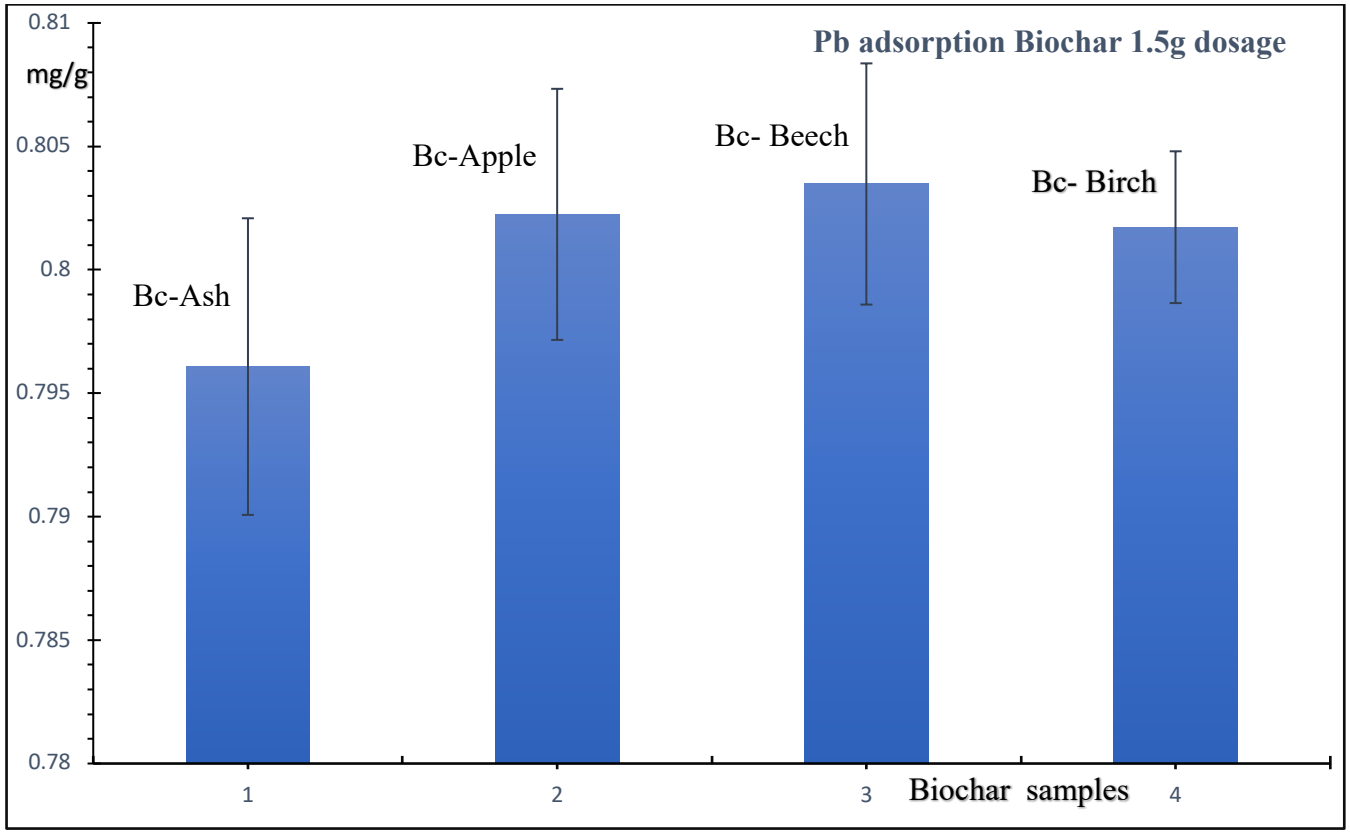


Figure 4.3 (b): Bar chart showing the derived biochar (Bc-Ash, Bc- Apple, Bc-Beech, and Bc-Birch) average adsorption values ± Standard deviation (n=4) of Pb^{2+} (mg/g) at the dosage of 1.5 g in an incubation time frame of 12 hours (1, 3, 5, 8 and 12 hours). A constant concentration of Pb^{2+} (500 ppm) was used, to monitor the sorption rate in relation to time and biochar mass and to infer the most effective biochar in terms of Pb^{2+} sorption.

4.2.2 Sorption Kinetics

In studies of environmental metal pollutants (such as Ni^{2+} and Pb^{2+}) and their interactions with the components of soil or its amendments such as biochar, it is necessary to understand the adsorbate behaviour on a sorption platform (active site). Experimentally, this requires assessing equilibrium reaction concentrations denoted by the maximum adsorption and distribution coefficients during binding. Thus, it is important to understand sorption kinetics and to use this information in order to improve remediation strategies by updating knowledge of contaminant mobility (time dependant). Determination of the associated sorption and binding mechanism and whether there is any observable desorption reaction at a given time (Strawn & Sparks, 2000). Adsorption isotherms and kinetics for sorption of Ni and Pb to different biomass-derived biochar (Bc-Ash, Bc-Apple, Bc-Beech and Bc-Birch) at different dosages (0.3 g, 0.5 g and 1.5 g) were determined, and the effect of contact time in adsorption was determined.

4.2.2.1 Effect of contact time and determination of the kinetic model for metal ion adsorption onto Ash, Apple, Beech, and Birch biochar

The effect of contact time (mins) can be seen in the kinetic models in Figures 4.4 to 4.6 of derived biochar (Bc-Ash, Bc-Apple, Bc-Beech and Bc-Birch) sorption of Ni^{2+} and Pb^{2+}. It was observed that the adsorption efficiency decreased with time and that the majority of adsorption happened during the first hour of contact. Sorption was relatively fast at 0.3 g biochar (0.8264 mg/g, 0.8268 mg/g, 0.8238 mg/g and 0.8268 mg/g for Ash, Apple, Beech and Birch biochar and Ni^{2+}) and (0.8134 mg/g, 0.7977 mg/g, 0.8043 mg/g, and 0.8043 mg/g for Ash, Apple, Beech and Birch biochar and Pb^{2+}), at 0.5 g biochar

(0.8248 mg/g, 0.8235 mg/g, 0.8150 mg/g, and 0.8235 mg/g for Ash, Apple, Beech and Birch biochar and Ni^{2+}) and (0.8011 mg/g, 0.7921 mg/g, 0.7974 mg/g, and 0.8023 mg/g for Ash, Apple, Beech and Birch biochar and Pb^{2+}) and for 1.5g biochar (0.8124 mg/g, 0.8108 mg/g, 0.7978 mg/g and 0.8055 mg/g for Ash, Apple, Beech and Birch biochar and Ni^{2+}) and (0.7959 mg/g, 0.8073 mg/g, 0.7979 mg/g, and 0.8017 mg/g for Ash, Apple, Beech and Birch biochar and Pb^{2+}) initially, after which the reaction tilted towards equilibrium (adsorption and desorption rates occurring at equivalent rates).

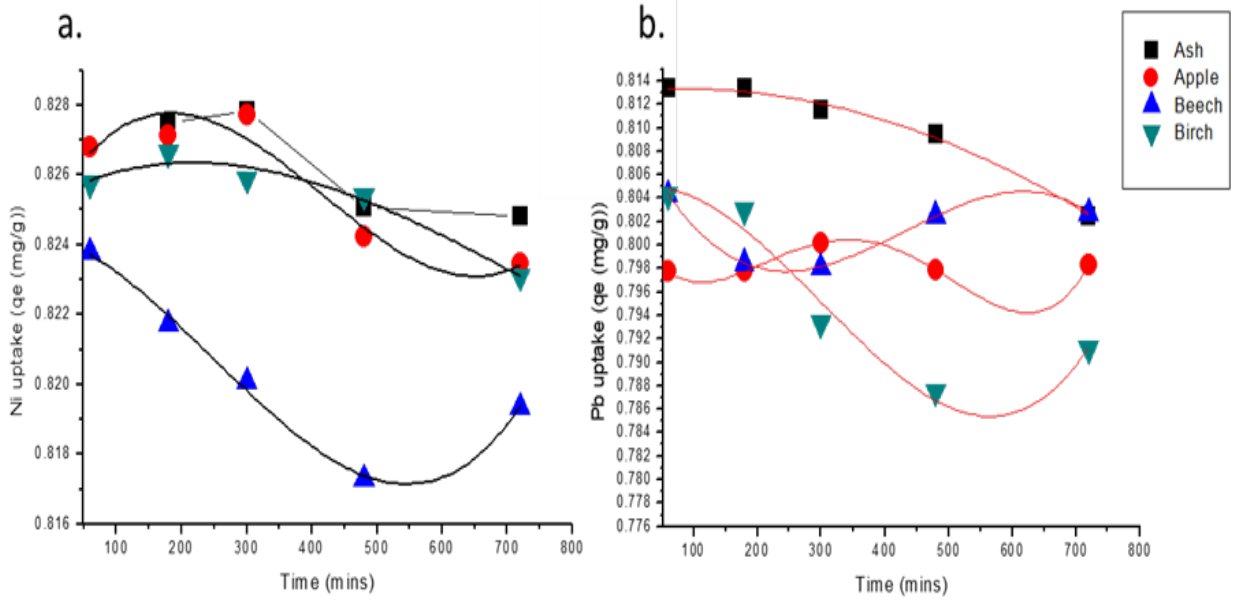


Figure 4.4: Plots showing the adsorption isotherms of derived biochar for (a) Ni^{2+} and (b) Pb^{2+} sorption to 0.3 g biochar over time (from 60 to 720 mins) and the recorded concentration q_e (mg/g) bound to biochar.

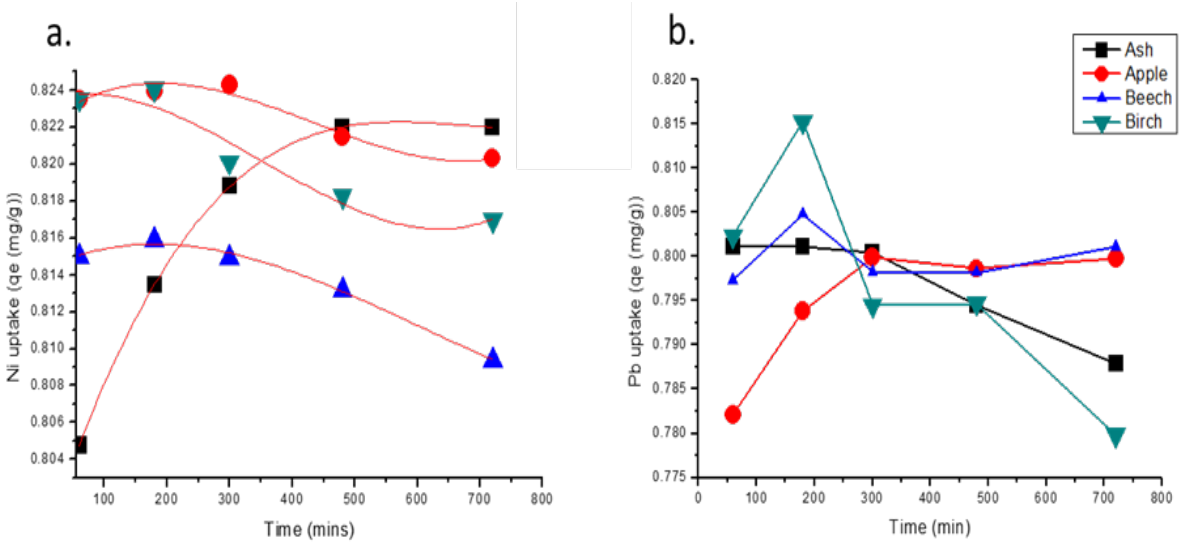


Figure 4.5: Plot of the adsorption isotherm for 0.5 g derived biochar for (a) Ni^{2+} and (b) Pb^{2+} sorption over time (from 60 to 720 mins) and the adsorbed concentration q_e (mg/g).

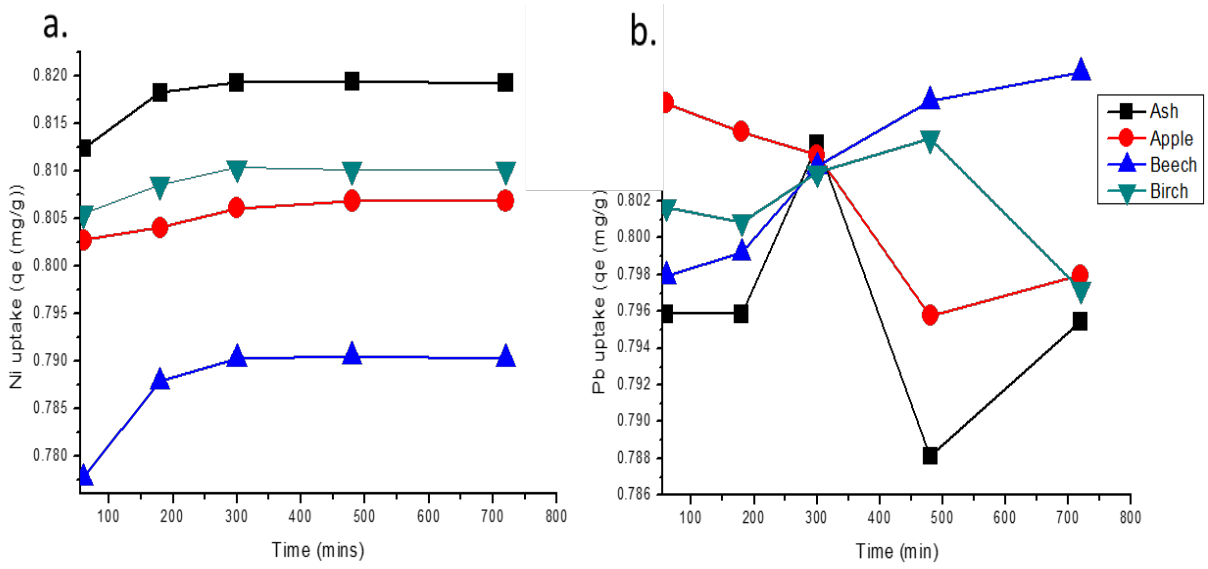


Figure 4.6: Plot of the adsorption isotherm at 1.5 g dosage of derived biochar for (a) Ni^{2+} and (b) Pb^{2+} sorption over time (from 60 to 720 mins) and the absorbed concentration q_e (mg/g).

Optimum adsorption was observed at 300 mins contact time with the 0.3 g dosage of adsorbent for all the biochar samples, Bc-Ash, Bc-Apple, Bc-Beech and Bc-Birch. Furthermore, the optimum contact time for adsorption when the adsorbent concentration was 0.5 g was 180 min, for Ash, 480 min for Apple, and 300 min for Beech and Birch. Similarly, the optimum contact time at 1.5 g adsorbents showed a similar trend to that observed with 0.5 g adsorbents. Generally, the adsorption interaction between biochar active sites and the targeted pollutant happened within the first hour and slowed as binding sites were utilised, moving towards an equilibrium state over time.

In general, the linear forms of a pseudo-first and second order models, and an Intraparticle diffusion can be expressed using equations 1 to 4 in appendix D (Georgin et al., 2018), where, k_1 and k_2 are the rate constants of pseudo first and second order respectively, q_e and q_t are amounts of metal ions biosorbed in mg g^{-1} at equilibrium and at time t (min), respectively. The rate constants, K_1 were calculated from the plots of log ($q_e - q_t$) against time t for different concentrations of metal ion. The kinetic parameters (q_e, k_1, and k_2) and the statistical information (coefficient of determination R^2) are presented in appendix D). Furthermore, the intra particle diffusion equation (Section 1.7.7) was used to investigate the behaviour of intra particle diffusion as the rate limiting step in the biosorption process. R is the percent metal ions sorted, K_d (mg g^{-1} $min^{-1/2}$) is the intra particle diffusion rate constant, t is the contact time, while b is the gradient of the linear plot (Appendix D).

5.3 Conclusion

This chapter worked with the hypothesis that the significance differences observed amongst the selected biomass samples would be transferred to the corresponding biochar samples, and thus that the derived biochar samples would demonstrate differences in terms of their sorption efficiencies which might arise due to the presence of a variety of different binding mechanisms amongst the biochar samples. Observations from experimental binding isotherms and the biochar characterization parameter shows that thermal dehydration energy (pyrolysis) eroded the significant differences in physico-chemical properties exhibited by the selected biomass samples (Ash, Apple, Beech and Birch) once they were carbonized into biochar.

The baseline adsorption experiments conducted at different biochar mass dosages (0.3g, 0.5 g, 1.0 g and 1.5 g) over a 12-hour incubation time frame (with samples taken at intervals for analysis) derived notable observations (maximum adsorption) from the experimental isotherm graphs (Figure 4.4 and Figure 4.5). The data showed that adsorption of the selected metal ions (Ni_{2+} or Pb^{2+}) was high and rapid, and that it all happened within the first hour (which is good because maximum adsorption capacity can be determined). Adsorption progressed slowly until it approached equilibrium (at between 3-8 hours of contact) and thereafter maintained a steady low rate before desorption.

Principal component analysis of the derived biochar characterization parameter for sorption of Ni^{2+} and Pb^{2+}gave three components each and accounted for 99.5% and 99.8% of the total variances respectively. These components pointed out biochar stability and suggested that sorption is a surface phenomenon (active sites in derived char has the

potential to provide a platform for interactions for adsorbate and adsorbent). The kinetic model (pseudo-first- (0.8185 – 0.9715) and (0.9865 – 0.9963) and Second order ((0.9998 -0.9999) and (1)) expresses a good fit for Ni^{2+} and Pb^{2+} respectively, with pseudo-first order exhibiting a less good fit for both contaminants (see Appendix D). However, it is important to note that most adsorption occurred during the first hour (Figures 4.4 - 4.6) and there might be slight possibility of inaccuracy in the kinetic model in appendix D. Nevertheless, our focus was to obtain the maximum adsorption value.

The main binding mechanism observed from the interactions between adsorbate and adsorbent on the active sites of biochar is hydrogen bond and electrostatic interaction (see Figure 1.6 for a schematic illustration of this process). The hypothesis underpinning this chapter was clearly rejected as none of what was hypothesised was observed on biochar sorption. A new hypothesis was adopted for the next chapter, which was that hybridization of the biochar with nanomaterials could be utilised to boost the morphological properties of the selected biochar leading to increased sorption potential and potentially providing a new binding mechanism.

A range of nanomaterials-functionalized Biochar samples are prepared, including magnetic biochar, hydroxyapatite Biochar, and Magnetic Hydroxyapatite Biochar. The aim is to increase the adsorption efficiency of the biochar and to potentially introduce a new attachment mechanism on the active site of hybrid biochar during sorption. The newly functionalized biochar will be subjected to sorption experiment in a mono and binary system (one metal and two metals respectively) and evaluated for their effectiveness in metal ion removal.

CHAPTER 5

CHARACTERIZATION OF SORPTION OF HEAVY METALS BY HYBRID DERIVED-BIOCHAR IN A MONO AND BINARY SYSTEM.

5.1 Introduction

In this chapter, we explore whether functionalisation of biochar with nanomaterials leads to enhanced adsorption capacity and potentially adds new modes of binding or interaction. Three hybrid biochar samples were produced - Hydroxyapatite-Biochar (Ha-Bc), Magnetic-Biochar(M-Bc) and Magnetic Hydroxyapatite-Biochar (MHa-Bc), as described in Sections 5.3.1 to 5.3.3.

In this chapter, we determine the adsorption of Ni^{2+} and Pb^{2+} in a mono (one metal at a time) and binary (two metals simultaneously) system by the hybrid biochar samples (Hydroxyapatite-Biochar (Ha-Bc), Magnetic-Biochar (M-Bc) and Magnetic Hydroxyapatite-Biochar (MHa-Bc)). The working hypothesis here was that modification of the morphological structure by reducing its hydrophobicity / increasing its hydrophilicity through introduction of a new surface functional group to aid adsorption, and/or by increasing its surface area and pore-sizes/volume, of a well-characterised woodchip biomass derived biochar would boost the maximum sorption capacity and potentially introduce a new binding mechanism for inorganic pollutants on the active sorption platform on the adsorbent.

The synergy between Biochar and the functionalising nanoscale materials (hydroxyapatite and/or magnetite) gives rise to improved properties, which can include greater stability, improved surface-area (active sites) and additional specific functional

groups which are responsible for facilitating sorption, and which can be designed to recognize and bind specific organic and inorganic pollutants for remediation of aqueous environments (Yin et al., 2020; Sizmur et al., 2017). Considering the properties (hydrophilicity, electronegativity, surface morphology-surface area, pore size) of hydroxyapatite, with those of Biochar led to a proposed combination of HA with biochar to produce a hybrid adsorbent (Ha-Bc) for Ni^{2+} and Pb^{2+} sorption. Additional approaches investigated included functionalization of biochar with magnetic nanomaterials and a combined Magnetic Hydroxyapatite-Biochar for sorption of Ni^{2+} and Pb^{2+}, as shown in Figure 5.1, based on the surface morphological properties of the nanomaterials as shown in Figure 4.1 (Iwamoto et al., 2016; Jose et al., 2021; Li et al., 2020b).

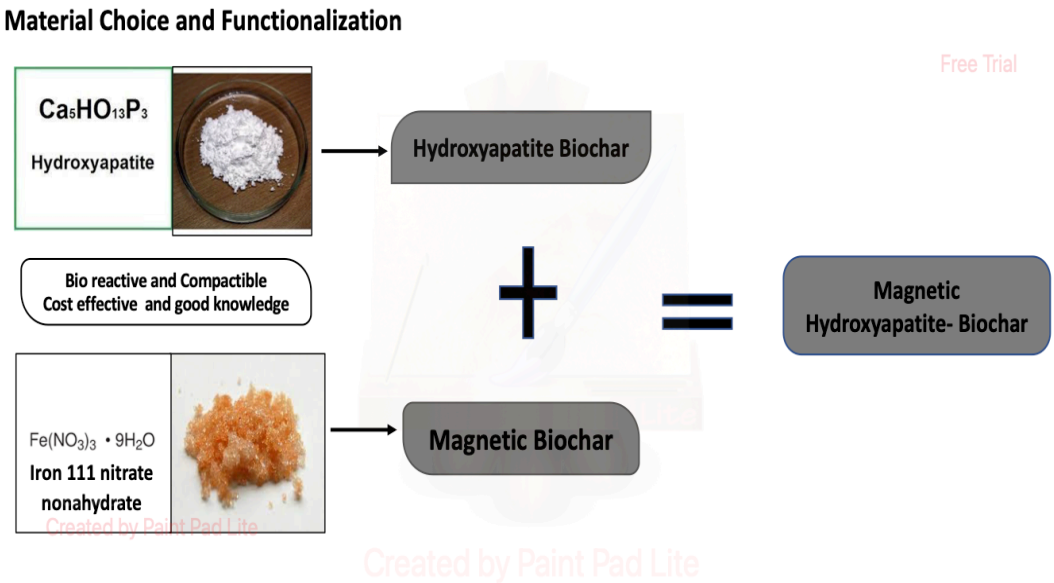


Figure 5.1: Schematic illustration of the process for functionalization of biochar with Hydroxyapatite or Iron (III) nitrate nonahydrate to produce the hybrid biochars Hydroxyapatite-Biochar and Magnetic Biochar, and the combination of both approaches to produce a super-hybrid (combination of hybrids) biochar, namely the Magnetic Hydroxyapatite-Biochar.

5.2 Biochar Hybridization Selection

All selected pyrolyzed samples (Bc-Ash, Bc-Apple, Bc-Beech, and Bc-Birch) fitted the potential choice of sample for functionalization. From the biochar baseline experimental observations, coupled with statistical evaluation (Table 3.3), the most suitable sample was chosen for Biochar hybridization. The ideal sample should have a reasonable surface area, a good carbon percentage, a well distributed pore size to volume ratio and a very good adsorption capacity. A nonparametric test on the Bc samples' characterization parameters (Carbon, Nitrogen, Hydrogen, pore size, pore volume, surface area and adsorption) was

the same across the different biochar categories (no significant differences observed) thus, the best sample choice for hybridization becomes difficult to select based on statistical differences. These biochar samples (BC-Ash, BC-Apple, BC-Birch, and BC-Beech) all have the potential to be selected (high carbon content and large surface area), but only one sample is required. The first choice that comes to mind is Bc-birch because it possesses the least surface area among the 4 samples, which gives the most room for increasing the surface area through functionalisation with nanomaterials. Thus, Bc-Beech was chosen as the preferred sample for modification. Hybridization of Bc-Beech, into Magnetized Biochar (MBc), Hydroxyapatite Biochar (Ha-Bc) and Magnetized hydroxyapatite Biochar (MHa-Bc-Beech) was achieved, the resulting hybrid materials were fully characterised and assessed for their sorption capability and mechanism(s) as described in Table 5.1 and Figure 5.2. Additionally, the ability of the hybrid biochar samples to bind the heavy metal ions when co-exposed to both metals simultaneously was also explored to determine if there was any preferential binding or both ions bound equally.

5.3 Method: Preparation of Hybrid Biochar

5.3.1 Hydroxyapatite and Hydroxyapatite Biochar (Ha-Bc) preparation

Ammonium phosphate dibasic and calcium nitrate tetrahydrate (purchased from Sigma Aldrich and Honeywell, respectively) were used to precipitate hydroxyapatite (HA). A wet precipitation method was adopted from (Chen et al., 2021) and (Papadiamantis et al., 2017). Briefly, 13.2627 g of PO_4 and 41.5170 g of Ca^{2+} (1.75 M) were dissolved separately in 100mL deionized water each, with ammonium hydroxide (NH_4OH) solution

used to regulate the pH ≥ 10 simultaneously with the addition of PO_4 in a dropwise manner. The resulting solution was enclosed with parafilm and foil and heated to 90 °C with a magnetic stirrer at 1000 rpm using a heating/stirring plate for 24 hours. After cooling the sample was washed with deionized water and centrifuged (3,000 rpm for 15 mins at 2e supernatant was discarded, then samples were freeze dried for 72 hours. For Hydroxyapatite Biochar (HABc), ammonium phosphate dibasic and calcium nitrate tetrahydrate (purchased from Sigma Aldrich and Honeywell respectively) were used to precipitate hydroxyapatite onto the Beech biochar. The method was exactly as described above, expect that 15 g of beech biochar was added to the tube containing Ca^{2+} before the dropwise addition of PO_4 solution (Figure 5.2). The Beech-HA biochar was freeze dried for characterisation and used for adsorption experiments as described above.

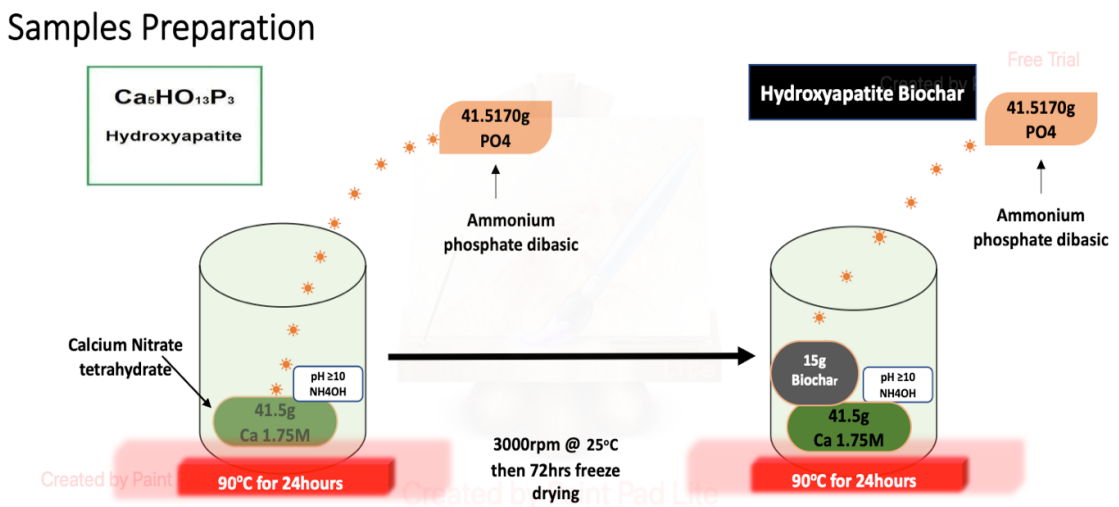


Figure 5.2: Schematic illustration of the steps in the synthesis of Hydroxyapatite and Hydroxyapatite Biochar with dropwise precipitation of PO_4 reactant into the solution plus use of NH_4OH to regulate the pH ≥ 10.

5.3.2 Magnetic Biochar (M-Bc) preparation

The iron (III) nitrate nonahydrate (Fe $(NO_3)_3.9H_2O$) used in the production of magnetic biochar was purchased form Sigma Aldrich. The method for preparation of magnetic biochar was adopted and modified from (Liang et al., 2019; Li et al., 2019). Briefly 0.076 M of Fe $(NO_3)_3$ was stirred in 100 mL of deionized water for 15 mins, before the addition of Beech Biochar (20 g). The mixture was further stirred until there was a homogenous mixture, heated to 90 ºC for 6 hours, after cooling, the mixture was centrifuged at 3,000 rpm for 15 mins at 25 ºC following which the supernatant was removed, and the biochar was freeze dried for 72 hours (Figure 5.3).

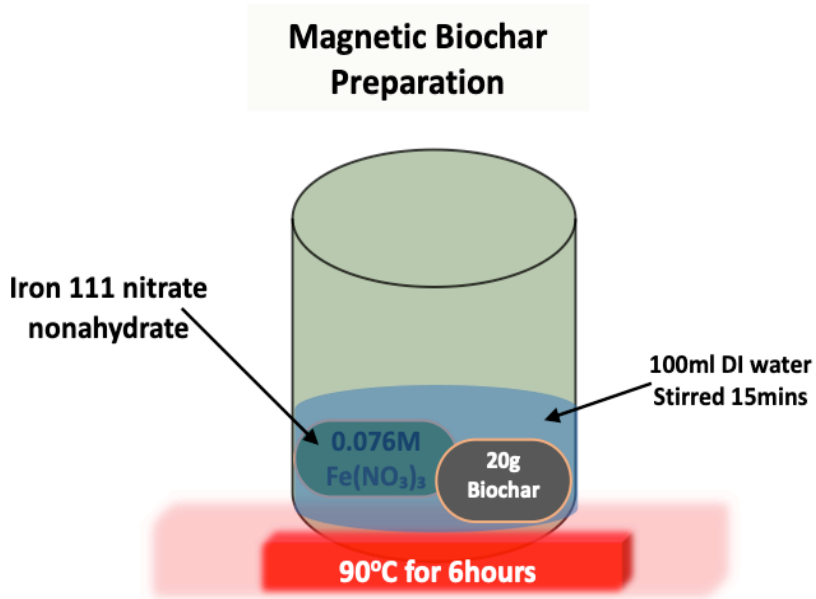


Figure 5.3 Schematic illustration of the synthesis of the Magnetic biochar preparation through heating for approximately 6 hours followed by then centrifugation at 3000 rpm at 25 ºC and freeze dried for 72 hours.

5.3.3 Magnetic Hydroxyapatite-Biochar (MHa-Bc) preparation

Briefly, 13.2627 g of PO_4 and 20 g of Fe $(NO_3)_3$ 0.076 M were dissolved into 100 mL deionized water while 15 g beech biochar and 41.5170 g of Ca $(NO_3)_2$ (1.75 M) were dispersed separately into 100 mL deionized water. A solution of NH_4OH was used to adjust the pH ≥ 10 initially of both mixtures (Calcium and Iron + biochar), followed by the dropwise addition of PO_4 (2.5 mL/min) to the mixtures (Figure 5.4). The resulting solution was enclosed with parafilm and foil and heated to 90 °C for the first 8 hours and last 5 hours with the temperature reduced to 40 °C during the intermediate 11 hours (24 hours heating in total) with a magnetic stirrer hotplate at 1000 rpm. After cooling, the sample was washed and centrifuged (at 3000 rpm for 15 mins at 25 °C) and the supernatant was discarded with the remaining sample freeze dried for 72 hours.

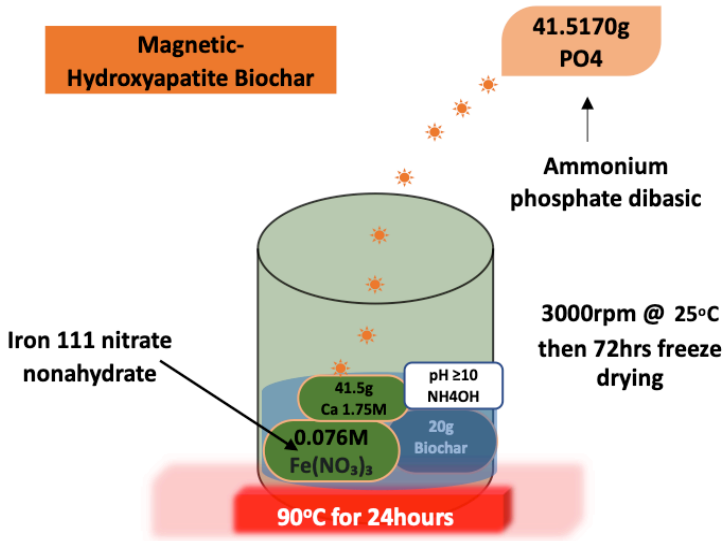


Figure 5.4: Schematic illustration of Magnetic Hydroxyapatite-biochar preparation. In detail, 20g of biochar in 100 ml DI water containing Fe $(NO_3)_3$ 0.076M + Ca1.75M 41.5g stirred for proper mixing, with NH4OH used to regulate the pH ≥ 10, then heated for 90°C

for approximately 6hours) then centrifuged at 3000 rpm and 25 ^{o}C and freeze dried over 72 hours.

5.4 Characterization of Functionalized Hybrid Biochar

The hybrid biochar samples (Hydroxyapatite-biochar, magnetic biochar and magnetic hydroxyapatite biochar) were characterized in terms of their morphological structure using scanning electron microscopy, their surface area using BET and their chemical composition and surface functional groups using FTIR, with the results presented in Figures 5.5a and 5.5b. The characterization results were compared to the original selected biochar (Bc-Beech) to observe the extent of the impact of functionalization on the surface morphological structures and feature of the derived hybrid, as discussed in section 5.4.1. Further BET details (BET summary report, isothermal linear plot, surface area plot, T-plot, dV/dt log of pore volume and pore Area, BJH Adsorption /Desorption dV/dlog of pore volume and pore area) on produced hybrid (MHA-Bc, HA-Bc, and MBc) and hydroxyapatite are contained in Appendix D.

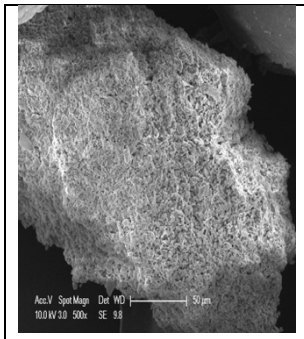
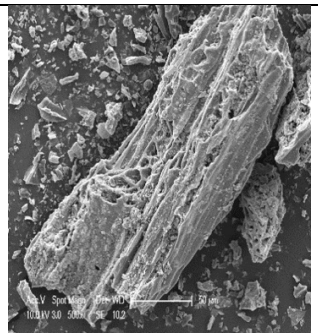
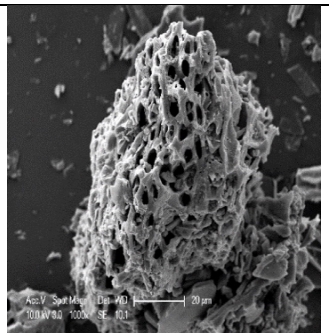
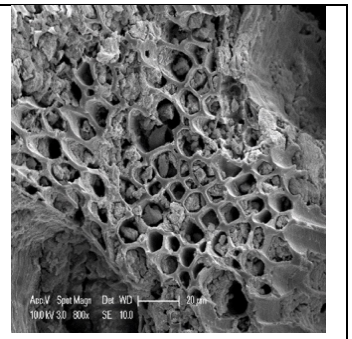
				
Hydroxyapatite (HA) **Surface Area:** **67.69±0.06 m^2/g** **Pore size:12.84nm** **Pore volume: 0.22cm^3/g**	**Hydroxyapatite Biochar (HA-Bc)** **Surface Area: 141.13± 1.95 m^2/g** **Pore size: 6.14nm** **Pore volume:0.22cm^3/g**	**Beech Biochar (Bc-Beech)** **Surface Area:** **305.07±7.25 m^2/g** **Pore size: 21.23nm** **Pore volume:0.16cm^3/g**	**Magnetic Biochar (MBc)** **Surface Area: 190.64±4.11 m^2/g** **Pore size: 2.37nm** **Pore volume: 0.11cm^3/g**	**Magnetic Hydroxyapatite Biochar (MHA-Bc)** **Surface Area:104.5±0.11 m^2/g** **Pore size: 13.62nm** **Pore volume: 0.36cm^3/g**

Figure 5.5a: Characterization of the hybrid biochar samples in terms of their morphology and surface area: SEM images and BET summary data for surface area, pore size/volume. compared to the original Beech-biochar. From Left to Right: Hydroxyapetite (alone, no biochar); hydroxyapatite modified Beech biochar (Ha-Bc), Beech Biochar, Magnetic biochar (M-Bc) and magnetic hydroxyapatite biochar (MHa-Bc).

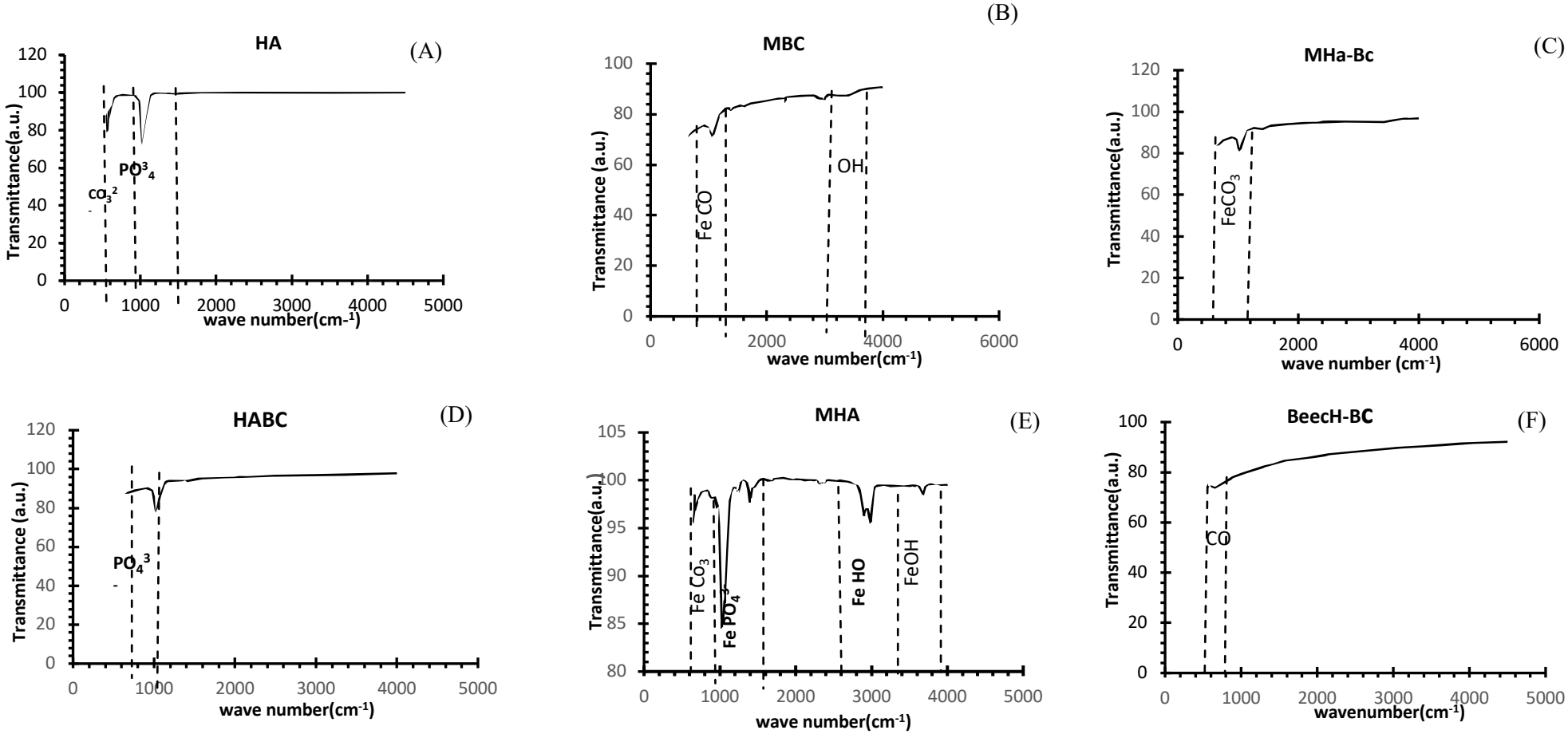


Figure 5.5b: FTIR spectral of (a) Hydroxyapatite (HA), (b) Hydroxyapatite Biochar (HABC), (c) Magnetic Biochar (MBC), (d) Magnetic Hydroxyapatite (MHA), (e) Magnetic Hydroxyapatite Biochar (MHABC) and (f) Beech Biochar (Beech-Bc) as the unmodified control.

5.4.1 Effect of functionalisation on the biochar physico-chemical characteristics

FTIR analysis of the functionalised biochar samples gave different characteristic peaks for the functionalized biochar samples compared to the original Beech-Bc. The new peaks are associated with additional functional groups (Figure 5.5b) introduced by the hybrid components, namely the hydroxyapatite and magnetite, with additional peaks ranging from 800 cm^{-1} to 4000 cm^{-1}. The spectra gave characteristic bands of PO_4^{3-}, CO_3^{2-}, Fe-PO_4^{3-}, and Fe-OH for the various functionalization's. Specifically, the hydroxyapatite-functionalized Biochar gained bands from PO_4^{3}- at 1090 cm^{-1}, while the Magnetic Hydroxyapatite gained bands from Fe-PO_4^{3-} and Fe-OH at 870 cm^{-1} and 3500 cm^{-1}, respectively, while the magnetic hydroxyapatite biochar gained a band from $FeCO_3$ at 1600 cm^{-1} (Eltaweil et al., 2020; Z. Tan et al., 2017; Reyes-Gasga et al., 2013).

Scanning Electron Microscopy (SEM) images of the functionalised biochar samples reveals structural and morphological modifications associated with the surface area, pore size and volume of HABC, MBC and MHABC relative to the original Beech biochar, which had a surface area of 305.07 m^2/g, an average pore size of 21.23 nm and a pore volume of 0.16 cm^3. Functionalisation of the Beech-Bc with hydroxyapetite (HA-Bc) led to a decrease in surface area to 141.13 m^2/g, indicative of a >50% decrease relative to the Beech biochar, while the pore size decreased to 16.1 nm and the pore volume increased to 0.57 cm^3 in the HA-Bc. The Magnetic Biochar showed a smaller decrease in surface area to 190.6 m^2/g resulting in a 38% decrease relative to the Beech biochar, while the pore size decreased significantly to only 2.37 nm, and the pore volume similarly decreased to just 0.11 cm^3, relative to the original Beech biochar. Finally, the Magnetic

Hydroxyapatite Biochar had the smallest surface area of any of the hybrid biochar samples, at just 104.5m^2/g, with its pore size being 13.62 nm and a pore volume of 0.36 cm^3 (Figure 5.5a).

The SEM images show that hydroxyapatite (HA) alone had a great porosity, which was maintained in the Hydroxyapetite biochar. with lots of pores distributed all over the structural matrix. The pore sizes and volume (12.85 nm and 0.22 cm^3/g respectively in the HA) are relatively large to encourage sorption, but the low surface area of 67.69 m^2/g counteracts this assumption. Hence, a combined synthesis which integrates the advantages of HA in terms of pore volume and pore distribution, with another functionalization approach to provide improved structural morphology in terms of its surface area, pore size / volume and surface functional groups/charges, was required. It was hoped that the combined magnetic and HA functionalised biochar would provide all the required features in an optimised format.

Magnetic Hydroxyapatite (MHA) had a morphological structure with a reasonable pore size and pore volume and low surface area (16.14 nm, 0.57 cm^3/g and 141.28 m^2/g, respectively) compared to its derived MHA-Bc which had the smallest overall surface area of any of the hybrid biochar samples, at 104.5m^2/g, but had the largest pore size (13.62 nm) and largest pore volume (0.36 cm) of any of the functionalised / hybrid biochar samples, as shown in Figure 5.5a, implying that the magnetic component (Fe) and impregnation method increased the pore size and volume (by reducing the number of blocked pores) and reduced the surface area (reduced the number of active sites). The

iron particles converted part of the surface area into active pores and increased its pore volume and further reduced the surface area of the MHA-biochar.

Hydroxyapatite biochar had a pore size, volume and surface area of 6.14 nm, 0.22 cm^3/g and 141.13 m^2/g respectively (Figure 5.5a). This is lower than the initial biochar (Bc-beech) which had a pore size volume and surface area of 2.12 nm, 0.16 cm^3/g and 305.07 m^2/g) stipulating that hybridization did not meet expectations in terms of surface morphology (reduced surface area). Evaluating the effect of impregnation on biochar, the pore sizes increased from 2.12 nm to 6.14 nm and the volume increased from 0.16 cm^3/g to 0.22 cm^3 /g resulting in a decrease in the surface area (active sites) as shown in Figure 5.5a.

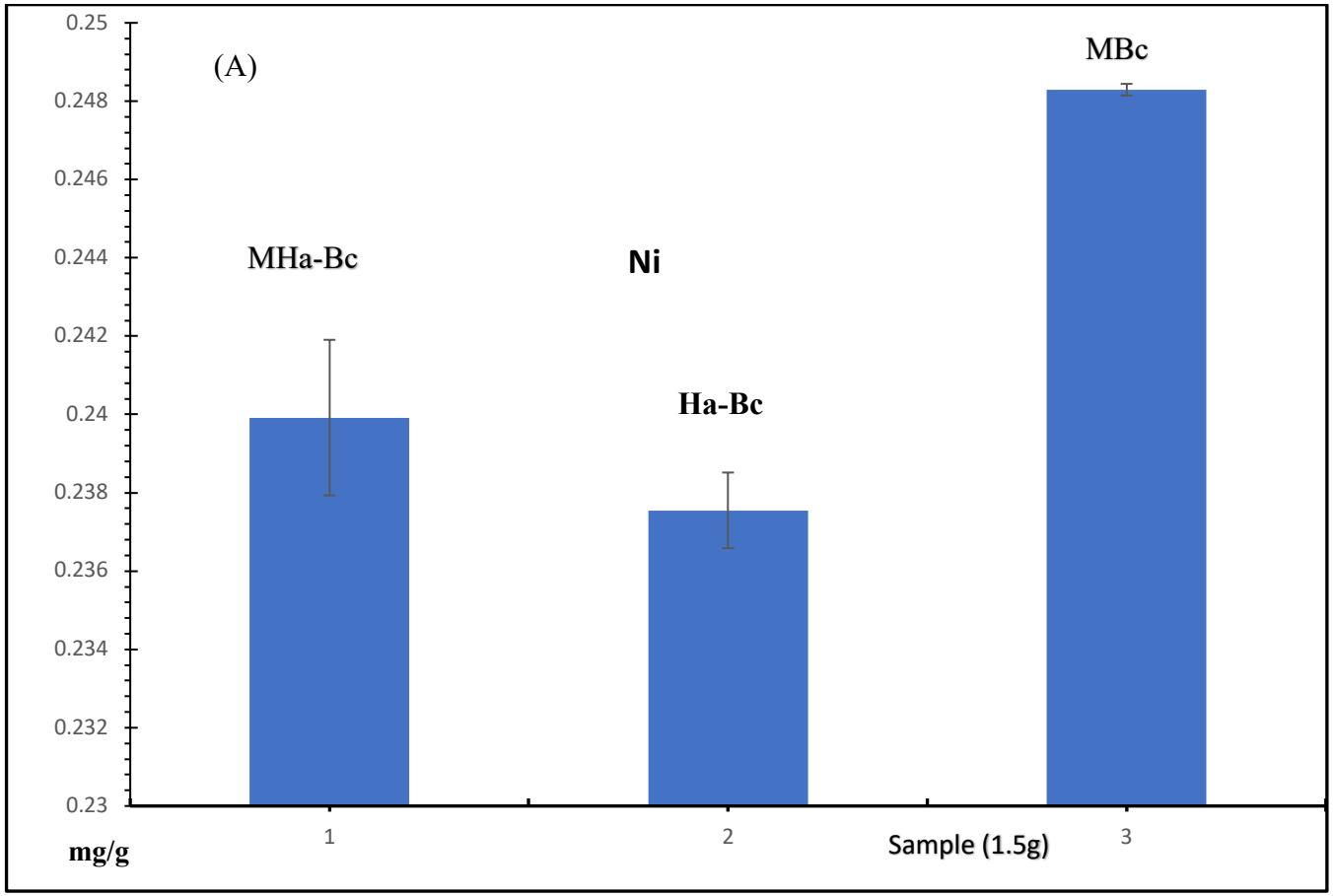
These observations might create a bias on sorption as it is meant to be a surface phenomenon rather than a whole bulk phenomenon. If the mechanism of sorption is meant to be across the whole bulk, then the reduced active sites might be relatively insignificant as far as sorption is concerned. But if the mechanism is surface driven or utilises both surface and bulk sites, then sorption will be truncated at a point when the whole bulk is actively involved in sorption while the surface-active sites get saturated with targeted adsorbate (Ni^{2+} and Pb^{2+}) gradually tilting towards a state of equilibrium. Thus, sorption might be incomplete as relating to reduced active sites, furthermore, the metal ions present might compete for sorption onto active sites.

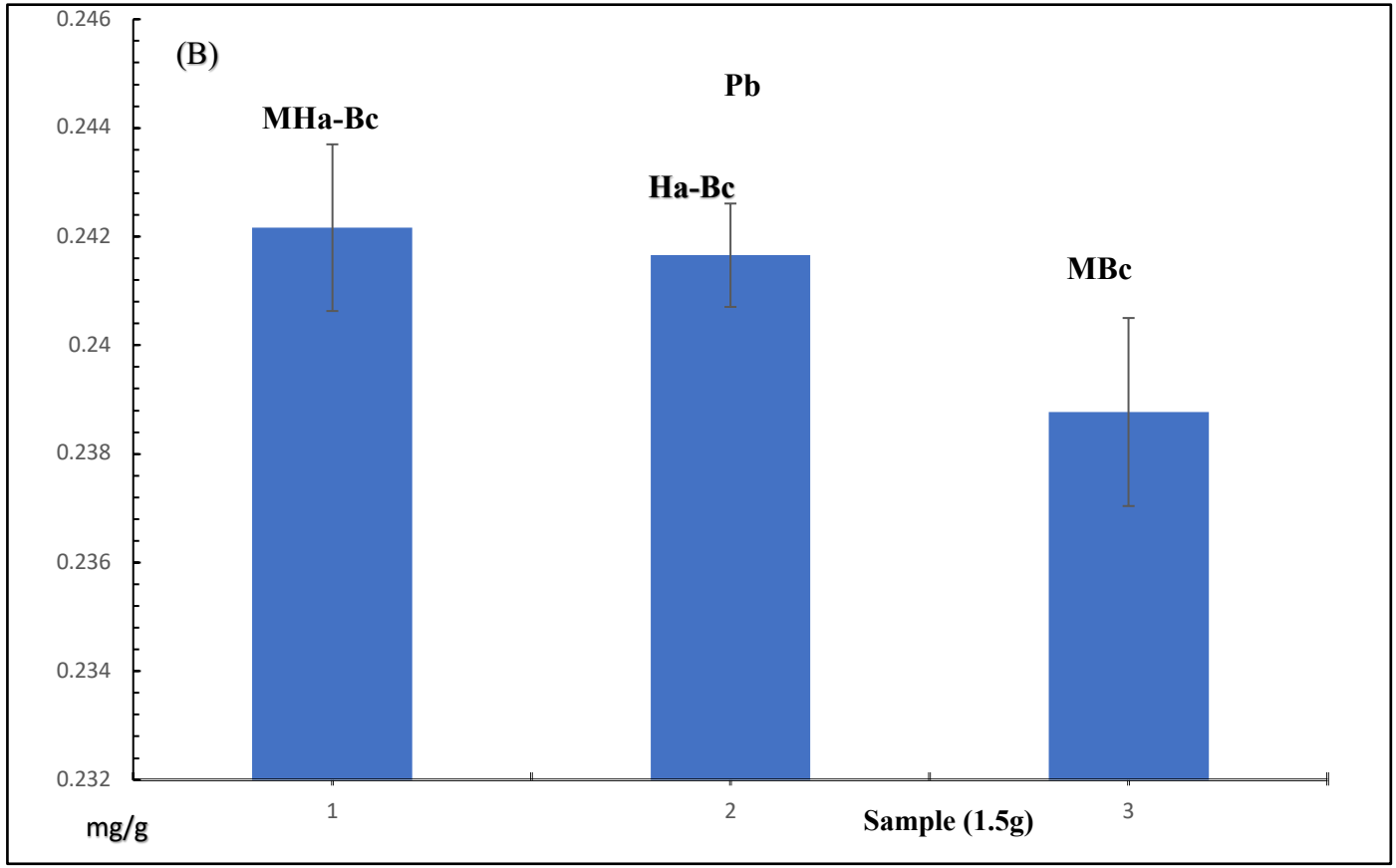
The surface area/active sites reduction as a result of nanomaterials functionalization of the Beech-Bc led to a significant increase in the pore sizes/volume within the hybrid biochar structural matrix. This observation directly affects sorption if it is mainly a

surface phenomenon (adsorption), because a lot of active sites would have been converted to increased pores/volume but might be different if sorption is dependent on the internal structural matrix (absorption). Thus, active site reduction might affect sorption depending on the mechanism utilised. In the next section, the sorption of metal ions, individually and as a pair is assessed to gain insights into the sorption mechanisms.

Table 5.1: Sorption results in mg/g of metal ions bound to the functionalized Biochar (Hydroxyapatite biochar (HABc), Magnetic Biochar (MBc) and Magnetic Hydroxyapatite Biochar) following incubation with Nickel and Lead in a mono and binary system over 12 hours.

Ni							**Pb**				
		1hr (mg/g)	**3hrs (mg/g)**	**5hrs (mg/g)**	**8hrs (mg/g)**	**12hrs (mg/g)**	**1hr (mg/g)**	**3hrs (mg/g)**	**5hrs (mg/g)**	**8hrs (mg/g)**	**12hrs (mg/g)**
Ni	**MHA-BC**	0.242	0.241	0.239	0.240	0.237					
	HA-BC	0.239	0.236	0.238	0.237	0.238					
	MBC	0.248	0.248	0.248	0.248	0.248					
Ni-Pb Binary system	**MHA-BC**	0.245	0.244	0.244	0.242	0.245	0.244	0.244	0.244	0.243	0.245
	HA-BC	0.243	0.242	0.243	0.239	0.243	0.244	0.243	0.244	0.242	0.244
	MBC	0.249	0.249	0.249	0.249	0.249	0.242	0.242	0.242	0.241	0.241
Pb	**MHA-BC**						0.243	0.243	0.243	0.239	0.242
	HA-BC						0.243	0.241	0.243	0.241	0.241
	MBC						0.239	0.240	0.240	0.236	0.238


(A)
MBc
MHa-Bc
Ni
Ha-Bc
0.25
0.248
0.246
0.244
0.242
0.24
0.238
0.236
0.234
0.232
0.23
mg/g
1
2
Sample (1.5g)
3


(B)
Pb
MHa-Bc
Ha-Bc
MBc
0.246
0.244
0.242
0.24
0.238
0.236
0.234
0.232
mg/g
1
2
3
Sample (1.5g)

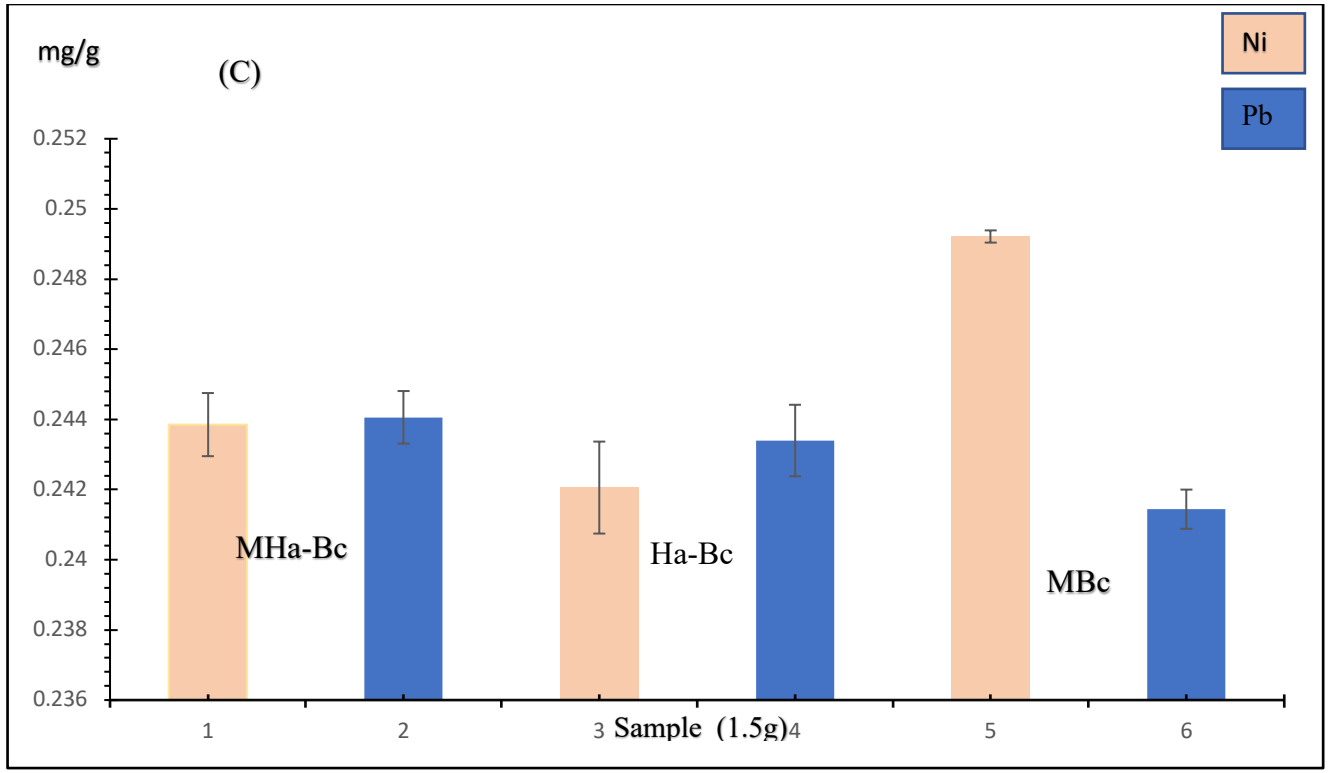


Figure 5.6: Plots of average adsorption ± standard deviation (mg/g) (n=3) of Ni^{2+} (A), Pb^{2+} (B) and Ni^{2+}- Pb^{2+} (C) exposed singularly (mono system) and simultaneously (binary system) to functionalized magnetic-Hydroxyapatite Biochar (MHA-Bc), Hydroxyapatite Biochar (Ha-Bc), and Magnetic biochar (MBc).

5.4.2 Sorption mechanisms of the Functionalized Biochar

Three functionalized biochar MBc, HA-Bc and MHABc were used to assess their maximum sorption capacity of Nickel (Ni^{2+}) and Lead (Pb^{2+}). The sorption experiment was performed in mono and binary system (one metal ion pollutant and two metals ions pollutants respectively) a similar manner as those reported previously in Chapter 5 (just that here a binary system is introduced, and functionalized biochar was introduced as the adsorbent). Experiments were performed with a constant mass (1g) of functionalised biochar and a fixed concentration of the pollutants (500 ppb) in the starting solution (500ppm of nickel and lead), sorption was monitored at room temperature in a shaker. Samples readings and measurements were obtained same way as explained in section 5.2.1 and Figure 5.1.

Magnetic Hydroxyapatite Biochar had a maximum sorption value Ni^{2+} and $Pb^{2+}$of 0.242 mg/g and 0.243 mg/g (mono system) respectively at the 1st hour insinuating a fast sorption of its active sites (Table 5.1 and Figure 5.6). This was quite different in the binary system for Ni^{2+} (0.245 mg/g) and Pb^{2+}(0.244 mg/g) as they displayed good sorption values and had almost equal affinities to the active site with a total adsorbed value of (0.489 mg/g) by the adsorbent.

The observations inferred that magnetic hydroxyapatite biochar (MHa-Bc) performed better in the binary system for Ni^{2+} and Pb^{2+} sorption than its application in a mono sorption system. Similarly, HA-Bc displayed a slightly high affinity for Pb^{2+}in both mono and binary adsorption system with 0.243 mg/g on the 1st hour while Ni^{2+} 0.239 mg/g and in the binary phase a total of 0.482 mg/g was observed. Results suggested that HA-Bc and MHa-Bc could be used for both adsorbate sorption but preferably for Pb^{2+}if

specificity is needed. Magnetic Biochar (MBc) gave a direct opposite observation from HA-Bc with a greater affinity of Ni^{2+} with 0.248 mg/g in the 1st hour while Pb^{2+} 0.240 mg/g as maximum sorption value (Table 5.1, Figures 5.5). In the binary system a total of MBc gave (0.491 mg/g) with Ni^{2+} having greater affinity for the active site followed by Magnetic Hydroxyapatite Biochar (0.4892 mg/g) and hydroxyapatite Biochar 0.4863 mg/g.

It is important to understand the binding mechanism displayed by the hybrid biochar samples (MBc, HA-Bc and MHABc). Firstly, the pristine biochar (BC-Beech) was hydrophobic in nature (high surface area and no surface functional groups) and its mode of contaminant attachment was basically physisorption (Hydrogen-bonding) by weak van der Waals forces, as seen in Figure 1.6. According to the second hypothesis (section 1.11.1) explored in this thesis, one of the primary objectives was to functionalize the pristine biochar (section 5.3) converting it from its hydrophobic nature to a hydrophilic nature by introducing surface functional groups onto the active sites of the biochar (Figure 5.5b). The functionalized biochar (MBc, HA-Bc and MHABc) gave good FTIR plots as seen in Figure 5.4b, with only MBc having -OH groups attached to it. The implication of this is that the functionalization was not successful in converting all hybrid biochar to a hydrophilic nature, except in the case of MBc. What this means is that adsorption using MBc will involve the use of its new hydrophilic nature (chemisorption-complexation) with the aid of the newly introduced -OH surface functional groups. The binding mechanisms observed from these hybrid biochar samples was hydrogen bonding for HA-Bc and MHA-Bc and complexation for MBc. The same observations were reported for straw biomass modified with $MgSO_4$ for the removal of Cadmium in wastewater (A. Li et al., 2023) . The functionalization of straw biomass via a one-pot co-precipitation

method introduced a new surface functional group (-OH) on the active site and brought about a new attachment mechanism (complexation) which was responsible for the removal of cadmium from wastewater. (H. Wang et al., 2024) reveals Similarly, reed straw derived biochar was functionalized with $NiCl_2.6H_2O$ and $FeSO_4.7H_2O$ for elimination of lead (Pb) and cadmium (Cd) contaminants was. The resulting biochar had an -OH functional group on its active site which influenced the attachment mechanism to be complexation.

In conclusions observations shows that MBc is most suitable for Nickel adsorption in a mono system and both (Ni^{2+} and Pb^{2+}) in a binary system because of the attached -OH functional group (which introduced a new binding mechanism).

The experimental working hypothesis (section 5.1) in this chapter was partially justified, as morphological modification of adsorbent active site did not meet the desired expectation to increase the surface area but rather reduced it and increase pore-sizes/volume (Figure 5.5a). On the other hand, an additional sorption attachment mechanism(complexation) was introduced by the introduction of a new surface functional group (-OH by the magnetic functionalization material) (Figure 5.5b, and Figure 1.6) on the magnetic biochar (M-Bc) which acts as an active surface driving binding to the surface of the adsorbent.

5.5 Conclusion

This chapter highlighted the biochar modification techniques used to improve the efficacy of the adsorbent, leading to a set of Hybrid biochar samples (HABc, MBc and MHABc), specifically the sorption of inorganic pollutants (Pb^{2+} & Ni^{2+}). This chapter addressed the hypothesis that functionalizing the selected biochar (Bc-Beech) with nanoscale materials would boost its surface properties (surface area, pore size/volume and surface functional groups) thus increasing the maximum sorption, and potentially introducing a new sorption attachment mechanism. The hybrid biochar samples (Hydroxyapatite Biochar, Magnetic biochar, and Magnetic Hydroxyapatite Biochar) were produced via wet precipitation.

These hybrid adsorbents were characterized for surface area, pore-size/volume and surface functional group (Figures 5.5a and 5.5b) and it was determined that the overall surface area was reduced, and that some pores were filled then collapsed and that the overall pore volume increased. All the functionalised biochar materials had additional function groups on their surfaces – HA-Bc gained bands from PO_4^{3-} at 1090 cm^{-1}, while the MA-Bc gained bands from Fe-PO_4^{3-} and Fe-OH at 870 cm^{-1} and 3500 cm^{-1}, respectively, while the MHa-Bc gained a band from $FeCO_3$ at 1600 cm^{-1}.

The functionalized biochar materials were used in metal ion sorption experiments in a mono (Ni^{2+} or Pb^{2+}) and binary (Ni^{2+} + Pb^{2+}) system, and it was observed that maximum rapid sorption took place within the first hour followed by achievement of an equilibrium reaction state where sorption and desorption took place at the same rate. MBc had a better affinity for Ni^{2+}, while HABC and MHa-Bc had the highest affinity for Pb^{2+} and MHa-Bc was more suitable for binary systems (Table 5.1, Figure 5.4). An additional sorption /

attachment mechanism (complexation) was observed in Magnetic Biochar amongst others (HABC and MHa-Bc) meeting part of the goal set by hypothesis 2. The derived hybrid biochar gave lower overall sorption than its pristine biochar (owing to its lower overall number of active sites) but introduced a new binding mechanism. It is important to note that sorption was rapid within the first hour and after that the reaction headed towards a state of equilibrium, and thus the lack of resolved data during the first how means that it was not possible to determine the reaction kinetics.

CHAPTER 6

OVERALL CONCLUSION AND RECOMMENDATIONS

Remediation of heavy metal pollutants, such as Ni^{2+} and Pb^{2+} introduced into the environment via natural or anthropogenic means, helps to preserve the environment (air water and land) by ensuring the removal of its toxic entities, thus leading to the increased survival of organisms, plants, and humans. Design of effective environmental remediation strategies and techniques has caught the attention of researchers globally, and the potential of biochar as a cost-effective adsorbent is being extensively explored. Biomass-derived biochar or various nanomaterial-functionalised hybrid biochar samples are being investigated for active removal of pollutants from the environment by physical adhesion of adsorbate to the active surface of an adsorbent such as biochar.

In this thesis a range of woodchip biomass samples were characterised, and a sub-set converted to biochar via pyrolysis and explored for their effectiveness in remediation (sorption) of representative heavy metals, Ni^{2+} and Pb^{2+} and then one of the biochar samples was functionalised to further enhance its sorption capabilities, resulting in three hybrid biochar samples (Bc, Ha-Bc, MBc, and MHa-Bc).

The focus of the thesis was to understand the mechanism of sorption of Ni^{2+} and Pb^{2+} with the derived biochar (from selected biomasses that were characterised in chapter 3) and utilise this understanding to design a series of functionalized biochar samples and to assess their mechanism(s) of sorption (chapter 5) in a mono and binary system. The adsorbents explored in this thesis achieved maximum sorption of the targeted pollutant with a corresponding possible attachment mechanism (Hydrogen bonding, electrostatic interaction, and complexation) noted and optimised.

Initially, seven woodchip biomasses (Ash, Apple, Alder, Beech, Birch, Cherry, and Oak) rich in lignin content and readily available were characterized and statistically evaluated to identify the most distinctive samples in terms of the physio-chemical properties most linked with sorption, resulting in a sub-set of the biomass (Ash, Apple, Birch, and Beech) (Table 3.8) for pyrolysis (at 550 ^{o}C for 5 hours) as shown schematically in Figure 6.0. The selected samples were subjected to sorption with the hypothesis that the significant difference observed amongst the characteristics of the biomass samples will be transferred to their derived biochar (Bc-Ash, Bc-Apple, Bc-Beech, and Beech) thus influencing their various sorption capacities and removal mechanism(s).

The binding mechanism observed in all cases was precipitation as the negatively charged active surface of the biochar samples accepted the positively charged cations ($Ni^{2+}$and Pb^{2+}) via precipitation onto the biochar surface. Thus, the biochar sorption experiments resulted in the initial hypothesis being rejected, as high pyrolysis temperature resulted in the observed significant differences in the properties of the selected biomass samples being lost in the derived biochar samples, which were very similar in their properties and their sorption behaviours when subjected to baseline-sorption experiments with Ni^{2+} and Pb^{2+}.

The rejection of the initial hypothesis led to the generation of a second hypothesis, which was that functionalization of the biochar with nanoscale materials could further increase the surface area for sorption, and/or add an additional sorption mechanism. Hypothesis 2 thus necessitated the functionalization of one of the biomass derived biochar samples, in this case the Beech biochar (Bc-beech) which was determined to have a good surface area (305.07 ± 7.275 g/m^2), a good pore size (21.2298 nm) and pore volume (0.1619 g/cm^3) but with room for improvement through functionalisation with nanoscale

materials, such as hydroxyapatite or magnetite to produce hybrid biochar for sorption of Ni^{2}+ and Pb^{2+} in mono and binary systems. The hydroxyapatite-functionalized Biochar gained bands from PO_4^{3}- at 1090 cm^{-1}, while the Magnetic Hydroxyapatite gained bands from Fe-PO_4^{3-} and Fe-OH at 870 cm^{-1} and 3500 cm^{-1}, respectively, while the magnetic hydroxyapatite biochar gained a band from $FeCO_3$ at 1600 cm^{-1} materials chosen for functionalisation of the biochar had to be biocompatible cost efficient, not generate secondary waste and be materials that we already had adequate knowledge about, resulting in the selection of hydroxyapatite and magnetite (in the form of iron (III) nitratenonahydrate) (see also Figure 5.5a,b and Figure 6.1).

Interestingly, the functionalized Beech biochar materials (Hydroxyapatite Biochar, Magnetic Biochar and Magnetic Hydroxyapatite Biochar) had lower surface areas, 141.1 ± 1.95 m^2/g, 190.6 ± 4.1 m^2/g and 104.5 ± 0.11 m^2/g, respectively than the initial Beech biochar (which was 305.07 ±7.25 m^2/g). SEM imaging showed expanded blocked pores within the functionalised materials, as a result of pore collapse, but increased pore volume, and reduced surface area (Figure 5.5a). The sorption behaviour of these hybrid biochar resulted in the following observations: Magnetic biochar shows a better affinity for Ni^{2+}, while Hydroxyapatite biochar and Magnetic-Hydroxyapatite had greater affinity for Pb^{2+} and Magnetic-Hydroxyapatite biochar gave the best adsorption performance in the binary system (Table 5.1 and Figure 5.6). Two binding mechanisms, namely physisorption (Hydrogen bonding and Electrostatic interaction) and chemisorption (Complexation) were observed, with the second (Complexation) being introduced by the -OH functional groups associated with the MBc.

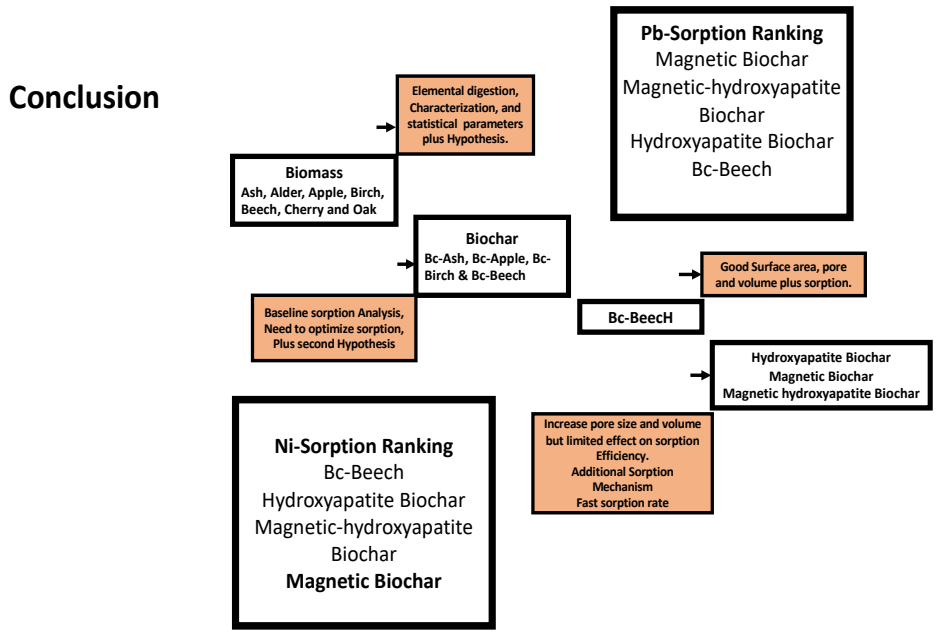


Figure 6.1: A summary of the experimental journey for the initial seven (7) biomasses, reduced by statistical evaluation to four (4) that were pyrolyzed to generate biochar, and then selection of one (1) for functionalized to create the hybrid biochar samples. Beech biochar was hybrid with hydroxyapatite, magnetite or both to produce the hybrid biochar (HaBc, MBc, MHaBc, respectively). The four biochar and three hybrid biochar samples were then used for sorption experiments with Ni^{2+} and Pb^{2+} in a mono (biochar and hybrid biochar) and binary (hybrid biochar samples only) system. Each adsorbent was ranked according to their sorption performance of Ni^{2+} or Pb^{2+} and Ni^{2+}+ Pb^{2+}).

Collectively, the data presented in this thesis demonstrate that the produced hybrid biochar samples had lower active sites for interactions than the initial Beech biochar but that the active sites were more functional as they possessed additional functional groups. For example, in the magnetite biochar (MBc), the introduction of -OH functional groups

on the biochar surface led to the introduction of a new sorption mechanism - complexation – in addition to the hydrogen bond and electrostatic interaction mechanism that dominated the beech biochar sorption in the Mono sorption system (Ni^{2+} or Pb^{2+}), MBc adsorbed 0.248 mg/g Ni^{2+} and 0.239 mg/g Pb^{2+}, while MHa-Bc absorbed 0.242 mg/g Ni^{2+} and 0.243 mg/g absorbed, and Ha-Bc absorbed 0.239 mg/g Ni^{2+} and 0.243 mg/g Pb^{2+}, compared to the sorption capacity of the initial Beech biochar of 0.80 mg/g Ni^{2+} and 0.82mg/g Pb^{2+}. The results showed that the affinities of the biochar samples for Ni^{2+} decreased in the order MBc, MHa-Bc and Ha-Bc, while for Pb^{2+} the MHa-Bc and Ha-Bc had greater affinity than MBc, as summarised also in Figure 6.1.

Observations from the binary systems (Ni^{2+}+ Pb^{2+}) as seen in Table 5.1 shows that the sorption performance of decreased in the order MBc (0.491 mg/g), MHa-Bc (0.489 mg/g) and Ha-Bc (0.487 mg/g). MBc and MHa-Bc had a greater affinity for Ni^{2+}(0.249 mg/g, 0.245 mg/g) than Pb^{2+}(0.242 mg/g, 0.244 mg/g) respectively, in the binary system, while Ha-Bc had a greater affinity for Pb^{2+} (0.244 mg/g) than Ni^{2+} (0.243 mg/g) in the binary system. Generally, the derived biochar performed better in the binary state than in the mono state with MBc having the highest overall sorption value (0.491 mg/g binary state) but only reaching a total adsorbed mass of 0.248 mg/g in the mono state for $Ni^{2+,}$ which can be attributed to the fact that the two metals precipitate or complex to different sites on the biochar.

In the MBc case, the presence of -OH functional group attached to its active site provides an additional sorption mechanism. The introduction of this functional group brought about a new sorption attachment mechanism (complexation), meaning that two

mechanisms are responsible for sorption (precipitation and complexation) of Ni^{2+} and Pb^{2+} in the mono and binary adsorption system with MBc.

It is important to note that the adsorption reaction was a rapid process, and it took place within the first hour of incubation within both the mono and binary systems (see for example Table 5.1 and Figures 5.5) and then drifted to a state of equilibrium. It is important to state that adsorption in this thesis was rapid within the first hour of a 12-hour incubation, followed by an equilibrium state, making the kinetics of the reaction difficult to determine. A detailed summary of the entire research and the key outcomes are presented in Figure 6.1 and Figure 6.2.

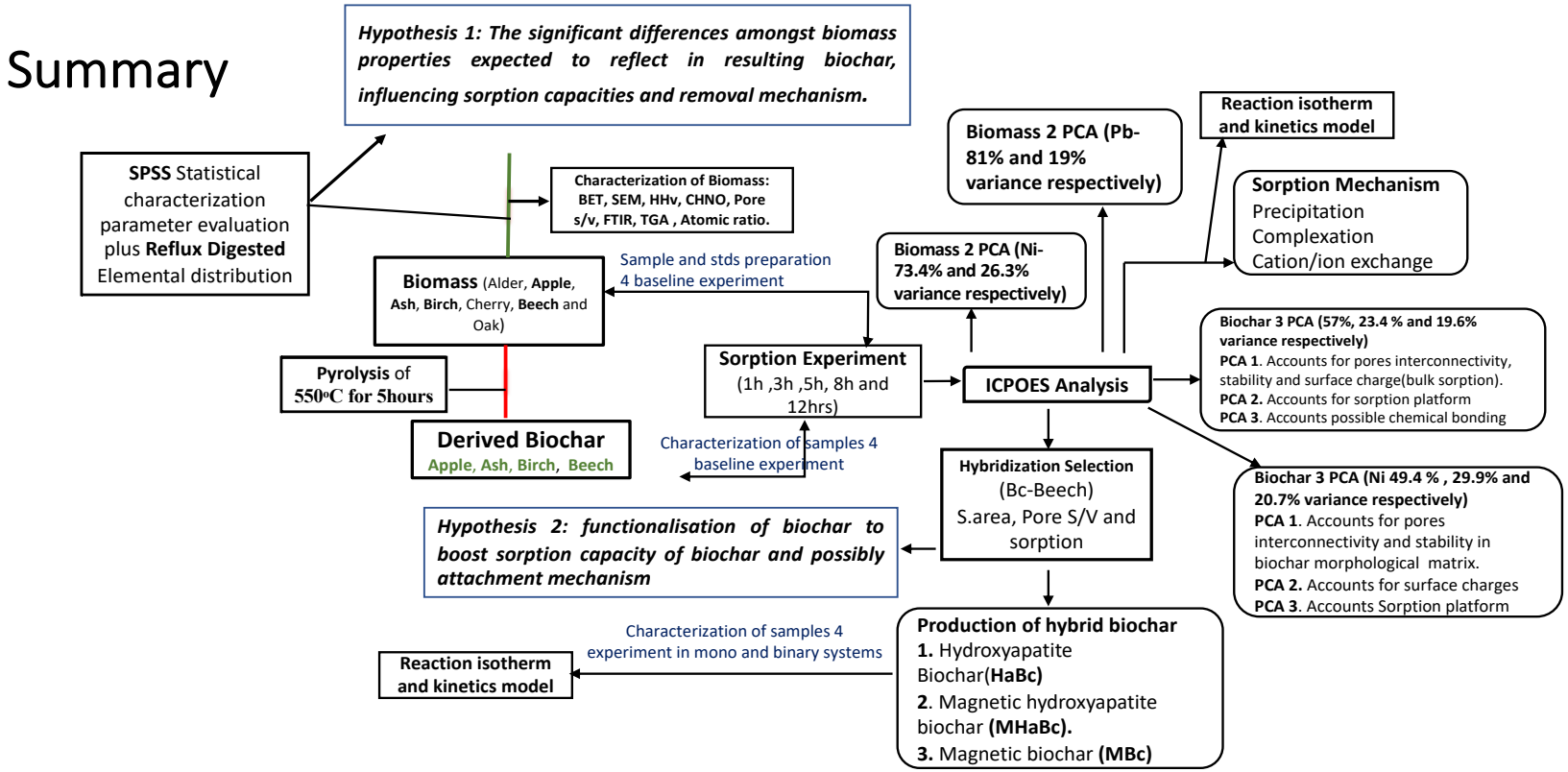


Figure 6.2: Summary of the research performed in this thesis: a systematic approach from Biomass selection and characterization to thermal degradation (showing hypothesis 1), base-line sorption experiments utilising the biomass-derived biochar samples, through to functionalization of the Beech biochar to produce hybrid biochar samples (showing hypothesis 2), then sorption in a mono and binary system.

6.1 Future Work and What I Would Do Differently

Based on the data and findings presented herein, there are a number of key questions that would be important to address as a next step. Some of these are presented below.

- A key parameter that we did not characterise, but which in hindsight would have been extremely informative, is the Cation Exchange Capacity. Thus, if I had known while in the experimental phase what I knew at the end of the write-up and interpretation phase about the different potential mechanisms of sorption, I would have characterised the CEC of the different biochar and functionalised biochar samples, to have a more completed set of mechanistic insights in terms of how the metal ions interact with the biochar. In part, this oversight came from the fact that the thesis was initially planned to focus on adsorption of organic contaminants such as PAHs where CEC may not have been such an important aspect.
- I would want to consider the potential of the hybridised biochar samples for remediation of organic pollutants and examine and evaluate how the produced biochar and derived hybrid biochar systems interact with these pollutants to identity possible removal mechanisms associated with each biochar and compare observations with the results from the inorganic (Ni^{2+} and Pb^{2+}) pollutant removal. I would also perform the experiments in different ways, both with the same timing at utilised here and with a shorter incubation time (60 mins) to enable fitting of the datasets to suitable kinetic models and to avoid equilibrium. Shorter runs would also facilitate increasing the range of conditions tested and the numbers of replicates thus increasing the statistical power of the data.
- A key experimental lesson learned is that mass-balance is important and to ensure mass-balance the distribution of the pollutants of interest across the system is

necessary. In the work presented here the amount of metal ions bound to the biochar was determined based only on the amount contained in the biochar pellet after centrifugation, whereas in the future while preparing samples for ICP-OES analysis I would make use of the supernatant also and deduct what was obtained from the original solution concentration, as this is simpler, and then the biochar samples would provide the total mass balance ensuring that the total recovered (supernatant + biochar) was equivalent to the initial concentration of the pollutant added.

- In the future, if I would repeat these experiments again to produce a hybrid biochar, I would use a lower ratio (1:5) of magnetic material and hydroxyapatite for functionalization of the biochar, then introduce a thermal dehydration phase after freeze drying. This might re-open blocked pores and give the chance for formation of micro-pores thus increasing active sites for sorption into the biochar and further allowing hybrid.
- I would like to produce biochar from a wider range of plant and animal-based biomass feedstocks and compare their characterised parameters then proceed to sorption removal efficiency in wastewater and associated mechanism plus use it as a filtration medium for air pollution. By having a baseline understanding of the properties of biochar and how to vary them, and the adsorption mechanisms available, it should be possible to optimise a range of low-cost pollution removal devices based on biochar – in the medium term I would like to spin-out a company making biochar-based remediation solutions.
- Lastly, I would want to produce hydrophobic and hydrophilic biochar and apply them separately and it combined forms to soil so see their effects on plant growth and soil nutrient properties. Degradation of soil quality is a major challenge

globally, and the need to feed a growing population sustainability is leading to an urgent need for bio-based solutions to enhance soil nutrient retention, facilitate uptake of nutrients into plants, and reduce the greenhouse gas emissions from agriculture. Biochar offers potential as part of the solution here, which is an exciting and emerging research direction.

7.1.1 What Was Learnt/Contribution to Knowledge.

- Functionalization of Beech biochar (produced at 550 °C through pyrolysis) with Iron (III)nitrate nonahydrate introduced a new attachment mechanism (complexation) to the existing precipitation-based sorption route. Thus, the magnetic beech biochar had two distinct mechanisms responsible for binding of metal ions, fulfilling the aim of adding a new sorption mechanism. The dual sorption mechanism resulted in the magnetic Beech biochar and hydroxyapatite biochar and magnetic hydroxyapatite biochar.
- Functionalization of Beech biochar with Hydroxyapatite and Iron (III) nitrate nonahydrate resulted in blocking of biochar pores and reduction of the active sites for sorption and thus further optimisation of the ratio of the two components is needed to enhance the usefulness of this super-hybrid biochar. A reasonable proportional ratio of 1:5 of magnetic nanomaterial and hydroxyapatite for functionalization of the biochar might be suitable with a short thermal dehydration phase.
- Pyrolysis erased the significance morphological differences observed amongst the biomass samples (Ash, Apple, Alder, Beech, Birch, Cherry, and Oak) that were the basis for selection of four samples (Ash, Apple, Beech, and Birch) for

carbonation (pyrolysis). A key remaining question is whether functionalisation of the biomass with HA and/or magnetic nanomaterials prior to pyrolysis might have help to retain some of the features of the original biomass samples, or whether the pyrolysis would anyway have resulted in the initial features being lost and homogenisation of the samples.

References

Abbaszade, G., Tserendorj, D., Salazar-Yanez, N., Zacháry, D., Völgyesi, P., Tóth, E., & Szabó, C. (2022). Lead and stable lead isotopes as tracers of soil pollution and human health risk assessment in former industrial cities of Hungary. *Applied Geochemistry*, *145*. https://doi.org/10.1016/j.apgeochem.2022.105397

Adigun, O. A., Oninla, V. O., & Babarinde, · N A Adesola. (2019). Application of sugarcane leaves as biomass in the removal of cadmium (II), lead(II) and zinc(II) ions from polluted water. *International Journal of Energy and Water Resources*, *3*(3), 141–152. https://doi.org/10.1007/s42108-019-00024-w

Afroze, S., Tushar, &, & Sen, K. (n.d.). *A Review on Heavy Metal Ions and Dye Adsorption from Water by Agricultural Solid Waste Adsorbents*. https://doi.org/10.1007/s11270-018-3869-z

Agrafioti, E., Kalderis, D., & Diamadopoulos, E. (2014). Arsenic and chromium removal from water using biochars derived from rice husk, organic solid wastes and sewage sludge. *Journal of Environmental Management*, *133*, 309–314. https://doi.org/10.1016/j.jenvman.2013.12.007

Ahmad, M., Lee, S. S., Dou, X., Mohan, D., Sung, J. K., Yang, J. E., & Ok, Y. S. (2012). Effects of pyrolysis temperature on soybean stover- and peanut shell-derived biochar properties and TCE adsorption in water. *Bioresource Technology*, *118*, 536–544. https://doi.org/10.1016/j.biortech.2012.05.042

Ahmad, M., Rajapaksha, A. U., Lim, J. E., Zhang, M., Bolan, N., Mohan, D., Vithanage, M., Lee, S. S., & Ok, Y. S. (2014). Biochar as a sorbent for contaminant management in soil and water: A review. *Chemosphere*, *99*, 19–23. https://doi.org/10.1016/j.chemosphere.2013.10.071

Ahmad, T., & Danish, M. (2022). A review of avocado waste-derived adsorbents: Characterizations, adsorption characteristics, and surface mechanism. *Chemosphere*, *296*. https://doi.org/10.1016/J.CHEMOSPHERE.2022.134036

Ahmed, M. B., Zhou, J. L., Ngo, H. H., Guo, W., & Chen, M. (2016). Progress in the preparation and application of modified biochar for improved contaminant removal from water and wastewater. *Bioresource Technology*, *214*, 836–851. https://doi.org/10.1016/j.biortech.2016.05.057

Ai, T., Jiang, X., Liu, Q., Lv, L., & Wu, H. (2019). Daptomycin adsorption on magnetic ultra-fine wood-based biochars from water: Kinetics, isotherms, and mechanism studies. *Bioresource Technology*, *273*(October 2018), 8–15. https://doi.org/10.1016/j.biortech.2018.10.039

Aidoo, E. N., Appiah, S. K., Awashie, G. E., Boateng, A., & Darko, G. (2021). Geographically weighted principal component analysis for characterising the spatial heterogeneity and connectivity of soil heavy metals in Kumasi, Ghana. *Heliyon*, *7*(9), e08039. https://doi.org/10.1016/j.heliyon.2021.e08039

Akpomie, K. G., Dawodu, F. A., & Adebowale, K. O. (2015). Mechanism on the sorption of heavy metals from binary-solution by a low cost montmorillonite and its desorption potential. *Alexandria Engineering Journal*, *54*(3), 757–767. https://doi.org/10.1016/J.AEJ.2015.03.025

Aljeboree, A. M., Alshirifi, A. N., & Alkaim, A. F. (2017). Kinetics and equilibrium study for the adsorption of textile dyes on coconut shell activated carbon. *Arabian Journal of Chemistry*, *10*, S3381–S3393. https://doi.org/10.1016/J.ARABJC.2014.01.020

Aller, D., Bakshi, S., & Laird, D. A. (2017). Modified method for proximate analysis of biochars. *Journal of Analytical and Applied Pyrolysis*, *124*(January 2017), 335–342. https://doi.org/10.1016/j.jaap.2017.01.012

Anastopoulos, I., Robalds, A., Nguyen Tran, H., Mitrogiannis, D., Giannakoudakis, D. A., Hosseini-Bandegharaei, A., & Dotto, G. L. (2019). Removal of heavy metals by leaves-derived biosorbents. *Environmental Chemistry Letters*, *17*, 755–766. https://doi.org/10.1007/s10311-018-00829-x

Arampatzidou, A. C., & Deliyanni, E. A. (2016). Comparison of activation media and pyrolysis temperature for activated carbons development by pyrolysis of potato peels for effective adsorption of endocrine disruptor bisphenol-A. *Journal of Colloid and Interface Science*, *466*, 101–112. https://doi.org/10.1016/j.jcis.2015.12.003

Atif, M., Haider, H. Z., Bongiovanni, R., Fayyaz, M., Razzaq, T., & Gul, S. (2022a). Physisorption and chemisorption trends in surface modification of carbon black. *Surfaces and Interfaces*, *31*. https://doi.org/10.1016/J.SURFIN.2022.102080

Atif, M., Haider, H. Z., Bongiovanni, R., Fayyaz, M., Razzaq, T., & Gul, S. (2022b). Physisorption and chemisorption trends in surface modification of carbon black. *Surfaces and Interfaces*, *31*. https://doi.org/10.1016/J.SURFIN.2022.102080

Azhar, U., Ahmad, H., Shafqat, H., Babar, M., Shahzad Munir, H. M., Sagir, M., Arif, M., Hassan, A., Rachmadona, N., Rajendran, S., Mubashir, M., & Khoo, K. S. (2022a). Remediation techniques for elimination of heavy metal pollutants from soil: A review. *Environmental Research*, *214*. https://doi.org/10.1016/J.ENVRES.2022.113918

Azhar, U., Ahmad, H., Shafqat, H., Babar, M., Shahzad Munir, H. M., Sagir, M., Arif, M., Hassan, A., Rachmadona, N., Rajendran, S., Mubashir, M., & Khoo, K. S. (2022b). Remediation techniques for elimination of heavy metal pollutants from soil: A review. *Environmental Research*, *214*(P4), 113918. https://doi.org/10.1016/j.envres.2022.113918

AZoSensors. (2015). Calorimeters - Structural Design and Applications. *AZoSensors*, 1–3. https://www.azosensors.com/article.aspx?ArticleID=355

Azouaou, N., Sadaoui, Z., Djaafri, A., & Mokaddem, H. (2010). Adsorption of cadmium from aqueous solution onto untreated coffee grounds: equilibrium, kinetics and thermodynamics. *Journal of Hazardous Materials*, *184*(1–3), 126–134. https://doi.org/10.1016/J.JHAZMAT.2010.08.014

Bajpai, P. (2016). *Pretreatment of Lignocellulosic Biomass for Biofuel Production*. https://doi.org/10.1007/978-981-10-0687-6

Bao, H., Wang, J., Zhang, H., Li, J., Li, H., & Wu, F. (2019). Effects of biochar and organic substrates on biodegradation of polycyclic aromatic hydrocarbons and microbial community structure in PAHs-contaminated soils. *Journal of Hazardous Materials*, 121595. https://doi.org/10.1016/j.jhazmat.2019.121595

Bardalai, M., & Mahanta, D. K. (2018). Characterisation of Biochar Produced by Pyrolysis from Areca Catechu Dust. *Materials Today: Proceedings*, *5*(1), 2089–2097. https://doi.org/10.1016/j.matpr.2017.09.205

Barquilha, C. E. R., & Braga, M. C. B. (2021). Adsorption of organic and inorganic pollutants onto biochars: Challenges, operating conditions, and mechanisms. *Bioresource Technology Reports*, *15*. https://doi.org/10.1016/J.BITEB.2021.100728

Beatrice, A., Varco, J. J., Dygert, A., Atsar, F. S., Solomon, S., Thirumalai, R. V. K. G., Pittman, C. U., & Mlsna, T. (2022). Lead immobilization in simulated polluted soil by Douglas fir biochar-supported phosphate. *Chemosphere*, *292*. https://doi.org/10.1016/j.chemosphere.2021.133355

Bispo, M. D., Schneider, J. K., Da Silva Oliveira, D., Tomasini, D., Da Silva MacIel, G. P., Schena, T., Onorevoli, B., Bjerk, T. R., Jacques, R. A., Krause, L. C., & Caramão, E. B. (2018). Production of activated biochar from coconut fiber for the removal of

organic compounds from phenolic. *Journal of Environmental Chemical Engineering*, *6*(2), 2743–2750. https://doi.org/10.1016/j.jece.2018.04.029

Brame, J., & Griggs, C. (2016). *Surface Area Analysis Using the Brunauer-Emmett-Teller (BET) Method Scient*. *September*, 23. https://doi.org/39180-6199

Budai, A., Calucci, L., Rasse, D. P., Strand, L. T., Pengerud, A., Wiedemeier, D., Abiven, S., & Forte, C. (2017). Effects of pyrolysis conditions on Miscanthus and corncob chars: Characterization by IR, solid state NMR and BPCA analysis. *Journal of Analytical and Applied Pyrolysis*, *128*(May), 335–345. https://doi.org/10.1016/j.jaap.2017.09.017

Bujdák, J. (2020). Adsorption kinetics models in clay systems. The critical analysis of pseudo-second order mechanism. *Applied Clay Science*, *191*. https://doi.org/10.1016/J.CLAY.2020.105630

Cai, X., Li, J., Liu, Y., Yan, Z., Tan, X., Liu, S., Zeng, G., Gu, Y., Hu, X., & Jiang, L. (2018). Titanium dioxide-coated biochar composites as adsorptive and photocatalytic degradation materials for the removal of aqueous organic pollutants. *Journal of Chemical Technology and Biotechnology*, *93*(3), 783–791. https://doi.org/10.1002/jctb.5428

Canatoy, R. C., Jeong, S. T., Galgo, S. J. C., Kim, P. J., & Cho, S. R. (2021). Biochar as soil amendment: Syngas recycling system is essential to create positive carbon credit. *Science of The Total Environment*, *xxxx*, 151140. https://doi.org/10.1016/j.scitotenv.2021.151140

Chai, W. S., Cheun, J. Y., Kumar, P. S., Mubashir, M., Majeed, Z., Banat, F., Ho, S. H., & Show, P. L. (2021). A review on conventional and novel materials towards heavy metal adsorption in wastewater treatment application. *Journal of Cleaner Production*, *296*, 126589. https://doi.org/10.1016/J.JCLEPRO.2021.126589

Chang, Y., Lai, J. Y., & Lee, D. J. (2016). Thermodynamic parameters for adsorption equilibrium of heavy metals and dyes from wastewaters: Research updated. *Bioresource Technology*, *222*, 513–516. https://doi.org/10.1016/J.BIORTECH.2016.09.125

Chen, J., Qiu, X., Fang, Z., Yang, M., Pokeung, T., Gu, F., Cheng, W., & Lan, B. (2012). Removal mechanism of antibiotic metronidazole from aquatic solutions by using nanoscale zero-valent iron particles. *Chemical Engineering Journal*, *181–182*, 113–119. https://doi.org/10.1016/j.cej.2011.11.037

Chen, M., Wang, F., Zhang, D. li, Yi, W. ming, & Liu, Y. (2021). Effects of acid modification on the structure and adsorption NH4+-N properties of biochar. *Renewable Energy*, *169*, 1343–1350. https://doi.org/10.1016/j.renene.2021.01.098

Chen, Q. L., Fan, X. T., Zhu, D., An, X. L., Su, J. Q., & Cui, L. (2018). Effect of biochar amendment on the alleviation of antibiotic resistance in soil and phyllosphere of Brassica chinensis L. *Soil Biology and Biochemistry*, *119*(January), 74–82. https://doi.org/10.1016/j.soilbio.2018.01.015

Chen, Y., Li, M., Li, Y., Liu, Y., Chen, Y., Li, H., Li, L., Xu, F., Jiang, H., & Chen, L. (2021). Hydroxyapatite modified sludge-based biochar for the adsorption of Cu2+ and Cd2+: Adsorption behavior and mechanisms. *Bioresource Technology*, *321*. https://doi.org/10.1016/j.biortech.2020.124413

Collin, M. S., Venkatraman, S. K., Vijayakumar, N., Kanimozhi, V., Arbaaz, S. M., Stacey, R. G. S., Anusha, J., Choudhary, R., Lvov, V., Tovar, G. I., Senatov, F., Koppala, S., & Swamiappan, S. (2022). Bioaccumulation of lead (Pb) and its effects on human: A review. *Journal of Hazardous Materials Advances*, *7*, 100094. https://doi.org/10.1016/j.hazadv.2022.100094

Crombie, K., Mašek, O., Sohi, S. P., Brownsort, P., & Cross, A. (2013). The effect of pyrolysis conditions on biochar stability as determined by three methods. *GCB Bioenergy*, *5*(2), 122–131. https://doi.org/10.1111/gcbb.12030

Dai, C., Han, Y., Duan, Y., Lai, X., Fu, R., Liu, S., Leong, K. H., Tu, Y., & Zhou, L. (2022). Review on the contamination and remediation of polycyclic aromatic hydrocarbons (PAHs) in coastal soil and sediments. *Environmental Research*, *205*. https://doi.org/10.1016/j.envres.2021.112423

Debiagi, P., Gentile, G., Cuoci, A., Frassoldati, A., Ranzi, E., & Faravelli, T. (2018). SC. *Journal of Analytical and Applied Pyrolysis*. https://doi.org/10.1016/j.jaap.2018.06.022

Definition, P., & Standards, S. (2015). *Standardized Product Definition and Product Testing Guidelines for Biochar That Is Used in Soil*. *November*, 1–61.

Demirbaş, A. (2001). Relationships between lignin contents and heating values of biomass. *Energy Conversion and Management*, *42*(2), 183–188. https://doi.org/10.1016/S0196-8904(00)00050-9

Demirbas, A. (2017). Higher heating values of lignin types from wood and non-wood lignocellulosic biomasses. *Energy Sources, Part A: Recovery, Utilization and Environmental Effects*, *39*(6), 592–598. https://doi.org/10.1080/15567036.2016.1248798

Den, W., Sharma, V. K., Lee, M., Nadadur, G., & Varma, R. S. (2018). Lignocellulosic Biomass Transformations via Greener Oxidative Pretreatment Processes: Access to Energy and Value-Added Chemicals. *Frontiers in Chemistry*, *6*(April), 1–23. https://doi.org/10.3389/fchem.2018.00141

Dhyani, V., & Bhaskar, T. (2019). Pyrolysis of Biomass. Cellulose. *Biofuels: Alternative Feedstocks and Conversion Processes for the Production of Liquid and Gaseous Biofuels*, 217–244. https://doi.org/10.1016/B978-0-12-816856-1.00009-9

Ding, S., Guan, D. X., Dai, Z. H., Su, J., Teng, H. H., Ji, J., Liu, Y., Yang, Z., & Ma, L. Q. (2022). Nickel bioaccessibility in soils with high geochemical background and anthropogenic contamination. *Environmental Pollution*, *310*. https://doi.org/10.1016/j.envpol.2022.119914

Ding, W., Dong, X., Ime, I. M., Gao, B., & Ma, L. Q. (2014). Pyrolytic temperatures impact lead sorption mechanisms by bagasse biochars. *Chemosphere*, *105*, 68–74. https://doi.org/10.1016/j.chemosphere.2013.12.042

Doyle, W. M. (n.d.). *Full-Text*.

Dutta, A. (2017). Fourier Transform Infrared Spectroscopy. In *Spectroscopic Methods for Nanomaterials Characterization* (Vol. 2). Elsevier B.V. https://doi.org/10.1016/B978-0-323-46140-5.00004-2

Eickhorst, T., & Seubert, A. (2004). Germanium dioxide as internal standard for simplified trace determination of bromate, bromide, iodate and iodide by on-line coupling ion chromatography-inductively coupled plasma mass spectrometry. *Journal of Chromatography A*, *1050*(1), 103–109. https://doi.org/10.1016/J.CHROMA.2004.04.084

Eltaweil, A. S., Ali Mohamed, H., Abd El-Monaem, E. M., & El-Subruiti, G. M. (2020). Mesoporous magnetic biochar composite for enhanced adsorption of malachite green dye: Characterization, adsorption kinetics, thermodynamics and isotherms. *Advanced Powder Technology*, *31*(3), 1253–1263. https://doi.org/10.1016/j.apt.2020.01.005

Emamgholizadeh, S., Bazoobandi, A., Mohammadi, B., Ghorbani, H., & Amel Sadeghi, M. (2022). Prediction of soil cation exchange capacity using enhanced machine learning approaches in the southern region of the Caspian Sea. *Ain Shams Engineering Journal*. https://doi.org/10.1016/J.ASEJ.2022.101876

Enang, R. K., Kips, P. A., Yerima, B. P. K., Kome, G. K., & Van Ranst, E. (2022). Pedotransfer functions for cation exchange capacity estimation in highly weathered soils of the tropical highlands of NW Cameroon. *Geoderma Regional*, *29*. https://doi.org/10.1016/J.GEODRS.2022.E00514

Fahmi, A. H., Samsuri, A. W., Jol, H., & Singh, D. (2018). Physical modification of biochar to expose the inner pores and their functional groups to enhance lead adsorption. *RSC Advances*, *8*(67), 38270–38280. https://doi.org/10.1039/c8ra06867d

Fan, Y., Wang, B., Yuan, S., Wu, X., Chen, J., & Wang, L. (2010). Adsorptive removal of chloramphenicol from wastewater by NaOH modified bamboo charcoal. *Bioresource Technology*, *101*(19), 7661–7664. https://doi.org/10.1016/j.biortech.2010.04.046

Genchi, G., Carocci, A., Lauria, G., & Sinicropi, M. S. (2020). Ijerph-17-00679-V3.Pdf. *International Journal of Environmental Research and Public Health*, *17*(3), 679–700.

Genchi, G., Carocci, A., Lauria, G., Sinicropi, M. S., & Catalano, A. (n.d.). *Nickel: Human Health and Environmental Toxicology*. https://doi.org/10.3390/ijerph17030679

Georgin, J., Marques, B. S., Chaves Peres, E., Allasia, D., Dotto, G. L., Chaves, E., Guilherme, P., & Dotto, L. (2018). *Biosorption of cationic dyes by Pará chestnut husk (Bertholletia excelsa)*. https://doi.org/10.2166/wst.2018.041

Ghorbel-Abid, I., & Trabelsi-Ayadi, M. (2015). Competitive adsorption of heavy metals on local landfill clay. *Arabian Journal of Chemistry*, *8*(1), 25–31. https://doi.org/10.1016/J.ARABJC.2011.02.030

Guizani, C., Jeguirim, M., Valin, S., Limousy, L., & Salvador, S. (2017). Biomass chars: The effects of pyrolysis conditions on their morphology, structure, chemical properties and reactivity. *Energies*, *10*(6). https://doi.org/10.3390/en10060796

Harris, W. (2009). *Dairy-Manure Derived Biochar Effectively Sorbs Lead and Atrazine*. 3285–3291. https://doi.org/10.1021/es803092k

Hart, A., Porbeni, D. W., Omonmhenle, S., & Peretomode, E. (2023). Waste bone char-derived adsorbents: characteristics, adsorption mechanism and model approach. In *Environmental Technology Reviews* (Vol. 12, Issue 1, pp. 175–204). Taylor and Francis Ltd. https://doi.org/10.1080/21622515.2023.2197128

Hasegawa, T. (2017). Quantitative infrared spectroscopy for understanding of a condensed matter. *Quantitative Infrared Spectroscopy for Understanding of a Condensed Matter*, 1–200. https://doi.org/10.1007/978-4-431-56493-5

Hassel, B. van, Pasini, J., & Limarga, A. (2010). IV. D. 6 Advancement of Systems Designs and Key Engineering Technologies for Materials Based-Hydrogen Storage. *Hydrogen.Energy.Gov*, 1–6. http://hydrogen.energy.gov/pdfs/progress12/iv_d_6_van_hassel_2012.pdf

Hendriks, A. T. W. M., & Zeeman, G. (2009). Pretreatments to enhance the digestibility of lignocellulosic biomass. *Bioresource Technology*, *100*(1), 10–18. https://doi.org/10.1016/j.biortech.2008.05.027

Hidayat B, Rauf, A., Sabrina, T., & Jamil, A. (2018). Potential of Several Biomass as Biochar for Heavy Metal Adsorbent. *Journal of Asian Scientific Research*, *8*(11), 293–300. https://doi.org/10.18488/journal.2.2018.811.293.300

Higashikawa, F. S., Conz, R. F., Colzato, M., Cerri, C. E. P., & Alleoni, L. R. F. (2016). Effects of feedstock type and slow pyrolysis temperature in the production of biochars on the removal of cadmium and nickel from water. *Journal of Cleaner Production*, *137*, 965–972. https://doi.org/10.1016/j.jclepro.2016.07.205

Huang, H. jun, Yang, T., Lai, F. ying, & Wu, G. qiang. (2017). Co-pyrolysis of sewage sludge and sawdust/rice straw for the production of biochar. *Journal of Analytical and Applied Pyrolysis*, *125*(April), 61–68. https://doi.org/10.1016/j.jaap.2017.04.018

Iamsaard, K., Weng, C.-H., Yen, L.-T., Tzeng, J.-H., Poonpakdee, C., & Lin, Y.-T. (2021). Adsorption of metal on pineapple leaf biochar: key affecting factors, mechanism identification, and regeneration evaluation. *Bioresource Technology*, *344*(PA), 126131. https://doi.org/10.1016/j.biortech.2021.126131

IBI. (2018). *List of frequently asked questions*. International Biochar Initiative. https://www.biochar-international.org/faqs/

Iftekhar, S., Ramasamy, D. L., Srivastava, V., Asif, M. B., & Sillanpää, M. (2018). Understanding the factors affecting the adsorption of Lanthanum using different adsorbents: A critical review. *Chemosphere*, *204*, 413–430. https://doi.org/10.1016/J.CHEMOSPHERE.2018.04.053

Igalavithana, A. D., Mandal, S., Niazi, N. K., Vithanage, M., Parikh, S. J., Mukome, F. N. D., Rizwan, M., Oleszczuk, P., Al-Wabel, M., Bolan, N., Tsang, D. C. W., Kim, K. H., & Ok, Y. S. (2017). Advances and future directions of biochar characterization methods and applications. *Critical Reviews in Environmental Science and Technology*, *47*(23), 2275–2330. https://doi.org/10.1080/10643389.2017.1421844

Inglezakis, V. J., Fyrillas, M. M., & Park, J. (2019). Variable diffusivity homogeneous surface diffusion model and analysis of merits and fallacies of simplified adsorption

kinetics equations. *Journal of Hazardous Materials*, *367*, 224–245. https://doi.org/10.1016/J.JHAZMAT.2018.12.023

Inyang, M., & Dickenson, E. (2015). The potential role of biochar in the removal of organic and microbial contaminants from potable and reuse water: A review. *Chemosphere*, *134*, 232–240. https://doi.org/10.1016/j.chemosphere.2015.03.072

Iwamoto, T., Hieda, Y., & Kogai, Y. (2016). Effect of hydroxyapatite surface morphology on cell adhesion. *Materials Science and Engineering C*, *69*, 1263–1267. https://doi.org/10.1016/J.MSEC.2016.07.056

Jafri, N., Wong, W. Y., Doshi, V., Yoon, L. W., & Cheah, K. H. (2018). SC. *Process Safety and Environmental Protection*. https://doi.org/10.1016/j.psep.2018.06.036

Jalees, M. I., Muhammad, ·, Farooq, U., Sarosh Basheer, ·, & Asghar, S. (2019). Removal of Heavy Metals from Drinking Water Using Chikni Mitti (Kaolinite): Isotherm and Kinetics. *Arabian Journal for Science and Engineering*, *44*, 6351–6359. https://doi.org/10.1007/s13369-019-03722-z

Jawed, A., Saxena, V., & Pandey, L. M. (2020). Engineered nanomaterials and their surface functionalization for the removal of heavy metals: A review. *Journal of Water Process Engineering*, *33*, 101009. https://doi.org/10.1016/J.JWPE.2019.101009

Jin, J., Sun, K., Liu, W., Li, S., Peng, X., Yang, Y., Han, L., Du, Z., & Wang, X. (2018). Isolation and characterization of biochar-derived organic matter fractions and their phenanthrene sorption. *Environmental Pollution*, *236*, 745–753. https://doi.org/10.1016/j.envpol.2018.02.015

Jose, S., Senthilkumar, M., Elayaraja, K., Haris, M., George, A., Raj, A. D., Sundaram, S. J., Bashir, A. K. H., Maaza, M., & Kaviyarasu, K. (2021). Preparation and

characterization of Fe doped n-hydroxyapatite for biomedical application. *Surfaces and Interfaces*, *25*, 101185. https://doi.org/10.1016/j.surfin.2021.101185

Jung, C., Oh, J., & Yoon, Y. (2015). Removal of acetaminophen and naproxen by combined coagulation and adsorption using biochar: influence of combined sewer overflow components. *Environmental Science and Pollution Research*, *22*(13), 10058–10069. https://doi.org/10.1007/s11356-015-4191-6

Jung, C., Park, J., Lim, K. H., Park, S., Heo, J., Her, N., Oh, J., Yun, S., & Yoon, Y. (2013). Adsorption of selected endocrine disrupting compounds and pharmaceuticals on activated biochars. *Journal of Hazardous Materials*, *263*, 702–710. https://doi.org/10.1016/j.jhazmat.2013.10.033

Khaleeq, A., Ahmed, M., Huma, R., Mujtaba, A., Noor, S., Rehman, R., Sheikh, T. A., Qamar, S., Iqbal, D. N., Alharthy, R. D., & Hameed, A. (2022). Evaluation of trace and heavy metals in different varieties of sauces to characterize their impact on human health. *Journal of Food Composition and Analysis*, *114*. https://doi.org/10.1016/J.JFCA.2022.104789

Khan, Z. H., Gao, M., Qiu, W., Islam, M. S., & Song, Z. (2020). Mechanisms for cadmium adsorption by magnetic biochar composites in an aqueous solution. *Chemosphere*, *246*. https://doi.org/10.1016/j.chemosphere.2019.125701

Kong, H., He, J., Gao, Y., Wu, H., & Zhu, X. (2011). Cosorption of phenanthrene and mercury(II) from aqueous solution by soybean stalk-based biochar. *Journal of Agricultural and Food Chemistry*, *59*(22), 12116–12123. https://doi.org/10.1021/jf202924a

Kong, L., Gao, Y., Zhou, Q., Zhao, X., & Sun, Z. (2018). Biochar accelerates PAHs biodegradation in petroleum-polluted soil by biostimulation strategy. *Journal of Hazardous Materials*, *343*, 276–284. https://doi.org/10.1016/j.jhazmat.2017.09.040

Krasucka, P., Pan, B., Sik Ok, Y., Mohan, D., Sarkar, B., & Oleszczuk, P. (2021). Engineered biochar – A sustainable solution for the removal of antibiotics from water. *Chemical Engineering Journal*, *405*, 126926. https://doi.org/10.1016/J.CEJ.2020.126926

Kushwaha, S., Soni, H., Ageetha, V., & Padmaja, P. (2013). Critical Reviews in Environmental Science and Technology An Insight Into the Production, Characterization, and Mechanisms of Action of Low-Cost Adsorbents for Removal of Organics From Aqueous Solution) An Insight Into the Production, Characterization, and Mechanisms of Action of Low-Cost Adsorbents for Removal of Organics From Aqueous Solution An Insight Into the Production, Characterization, and Mechanisms of Action of Low-Cost Adsorbents for Removal of Organics From Aqueous Solution. *Critical Reviews in Environmental Science and Technology*, *43*(5), 443–549. https://doi.org/10.1080/10643389.2011.604263

Lam, S. S., Liew, R. K., Cheng, C. K., Rasit, N., Ooi, C. K., Ma, N. L., Ng, J. H., Lam, W. H., Chong, C. T., & Chase, H. A. (2018). Pyrolysis production of fruit peel biochar for potential use in treatment of palm oil mill effluent. *Journal of Environmental Management*, *213*, e74–e74. https://doi.org/10.1016/j.jenvman.2018.02.092

Largitte, L., & Pasquier, R. (2016). A review of the kinetics adsorption models and their application to the adsorption of lead by an activated carbon. *Chemical Engineering Research and Design*, *109*, 495–504. https://doi.org/10.1016/J.CHERD.2016.02.006

Li, A., Ye, C., Jiang, Y., & Deng, H. (2023). Enhanced removal performance of magnesium-modified biochar for cadmium in wastewaters: Role of active functional groups, processes, and mechanisms. *Bioresource Technology*, *386*, 129515. https://doi.org/10.1016/j.biortech.2023.129515

Li, B., Yang, L., Wang, C. quan, Zhang, Q. pei, Liu, Q. cheng, Li, Y. ding, & Xiao, R. (2017). Adsorption of Cd(II) from aqueous solutions by rape straw biochar derived from different modification processes. *Chemosphere*, *175*, 332–340. https://doi.org/10.1016/j.chemosphere.2017.02.061

Li, C., Zhang, L., Gao, Y., & Li, A. (2018). Facile synthesis of nano ZnO/ZnS modified biochar by directly pyrolyzing of zinc contaminated corn stover for Pb(II), Cu(II) and Cr(VI) removals. *Waste Management*, *79*, 625–637. https://doi.org/10.1016/j.wasman.2018.08.035

Li, H., Dong, X., da Silva, E. B., de Oliveira, L. M., Chen, Y., & Ma, L. Q. (2017a). Mechanisms of metal sorption by biochars: Biochar characteristics and modifications. *Chemosphere*, *178*, 466–478. https://doi.org/10.1016/j.chemosphere.2017.03.072

Li, H., Dong, X., da Silva, E. B., de Oliveira, L. M., Chen, Y., & Ma, L. Q. (2017b). Mechanisms of metal sorption by biochars: Biochar characteristics and modifications. *Chemosphere*, *178*, 466–478. https://doi.org/10.1016/j.chemosphere.2017.03.072

Li, H., Dong, X., da Silva, E. B., de Oliveira, L. M., Chen, Y., & Ma, L. Q. (2017c). Mechanisms of metal sorption by biochars: Biochar characteristics and modifications. In *Chemosphere* (Vol. 178, pp. 466–478). Elsevier Ltd. https://doi.org/10.1016/j.chemosphere.2017.03.072

Li, M., Liu, H., Chen, T., Dong, C., & Sun, Y. (2019). Synthesis of magnetic biochar composites for enhanced uranium(VI) adsorption. *Science of the Total Environment*, *651*, 1020–1028. https://doi.org/10.1016/j.scitotenv.2018.09.259

Li, X., Wang, C., Zhang, J., Liu, J., Liu, B., & Chen, G. (2020). Preparation and application of magnetic biochar in water treatment: A critical review. *Science of the Total Environment*, *711*, 134847. https://doi.org/10.1016/j.scitotenv.2019.134847

Li, Y., Shao, J., Wang, X., Deng, Y., Yang, H., & Chen, H. (2014). Characterization of modified biochars derived from bamboo pyrolysis and their utilization for target component (furfural) adsorption. *Energy and Fuels*, *28*(8), 5119–5127. https://doi.org/10.1021/ef500725c

Li, Z., Cheng, J., & Wu, Q. (2016). Analyzing regional economic development patterns in a fast developing province of China through geographically weighted principal component analysis. *Letters in Spatial and Resource Sciences*, *9*(3), 233–245. https://doi.org/10.1007/s12076-015-0154-2

Li, Z., Wang, Z., Wu, X., Li, M., & Liu, X. (2020a). Competitive adsorption of tylosin, sulfamethoxazole and Cu(II) on nano-hydroxyapatitemodified biochar in water. *Chemosphere*, *240*. https://doi.org/10.1016/j.chemosphere.2019.124884

Li, Z., Wang, Z., Wu, X., Li, M., & Liu, X. (2020b). Competitive adsorption of tylosin, sulfamethoxazole and Cu(II) on nano-hydroxyapatitemodified biochar in water. *Chemosphere*, *240*, 124884. https://doi.org/10.1016/j.chemosphere.2019.124884

Liang, S., Shi, S., Zhang, H., Qiu, J., Yu, W., Li, M., Gan, Q., Yu, W., Xiao, K., Liu, B., Hu, J., Hou, H., & Yang, J. (2019). One-pot solvothermal synthesis of magnetic biochar from waste biomass: Formation mechanism and efficient adsorption of Cr(VI) in an aqueous solution. *Science of the Total Environment*, *695*, 133886. https://doi.org/10.1016/j.scitotenv.2019.133886

Liao, T., Li, T., Su, X., Yu, X., Song, H., Zhu, Y., & Zhang, Y. (2018). La(OH)3-modified magnetic pineapple biochar as novel adsorbents for efficient phosphate removal.

Bioresource Technology, *263*(April), 207–213. https://doi.org/10.1016/j.biortech.2018.04.108

Lim, K. Y., & Foo, K. Y. (2021). Hazard identification and risk assessment of the organic, inorganic and microbial contaminants in the surface water after the high magnitude of flood event. *Environment International*, *157*. https://doi.org/10.1016/J.ENVINT.2021.106851

Liu, L., Liu, X., Wang, D., Lin, H., & Huang, L. (2020). Removal and reduction of Cr(VI) in simulated wastewater using magnetic biochar prepared by co-pyrolysis of nano-zero-valent iron and sewage sludge. *Journal of Cleaner Production*, *257*, 120562. https://doi.org/10.1016/j.jclepro.2020.120562

Liu, Q., Gui, Z., Xiong, S., & Zhan, M. (2021). A principal component analysis dominance mechanism based many-objective scheduling optimization. *Applied Soft Computing*, *113*, 107931. https://doi.org/10.1016/j.asoc.2021.107931

Liu, X., & Lee, D. J. (2014). Thermodynamic parameters for adsorption equilibrium of heavy metals and dyes from wastewaters. *Bioresource Technology*, *160*, 24–31. https://doi.org/10.1016/J.BIORTECH.2013.12.053

Liu, Y., Chen, Y., Li, Y., Chen, L., Jiang, H., Li, H., Luo, X., Tang, P., Yan, H., Zhao, M., Yuan, Y., & Hou, S. (2022). Fabrication, application, and mechanism of metal and heteroatom co-doped biochar composites (MHBCs) for the removal of contaminants in water: A review. *Journal of Hazardous Materials*, *431*. https://doi.org/10.1016/J.JHAZMAT.2022.128584

Liu, Y., Lonappan, L., Brar, S. K., & Yang, S. (2018). Impact of biochar amendment in agricultural soils on the sorption, desorption, and degradation of pesticides: A review. *Science of the Total Environment*, *645*, 60–70. https://doi.org/10.1016/j.scitotenv.2018.07.099

Liu, Z., Singer, S., Tong, Y., Kimbell, L., Anderson, E., Hughes, M., Zitomer, D., & McNamara, P. (2018). Characteristics and applications of biochars derived from wastewater solids. *Renewable and Sustainable Energy Reviews*, *90*(May 2017), 650–664. https://doi.org/10.1016/j.rser.2018.02.040

Lu, H., Zhang, W., Yang, Y., Huang, X., Wang, S., & Qiu, R. (2012). Relative distribution of Pb2+sorption mechanisms by sludge-derived biochar. *Water Research*, *46*(3), 854–862. https://doi.org/10.1016/j.watres.2011.11.058

Luo, M., Lin, H., Li, B., Dong, Y., He, Y., & Wang, L. (2018). A novel modification of lignin on corncob-based biochar to enhance removal of cadmium from water. *Bioresource Technology*, *259*(March), 312–318. https://doi.org/10.1016/j.biortech.2018.03.075

Luz, F. C., Cordiner, S., Manni, A., Mulone, V., & Rocco, V. (2018). Biochar Characteristics and Early Applications in Anaerobic Digestion-a Review. *Journal of Environmental Chemical Engineering*, *6*(2), 2892–2909. https://doi.org/10.1016/j.jece.2018.04.015

Ma, Y., Liu, W. J., Zhang, N., Li, Y. S., Jiang, H., & Sheng, G. P. (2014). Polyethylenimine modified biochar adsorbent for hexavalent chromium removal from the aqueous solution. *Bioresource Technology*, *169*, 403–408. https://doi.org/10.1016/j.biortech.2014.07.014

Mahdi, Z., Yu, Q. J., & El Hanandeh, A. (2018a). Investigation of the kinetics and mechanisms of nickel and copper ions adsorption from aqueous solutions by date seed derived biochar. *Journal of Environmental Chemical Engineering*, *6*(1), 1171–1181. https://doi.org/10.1016/j.jece.2018.01.021

Mahdi, Z., Yu, Q. J., & El Hanandeh, A. (2018b). Investigation of the kinetics and mechanisms of nickel and copper ions adsorption from aqueous solutions by date

seed derived biochar. *Journal of Environmental Chemical Engineering*, *6*(1), 1171–1181. https://doi.org/10.1016/j.jece.2018.01.021

Manufacturing, C. B. (2014). *Standard Test Method for Carbon Black — Total and External Surface Area by Nitrogen*. *i*, 1–5. https://doi.org/10.1520/D6556-14.2

Manyà, J. J., Ortigosa, M. A., Laguarta, S., & Manso, J. A. (2014). Experimental study on the effect of pyrolysis pressure, peak temperature, and particle size on the potential stability of vine shoots-derived biochar. *Fuel*, *133*, 163–172. https://doi.org/10.1016/j.fuel.2014.05.019

Masebinu, S. O., Akinlabi, E. T., Muzenda, E., & Aboyade, A. O. (2019). A review of biochar properties and their roles in mitigating challenges with anaerobic digestion. *Renewable and Sustainable Energy Reviews*, *103*, 291–307. https://doi.org/10.1016/J.RSER.2018.12.048

Mašek, O., Buss, W., Roy-Poirier, A., Lowe, W., Peters, C., Brownsort, P., Mignard, D., Pritchard, C., & Sohi, S. (2018). Consistency of biochar properties over time and production scales: A characterisation of standard materials. *Journal of Analytical and Applied Pyrolysis*, *132*(February), 200–210. https://doi.org/10.1016/j.jaap.2018.02.020

Matouq, M., Jildeh, N., Qtaishat, M., Hindiyeh, M., & Al Syouf, M. Q. (2015). The adsorption kinetics and modeling for heavy metals removal from wastewater by Moringa pods. *Journal of Environmental Chemical Engineering*, *3*(2), 775–784. https://doi.org/10.1016/j.jece.2015.03.027

Mei, M., Hu, X., Song, Z., Chen, L., Deng, L., & Qi, Z. (2022). CO2 capture by 1-ethyl-3-methylimidazolium acetate: Solubility at low pressure and quantification of chemisorption and physisorption. *Journal of Molecular Liquids*, *348*. https://doi.org/10.1016/J.MOLLIQ.2021.118036

Minerals, B. C., Required, I. C., Class, M., Declaration, R., Declaration, R., Method, S. T., Determination, R., Content, C., Method, S. T., Analysis, C., Charcoal, W., & Iso, D. I. N. E. N. (2014). *Comparison of European Biochar Certificate Version 4 . 8 and IBI Biochar Standards Version 2 . 0 European Biochar Certificate first publication March 2012 http://www.european-biochar.org/en/home IBI Biochar Standards first publication May 2012 http://www. October*, 1–5.

Mirheidari, A., Torbatinejad, N. M., Shakeri, P., & Mokhtarpour, A. (2020). Effects of biochar produced from different biomass sources on digestibility, ruminal fermentation, microbial protein synthesis and growth performance of male lambs. *Small Ruminant Research*, *183*, 106042. https://doi.org/10.1016/j.smallrumres.2019.106042

Mitra, S., Chakraborty, A. J., Tareq, A. M., Emran, T. Bin, Nainu, F., Khusro, A., Idris, A. M., Khandaker, M. U., Osman, H., Alhumaydhi, F. A., & Simal-Gandara, J. (2022). Impact of heavy metals on the environment and human health: Novel therapeutic insights to counter the toxicity. *Journal of King Saud University - Science*, *34*(3). https://doi.org/10.1016/J.JKSUS.2022.101865

Mondal, S., Bobde, K., Aikat, K., & Halder, G. (2016). Biosorptive uptake of ibuprofen by steam activated biochar derived from mung bean husk: Equilibrium, kinetics, thermodynamics, modeling and eco-toxicological studies. *Journal of Environmental Management*, *182*, 581–594. https://doi.org/10.1016/j.jenvman.2016.08.018

Nartey, O. D., & Zhao, B. (2014). Biochar preparation, characterization, and adsorptive capacity and its effect on bioavailability of contaminants: An overview. *Advances in Materials Science and Engineering*, *2014*. https://doi.org/10.1155/2014/715398

Netzsch. (2011). *Thermogravimetric Analysis – TGA Method , Technique , Applications*. 1–20.

Nur, S., Abas, A., Halim, M., Ismail, S., Kamal, L., & Izhar, S. (2013). Adsorption Process of Heavy Metals by Low-Cost Adsorbent: A Review. *World Applied Sciences Journal*, *28*(11), 1518–1530. https://doi.org/10.5829/idosi.wasj.2013.28.11.1874

Oliveira, F. R., Patel, A. K., Jaisi, D. P., Adhikari, S., Lu, H., & Khanal, S. K. (2017). Environmental application of biochar: Current status and perspectives. *Bioresource Technology*, *246*(August), 110–122. https://doi.org/10.1016/j.biortech.2017.08.122

Oninla, V. O., Olatunde, A. M., Babalola, J. O., Adesanmi, O. J., Towolawi, G. S., & Awokoya, K. N. (2018). Qualitative assessments of the biomass from oil palm calyxes and its application in heavy metals removal from polluted water. *Journal of Environmental Chemical Engineering*, *6*(4), 4044–4053. https://doi.org/10.1016/J.JECE.2018.05.030

Onorevoli, B., da Silva Maciel, G. P., Machado, M. E., Corbelini, V., Caramão, E. B., & Jacques, R. A. (2018). Characterization of feedstock and biochar from energetic tobacco seed waste pyrolysis and potential application of biochar as an adsorbent. *Journal of Environmental Chemical Engineering*, *6*(1), 1279–1287. https://doi.org/10.1016/j.jece.2018.01.039

Pace, B., Munroe, P., Marjo, C. E., Thomas, P., Gong, B., Shepherd, J., Buss, W., & Joseph, S. (2018). The mechanisms and consequences of inorganic reactions during the production of ferrous sulphate enriched bamboo biochars. *Journal of Analytical and Applied Pyrolysis*, *131*(February), 101–112. https://doi.org/10.1016/j.jaap.2018.01.028

Papadiamantis, A. G. (2017). *MATURATION AND AGEING IN BIOMINERALS WITH APPLICATION TO ENAMEL MATURATION*.

Parmar, S., Daki, S., & Shrivastav, A. (2021). Application of Biochar for Soil Remediation. *Biochar and Its Application in Bioremediation*, *98104*, 455–471. https://doi.org/10.1007/978-981-16-4059-9_21

Parr instrument company. (2007). Introduction to Bomb Calorimetry. *Parr Instrument Company*, *483*, 1–11. http://www.scimed.co.uk/wp-content/uploads/2013/03/Introduction-to-bomb-calorimetry.pdf

PerkinElmer. (2013). *Thermogravimetric Analysis (TGA) PerkinElmer's TGA - A Beginner's Guide*. https://doi.org/10.1198/tech.2005.s328

Petrovic, B., Gorbounov, M., & Masoudi Soltani, S. (2021). Influence of surface modification on selective CO2 adsorption: A technical review on mechanisms and methods. *Microporous and Mesoporous Materials*, *312*. https://doi.org/10.1016/J.MICROMESO.2020.110751

Ping, L. F., Luo, Y. M., Zhang, H. B., Li, Q. B., & Wu, L. H. (2007). Distribution of polycyclic aromatic hydrocarbons in thirty typical soil profiles in the Yangtze River Delta region, east China. *Environmental Pollution*, *147*(2), 358–365. https://doi.org/10.1016/j.envpol.2006.05.027

Qiao, K., Tian, W., Bai, J., Dong, J., Zhao, J., Gong, X., & Liu, S. (2018). Preparation of biochar from Enteromorpha prolifera and its use for the removal of polycyclic aromatic hydrocarbons (PAHs) from aqueous solution. *Ecotoxicology and Environmental Safety*, *149*(November 2017), 80–87. https://doi.org/10.1016/j.ecoenv.2017.11.027

Raghav, S., & Kumar, D. (2018). *Adsorption Equilibrium, Kinetics, and Thermodynamic Studies of Fluoride Adsorbed by Tetrametallic Oxide Adsorbent*. https://doi.org/10.1021/acs.jced.8b00024

Rahmani, A., Mousavi, H. Z., & Fazli, M. (2010). Effect of nanostructure alumina on adsorption of heavy metals. *Desalination*, *253*(1–3), 94–100. https://doi.org/10.1016/J.DESAL.2009.11.027

Rajapaksha, A. U., Chen, S. S., Tsang, D. C. W., Zhang, M., Vithanage, M., Mandal, S., Gao, B., Bolan, N. S., & Ok, Y. S. (2016). Engineered/designer biochar for contaminant removal/immobilization from soil and water: Potential and implication of biochar modification. *Chemosphere*, *148*, 276–291. https://doi.org/10.1016/j.chemosphere.2016.01.043

Rajendran, S., Priya, A. K., Senthil Kumar, P., Hoang, T. K. A., Sekar, K., Chong, K. Y., Khoo, K. S., Ng, H. S., & Show, P. L. (2022a). A critical and recent developments on adsorption technique for removal of heavy metals from wastewater-A review. *Chemosphere*, *303*. https://doi.org/10.1016/J.CHEMOSPHERE.2022.135146

Rajendran, S., Priya, A. K., Senthil Kumar, P., Hoang, T. K. A., Sekar, K., Chong, K. Y., Khoo, K. S., Ng, H. S., & Show, P. L. (2022b). A critical and recent developments on adsorption technique for removal of heavy metals from wastewater-A review. *Chemosphere*, *303*, 135146. https://doi.org/10.1016/J.CHEMOSPHERE.2022.135146

Rápó, E., & Tonk, S. (2017a). *molecules Factors Affecting Synthetic Dye Adsorption; Desorption Studies: A Review of Results from the Last Five Years (2017-2021)*. *26*, 5419. https://doi.org/10.3390/molecules26175419

Rápó, E., & Tonk, S. (2017b). *molecules Factors Affecting Synthetic Dye Adsorption; Desorption Studies: A Review of Results from the Last Five Years (2017-2021)*. *26*, 5419. https://doi.org/10.3390/molecules26175419

Rasheed, T. (2022). Covalent organic frameworks as promising adsorbent paradigm for environmental pollutants from aqueous matrices: Perspective and challenges.

Science of The Total Environment, *833*, 155279. https://doi.org/10.1016/J.SCITOTENV.2022.155279

Reac, L. M. (2001). *Contaminated Soils*. *April*. https://doi.org/10.13140/2.1.1074.9448

rees. (2014). Short-term effects of biochar on soil heavy metal mobility are controlled by intra-particle diffusion and soil pH increase. *European Journal of Soil Science*, *65*, 149–161. https://doi.org/10.1111/ejss.12107

Revellame, E. D., Fortela, D. L., Sharp, W., Hernandez, R., & Zappi, M. E. (2020). Adsorption kinetic modeling using pseudo-first order and pseudo-second order rate laws: A review. *Cleaner Engineering and Technology*, *1*, 100032. https://doi.org/10.1016/J.CLET.2020.100032

Reyes-Gasga, J., Martínez-Piñeiro, E. L., Rodríguez-Álvarez, G., Tiznado-Orozco, G. E., García-García, R., & Brès, E. F. (2013). XRD and FTIR crystallinity indices in sound human tooth enamel and synthetic hydroxyapatite. *Materials Science and Engineering C*, *33*(8), 4568–4574. https://doi.org/10.1016/j.msec.2013.07.014

Saha, P., Chowdhury, S., Gupta, S., & Kumar, I. (2010). Insight into adsorption equilibrium, kinetics and thermodynamics of Malachite Green onto clayey soil of Indian origin. *Chemical Engineering Journal*, *165*(3), 874–882. https://doi.org/10.1016/J.CEJ.2010.10.048

Sahmoune, M. N. (2019). Evaluation of thermodynamic parameters for adsorption of heavy metals by green adsorbents. *Environmental Chemistry Letters*, *17*, 697–704. https://doi.org/10.1007/s10311-018-00819-z

Sahoo, S. S., Vijay, V. K., Chandra, R., & Kumar, H. (2021). Production and characterization of biochar produced from slow pyrolysis of pigeon pea stalk and bamboo. *Cleaner Engineering and Technology*, *3*, 100101. https://doi.org/10.1016/J.CLET.2021.100101

Sakhiya, A. K., Anand, A., Aier, I., Vijay, V. K., & Kaushal, P. (2021). Suitability of rice straw for biochar production through slow pyrolysis: Product characterization and thermodynamic analysis. *Bioresource Technology Reports*, *15*, 100818. https://doi.org/10.1016/J.BITEB.2021.100818

Schreiter, I. J., Schmidt, W., & Schüth, C. (2018). Sorption mechanisms of chlorinated hydrocarbons on biochar produced from different feedstocks: Conclusions from single- and bi-solute experiments. *Chemosphere*, *203*, 34–43. https://doi.org/10.1016/j.chemosphere.2018.03.173

Sharma, S. P. (2018). Biochar for Carbon Sequestration. In *Omics Technologies and Bio-Engineering*. Elsevier Inc. https://doi.org/10.1016/B978-0-12-815870-8.00020-6

Shen, B., Chen, J., Yue, S., & Li, G. (2015). A comparative study of modified cotton biochar and activated carbon based catalysts in low temperature SCR. *Fuel*, *156*, 47–53. https://doi.org/10.1016/j.fuel.2015.04.027

Shen, B., Li, G., Wang, F., Wang, Y., He, C., Zhang, M., & Singh, S. (2015). Elemental mercury removal by the modified bio-char from medicinal residues. *Chemical Engineering Journal*, *272*, 28–37. https://doi.org/10.1016/j.cej.2015.03.006

Shen, J., Liu, J., Xing, Y., Zhang, H., Luo, L., & Jiang, X. (2018). Journal of Analytical and Applied Pyrolysis Application of TG-FTIR analysis to super fi ne pulverized coal. *Journal of Analytical and Applied Pyrolysis*, *133*(April), 154–161. https://doi.org/10.1016/j.jaap.2018.04.007

Shen, W., Li, Z., & Liu, Y. (2010). Surface Chemical Functional Groups Modification of Porous Carbon. *Recent Patents on Chemical Engineering*, *1*(1), 27–40. https://doi.org/10.2174/1874478810801010027

Shrestha, R., Ban, S., Devkota, S., Sharma, S., Joshi, R., Tiwari, A. P., Kim, H. Y., & Joshi, M. K. (2021a). Technological trends in heavy metals removal from industrial

wastewater: A review. *Journal of Environmental Chemical Engineering*, *9*(4), 105688. https://doi.org/10.1016/J.JECE.2021.105688

Shrestha, R., Ban, S., Devkota, S., Sharma, S., Joshi, R., Tiwari, A. P., Kim, H. Y., & Joshi, M. K. (2021b). Technological trends in heavy metals removal from industrial wastewater: A review. *Journal of Environmental Chemical Engineering*, *9*(4), 105688. https://doi.org/10.1016/J.JECE.2021.105688

Silva, L. M. S., Muñoz-Peña, M. J., Domínguez-Vargas, J. R., González, T., & Cuerda-Correa, E. M. (2021a). Kinetic and equilibrium adsorption parameters estimation based on a heterogeneous intraparticle diffusion model. *Surfaces and Interfaces*, *22*, 100791. https://doi.org/10.1016/J.SURFIN.2020.100791

Silva, L. M. S., Muñoz-Peña, M. J., Domínguez-Vargas, J. R., González, T., & Cuerda-Correa, E. M. (2021b). Kinetic and equilibrium adsorption parameters estimation based on a heterogeneous intraparticle diffusion model. *Surfaces and Interfaces*, *22*. https://doi.org/10.1016/J.SURFIN.2020.100791

Singh, A. K. (2022). Engineered biochar for oil/water separation: Processing and mechanism. *Bioresource Technology Reports*, *20*. https://doi.org/10.1016/j.biteb.2022.101269

Singh, Y. D., Mahanta, P., & Bora, U. (2017). Comprehensive characterization of lignocellulosic biomass through proximate, ultimate and compositional analysis for bioenergy production. *Renewable Energy*, *103*, 490–500. https://doi.org/10.1016/j.renene.2016.11.039

Sizmur, T., Fresno, T., Akgül, G., Frost, H., & Moreno-Jiménez, E. (2017). Biochar modification to enhance sorption of inorganics from water. In *Bioresource Technology* (Vol. 246, pp. 34–47). Elsevier Ltd. https://doi.org/10.1016/j.biortech.2017.07.082

Smoak, R. A., & Schnoor, J. L. (2022). Nickel Hyperaccumulator Biochar as a Ni-Adsorbent and Enhanced Bio-ore. *ACS Environmental Au*, *2*(1), 65–73. https://doi.org/10.1021/acsenvironau.1c00018

Song, B., Chen, M., Zhao, L., Qiu, H., & Cao, X. (2019). Physicochemical property and colloidal stability of micron- and nano-particle biochar derived from a variety of feedstock sources. *Science of the Total Environment*, *661*, 685–695. https://doi.org/10.1016/j.scitotenv.2019.01.193

Spokas, K. A. (2010). Review of the stability of biochar in soils: Predictability of O:C molar ratios. *Carbon Management*, *1*(2), 289–303. https://doi.org/10.4155/cmt.10.32

Sponsors, S., & News, L. N. (2015). The History and Working Principle of the Scanning Electron Microscope (SEM). *Mar 20 2015*, 1–8. https://www.azonano.com/article.aspx?ArticleID=3995

Strawn, D. G., & Sparks, D. L. (2000). Effects of Soil Organic Matter on the Kinetics and Mechanisms of Pb(II) Sorption and Desorption in Soil. *Soil Science Society of America Journal*, *64*(1), 144–156. https://doi.org/10.2136/SSSAJ2000.641144X

Suliman, W., Harsh, J. B., Abu-Lail, N. I., Fortuna, A. M., Dallmeyer, I., & Garcia-Perez, M. (2016). Influence of feedstock source and pyrolysis temperature on biochar bulk and surface properties. *Biomass and Bioenergy*, *84*, 37–48. https://doi.org/10.1016/j.biombioe.2015.11.010

Tafur-marinos, J. A., Ginepro, M., Pastero, L., Zelano, V., Ginepro, M., & Pastero, L. (2016). Digestion Procedures for the Elemental Analysis of Wood by Inductively Coupled Plasma Optical Emission Spectrometry Digestion Procedures for the Elemental Analysis of Wood by. *Analytical Letters*, *49*(11), 1722–1733. https://doi.org/10.1080/00032719.2015.1120309

Tamjidi, S., Esmaeili, H., & Kamyab, B. (n.d.). *IOP Conference Series: Earth and Environmental Science Adsorption mechanisms for heavy metal removal using low cost adsorbents: A review You may also like A review of the function of using carbon nanomaterials in membrane filtration for contaminant removal from wastewater Utkarsh Chadha, Senthil Kumaran Selvaraj, S Vishak Thanu et al.-Application of magnetic adsorbents for removal of heavy metals from wastewater: a review study*. https://doi.org/10.1088/1755-1315/614/1/012166

Tan, K. L., & Hameed, B. H. (2017). Insight into the adsorption kinetics models for the removal of contaminants from aqueous solutions. *Journal of the Taiwan Institute of Chemical Engineers*, *74*, 25–48. https://doi.org/10.1016/J.JTICE.2017.01.024

Tan, X. F., Zhu, S. S., Wang, R. P., Chen, Y. Di, Show, P. L., Zhang, F. F., & Ho, S. H. (2021). Role of biochar surface characteristics in the adsorption of aromatic compounds: Pore structure and functional groups. *Chinese Chemical Letters*, *32*(10), 2939–2946. https://doi.org/10.1016/J.CCLET.2021.04.059

Tan, Z., Wang, Y., Kasiulienė, A., Huang, C., & Ai, P. (2017). Cadmium removal potential by rice straw-derived magnetic biochar. *Clean Technologies and Environmental Policy*, *19*(3), 761–774. https://doi.org/10.1007/S10098-016-1264-2/FIGURES/12

Tang, L., Yu, J., Pang, Y., Zeng, G., Deng, Y., Wang, J., Ren, X., Ye, S., Peng, B., & Feng, H. (2018). Sustainable efficient adsorbent: Alkali-acid modified magnetic biochar derived from sewage sludge for aqueous organic contaminant removal. *Chemical Engineering Journal*, *336*(September 2017), 160–169. https://doi.org/10.1016/j.cej.2017.11.048

Tarafdar, J., & Adhikari, T. (2015). Nanotechnology in Soil Science. *Soil Science: An Introduction*, *December*, 775–807.

Teixidó, M., Pignatello, J. J., Beltrán, J. L., Granados, M., & Peccia, J. (2011). Speciation of the ionizable antibiotic sulfamethazine on black carbon (Biochar). *Environmental Science and Technology*, *45*(23), 10020–10027. https://doi.org/10.1021/es202487h

Telmo, C., & Lousada, J. (2011). The explained variation by lignin and extractive contents on higher heating value of wood. *Biomass and Bioenergy*, *35*(5), 1663–1667. https://doi.org/10.1016/J.BIOMBIOE.2010.12.038

Thompson, M. (2008). *CHNS elemental analysers*. *29*, 1–2. https://doi.org/10.1260/0957456991496844

Tong, Y., McNamara, P. J., & Mayer, B. K. (2019). Adsorption of organic micropollutants onto biochar: a review of relevant kinetics, mechanisms and equilibrium. *Environmental Science: Water Research & Technology*, *5*(5), 821–838. https://doi.org/10.1039/C8EW00938D

Tong, Y., Mcnamara, P. J., & Mayer, B. K. (2019). Environmental Science Water Research & Technology TUTORIAL REVIEW Adsorption of organic micropollutants onto biochar: a review of relevant kinetics, mechanisms and equilibrium. *Cite This: Environ. Sci.: Water Res. Technol*, *5*, 821. https://doi.org/10.1039/c8ew00938d

Turk Sekulić, M., Pap, S., Stojanović, Z., Bošković, N., Radonić, J., & Šolević Knudsen, T. (2018). Efficient removal of priority, hazardous priority and emerging pollutants with Prunus armeniaca functionalized biochar from aqueous wastes: Experimental optimization and modeling. *Science of the Total Environment*, *613–614*, 736–750. https://doi.org/10.1016/j.scitotenv.2017.09.082

Turkulin, H., Holzer, L., Richter, K., & Sell, J. (2005). Application of the ESEM technique in wood research. Part II. Comparison of operational modes. *Wood and Fiber Science*, *37*(4), 565–573.

Uchimiya, M., Chang, S., & Klasson, K. T. (2011). Screening biochars for heavy metal retention in soil: Role of oxygen functional groups. *Journal of Hazardous Materials*, *190*(1–3), 432–441. https://doi.org/10.1016/j.jhazmat.2011.03.063

Uchimiya, M., Klasson, K. T., Wartelle, L. H., & Lima, I. M. (2011). Influence of soil properties on heavy metal sequestration by biochar amendment: 1. Copper sorption isotherms and the release of cations. *Chemosphere*, *82*(10), 1431–1437. https://doi.org/10.1016/j.chemosphere.2010.11.050

USEPA, Pah. (2000). *Polycyclic aromatic hydrocarbons (PAHs)*. *3*, 1–24.

Wang, C., Liu, J., Shen, J., Chen, D., Li, Y., Jiang, B., & Wu, J. (2018). Effects of biochar amendment on net greenhouse gas emissions and soil fertility in a double rice cropping system: A 4-year field experiment. *Agriculture, Ecosystems and Environment*, *262*(November 2017), 83–96. https://doi.org/10.1016/j.agee.2018.04.017

Wang, C., & Wang, H. (2018). Pb(II) sorption from aqueous solution by novel biochar loaded with nano-particles. *Chemosphere*, *192*, 1–4. https://doi.org/10.1016/j.chemosphere.2017.10.125

Wang, H., Chen, Q., Xia, H., Liu, R., & Zhang, Y. (2024). Enhanced complexation and electrostatic attraction through fabrication of amino-or hydroxyl-functionalized Fe/Ni-biochar composite for the adsorption of Pb(II) and Cd(II). *Separation and Purification Technology*, *328*, 125074. https://doi.org/10.1016/j.seppur.2023.125074

Wang, H., Nan, Q., Waqas, M., & Wu, W. (2021). Stability of biochar in mineral soils: Assessment methods, influencing factors and potential problems. *Science of The Total Environment*, 150789. https://doi.org/10.1016/j.scitotenv.2021.150789

Wang, J., & Guo, X. (2020). Adsorption isotherm models: Classification, physical meaning, application and solving method. *Chemosphere*, *258*, 127279. https://doi.org/10.1016/J.CHEMOSPHERE.2020.127279

Wang, J., Zhang, D., Liu, S., & Wang, C. (2020). Enhanced removal of chromium(III) for aqueous solution by EDTA modified attapulgite: Adsorption performance and mechanism. *Science of the Total Environment*, *720*. https://doi.org/10.1016/J.SCITOTENV.2020.137391

Wang, J., & Zhuang, S. (2018). *Critical Reviews in Environmental Science and Technology Removal of various pollutants from water and wastewater by modified chitosan adsorbents Removal of various pollutants from water and wastewater by modified chitosan adsorbents*. https://doi.org/10.1080/10643389.2017.1421845

Wang, L., Wang, Y., Ma, F., Tankpa, V., Bai, S., Guo, X., & Wang, X. (2019a). Mechanisms and reutilization of modified biochar used for removal of heavy metals from wastewater: A review. *Science of the Total Environment*, *668*, 1298–1309. https://doi.org/10.1016/J.SCITOTENV.2019.03.011

Wang, L., Wang, Y., Ma, F., Tankpa, V., Bai, S., Guo, X., & Wang, X. (2019b). Mechanisms and reutilization of modified biochar used for removal of heavy metals from wastewater: A review. In *Science of the Total Environment* (Vol. 668, pp. 1298–1309). Elsevier B.V. https://doi.org/10.1016/j.scitotenv.2019.03.011

Weber, K., & Quicker, P. (2018). Properties of biochar. *Fuel*, *217*(September 2017), 240–261. https://doi.org/10.1016/j.fuel.2017.12.054

Wu, F. C., & Chyu, C. C. (2004). Optimization of correlated multiple quality characteristics robust design using principal component analysis. *Journal of Manufacturing Systems*, *23*(2), 134–143. https://doi.org/10.1016/S0278-6125(05)00005-1

Wu, F., & Management, I. (2004). *Optimization of Correlated Multiple Quality Characteristics Robust Design Using Principal Component Analysis*. *23*(2).

Xie, T., Reddy, K. R., Wang, C., Yargicoglu, E., & Spokas, K. (2015). Characteristics and applications of biochar for environmental remediation: A review. *Critical Reviews in Environmental Science and Technology*, *45*(9), 939–969. https://doi.org/10.1080/10643389.2014.924180

Xu, H., Zhang, X., & Zhang, Y. (2018). Modification of biochar by Fe2O3for the removal of pyridine and quinoline. *Environmental Technology (United Kingdom)*, *39*(11), 1470–1480. https://doi.org/10.1080/09593330.2017.1332103

Xu, R. kou, Xiao, S. cheng, Yuan, J. hua, & Zhao, A. zhen. (2011). Adsorption of methyl violet from aqueous solutions by the biochars derived from crop residues. *Bioresource Technology*, *102*(22), 10293–10298. https://doi.org/10.1016/j.biortech.2011.08.089

Xu, X., Cao, X., & Zhao, L. (2013). Comparison of rice husk- and dairy manure-derived biochars for simultaneously removing heavy metals from aqueous solutions: Role of mineral components in biochars. *Chemosphere*, *92*(8), 955–961. https://doi.org/10.1016/j.chemosphere.2013.03.009

Yadav, D., Rangabhashiyam, S., Verma, P., Singh, P., Devi, P., Kumar, P., Hussain, C. M., Gaurav, G. K., & Kumar, K. S. (2021). Environmental and health impacts of contaminants of emerging concerns: Recent treatment challenges and approaches. *Chemosphere*, *272*. https://doi.org/10.1016/J.CHEMOSPHERE.2020.129492

Yang, H., Yan, R., Chen, H., Lee, D. H., & Zheng, C. (2007a). Characteristics of hemicellulose, cellulose and lignin pyrolysis. *Fuel*, *86*(12–13), 1781–1788. https://doi.org/10.1016/j.fuel.2006.12.013

Yang, H., Yan, R., Chen, H., Lee, D. H., & Zheng, C. (2007b). Characteristics of hemicellulose, cellulose and lignin pyrolysis. *Fuel*, *86*(12–13), 1781–1788. https://doi.org/10.1016/j.fuel.2006.12.013

Yi, Y., Huang, Z., Lu, B., Xian, J., Tsang, E. P., Cheng, W., Fang, J., & Fang, Z. (2019). Magnetic biochar for environmental remediation: A review. *Bioresource Technology*, *298*(September 2019). https://doi.org/10.1016/j.biortech.2019.122468

Yi, Y., Li, C., Zhao, L., Du, X., Gao, L., Chen, J., Zhai, Y., & Zeng, G. (2018). The synthetic evaluation of CuO-MnOx-modified pinecone biochar for simultaneous removal formaldehyde and elemental mercury from simulated flue gas. *Environmental Science and Pollution Research*, *25*(5), 4761–4775. https://doi.org/10.1007/s11356-017-0855-8

Yi, Y., Tu, G., Ying, G., Fang, Z., & Tsang, E. P. (2021). Magnetic biochar derived from rice straw and stainless steel pickling waste liquor for highly efficient adsorption of crystal violet. *Bioresource Technology*, *341*. https://doi.org/10.1016/J.BIORTECH.2021.125743

Yi, Y., Tu, G., Zhao, D., Tsang, P. E., & Fang, Z. (2019). Biomass waste components significantly influence the removal of Cr(VI) using magnetic biochar derived from four types of feedstocks and steel pickling waste liquor. *Chemical Engineering Journal*, *360*(November 2018), 212–220. https://doi.org/10.1016/j.cej.2018.11.205

Yin, Q., Wang, R., & Zhao, Z. (2018). Application of Mg–Al-modified biochar for simultaneous removal of ammonium, nitrate, and phosphate from eutrophic water. *Journal of Cleaner Production*, *176*, 230–240. https://doi.org/10.1016/j.jclepro.2017.12.117

Yin, Z., Xu, S., Liu, S., Xu, S., Li, J., & Zhang, Y. (2020). A novel magnetic biochar prepared by K2FeO4-promoted oxidative pyrolysis of pomelo peel for adsorption of

hexavalent chromium. *Bioresource Technology*, *300*(October 2019), 122680. https://doi.org/10.1016/j.biortech.2019.122680

Zhang, J., Fan, S. kai, Yang, J. cheng, Du, X. ming, Li, F. sheng, & Hou, H. (2014). Petroleum contamination of soil and water, and their effects on vegetables by statistically analyzing entire data set. *Science of the Total Environment*, *476–477*, 258–265. https://doi.org/10.1016/j.scitotenv.2014.01.023

Zhang, K., Cheng, X., Dang, H., Ye, C., Zhang, Y., & Zhang, Q. (2013). Linking litter production, quality and decomposition to vegetation succession following agricultural abandonment. *Soil Biology and Biochemistry*, *57*, 803–813. https://doi.org/10.1016/j.soilbio.2012.08.005

Zhang, P., O'Connor, D., Wang, Y., Jiang, L., Xia, T., Wang, L., Tsang, D. C. W., Ok, Y. S., & Hou, D. (2020). A green biochar/iron oxide composite for methylene blue removal. *Journal of Hazardous Materials*, *384*. https://doi.org/10.1016/j.jhazmat.2019.121286

Zhang, X., Lv, L., Qin, Y., Xu, M., Jia, X., & Chen, Z. (2018). Removal of aqueous Cr(VI) by a magnetic biochar derived from Melia azedarach wood. *Bioresource Technology*, *256*(January), 1–10. https://doi.org/10.1016/j.biortech.2018.01.145

Zhang, Y., Zhu, C., Liu, F., Yuan, Y., Wu, H., & Li, A. (2019). Effects of ionic strength on removal of toxic pollutants from aqueous media with multifarious adsorbents: A review. *Science of the Total Environment*, *646*, 265–279. https://doi.org/10.1016/J.SCITOTENV.2018.07.279

Zhao, H., & Lang, Y. (2018). Adsorption behaviors and mechanisms of florfenicol by magnetic functionalized biochar and reed biochar. *Journal of the Taiwan Institute of Chemical Engineers*, *0*, 1–9. https://doi.org/10.1016/j.jtice.2018.03.049

Zhao, L., Yang, F., Jiang, Q., Zhu, M., Jiang, Z., Tang, Y., & Zhang, Y. (2018). Characterization of modified biochars prepared at low pyrolysis temperature as an efficient adsorbent for atrazine removal. *Environmental Science and Pollution Research*, *25*(2), 1405–1417. https://doi.org/10.1007/s11356-017-0492-2

Zhao, M., Dai, Y., Zhang, M., Feng, C., Qin, B., Zhang, W., Zhao, N., Li, Y., Ni, Z., Xu, Z., Tsang, D. C. W., & Qiu, R. (2020, January). *Mechanisms of Pb and/or Zn adsorption by different biochars: Biochar characteristics, stability, and binding energies*. Science of The Total Environment. https://doi.org/10.1016/j.scitotenv.2020.136894

Zhao, Z., Nie, T., & Zhou, W. (2019). Enhanced biochar stabilities and adsorption properties for tetracycline by synthesizing silica-composited biochar. *Environmental Pollution*, *254*. https://doi.org/10.1016/j.envpol.2019.113015

Zhen, M., Song, B., Liu, X., Chandankere, R., & Tang, J. (2018). Biochar-mediated regulation of greenhouse gas emission and toxicity reduction in bioremediation of organophosphorus pesticide-contaminated soils. *Chinese Journal of Chemical Engineering*, 1–9. https://doi.org/10.1016/j.cjche.2018.01.028

Zhou, L., Liu, Y., Liu, S., Yin, Y., Zeng, G., Tan, X., Hu, X., Hu, X., Jiang, L., Ding, Y., Liu, S., & Huang, X. (2016). Investigation of the adsorption-reduction mechanisms of hexavalent chromium by ramie biochars of different pyrolytic temperatures. *Bioresource Technology*, *218*, 351–359. https://doi.org/10.1016/j.biortech.2016.06.102

Zhou, X., Liu, Y., Zhou, J., Guo, J., Ren, J., & Zhou, F. (2018). Efficient removal of lead from aqueous solution by urea-functionalized magnetic biochar: Preparation, characterization and mechanism study. *Journal of the Taiwan Institute of Chemical Engineers*, *0*, 1–11. https://doi.org/10.1016/j.jtice.2018.04.018

Zhou, Y., Gao, B., Zimmerman, A. R., Chen, H., Zhang, M., & Cao, X. (2014). Biochar-supported zerovalent iron for removal of various contaminants from aqueous solutions. *Bioresource Technology*, *152*, 538–542. https://doi.org/10.1016/j.biortech.2013.11.021

Zhou, Y., Gao, B., Zimmerman, A. R., Fang, J., Sun, Y., & Cao, X. (2013). Sorption of heavy metals on chitosan-modified biochars and its biological effects. *Chemical Engineering Journal*, *231*, 512–518. https://doi.org/10.1016/j.cej.2013.07.036

Zhu, X., Chen, B., Zhu, L., & Xing, B. (2017). Effects and mechanisms of biochar-microbe interactions in soil improvement and pollution remediation: A review. *Environmental Pollution*, *227*, 98–115. https://doi.org/10.1016/j.envpol.2017.04.032

Zong, Y., Xiao, Q., Malik, Z., Su, Y., Wang, Y., & Lu, S. (2021). Crop straw-derived biochar alleviated cadmium and copper phytotoxicity by reducing bioavailability and accumulation in a field experiment of rice-rape-corn rotation system. *Chemosphere*, *280*. https://doi.org/10.1016/J.CHEMOSPHERE.2021.130830

APPENDIX

Appendix A

FUNCTIONAL GROUP

This section contains information on FTIR data interpretation of surface functional group observed on the surface of biomass, its derived char and functionalized biochar. The information is presented in a tabular form having four columns representing Adsorption wavelength (cm^{-1}), Appearances (Strong, Sharp, Medium, and weak Bond), Bond present (free Hydroxyl, O-H stretch, N-H Stretch, C-H stretch, C=O stretch, C=C stretch, O=C=O stretch, and H-Bonded) and functional group (Alcohols, Carboxyl, aldehyde, Aromatic amine, Ester, alkyne, akene, Nitro-compound etc). Table 1 was used in data interpretation in sections 4.2.1 (Table 4.3 and 4.3.1) and section 6.4 (figure6.6).

Table A-1.0: Infrared Spectroscopy Absorption

Absorption cm^{-1}	Appearance	Bond present	Functional group
Frequency Range 4000-3000cm^{-1}			
3700-3584	Medium,sharp	O-H stretch, free hydroxyl	Alcohol

3550-3200	Strong broad	O-H stretch, H- bonded	Alcohols
3500	Medium	N-H stretch	1*,2* amines, amides
3400-3300	Medium	N-H stretching	Aliphatic primary amine
3300-2500	Strong broad	O-H stretching	Carboxylic acid
3200- 2700	Weak broad	O-H stretching	Alcohols

Frequency Range 3000 -2500 cm^{-1}

3333-3267	Strong	C-H stretching	alkyne
3100-3000	Medium	C-H stretching	alkene
3000-2840	Medium	C-H stretching	Alkane
2830-2695	medium	C-H stretching	aldehyde
2600-2550	Weak	S-H stretching	Thiol

Frequency range 2400-2000cm^{-1}

2349	Strong	O=C=O Stretching	Carbon-dioxide
2160-2120	Strong	N=N=N stretching	Azide
2150		C=C=O stretching	Ketene

Frequency range 2000-1650cm^{-1}

2000-1650	weak	C-H bending	Aromatic compound

Frequency range 1870-1540cm^{-1}

1818-1750	Strong	C=O stretching	Anhydride
1815-1785	Strong	C=O stretching	Acid halide
1800-1770	strong	C=O stretching	Conjugated acid halide
1775, 1720	Strong	C=O stretching	Conjugated anhydride
1770-1780	Strong	C=O stretching	Vinyl/ phenyl ester
1760	Strong	C=O stretching	Carboxylic acid
1740- 1720	Strong	C=O stretching	Aldehyde
1725-1705	Strong	C=O stretching	Aliphatic ketones
1720-1706	Strong	C=O stretching	Carboxylic acid
1710-1685	Strong	C=O stretching	Conjugated aldehyde

Frequency range 1670-1600cm^{-1}

1678-1668	Weak	C=C stretching	Alkene
1675-1665	Weak	C=C stretching	Alkene
1675 -1665	Weak	C=C stretching	Alkene
1658-1648	Medium	C=C stretching	Alkene
1650-1600	Medium	C=C stretching	Conjugated alkene
1650-1580	Medium	N-H bending	Amine
1648-1638	Strong	C=C stretching	Alkene
1620-1610	Strong	C=C stretching	αβ-unsaturated ketone

Frequency range 1600-1300cm^{-1}

1550-1500	Strong	N-O stretching	Nitro compound
1372-1290	Strong		
1465	Medium	C-H bending	Alkane
1450-1375	Medium	C-H bending	Alkane
1390-1380	Medium	C-H bending	Aldehyde
1385-1380	Medium	C-H bending	Alkane

Frequency range 1400-1000cm^{-1}

1440-1395	Medium	O-H bending	Carboxylic acid
1420-1330	Medium	O-H bending	Alcohol
1390-1310	Medium	O-H bending	Phenol
1342-1266	Strong	C-N stretching	Aromatic amine
	Strong	C-O stretching	Aromatic ester
1275-1200	Strong	C-O stretching	Alkyl ayrl ether
1075-1020			
1250-1020	Medium	C-N stretching	Amine
1225-1200	Strong	C-O stretching	Vinyl ether
1210-1163	Strong	C-O stretching	Ester
1205-1124	Strong	C-O stretching	Tertiary alcohol
1150-1085	Strong	C-O stretching	Aliphatic ether
1124-1087	Strong	C-O stretching	Secondary alcohol
1085-1050	Strong	C-O stretching	Primary alcohol
1050-1040	Strong	CO-O-CO stretching	Anhydride

Frequency range 1000-650cm^{-1}

995-985	Strong	C=C Bending	Alkene
915-905			
980-960	Strong	C=C Bending	Alkene

895-885	Strong	C=C Bending	Alkene
850-550	Strong	C-Cl Stretching	Halo compound
840-790	Medium	C=C Bending	Alkene
730-665	Strong	C=C Bending	Alkene
690-515	Strong	C-Br Stretching	Halo compound
600-500	Strong	C-l Stretching	Halo compound
		Frequency Range 900 -700cm^{-1}	
880 ± 20	Strong	C-H bending	1,2,4-trisbustituted

APPENDIX B

CALIBRATION

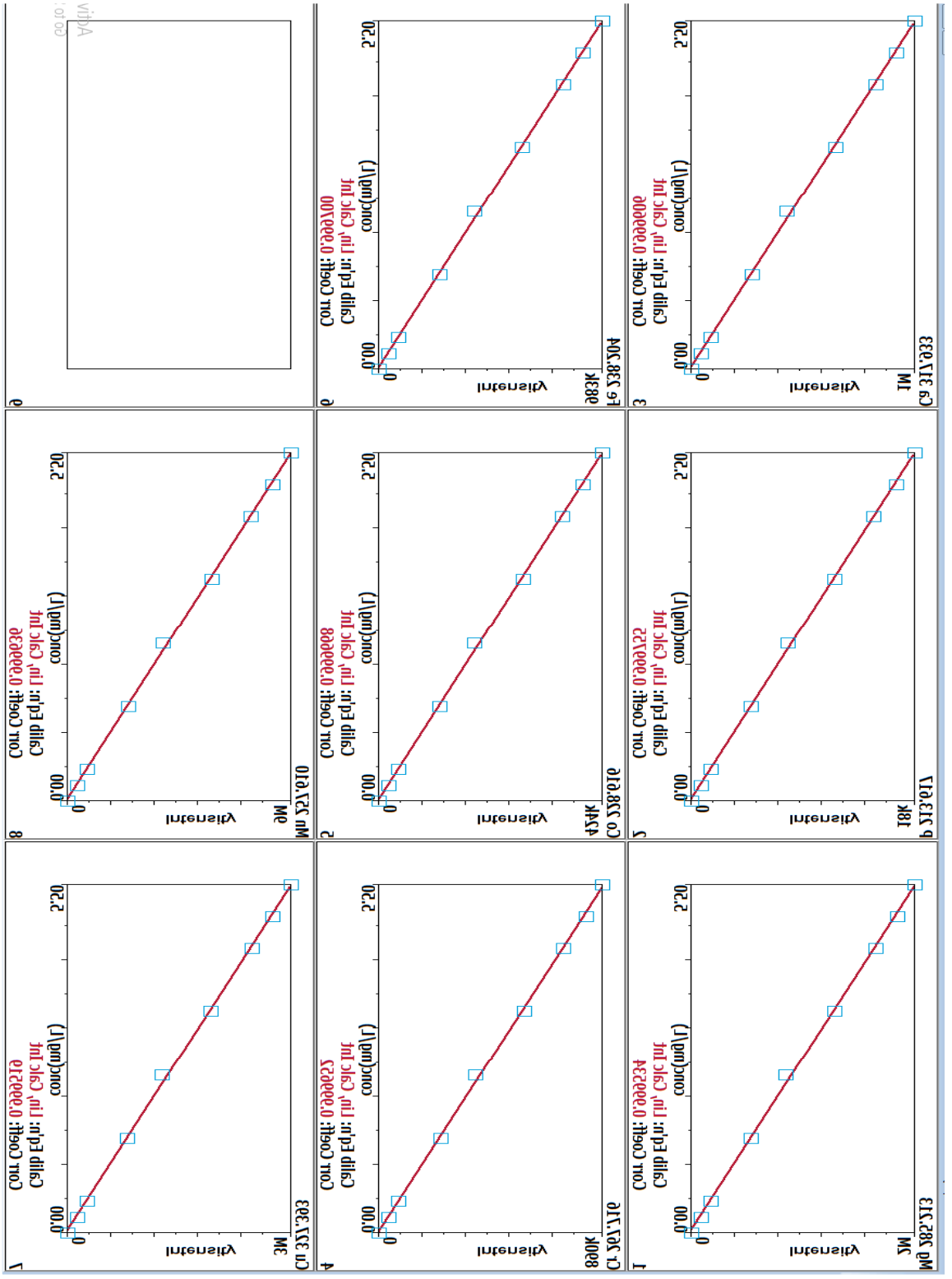


Figure B-2.1a: Calibration curves for selected elements hypothesized to be present in biomass.

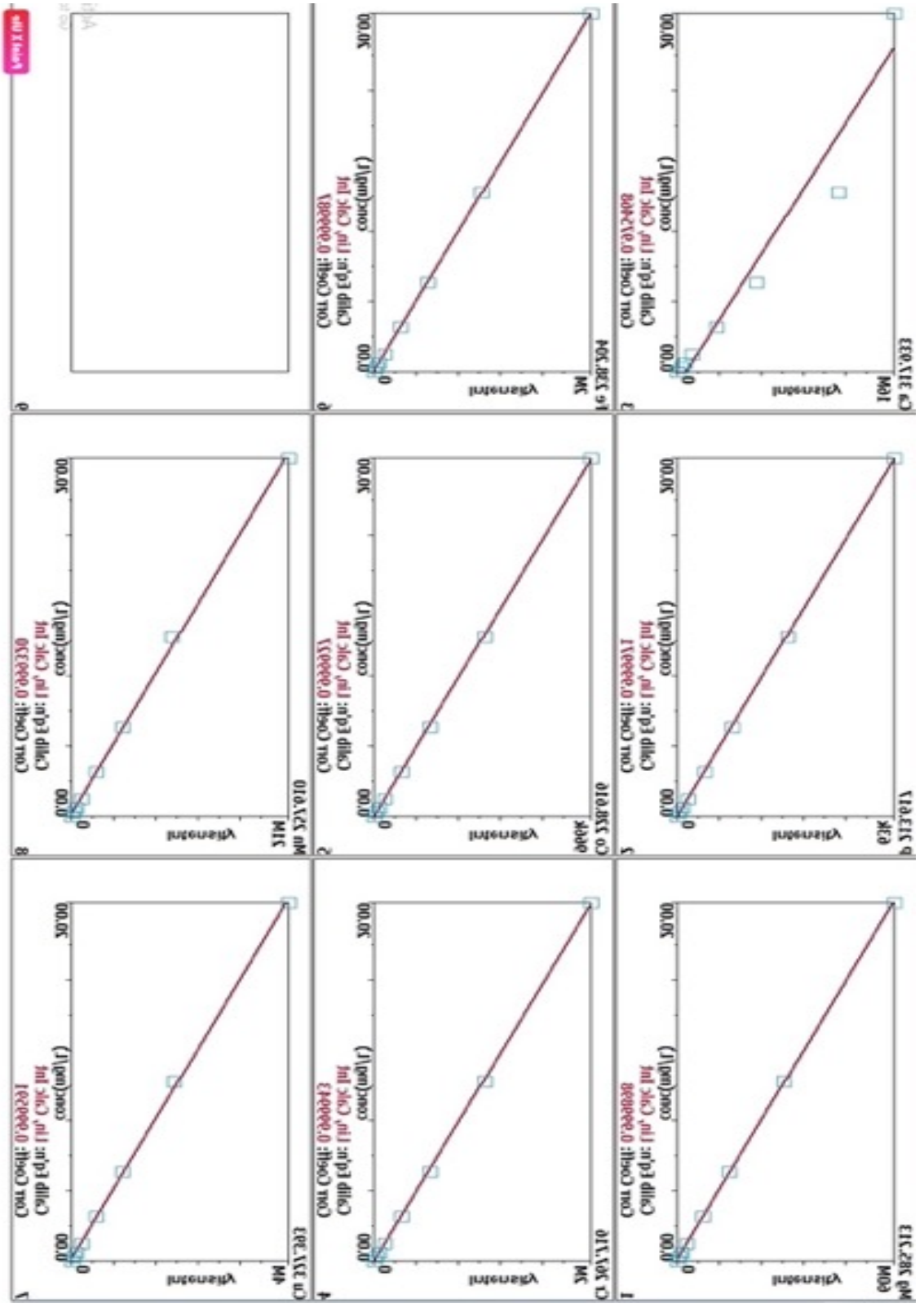


Figure B-2.1b: Calibration curves for selected elements hypothesized to be present in biomass.

APPENDIX C

BET SAMPLES ANALYSIS

APPLE SUMMARY REPORT

Surface Area

Single point surface area at p/p° = 0.300000000: 290.3387 m²/g

BET Surface Area: 314.2137 m²/g

Langmuir Surface Area: 464.6134 m²/g

BJH Adsorption cumulative surface area of pores between 17.000 Å and 3,000.000 Å diameter: 34.095 m²/g

BJH Desorption cumulative surface area of pores between 17.000 Å and 3,000.000 Å diameter: 9.9570m²/g

Pore Volume

Single point adsorption total pore volume of pores less than 2,896.722 Å diameter at p/p° = 0.993294104: 0.165392 cm³/g

BJH Adsorption cumulative volume of pores between 17.000 Å and 3,000.000 Å diameter: 0.029211 cm³/g

BJH Desorption cumulative volume of pores between 17.000 Å and 3,000.000 Å diameter: 0.012516 cm³/g

Pore Size

Adsorption average pore diameter (4V/A by BET): 21.0548 Å BJH Adsorption average pore diameter (4V/A): 34.269 Å

BJH Desorption average Por diameter (4V/A): 50.281 Å

Table C-1.0: Bc-Apple Isotherm Tabular Report

Relative Pressure (P/P^o)	**Absolute pressure (mmHg)**	**Quantity Adsorbed (cm^3/g STP)**	**Elapsed Time (h: min)**	**Saturation pressure (mmHg)**
0.009657658	7.296658	83.9654	00:40	759.455200
0.063012009	47.542500	93.4471	11:50	755.530762
0.080086876	60.403645	94.7049	14:50	754.499023
0.127823610	96.396439	96.5110	15:26	754.226501
0.168974576	127.422043	97.5554	15:54	754.136414
0.210858280	158.998520	98.3921	16:09	754.090027
0.235582746	177.618607	98.8288	16:20	754.053955
0.246748130	186.028000	99.0463	16:27	753.954224
0.332640150	250.773621	99.9536	16:32	753.918579
0.356642010	268.857422	100.2256	16:40	753.888611
0.447164139	337.088562	100.8725	16:44	753.857971
0.467456804	352.388306	101.0626	16:49	753.836304
0.549975361	414.579041	101.5085	16:52	753.841431
0.574582987	433.114441	101.6864	16:55	753.813843
0.648911940	489.127197	102.0142	16:58	753.789185
0.683284736	515.040466	102.2125	17:00	753.765137
0.738149342	556.370605	102.4740	17:02	753.771362

0.773611990	583.074341	102.6738	17:05	753.737183
0.798620787	601.935608	102.8382	17:06	753.703857
0.838136545	631.676514	103.0786	17:08	753.718933
0.872443936	657.527405	103.3408	17:09	753.667786
0.884733955	666.775879	103.4918	17:11	753.661499
0.904544451	681.690735	103.7144	17:12	753.645630
0.923362560	695.863586	103.9674	17:14	753.628784
0.938772581	707.474121	104.2408	17:15	753.619019
0.951901508	717.350281	104.5580	17:16	753.616089
0.963185408	725.845154	104.9030	17:18	753.597168
0.970388160	731.258789	105.1959	17:19	753.588196
0.976536817	735.843201	105.5087	17:20	753.573486
0.981549442	739.621887	105.8202	17:22	753.523254
0.983829397	741.290710	106.0084	17:23	753.524841
0.986040609	742.919128	106.1977	17:25	753.474854
0.987811971	744.180725	106.3738	17:26	753.436646
0.988793811	744.952454	106.5199	17:27	753.362732
0.993294104	748.306152	106.9255	17:28	753.395142
0.976005158	735.286865	106.1099	17:30	753.358093
0.957217638	721.133789	105.5283	17:32	753.363708
0.937122748	705.943420	105.1868	17:33	753.364502
0.909557040	685.188293	104.8462	17:35	753.309448
0.887989752	668.937195	104.6538	17:36	753.320862
0.876014738	659.923706	104.5741	17:37	753.316345

0.842080330	634.367371	104.4138	17:39	753.324890
0.802527876	604.555603	104.2663	17:40	753.333557
0.743030343	559.755859	104.0939	17:41	753.314148
0.654710274	493.199036	103.8532	17:43	753.341858
0.554690932	417.845490	103.5579	17:45	753.308838
0.454584233	342.427948	103.1695	17:47	753.294250
0.354326384	266.903442	102.6269	17:50	753.277222
0.242683287	182.782730	101.7281	17:54	753.270020

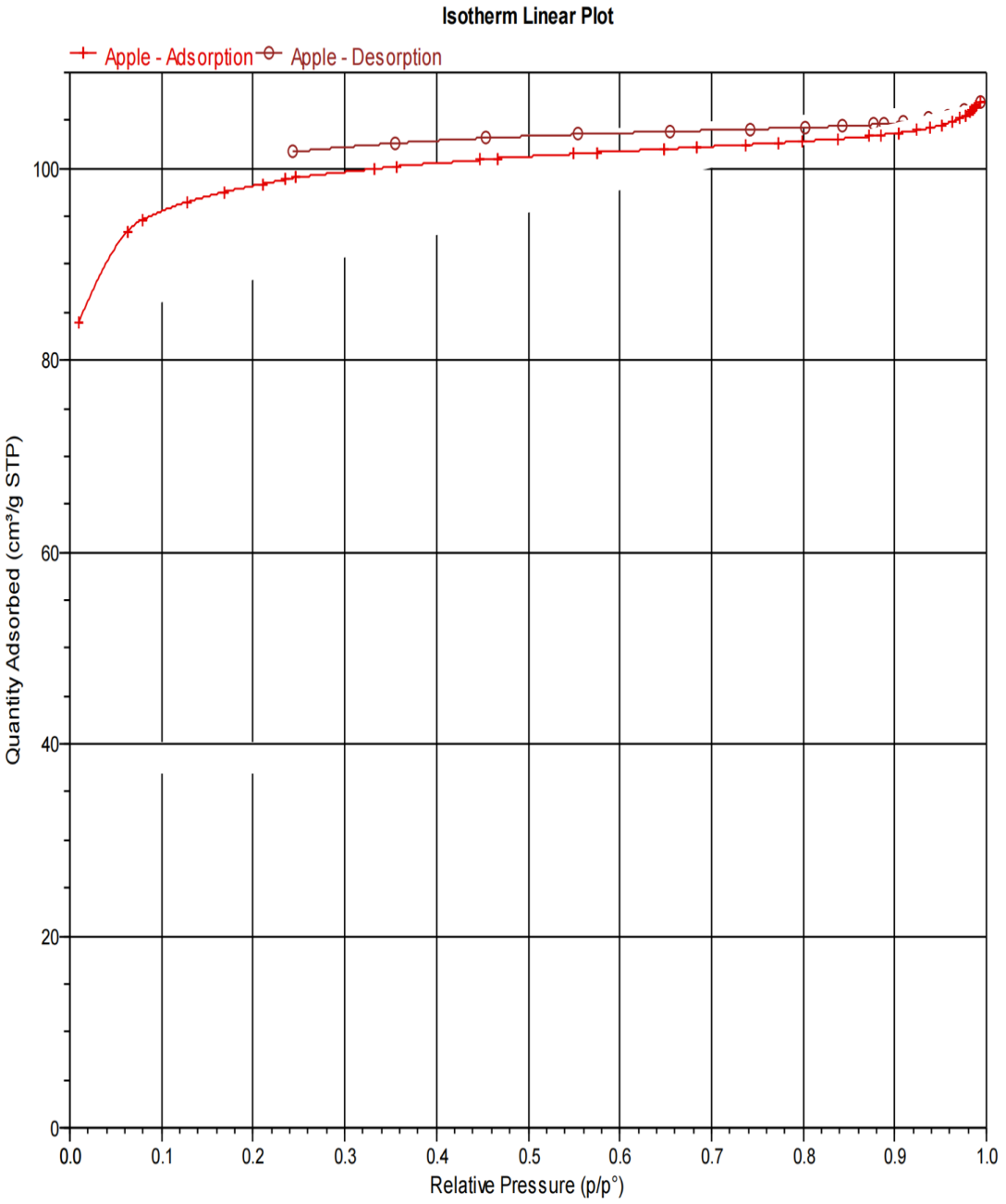


Figure C-1.0: Bc-Apple Isothermal Linear Plot

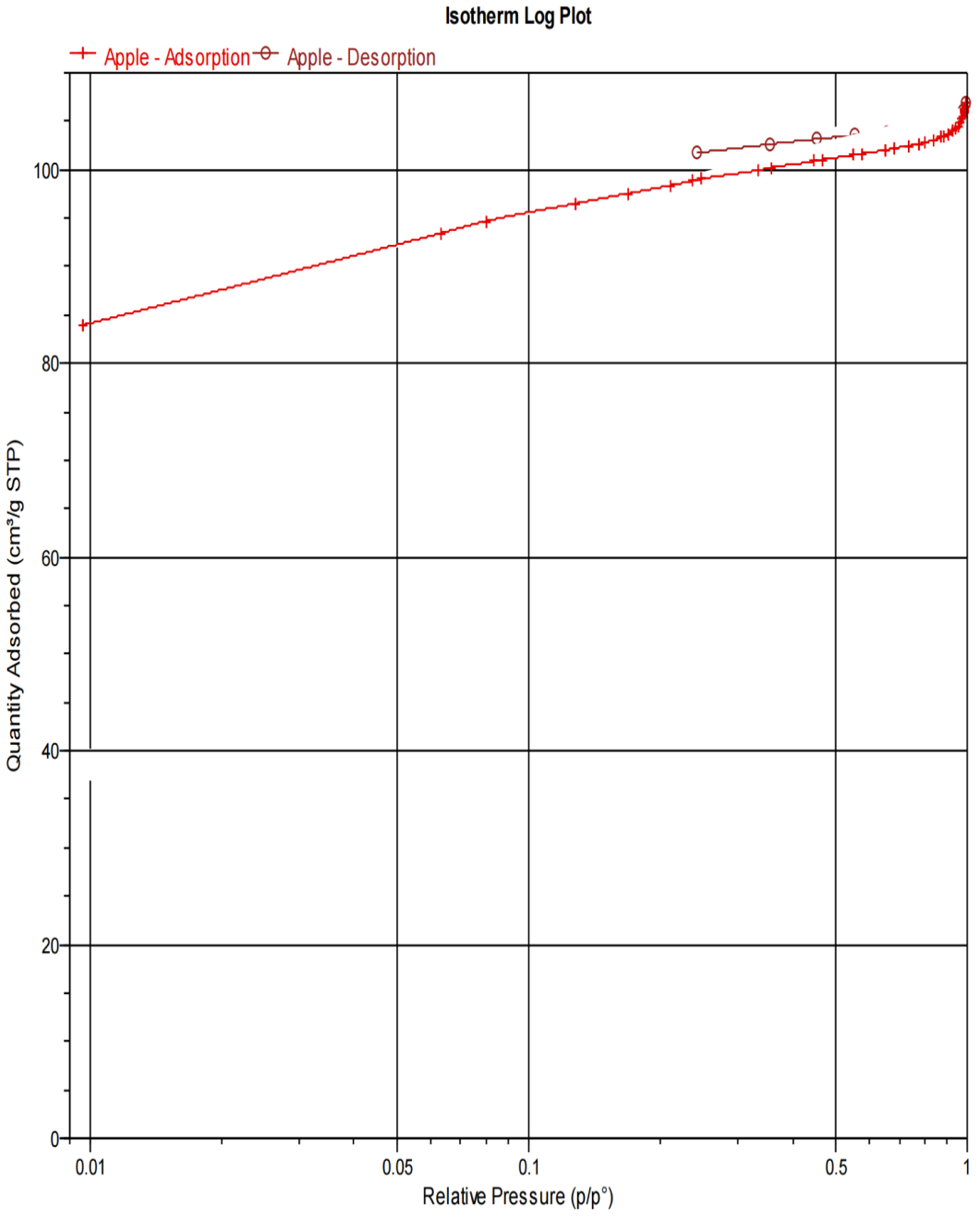


Figure C-1.1: Bc-Apple Isothermal Log Plot

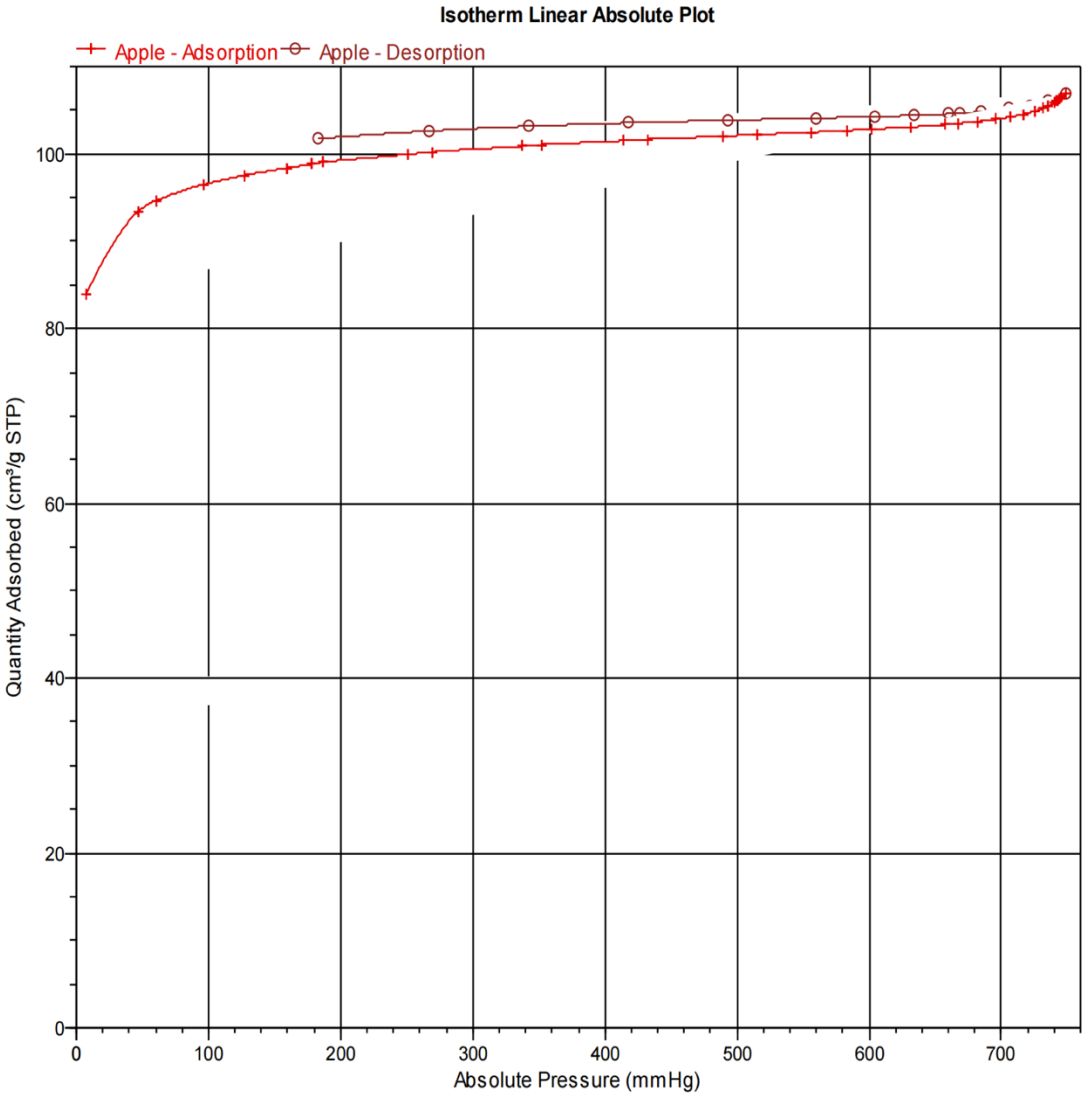


Figure C-1.3: Bc-Apple Isothermal Linear Absolute Plot

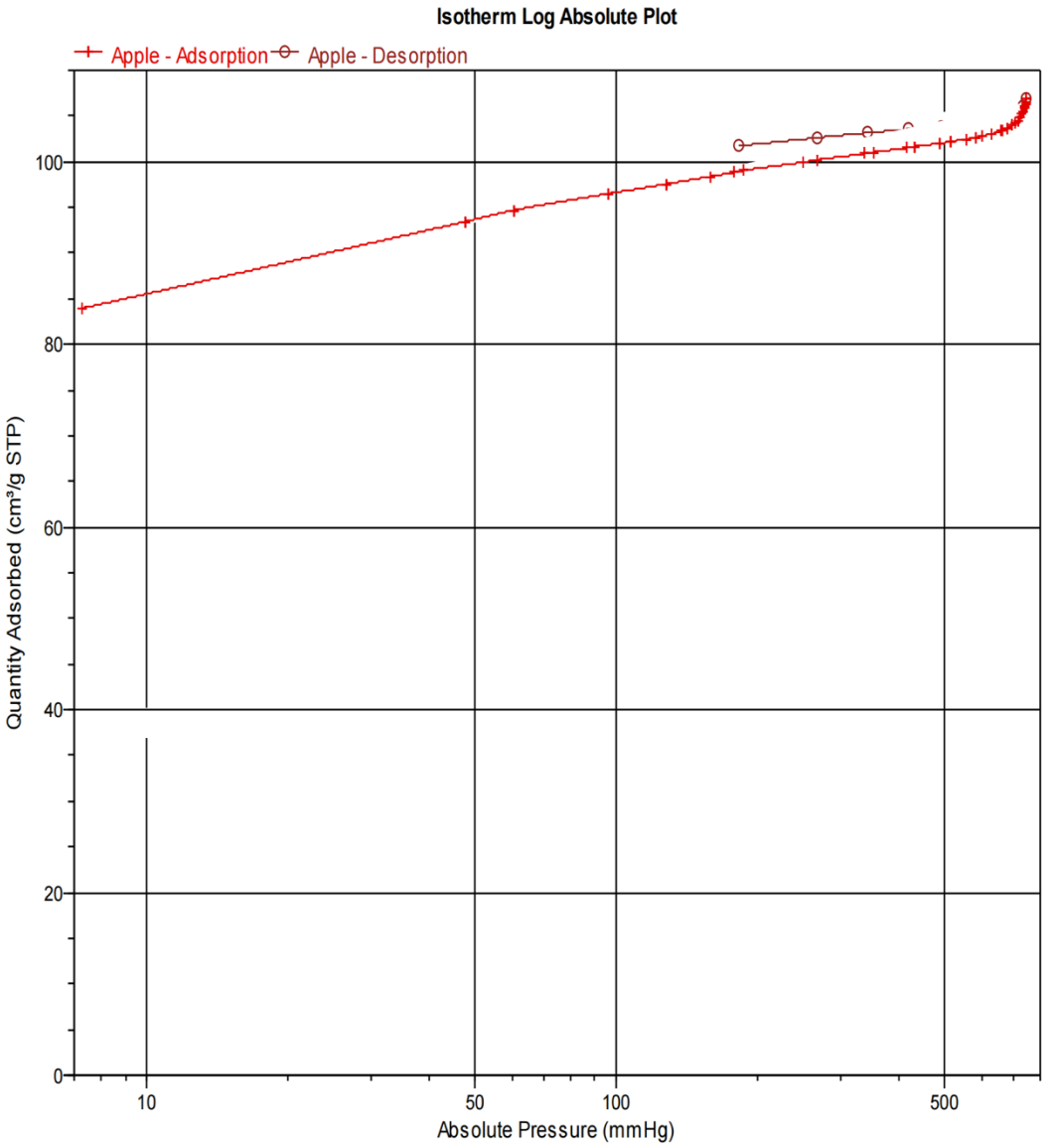


Figure C-1.4: Bc-Apple Isothermal Log Absolute Plot

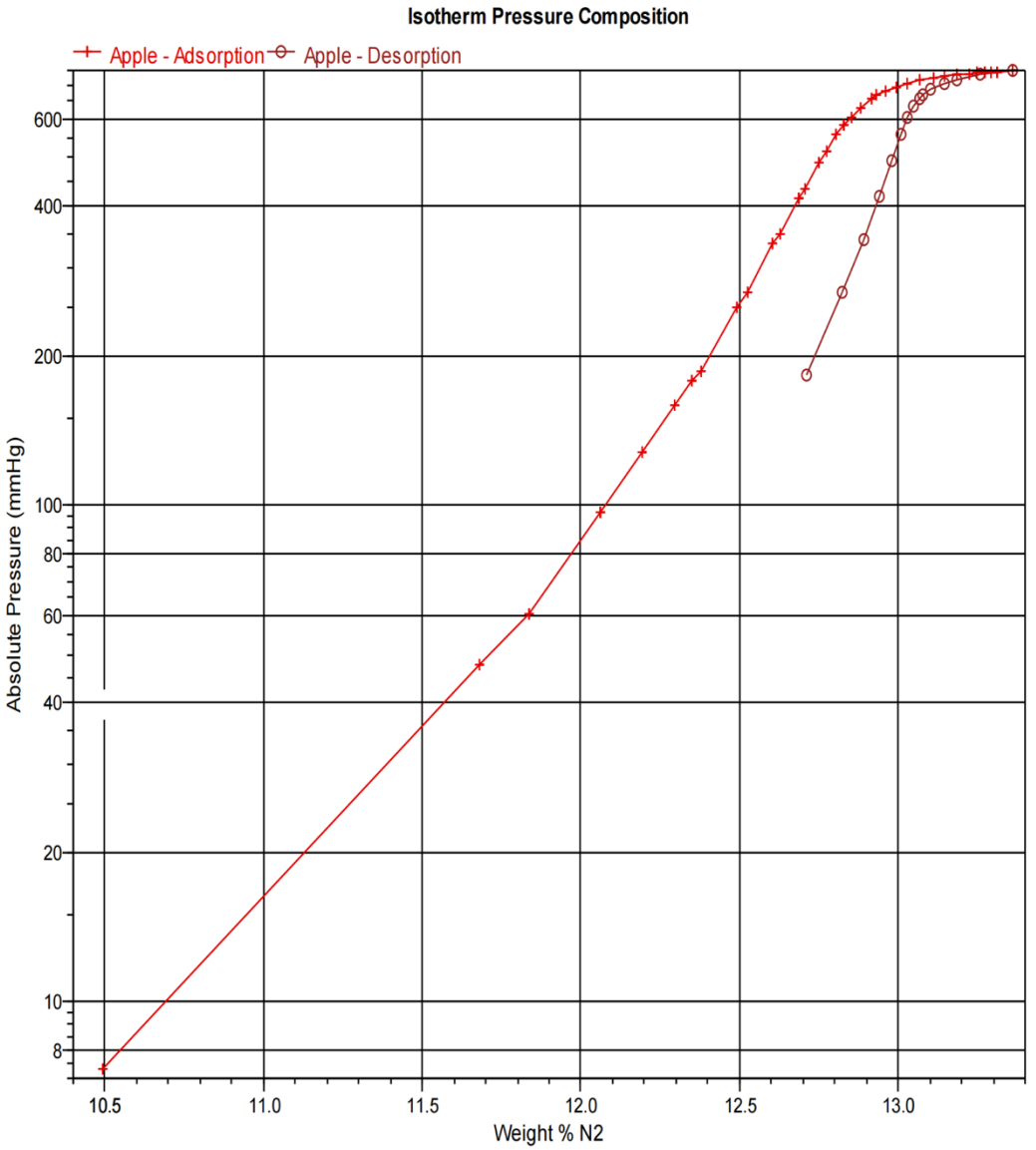


Figure C-1.5: Bc-Apple Isothermal pressure composition

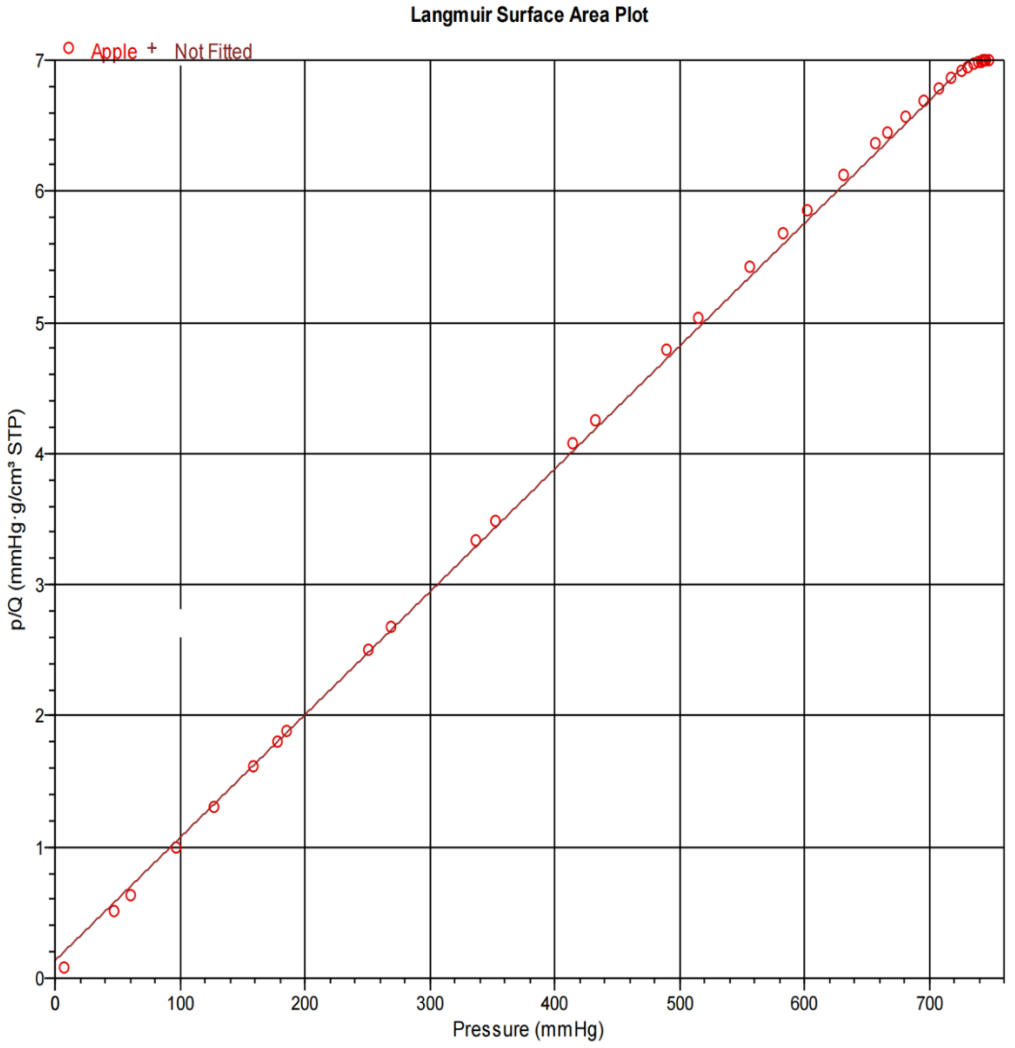


Figure C-1.6: Bc-Apple Langmuir surface area Plot

Langmuir Report

Langmuir Surface Area: 464.6134 ± 2.3726 m^2/g

Slope: 0.009368 ± 0.000048 g/cm^3 STP

Y-Intercept: 0.133 ± 0.026 $mmHg \cdot g/cm^3$

STP b: 0.070222 1/mmHg

Qm: 106.7444 cm^3/g STP

Correlation Coefficient: 0.999570

Molecular Cross-Sectional Area: 0.1620 nm^2

Table C-1.1: Bc-Apple Langmuir Report

Pressure (mmHg)	**Quality Adsorbed cm^3/g STP**	**p/Q(mmHg g/cm^3 STP**
7.585598	83.3589	0.091
46.151634	92.2460	0.500
62.309990	93.3770	0.667
95.734222	94.7759	1.010
125.357498	95.6132	1.311
156.860764	96.2490	1.630
175.982529	96.6404	1.821
184.377304	96.8250	1.904
251.792709	97.5311	2.582
267.414337	97.7360	2.736
337.876068	98.1870	3.441
352.615936	98.3262	3.586
413.750031	98.6301	4.195
433.119598	98.7646	4.385
488.184174	99.0022	4.931
514.988647	99.1464	5.194
555.695496	99.3321	5.594
582.742493	99.4912	5.857
601.472473	99.6335	6.037
631.200684	99.8128	6.324
656.894592	100.0289	6.567

666.223206	100.1725	6.651
681.114807	100.3622	6.787
695.177979	100.5814	6.912
706.793274	100.8337	7.009
716.833435	101.1141	7.089
725.128296	101.4271	7.149
730.742065	101.6971	7.185
735.132629	101.9793	7.209
739.039124	102.2889	7.225
740.678894	102.4755	7.228
742.432068	102.6660	7.232

Table C.1.2: Bc-Apple BjH Adsorption Pore Distribution Report

Pore Diameter Range (Å)	Average Diameter (Å)	Incremental Pore volume (cm^3/g)	Cumulative Pore Volume (cm^3/g)	Incremental Pore Area($m^{2/}g$)	Cumulative pore area ($m^{2/}g$)
2896.7 - 1745.2	2048.2	0.000662	0.000662	0.013	0.013
1745.2 - 1606.7	1670.1	0.000240	0.000902	0.006	0.019
1606.7 - 1405.9	1492.7	0.000289	0.001191	0.008	0.026
1405.9 - 1216.8	1297.5	0.000312	0.001503	0.010	0.036
1216.8 - 1069.1	1133.2	0.000312	0.001815	0.011	0.047
1069.1 - 844.8	930.3	0.000520	0.002335	0.022	0.069
844.8 - 673.0	739.0	0.000527	0.002862	0.029	0.098
673.0 - 544.2	594.6	0.000499	0.003361	0.034	0.131
544.2 - 419.6	465.4	0.000595	0.003956	0.051	0.183
419.6 - 332.0	365.2	0.000557	0.004513	0.061	0.244
332.0 - 267.1	292.2	0.000485	0.004998	0.066	0.310
267.1 - 216.0	235.8	0.000456	0.005454	0.077	0.387
216.0 - 180.0	194.5	0.000410	0.005865	0.084	0.472
180.0 - 163.2	170.7	0.000289	0.006153	0.068	0.540
163.2 - 129.5	142.1	0.000496	0.006650	0.140	0.679

129.5 - 104.6	114.2	0.000469	0.007119	0.164	0.844
104.6 - 93.3	98.2	0.000341	0.007460	0.139	0.983
93.3 - 80.8	86.0	0.000422	0.007882	0.196	1.179
80.8 - 66.7	72.2	0.000569	0.008451	0.315	1.494
66.7 - 60.1	63.0	0.000471	0.008922	0.299	1.793
60.1 - 49.1	53.3	0.000783	0.009705	0.588	2.380
49.1 - 46.2	47.6	0.000490	0.010195	0.412	2.793
46.2 - 38.3	41.4	0.001220	0.011415	1.180	3.972
38.3 - 36.7	37.5	0.000599	0.012014	0.640	4.612
36.7 - 30.5	32.8	0.002022	0.014036	2.463	7.075
30.5 - 29.0	29.7	0.000964	0.015001	1.299	8.374
29.0 - 24.4	26.2	0.003272	0.018273	4.993	13.366
24.4 - 23.9	24.2	0.000912	0.019185	1.511	14.877
23.9 - 22.7	23.2	0.001795	0.020980	3.089	17.966
22.7 - 20.7	21.6	0.003550	0.024530	6.582	24.548
20.7 - 18.8	19.6	0.004681	0.029211	9.547	34.095

Table 1.3: Bc-Ash BJH Desorption pore Distribution Report

Pore Diameter Range (Å)	Average Diameter (Å)	Incremental Pore volume (cm^3/g)	Cumulative Pore Volume (cm^3/g)	Incremental Pore Area($m^{2/}g$)	Cumulative pore area ($m^{2/}g$)
2896.7 - 826.5	974.9	0.001377	0.001377	0.056	0.056
826.5 - 470.2	554.5	0.000999	0.002376	0.072	0.129
470.2 - 323.6	369.4	0.000595	0.002972	0.064	0.193
323.6 - 227.6	258.3	0.000614	0.003585	0.095	0.288
227.6 - 185.0	201.6	0.000353	0.003938	0.070	0.358
185.0 - 167.7	175.5	0.000146	0.004083	0.033	0.391
167.7 - 132.6	145.7	0.000293	0.004377	0.080	0.472
132.6 - 106.7	116.6	0.000278	0.004655	0.096	0.567
106.7 - 82.3	91.0	0.000339	0.004994	0.149	0.716
82.3 - 61.1	68.1	0.000527	0.005521	0.309	1.026
61.1 - 46.8	51.7	0.000735	0.006256	0.569	1.594
46.8 - 37.3	40.7	0.001115	0.007371	1.095	2.690
37.3 - 30.3	32.9	0.001774	0.009144	2.157	4.846
30.3 - 24.2	26.4	0.003372	0.012516	5.111	9.957

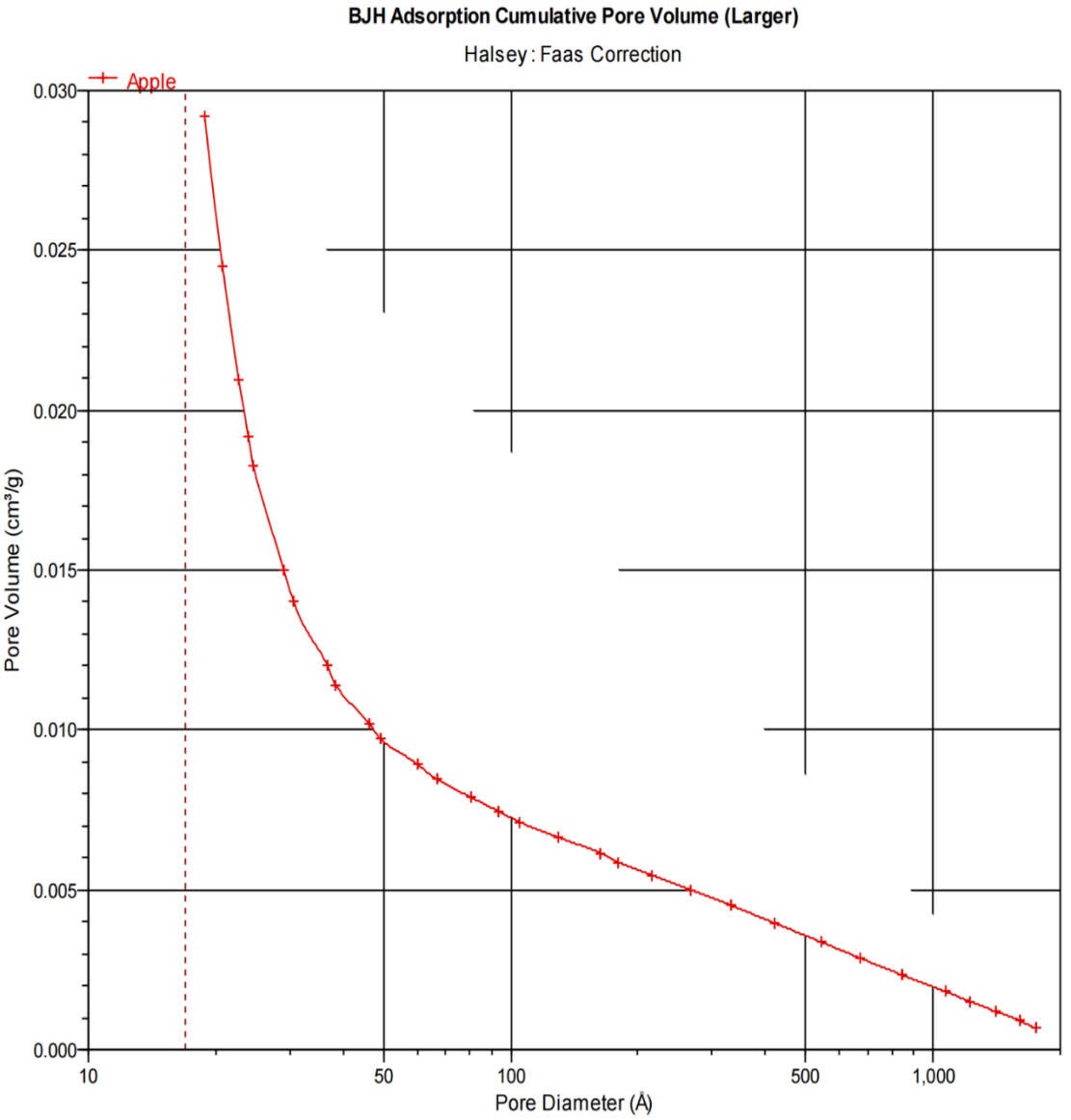


Figure C-1.7: BJH Adsorption Cumulative Pore Volume (Larger)

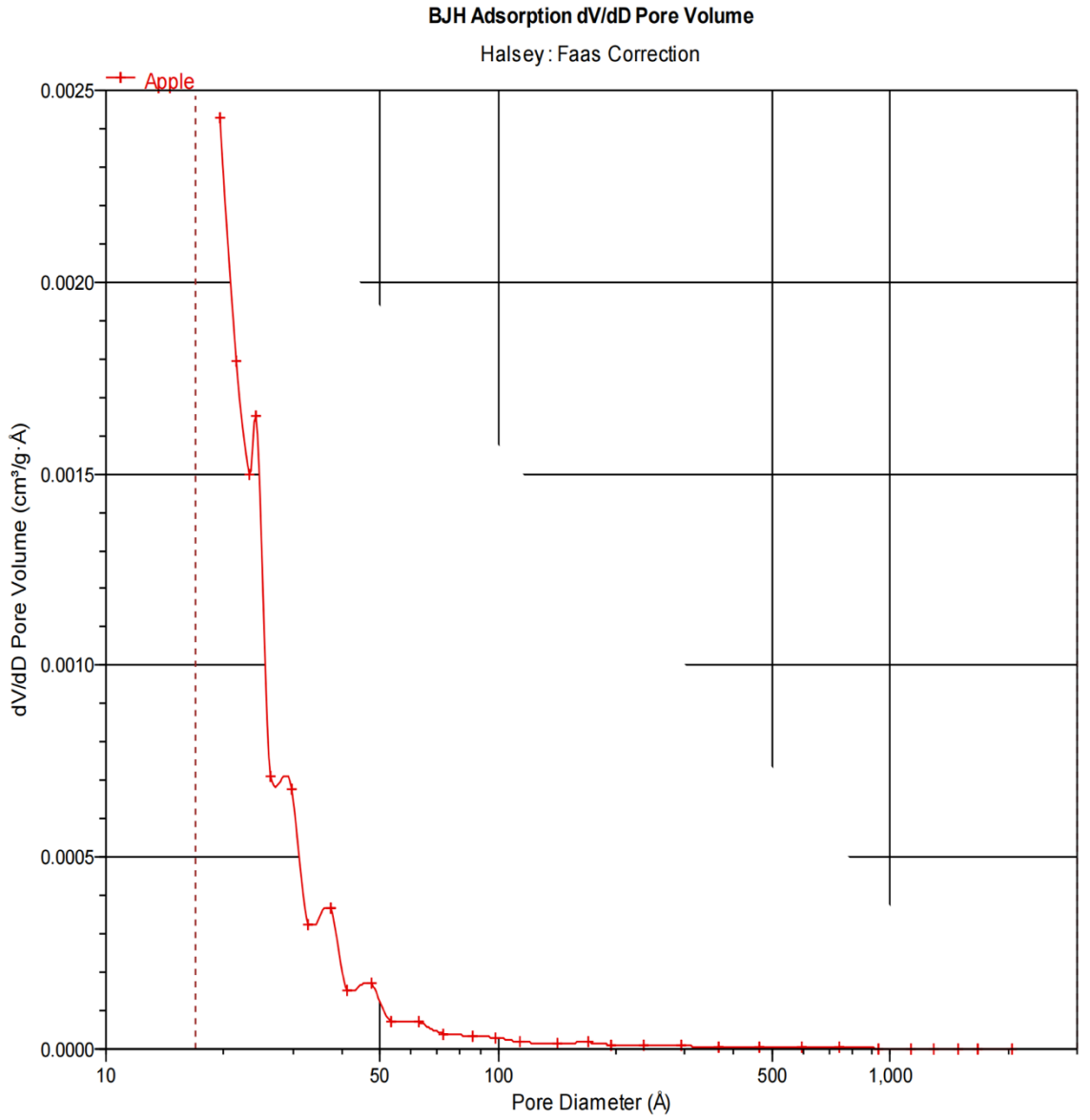


Figure C-1.8: Bc- Apple BJH adsorption DV/dD Pore Volume (Larger)

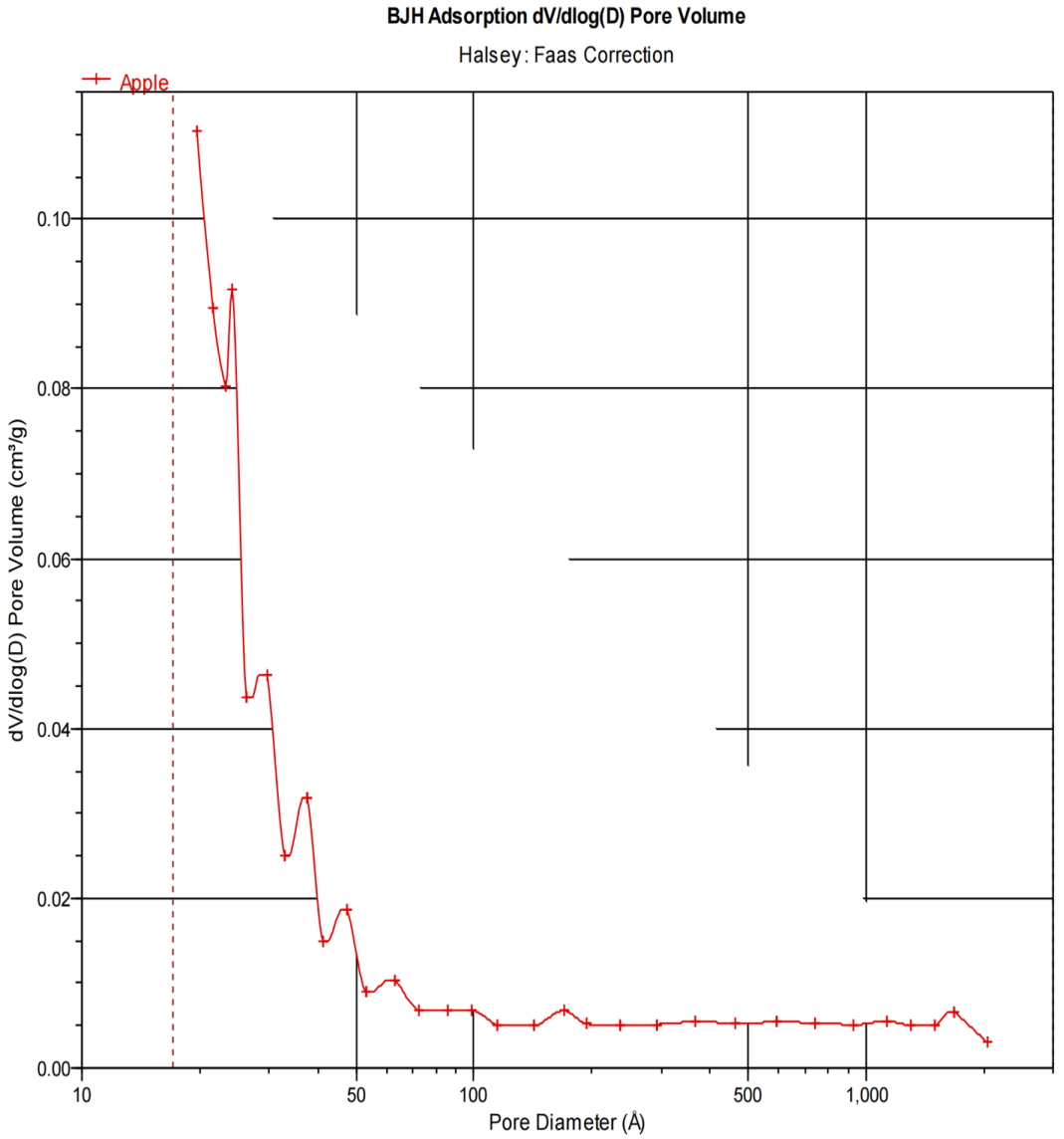


Figure C-1.9: Bc- Apple BJH adsorption DV/d log (D) Pore Volume

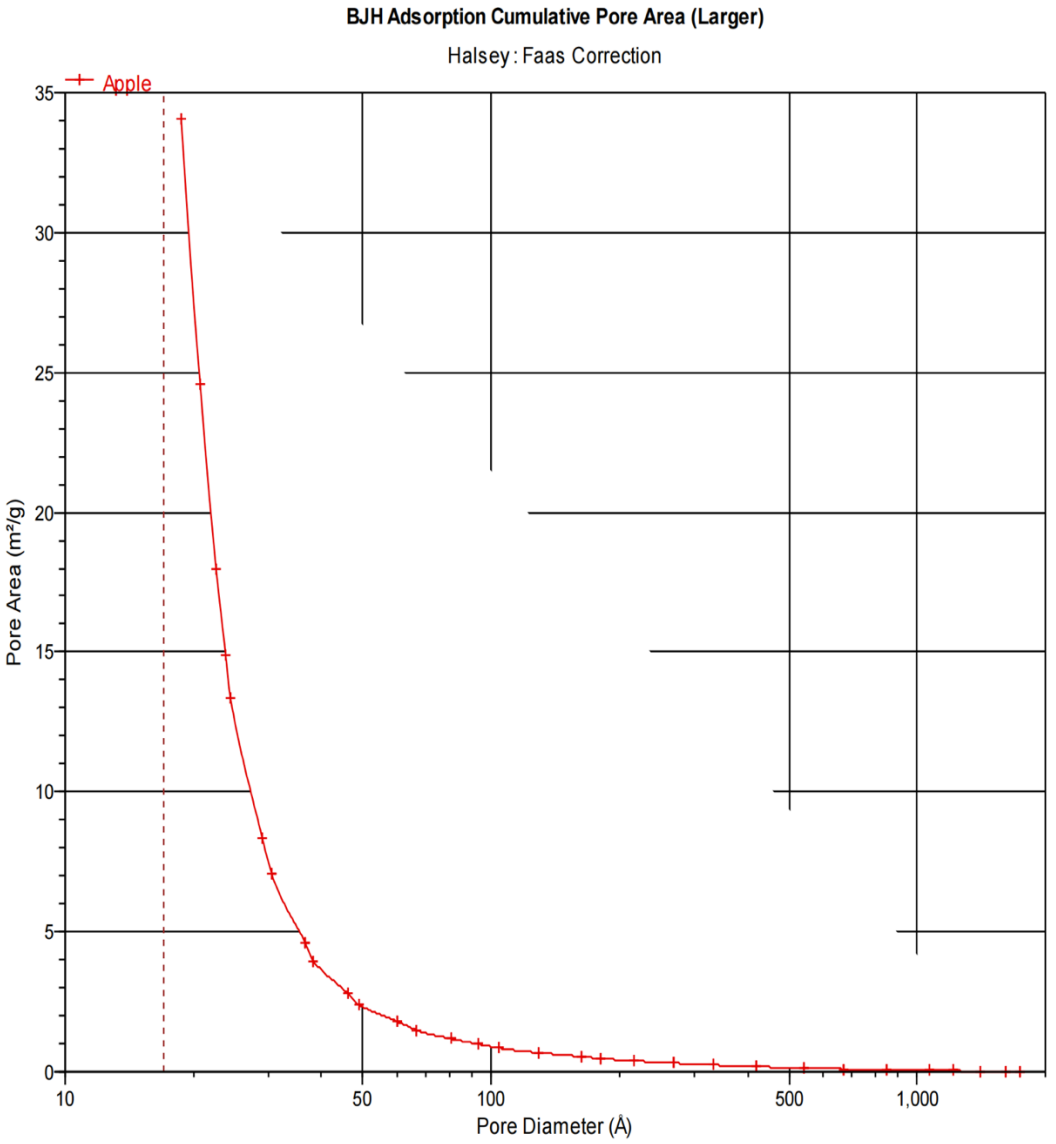


Figure C-1.10: Bc- Apple BJH adsorption DV/dD Pore Volume (Larger)

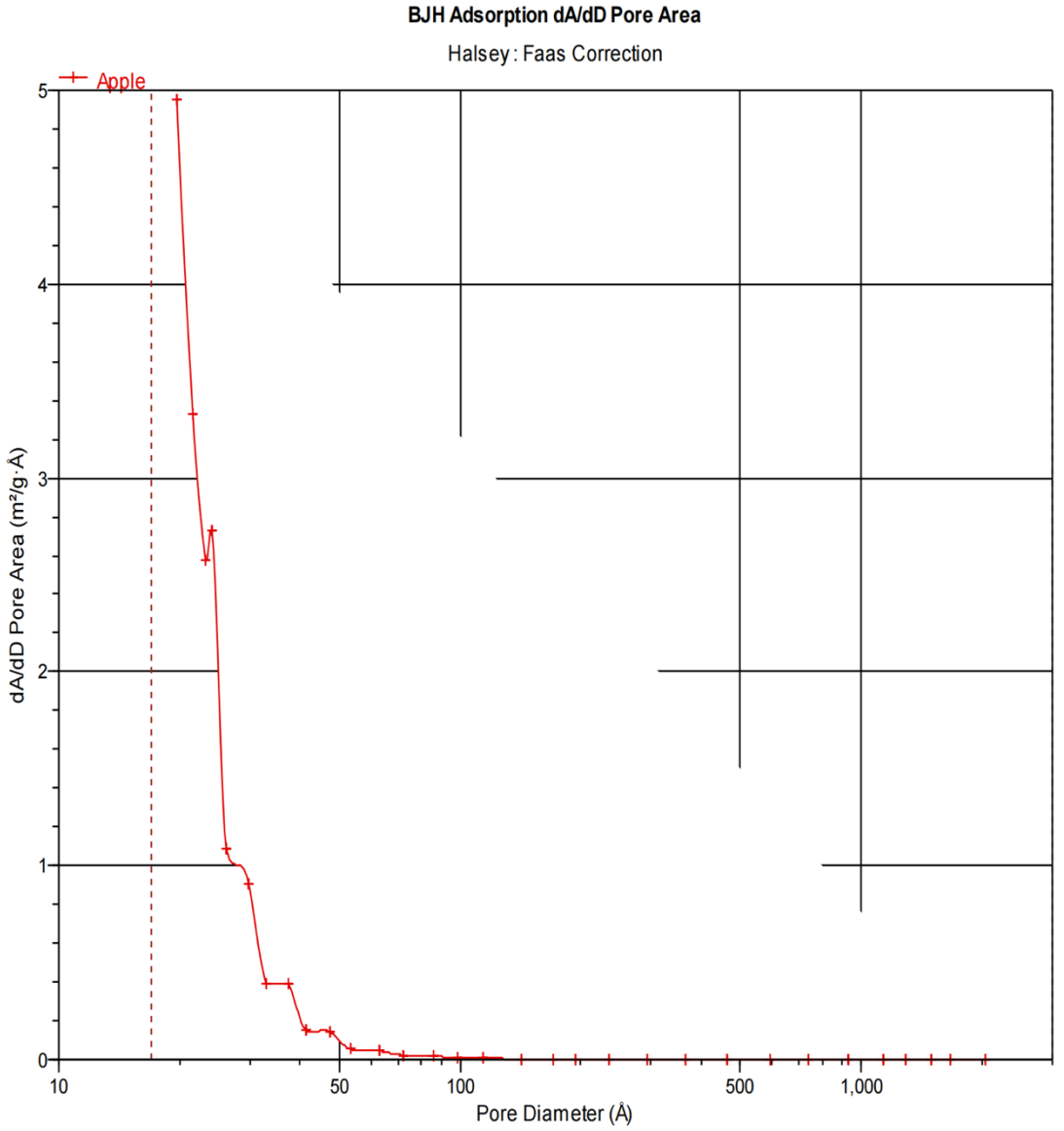


Figure C-1.11: Bc- Apple BJH adsorption DV/dD Pore area

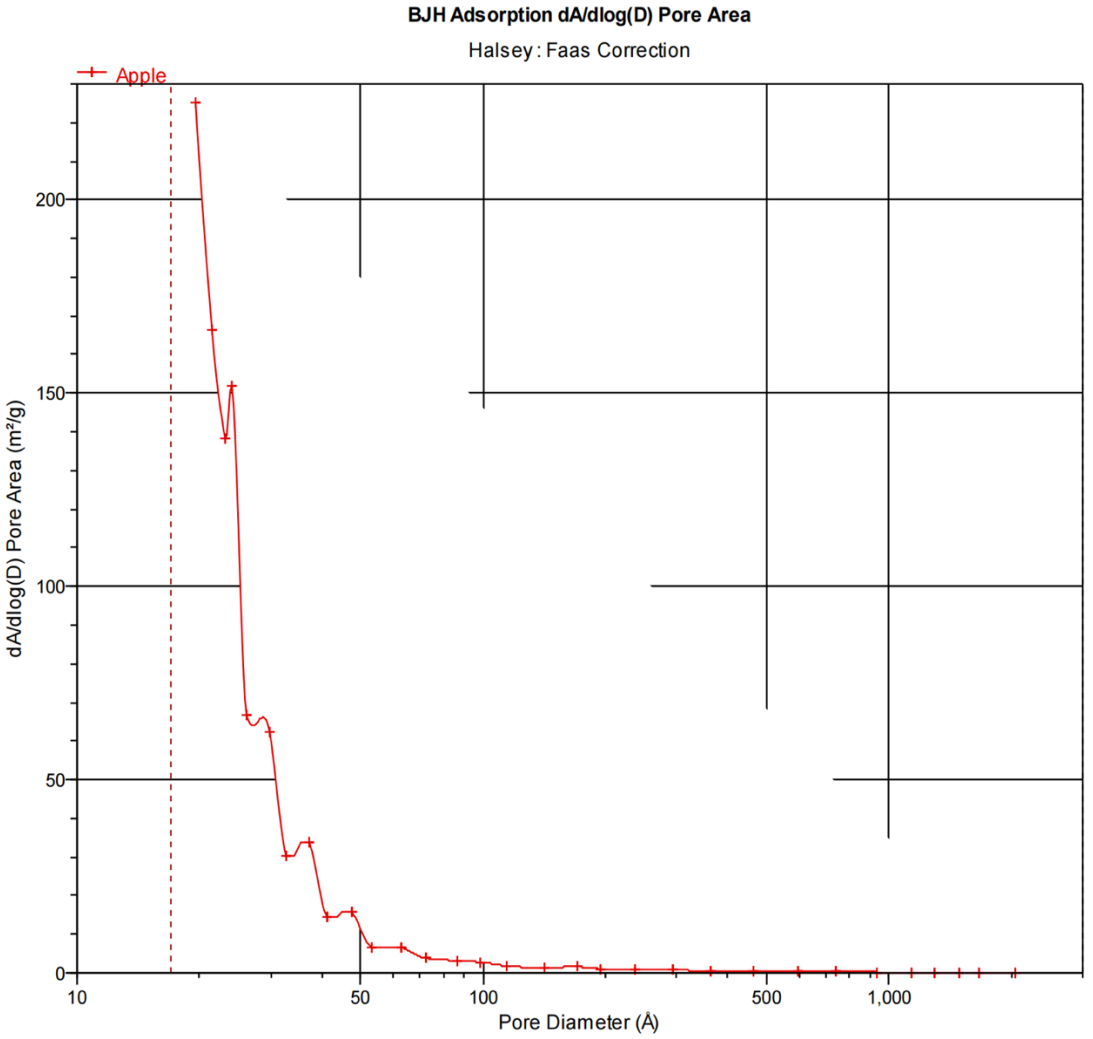


Figure C-1.12: Bc- Apple BJH adsorption DV/dlog(D) Pore area

Table 1.4: Bc-Ash BJH Desorption pore Distribution Report

Pore Diameter Range (Å)	Average Diameter (Å)	Incremental Pore volume (cm^3/g)	Cumulative Pore Volume (cm^3/g)	Incremental Pore Area($m^{2/}g$)	Cumulative pore area ($m^{2/}g$)
2896.7 - 826.5	974.9	0.001377	0.001377	0.056	0.056
826.5 - 470.2	554.5	0.000999	0.002376	0.072	0.129
470.2 - 323.6	369.4	0.000595	0.002972	0.064	0.193
323.6 - 227.6	258.3	0.000614	0.003585	0.095	0.288
227.6 - 185.0	201.6	0.000353	0.003938	0.070	0.358
185.0 - 167.7	175.5	0.000146	0.004083	0.033	0.391
167.7 - 132.6	145.7	0.000293	0.004377	0.080	0.472
132.6 - 106.7	116.6	0.000278	0.004655	0.096	0.567
106.7 - 82.3	91.0	0.000339	0.004994	0.149	0.716
82.3 - 61.1	68.1	0.000527	0.005521	0.309	1.026
61.1 - 46.8	51.7	0.000735	0.006256	0.569	1.594
46.8 - 37.3	40.7	0.001115	0.007371	1.095	2.690
37.3 - 30.3	32.9	0.001774	0.009144	2.157	4.846
30.3 - 24.2	26.4	0.003372	0.012516	5.111	9.957

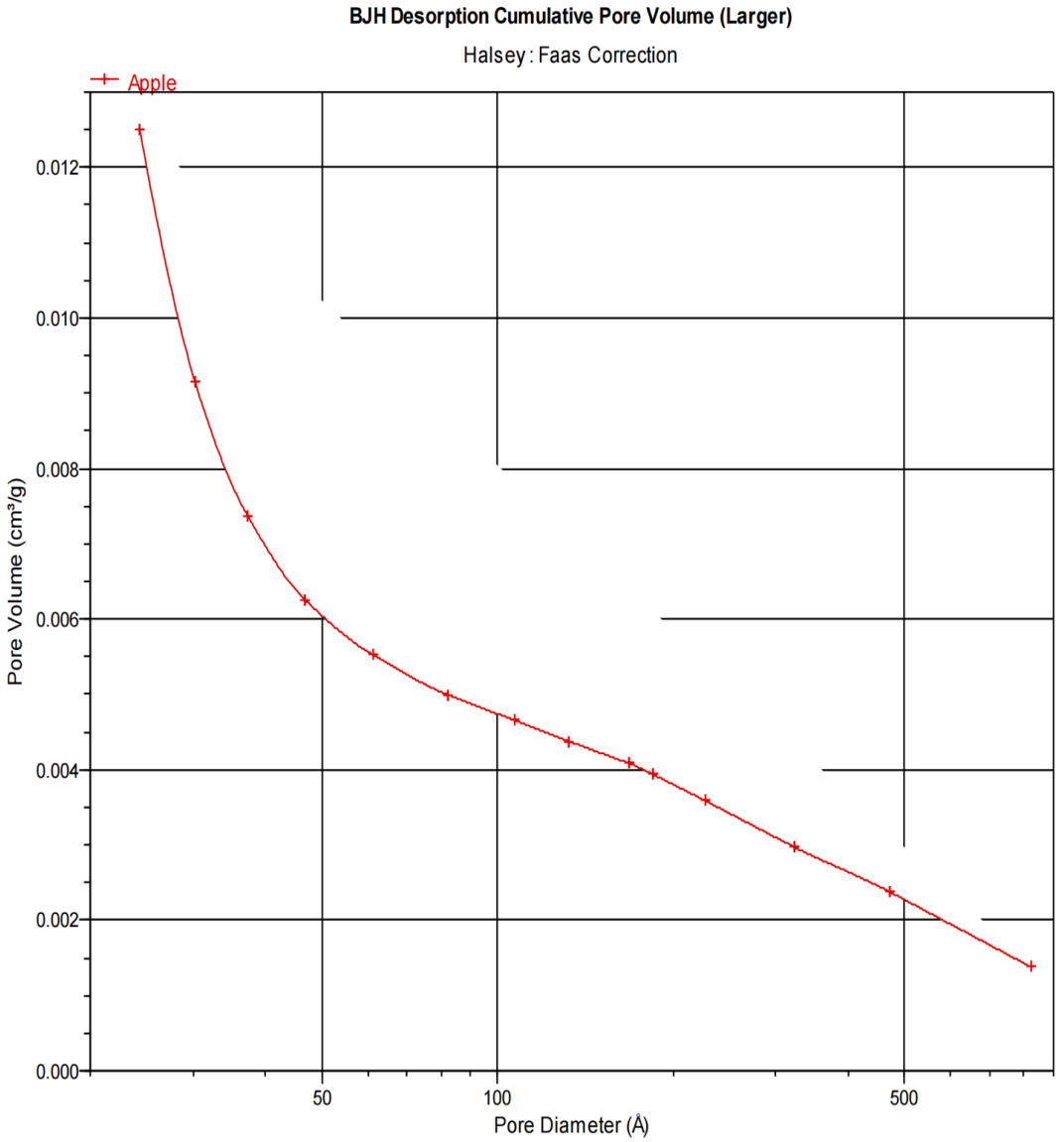


Figure C-1.13: Bc-Apple BJH Desorption cumulative dA/dD pore volume

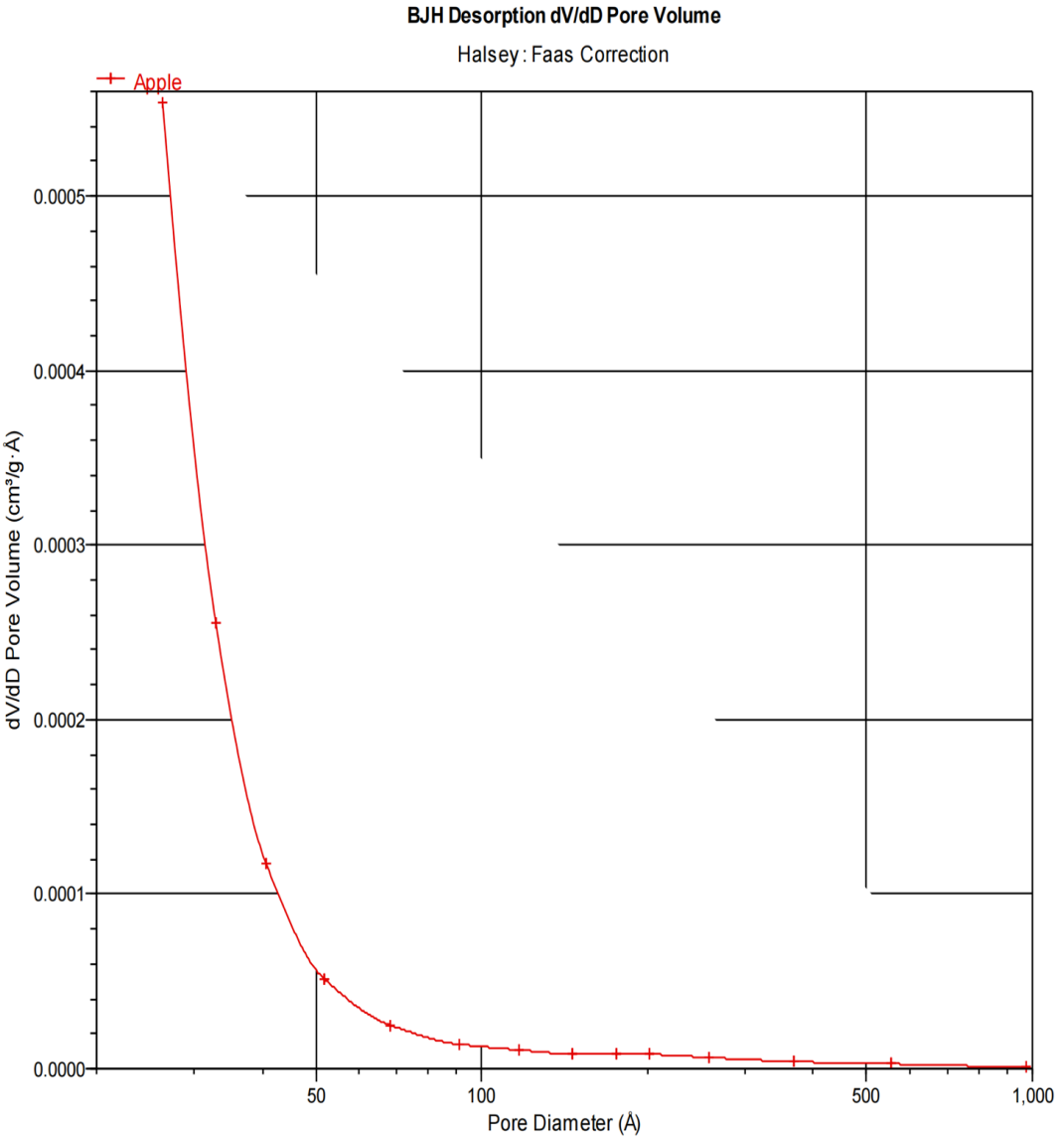


Figure C-1.14: Bc-Apple BJH Desorption dA/dD pore volume

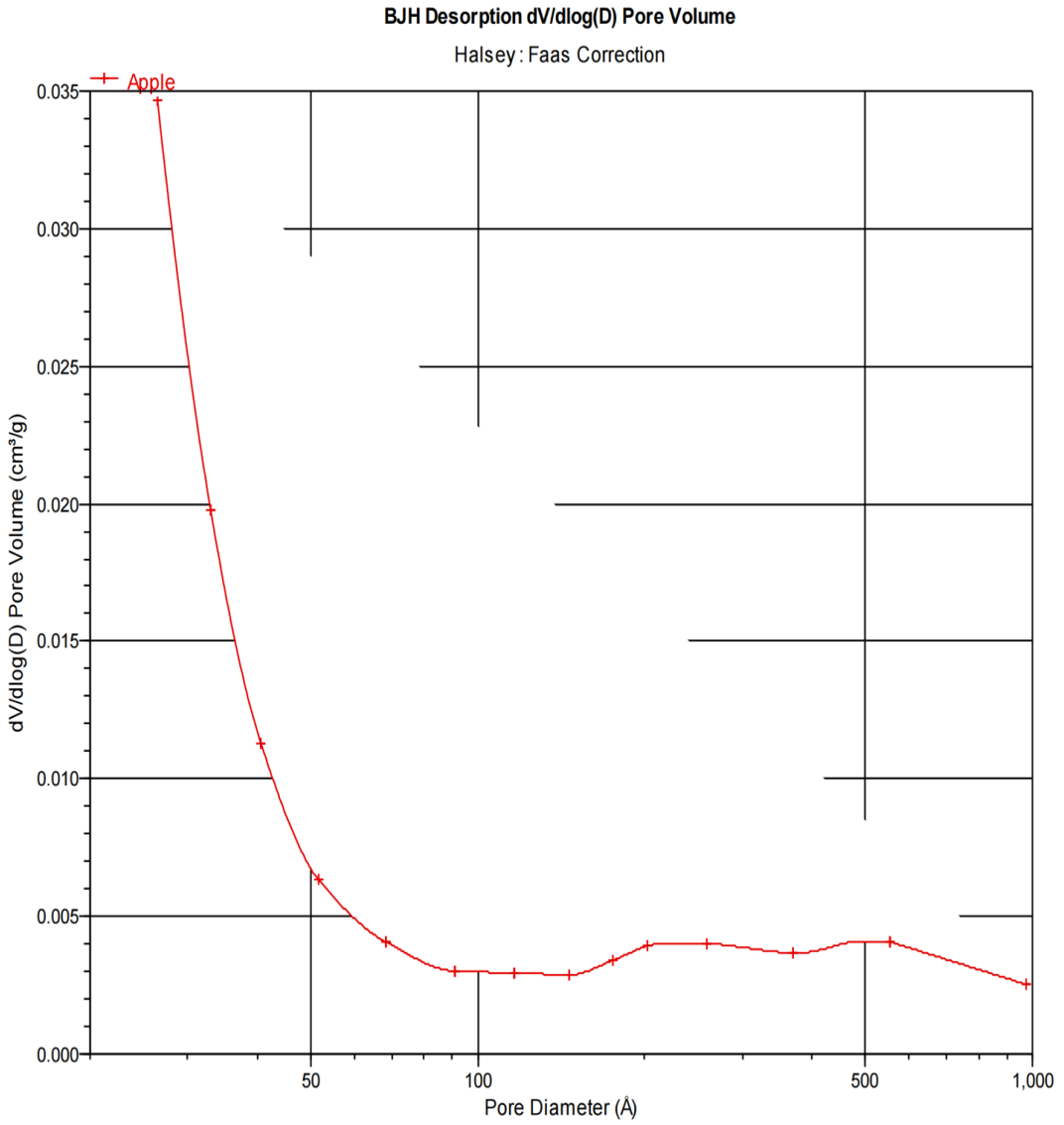


Figure C-1.15: Bc-Apple BJH Desorption dA/dlog(D) pore volume

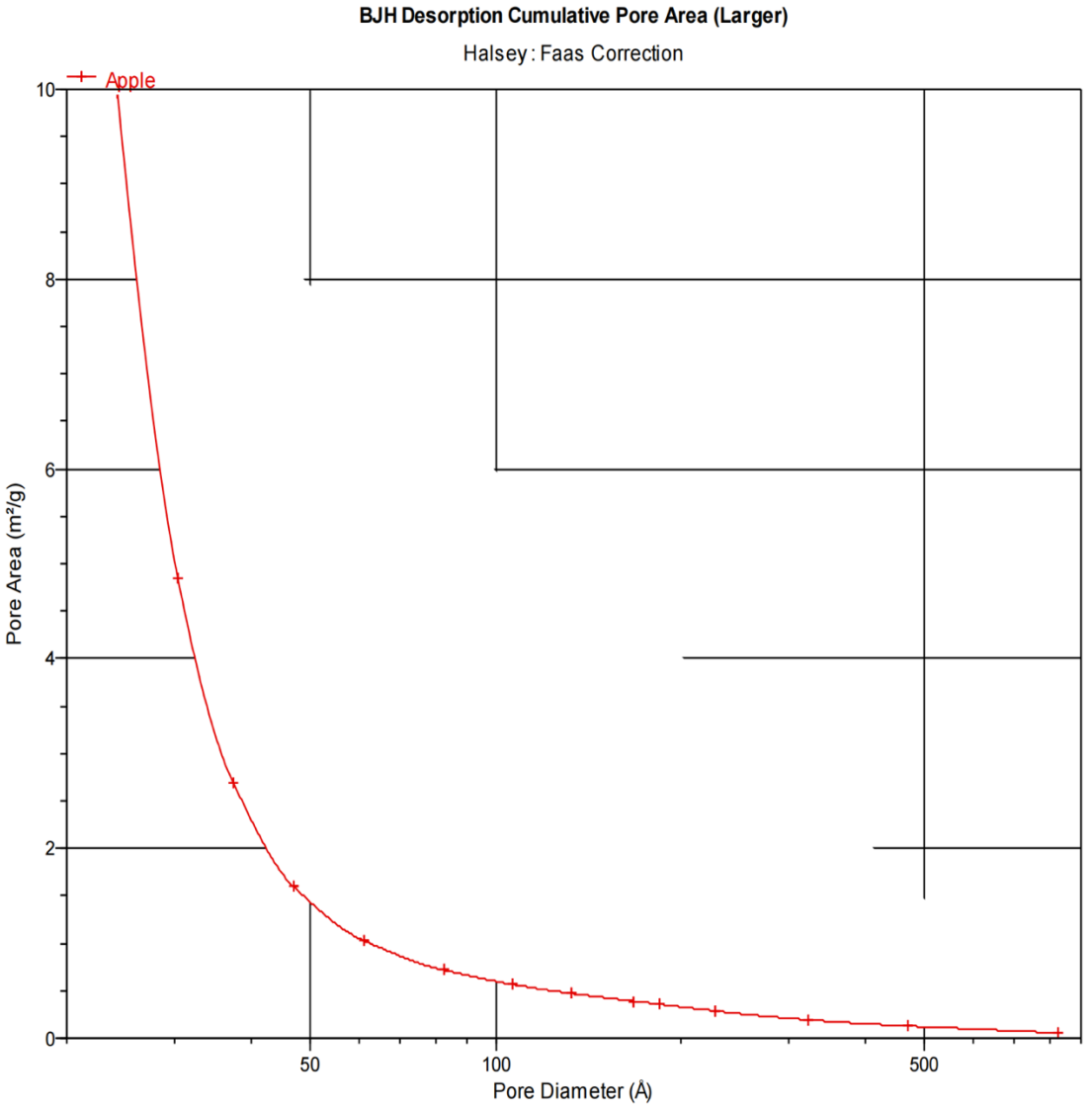


Figure C-1.16: Bc-Apple BJH Desorption cumulative pore area (larger)

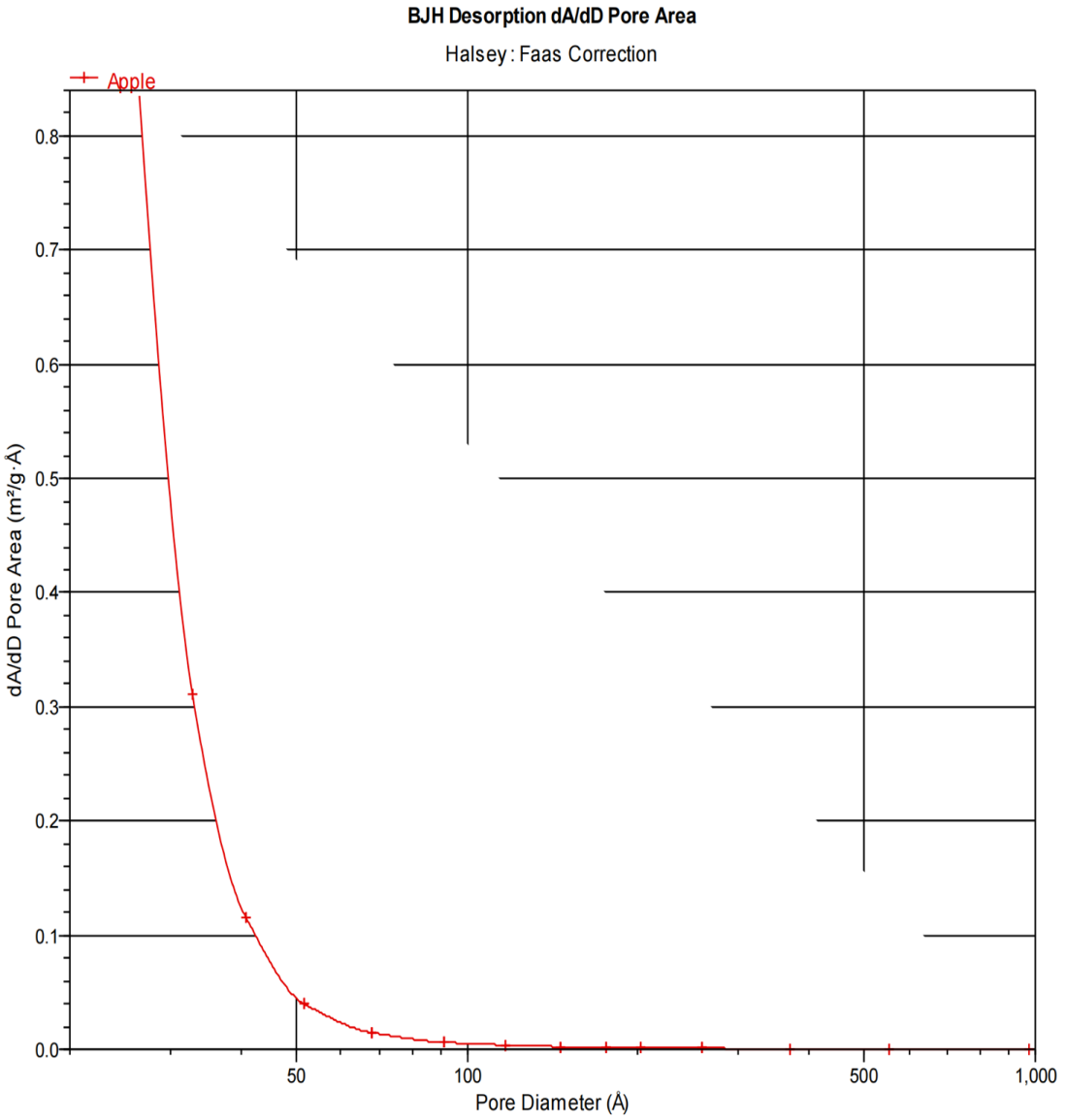


Figure C-1.17: Bc-Apple BJH Desorption dA/dD pore Area

Ash Summary Report

Single point surface area at p/p° = 0.300000000: 282.5944 m^2/g

BET Surface Area: 307.3071 m^2/g

Langmuir Surface Area: 448.1112 m^2/g

BJH Adsorption cumulative surface area of pores

between 17.000 Å and 3,000.000 Å diameter: 27.085 m^2/g

BJH Desorption cumulative surface

area of pores between 17.000 Å and

3,000.000 Å diameter: 6.8106 m^2/g

Pore Volume

Single point adsorption total pore

volume of pores less than 1,683.837

Å diameter at p/p° = 0.988379095:

0.159254cm^3/g

Single point desorption total pore

volume of pores. less than 2,975.211

Å diameter at p/p° = 0.993473013:

0.160026cm^3/g

BJH Adsorption cumulative volume of pores

between 17.000 Å and 3,000.000 Å diameter: 0.023795 cm^3/g

BJH Desorption cumulative volume of pores

between 17.000 Å and 3,000.000 Å diameter: 0.009226 $cm^3/$

Pore Size

Adsorption average pore diameter (4V/A by BET):20.7290Å

Desorption average pore diameter (4V/A by BET): 20.8294 Å

BJH Adsorption average pore diameter (4V/A): 35.142 Å BJH Desorption average pore diameter (4V/A): 54.186 Å

BET Report

BET Surface Area: 307.3071 ± 7.3074 m^2/g

Slope: 0.014400 ± 0.000332 g/cm^3 STP

Y-Intercept: -0.000237 ± 0.000058 g/cm^3

STP C: -59.884403 Qm: 70.6035 cm^3/g

STP Correlation Coefficient: 0.9986754

Molecular Cross-Sectional Area: 0.1620 nm^2

Table C 2.0: Bc-Ash Isotherm Tabular Report

Relative Pressure (P/P^o)	Absolute pressure (mmHg)	Quantity Adsorbed (cm^3/g STP)	Elapsed Time (h: min)	Saturation pressure (mmHg)
0.010045927	7.585598	83.3589	00:40	759.455200
0.061212691	46.151634	92.2460	12:46	755.091919
0.082663079	62.309990	93.3770	16:28	753.955322
0.127047088	95.734222	94.7759	16:58	753.782593
0.166406271	125.357498	95.6132	17:22	753.533386
0.208233511	156.860764	96.2490	17:36	753.321960
0.233619386	175.982529	96.6404	17:45	753.292603
0.244782395	184.377304	96.8250	17:52	753.287354
0.334307485	251.792709	97.5311	17:57	753.229431
0.355051484	267.414337	97.7360	18:04	753.177002
0.448574031	337.876068	98.1870	18:07	753.170593
0.468166626	352.615936	98.3262	18:11	753.222534
0.549372336	413.750031	98.6301	18:13	753.184692
0.575127651	433.119598	98.7646	18:16	753.132263
0.648313333	488.184174	99.0022	18:18	753.084290
0.683890423	514.988647	99.1464	18:21	753.006531
0.737916570	555.695496	99.3321	18:23	753.028015
0.773860039	582.742493	99.4912	18:25	753.060059
0.798797879	601.472473	99.6335	18:26	753.033447
0.838239563	631.200684	99.8128	18:28	752.972046

0.872435672	656.894592	100.0289	18:29	753.007507
0.884865298	666.223206	100.1725	18:31	752.943298
0.904620727	681.114807	100.3622	18:32	752.909180
0.923302805	695.177979	100.5814	18:33	752.928589
0.938763560	706.793274	100.8337	18:34	752.925232
0.952021427	716.833435	101.1141	18:36	752.898071
0.963073840	725.128296	101.4271	18:37	752.959351
0.970569852	730.742065	101.6971	18:38	752.931152
0.976388724	735.132629	101.9793	18:40	752.900024
0.981595635	739.039124	102.2889	18:41	752.909790
0.983753489	740.678894	102.4755	18:42	752.895691
0.986072344	742.432068	102.6660	18:44	752.911072
0.987439101	743.432617	102.8578	18:45	752.918457
0.989322151	744.856384	103.0525	18:46	752.889587
0.993473013	748.016113	103.4559	18:47	752.895691
0.975736192	734.610840	102.6533	18:49	752.930481
0.956740990	720.328796	102.0888	18:50	752.878540
0.936944969	705.429321	101.7461	18:52	752.898438
0.909035210	684.428833	101.4557	18:54	752.903687
0.887345567	668.090027	101.3180	18:55	752.917847
0.857724664	645.804321	101.1944	18:57	752.908508
0.841313339	633.455078	101.1438	18:58	752.927307
0.802094432	603.862061	101.0686	18:59	752.935974
0.743217032	559.530334	100.9783	19:01	752.856567

0.654251457	492.520569	100.8626	19:02	752.849182
0.554472675	417.394806	100.7095	19:04	752.800110
0.454280951	341.945374	100.4687	19:06	752.777954
0.353752774	266.264557	100.1047	19:08	752.717834
0.242006787	182.152145	99.4630	19:12	752.685425

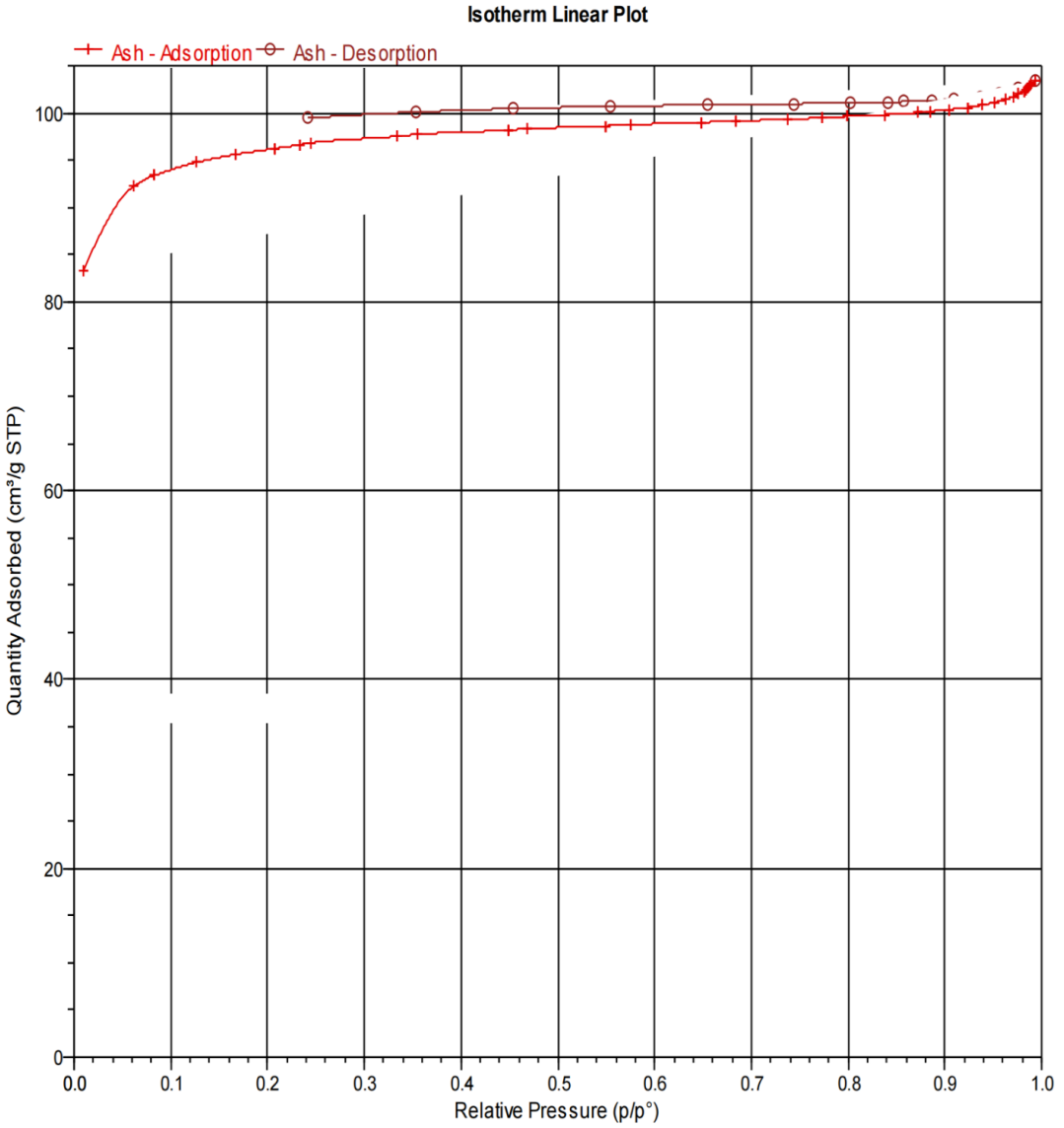


Figure C-2.0: Bc-Ash BET Isotherm Linear Plot

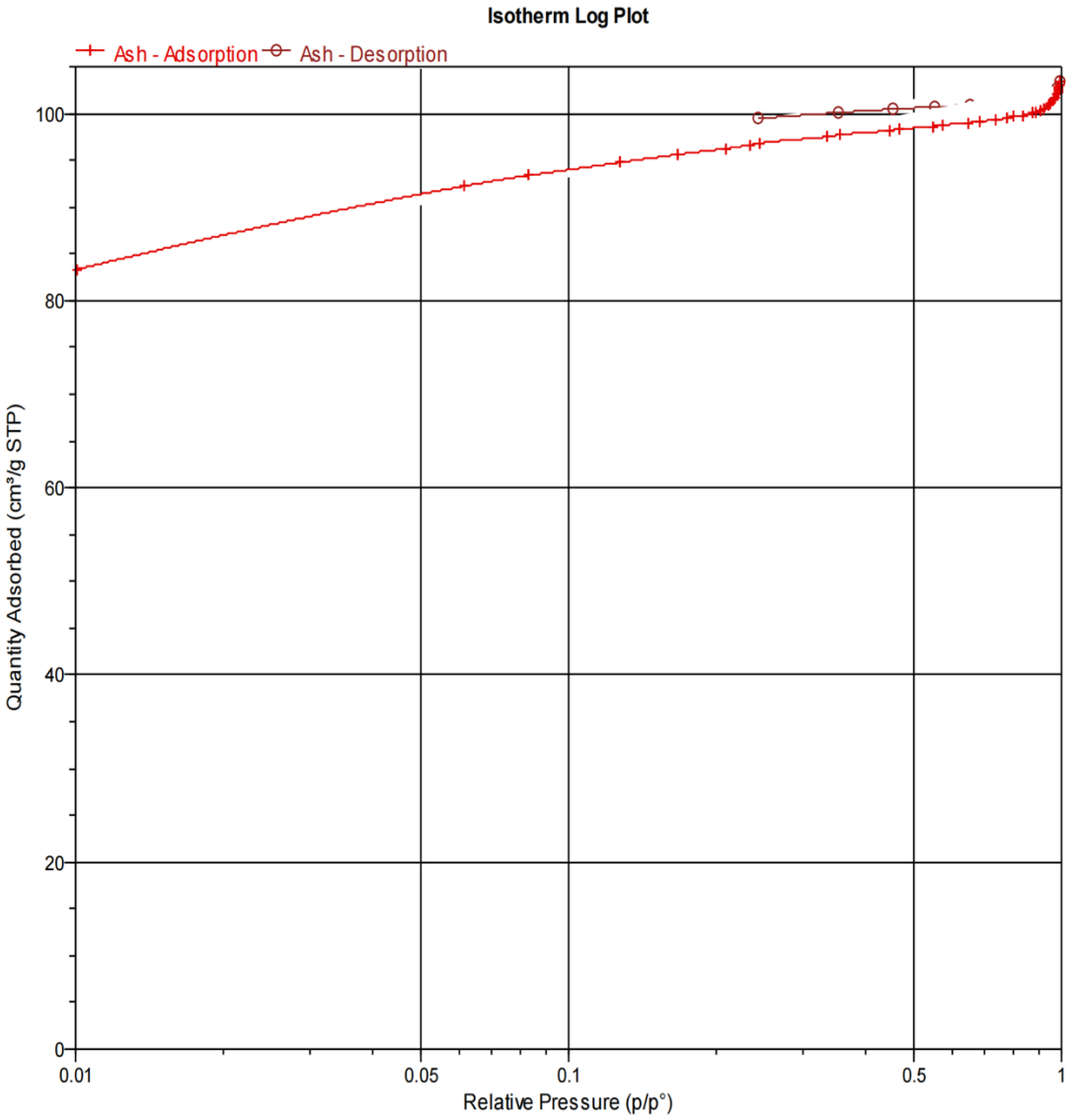


Figure C-2.1: Bc-Ash BET Isotherm Log Plot

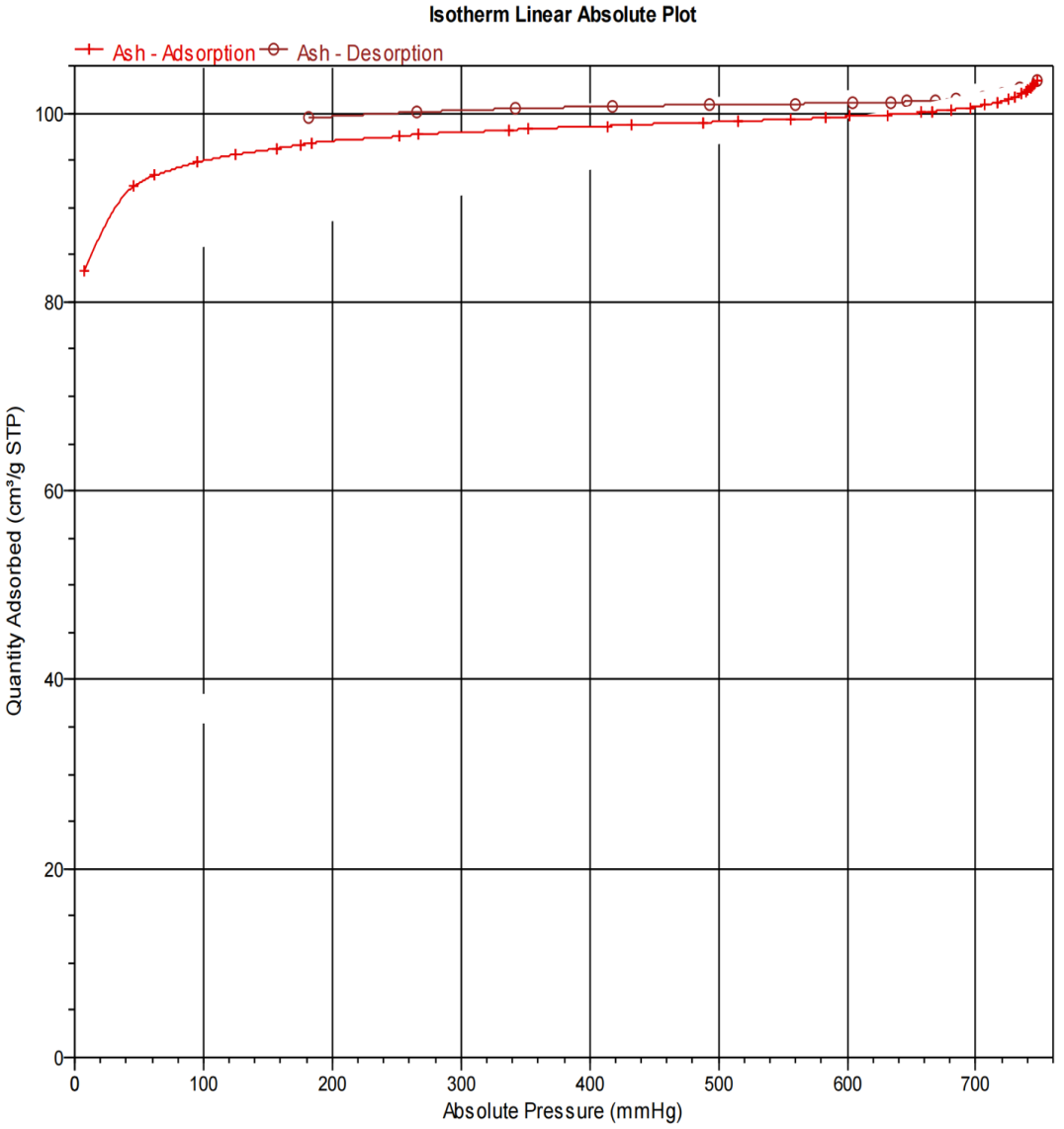


Figure C-2.2: Isotherm Linear Absolute Plot

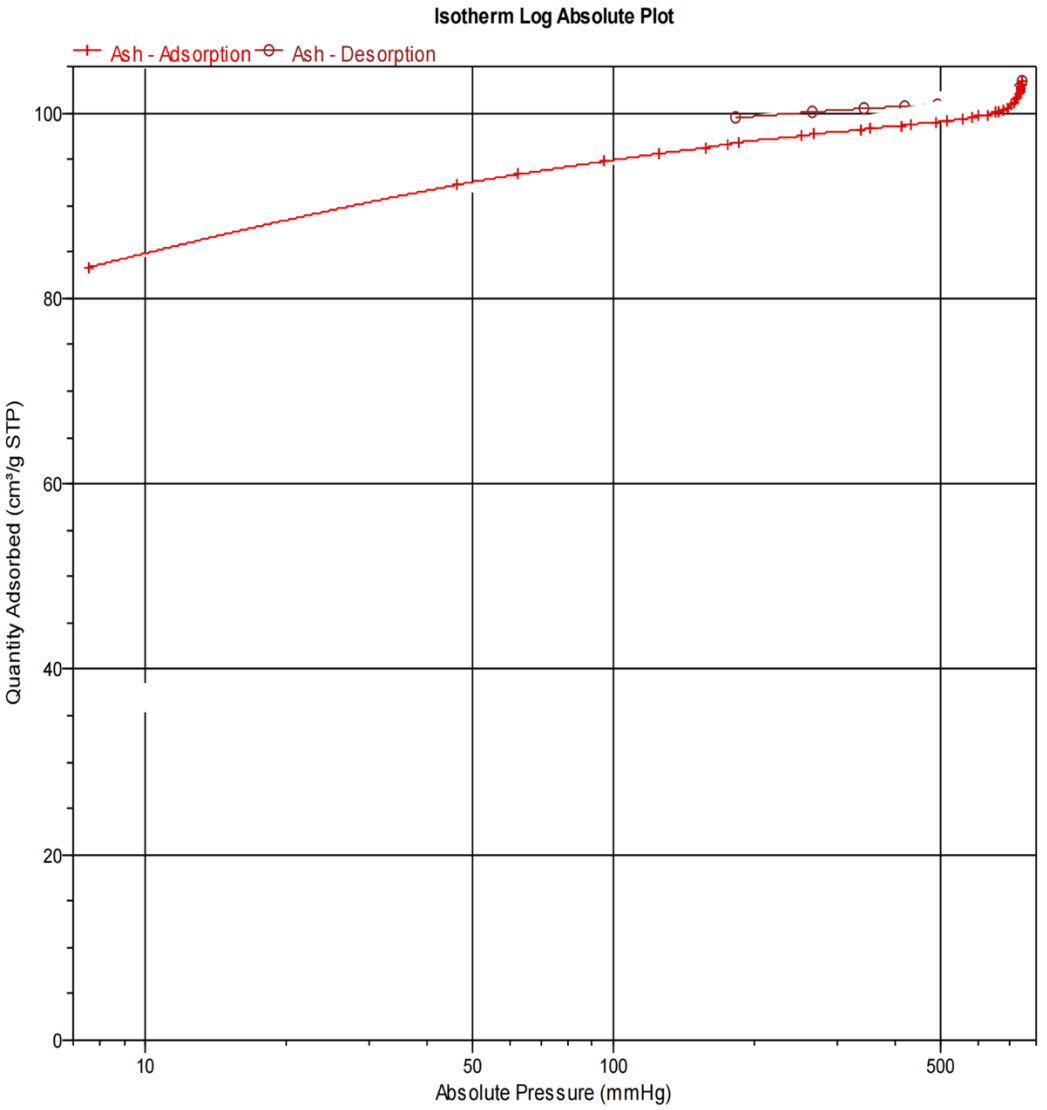


Figure C-2.3: Bc-Ash BET Isotherm Log Plot

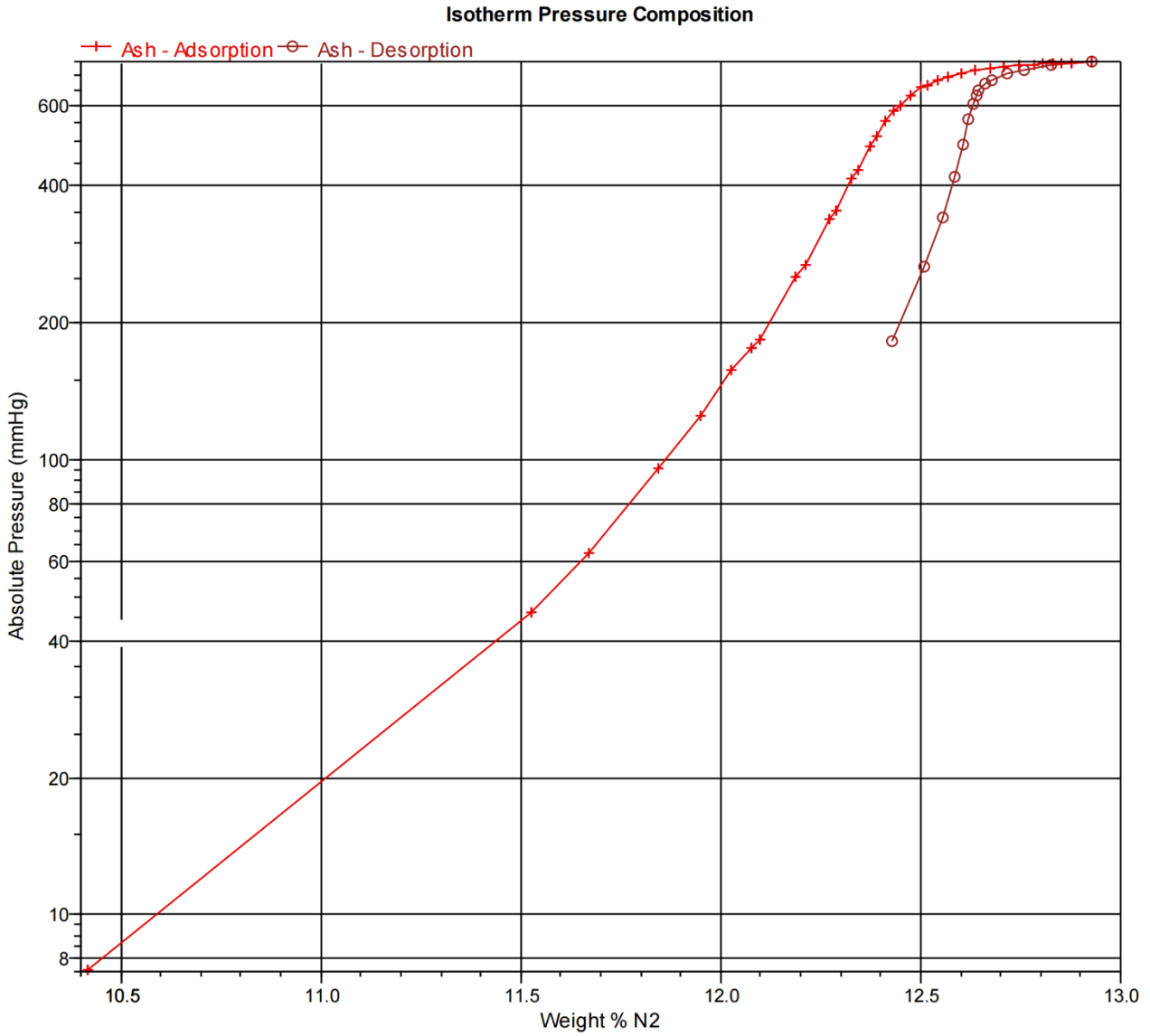


Figure C-2.4: Isotherm Pressure Composition

Table C-2.1: Bc-Ash Bet report showing relative pressure and quantity adsorbed at STP.

Relative pressure p/p^o	**Quantity adsorbed (cm3/g STP)**	**1/[Q(p°/p - 1)]**
0.061212691	92.2460	0.000707
0.082663079	93.3770	0.000965
0.127047088	94.7759	0.001536
0.166406271	95.6132	0.002088
0.208233511	96.2490	0.002732
0.233619386	96.6404	0.003154
0.244782395	96.8250	0.003348

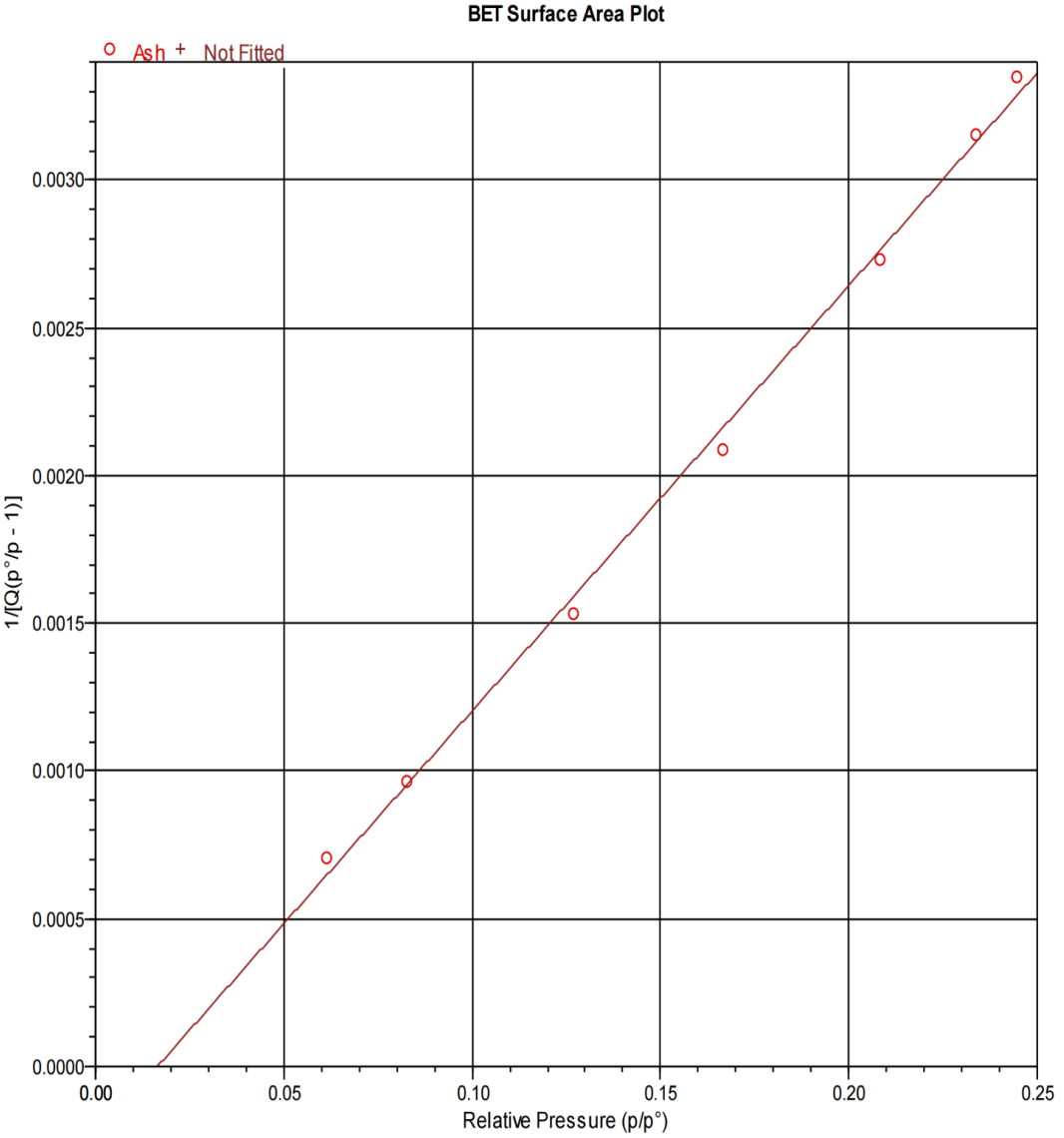


Figure C-2.5: Bc-Ash BET Surface Area Plot

Langmuir Report

Langmuir Surface Area: 448.1112 ± 2.1387 m^2/g

Slope: 0.009713 ± 0.000046 g/cm^3 STP

Y-Intercept: 0.115 ± 0.025 $mmHg \cdot g/cm^3$

STP b: 0.084108 1/mmHg

Qm: 102.9530 cm^3/g STP

Correlation Coefficient: 0.999624

Molecular Cross-Sectional Area: 0.1620 nm^2

Table C- 2.2: Bc-Ash Langmuir Data Representation.

Pressure (mmHg)	Quality Adsorbed cm^3/g STP	p/Q (mmHg g/cm^3 STP
7.585598	83.3589	0.091
46.151634	92.2460	0.500
62.309990	93.3770	0.667
95.734222	94.7759	1.010
125.357498	95.6132	1.311
156.860764	96.2490	1.630
175.982529	96.6404	1.821
184.377304	96.8250	1.904
251.792709	97.5311	2.582
267.414337	97.7360	2.736
337.876068	98.1870	3.441
352.615936	98.3262	3.586
413.750031	98.6301	4.195
433.119598	98.7646	4.385
488.184174	99.0022	4.931
514.988647	99.1464	5.194
555.695496	99.3321	5.594
582.742493	99.4912	5.857
601.472473	99.6335	6.037
631.200684	99.8128	6.324
656.894592	100.0289	6.567

666.223206	100.1725	6.651
681.114807	100.3622	6.787
695.177979	100.5814	6.912
706.793274	100.8337	7.009
716.833435	101.1141	7.089
725.128296	101.4271	7.149
730.742065	101.6971	7.185
735.132629	101.9793	7.209
739.039124	102.2889	7.225
740.678894	102.4755	7.228
742.432068	102.6660	7.232

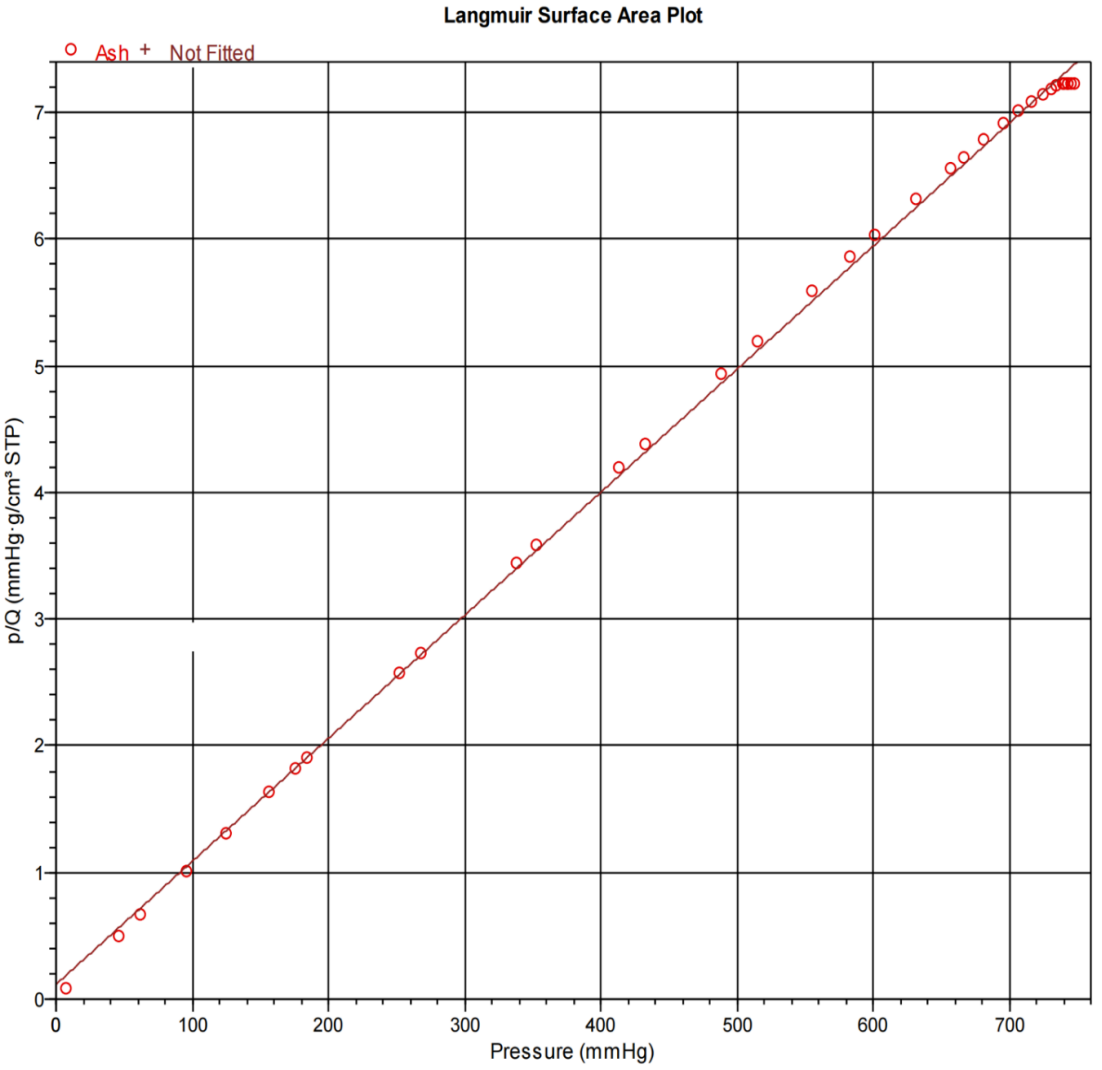


Figure C-2.6: Langmuir Surface Area Plot

Table C 2.3: Bc-Ash BJH Adsorption Pore Distribution Report

Pore Diameter Range (Å)	Average Diameter (Å)	Incremental Pore vol(cm^3/g)	Cumulative Pore Vol (cm^3/g)	Incremental Pore Area(m^2/g)	Cumulative pore area (m^2/g)
2975.2 - 1830.2	2141.1	0.000657	0.000657	0.012	0.012
1830.2 - 1559.7	1673.1	0.000319	0.000976	0.008	0.020
1559.7 - 1409.1	1476.6	0.000316	0.001292	0.009	0.028
1409.1 - 1211.2	1294.9	0.000314	0.001606	0.010	0.038
1211.2 - 1071.7	1132.7	0.000309	0.001915	0.011	0.049
1071.7 - 839.6	927.1	0.000516	0.002431	0.022	0.071
839.6 - 677.0	740.5	0.000475	0.002906	0.026	0.097
677.0 - 542.6	594.6	0.000458	0.003364	0.031	0.128
542.6 - 420.6	465.8	0.000539	0.003903	0.046	0.174
420.6 - 332.0	365.5	0.000490	0.004393	0.054	0.228
332.0 - 266.9	292.0	0.000448	0.004840	0.061	0.289
266.9 - 216.2	235.9	0.000393	0.005233	0.067	0.356
216.2 - 180.2	194.7	0.000347	0.005580	0.071	0.427
180.2 - 163.2	170.7	0.000275	0.005856	0.064	0.491

163.2 - 129.6	142.2	0.000404	0.006259	0.114	0.605
129.6 - 104.7	114.2	0.000339	0.006598	0.119	0.724
104.7 - 93.4	98.3	0.000295	0.006893	0.120	0.844
93.4 - 80.7	86.0	0.000330	0.007223	0.154	0.997
80.7 - 66.9	72.3	0.000389	0.007613	0.215	1.213
66.9 - 60.0	63.0	0.000333	0.007945	0.211	1.424
60.0 - 49.2	53.3	0.000556	0.008501	0.417	1.841
49.2 - 46.2	47.6	0.000366	0.008867	0.308	2.148
46.2 - 38.4	41.4	0.000809	0.009676	0.782	2.930
38.4 - 36.8	37.5	0.000439	0.010115	0.468	3.398
36.8 - 30.4	32.8	0.001377	0.011492	1.679	5.077
30.4 - 29.1	29.7	0.000751	0.012242	1.011	6.088
29.1 - 24.3	26.2	0.002558	0.014801	3.910	9.998
24.3 - 23.8	24.1	0.000794	0.015595	1.321	11.319
23.8 - 22.6	23.1	0.001664	0.017260	2.878	14.197
22.6 - 20.6	21.4	0.002687	0.019947	5.012	19.209
20.6 - 18.7	19.5	0.003848	0.023795	7.876	27.085

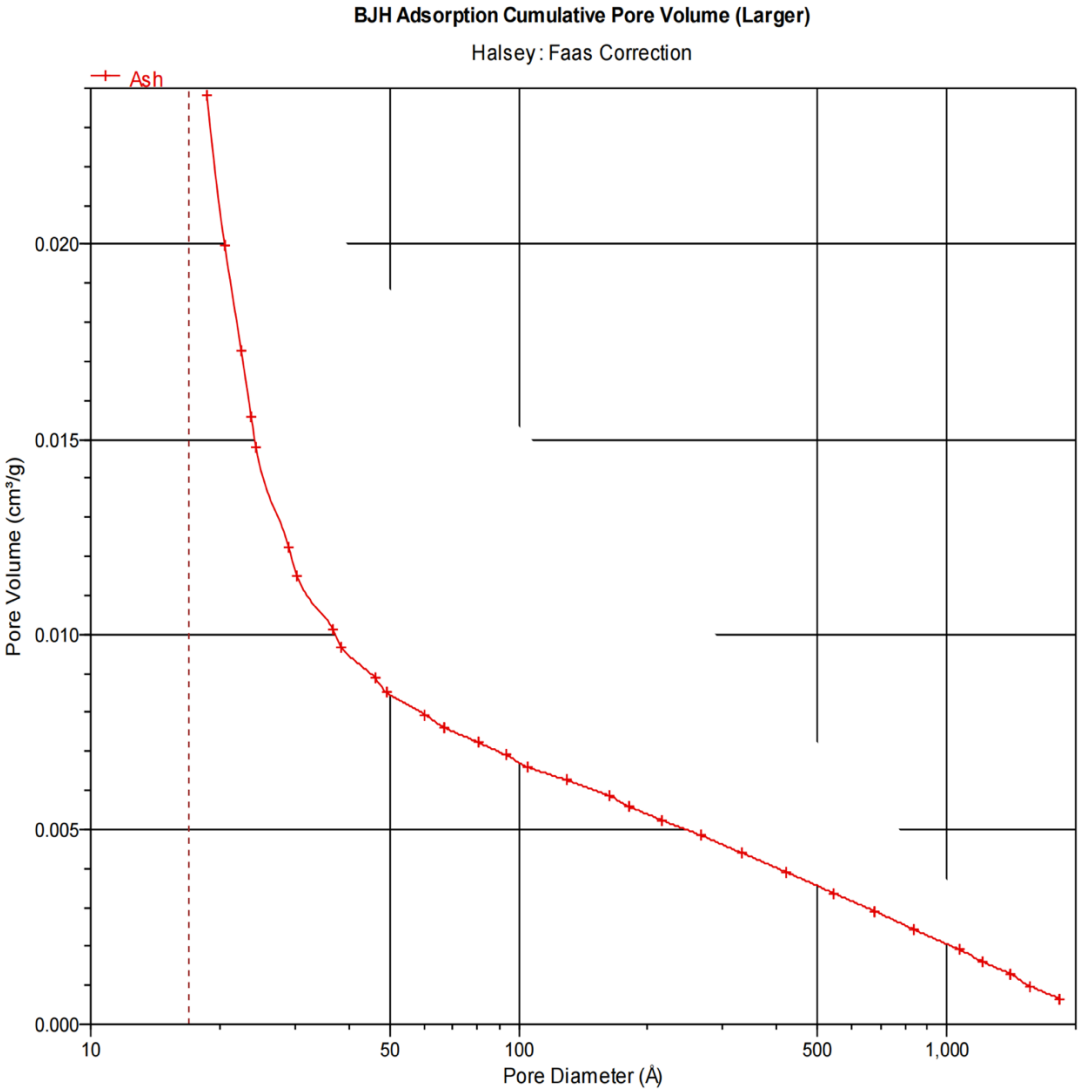


Figure C-2.7: Bc-Ash BJH Adsorption Cumulative Pore Volume Halsey Faas Correction

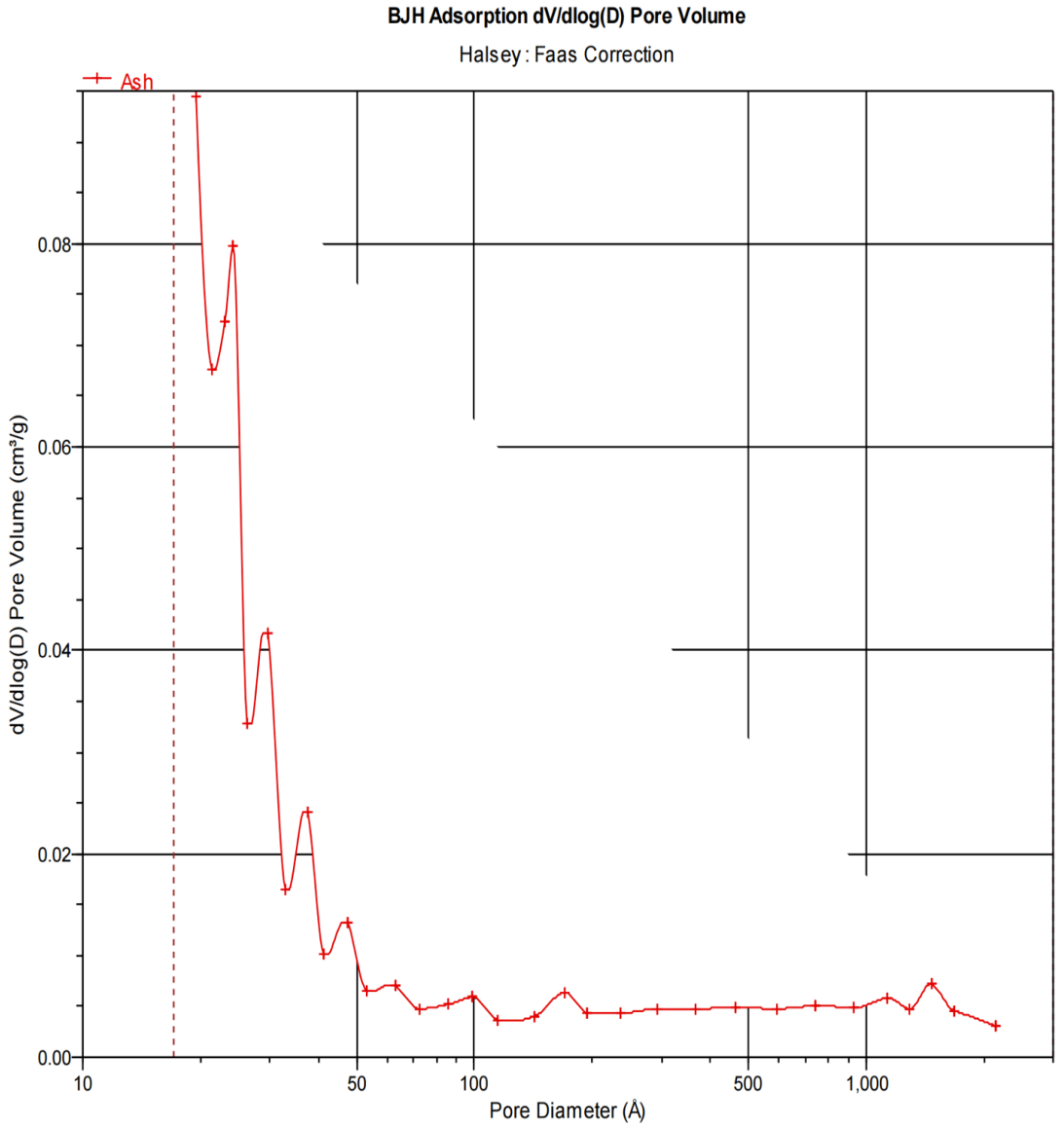


Figure C-2.8: Bc-Ash BJH Adsorption dV/dlog(D) Pore Volume (Halsey Faas Correction)

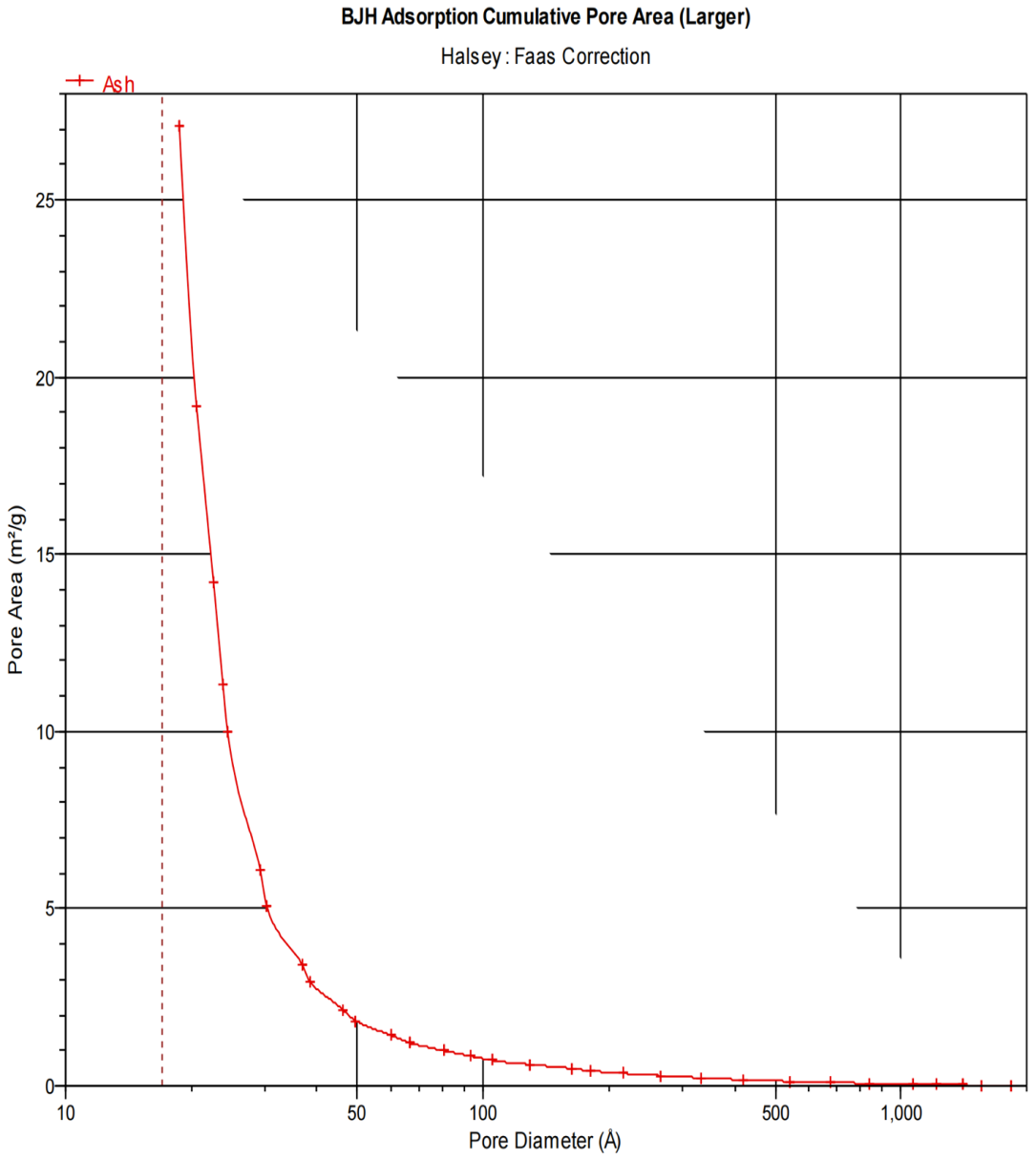


Figure C-2.9: BJH Adsorption Cumulative Pore Area (Larger) (Halsey: Faas Correction

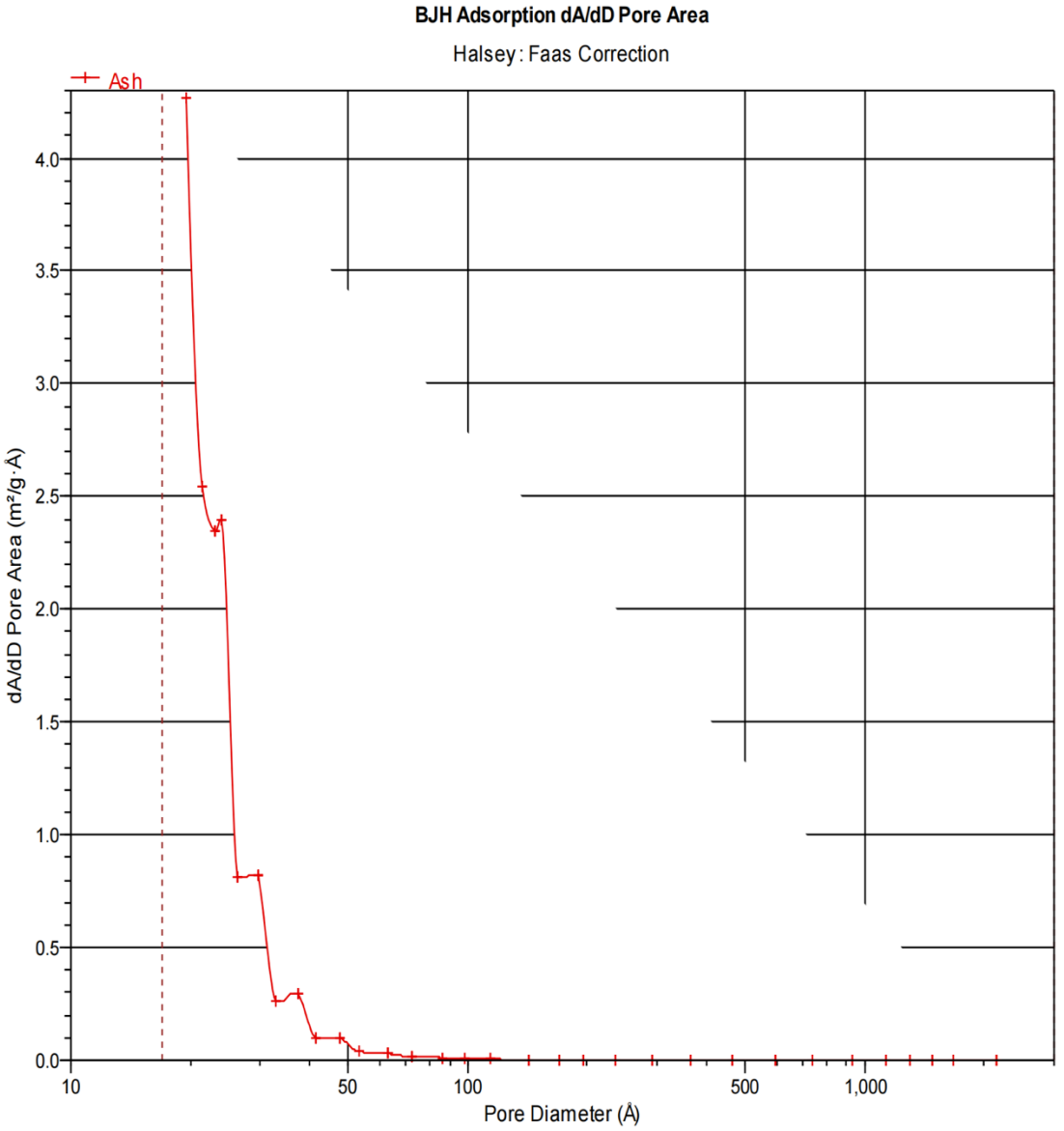


Figure C-2.10: Bc-Ash BJH Adsorption dA/dD Pore Area (Halsey: Faas Correction)

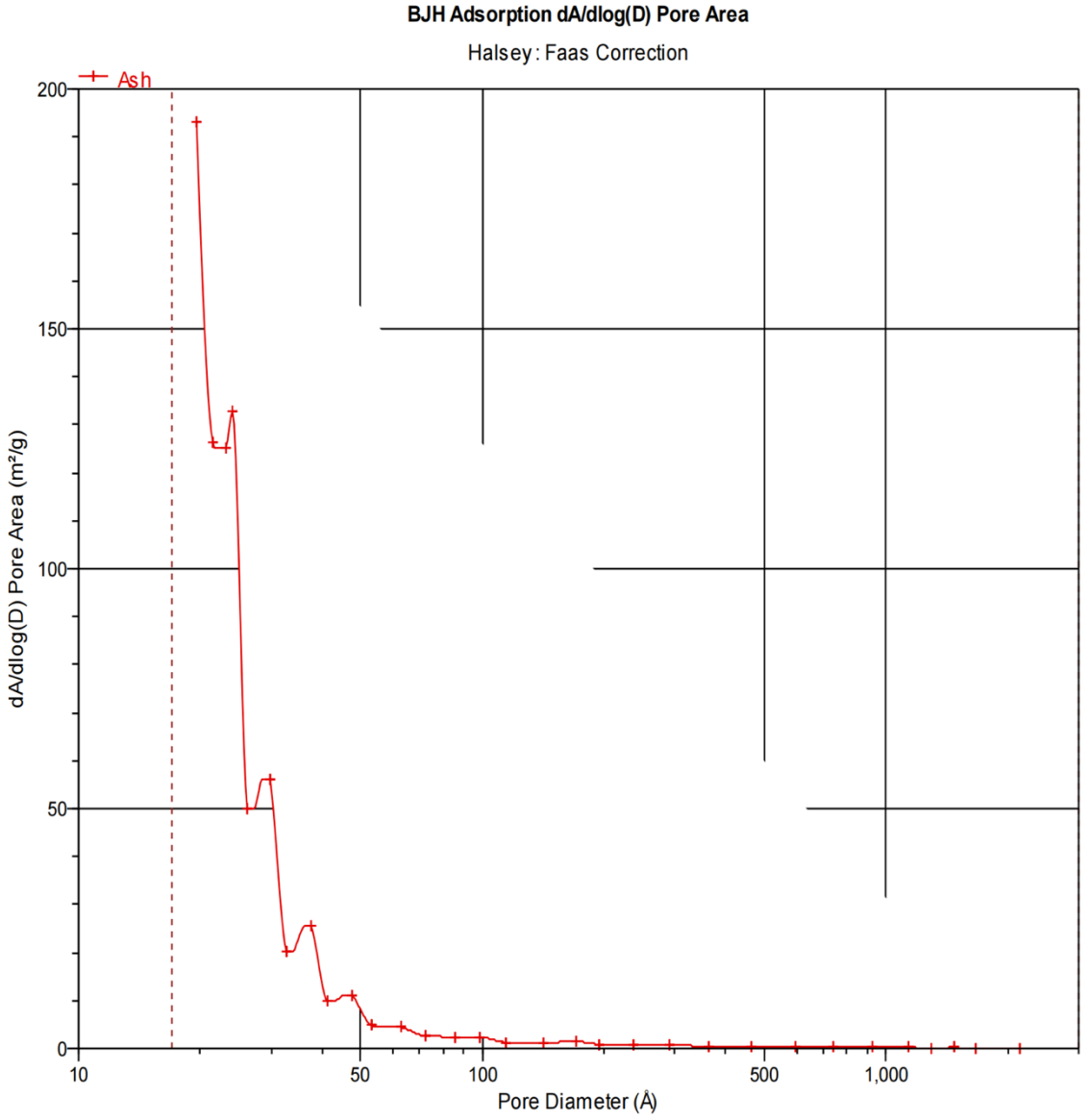


Figure.C-2.11: Bc-Ash BJH Adsorption dA/dlog(D) Pore Area

Table C 2.4: Bc-Ash BJH Desorption Pore Distribution Report

Pore Diameter Range (Å)	Average Diameter (Å)	Incremental Pore volume (cm^3/g)	Cumulative Pore Volume (cm^3/g)	Incremental Pore Area($m^{2/}g$)	Cumulative pore area ($m^{2/}g$)
2975.2 - 817.5	961.6	0.001356	0.001356	0.056	0.056
817.5 - 465.2	548.5	0.000970	0.002326	0.071	0.127
465.2 - 322.7	367.8	0.000599	0.002925	0.065	0.192
322.7 - 226.3	257.1	0.000518	0.003443	0.081	0.273
226.3 - 184.0	200.5	0.000245	0.003688	0.049	0.322
184.0 - 146.8	160.9	0.000219	0.003907	0.054	0.376
146.8 - 132.0	138.5	0.000089	0.003995	0.026	0.402
132.0 - 106.4	116.2	0.000124	0.004119	0.043	0.444
106.4 - 82.4	91.0	0.000158	0.004277	0.069	0.514
82.4 - 61.0	68.1	0.000225	0.004502	0.132	0.646
61.0 - 46.7	51.7	0.000363	0.004865	0.281	0.927
46.7 - 37.2	40.7	0.000696	0.005561	0.684	1.611

37.2 - 30.3	32.9	0.001209	0.006770	1.472	3.083
30.3 - 24.2	26.4	0.002456	0.009226	3.728	6.811

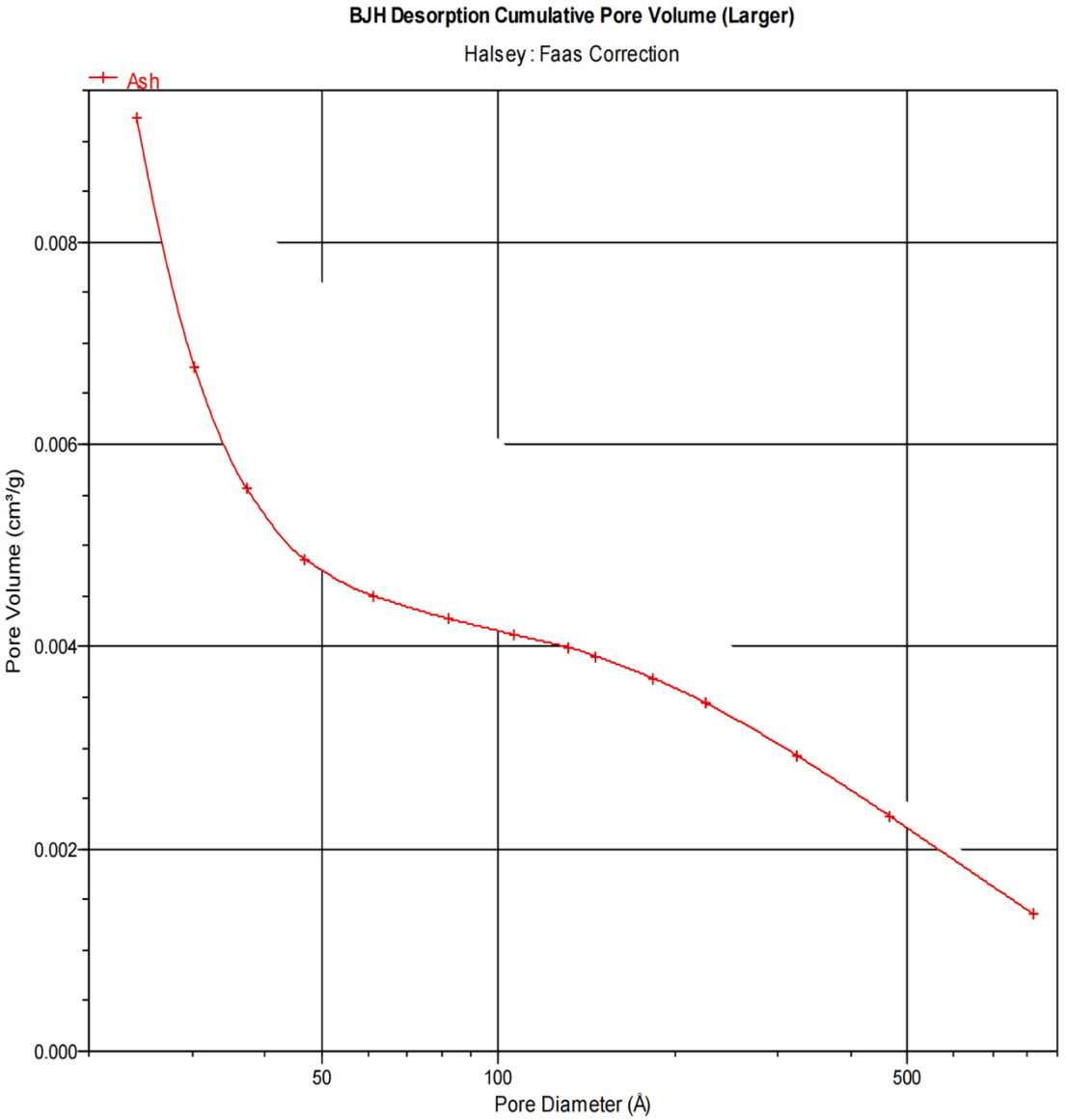


Figure C-2.12: Bc-Ash BJH Desorption Cumulative Pore Volume (Larger)

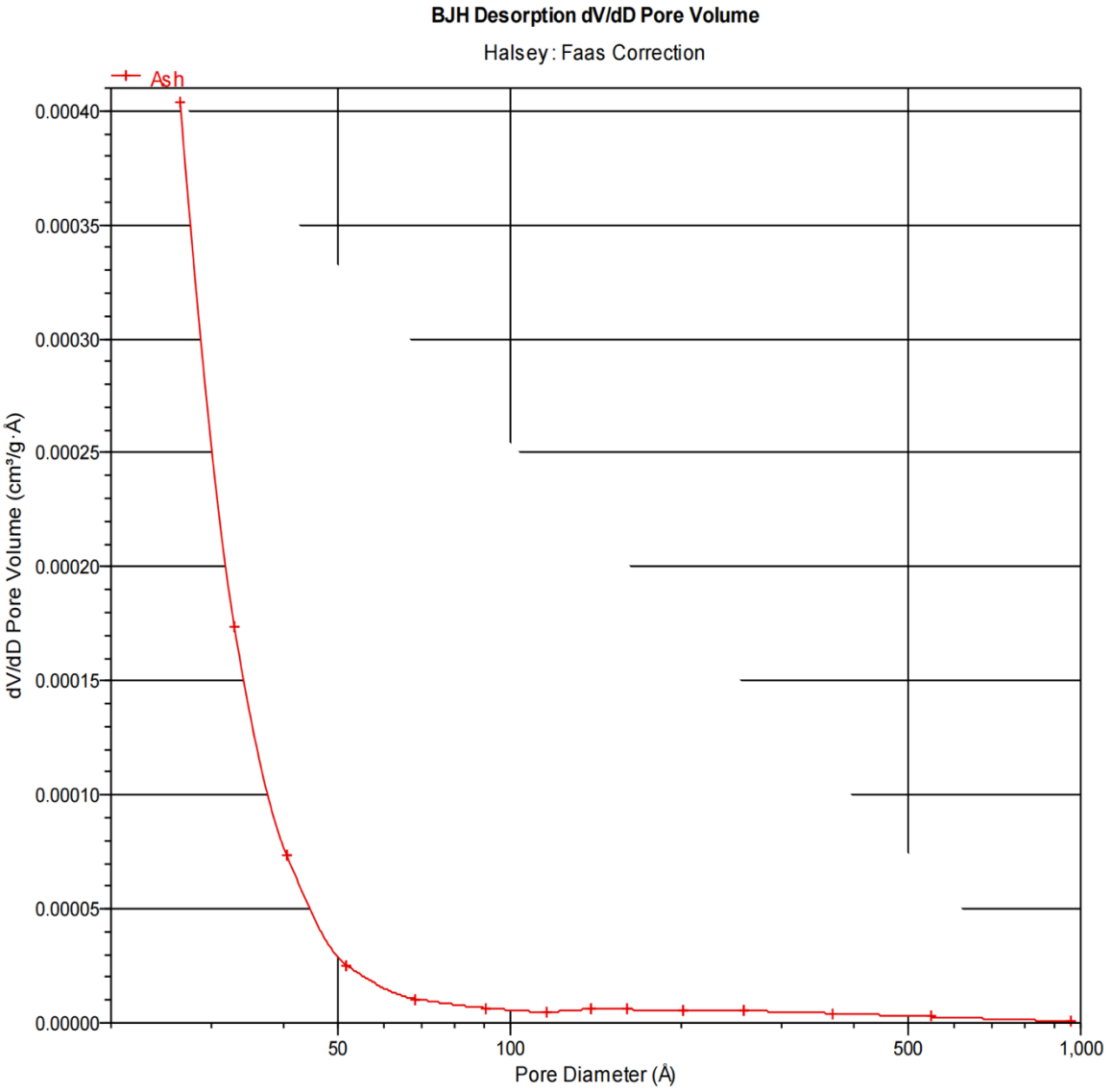


Figure C-2.13: Bc-Ash BJH Desorption dA/dD Pore volume

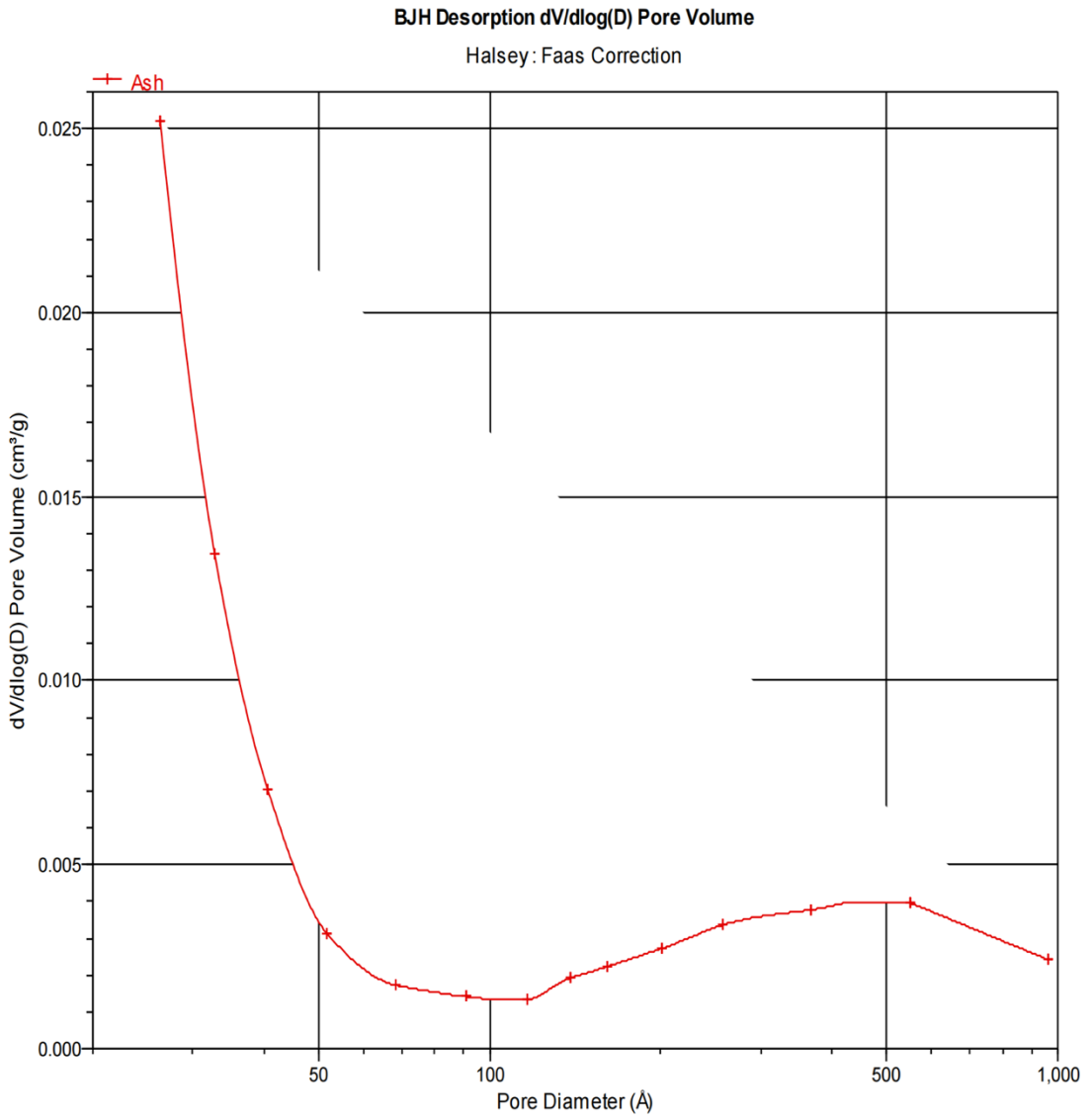


Figure C-2.14: Bc-Ash BJH Desorption dv/dlog(D) Pore

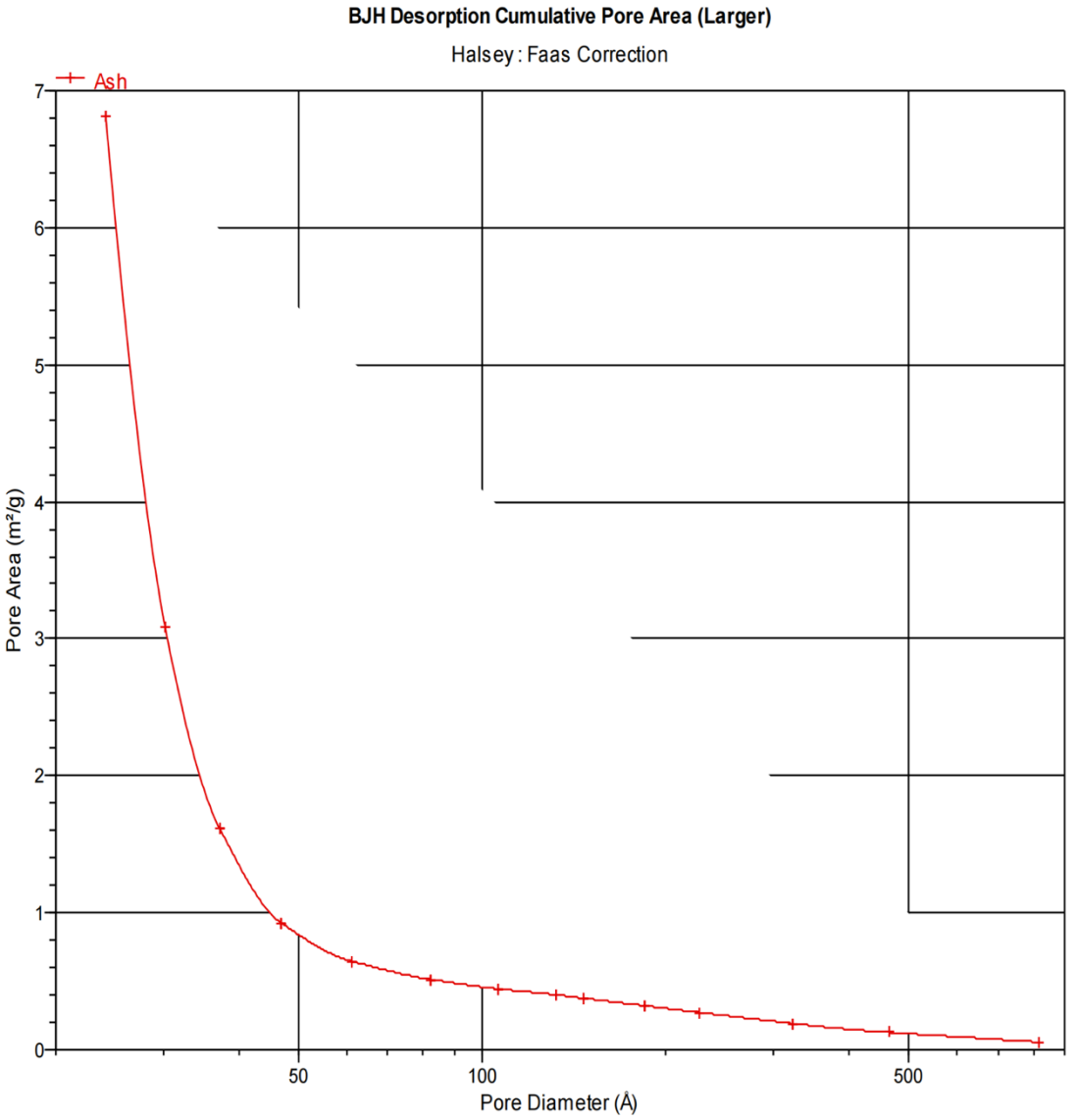


Figure C-2.15: Bc-Ash BJH Desorption cumulative pore area

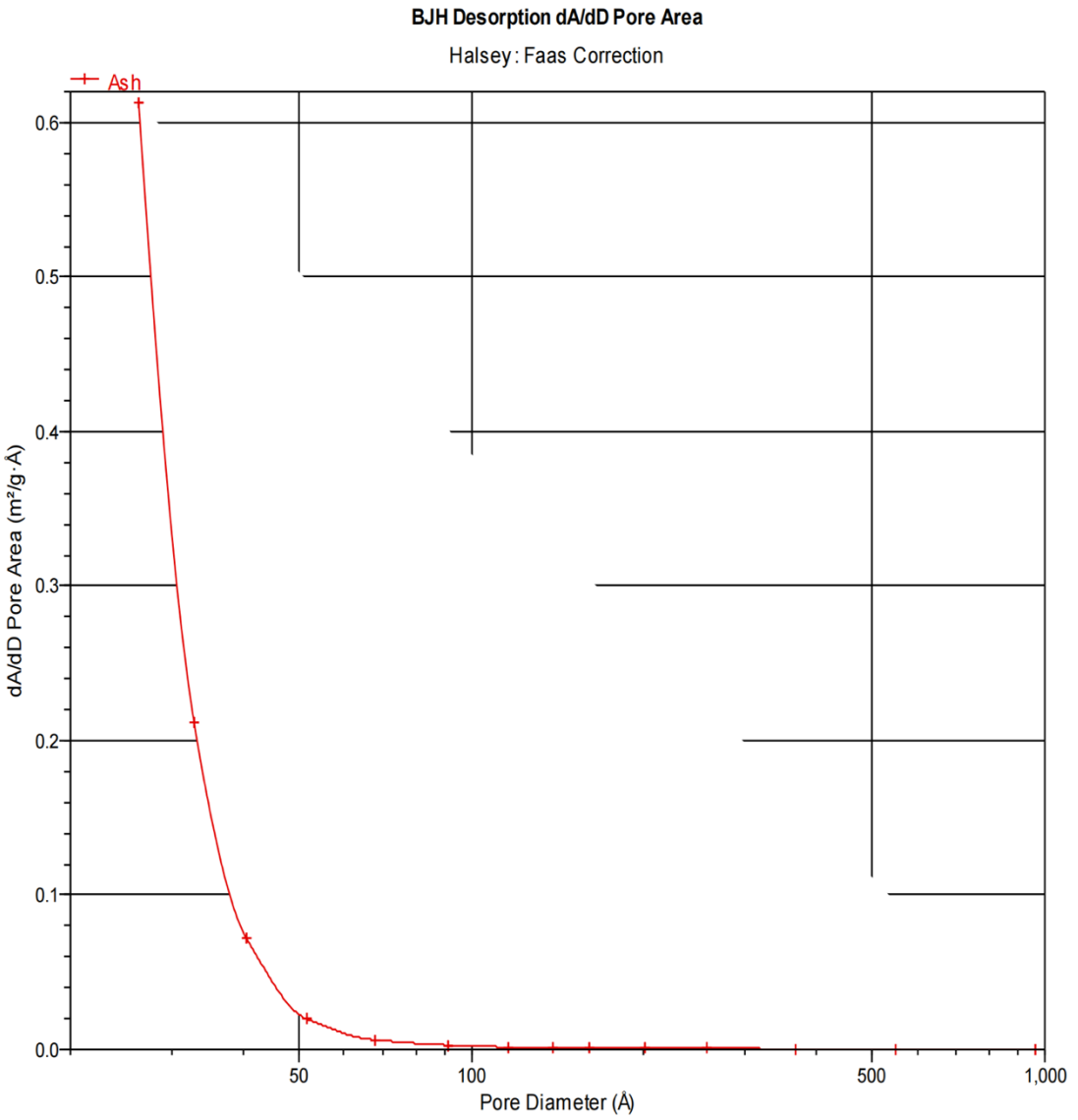


Figure C-2.16: Bc-Ash BJH Desorption dA/dlog(D) Pore Area

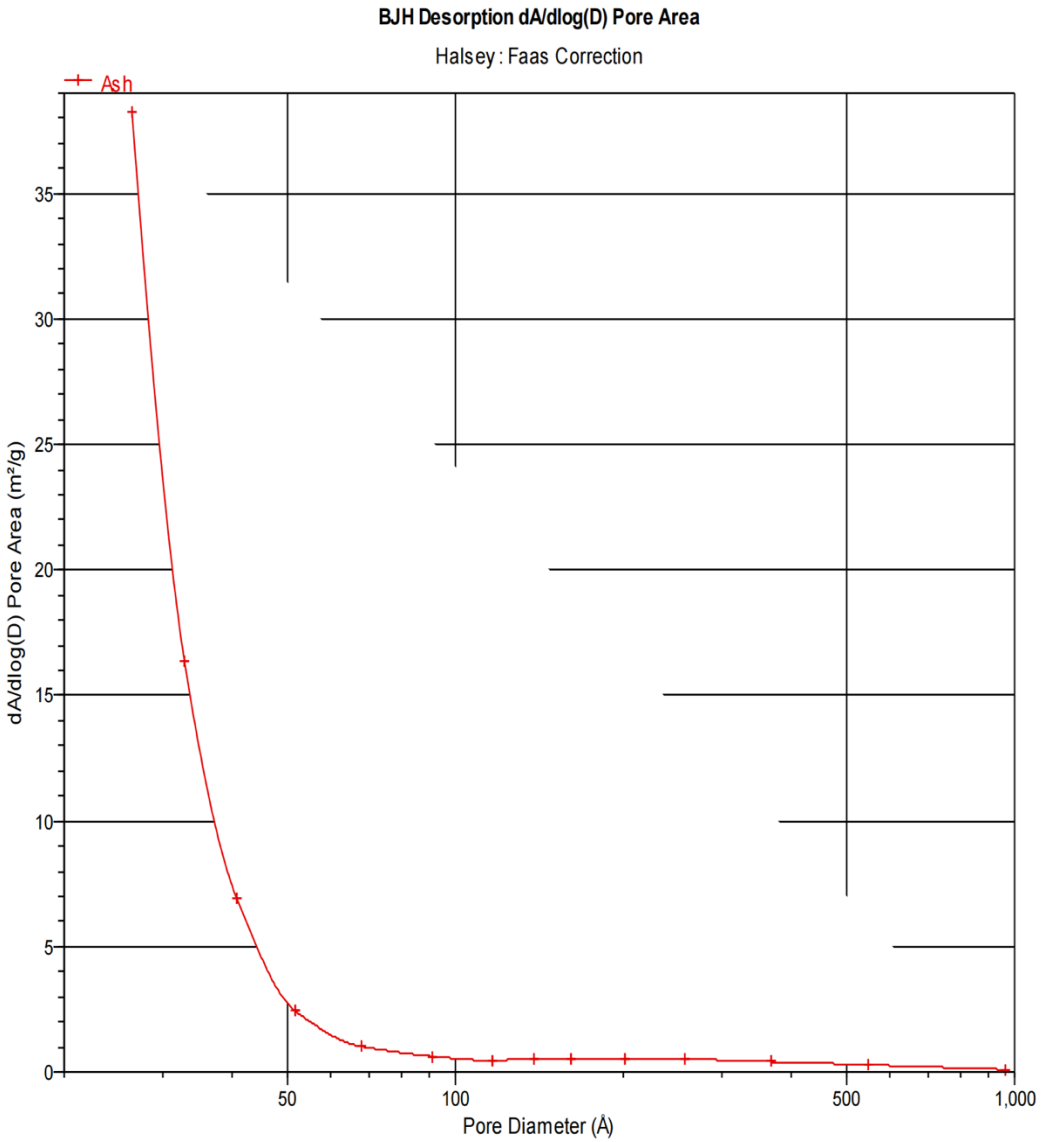


Figure C-2.17: Bc-Ash BJH Desorption dA/dlog(D) Pore Area

BEECH SUMMARY REPORT

Single point surface area at p/p° = 0.300000000: 290.3387 m²/g

BET Surface Area: 314.2137 m²/g

Langmuir Surface Area:464.6134 m²/g

BJH Adsorption cumulative surface area of pores

between 17.000 Å and 3,000.000 Å diameter: 34.095

m²/g

BJH Desorption cumulative surface area of pores

between 17.000 Å and 3,000.000 Å diameter: 9.9570

m²/g

Pore Volume

Single point adsorption total pore

volume of pores less than 2,896.722

Å diameter at p/p° = 0.993294104:

0.16539 cm³/g

BJH Adsorption cumulative volume of pores between 17.000 Å and 3,000.000 Å

diameter: 0.029211 cm³/g

BJH Desorption cumulative volume of pores between 17.000 Å and 3,000.000 Å

diameter: 0.012516 cm³/g

Pore Size

Adsorption average pore diameter (4V/A

byBET): 21.0548 Å BJH Adsorption

average pore diameter (4V/A): 34.269 Å

BJH Desorption average pore diameter

(4V/A): 50.281 Å

Table C-3.0: Bc- BeecH Isotherm Tabular Report

Relative Pressure (P/P^o)	**Absolute pressure (mmHg)**	**Quantity Adsorbed (cm^3/g STP)**	**Elapsed Time (h: min)**	**Saturation pressure (mmHg)**
			00:40	759.455200
0.009657658	7.296658	83.9654	11:50	755.530762
0.063012009	47.542500	93.4471	14:50	754.499023
0.080086876	60.403645	94.7049	15:26	754.226501
0.127823610	96.396439	96.5110	15:54	754.136414
0.168974576	127.422043	97.5554	16:09	754.090027
0.210858280	158.998520	98.3921	16:20	754.053955
0.235582746	177.618607	98.8288	16:27	753.954224
0.246748130	186.028000	99.0463	16:32	753.918579
0.332640150	250.773621	99.9536	16:40	753.888611
0.356642010	268.857422	100.2256	16:44	753.857971
0.447164139	337.088562	100.8725	16:49	753.836304
0.467456804	352.388306	101.0626	16:52	753.841431
0.549975361	414.579041	101.5085	16:55	753.813843
0.574582987	433.114441	101.6864	16:58	753.789185
0.648911940	489.127197	102.0142	17:00	753.765137

0.683284736	515.040466	102.2125	17:02	753.771362
0.738149342	556.370605	102.4740	17:05	753.737183
0.773611990	583.074341	102.6738	17:06	753.703857
0.798620787	601.935608	102.8382	17:08	753.718933
0.838136545	631.676514	103.0786	17:09	753.667786
0.872443936	657.527405	103.3408	17:11	753.661499
0.884733955	666.775879	103.4918	17:12	753.645630
0.904544451	681.690735	103.7144	17:14	753.628784
0.923362560	695.863586	103.9674	17:15	753.619019
0.938772581	707.474121	104.2408	17:16	753.616089
0.951901508	717.350281	104.5580	17:18	753.597168
0.963185408	725.845154	104.9030	17:19	753.588196
0.970388160	731.258789	105.1959	17:20	753.573486
0.976536817	735.843201	105.5087	17:22	753.523254
0.981549442	739.621887	105.8202	17:23	753.524841
0.983829397	741.290710	106.0084	17:25	753.474854
0.986040609	742.919128	106.1977	17:26	753.436646
0.987811971	744.180725	106.3738	17:27	753.362732
0.988793811	744.952454	106.5199	17:28	753.395142
0.993294104	748.306152	106.9255	17:30	753.358093
0.976005158	735.286865	106.1099	17:32	753.363708
0.957217638	721.133789	105.5283	17:33	753.364502
0.937122748	705.943420	105.1868	17:35	753.309448

0.909557040	685.188293	104.8462	17:36	753.320862
0.887989752	668.937195	104.6538	17:37	753.316345
0.876014738	659.923706	104.5741	17:39	753.324890
0.842080330	634.367371	104.4138	17:40	753.333557
0.802527876	604.555603	104.2663	17:41	753.314148
0.743030343	559.755859	104.0939	17:43	753.341858
0.654710274	493.199036	103.8532	17:45	753.308838
0.554690932	417.845490	103.5579	17:47	753.294250
0.454584233	342.427948	103.1695	17:50	753.277222
0.354326384	266.903442	102.6269	17:54	753.270020
0.242683287	182.782730	101.7281	18:02	753.173950

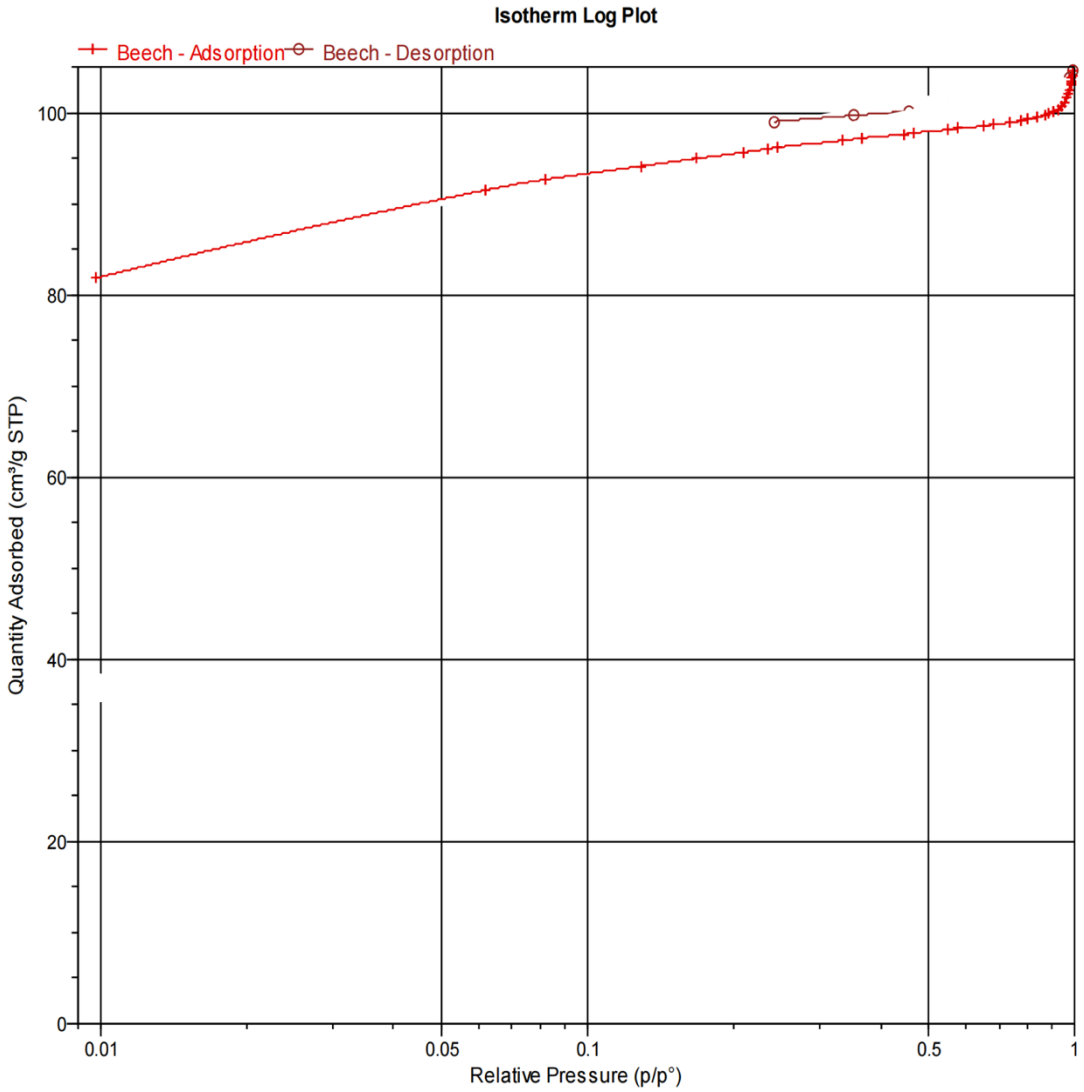


Figure C-3.0: Bc-Beech-isothermal Log plot

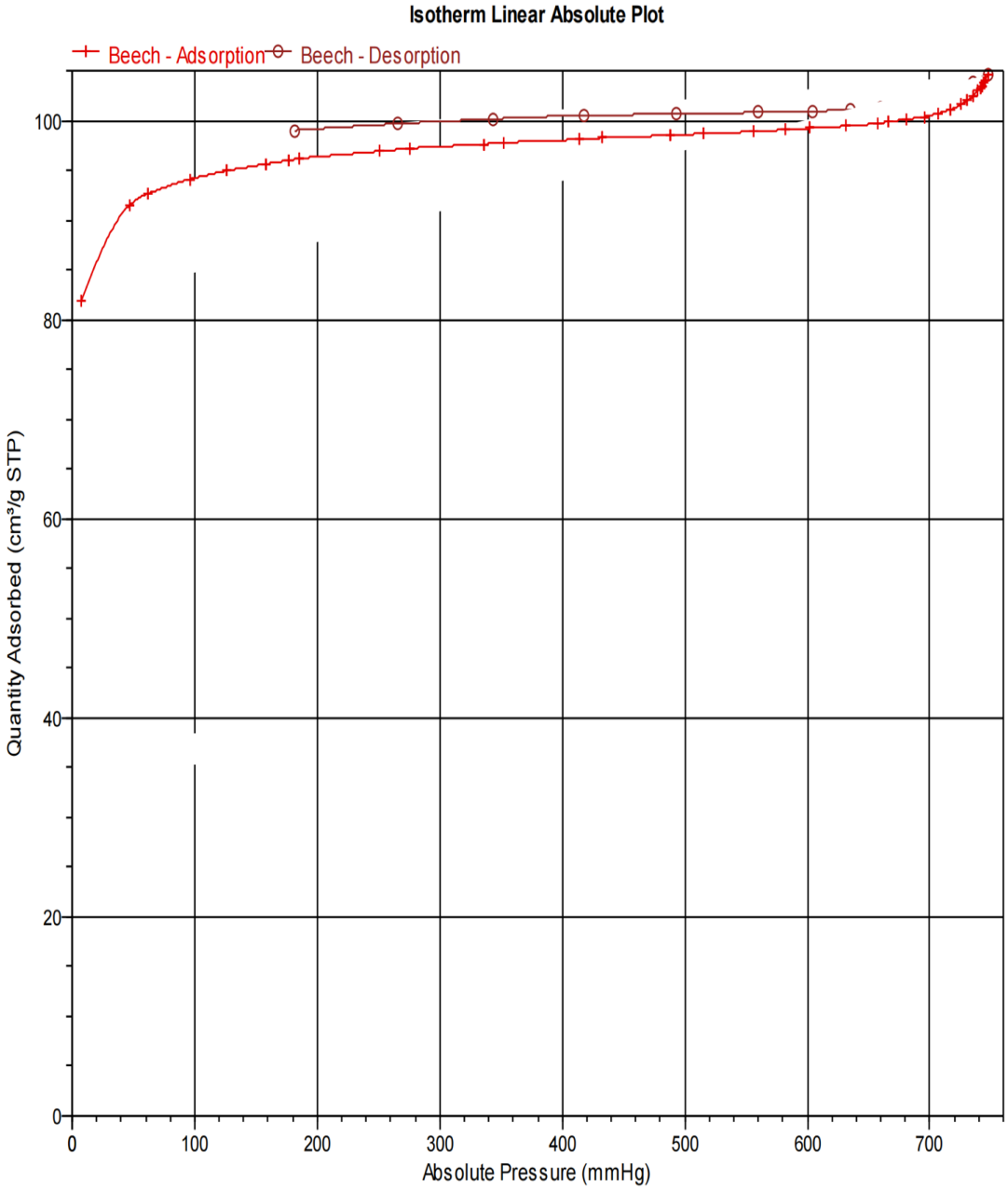


Figure C-3.1: Bc-Beech isothermal Log Absolute plot

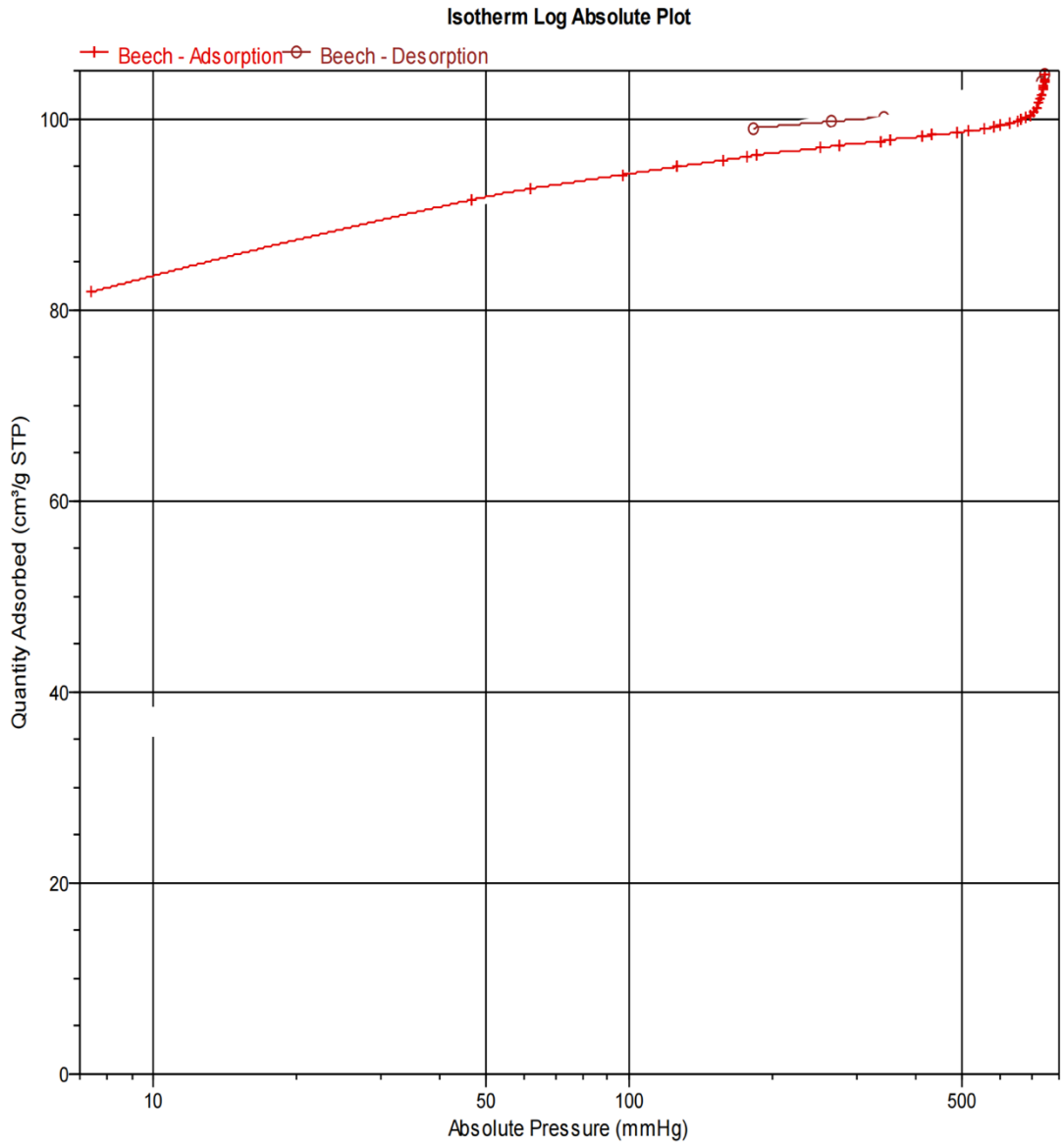


Figure C-3.2: Bc-Beech isothermal Log Absolute plot

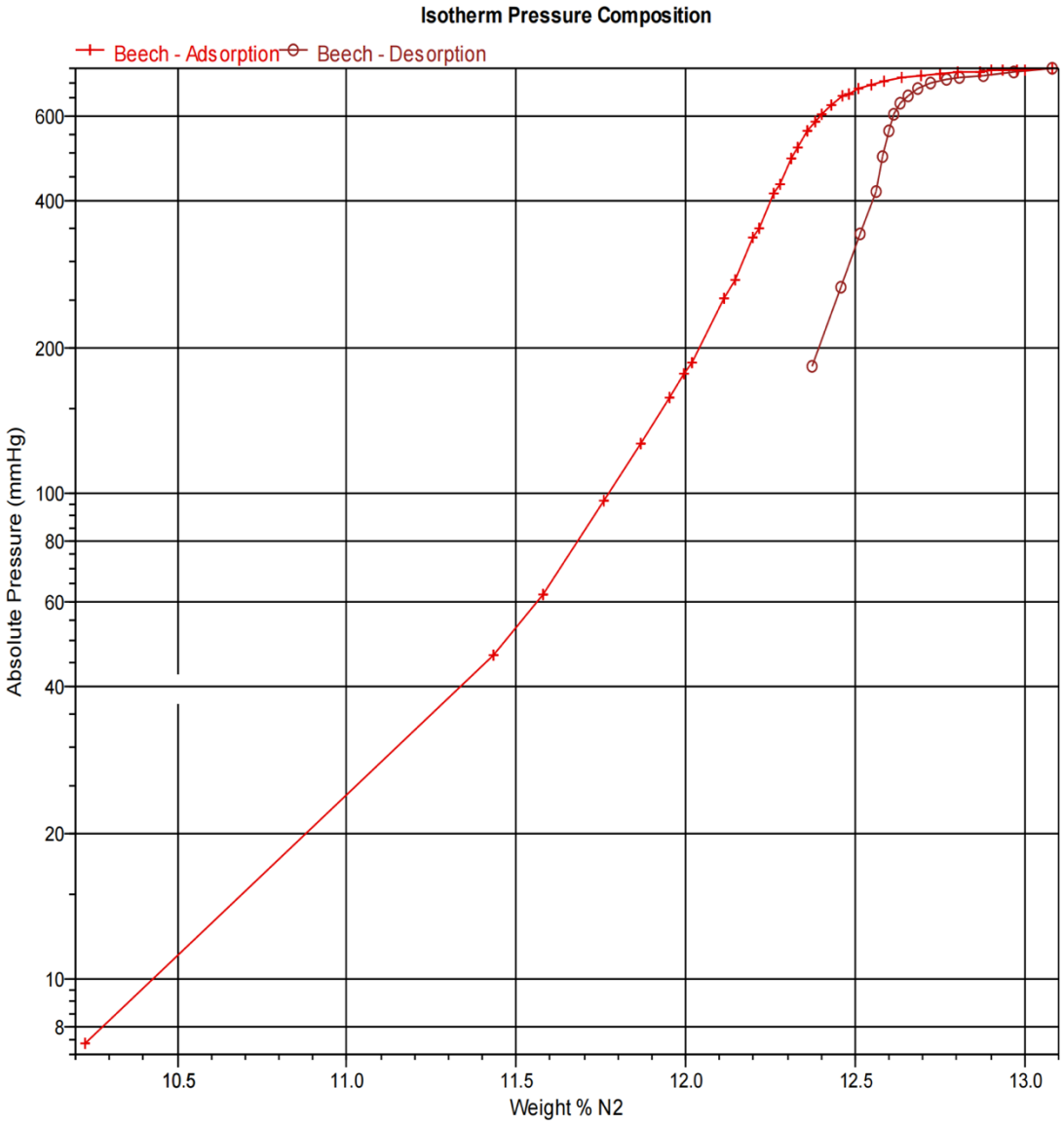


Figure C- 3.3: Bc-Beech isothermal pressure Composition plot

BET Report

BET Surface Area: 314.2137 ± 7.3119 m^2/g

Slope: 0.014076 ± 0.000317 g/cm^3 STP

Y-Intercept: -0.000224 ± 0.000056 g/cm^3 STP

C: -61.909683

Qm: 72.1903 cm^3/g STP

Correlation Coefficient: 0.9987306

Molecular Cross-Sectional Area: 0.1620 nm^2

Table C3.1: Bc-Beech Tabular data Report Report

Relative pressure (p/p^o)	**Quantity adsorbed (cm3/g) STP**	**1/[Q(p°/p - 1)]**
0.063012009	93.4471	0.000720
0.080086876	94.7049	0.000919
0.127823610	96.5110	0.001519
0.168974576	97.5554	0.002084
0.210858280	98.3921	0.002716
0.235582746	98.8288	0.003118
0.246748130	99.0463	0.003307

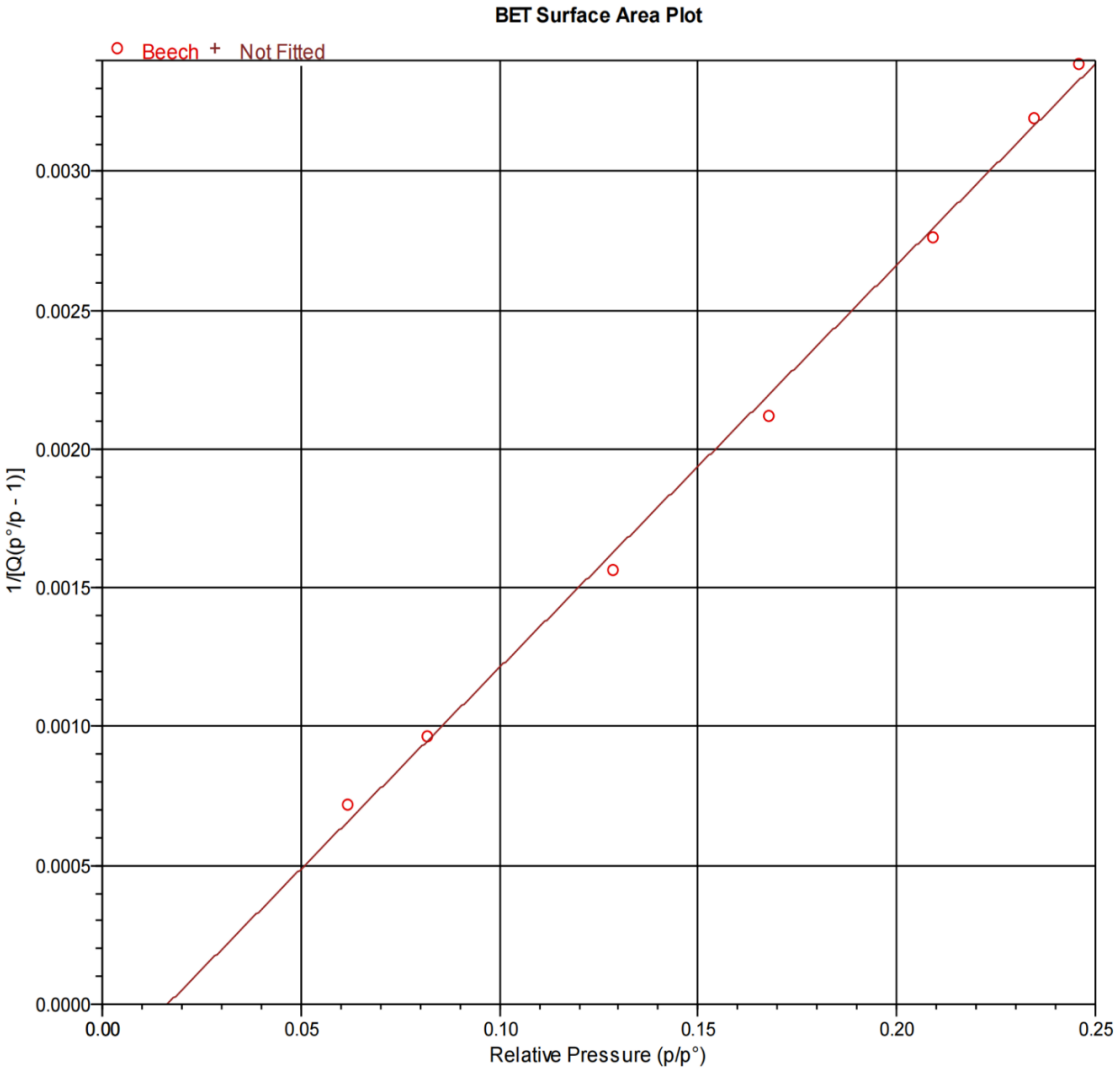


Figure C-3.4: Bc-Beech BET Surface Area plot

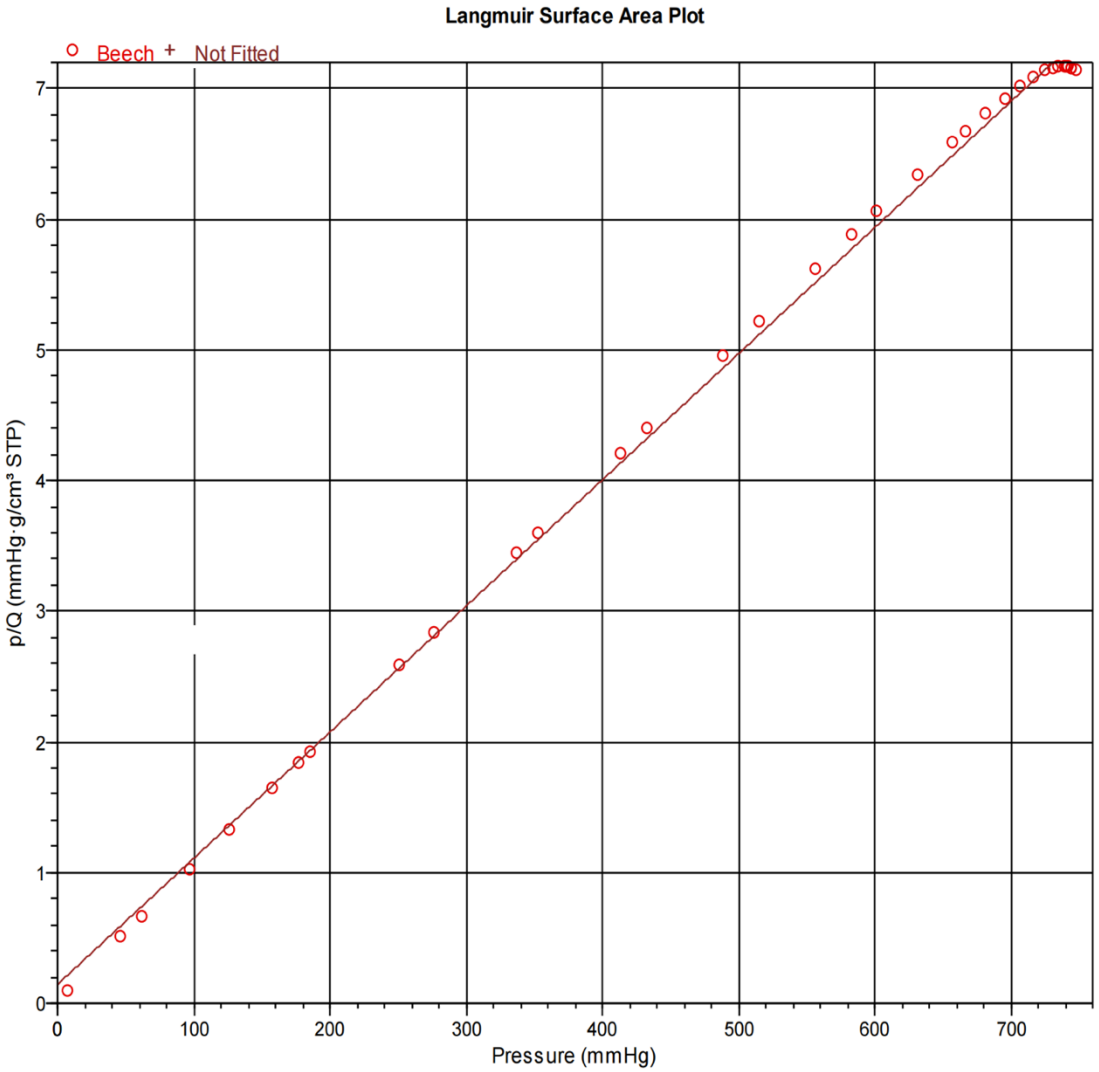


Figure C-3.5: Bc-Beech Langmuir Surface Area plot

Langmuir Report

Langmuir Surface Area: 464.6134 ± 2.3726 m^2/g

Slope: 0.009368 ± 0.000048 g/cm^3 STP

Y-Intercept: 0.133 ± 0.026 $mmHg \cdot g/cm^3$ STP b: 0.070222

1/mmHg

Qm: 106.7444 cm^3/g STP

Correlation Coefficient: 0.999570

Molecular Cross-Sectional Area: 0.1620 nm^2

Table C-3.2: Bc-Beech Langmuir Tabular data Report

Pressure (mmHg)	**Quantity Adsorbed (cm^3/g STP**	**p/Q (mmhg g/cm3 STP**
7.296658	83.9654	0.087
47.542500	93.4471	0.509
60.403645	94.7049	0.638
96.396439	96.5110	0.999
127.422043	97.5554	1.306
158.998520	98.3921	1.616
177.618607	98.8288	1.797
186.028000	99.0463	1.878
250.773621	99.9536	2.509
268.857422	100.2256	2.683

337.088562	100.8725	3.342
352.388306	101.0626	3.487
414.579041	101.5085	4.084
433.114441	101.6864	4.259
489.127197	102.0142	4.795
515.040466	102.2125	5.039
556.370605	102.4740	5.429
583.074341	102.6738	5.679
601.935608	102.8382	5.853
631.676514	103.0786	6.128
657.527405	103.3408	6.363
666.775879	103.4918	6.443
681.690735	103.7144	6.573
695.863586	103.9674	6.693
707.474121	104.2408	6.787
717.350281	104.5580	6.861
725.845154	104.9030	6.919
731.258789	105.1959	6.951
735.843201	105.5087	6.974
739.621887	105.8202	6.989
741.290710	106.0084	6.993
742.919128	106.1977	6.996
744.180725	106.3738	6.996

744.952454	106.5199	6.994
748.306152	106.9255	6.998

Table C-3.3: Bc-BeecH BJH Adsorption pore Distribution Report

Pore Diameter Range (Å)	**Average Diameter (Å)**	**Incremental Pore volume (cm^3/g)**	**Cumulative Pore Volume (cm^3/g)**	**Incremental Pore Area(m^2/g)**	**Cumulative pore area (m^2/g)**
2696.1 - 1773.7	2049.6	0.001034	0.001034	0.020	0.020
1773.7 - 1597.7	1676.4	0.000341	0.001375	0.008	0.028
1597.7 - 1382.5	1474.3	0.000531	0.001906	0.014	0.043
1382.5 - 1225.4	1294.3	0.000421	0.002328	0.013	0.056
1225.4 - 1058.2	1129.3	0.000487	0.002815	0.017	0.073
1058.2 - 835.5	920.3	0.000833	0.003648	0.036	0.109

835.5 - 675.3	738.0	0.000757	0.004405	0.041	0.150
675.3 - 538.0	590.7	0.000747	0.005152	0.051	0.201
538.0 - 419.4	463.6	0.000798	0.005950	0.069	0.270
419.4 - 332.0	365.2	0.000664	0.006614	0.073	0.342
332.0 - 266.4	291.7	0.000584	0.007198	0.080	0.422
266.4 - 215.9	235.5	0.000517	0.007715	0.088	0.510
215.9 - 180.0	194.4	0.000415	0.008130	0.085	0.596
180.0 - 163.1	170.7	0.000287	0.008417	0.067	0.663
163.1 - 129.3	142.0	0.000492	0.008909	0.139	0.802
129.3 - 104.8	114.2	0.000433	0.009342	0.152	0.953
104.8 - 93.2	98.2	0.000289	0.009630	0.118	1.071
93.2 - 80.7	86.0	0.000385	0.010015	0.179	1.250
80.7 - 66.8	72.2	0.000422	0.010438	0.234	1.484
66.8 - 60.0	62.9	0.000367	0.010804	0.233	1.717
60.0 - 49.2	53.3	0.000598	0.011402	0.449	2.165
49.2 - 46.1	47.5	0.000386	0.011788	0.325	2.491
46.1 - 38.3	41.3	0.000881	0.012669	0.852	3.343
38.3 - 36.7	37.5	0.000475	0.013144	0.507	3.850
36.7 - 31.1	33.3	0.001279	0.014423	1.537	5.387
31.1 - 29.1	30.0	0.000983	0.015406	1.311	6.698
29.1 - 24.4	26.2	0.002589	0.017995	3.954	10.652
24.4 - 23.8	24.1	0.000840	0.018835	1.394	12.046
23.8 - 22.6	23.2	0.001494	0.020328	2.578	14.624

22.6 - 20.6	21.5	0.002903	0.023232	5.401	20.025
20.6 - 18.8	19.6	0.003807	0.027038	7.766	27.791

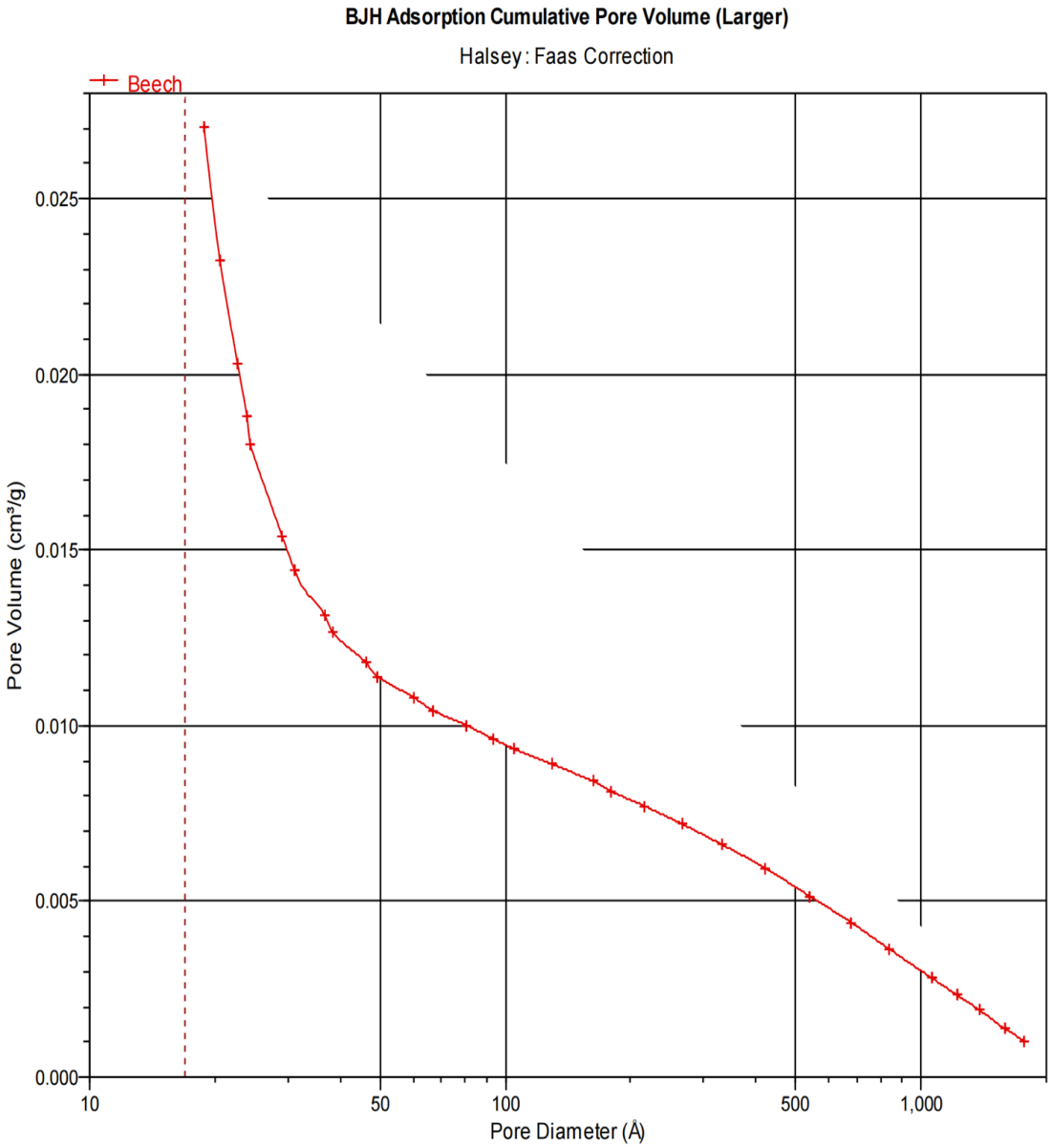
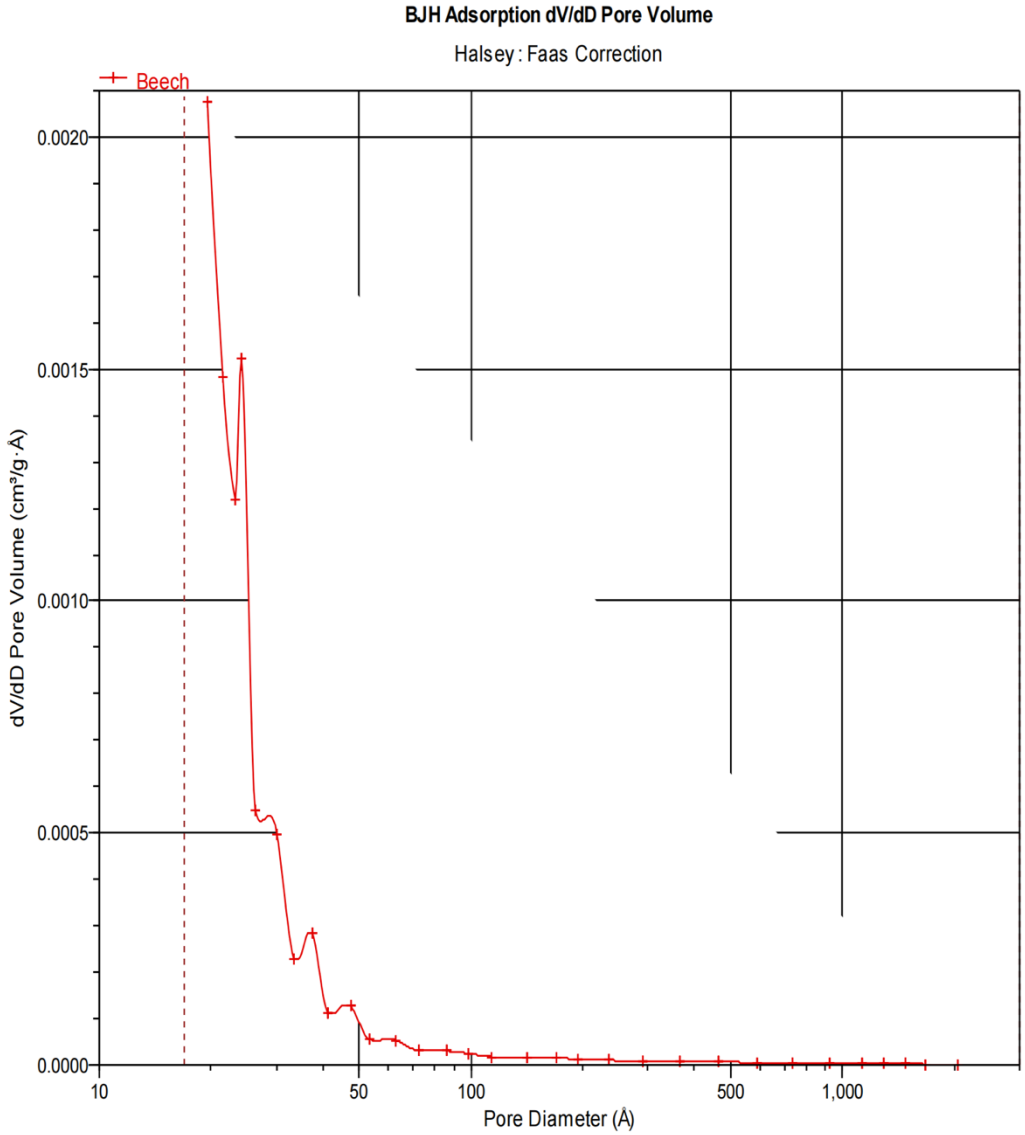


Figure C-3.6: Bc-Beech BJH adsorption cumulative pore volume (large)



FigureC-3.7: Bc-Beech BJH adsorption dV/d(D) pore volume

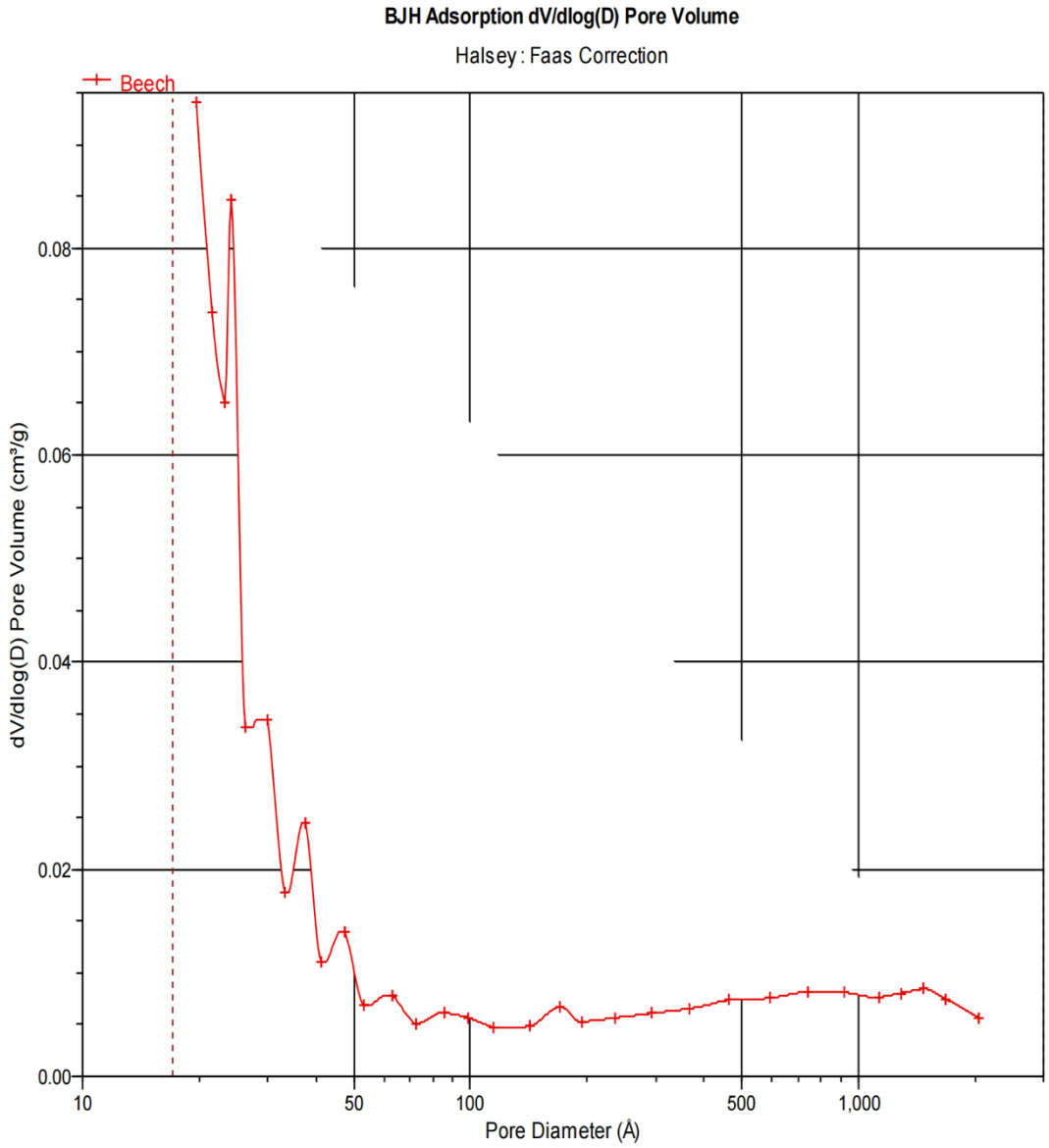


Figure C-3.8: Bc-Beech BJH adsorption dV/dlog(D) pore volume

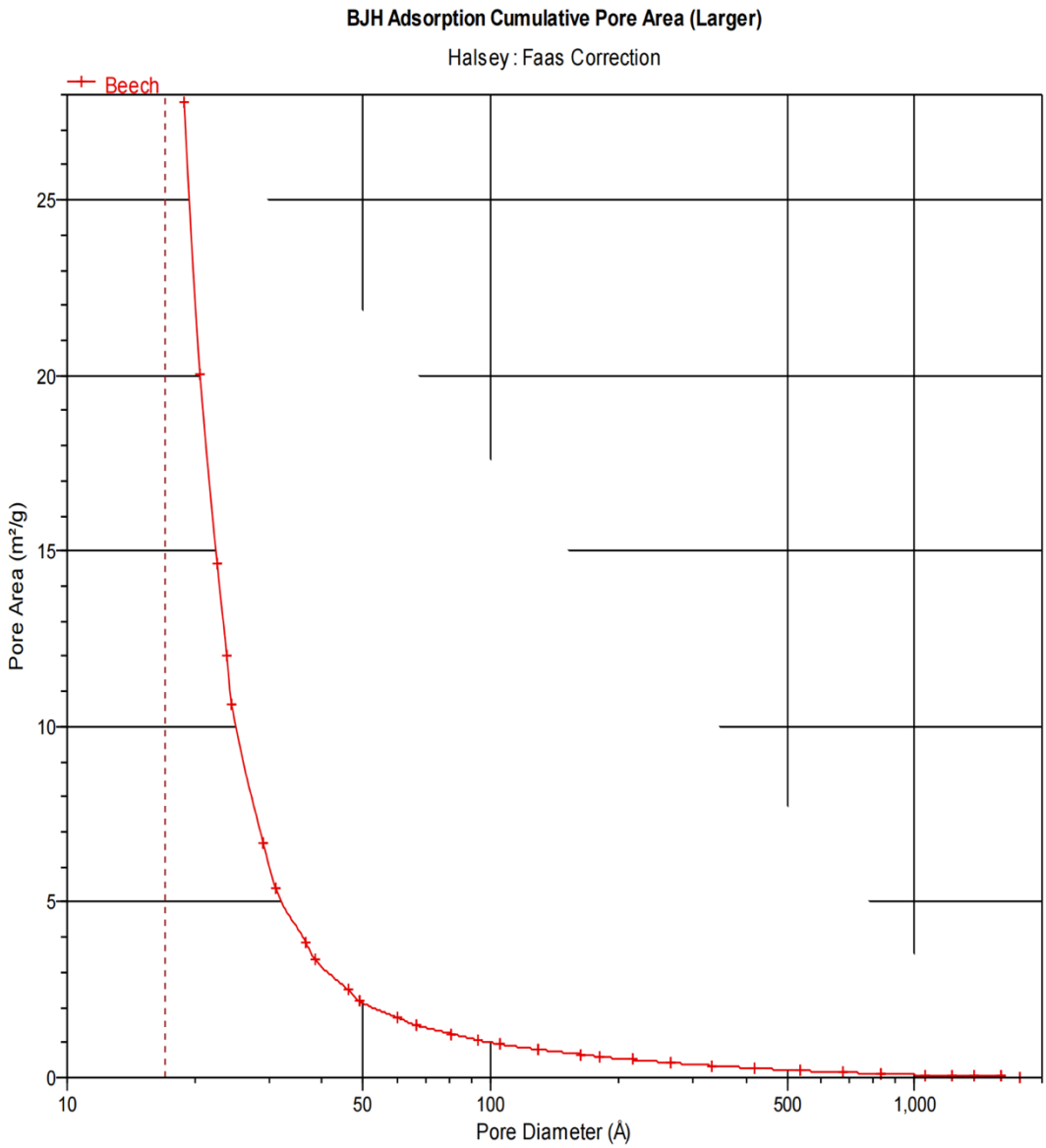


Figure 3.9: Bc-Beech BJH adsorption dV/dlog(D) pore volume

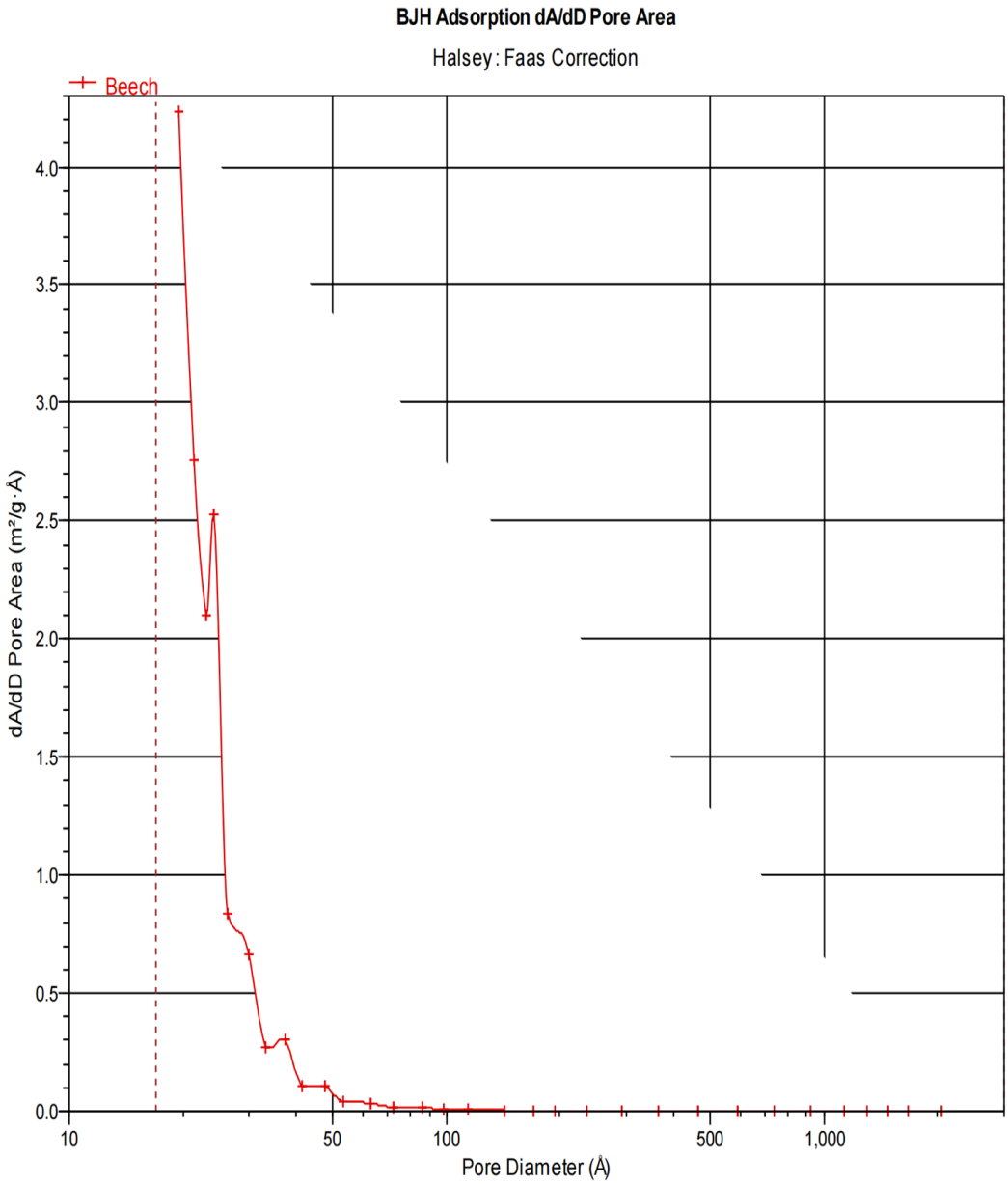


Figure C-3.10: Bc-Beech Adsorption dA/dD pore Area

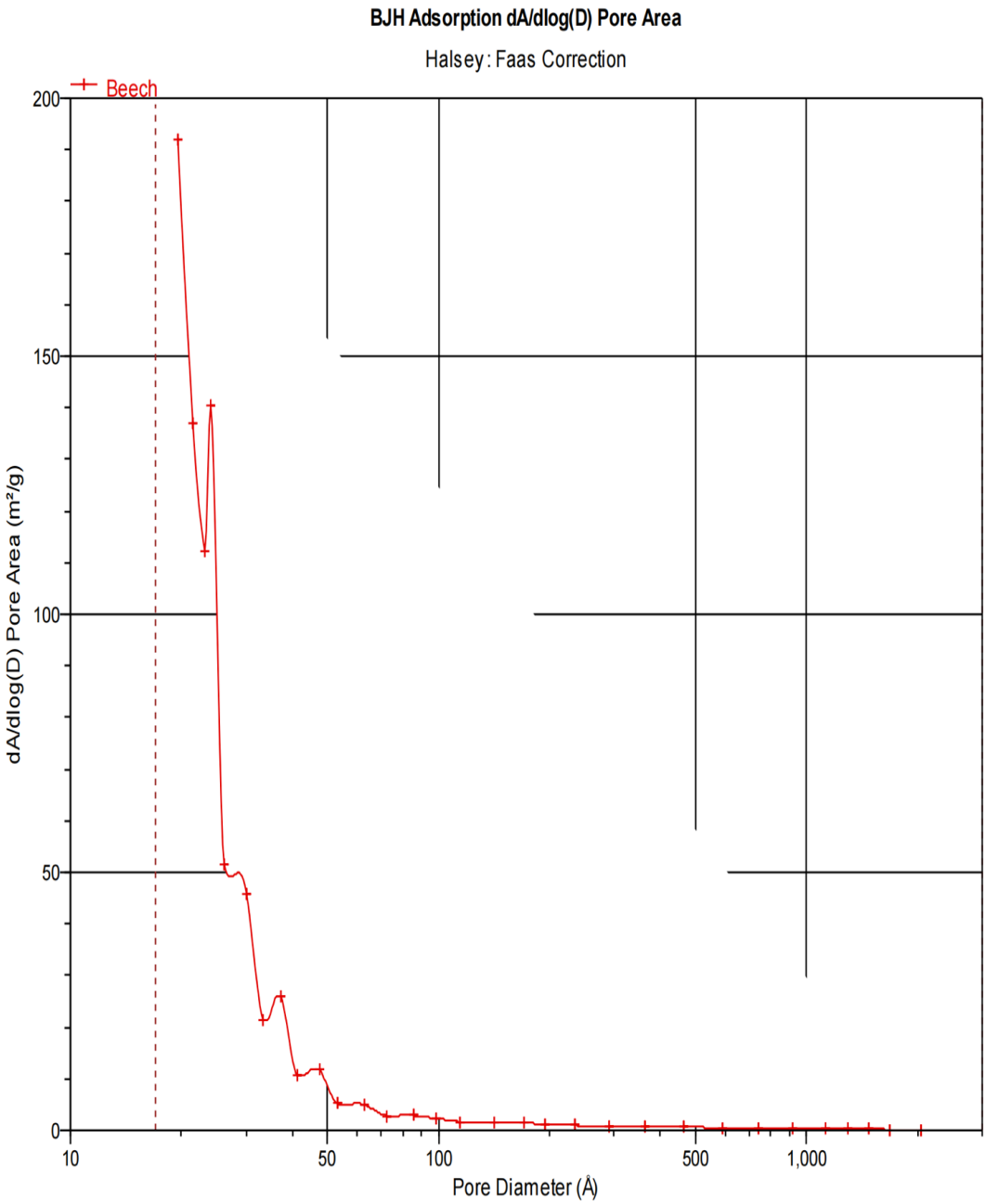


Figure C-3.11: Bc-Beech Adsorption dA/dlog(D) pore Area

BJH Desorption Pore Distribution Report

Faas Correction Halsey

t = 3.54 [-5 / ln(p/p°)] ^ 0.333

Diameter Range: 17.000 Å to 3,000.000 Å

Adsorbate Property Factor: 9.53000 Å

Density Conversion Factor: 0.0015468

Fraction of Pores Open at Both Ends: 0.00

Table C-3.4: Bc-Beech BJH Desorption pore Distribution Report

Pore Diameter Range (Å)	**Average Diameter (Å)**	**Incremental Pore volume (cm^3/g)**	**Cumulative Pore Volume (cm^3/g)**	**Incremental Pore Area(m^2/g)**	**Cumulative pore area (m^2/g)**
2696.1 - 867.5	1031.8	0.001506	0.001506	0.058	0.058
867.5 - 563.4	651.7	0.001222	0.002728	0.075	0.133
563.4 - 408.2	460.6	0.001045	0.003774	0.091	0.224
408.2 - 346.4	372.0	0.000521	0.004294	0.056	0.280

346.4 - 277.9	304.3	0.000622	0.004916	0.082	0.362
277.9 - 220.6	242.3	0.000546	0.005462	0.090	0.452
220.6 - 169.2	187.7	0.000450	0.005912	0.096	0.548
169.2 - 133.4	146.7	0.000323	0.006235	0.088	0.636
133.4 - 106.8	116.8	0.000231	0.006466	0.079	0.715
106.8 - 82.4	91.1	0.000206	0.006672	0.090	0.806
82.4 - 61.1	68.2	0.000257	0.006930	0.151	0.957
61.1 - 46.8	51.7	0.000344	0.007274	0.266	1.223
46.8 - 37.3	40.8	0.001032	0.008306	1.013	2.236
37.3 - 30.3	32.9	0.001508	0.009814	1.835	4.071
30.3 - 24.2	26.3	0.002512	0.012327	3.816	7.887

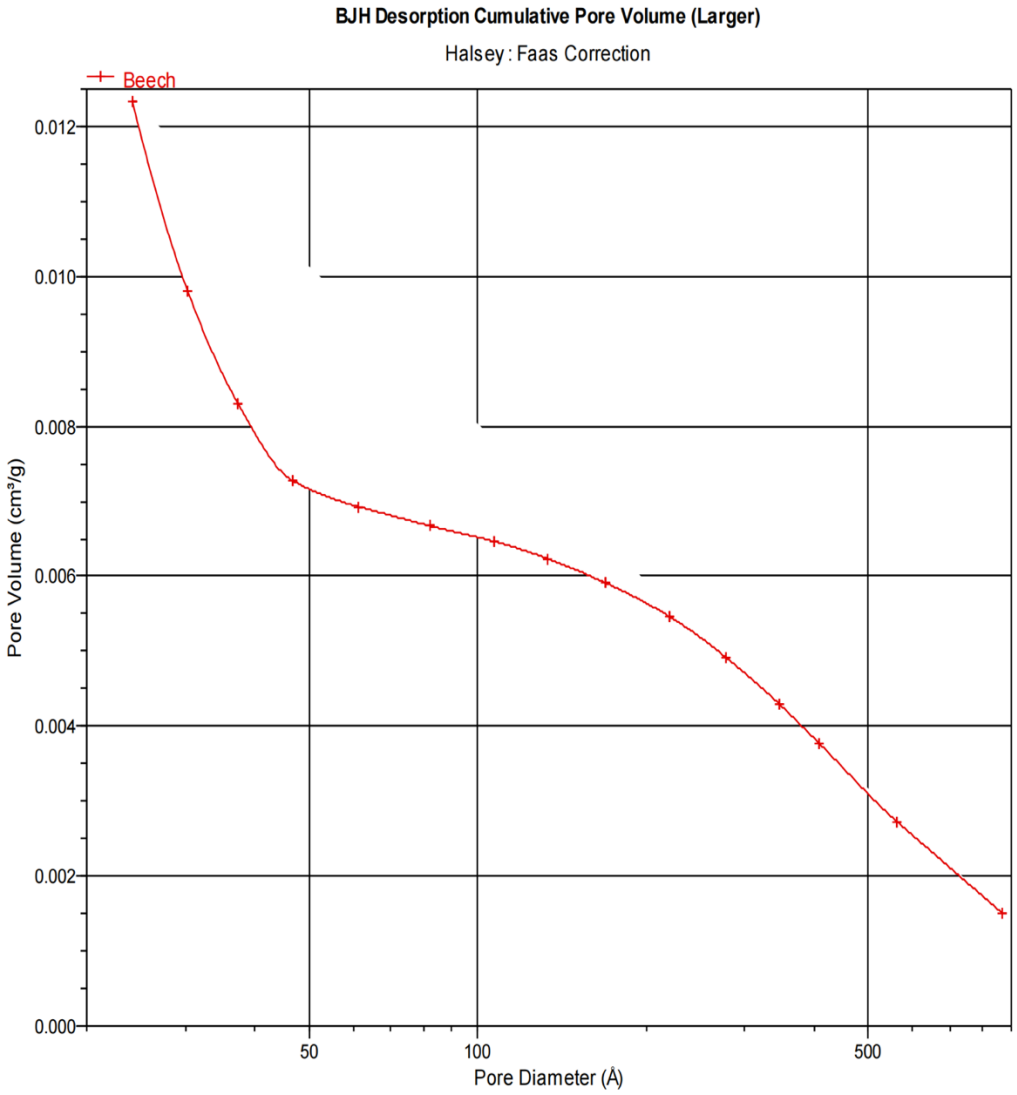


Figure C-3.12: Bc-Beech desorption cumulative pore volume (larger)

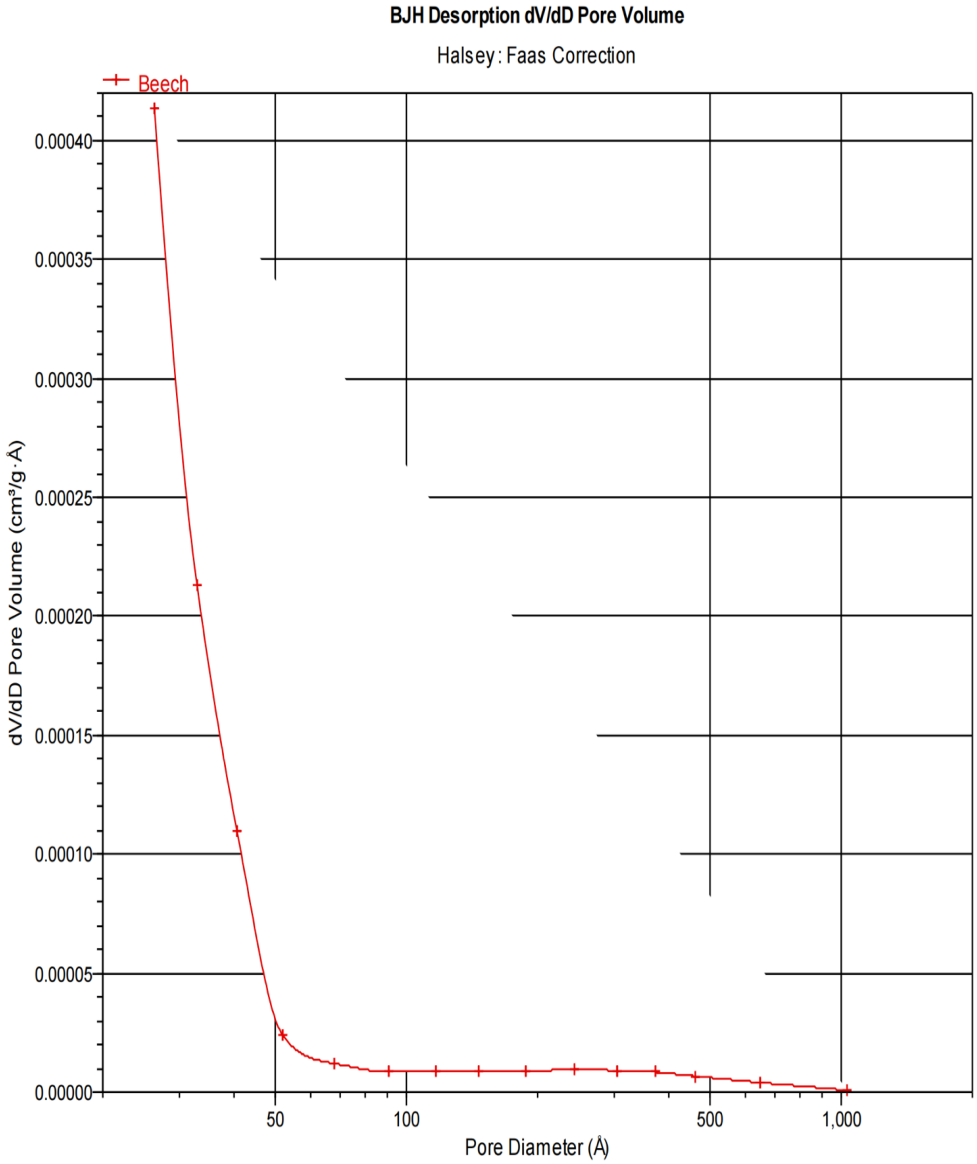


Figure C-3.13: Bc-Beech desorption dV/dD pore volume

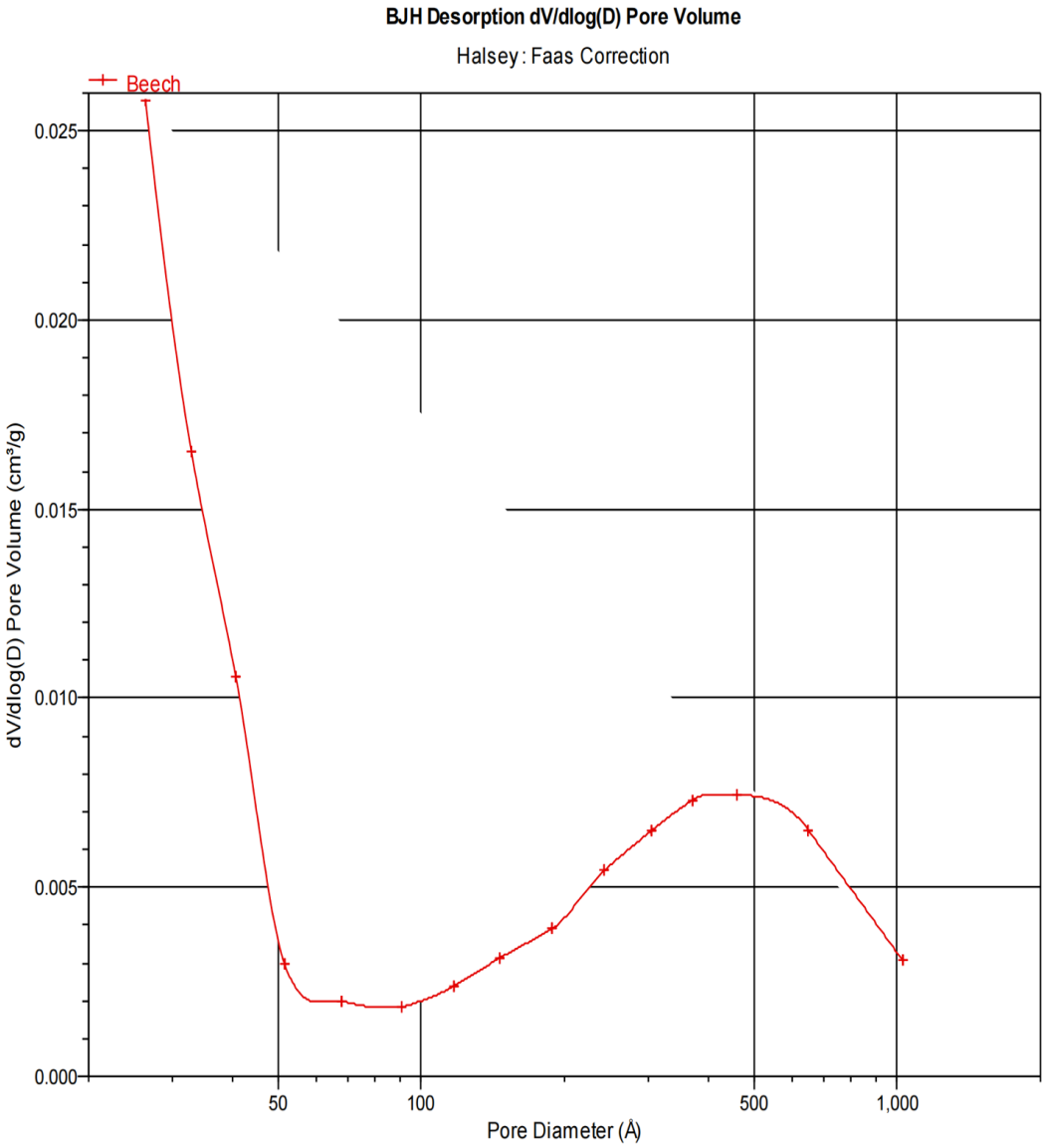


Figure C-3.14: Bc-Beech desorption dV/dlog(D)pore volume

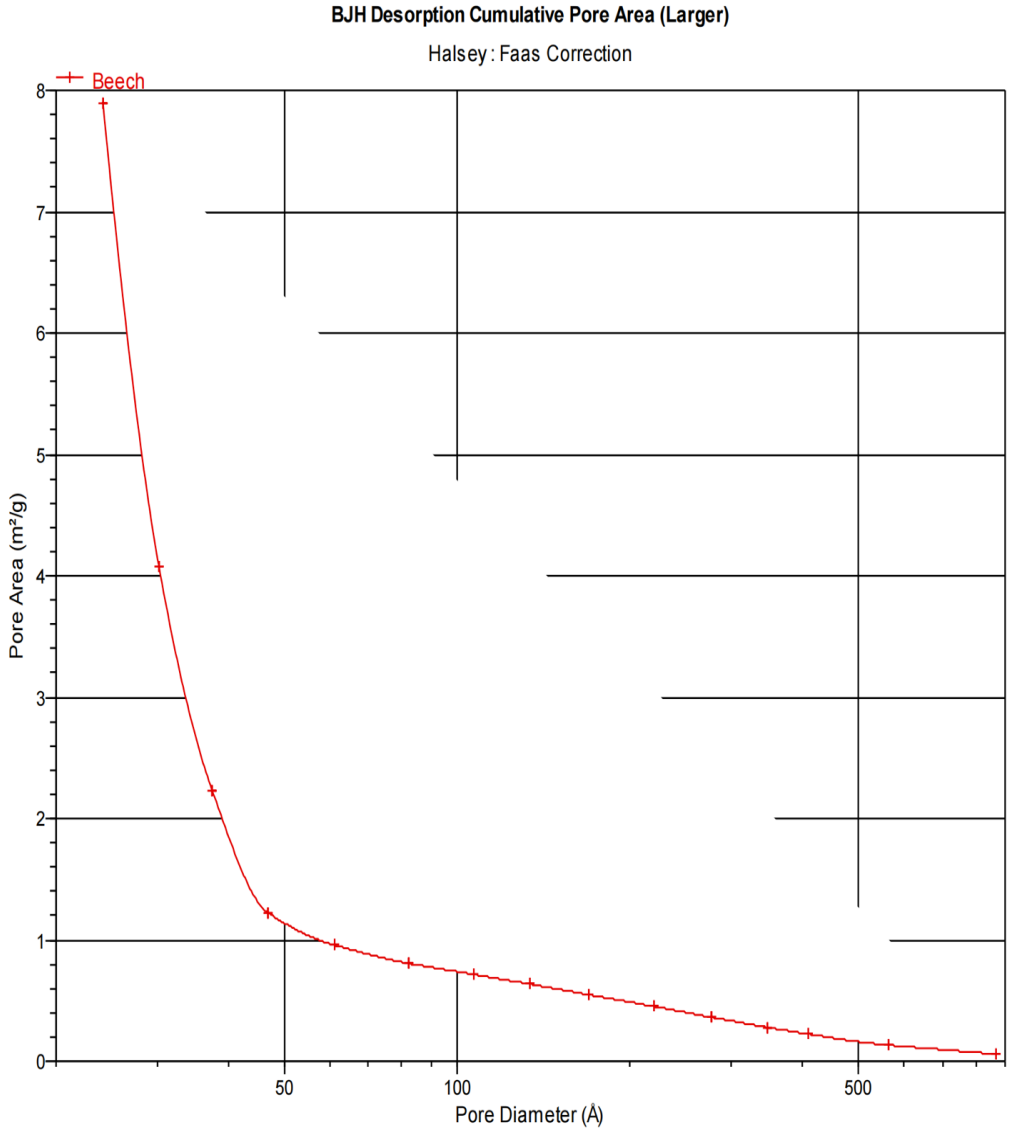


Figure C-3.15: Bc-Beech desorption cumulative pore Area (larger)

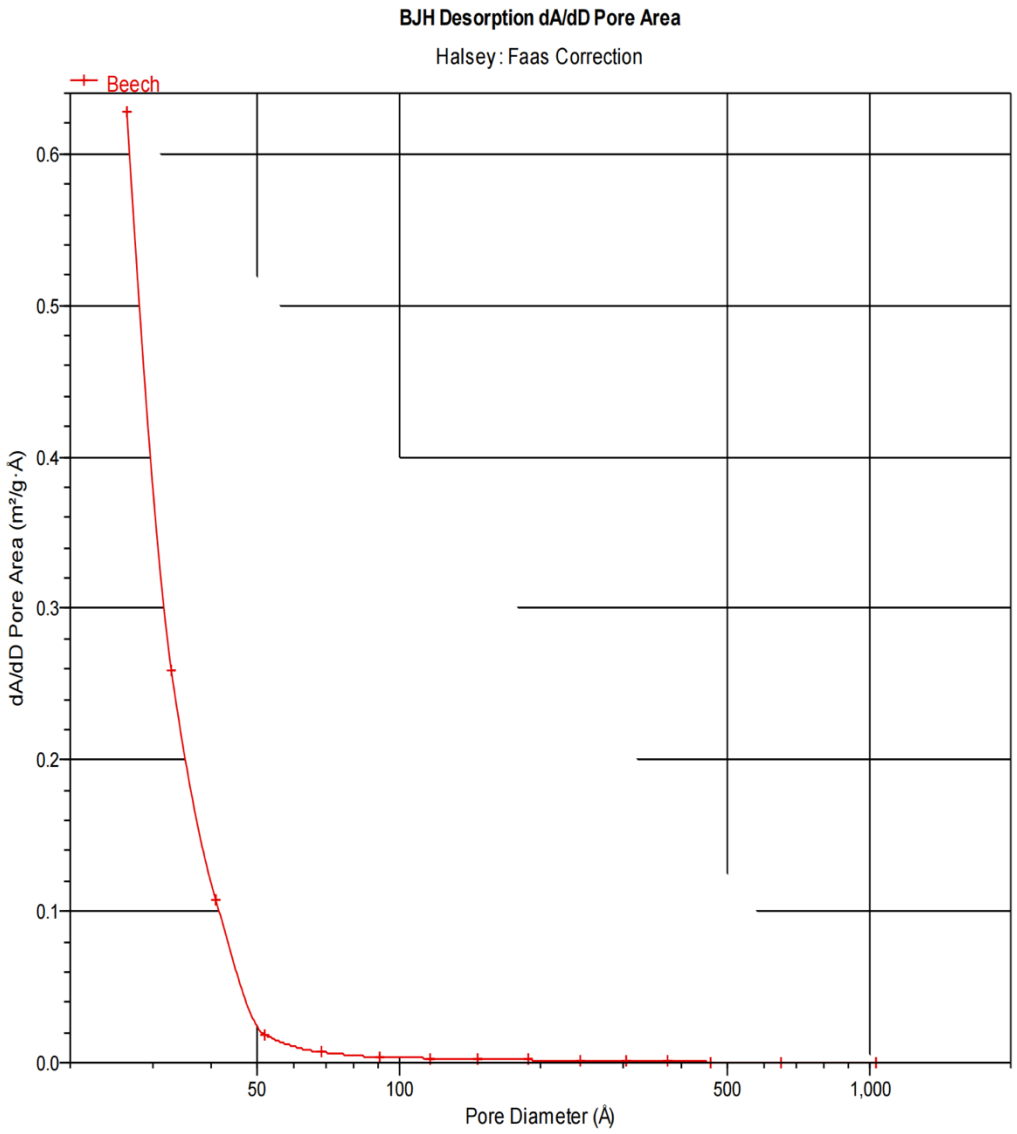


Figure C-3.16: Bc-Beech desorption dA/dD pore area

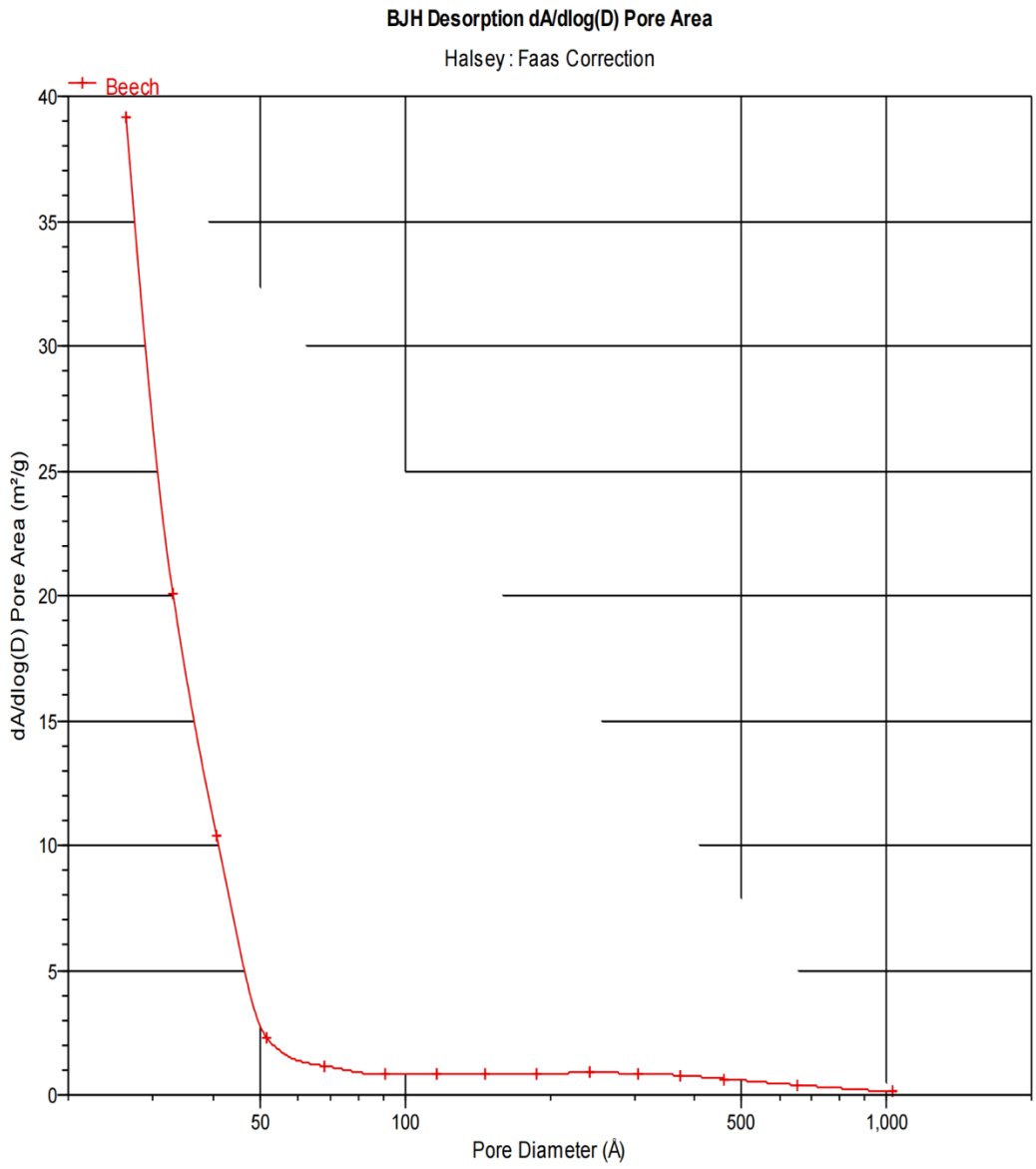


Figure C-3.17: Bc-Beech desorption dA/dlog(D) pore area

BIRCH SUMMARY REPORT

Summary Report Surface Area

Single point surface area at p/p° = 0.300000000: 264.2830 m²/g

BET Surface Area: 287.3206 m²/g

Langmuir Surface Area: 423.4764m²/g

BJH Adsorption cumulative surface area of pores

between 17.000 Å and 3,000.000 Å diameter: 28.958

m²/g

BJH Desorption cumulative surface area of pores

between 17.000 Å and 3,000.000 Å diameter: 6.7111

m²/g

Pore Volume

Single point adsorption total pore

volume of pores less than 2,816.256

Å diameter at p/p° = 0.993100243:

0.151366 cm³/g

BJH Adsorption cumulative volume of pores between 17.000 Å and 3,000.000 Å

diameter: 0.026079 cm³/g

BJH Desorption cumulative volume of pores between 17.000 Å and 3,000.000 Å

diameter: 0.009894 cm³/g

Pore Size

Adsorption average pore diameter (4V/A

byBET):

21.0727 Å BJH Adsorption average pore

diameter

(4V/A): 36.024 Å BJH Desorption average

pore diameter (4V/A): 58.971 Å

Table C-4.0: Bc-BircH showing isothermal Tabular Report

Relative Pressure (P/P^o)	**Absolute pressure (mmHg)**	**Quantity Adsorbed (cm^3/g STP)**	**Elapsed Time (h: min)**	**Saturation pressure (mmHg)**
			00:37	753.255737
0.009677042	7.232509	74.9950	15:08	747.388428
0.061155089	45.716591	85.4249	20:22	747.551697
0.080034790	59.888611	86.6878	21:08	748.282227
0.128694898	96.345200	88.1855	21:35	748.632629
0.167278118	125.278763	89.0626	21:52	748.924988
0.208851451	156.433472	89.7725	22:04	749.017883
0.234074103	175.354248	90.1745	22:12	749.139893
0.245425667	183.861633	90.3892	22:17	749.154053
0.333648833	250.003922	91.1212	22:26	749.302551
0.366380656	274.561737	91.4005	22:30	749.389282
0.446508366	334.645538	91.8303	22:35	749.472046
0.467697226	350.521515	91.9952	22:37	749.462463
0.548780078	411.346039	92.3171	22:41	749.564453

0.574761489	430.851196	92.4653	22:43	749.617371
0.648078343	485.842072	92.7256	22:46	749.665649
0.683622472	512.529175	92.8791	22:48	749.725464
0.737647644	553.054382	93.0891	22:50	749.754150
0.773685991	580.069702	93.2637	22:52	749.748230
0.798623372	598.769043	93.4068	22:53	749.751465
0.837936278	628.289368	93.6186	22:55	749.805664
0.872280999	654.059814	93.8686	22:56	749.826965
0.884666933	663.377197	94.0199	22:58	749.860962
0.904520708	678.256653	94.2419	22:59	749.851990
0.923186505	692.269409	94.5039	23:00	749.869507
0.938566629	703.814697	94.8079	23:02	749.882507
0.951980028	713.897400	95.1484	23:03	749.907959
0.962675271	721.950928	95.5405	23:05	749.942322
0.970402594	727.768066	95.9082	23:06	749.965088
0.976377803	732.264282	96.2679	23:08	749.980469
0.981375115	736.045532	96.6409	23:09	750.014465
0.983726272	737.818420	96.8727	23:10	750.024109
0.986068702	739.586975	97.0800	23:12	750.035950
0.987453023	740.617371	97.2564	23:13	750.027954
0.989188600	741.916687	97.4394	23:14	750.025513
0.993100243	744.876038	97.8574	23:16	750.051208
0.975916952	731.958740	97.0658	23:18	750.021545

0.957482272	718.168274	96.4422	23:19	750.059082
0.937883064	703.519287	96.0011	23:21	750.114075
0.926864657	695.223450	95.8084	23:22	750.080872
0.906213320	679.752747	95.5705	23:23	750.102356
0.877205038	657.976379	95.3475	23:24	750.082764
0.842290784	631.807129	95.1706	23:26	750.105713
0.802397961	601.885498	95.0411	23:27	750.108459
0.743292065	557.554565	94.9150	23:28	750.115051
0.654441170	490.904694	94.7793	23:30	750.112793
0.554615764	416.034332	94.6242	23:32	750.130737
0.454491602	340.908508	94.3767	23:35	750.087585
0.353515397	265.157715	94.0420	23:39	750.059875
0.242655260	182.035477	93.4141	23:46	750.181458

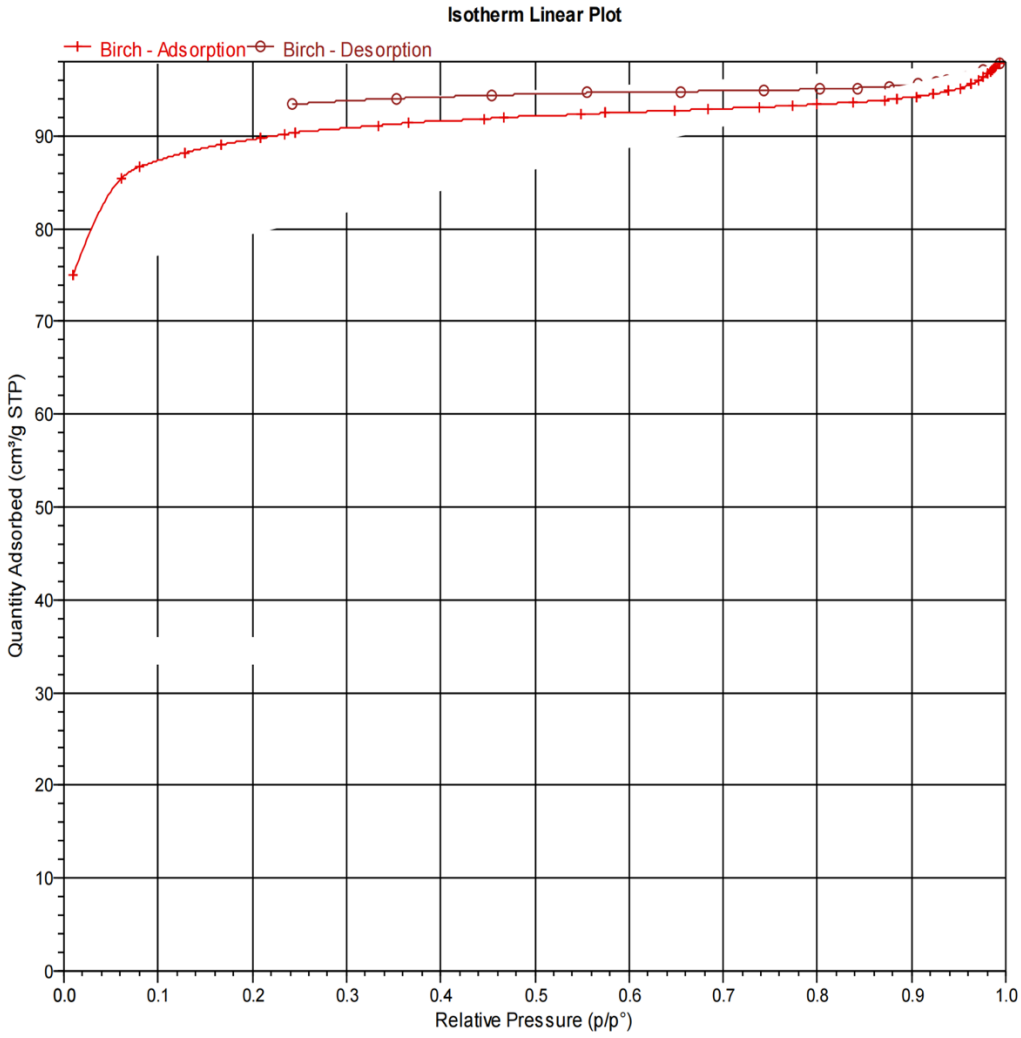


Figure C- 4.0: Bc-BircH isothermal Linear Plot

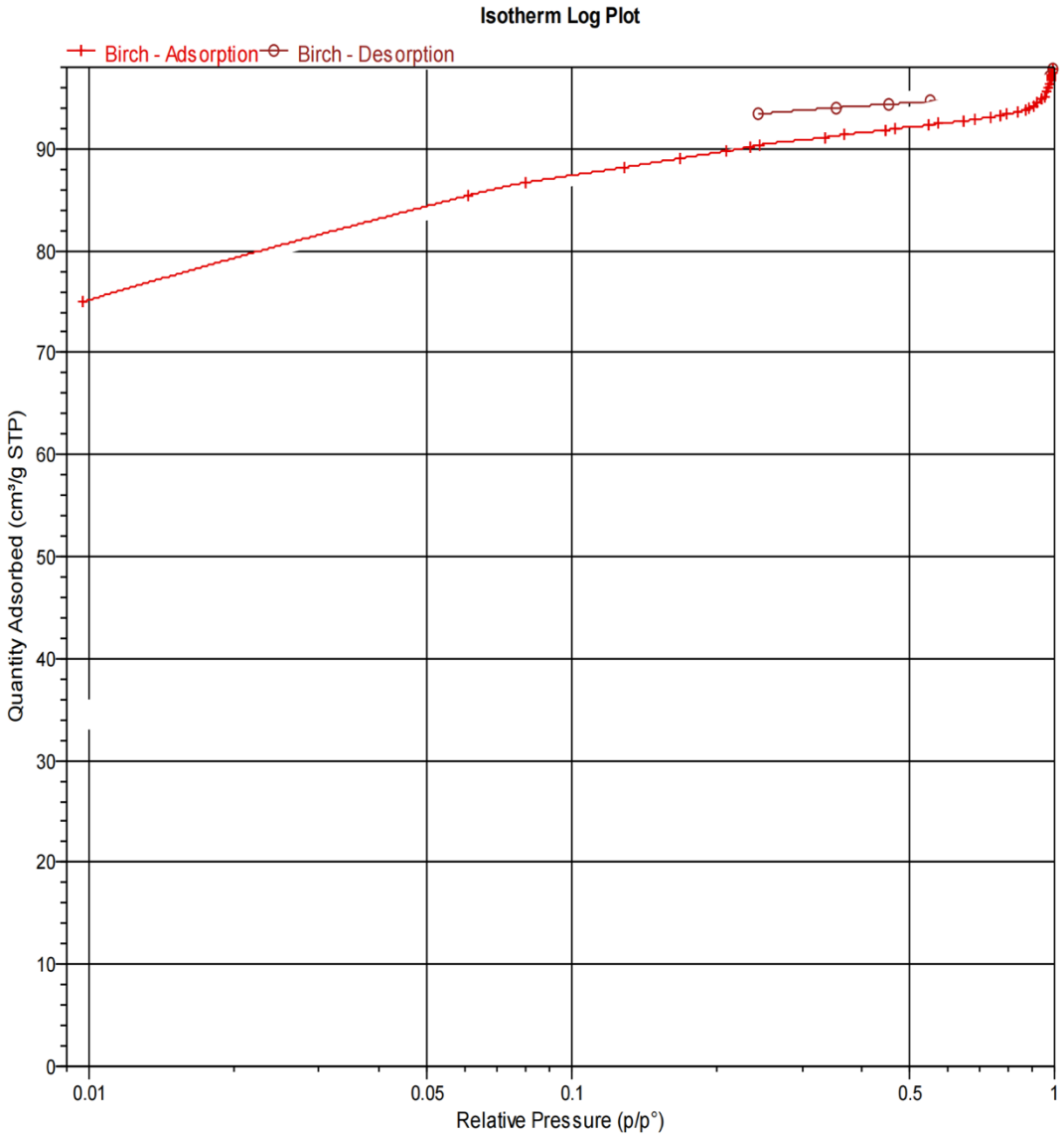


Figure C- 4.1: Bc-BircH Isothermal log Plot

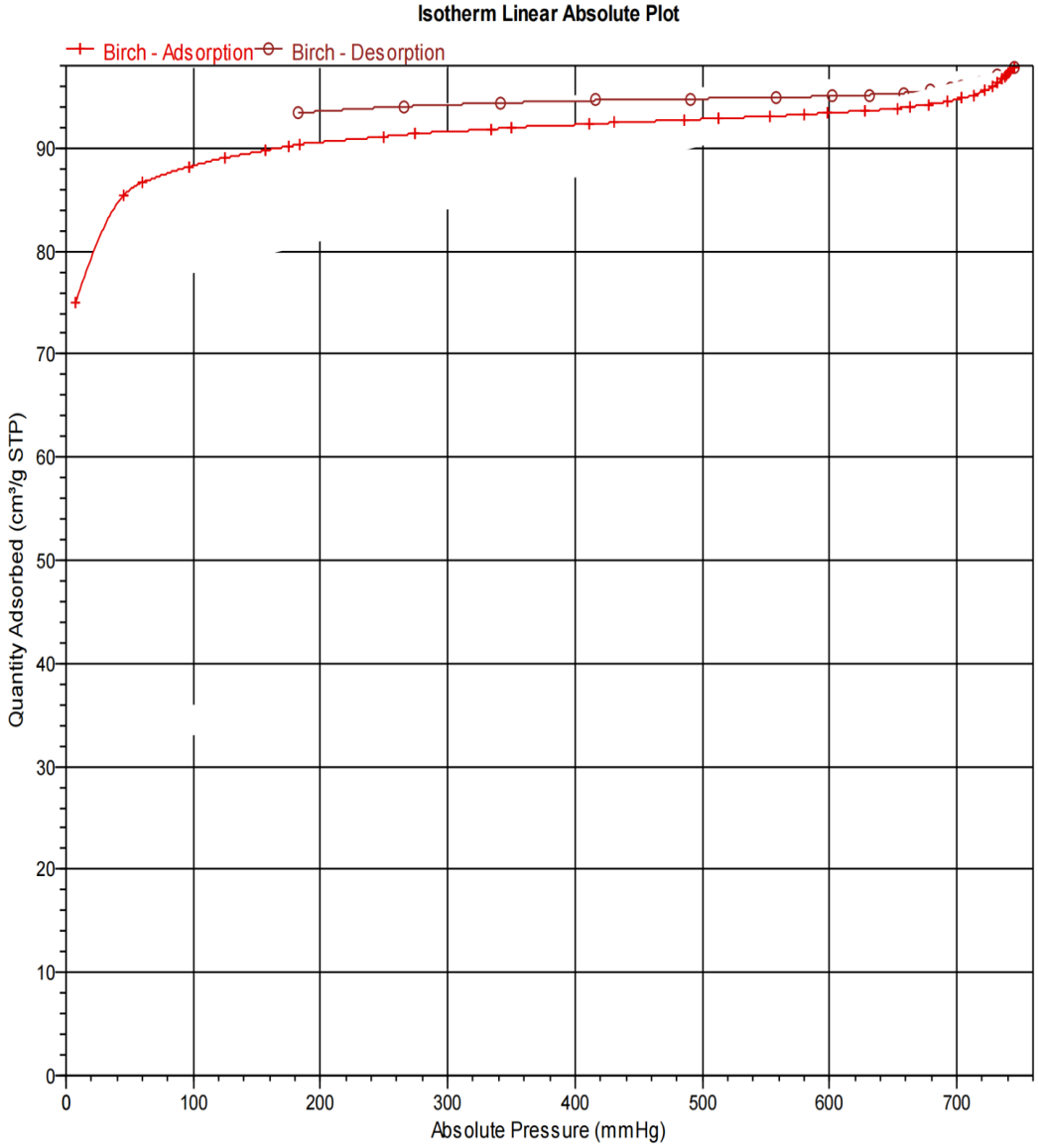


Figure C-4.2: Bc-BircH Isothermal Linear Absolute Plot

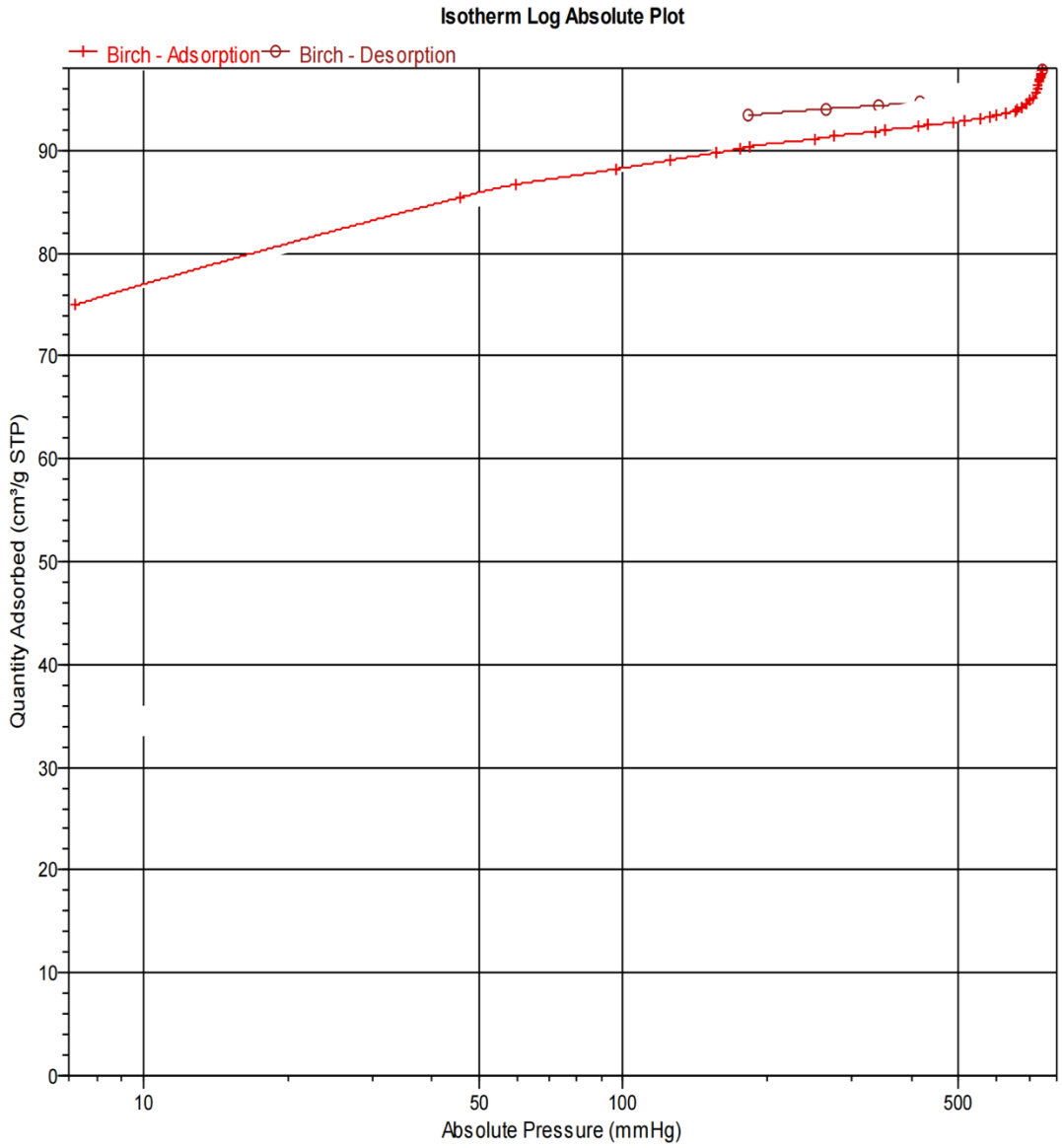


Figure C- 4.3: Bc-BircH Isothermal Log Absolute Plot

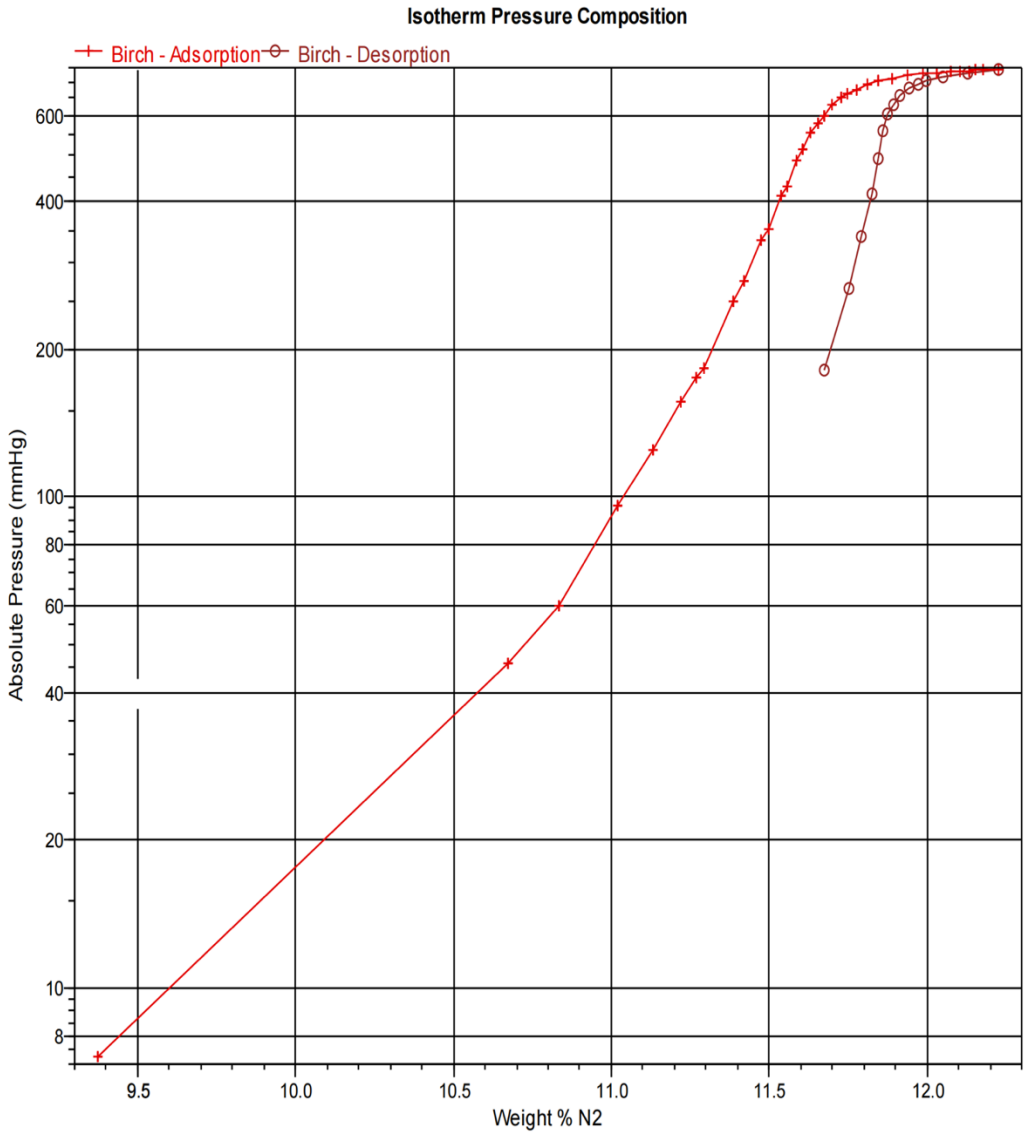


Figure C- 4.4: Bc-BircH Isothermal Pressure Composition Plot

Birch BET Report

BET Surface Area: 287.3206 ± 6.7680 m^2/g

Slope: 0.015392 ± 0.000352 g/cm^3 STP

Y-Intercept: -0.000243 ± 0.000061 g/cm^3

STP C: -62.419348

Qm: 66.0116 cm^3/g STP

Correlation Coefficient: 0.9986985

Table C-4.1: Bc-Birch BET Tabula data Report

Relative pressure (p/p^o)	**Quality adsorbed Cm^3/g STP**	**1/[Q(p°/p - 1)]**
0.061155089	85.4249	0.000763
0.080034790	86.6878	0.001004
0.128694898	88.1855	0.001675
0.167278118	89.0626	0.002256
0.208851451	89.7725	0.002941
0.234074103	90.1745	0.003389
0.245425667	90.3892	0.003598

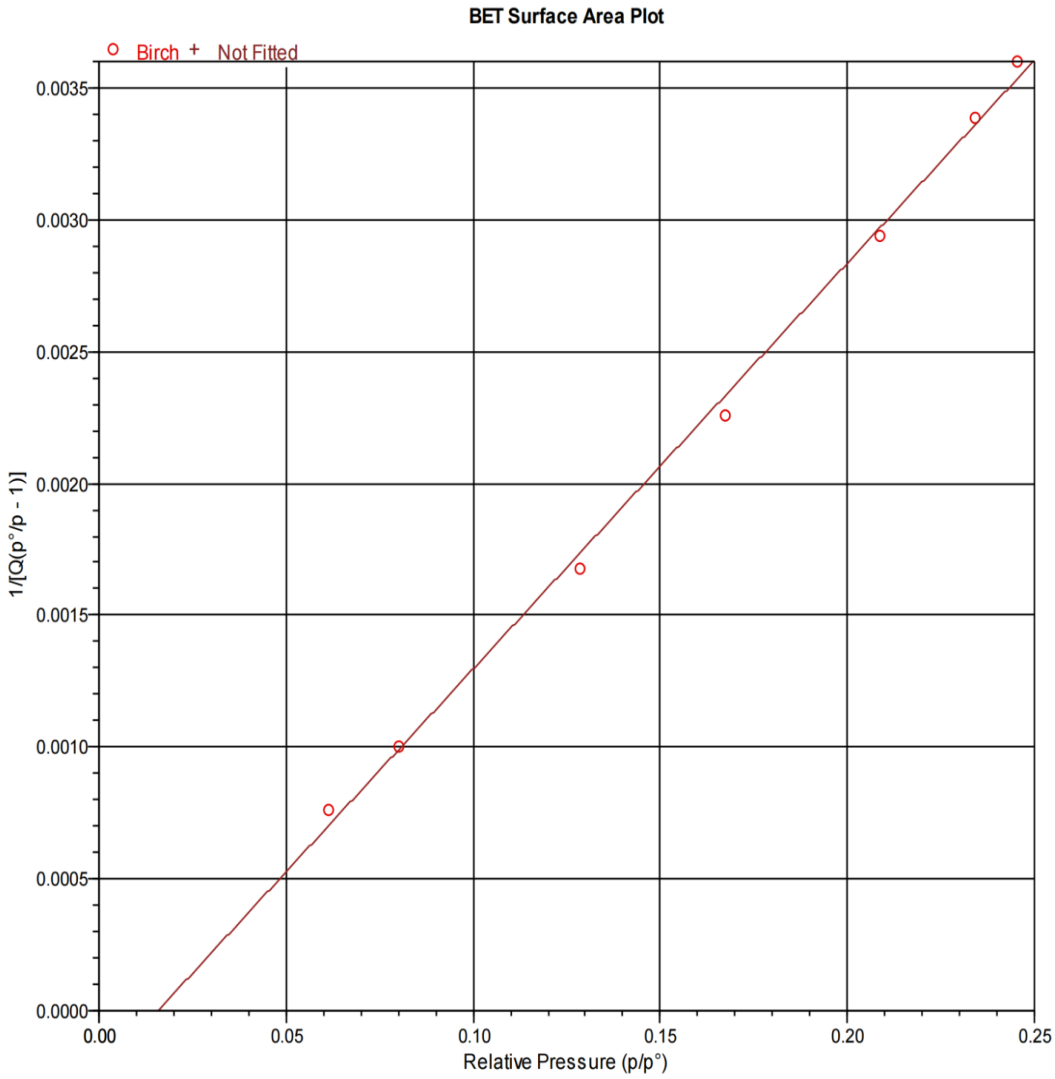


Figure C- 4.5: Bc-BircH BET surface Area Plot

Table C- 4.2: Bc-Birch BET Langmuir Tabular Report

Pressure (mmHg)	**Quantity Adsorbed (cm^3/g STP**	**p/Q (mmhg g/cm3 STP**
7.232509	74.9950	0.096
45.716591	85.4249	0.535
59.888611	86.6878	0.691
96.345200	88.1855	1.093
125.278763	89.0626	1.407
156.433472	89.7725	1.743
175.354248	90.1745	1.945
183.861633	90.3892	2.034
250.003922	91.1212	2.744
274.561737	91.4005	3.004
334.645538	91.8303	3.644
350.521515	91.9952	3.810
411.346039	92.3171	4.456
430.851196	92.4653	4.660
485.842072	92.7256	5.240
512.529175	92.8791	5.518
553.054382	93.0891	5.941
580.069702	93.2637	6.220
598.769043	93.4068	6.410

628.289368	93.6186	6.711
654.059814	93.8686	6.968
663.377197	94.0199	7.056
678.256653	94.2419	7.197
692.269409	94.5039	7.325
703.814697	94.8079	7.424
713.897400	95.1484	7.503
721.950928	95.5405	7.556
727.768066	95.9082	7.588
732.264282	96.2679	7.607
736.045532	96.6409	7.616
737.818420	96.8727	7.616
739.586975	97.0800	7.618

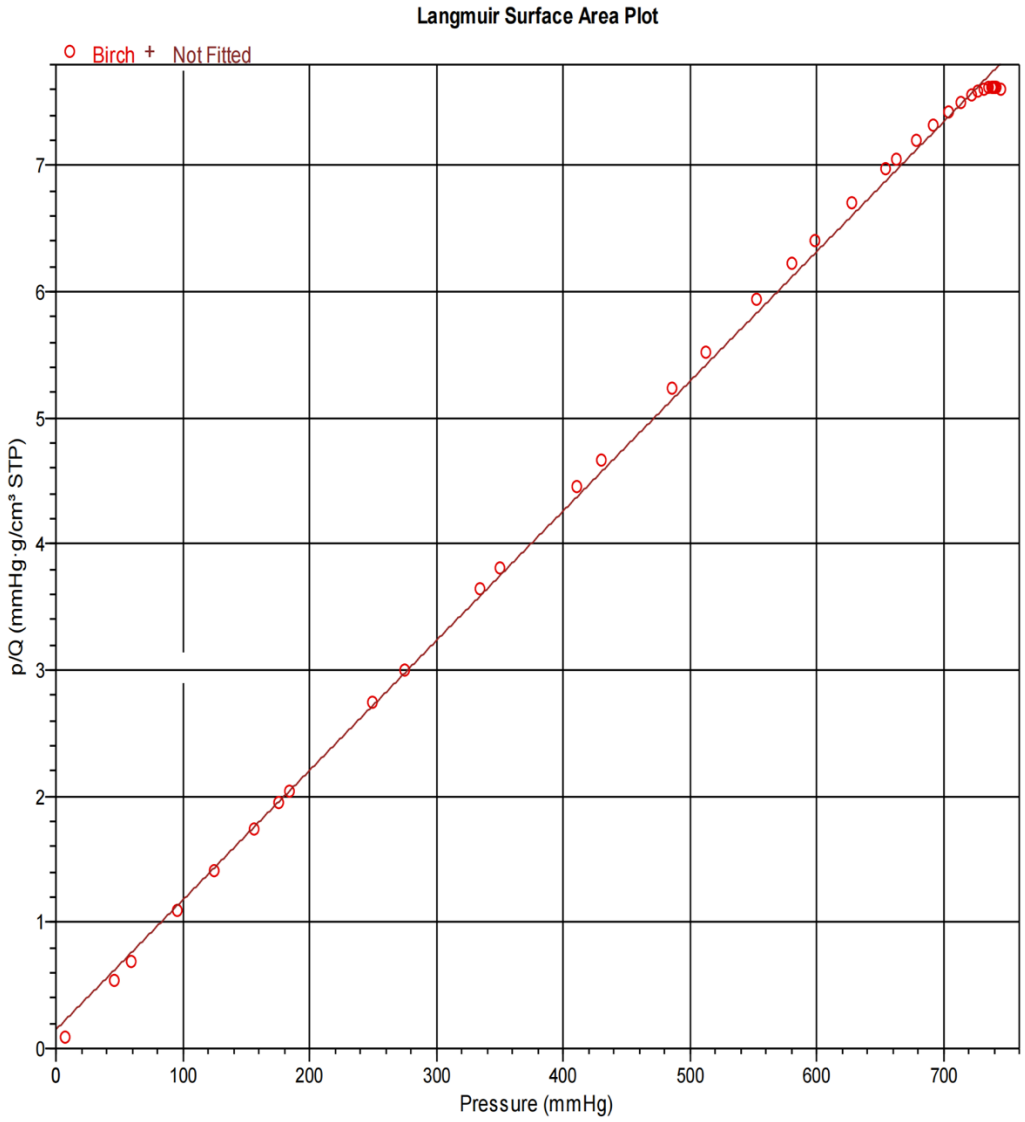


Figure C-4.6: Bc-BircH BET Langmuir surface Area Plot

Table C- 4.3: Bc-Birch BJH Adsorption Pore Distribution Report

Pore Diameter Range (Å)	**Average Diameter (Å)**	**Incremental Pore volume (cm^3/g)**	**Cumulative Pore Volume(cm^3/g)**	**Incremental Pore Area(m^2/g)**	**Cumulative pore area(m^2/g)**
2816.3 - 1807.9	2099.2	0.000681	0.000681	0.013	0.013
1807.9 - 1561.4	1666.4	0.000300	0.000981	0.007	0.020
1561.4 - 1408.7	1477.1	0.000290	0.001272	0.008	0.028
1408.7 - 1209.2	1293.5	0.000342	0.001614	0.011	0.039
1209.2 - 1059.2	1124.1	0.000385	0.001999	0.014	0.052
1059.2 - 839.3	923.4	0.000624	0.002622	0.027	0.079
839.3 - 673.3	737.7	0.000607	0.003229	0.033	0.112
673.3 - 537.0	589.4	0.000627	0.003856	0.043	0.155
537.0 - 420.3	464.0	0.000678	0.004534	0.058	0.213

420.3 - 330.9	364.6	0.000594	0.005128	0.065	0.278
330.9 - 266.5	291.5	0.000539	0.005667	0.074	0.352
266.5 - 216.0	235.6	0.000469	0.006136	0.080	0.432
216.0 - 179.9	194.4	0.000404	0.006541	0.083	0.515
179.9 - 163.0	170.5	0.000287	0.006828	0.067	0.583
163.0 - 129.3	142.0	0.000465	0.007293	0.131	0.714
129.3 - 104.7	114.1	0.000401	0.007694	0.141	0.854
104.7 - 93.3	98.2	0.000289	0.007983	0.118	0.972
93.3 - 80.6	85.9	0.000358	0.008341	0.167	1.139
80.6 - 66.8	72.2	0.000439	0.008781	0.243	1.382
66.8 - 59.9	62.9	0.000349	0.009130	0.222	1.604

59.9 - 49.1	53.3	0.000604	0.009733	0.453	2.057
49.1 - 46.1	47.5	0.000402	0.010135	0.338	2.395
46.1 - 38.3	41.3	0.000845	0.010980	0.818	3.213
38.3 - 36.6	37.4	0.000521	0.011501	0.556	3.770
36.6 - 31.1	33.3	0.001305	0.012806	1.569	5.339
31.1 - 29.1	30.0	0.000974	0.013780	1.299	6.638
29.1 - 24.4	26.2	0.002627	0.016407	4.013	10.651
24.4 - 23.8	24.1	0.000932	0.017339	1.548	12.199
23.8 - 22.6	23.2	0.001693	0.019032	2.924	15.123
22.6 - 20.6	21.5	0.003037	0.022068	5.653	20.776
20.6 - 18.8	19.6	0.004011	0.026079	8.182	28.958

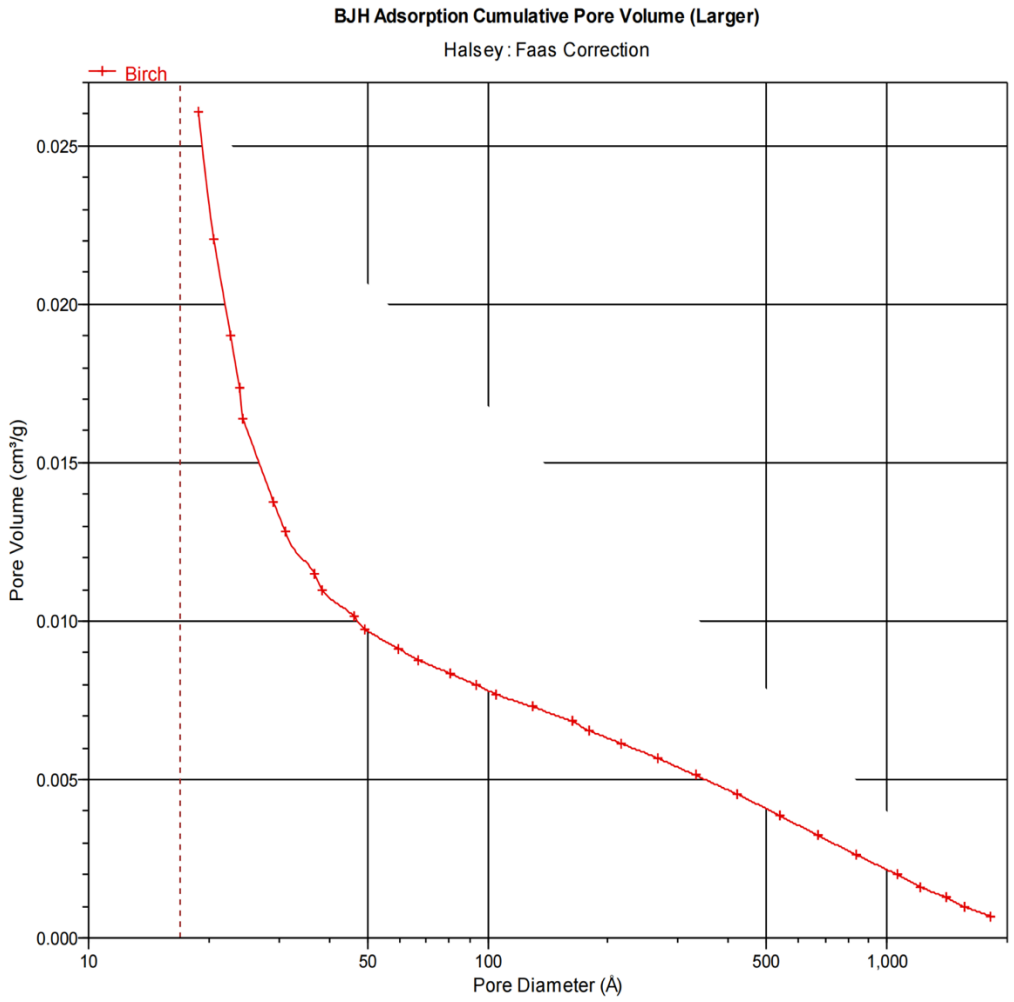


Figure C-4.7: Bc-BircH BJH Adsorption cumulative pore volume (large).

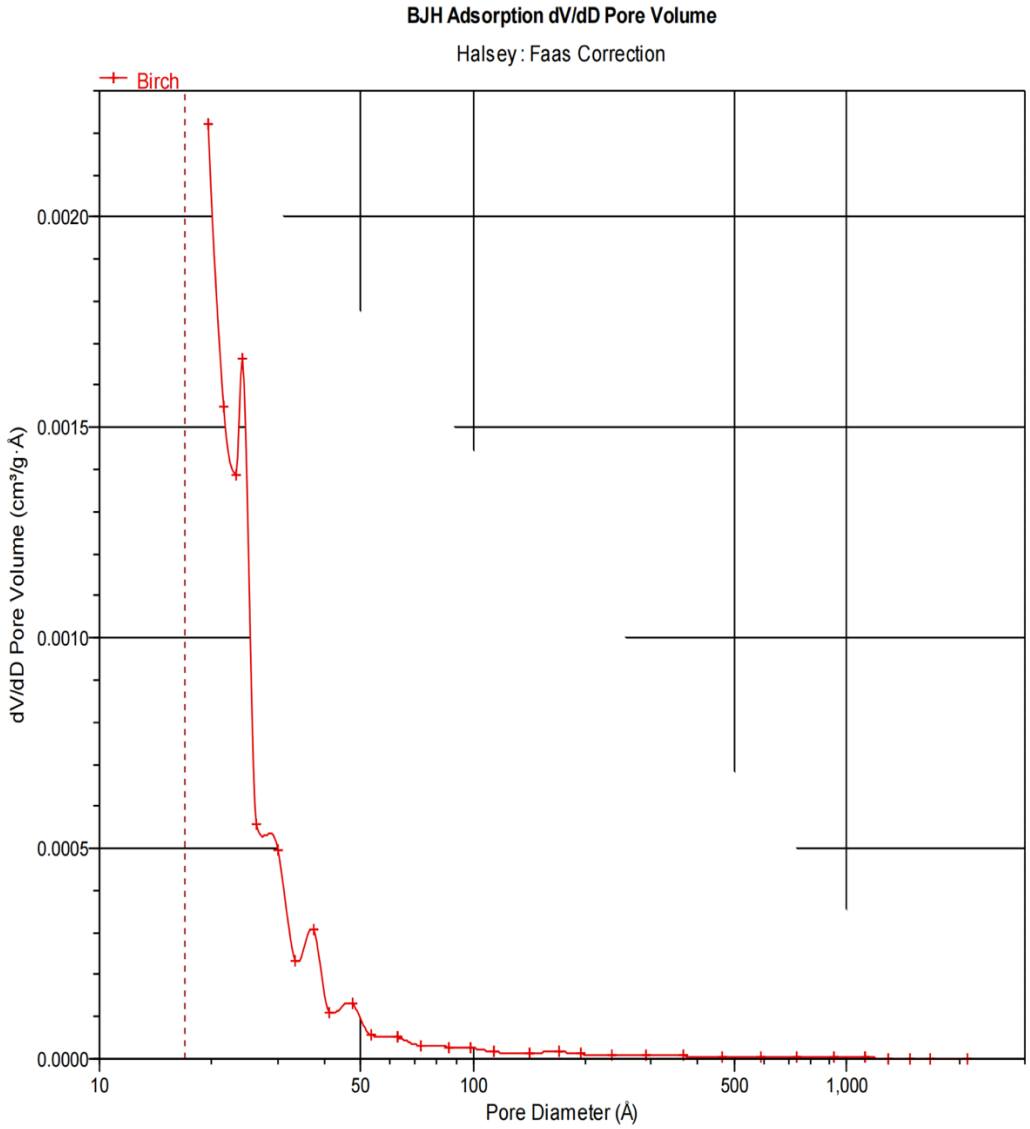


Figure C-4.8: Bc-BircH BJH Adsorption dV/dD pore volume

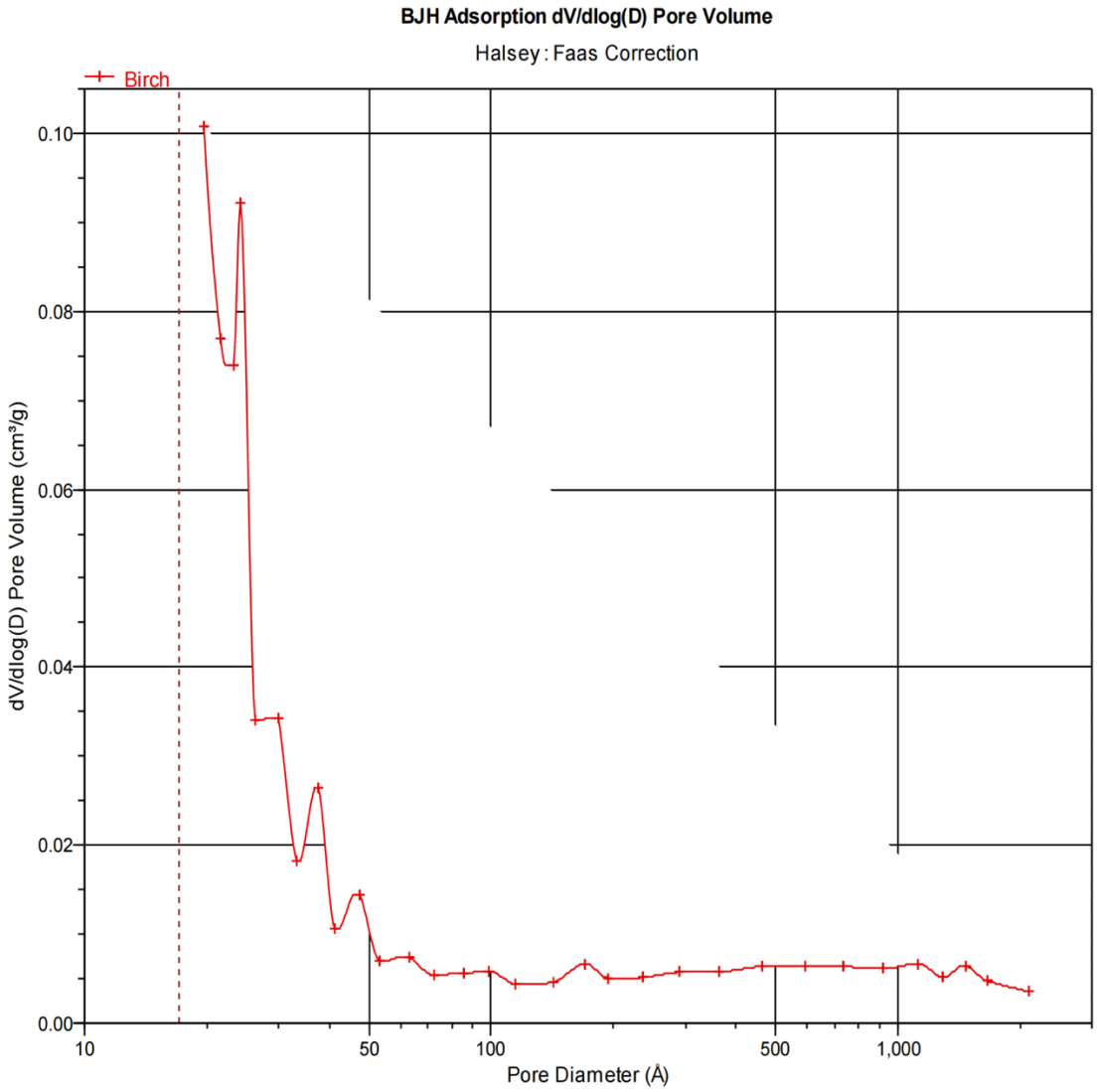


Figure C- 4.9: Bc-BircH BJH Adsorption dV/dlog (D) pore volume

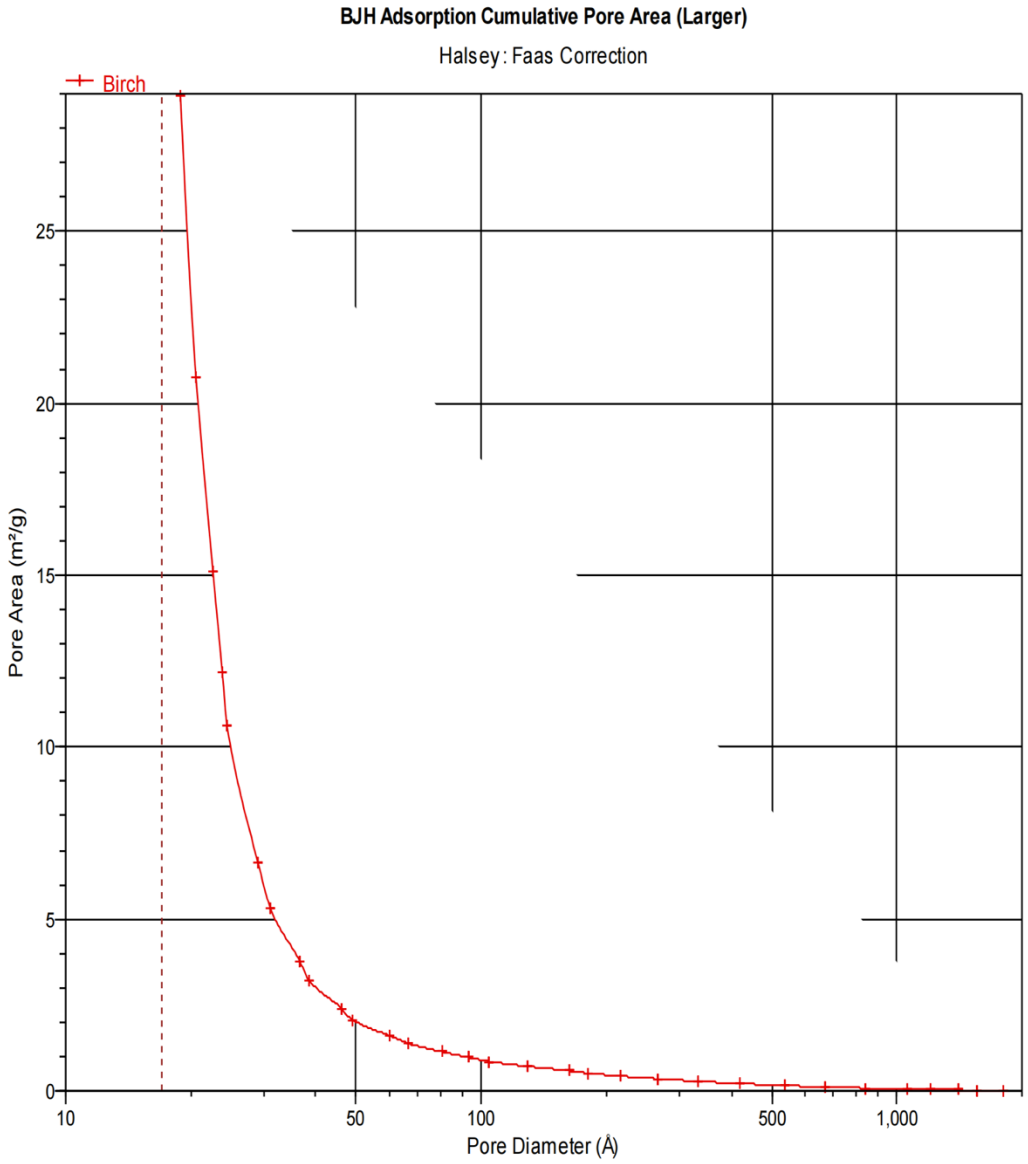


Figure C- 4.10: Bc-BircH BJH Adsorption cumulative pore area(larger)

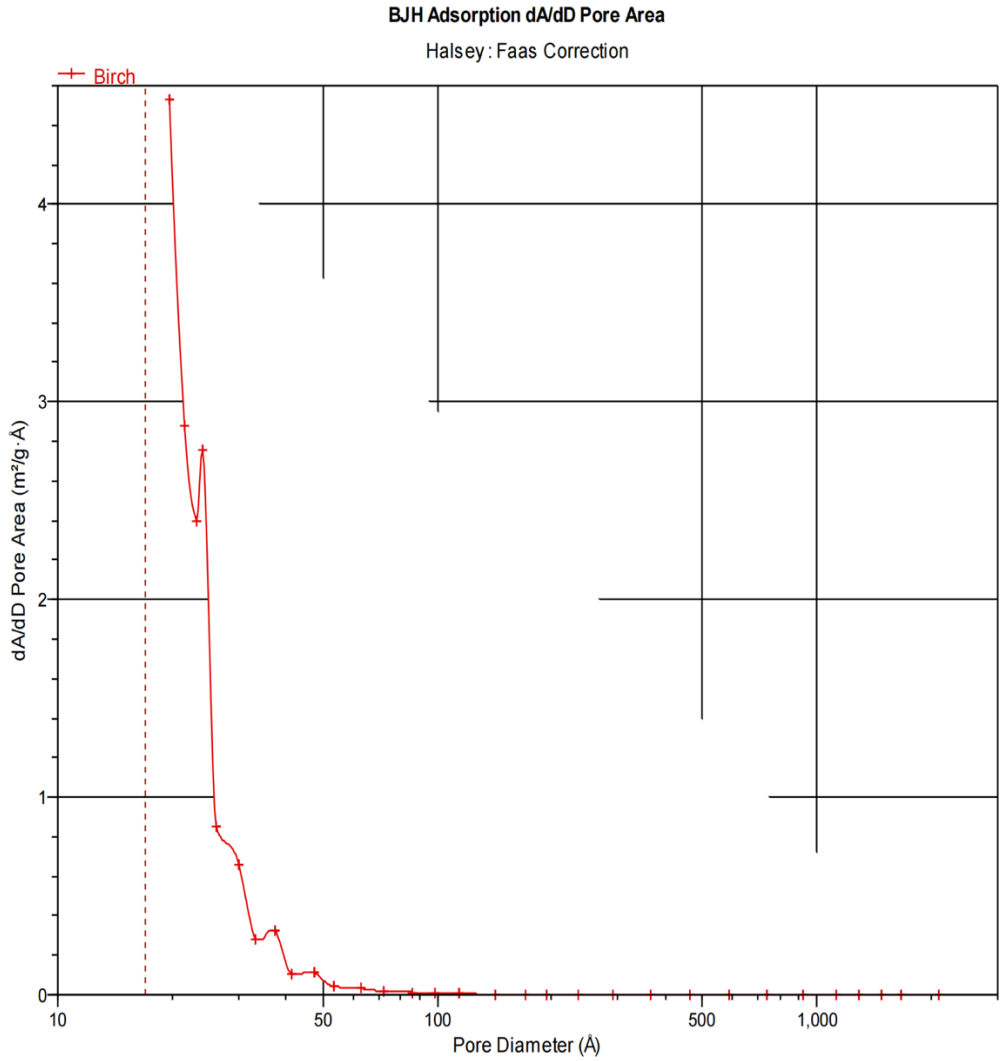


Figure C- 4.11: Bc-BircH BJH Adsorption dA/dD pore area

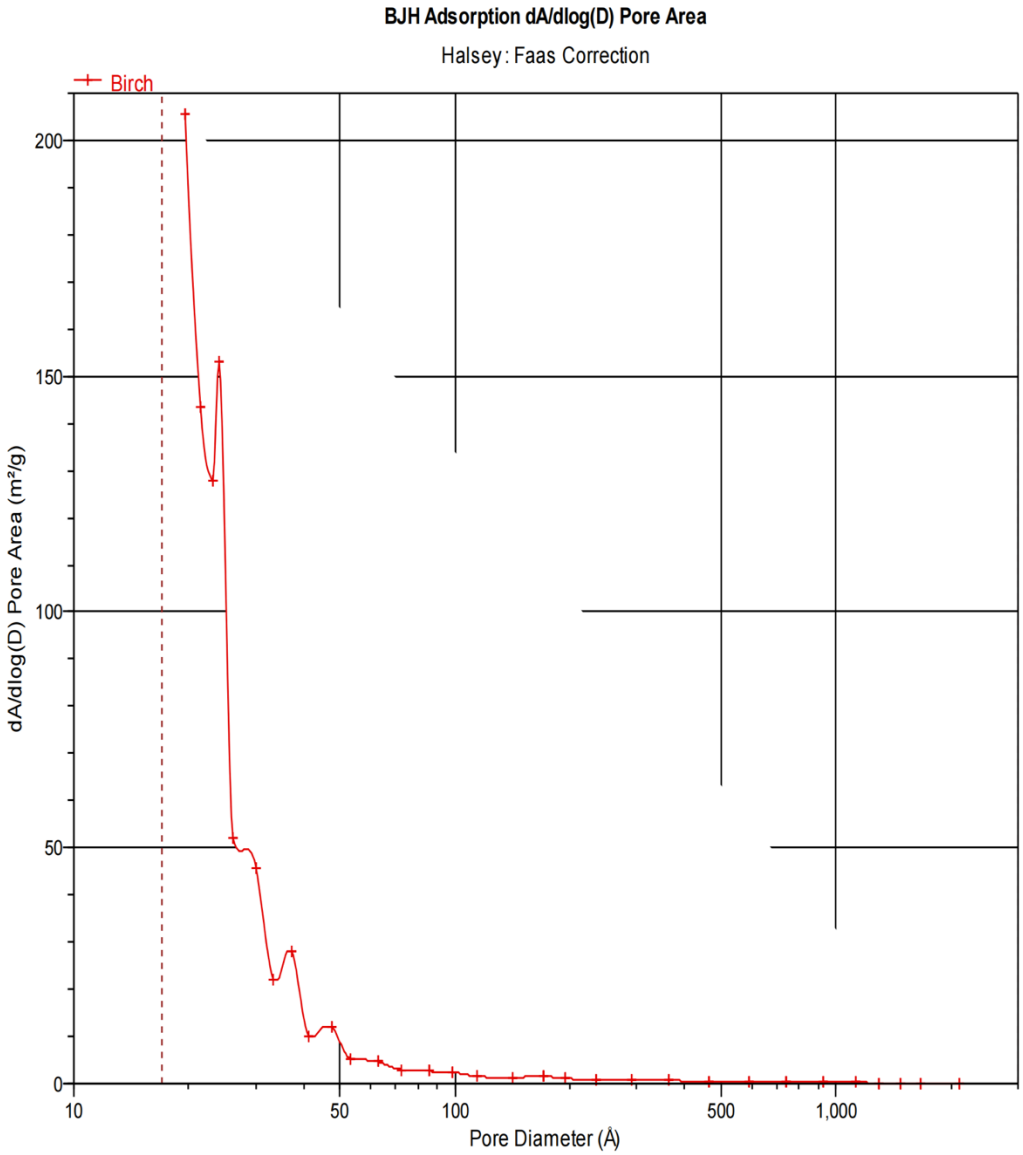


Figure C- 4.12: Bc-BircH BJH Adsorption dA/dlog (D) pore area

BJH Adsorption Pore Distribution Report

Faas Correction Halsey

t = 3.54 [-5 / ln(p/p°)] ^ 0.333

Diameter Range: 17.000 Å to 3,000.000 Å

Adsorbate Property Factor: 9.53000 Å

Density Conversion Factor: 0.0015468

Fraction of Pores Open at Both Ends: 0.00

Table C- 4.4: Bc-Birch BJH Desorption Pore Distribution Report

Pore Diameter Range (Å)	**Average Diameter (Å)**	**Incremental Pore volume (cm^3/g)**	**Cumulative Pore Volume(cm^3/g)**	**Incremental Pore Area(m^2/g)**	**Cumulative pore area(m^2/g)**
2816.3 - 823.5	973.1	0.001336	0.001336	0.055	0.055
823.5 - 473.1	557.3	0.001074	0.002410	0.077	0.132
473.1 - 327.4	373.4	0.000777	0.003187	0.083	0.215
327.4 - 279.5	299.5	0.000344	0.003530	0.046	0.261

279.5 - 219.7	242.1	0.000426	0.003957	0.070	0.332
219.7 - 169.3	187.5	0.000404	0.004361	0.086	0.418
169.3 - 132.8	146.3	0.000323	0.004684	0.088	0.506
132.8 - 106.6	116.5	0.000233	0.004917	0.080	0.586
106.6 - 82.4	91.0	0.000225	0.005142	0.099	0.685
82.4 - 61.1	68.1	0.000252	0.005394	0.148	0.833
61.1 - 46.8	51.7	0.000342	0.005736	0.265	1.097
46.8 - 37.3	40.7	0.000695	0.006431	0.683	1.781
37.3 - 30.3	32.9	0.001075	0.007505	1.308	3.089
30.3 - 24.2	26.4	0.002389	0.009894	3.622	6.711

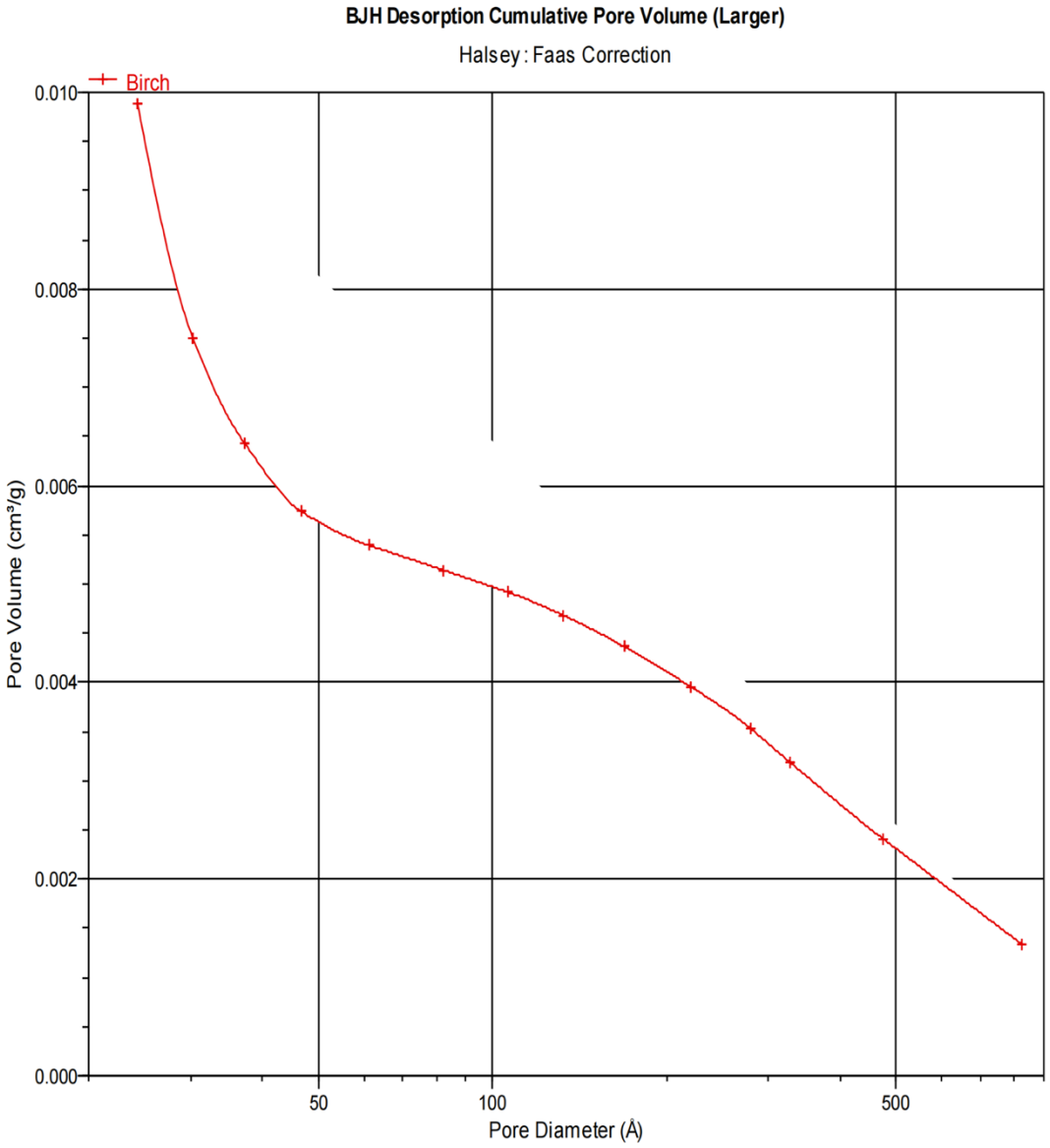


Figure C- 4.13: Bc-BircH BJH Desorption cumulative pore volume

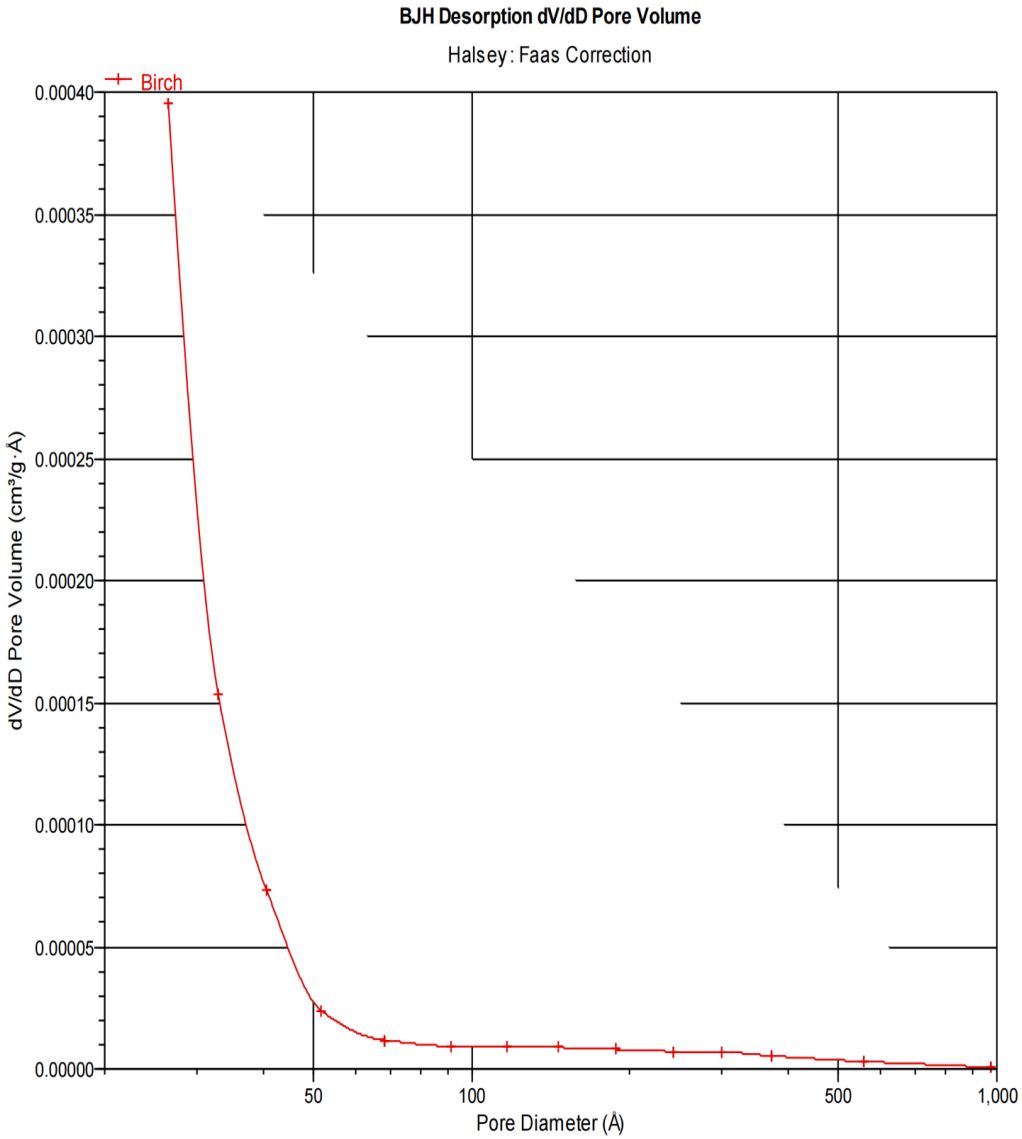


Figure C- 4.14: Bc-BircH BJH Desorption dV/dD pore volume

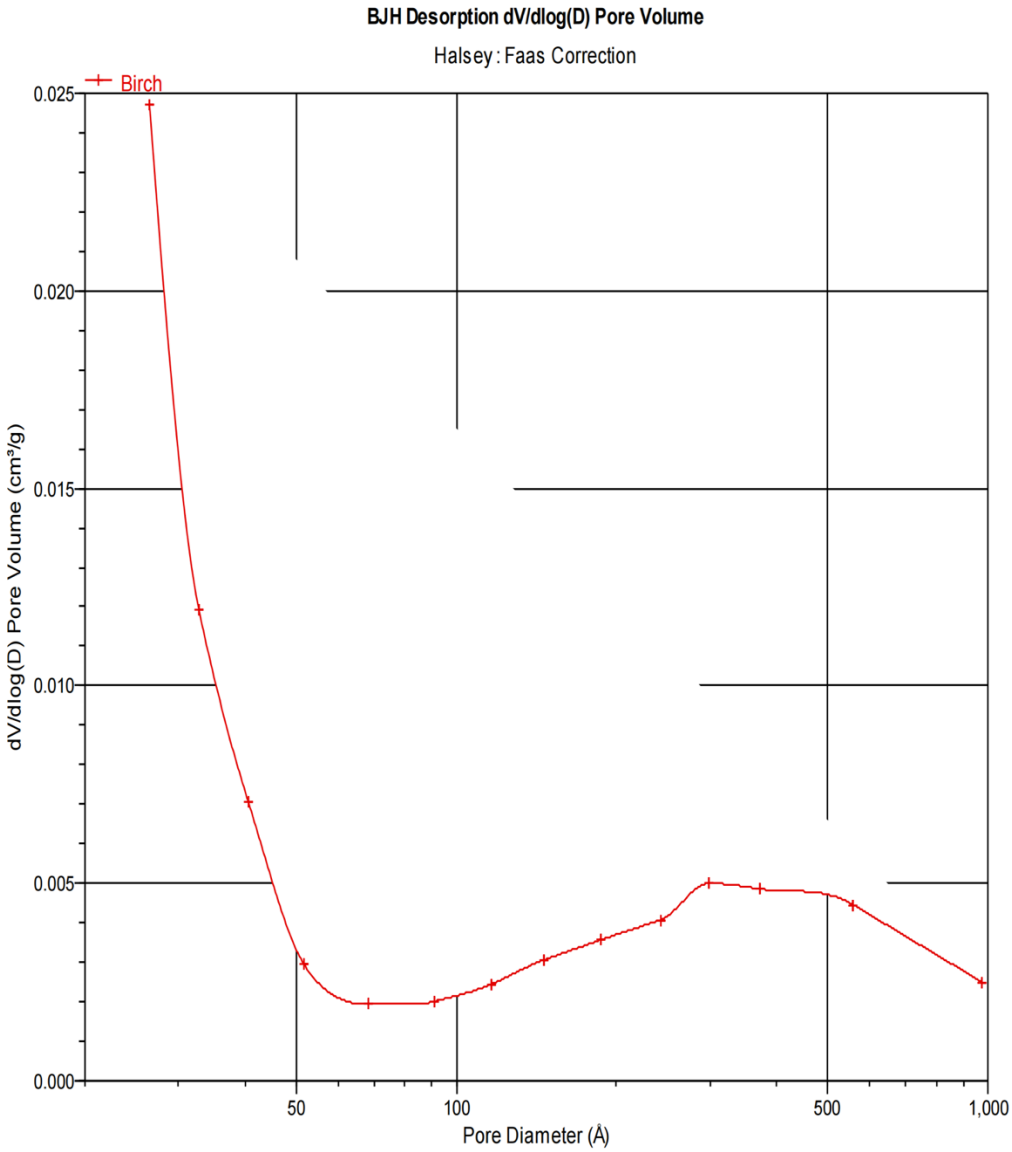


Figure C- 4.15: Bc-BircH BJH Desorption dV/dlog(D) pore volume

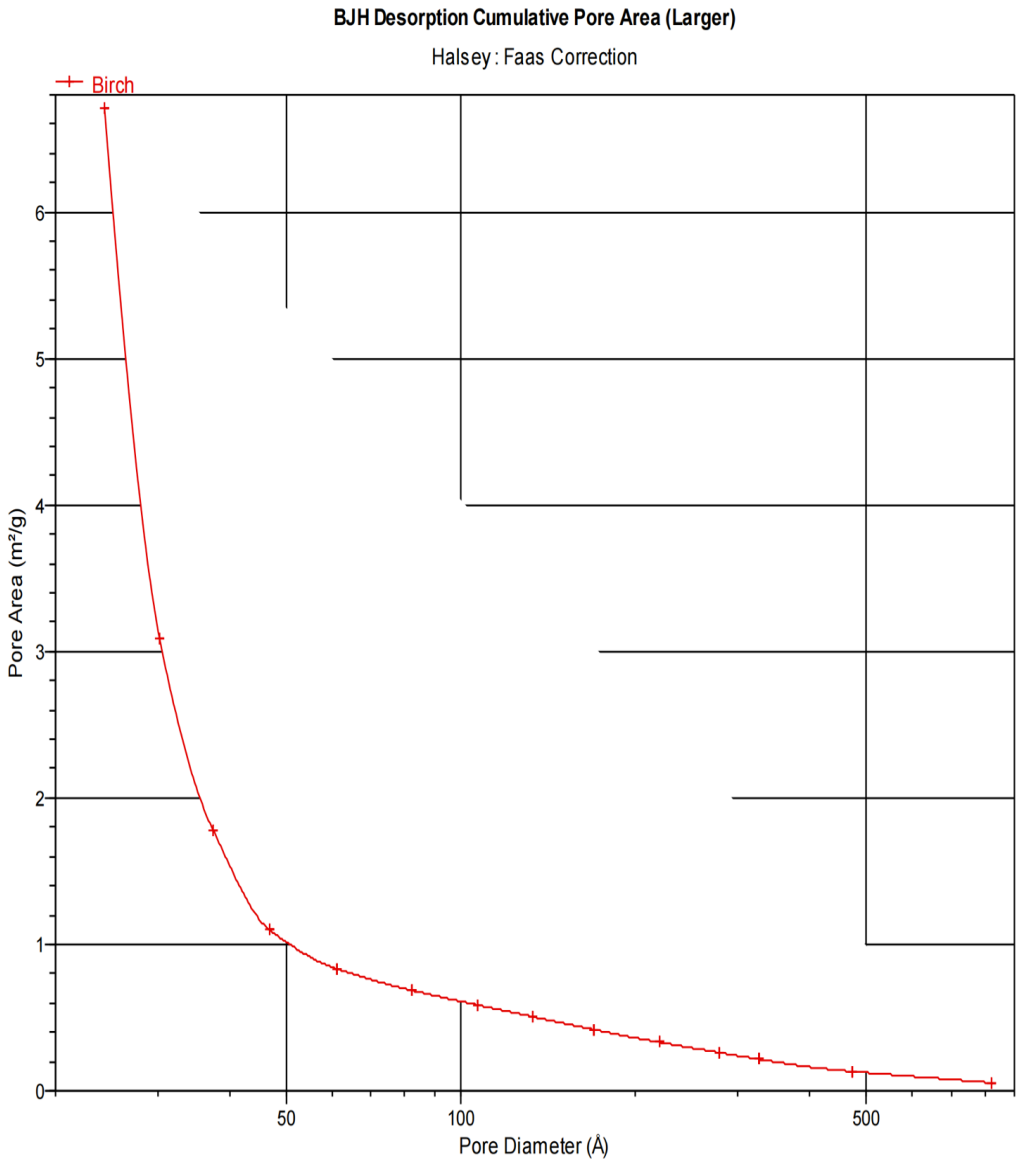


Figure C-4.16: Bc-BircH BJH Desorption cumulative pore area(larger)

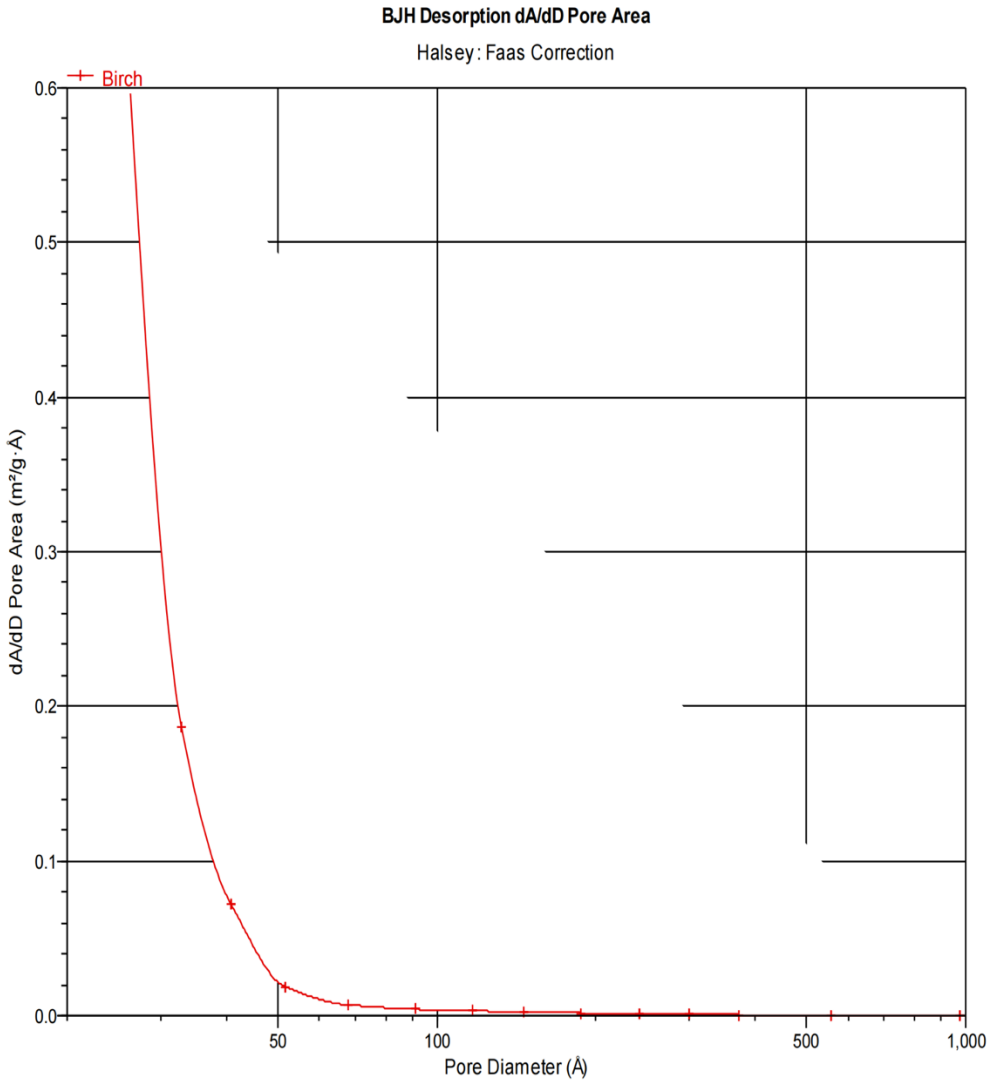


Figure C-4.17: Bc-BircH BJH Desorption dV/dD pore volume

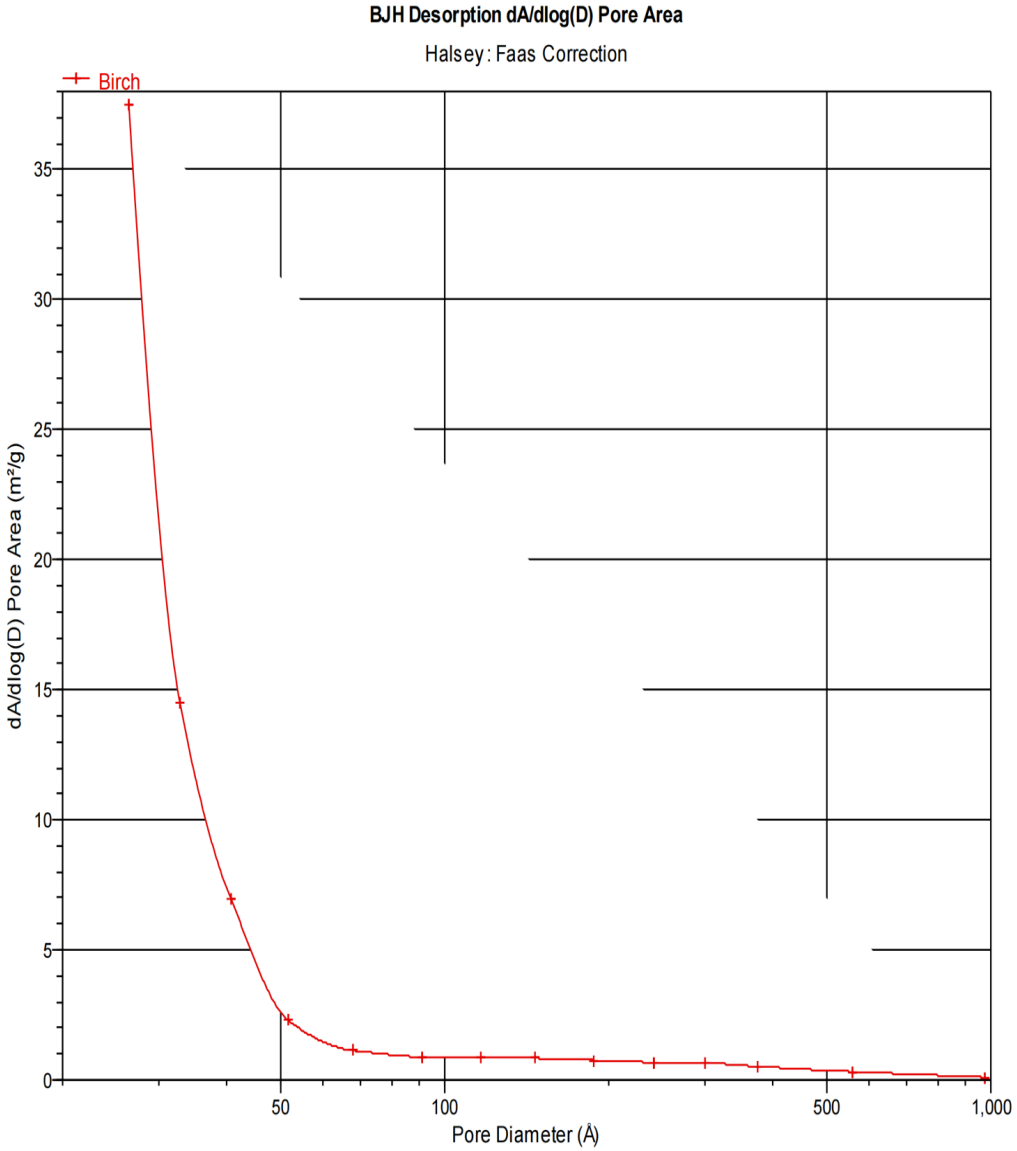


Figure C- 4.18: Bc-BircH BJH Desorption dV/dlog(D) pore volume

APPENDIX D

FUNCTIONALIZE SAMPLES

MAGNETIC HYDROXYAPPETITE BIOCHARA-(MHA-BC) SUMMARY REPORT

Surface Area	
BET Surface Area:	104.4699 m²/g
Pore Volume	
Single point adsorption total pore volume of pores less than 172.6376 nm width at P/Po = 0.988775010:	0.355675 cm³/g
BJH Adsorption cumulative volume of pores between 2.0000 nm and 500.0000 nm width:	0.351696 cm³/g
BJH Desorption cumulative volume of pores between 1.7000 nm and 300.0000 nm width:	0.351128 cm³/g
Pore Size	
Adsorption average pore diameter (4V/A by BET):	13.6183 nm
Desorption average pore diameter (4V/A by BET):	12.6378 nm
BJH Adsorption average pore width (4V/A):	13.9217 nm
BJH Desorption average pore width (4V/A):	13.1116 nm

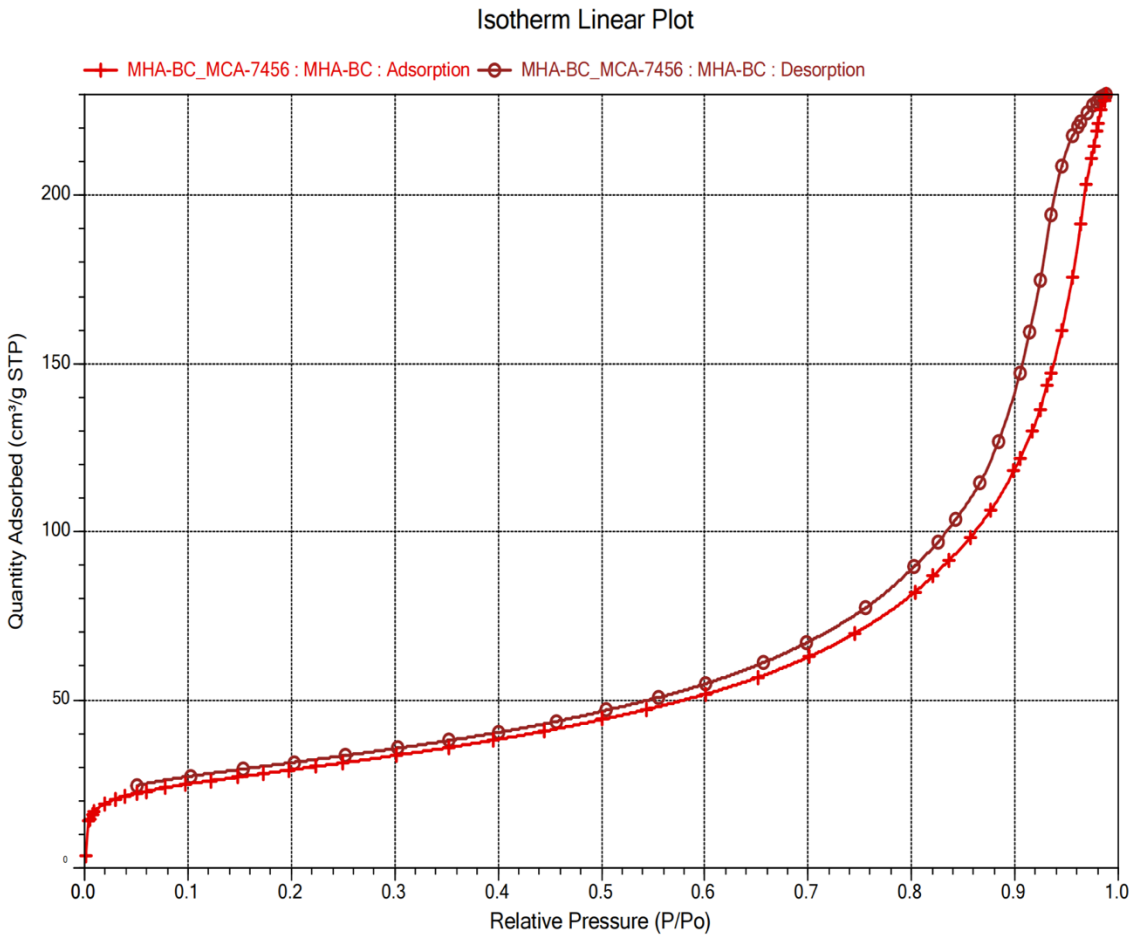


Figure D-1.0: MHA-Bc Isothermal Linear Plot

BET Report

BET surface area:	104.4699 ± 0.1145 m²/g
Slope:	0.041349 ± 0.000045 g/cm³ STP
Y-intercept:	0.000315 ± 0.000007 g/cm³ STP
C:	132.470768
Qm:	24.0018 cm³/g STP
Correlation coefficient:	0.9999952
Molecular cross-sectional area:	0.1620 nm²

Relative Pressure (P/Po)	Quantity Adsorbed (cm³/g STP)	1/[Q(Po/P - 1)]
0.050158703	22.1948	0.002379
0.059573877	22.8110	0.002777
0.078657598	23.8710	0.003576
0.098139695	24.8355	0.004382
0.122774104	25.9368	0.005396
0.147773162	26.9988	0.006422
0.172878749	28.0422	0.007454
0.198170931	29.0852	0.008497
0.223643610	30.1403	0.009558
0.249186991	31.2163	0.010632

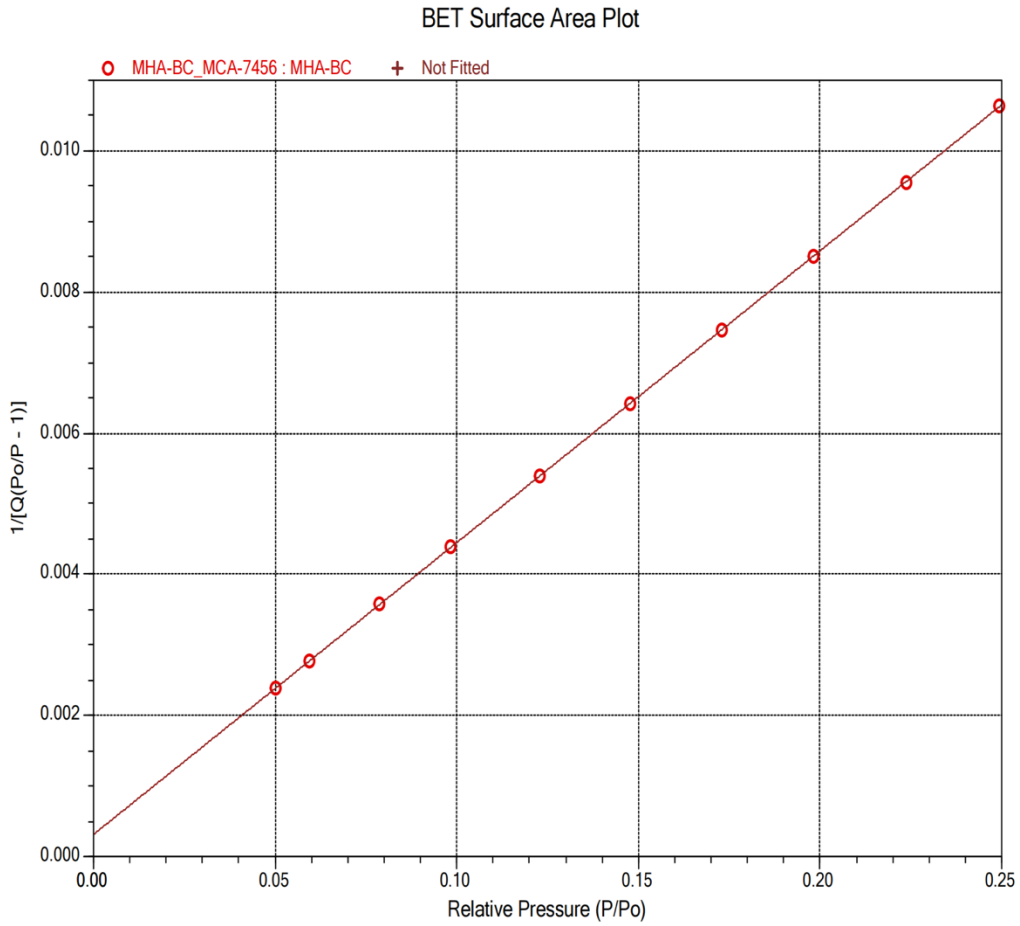


Figure D-1.0: MHA-Bc Surface Area Plot

t-Plot Report

Micropore volume:	0.003176 cm³/g
Micropore area:	8.3941 m²/g
External surface area:	96.0758 m²/g
Slope:	62.112606 ± 0.404767 cm³/g·nm STP
Y-intercept:	2.053578 ± 0.166671 cm³/g STP
Correlation coefficient:	0.999873
Surface area correction factor:	1.000
Density conversion factor:	0.0015468
Total surface area (BET):	104.4699 m²/g
Thickness range:	0.35000 to 0.50000 nm
Thickness equation:	Harkins and Jura

Thickness Curve

$$t = [\ 13.99 / (\ 0.034 - \log(P/Po)\ )\ ]\ ^{\wedge}\ 0.5$$

t-Plot Report - Data

Relative Pressure (P/Po)	Statistical Thickness (nm)	Quantity Adsorbed (cm³/g STP)	Fitted
0.050158703	0.32388	22.1948	
0.059573877	0.33335	22.8110	
0.078657598	0.35058	23.8710	
0.098139695	0.36639	24.8355	
0.122774104	0.38478	25.9368	
0.147773162	0.40230	26.9988	
0.172878749	0.41916	28.0422	
0.198170931	0.43570	29.0852	
0.223643610	0.45211	30.1403	
0.249186991	0.46847	31.2163	
0.302275277	0.50270	33.5168	
0.352378370	0.53598	35.8398	
0.395436857	0.56586	37.9990	
0.444332344	0.60180	40.6650	

t-Plot Report - Data

Relative Pressure (P/Po)	Statistical Thickness (nm)	Quantity Adsorbed (cm^3/g STP)	Fitted
0.501166026	0.64718	44.1468	
0.544175421	0.68487	47.1376	
0.600341976	0.73982	51.6845	
0.651118005	0.79682	56.6841	

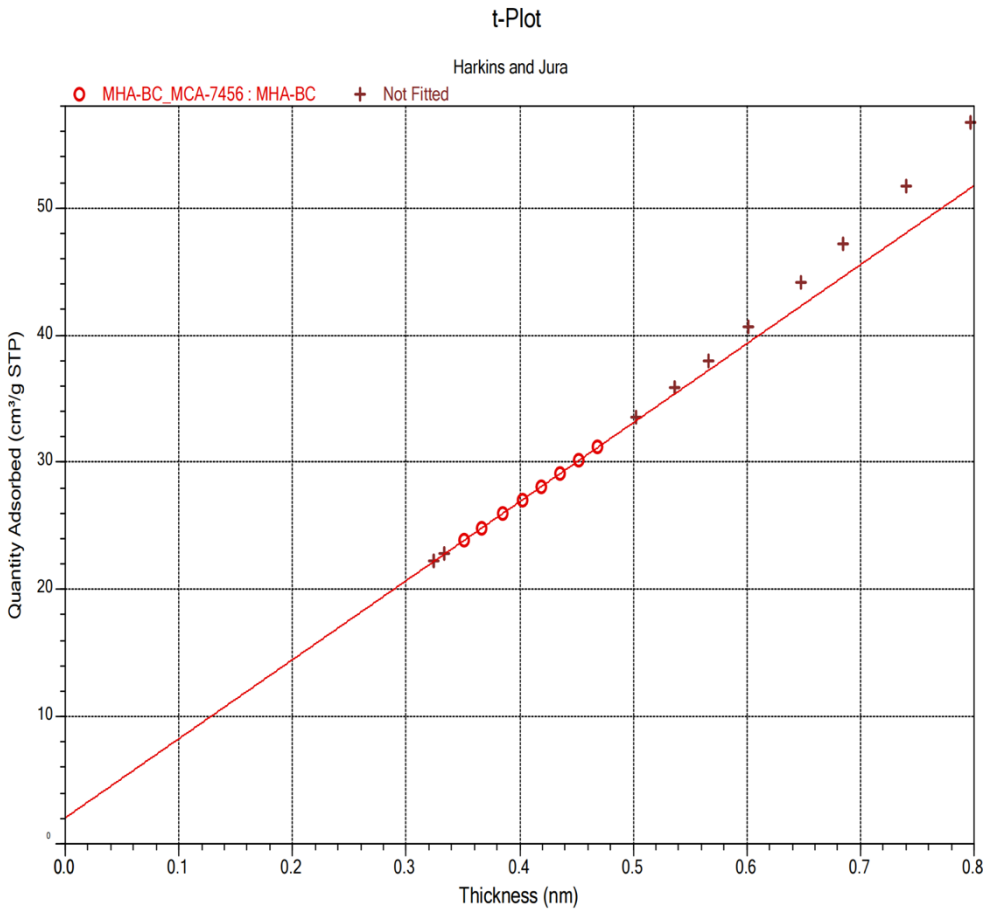


Figure D-1.1: MHA-Bc t- Plot

BJH Adsorption Pore Distribution Report

Faas Correction

Harkins and Jura

$t = [13.99 / (0.034 - \log(P/Po))]^{0.5}$

Width range:	2.0000 to 500.0000 nm
Adsorbate property factor:	0.95300 nm
Density conversion factor:	0.0015468
Fraction of pores open at both ends:	0.00

Pore Width Range (nm)	Average Width (nm)	Incremental Pore Volume (cm^3/g)	Cumulative Pore Volume (cm^3/g)	Incremental Pore Area (m^2/g)	Cumulative Pore Area (m^2/g)
172.6 - 143.3	155.2	0.002852	0.002852	0.074	0.074
143.3 - 119.7	129.3	0.004620	0.007473	0.143	0.216
119.7 - 103.4	110.3	0.006677	0.014150	0.242	0.458
103.4 - 96.3	99.6	0.003579	0.017729	0.144	0.602
96.3 - 82.6	88.4	0.007621	0.025350	0.345	0.947
82.6 - 75.9	79.0	0.006120	0.031471	0.310	1.257
75.9 - 64.7	69.4	0.013459	0.044930	0.776	2.033
64.7 - 55.4	59.3	0.020342	0.065272	1.372	3.405
55.4 - 44.9	49.0	0.027904	0.093177	2.278	5.684
44.9 - 37.0	40.2	0.027640	0.120817	2.752	8.436
37.0 - 31.3	33.7	0.023580	0.144396	2.802	11.238
31.3 - 29.7	30.4	0.006435	0.150831	0.846	12.084
29.7 - 27.0	28.2	0.013059	0.163890	1.854	13.938
27.0 - 24.7	25.7	0.012125	0.176015	1.886	15.824
24.7 - 21.7	23.0	0.015333	0.191347	2.671	18.495
21.7 - 20.6	21.1	0.007063	0.198410	1.339	19.835
20.6 - 16.8	18.3	0.022016	0.220426	4.809	24.643
16.8 - 14.8	15.6	0.015088	0.235515	3.857	28.500
14.8 - 12.9	13.7	0.013232	0.248746	3.862	32.362
12.9 - 11.8	12.3	0.008801	0.257547	2.858	35.220
11.8 - 10.8	11.3	0.009084	0.266631	3.228	38.449
10.8 - 8.3	9.2	0.023967	0.290598	10.403	48.851

Pore Width Range (nm)	Average Width (nm)	Incremental Pore Volume (cm^3/g)	Cumulative Pore Volume (cm^3/g)	Incremental Pore Area (m^2/g)	Cumulative Pore Area (m^2/g)
8.3 - 7.1	7.6	0.013013	0.303610	6.848	55.699
7.1 - 6.0	6.5	0.011043	0.314653	6.829	62.528
6.0 - 5.2	5.6	0.008556	0.323209	6.159	68.687
5.2 - 4.5	4.8	0.007318	0.330527	6.101	74.788
4.5 - 4.1	4.3	0.004501	0.335028	4.236	79.024
4.1 - 3.6	3.8	0.004913	0.339941	5.220	84.244
3.6 - 3.2	3.3	0.003437	0.343378	4.109	88.353
3.2 - 2.9	3.0	0.002545	0.345923	3.364	91.717
2.9 - 2.6	2.7	0.002404	0.348327	3.524	95.240
2.6 - 2.3	2.4	0.001964	0.350291	3.229	98.470
2.3 - 2.2	2.2	0.000775	0.351066	1.384	99.854
2.2 - 2.0	2.1	0.000630	0.351696	1.196	101.050

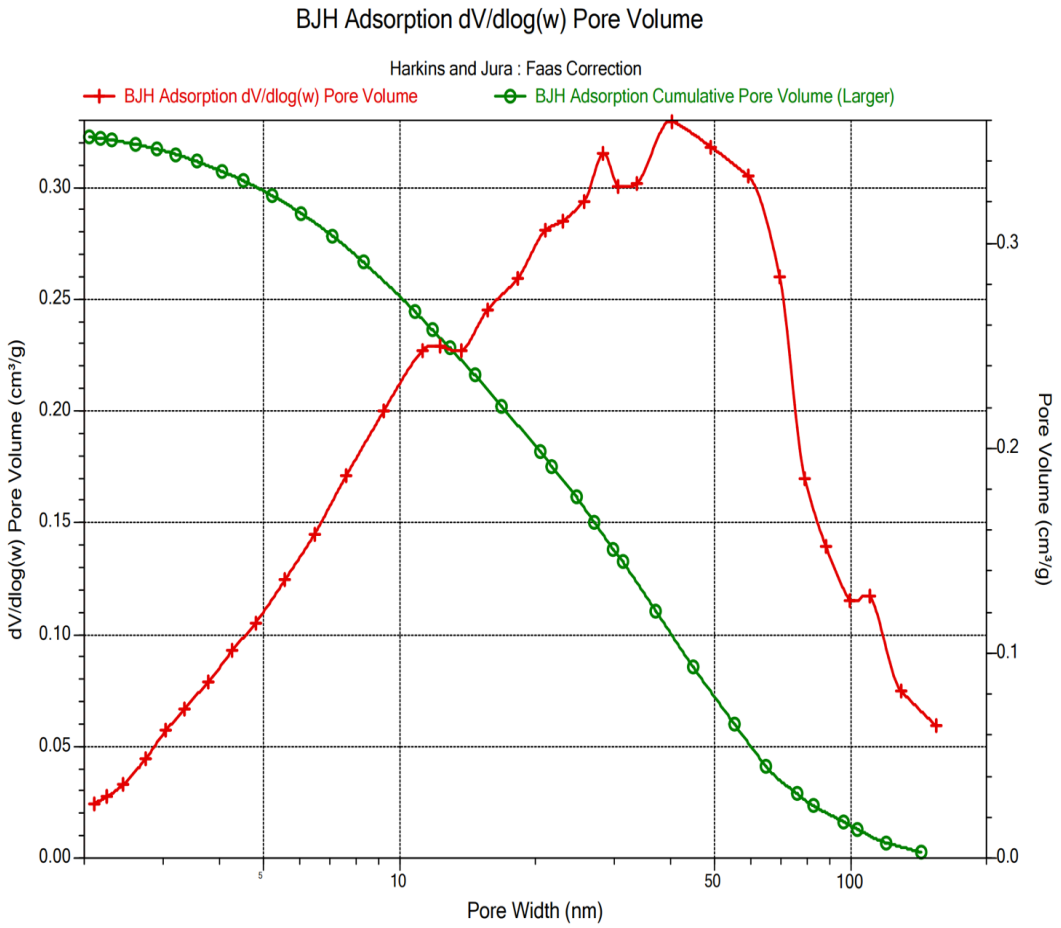


Figure D-1.2: MHA-Bc BJH Adsorption dV/dLog(w) Pore Volume

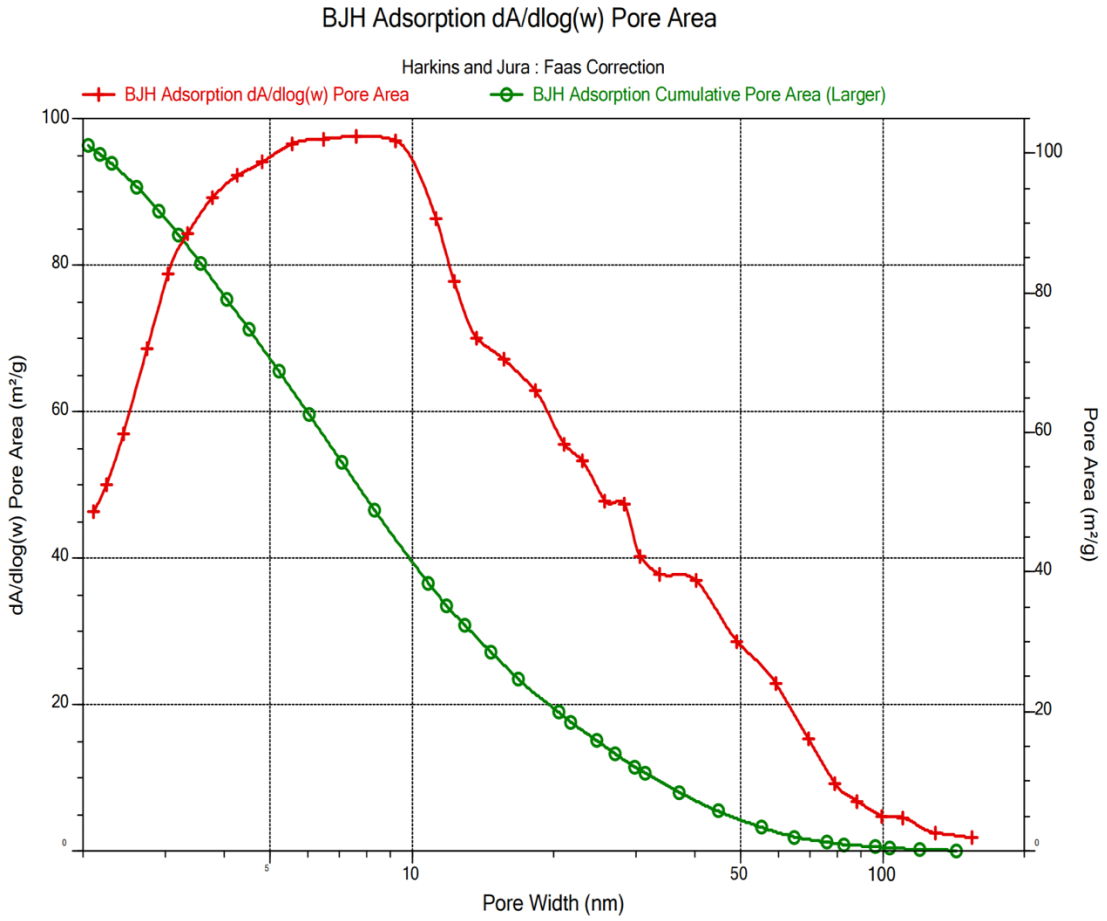


Figure D-1.3: MHA-Bc BJH Adsorption dA/dLog(w) Pore Area

BJH Desorption Pore Distribution Report

Faas Correction

Harkins and Jura

$t = [13.99 / (0.034 - \log(P/Po))] ^ {0.5}$

Width range:	1.7000 to 300.0000 nm
Adsorbate property factor:	0.95300 nm
Density conversion factor:	0.0015468
Fraction of pores open at both ends:	0.00

Pore Width Range (nm)	Average Width (nm)	Incremental Pore Volume (cm^3/g)	Cumulative Pore Volume (cm^3/g)	Incremental Pore Area (m^2/g)	Cumulative Pore Area (m^2/g)
172.6 - 137.2	150.8	0.000577	0.000577	0.015	0.015
137.2 - 118.4	126.4	0.000809	0.001385	0.026	0.041
118.4 - 105.7	111.3	0.000948	0.002334	0.034	0.075
105.7 - 92.9	98.5	0.001368	0.003702	0.056	0.131
92.9 - 81.2	86.3	0.001662	0.005365	0.077	0.208
81.2 - 65.2	71.4	0.003635	0.008999	0.204	0.411
65.2 - 54.7	59.0	0.004441	0.013440	0.301	0.712
54.7 - 50.9	52.7	0.002494	0.015934	0.189	0.902
50.9 - 45.3	47.7	0.005252	0.021185	0.440	1.342
45.3 - 37.0	40.3	0.015727	0.036912	1.562	2.904
37.0 - 31.5	33.8	0.026756	0.063668	3.165	6.069
31.5 - 27.4	29.1	0.037066	0.100734	5.088	11.157
27.4 - 24.2	25.6	0.029618	0.130352	4.636	15.793
24.2 - 21.9	22.9	0.022856	0.153208	3.987	19.779
21.9 - 18.0	19.6	0.039510	0.192718	8.083	27.862
18.0 - 15.6	16.6	0.024529	0.217247	5.896	33.758
15.6 - 13.4	14.4	0.020638	0.237885	5.749	39.507
13.4 - 12.1	12.7	0.012679	0.250563	3.986	43.493
12.1 - 10.8	11.4	0.014113	0.264677	4.969	48.462
10.8 - 8.7	9.5	0.023299	0.287976	9.835	58.297
8.7 - 7.0	7.7	0.018852	0.306829	9.853	68.150
7.0 - 6.1	6.5	0.010280	0.317109	6.320	74.470

Pore Width Range (nm)	Average Width (nm)	Incremental Pore Volume (cm^3/g)	Cumulative Pore Volume (cm^3/g)	Incremental Pore Area (m^2/g)	Cumulative Pore Area (m^2/g)
6.1 - 5.2	5.6	0.010365	0.327474	7.414	81.884
5.2 - 4.6	4.9	0.006022	0.333497	4.929	86.813
4.6 - 4.1	4.3	0.005109	0.338606	4.732	91.545
4.1 - 3.6	3.8	0.004235	0.342841	4.415	95.960
3.6 - 3.2	3.4	0.003547	0.346388	4.171	100.131
3.2 - 2.9	3.0	0.001923	0.348311	2.535	102.666
2.9 - 2.6	2.7	0.001441	0.349752	2.115	104.780
2.6 - 2.3	2.4	0.000958	0.350710	1.571	106.351
2.3 - 2.1	2.2	0.000418	0.351128	0.768	107.119

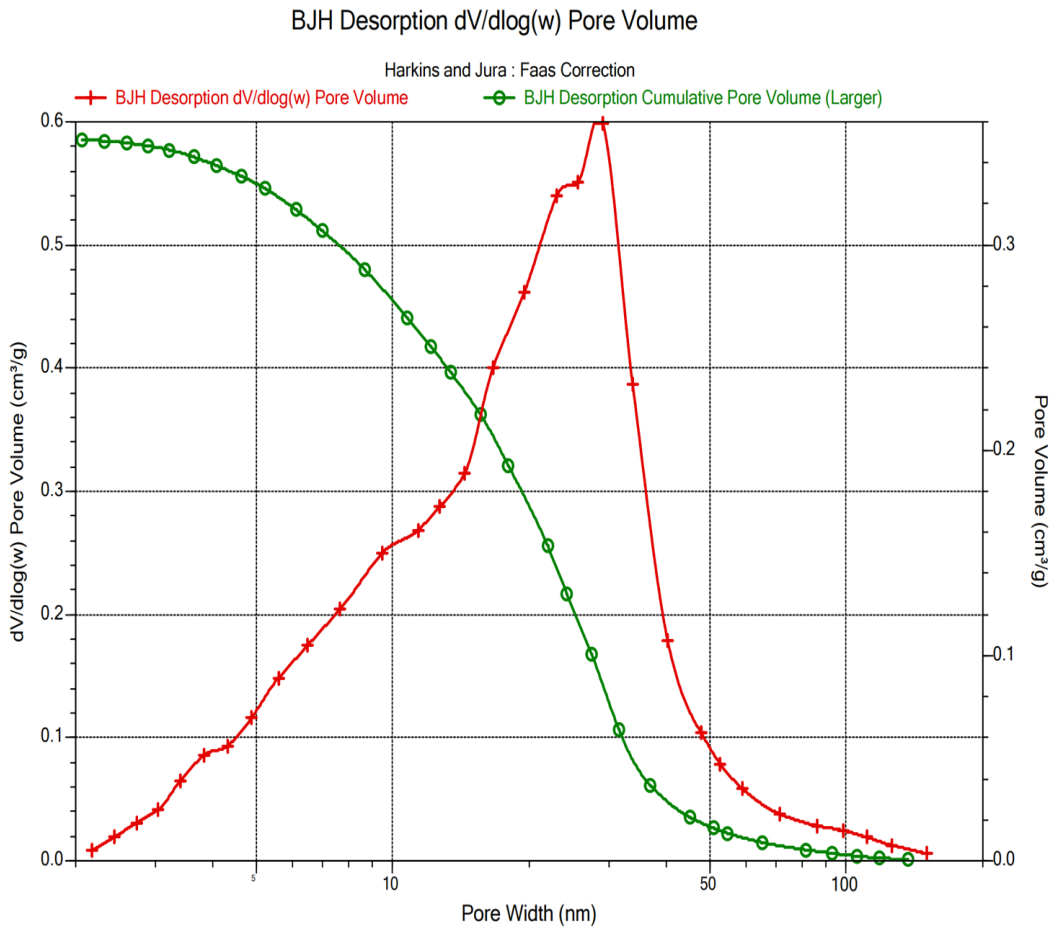


Figure D-1.4: MHA-Bc BJH Desorption dV/dLog(w) Pore Volume

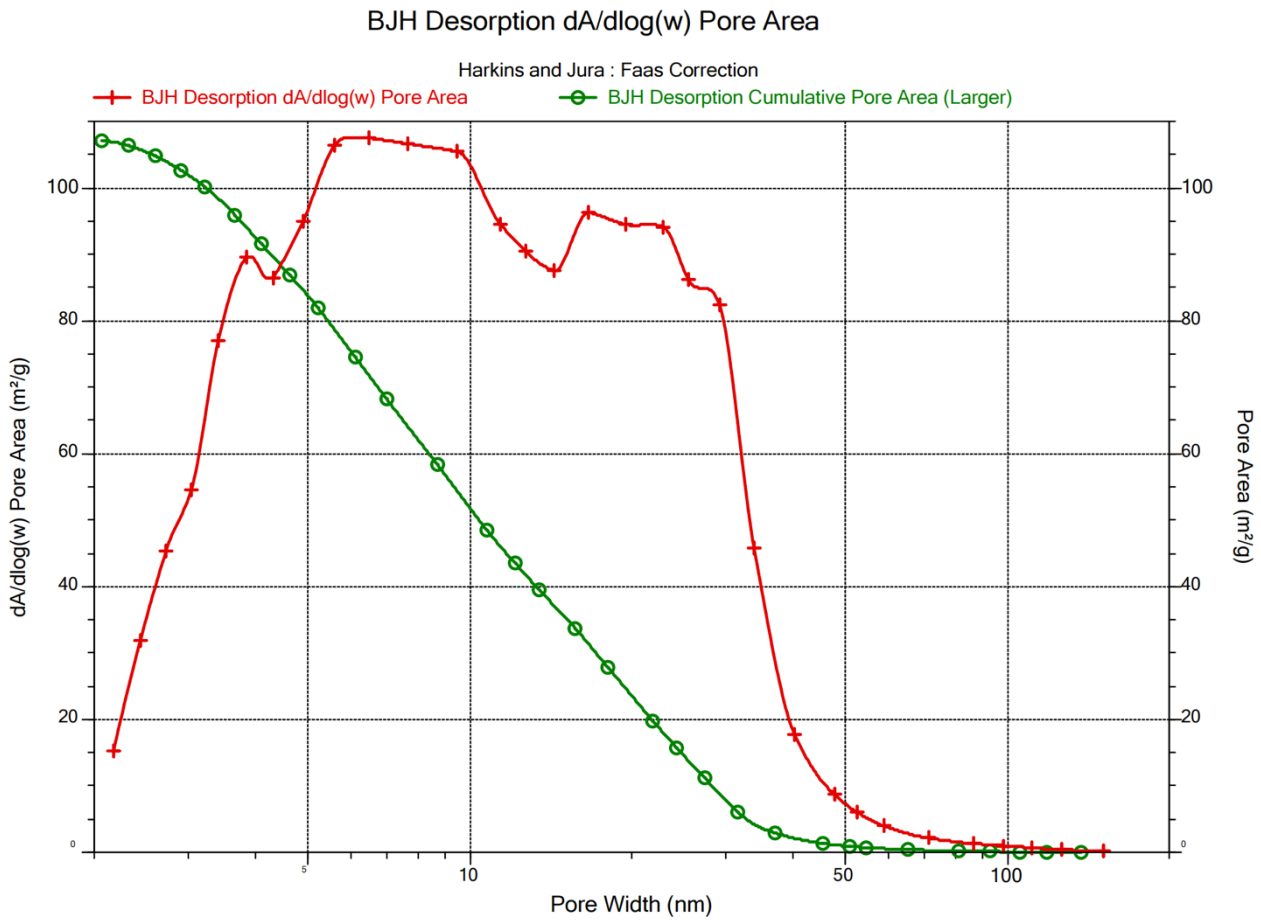


Figure D-1.5: MHA-Bc BJH Desorption dV/dLog(w) Pore Area

HYDROXYAPPATIE -BIOCHAR (HA-Bc) SUMMARY REPORT

Surface Area	
BET Surface Area:	141.1385 m²/g
Pore Volume	
Single point adsorption total pore volume of pores less than 320.6222 nm width at P/Po = 0.994000000:	0.216671 cm³/g
BJH Adsorption cumulative volume of pores between 2.0000 nm and 500.0000 nm width:	0.179726 cm³/g
BJH Desorption cumulative volume of pores between 1.7000 nm and 300.0000 nm width:	0.173670 cm³/g
Pore Size	
Adsorption average pore diameter (4V/A by BET):	6.1407 nm
Desorption average pore diameter (4V/A by BET):	5.2420 nm
BJH Adsorption average pore width (4V/A):	10.5743 nm
BJH Desorption average pore width (4V/A):	9.6275 nm

BET Report of Hydroxyapatite Biochar

BET Report

BET surface area:	141.2850 ± 0.2010 m²/g
Slope:	0.030472 ± 0.000043 g/cm³ STP
Y-intercept:	0.000335 ± 0.000007 g/cm³ STP
C:	91.865157
Qm:	32.4601 cm³/g STP
Correlation coefficient:	0.9999929
Molecular cross-sectional area:	0.1620 nm²

Relative Pressure (P/Po)	Quantity Adsorbed (cm³/g STP)	1/[Q(Po/P - 1)]
0.058734997	29.5670	0.002110
0.076902838	31.0916	0.002679
0.097780060	32.6097	0.003323
0.122060961	34.2097	0.004064
0.146931347	35.7481	0.004818
0.172270484	37.2680	0.005585
0.197224496	38.7472	0.006341
0.222577665	40.2543	0.007112
0.248118555	41.7902	0.007897

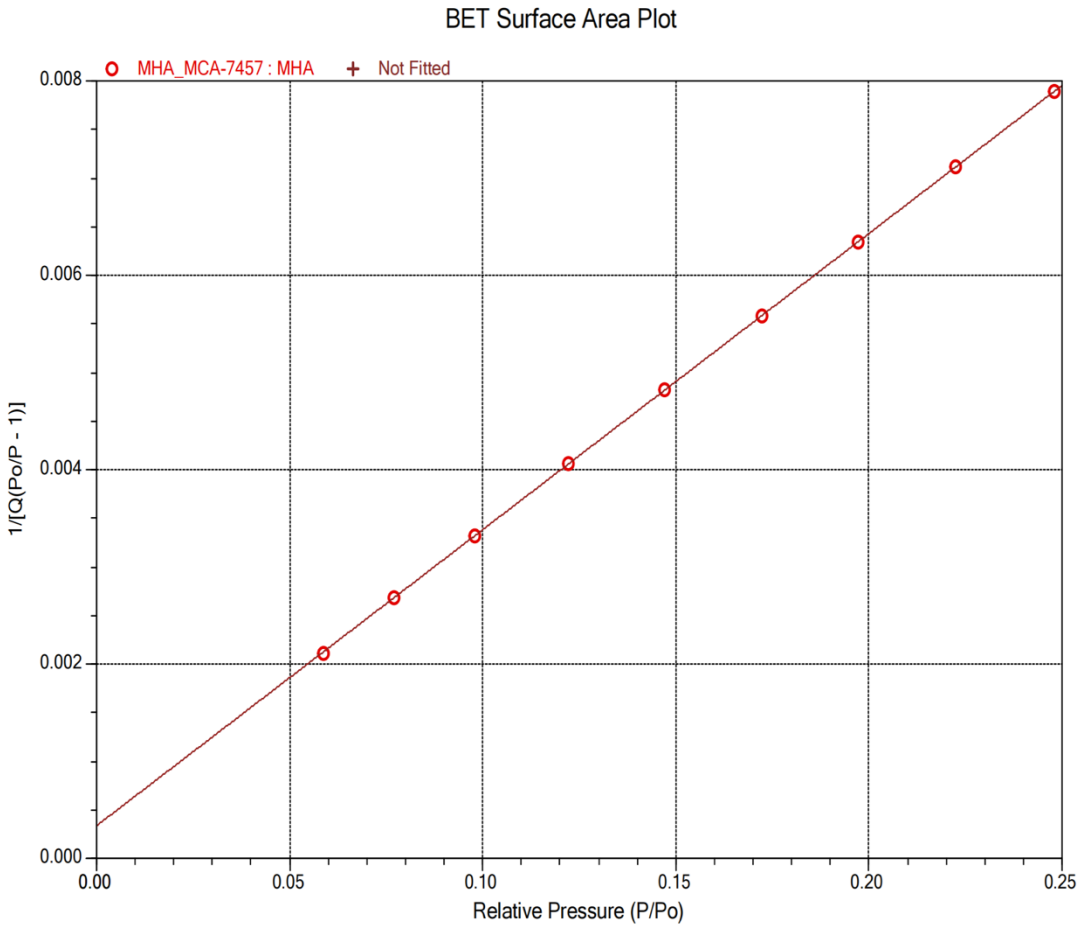


Figure D-2.0: HA-Bc Surface Area Plot

t-Plot Report

Micropore volume:	-0.000691 cm³/g
Micropore area:	
External surface area:	139.4706 m²/g
Slope:	90.167173 ± 0.488887 cm³/g·nm STP
Y-intercept:	-0.446499 ± 0.204962 cm³/g STP
Correlation coefficient:	0.999927
Surface area correction factor:	1.000
Density conversion factor:	0.0015468
Total surface area (BET):	141.2850 m²/g
Thickness range:	0.35000 to 0.50000 nm
Thickness equation:	Harkins and Jura

Thickness Curve

$$t = [\ 13.99 / (\ 0.034 - \log(P/Po)\ )\ ]^{0.5}$$

t-Plot Report - Data

Relative Pressure (P/Po)	Statistical Thickness (nm)	Quantity Adsorbed (cm³/g STP)	Fitted
0.058734997	0.33254	29.5670	
0.076902838	0.34908	31.0916	
0.097780060	0.36611	32.6097	
0.122060961	0.38427	34.2097	
0.146931347	0.40172	35.7481	
0.172270484	0.41876	37.2680	
0.197224496	0.43509	38.7472	
0.222577665	0.45142	40.2543	
0.248118555	0.46778	41.7902	
0.300495834	0.50154	45.0435	
0.344648278	0.53076	47.9439	
0.393830462	0.56472	51.4062	
0.450995562	0.60690	55.8100	
0.493658539	0.64092	59.4950	

t-Plot Report - Data

Relative Pressure (P/Po)	Statistical Thickness (nm)	Quantity Adsorbed (cm^3/g STP)	Fitted
0.551514601	0.69165	65.0620	
0.601158466	0.74068	70.6231	
0.646915576	0.79179	76.7023	
0.694793611	0.85329	84.3826	

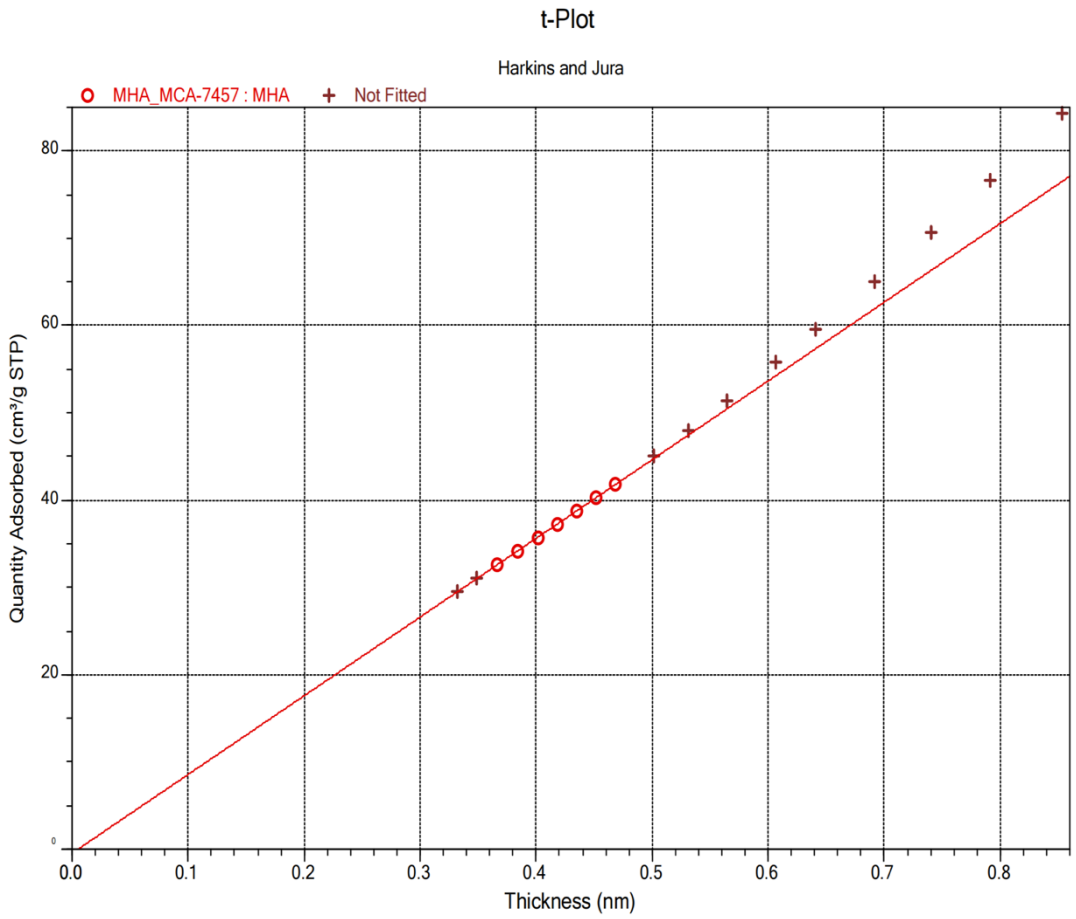


Figure D-2.1: HA-Bc Surface Area Plot

BJH Adsorption Pore Distribution Report

Faas Correction

Harkins and Jura

t = [13.99 / (0.034 - log(P/Po))] ^ 0.5

Width range:	2.0000 to 500.0000 nm
Adsorbate property factor:	0.95300 nm
Density conversion factor:	0.0015468
Fraction of pores open at both ends:	0.00

Pore Width Range (nm)	Average Width (nm)	Incremental Pore Volume (cm^3/g)	Cumulative Pore Volume (cm^3/g)	Incremental Pore Area (m^2/g)	Cumulative Pore Area (m^2/g)
170.9 - 141.8	153.6	0.004242	0.004242	0.110	0.110
141.8 - 120.7	129.5	0.005764	0.010005	0.178	0.288
120.7 - 105.6	112.1	0.007491	0.017496	0.267	0.556
105.6 - 92.7	98.3	0.009400	0.026896	0.383	0.938
92.7 - 83.8	87.8	0.010067	0.036963	0.459	1.397
83.8 - 74.7	78.7	0.013798	0.050761	0.701	2.098
74.7 - 64.2	68.7	0.028216	0.078977	1.643	3.741
64.2 - 57.8	60.7	0.034422	0.113399	2.269	6.011
57.8 - 44.1	49.1	0.058633	0.172033	4.779	10.789
44.1 - 35.9	39.1	0.054327	0.226360	5.557	16.347
35.9 - 31.1	33.1	0.030867	0.257227	3.729	20.076
31.1 - 28.8	29.8	0.019148	0.276375	2.568	22.643
28.8 - 27.4	28.0	0.012988	0.289364	1.854	24.497
27.4 - 24.7	25.9	0.024758	0.314121	3.826	28.323
24.7 - 21.6	22.9	0.026712	0.340833	4.666	32.989
21.6 - 20.3	20.9	0.013915	0.354748	2.663	35.652
20.3 - 17.1	18.4	0.033551	0.388299	7.284	42.936
17.1 - 14.6	15.7	0.027602	0.415901	7.052	49.988
14.6 - 12.8	13.6	0.021713	0.437614	6.406	56.395
12.8 - 11.5	12.1	0.015352	0.452966	5.079	61.474
11.5 - 10.9	11.2	0.007718	0.460684	2.754	64.228
10.9 - 8.5	9.4	0.031739	0.492423	13.566	77.793

Pore Width Range (nm)	Average Width (nm)	Incremental Pore Volume (cm^3/g)	Cumulative Pore Volume (cm^3/g)	Incremental Pore Area (m^2/g)	Cumulative Pore Area (m^2/g)
8.5 - 7.0	7.6	0.019748	0.512171	10.437	88.231
7.0 - 6.0	6.4	0.012686	0.524857	7.919	96.149
6.0 - 5.3	5.6	0.009580	0.534438	6.867	103.016
5.3 - 4.6	4.9	0.008265	0.542703	6.746	109.762
4.6 - 4.0	4.3	0.007808	0.550511	7.302	117.065
4.0 - 3.7	3.8	0.004933	0.555445	5.172	122.237
3.7 - 3.2	3.4	0.005379	0.560824	6.327	128.563
3.2 - 2.9	3.0	0.003845	0.564669	5.068	133.631
2.9 - 2.6	2.7	0.002855	0.567524	4.157	137.788
2.6 - 2.3	2.5	0.002715	0.570239	4.401	142.189
2.3 - 2.2	2.3	0.001049	0.571288	1.844	144.033
2.2 - 2.1	2.1	0.000873	0.572161	1.628	145.660
2.1 - 2.0	2.0	0.000691	0.572852	1.368	147.028

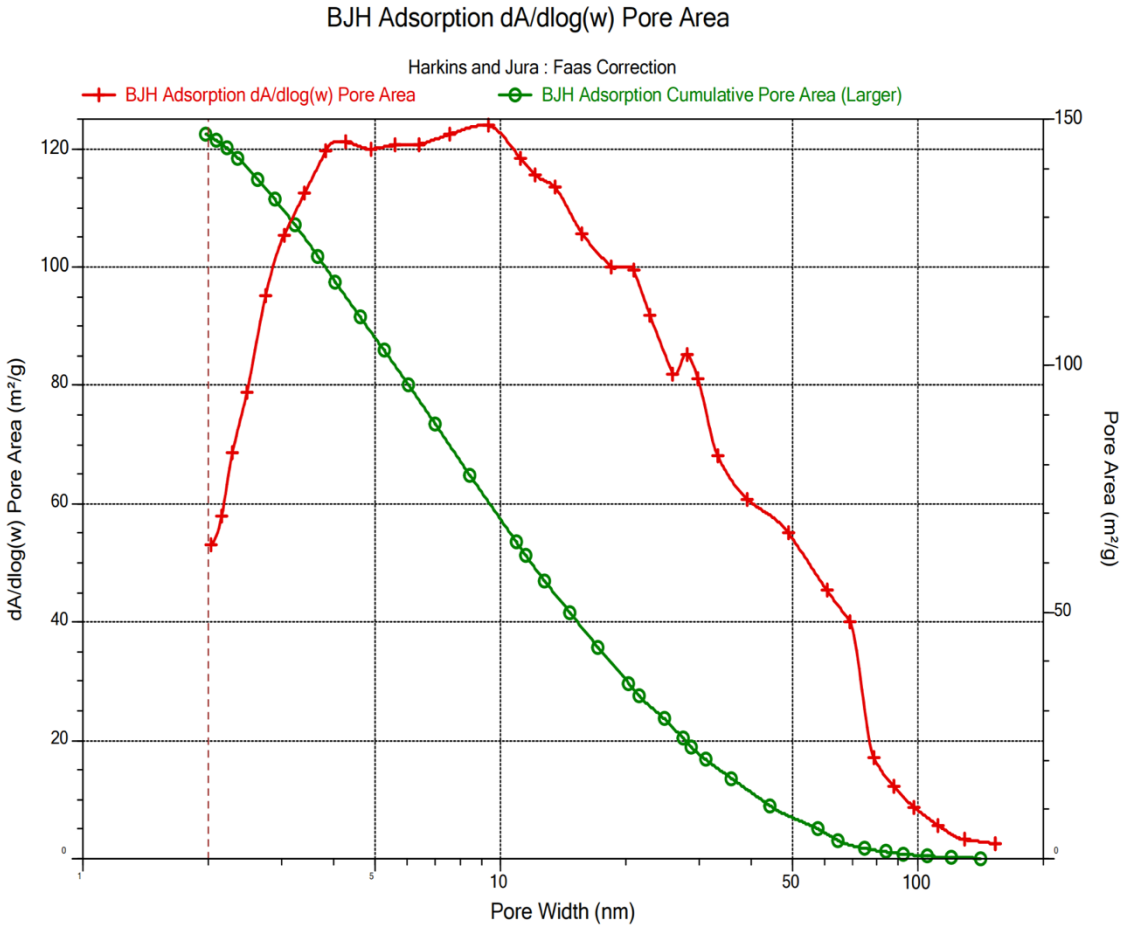


Figure D-2.2: MHA-BJH Adsorption dV/dlog(w) pore volume

BJH Desorption Pore Distribution Report

Faas Correction

Harkins and Jura

$t = [13.99 / (0.034 - \log(P/Po))]^{0.5}$

Width range:	1.7000 to 300.0000 nm
Adsorbate property factor:	0.95300 nm
Density conversion factor:	0.0015468
Fraction of pores open at both ends:	0.00

Pore Width Range (nm)	Average Width (nm)	Incremental Pore Volume (cm^3/g)	Cumulative Pore Volume (cm^3/g)	Incremental Pore Area (m^2/g)	Cumulative Pore Area (m^2/g)
170.9 - 139.5	152.0	0.000450	0.000450	0.012	0.012
139.5 - 124.3	131.0	0.000640	0.001091	0.020	0.031
124.3 - 113.5	118.4	0.000759	0.001850	0.026	0.057
113.5 - 100.5	106.2	0.001143	0.002993	0.043	0.100
100.5 - 80.8	88.4	0.002716	0.005710	0.123	0.223
80.8 - 67.3	72.7	0.003581	0.009291	0.197	0.420
67.3 - 58.6	62.3	0.004090	0.013381	0.263	0.683
58.6 - 50.1	53.7	0.006571	0.019951	0.490	1.172
50.1 - 45.9	47.8	0.005754	0.025705	0.481	1.654
45.9 - 37.1	40.5	0.022578	0.048283	2.230	3.883
37.1 - 32.0	34.2	0.037478	0.085761	4.390	8.273
32.0 - 27.8	29.6	0.062640	0.148401	8.464	16.736
27.8 - 24.1	25.6	0.070034	0.218435	10.925	27.661
24.1 - 21.8	22.8	0.045767	0.264202	8.018	35.679
21.8 - 18.3	19.7	0.067892	0.332094	13.754	49.433
18.3 - 15.6	16.7	0.051299	0.383394	12.265	61.699
15.6 - 13.7	14.5	0.033082	0.416475	9.134	70.833
13.7 - 11.8	12.6	0.025606	0.442081	8.134	78.967
11.8 - 10.8	11.3	0.015913	0.457994	5.648	84.615
10.8 - 8.8	9.6	0.038621	0.496614	16.076	100.691
8.8 - 7.1	7.8	0.026593	0.523207	13.675	114.365
7.1 - 6.1	6.5	0.012771	0.535978	7.825	122.190

Pore Width Range (nm)	Average Width (nm)	Incremental Pore Volume (cm^3/g)	Cumulative Pore Volume (cm^3/g)	Incremental Pore Area (m^2/g)	Cumulative Pore Area (m^2/g)
6.1 - 5.2	5.6	0.010315	0.546293	7.369	129.559
5.2 - 4.6	4.9	0.006876	0.553169	5.630	135.189
4.6 - 4.1	4.3	0.005579	0.558748	5.187	140.376
4.1 - 3.6	3.8	0.004670	0.563418	4.902	145.278
3.6 - 3.2	3.4	0.003862	0.567280	4.576	149.853
3.2 - 2.9	3.0	0.002087	0.569368	2.764	152.618
2.9 - 2.6	2.7	0.001604	0.570972	2.360	154.977
2.6 - 2.3	2.4	0.001028	0.572000	1.692	156.669
2.3 - 2.0	2.2	0.000423	0.572423	0.785	157.455

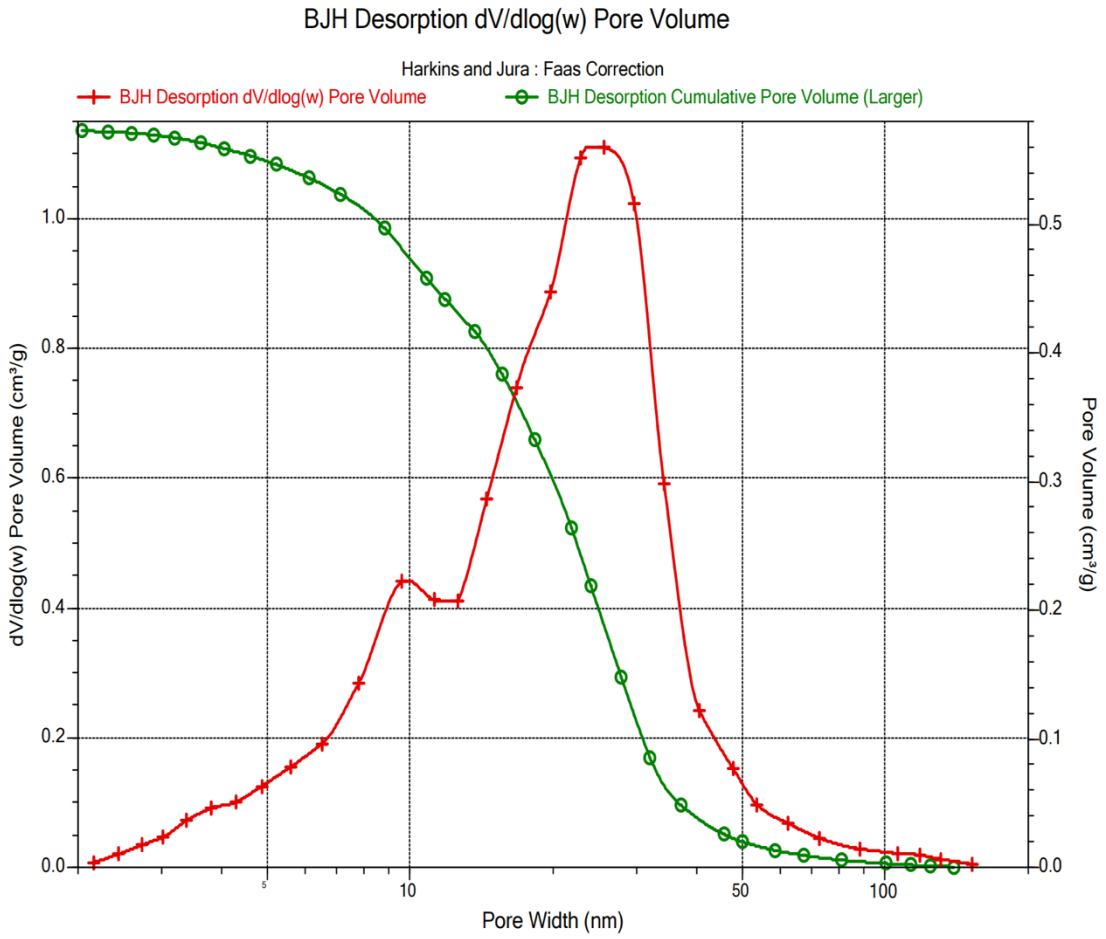


Figure D-2.3: MHA-BJH Desorption dV/dlog(w) pore volume

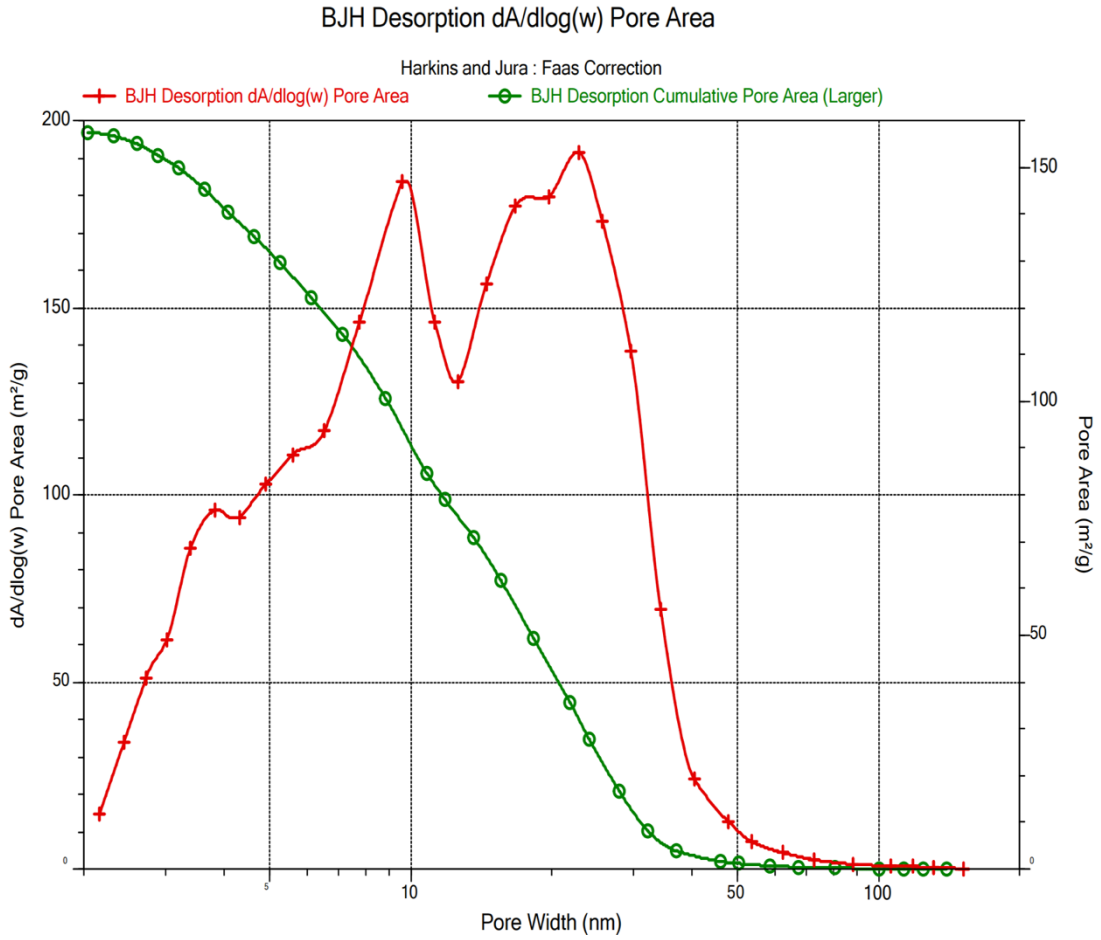


Figure D-2.4: MHA-BJH Desorption dV/dlog(w) pore area

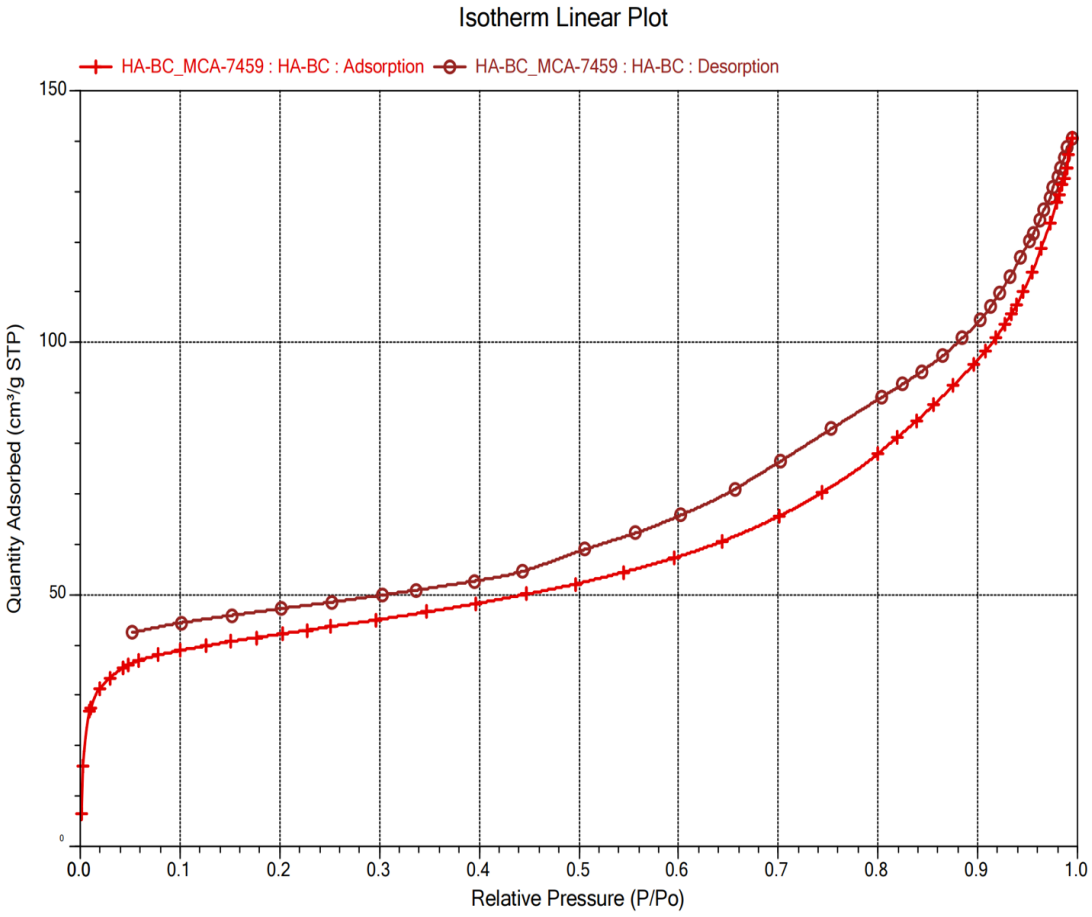
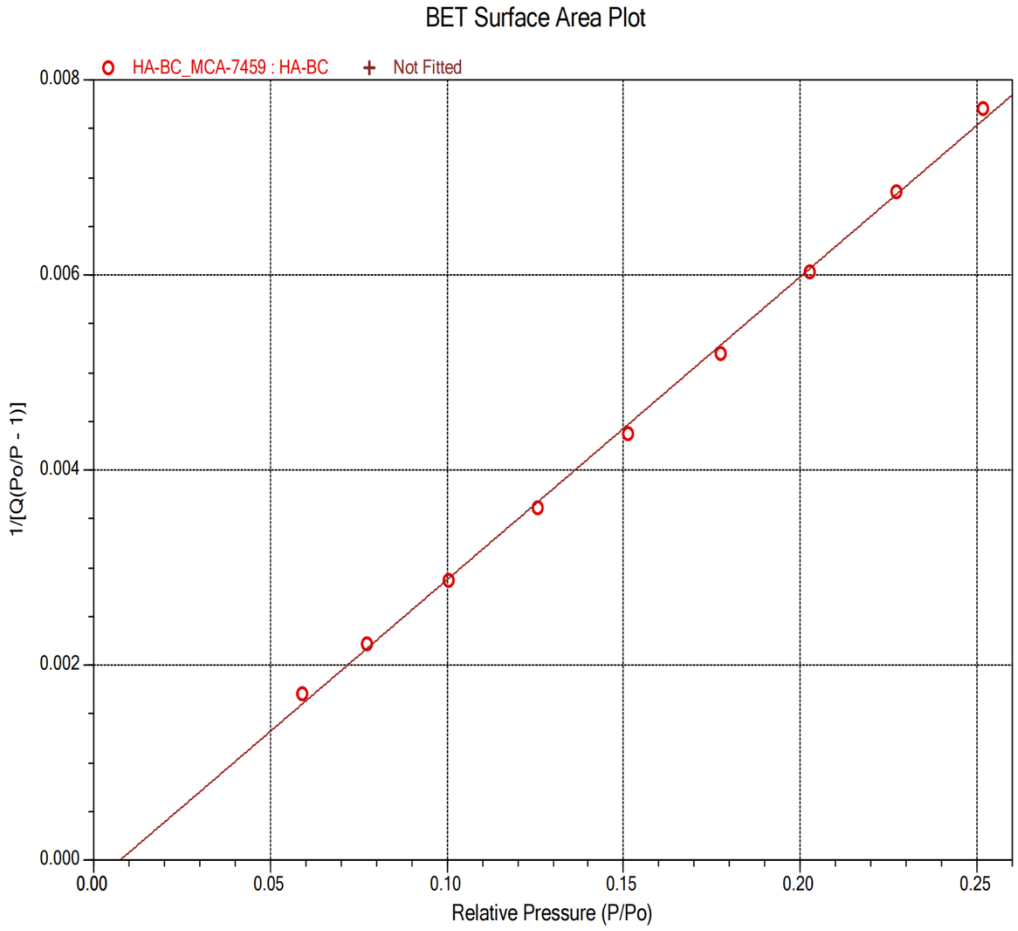


Figure.D-2.5: HA-Bc Isothermal Linear Plot



FigureD-2.6: HA-Bc surface Area Plot

t-Plot Report

Micropore volume:	0.033984 cm³/g
Micropore area:	69.8009 m²/g
External surface area:	71.3376 m²/g
Slope:	46.119474 ± 0.324207 cm³/g·nm STP
Y-intercept:	21.970775 ± 0.140211 cm³/g STP
Correlation coefficient:	0.999852
Surface area correction factor:	1.000
Density conversion factor:	0.0015468
Total surface area (BET):	141.1385 m²/g
Thickness range:	0.35000 to 0.50000 nm
Thickness equation:	Harkins and Jura

Thickness Curve

$$t = [\ 13.99 / (\ 0.034 - \log(P/Po)\ )\ ]\ ^{\wedge}\ 0.5$$

t-Plot Report - Data

Relative Pressure (P/Po)	Statistical Thickness (nm)	Quantity Adsorbed (cm³/g STP)	Fitted
0.059008220	0.33281	36.9168	
0.077487716	0.34958	37.9513	
0.100568593	0.36827	38.8961	
0.125744561	0.38692	39.8148	
0.151222353	0.40465	40.6858	
0.177396134	0.42214	41.4735	
0.202846920	0.43872	42.2191	
0.227369410	0.45449	42.9184	
0.251623079	0.47003	43.6454	
0.296616405	0.49902	44.9598	
0.347275296	0.53253	46.5192	
0.397194412	0.56711	48.1994	
0.446980704	0.60382	50.0549	
0.496777100	0.64351	52.1021	

t-Plot Report - Data

Relative Pressure (P/Po)	Statistical Thickness (nm)	Quantity Adsorbed (cm^3/g STP)	Fitted
0.545321193	0.68592	54.4540	
0.595569052	0.73486	57.2587	
0.643645420	0.78791	60.5651	

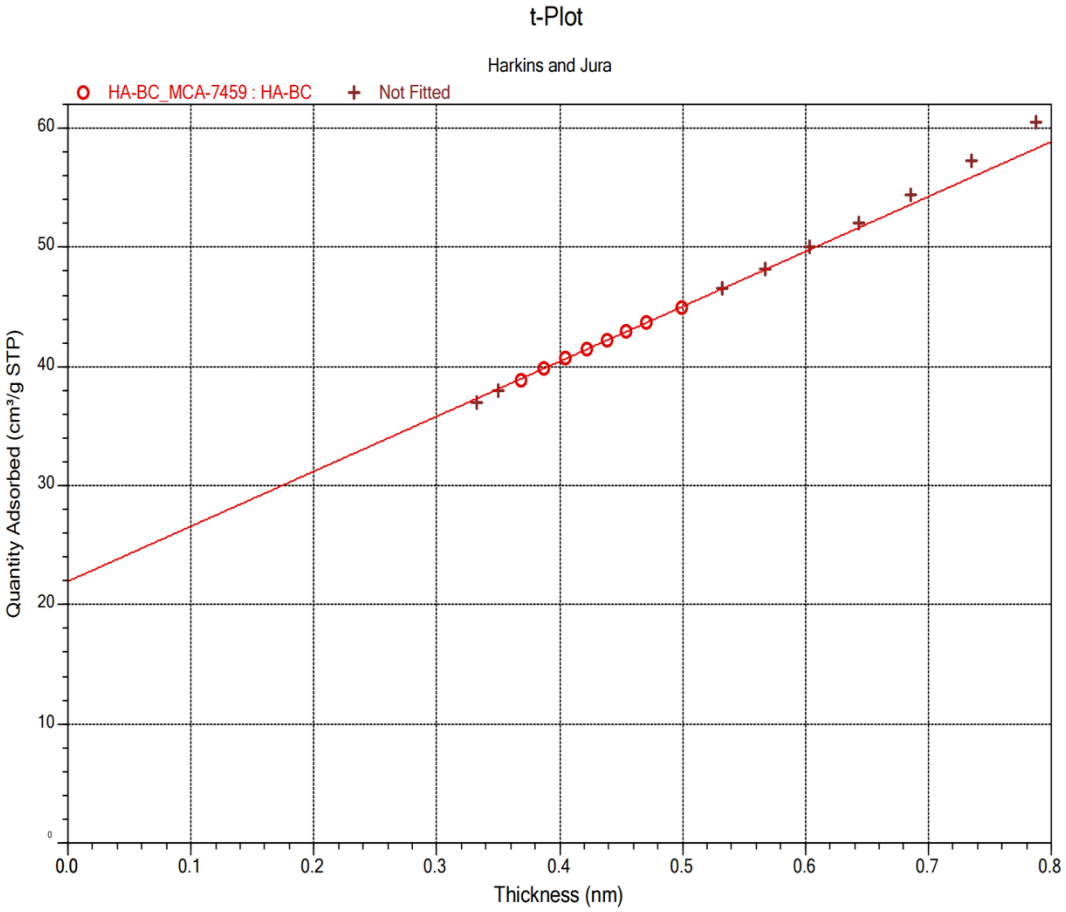


Figure D-2.7: HA-Bc t-Plot

BJH Adsorption Pore Distribution Report

Faas Correction

Harkins and Jura

t = [13.99 / (0.034 - log(P/Po))] ^ 0.5

Width range:	2.0000 to 500.0000 nm
Adsorbate property factor:	0.95300 nm
Density conversion factor:	0.0015468
Fraction of pores open at both ends:	0.00

Pore Width Range (nm)	Average Width (nm)	Incremental Pore Volume (cm³/g)	Cumulative Pore Volume (cm³/g)	Incremental Pore Area (m²/g)	Cumulative Pore Area (m²/g)
349.3 - 224.7	260.9	0.005265	0.005265	0.081	0.081
224.7 - 176.0	194.4	0.004250	0.009515	0.087	0.168
176.0 - 145.8	158.0	0.003265	0.012780	0.083	0.251
145.8 - 129.6	136.7	0.001898	0.014678	0.056	0.306
129.6 - 106.6	115.8	0.003492	0.018171	0.121	0.427
106.6 - 95.0	100.1	0.002661	0.020832	0.106	0.533
95.0 - 71.7	80.0	0.006973	0.027804	0.348	0.882
71.7 - 55.6	61.6	0.008319	0.036123	0.540	1.422
55.6 - 43.9	48.3	0.008619	0.044742	0.713	2.136
43.9 - 37.3	40.0	0.006631	0.051373	0.663	2.798
37.3 - 33.3	35.1	0.004859	0.056232	0.554	3.352
33.3 - 30.8	31.9	0.003207	0.059439	0.402	3.754
30.8 - 28.3	29.4	0.003585	0.063024	0.488	4.241
28.3 - 25.0	26.4	0.005187	0.068211	0.785	5.026
25.0 - 22.3	23.5	0.004950	0.073161	0.842	5.868
22.3 - 20.0	21.1	0.004870	0.078031	0.925	6.793
20.0 - 16.8	18.1	0.008248	0.086279	1.820	8.613
16.8 - 14.6	15.6	0.007441	0.093721	1.913	10.526
14.6 - 13.1	13.8	0.006341	0.100061	1.844	12.370
13.1 - 11.7	12.3	0.006636	0.106698	2.157	14.527
11.7 - 10.6	11.1	0.006750	0.113448	2.434	16.961
10.6 - 8.3	9.1	0.016225	0.129673	7.110	24.071

Pore Width Range (nm)	Average Width (nm)	Incremental Pore Volume (cm³/g)	Cumulative Pore Volume (cm³/g)	Incremental Pore Area (m²/g)	Cumulative Pore Area (m²/g)
8.3 - 7.1	7.6	0.009803	0.139476	5.167	29.239
7.1 - 5.9	6.4	0.010365	0.149841	6.503	35.742
5.9 - 5.1	5.5	0.006540	0.156381	4.786	40.528
5.1 - 4.5	4.8	0.005220	0.161600	4.365	44.893
4.5 - 4.0	4.2	0.004191	0.165792	3.965	48.857
4.0 - 3.6	3.8	0.003323	0.169114	3.532	52.389
3.6 - 3.2	3.4	0.002852	0.171966	3.393	55.782
3.2 - 2.9	3.0	0.002342	0.174308	3.111	58.893
2.9 - 2.6	2.7	0.001902	0.176210	2.821	61.714
2.6 - 2.3	2.4	0.001411	0.177621	2.324	64.038
2.3 - 2.2	2.3	0.000814	0.178435	1.445	65.483
2.2 - 2.1	2.1	0.000622	0.179057	1.168	66.650
2.1 - 1.9	2.0	0.000669	0.179726	1.335	67.986

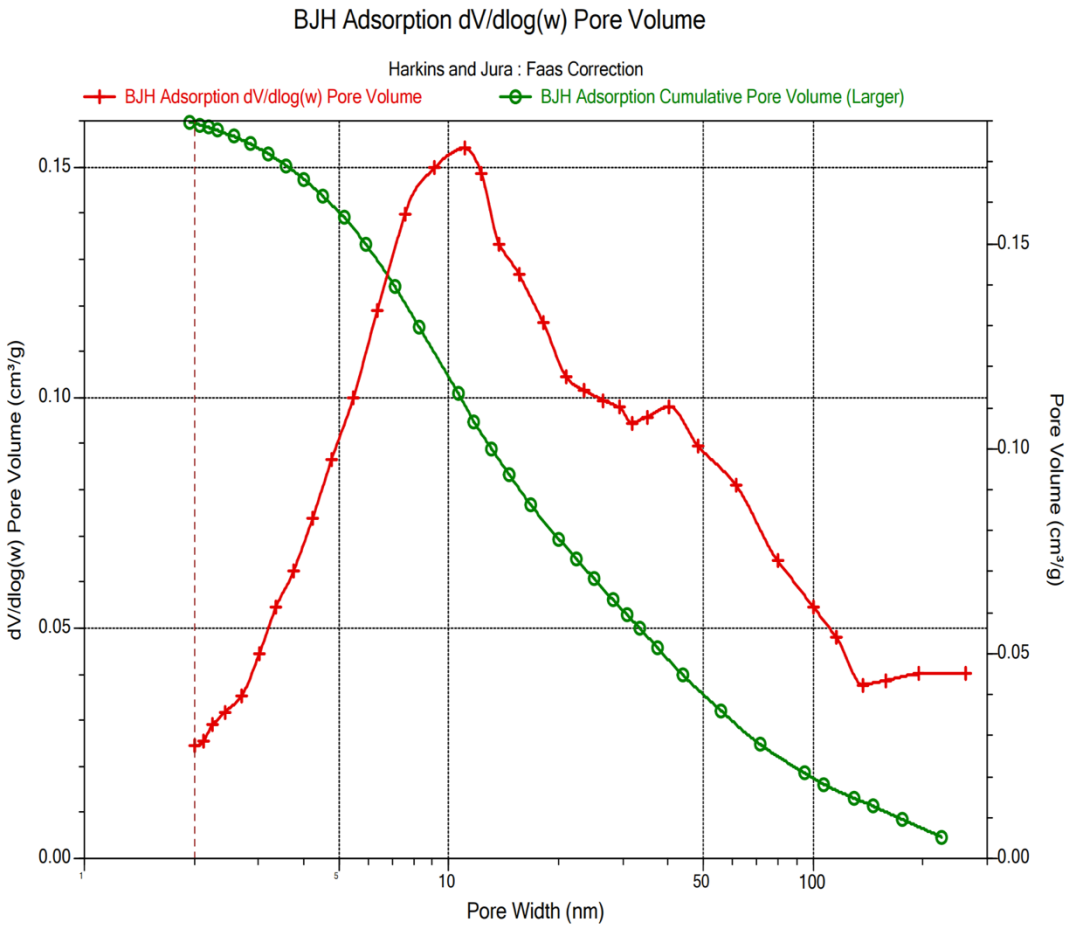


Figure D-2.8: HA-Bc BJH Adsorption dV/dLog (w) Pore Volume

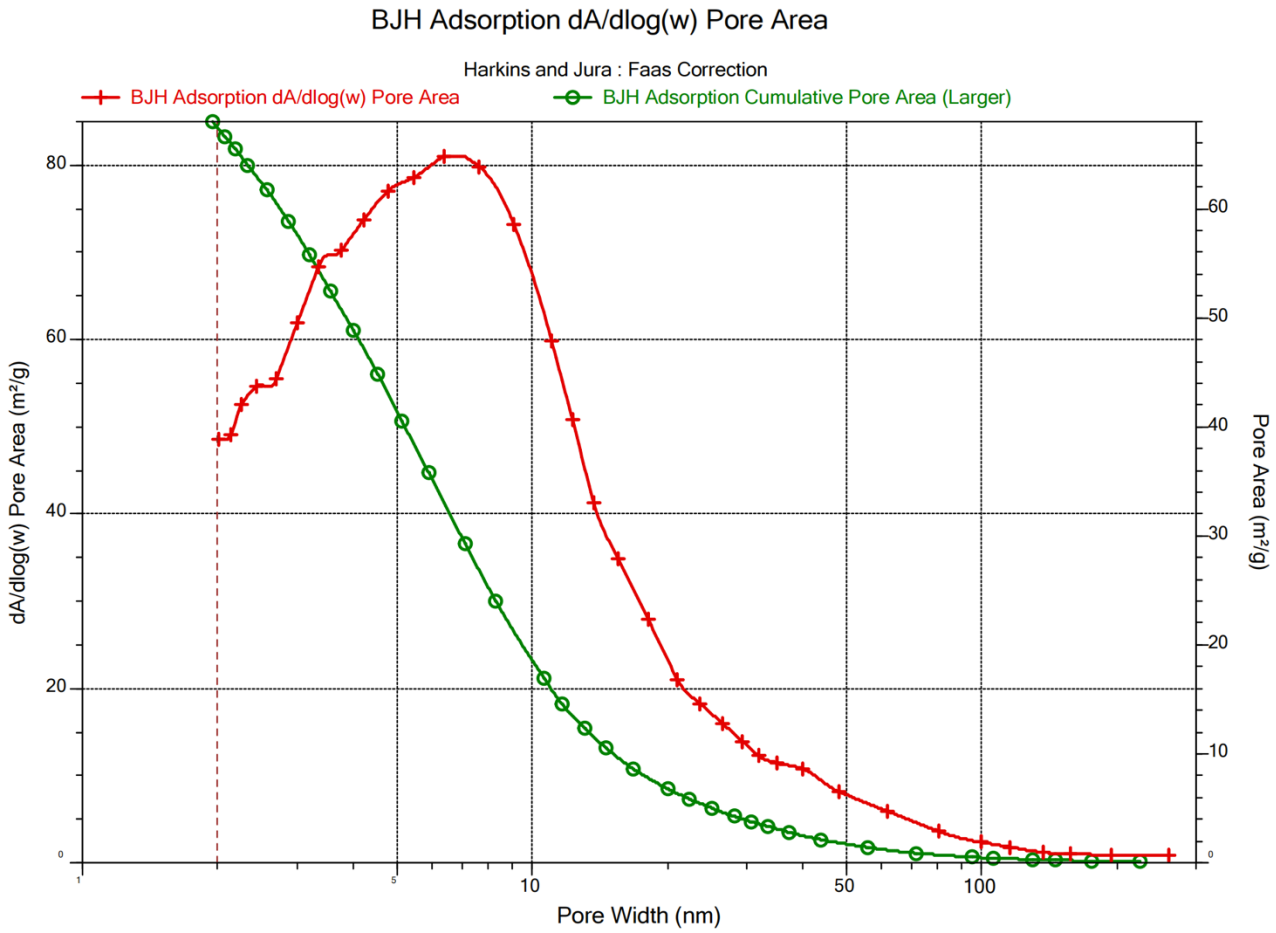


Figure D-2.9: HA-Bc BJH Adsorption dA/dLog (w) Pore Area

BJH Desorption Pore Distribution Report

Faas Correction

Harkins and Jura

t = [13.99 / (0.034 - log(P/Po))] ^ 0.5

Width range:	1.7000 to 300.0000 nm
Adsorbate property factor:	0.95300 nm
Density conversion factor:	0.0015468
Fraction of pores open at both ends:	0.00

Pore Width Range (nm)	Average Width (nm)	Incremental Pore Volume (cm^3/g)	Cumulative Pore Volume (cm^3/g)	Incremental Pore Area (m^2/g)	Cumulative Pore Area (m^2/g)
349.3 - 196.1	232.3	0.003158	0.003158	0.054	0.054
196.1 - 148.7	165.8	0.003028	0.006186	0.073	0.127
148.7 - 119.2	130.7	0.003366	0.009552	0.103	0.230
119.2 - 99.3	107.4	0.003119	0.012671	0.116	0.347
99.3 - 81.5	88.6	0.003501	0.016173	0.158	0.505
81.5 - 71.2	75.6	0.003271	0.019444	0.173	0.678
71.2 - 59.2	64.0	0.004311	0.023754	0.269	0.947
59.2 - 53.1	55.8	0.003209	0.026964	0.230	1.177
53.1 - 44.8	48.2	0.005011	0.031975	0.416	1.593
44.8 - 41.7	43.1	0.002364	0.034339	0.219	1.812
41.7 - 35.5	38.0	0.006129	0.040467	0.645	2.456
35.5 - 30.0	32.2	0.007051	0.047518	0.875	3.331
30.0 - 26.4	27.9	0.005695	0.053213	0.815	4.147
26.4 - 23.5	24.8	0.005319	0.058531	0.859	5.005
23.5 - 21.3	22.3	0.004810	0.063341	0.864	5.870
21.3 - 18.1	19.4	0.007050	0.070392	1.452	7.322
18.1 - 15.5	16.6	0.006741	0.077133	1.623	8.946
15.5 - 13.5	14.4	0.005932	0.083065	1.649	10.595
13.5 - 12.0	12.7	0.005213	0.088278	1.642	12.237
12.0 - 10.8	11.4	0.005168	0.093446	1.818	14.055
10.8 - 8.6	9.4	0.013268	0.106714	5.619	19.674
8.6 - 7.1	7.7	0.014105	0.120819	7.329	27.003

Pore Width Range (nm)	Average Width (nm)	Incremental Pore Volume (cm^3/g)	Cumulative Pore Volume (cm^3/g)	Incremental Pore Area (m^2/g)	Cumulative Pore Area (m^2/g)
7.1 - 6.1	6.5	0.012486	0.133305	7.641	34.644
6.1 - 5.2	5.6	0.011601	0.144906	8.276	42.920
5.2 - 4.6	4.9	0.007593	0.152499	6.197	49.116
4.6 - 4.1	4.3	0.006480	0.158979	5.981	55.098
4.1 - 3.5	3.8	0.009499	0.168478	10.066	65.164
3.5 - 3.2	3.3	0.002448	0.170926	2.933	68.097
3.2 - 2.8	3.0	0.001411	0.172337	1.905	70.002
2.8 - 2.6	2.7	0.000559	0.172896	0.830	70.832
2.6 - 2.3	2.4	0.000539	0.173435	0.881	71.713
2.3 - 2.1	2.2	0.000193	0.173628	0.355	72.068
2.1 - 1.8	1.9	0.000042	0.173670	0.088	72.156

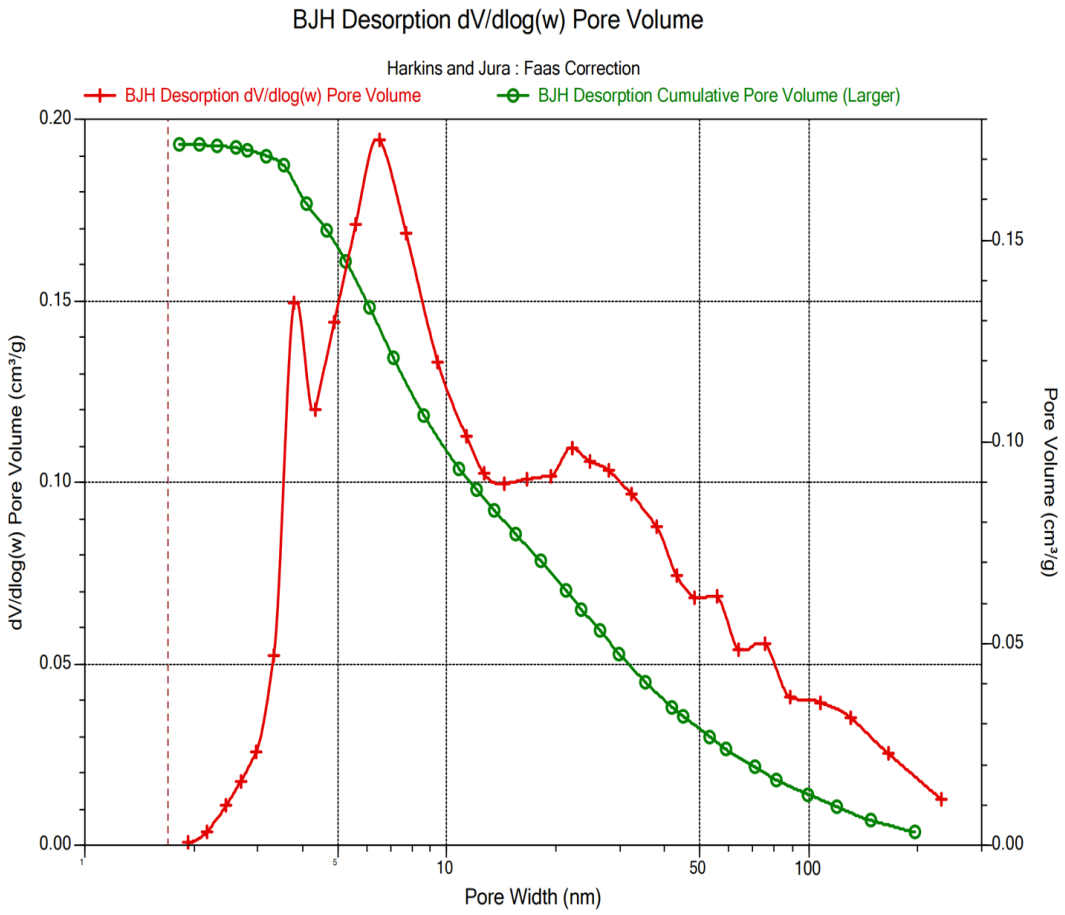


Figure D-2.10: HA-Bc BJH Desorption dV/dLog (w) Pore Volume

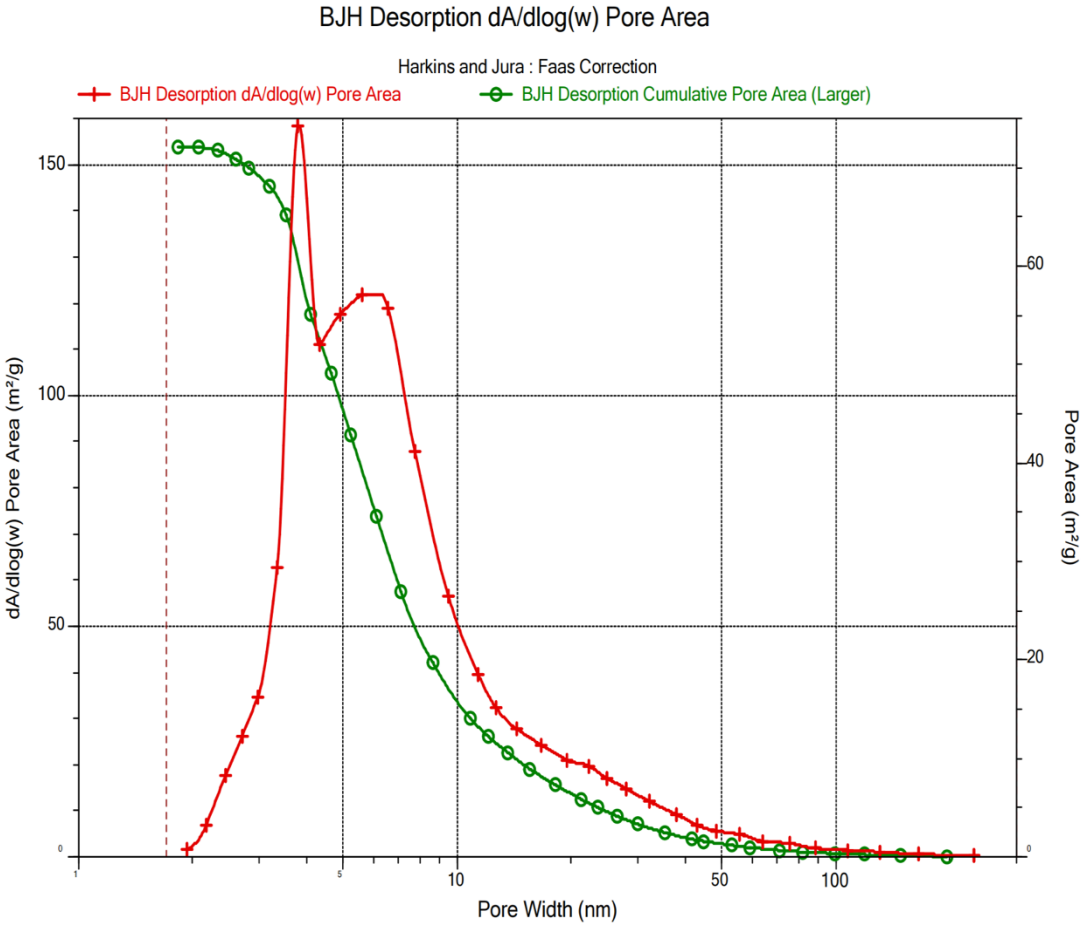


Figure D-2.11: HA-Bc BJH Desorption dA/dLog (w) Pore Area

HYDROXY APPATITE (HA) SUMMARY REPORT

Surface Area	
BET Surface Area:	67.6926 m²/g
Pore Volume	
Single point adsorption total pore volume of pores less than 290.0702 nm width at P/Po = 0.993361882:	0.217262 cm³/g
BJH Adsorption cumulative volume of pores between 2.0000 nm and 500.0000 nm width:	0.218652 cm³/g
BJH Desorption cumulative volume of pores between 1.7000 nm and 300.0000 nm width:	0.218389 cm³/g
Pore Size	
Adsorption average pore diameter (4V/A by BET):	12.8382 nm
Desorption average pore diameter (4V/A by BET):	12.0516 nm
BJH Adsorption average pore width (4V/A):	11.5259 nm
BJH Desorption average pore width (4V/A):	9.2425 nm

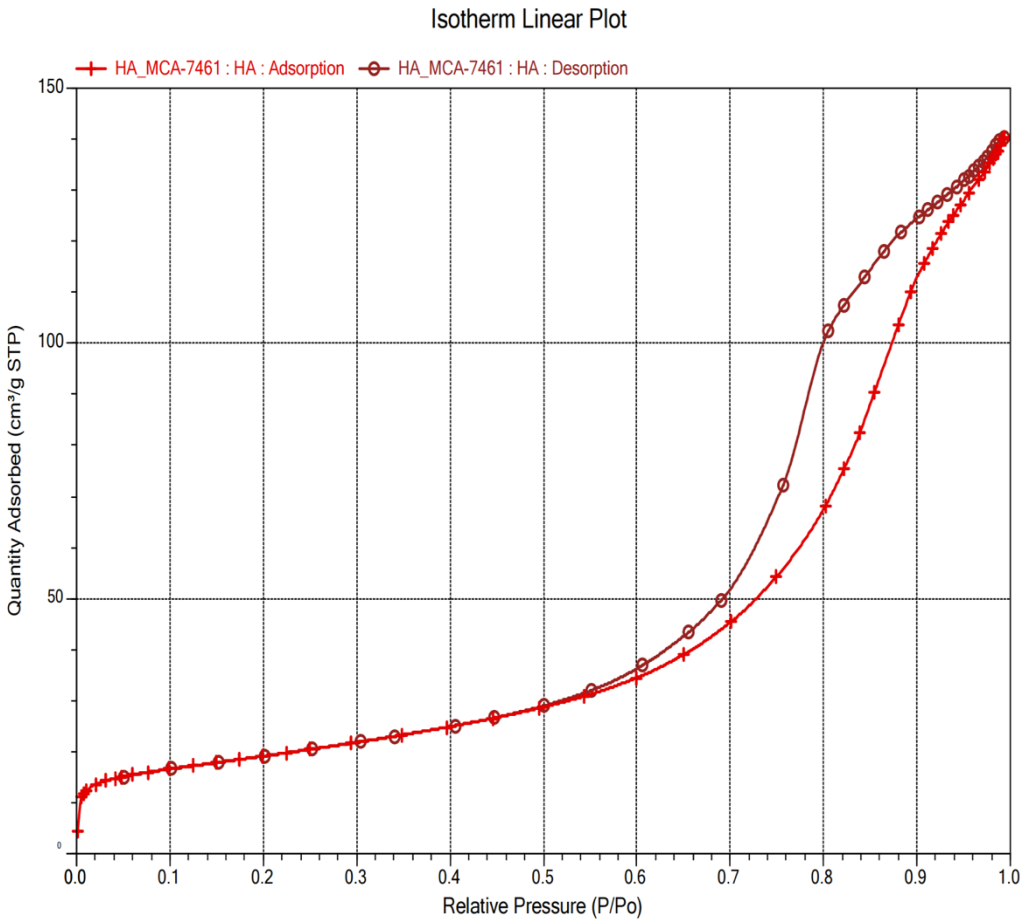


Figure D-3.1: HA Isothermal Linear Plot

BET Report

BET surface area:	67.6926 ± 0.0651 m²/g
Slope:	0.064019 ± 0.000061 g/cm³ STP
Y-intercept:	0.000280 ± 0.000010 g/cm³ STP
C:	229.545195
Qm:	15.5523 cm³/g STP
Correlation coefficient:	0.9999968
Molecular cross-sectional area:	0.1620 nm²

Relative Pressure (P/Po)	Quantity Adsorbed (cm³/g STP)	1/[Q(Po/P - 1)]
0.059475592	15.4602	0.004090
0.076696872	15.9837	0.005197
0.099426404	16.6011	0.006650
0.124350454	17.2330	0.008241
0.149304940	17.8524	0.009831
0.174301483	18.4744	0.011426
0.199334772	19.1091	0.013028
0.224431642	19.7593	0.014645
0.249606912	20.4307	0.016281

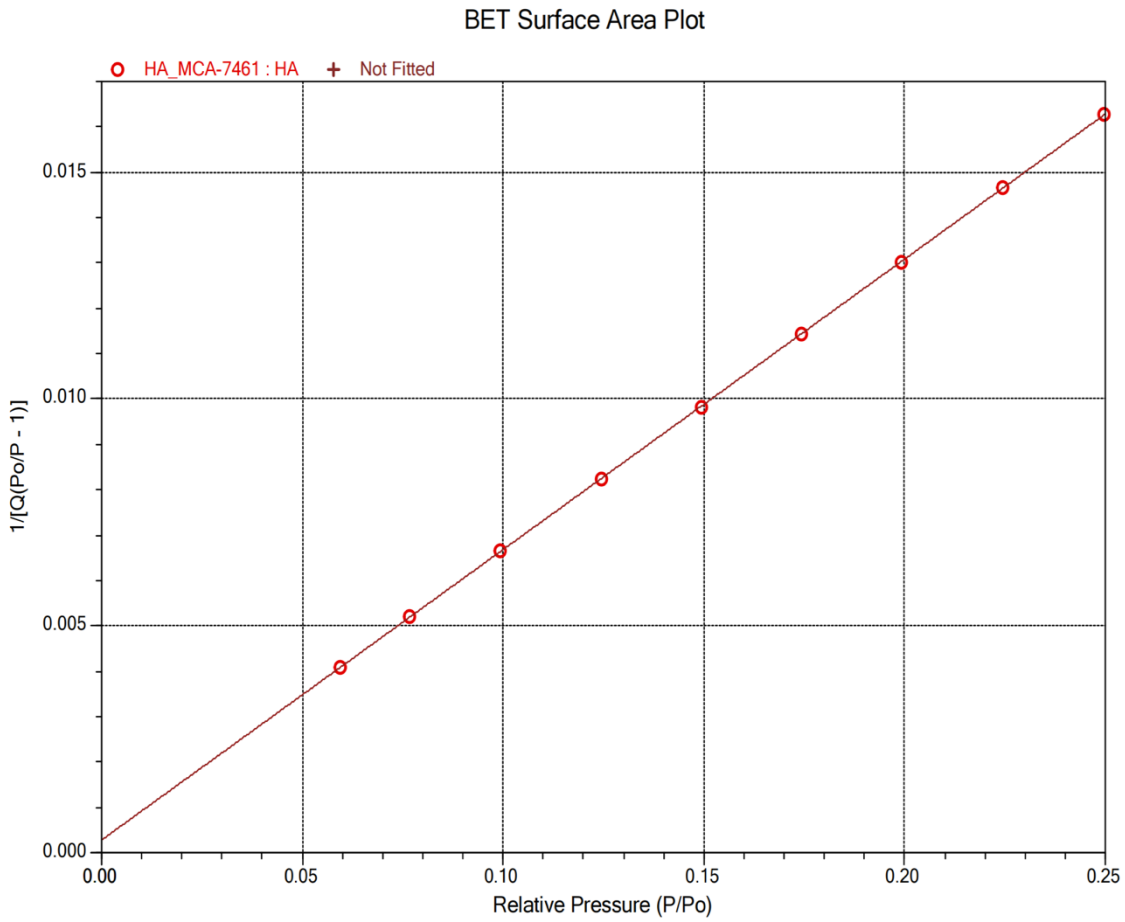


Figure D-3.2: HA Surface Area Plot

t-Plot Report

Micropore volume:	0.003413 cm³/g
Micropore area:	7.5361 m²/g
External surface area:	60.1564 m²/g
Slope:	38.890893 ± 0.694586 cm³/g·nm STP
Y-intercept:	2.206313 ± 0.299282 cm³/g STP
Correlation coefficient:	0.999044
Surface area correction factor:	1.000
Density conversion factor:	0.0015468
Total surface area (BET):	67.6926 m²/g
Thickness range:	0.35000 to 0.50000 nm
Thickness equation:	Harkins and Jura

Thickness Curve

$$t = [\ 13.99 / (\ 0.034 - \log(P/Po)\ )\ ]^{0.5}$$

t-Plot Report - Data

Relative Pressure (P/Po)	Statistical Thickness (nm)	Quantity Adsorbed (cm³/g STP)	Fitted
0.059475592	0.33326	15.4602	
0.076696872	0.34890	15.9837	
0.099426404	0.36739	16.6011	
0.124350454	0.38592	17.2330	
0.149304940	0.40335	17.8524	
0.174301483	0.42010	18.4744	
0.199334772	0.43645	19.1091	
0.224431642	0.45261	19.7593	
0.249606912	0.46873	20.4307	
0.293660259	0.49710	21.6504	
0.348927361	0.53364	23.2780	
0.396698150	0.56675	24.8028	
0.445930723	0.60302	26.5369	
0.494879790	0.64193	28.5048	

t-Plot Report - Data

Relative Pressure (P/Po)	Statistical Thickness (nm)	Quantity Adsorbed (cm^3/g STP)	Fitted
0.543495207	0.68425	30.8468	
0.599891389	0.73935	34.4221	
0.650480720	0.79606	39.0141	

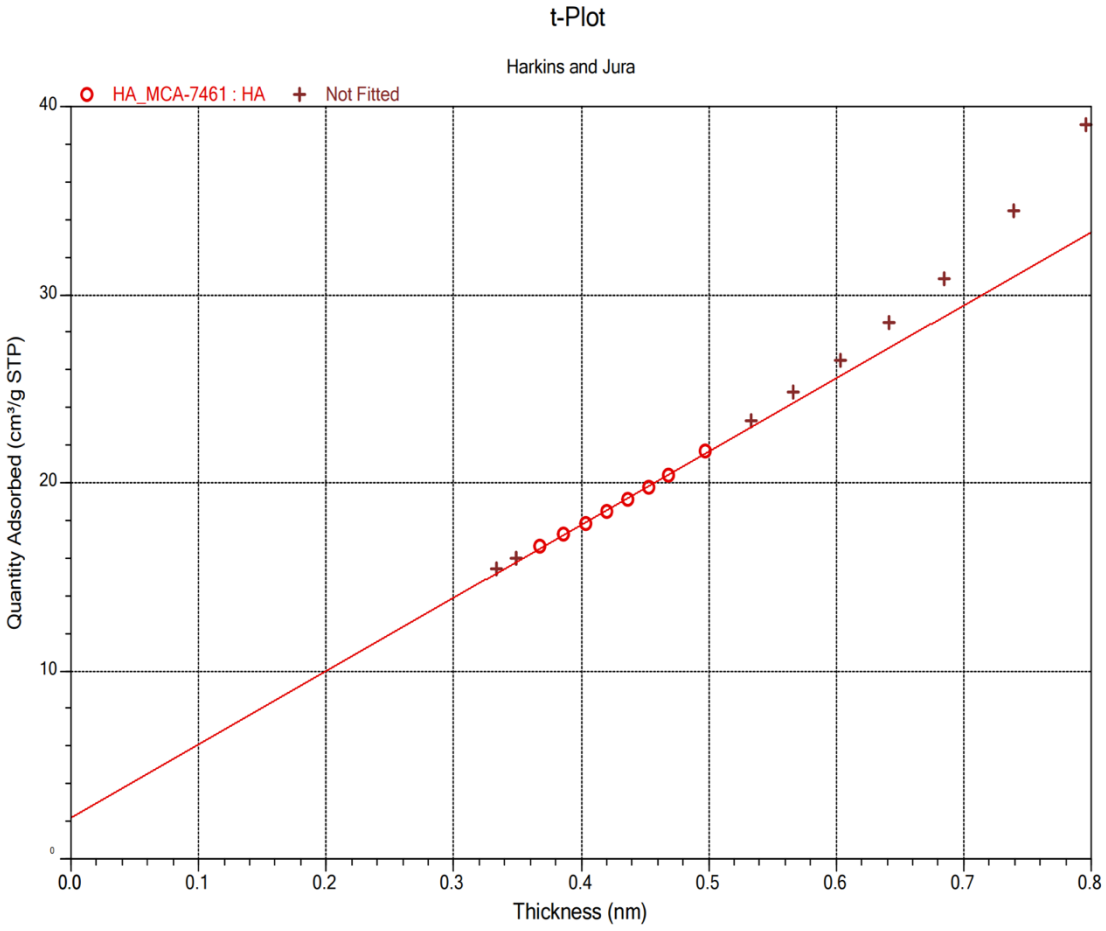


Figure D-3.3: HA t-Plot

BJH Adsorption Pore Distribution Report

Faas Correction

Harkins and Jura

$t = [13.99 / (0.034 - \log(P/Po))] ^ {0.5}$

Width range:	2.0000 to 500.0000 nm
Adsorbate property factor:	0.95300 nm
Density conversion factor:	0.0015468
Fraction of pores open at both ends:	0.00

Pore Width Range (nm)	Average Width (nm)	Incremental Pore Volume (cm^3/g)	Cumulative Pore Volume (cm^3/g)	Incremental Pore Area (m^2/g)	Cumulative Pore Area (m^2/g)
290.1 - 264.5	276.1	0.000803	0.000803	0.012	0.012
264.5 - 179.7	206.2	0.001925	0.002728	0.037	0.049
179.7 - 148.4	161.0	0.001561	0.004289	0.039	0.088
148.4 - 125.5	135.0	0.001349	0.005638	0.040	0.128
125.5 - 107.2	114.9	0.001359	0.006997	0.047	0.175
107.2 - 91.2	97.9	0.001535	0.008532	0.063	0.238
91.2 - 71.9	79.2	0.002613	0.011146	0.132	0.370
71.9 - 59.6	64.6	0.002483	0.013629	0.154	0.524
59.6 - 45.1	50.3	0.004650	0.018279	0.370	0.893
45.1 - 37.6	40.6	0.004456	0.022735	0.439	1.332
37.6 - 33.3	35.2	0.003474	0.026209	0.395	1.727
33.3 - 30.6	31.9	0.002521	0.028730	0.317	2.043
30.6 - 27.5	28.9	0.004293	0.033024	0.595	2.638
27.5 - 24.7	25.9	0.005222	0.038245	0.805	3.443
24.7 - 22.3	23.3	0.005899	0.044144	1.011	4.454
22.3 - 19.5	20.7	0.010866	0.055010	2.103	6.557
19.5 - 17.5	18.3	0.012824	0.067835	2.796	9.353
17.5 - 14.4	15.6	0.027524	0.095358	7.050	16.402
14.4 - 13.0	13.6	0.016781	0.112140	4.921	21.324
13.0 - 11.9	12.4	0.014644	0.126783	4.732	26.056
11.9 - 10.7	11.2	0.015099	0.141882	5.385	31.441
10.7 - 8.5	9.3	0.029583	0.171465	12.739	44.180

Pore Width Range (nm)	Average Width (nm)	Incremental Pore Volume (cm^3/g)	Cumulative Pore Volume (cm^3/g)	Incremental Pore Area (m^2/g)	Cumulative Pore Area (m^2/g)
8.5 - 7.1	7.6	0.017734	0.189199	9.311	53.490
7.1 - 6.0	6.4	0.012165	0.201364	7.558	61.049
6.0 - 5.2	5.5	0.007653	0.209017	5.535	66.583
5.2 - 4.5	4.8	0.004652	0.213669	3.898	70.482
4.5 - 4.0	4.2	0.002184	0.215854	2.084	72.566
4.0 - 3.5	3.7	0.001311	0.217165	1.405	73.971
3.5 - 3.2	3.3	0.000804	0.217969	0.963	74.934
3.2 - 2.9	3.0	0.000458	0.218427	0.611	75.545
2.9 - 2.5	2.7	0.000225	0.218652	0.337	75.882

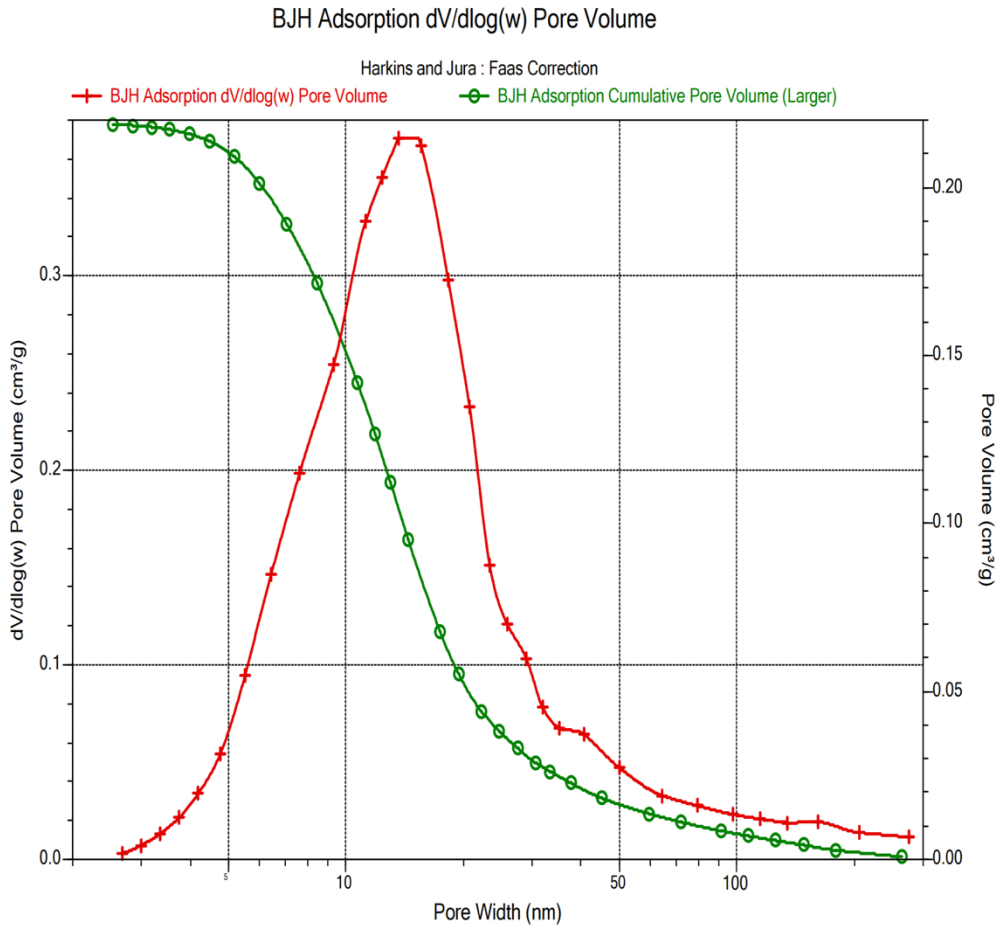


Figure.D-3.4: HA BJH Adsorption dV/dLog (w) Pore Volume

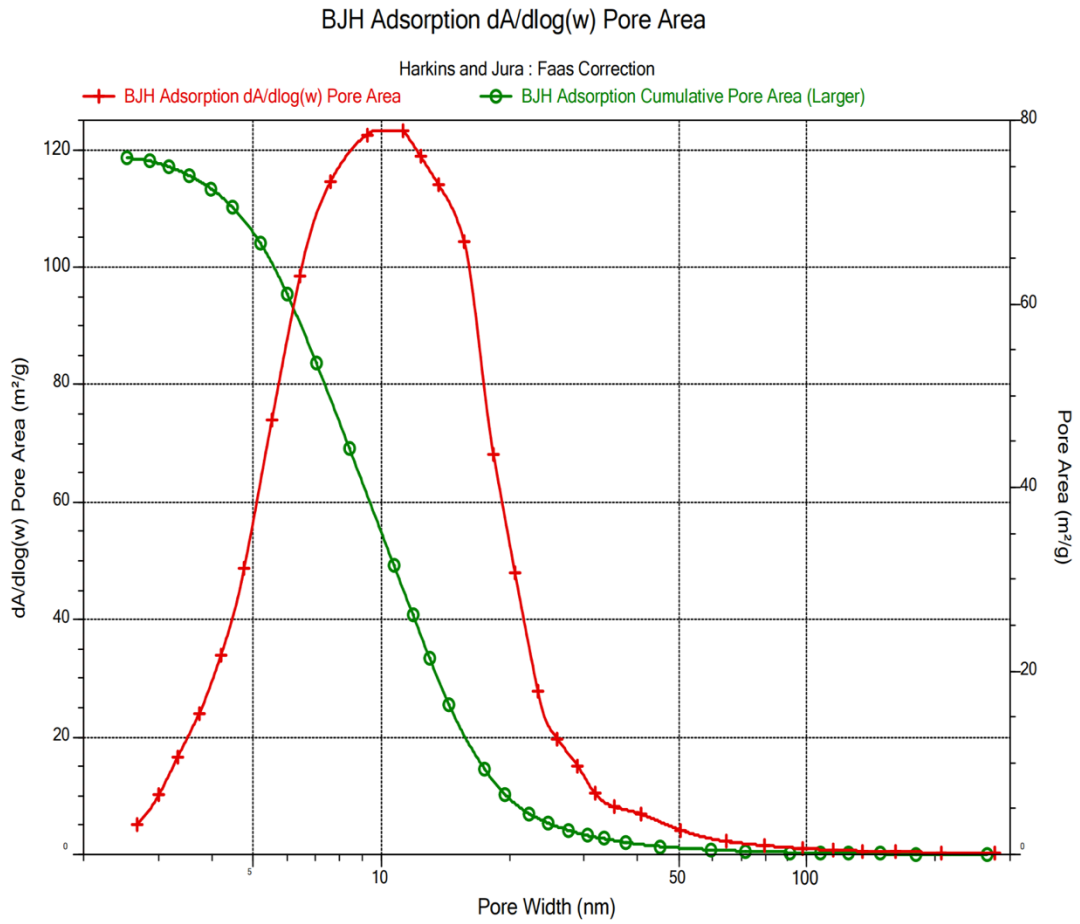


Figure D-3.5: HA BJH Adsorption dA/dLog (w) Pore Area

BJH Desorption Pore Distribution Report

Faas Correction

Harkins and Jura

t = [13.99 / (0.034 - log(P/Po))] ^ 0.5

Width range:	1.7000 to 300.0000 nm
Adsorbate property factor:	0.95300 nm
Density conversion factor:	0.0015468
Fraction of pores open at both ends:	0.00

Pore Width Range (nm)	Average Width (nm)	Incremental Pore Volume (cm^3/g)	Cumulative Pore Volume (cm^3/g)	Incremental Pore Area (m^2/g)	Cumulative Pore Area (m^2/g)
289.8 - 172.6	202.9	0.001210	0.001210	0.024	0.024
172.6 - 127.9	143.6	0.001501	0.002712	0.042	0.066
127.9 - 102.3	112.2	0.001596	0.004308	0.057	0.123
102.3 - 80.9	89.0	0.001960	0.006268	0.088	0.211
80.9 - 68.3	73.5	0.001617	0.007885	0.088	0.299
68.3 - 57.8	62.1	0.001743	0.009628	0.112	0.411
57.8 - 51.5	54.3	0.001409	0.011037	0.104	0.515
51.5 - 45.1	47.8	0.001748	0.012785	0.146	0.661
45.1 - 41.0	42.8	0.001348	0.014133	0.126	0.787
41.0 - 35.2	37.6	0.002337	0.016470	0.248	1.035
35.2 - 29.8	32.1	0.002896	0.019366	0.361	1.396
29.8 - 26.2	27.8	0.002708	0.022074	0.390	1.786
26.2 - 23.0	24.4	0.002866	0.024940	0.470	2.256
23.0 - 21.0	21.9	0.002389	0.027329	0.436	2.693
21.0 - 17.5	18.9	0.005880	0.033209	1.244	3.937
17.5 - 15.2	16.2	0.007137	0.040346	1.762	5.699
15.2 - 13.2	14.1	0.010566	0.050912	3.001	8.701
13.2 - 11.7	12.3	0.011114	0.062026	3.604	12.305
11.7 - 10.6	11.1	0.010764	0.072790	3.883	16.188
10.6 - 8.5	9.3	0.066839	0.139629	28.797	44.985
8.5 - 6.6	7.3	0.048149	0.187778	26.454	71.439
6.6 - 5.9	6.2	0.011450	0.199229	7.416	78.855

Pore Width Range (nm)	Average Width (nm)	Incremental Pore Volume (cm^3/g)	Cumulative Pore Volume (cm^3/g)	Incremental Pore Area (m^2/g)	Cumulative Pore Area (m^2/g)
5.9 - 5.0	5.4	0.010649	0.209878	7.914	86.769
5.0 - 4.3	4.6	0.006061	0.215939	5.241	92.010
4.3 - 3.8	4.0	0.001978	0.217917	1.969	93.980
3.8 - 3.3	3.5	0.000472	0.218389	0.536	94.515

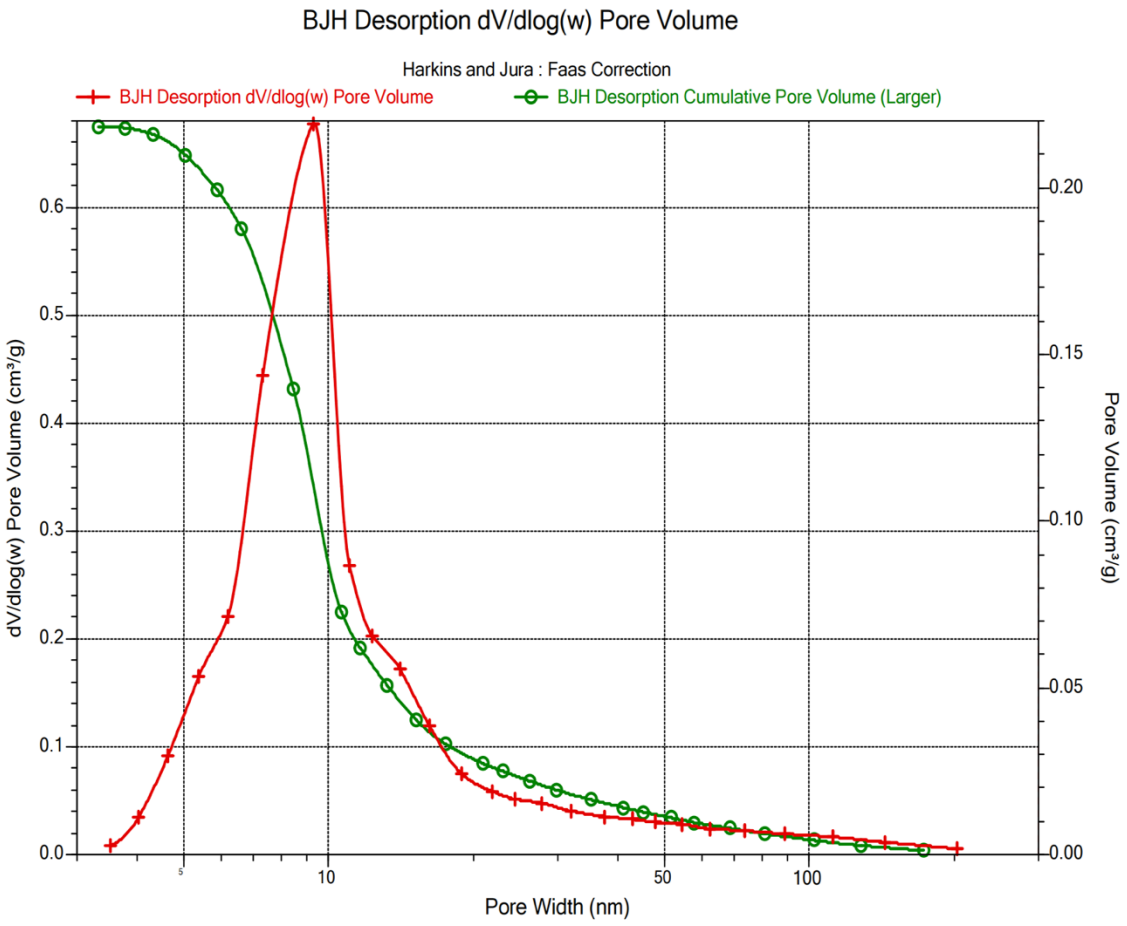


Figure D-3.6: HA BJH Desorption dV/dLog (w) Pore Volume

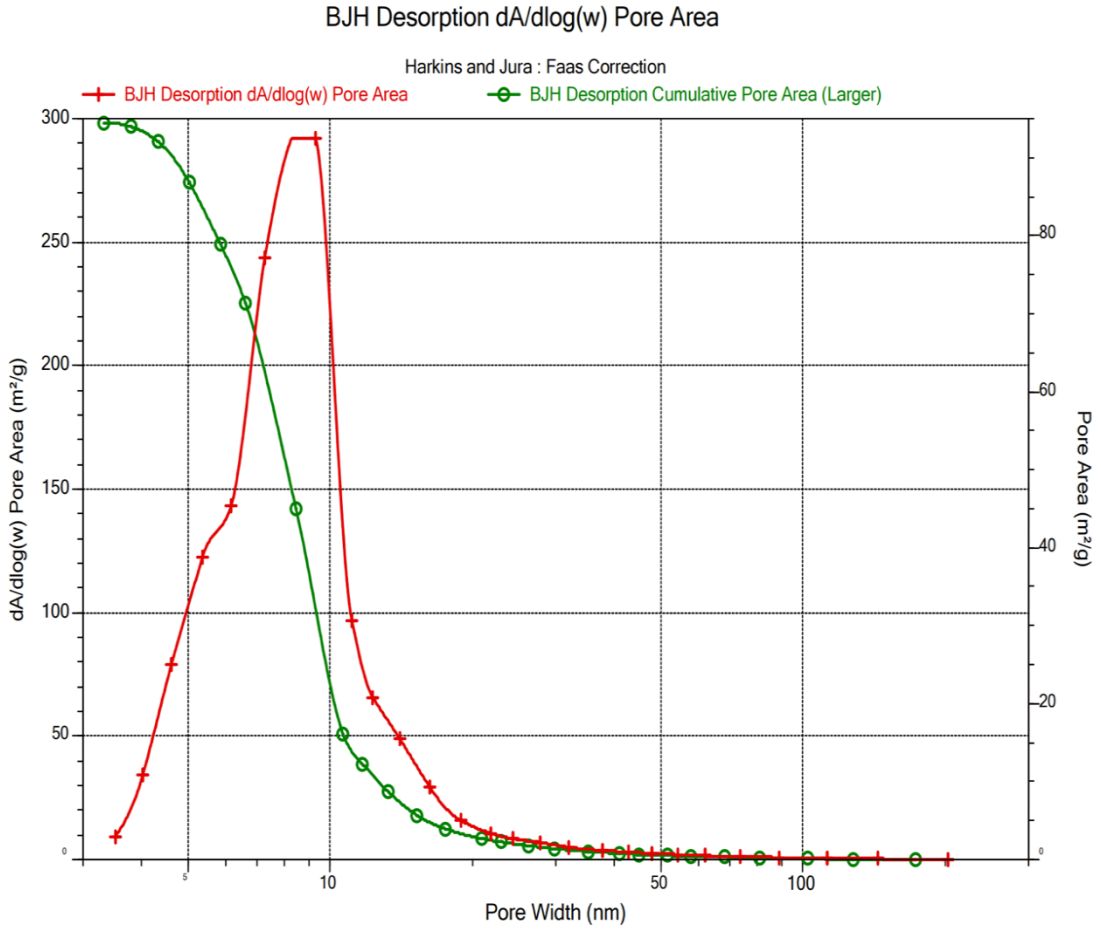


Figure D-3.7: HA BJH Desorption dA/dLog (w) Pore Area

MAGNETIC BIOCHAR (MBC) SUMMARY REPORT

Surface Area	
BET Surface Area:	190.6357 m^2/g
Pore Volume	
Single point adsorption total pore volume of pores less than 320.6222 nm width at P/Po = 0.994000000:	0.112855 cm^3/g
BJH Adsorption cumulative volume of pores between 2.0000 nm and 500.0000 nm width:	0.025794 cm^3/g
BJH Desorption cumulative volume of pores between 1.7000 nm and 300.0000 nm width:	0.021870 cm^3/g
Pore Size	
Adsorption average pore diameter (4V/A by BET):	2.3680 nm
Desorption average pore diameter (4V/A by BET):	2.1840 nm
BJH Adsorption average pore width (4V/A):	10.2858 nm
BJH Desorption average pore width (4V/A):	9.1855 nm

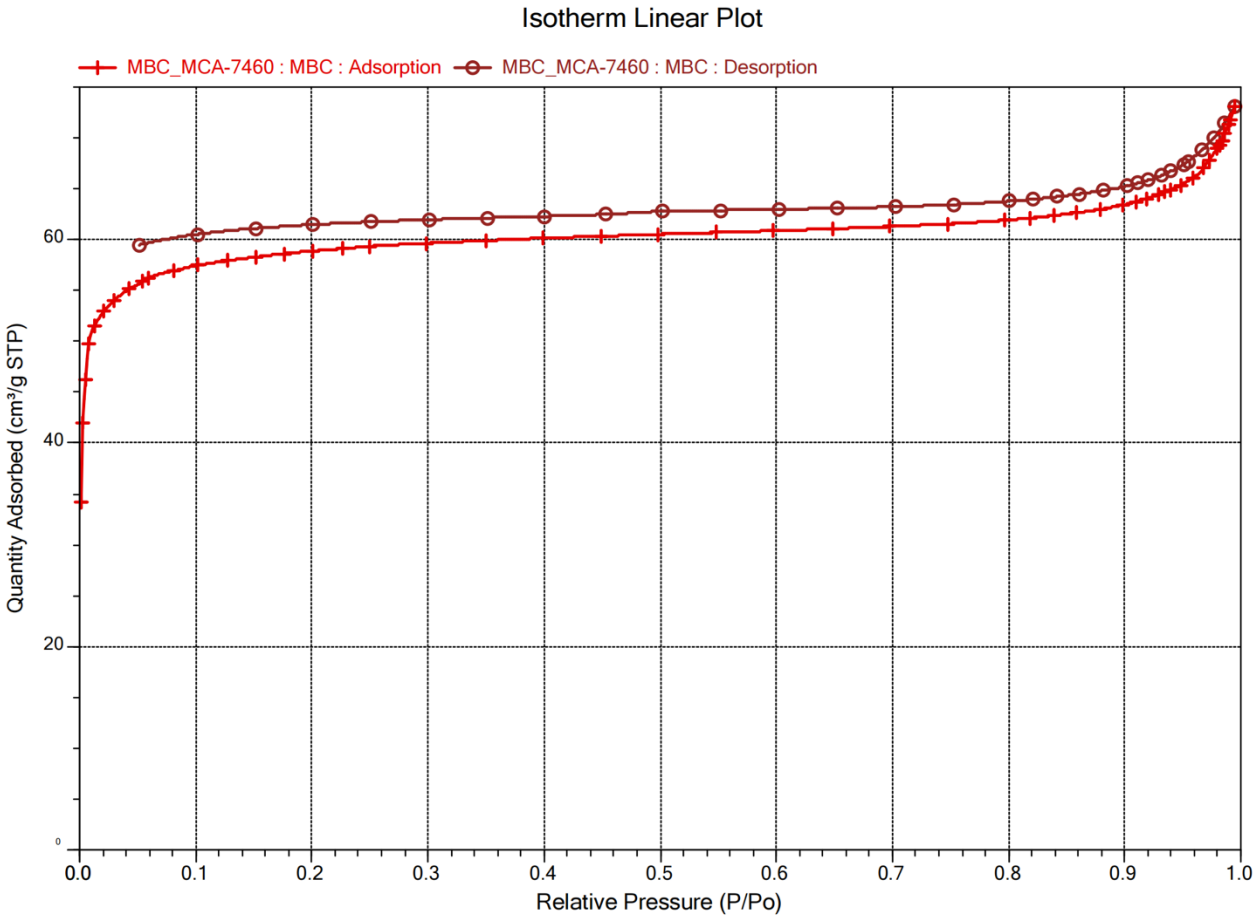


Figure D-4.0: MBc Isothermal Linear Plot

BET Report

BET surface area:	190.6357 ± 4.1087 m²/g
Slope:	0.023168 ± 0.000486 g/cm³ STP
Y-intercept:	-0.000336 ± 0.000077 g/cm³ STP
C:	-67.914389
Qm:	43.7983 cm³/g STP
Correlation coefficient:	0.9982437
Molecular cross-sectional area:	0.1620 nm²

Relative Pressure (P/Po)	Quantity Adsorbed (cm³/g STP)	1/[Q(Po/P - 1)]
0.053671789	55.8542	0.001015
0.059033583	56.2362	0.001116
0.080737954	56.9434	0.001542
0.101668455	57.4768	0.001969
0.127713490	57.9349	0.002527
0.151894673	58.2979	0.003072
0.176395394	58.6269	0.003653
0.200999520	58.8885	0.004272
0.225931512	59.1150	0.004937
0.250236275	59.3394	0.005624

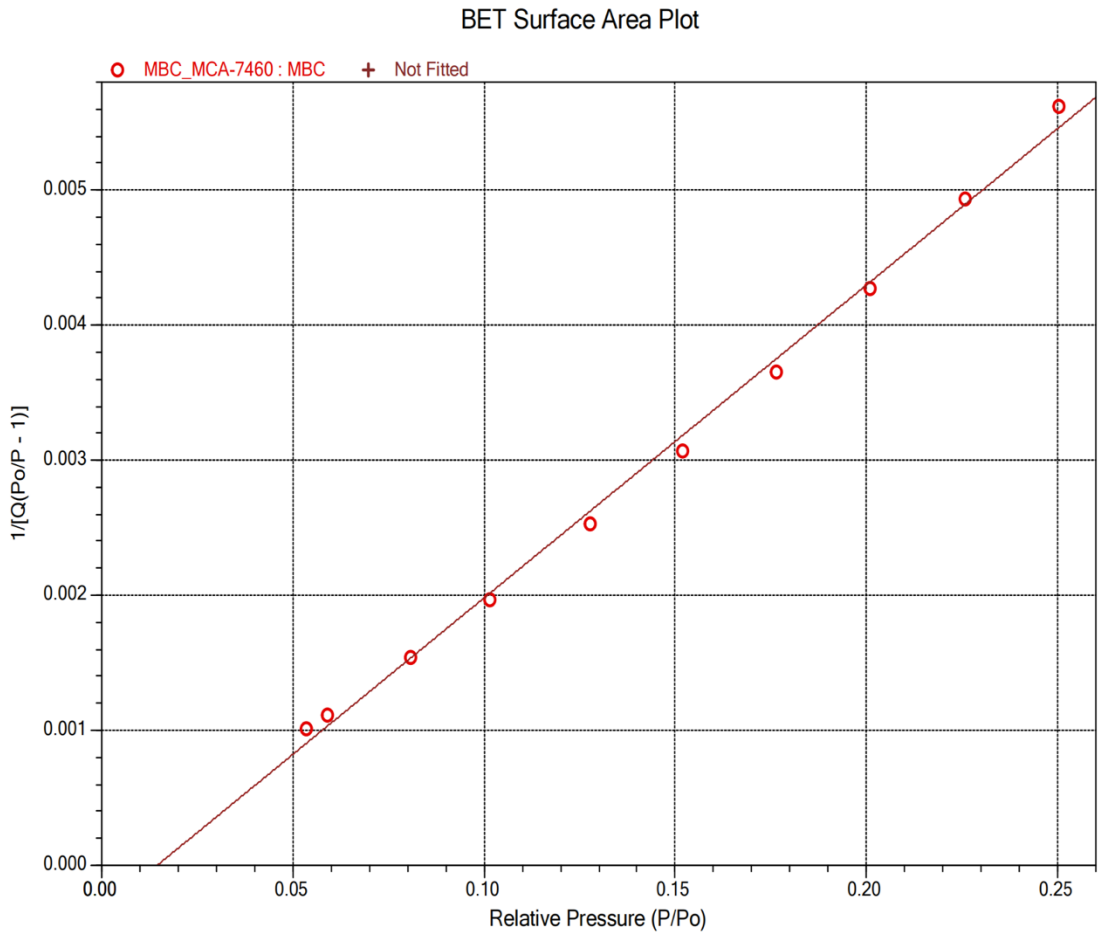


Figure D-4.1: MBc Surface Area Plot

t-Plot Report

Micropore volume:	0.077395 cm³/g
Micropore area:	159.5089 m²/g
External surface area:	31.1267 m²/g
Slope:	20.123307 ± 1.118954 cm³/g·nm STP
Y-intercept:	50.035523 ± 0.463083 cm³/g STP
Correlation coefficient:	0.990851
Surface area correction factor:	1.000
Density conversion factor:	0.0015468
Total surface area (BET):	190.6357 m²/g
Thickness range:	0.35000 to 0.50000 nm
Thickness equation:	Harkins and Jura

Thickness Curve

$$t = [\ 13.99 / (\ 0.034 - \log(P/Po)\ )\ ]\ ^{\wedge}\ 0.5$$

t-Plot Report - Data

Relative Pressure (P/Po)	Statistical Thickness (nm)	Quantity Adsorbed (cm³/g STP)	Fitted
0.053671789	0.32751	55.8542	
0.059033583	0.33283	56.2362	
0.080737954	0.35234	56.9434	
0.101668455	0.36912	57.4768	
0.127713490	0.38832	57.9349	
0.151894673	0.40511	58.2979	
0.176395394	0.42148	58.6269	
0.200999520	0.43753	58.8885	
0.225931512	0.45357	59.1150	
0.250236275	0.46914	59.3394	
0.298936691	0.50053	59.6426	
0.349693082	0.53416	59.9084	
0.398362098	0.56794	60.1474	
0.448654455	0.60510	60.3409	

t-Plot Report - Data

Relative Pressure (P/Po)	Statistical Thickness (nm)	Quantity Adsorbed (cm^3/g STP)	Fitted
0.498095990	0.64461	60.5305	
0.548289665	0.68866	60.6991	
0.597752745	0.73712	60.8756	
0.648114924	0.79322	61.0711	
0.697446885	0.85699	61.2888	

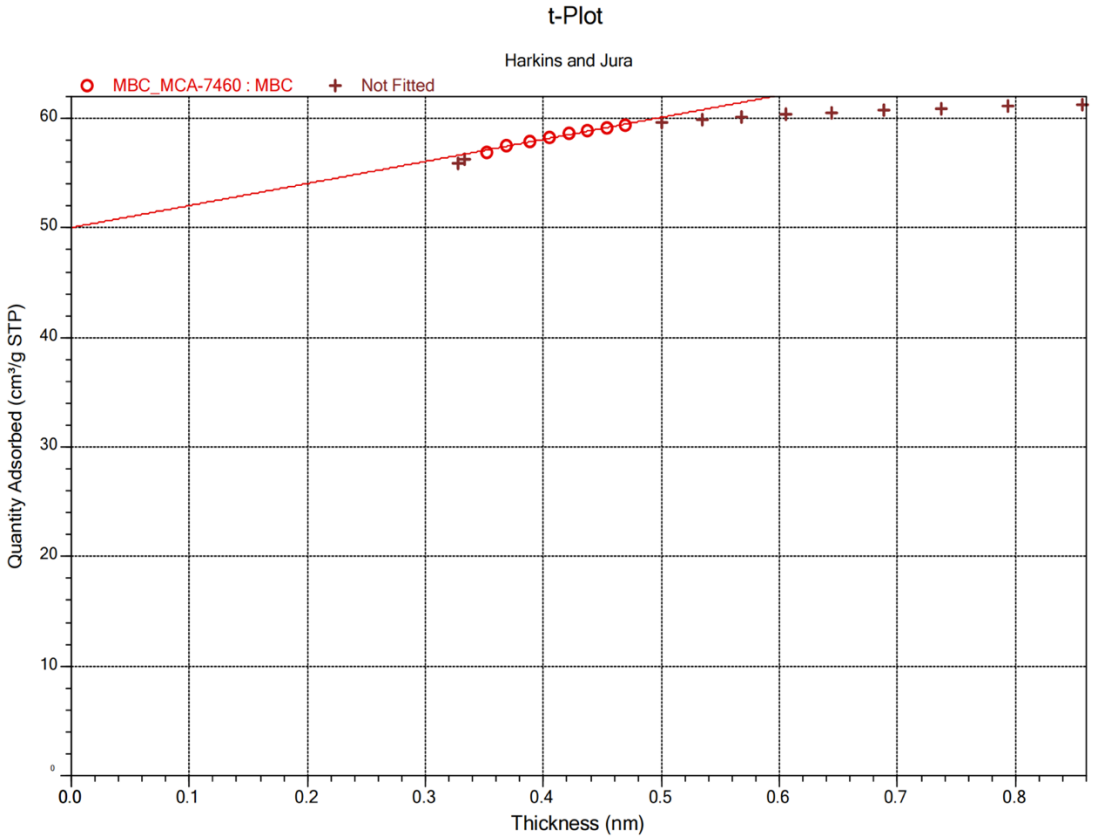


Figure D-4.2: MBc t-Plot

BJH Adsorption Pore Distribution Report

Faas Correction

Harkins and Jura

t = [13.99 / (0.034 - log(P/Po))] ^ 0.5

Width range:	2.0000 to 500.0000 nm
Adsorbate property factor:	0.95300 nm
Density conversion factor:	0.0015468
Fraction of pores open at both ends:	0.00

Pore Width Range (nm)	Average Width (nm)	Incremental Pore Volume (cm^3/g)	Cumulative Pore Volume (cm^3/g)	Incremental Pore Area (m^2/g)	Cumulative Pore Area (m^2/g)
341.4 - 214.2	249.8	0.002016	0.002016	0.032	0.032
214.2 - 190.2	200.7	0.000823	0.002839	0.016	0.049
190.2 - 139.4	157.0	0.001394	0.004234	0.036	0.084
139.4 - 121.4	129.1	0.001159	0.005393	0.036	0.120
121.4 - 107.6	113.6	0.000820	0.006213	0.029	0.149
107.6 - 97.7	102.2	0.000547	0.006760	0.021	0.170
97.7 - 74.2	82.7	0.001780	0.008539	0.086	0.256
74.2 - 62.5	67.3	0.001411	0.009951	0.084	0.340
62.5 - 47.9	53.2	0.001627	0.011577	0.122	0.463
47.9 - 38.9	42.4	0.001249	0.012827	0.118	0.580
38.9 - 33.6	35.8	0.000845	0.013672	0.094	0.675
33.6 - 31.2	32.3	0.000446	0.014118	0.055	0.730
31.2 - 28.9	29.9	0.000417	0.014536	0.056	0.786
28.9 - 25.3	26.8	0.000719	0.015255	0.107	0.893
25.3 - 22.9	23.9	0.000578	0.015833	0.097	0.990
22.9 - 20.4	21.5	0.000539	0.016372	0.100	1.090
20.4 - 17.2	18.5	0.000799	0.017171	0.172	1.262
17.2 - 14.9	15.9	0.000609	0.017780	0.154	1.416
14.9 - 13.1	13.9	0.000510	0.018290	0.147	1.563
13.1 - 11.7	12.3	0.000437	0.018727	0.142	1.705
11.7 - 10.5	11.0	0.000411	0.019138	0.150	1.855
10.5 - 8.4	9.2	0.000596	0.019734	0.259	2.114

Pore Width Range (nm)	Average Width (nm)	Incremental Pore Volume (cm^3/g)	Cumulative Pore Volume (cm^3/g)	Incremental Pore Area (m^2/g)	Cumulative Pore Area (m^2/g)
8.4 - 7.0	7.6	0.000438	0.020172	0.232	2.345
7.0 - 6.0	6.4	0.000357	0.020529	0.223	2.568
6.0 - 5.2	5.5	0.000323	0.020852	0.234	2.803
5.2 - 4.5	4.8	0.000299	0.021151	0.248	3.051
4.5 - 4.0	4.2	0.000293	0.021444	0.276	3.327
4.0 - 3.6	3.8	0.000386	0.021831	0.409	3.736
3.6 - 3.2	3.4	0.000409	0.022239	0.485	4.221
3.2 - 2.9	3.0	0.000596	0.022835	0.788	5.009
2.9 - 2.6	2.7	0.000684	0.023519	1.009	6.018
2.6 - 2.3	2.4	0.000842	0.024361	1.386	7.405
2.3 - 2.2	2.2	0.000724	0.025085	1.290	8.694
2.2 - 2.1	2.1	0.000709	0.025794	1.337	10.031

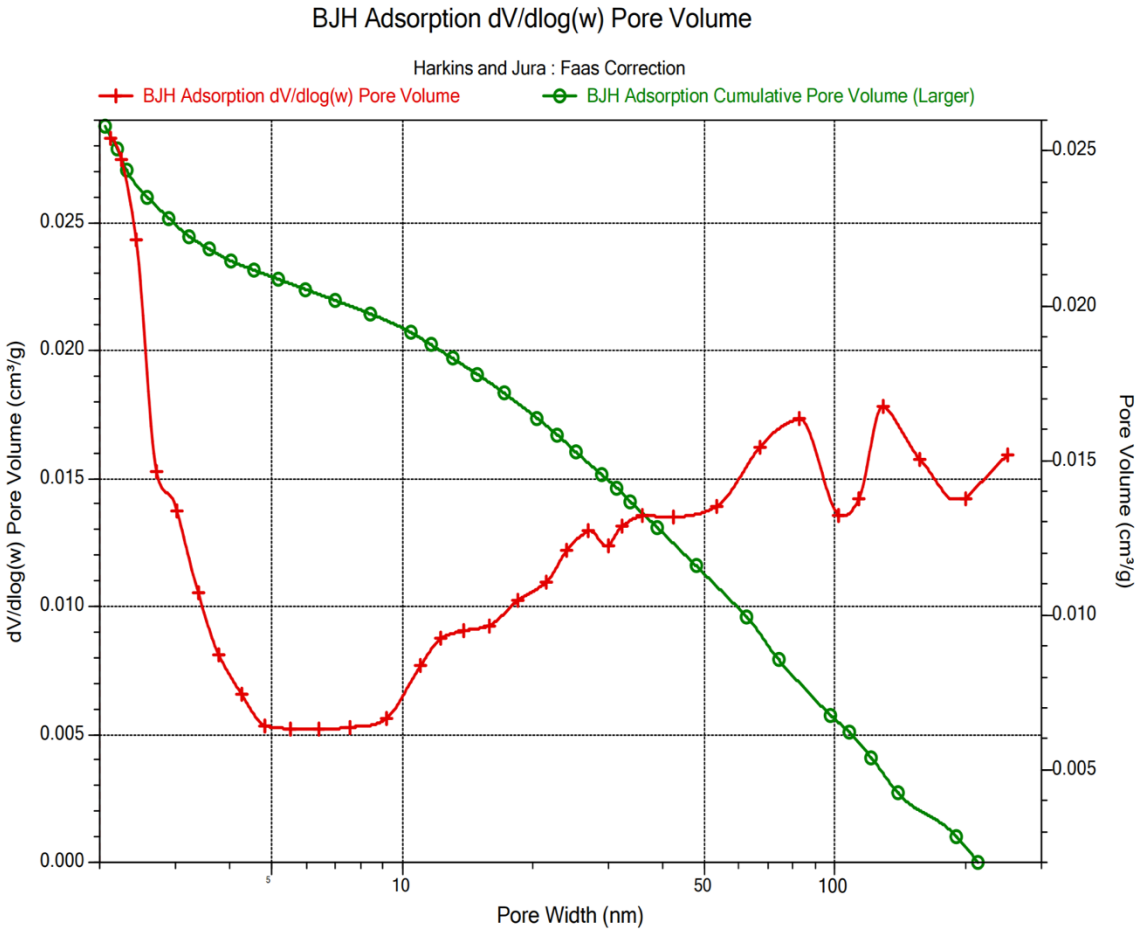


Figure D-4.3: MBc BJH Adsorption dV/dlog (w) Pore Volume

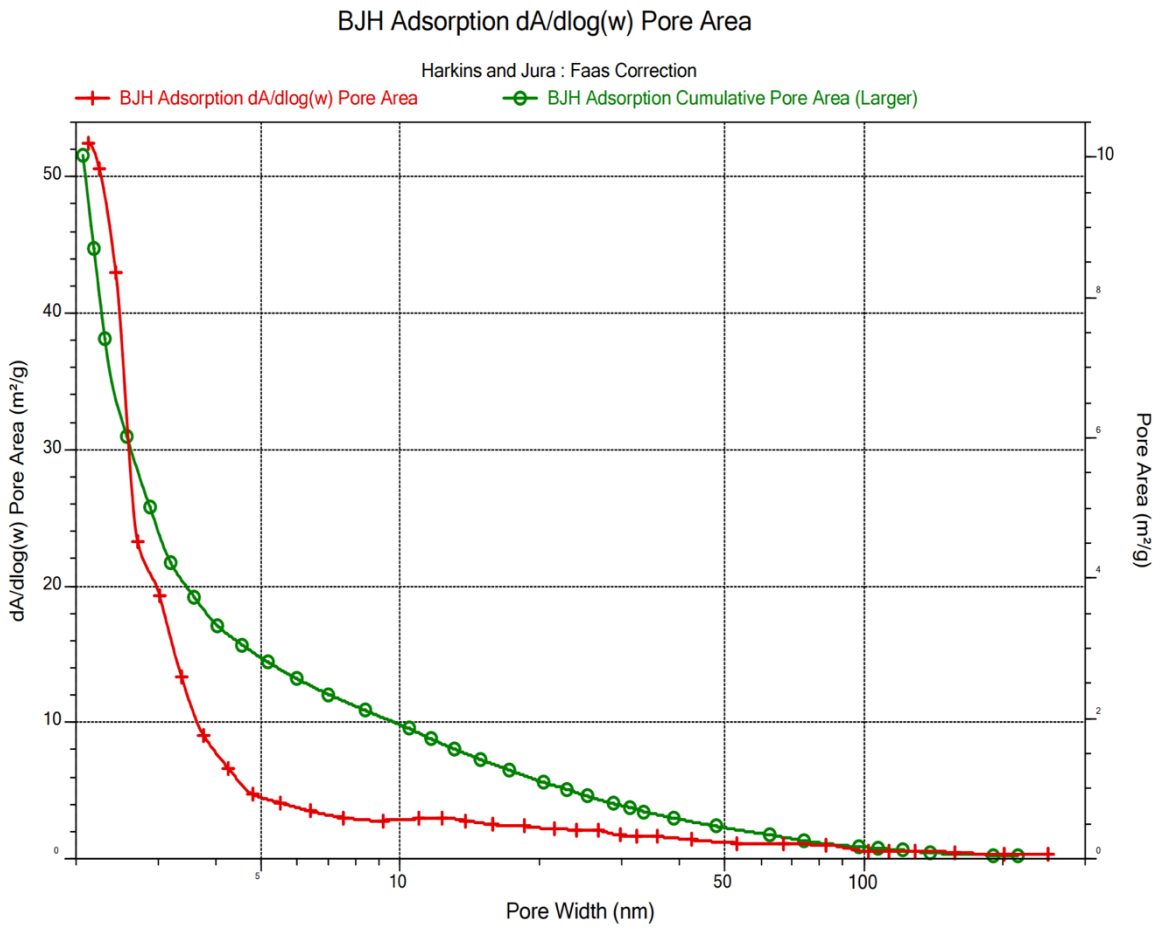


Figure D- 4.4: MBc BJH Adsorption dA/dlog (w) Pore Area

BJH Desorption Pore Distribution Report

Faas Correction

Harkins and Jura

t = [13.99 / (0.034 - log(P/Po))] ^ 0.5

Width range:	1.7000 to 300.0000 nm
Adsorbate property factor:	0.95300 nm
Density conversion factor:	0.0015468
Fraction of pores open at both ends:	0.00

Pore Width Range (nm)	Average Width (nm)	Incremental Pore Volume (cm^3/g)	Cumulative Pore Volume (cm^3/g)	Incremental Pore Area (m^2/g)	Cumulative Pore Area (m^2/g)
341.4 - 139.8	168.0	0.002740	0.002740	0.065	0.065
139.8 - 85.8	100.3	0.002276	0.005016	0.091	0.156
85.8 - 58.7	67.1	0.002138	0.007153	0.127	0.283
58.7 - 44.4	49.5	0.001856	0.009009	0.150	0.433
44.4 - 41.5	42.9	0.000527	0.009536	0.049	0.483
41.5 - 33.7	36.8	0.001253	0.010789	0.136	0.619
33.7 - 30.0	31.7	0.000746	0.011536	0.094	0.713
30.0 - 25.9	27.6	0.000833	0.012368	0.121	0.834
25.9 - 23.2	24.4	0.000537	0.012905	0.088	0.922
23.2 - 21.1	22.0	0.000491	0.013395	0.089	1.011
21.1 - 17.6	19.0	0.000811	0.014207	0.171	1.182
17.6 - 15.1	16.2	0.000622	0.014828	0.154	1.335
15.1 - 13.3	14.1	0.000525	0.015354	0.149	1.484
13.3 - 11.8	12.5	0.000452	0.015806	0.145	1.629
11.8 - 10.7	11.2	0.000319	0.016125	0.114	1.743
10.7 - 8.6	9.4	0.000566	0.016691	0.241	1.984
8.6 - 7.1	7.7	0.000329	0.017020	0.171	2.155
7.1 - 6.1	6.5	0.000176	0.017196	0.109	2.264
6.1 - 5.2	5.6	0.000089	0.017285	0.063	2.327
5.2 - 4.6	4.9	0.000103	0.017387	0.084	2.412
4.6 - 4.1	4.3	0.000111	0.017499	0.104	2.515
4.1 - 3.6	3.8	0.000811	0.018310	0.851	3.366

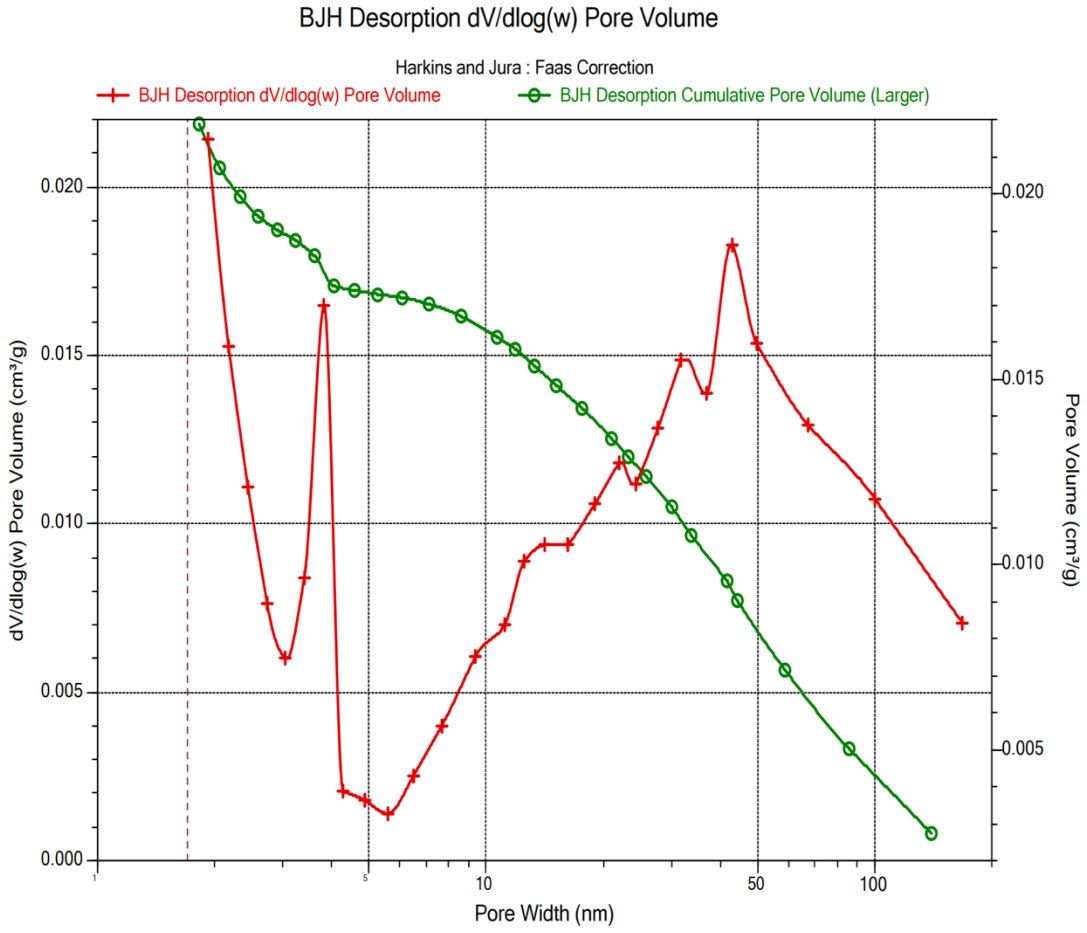


Figure D-4.5: MBc BJH Desorption dV/dlog (w) Pore Volume

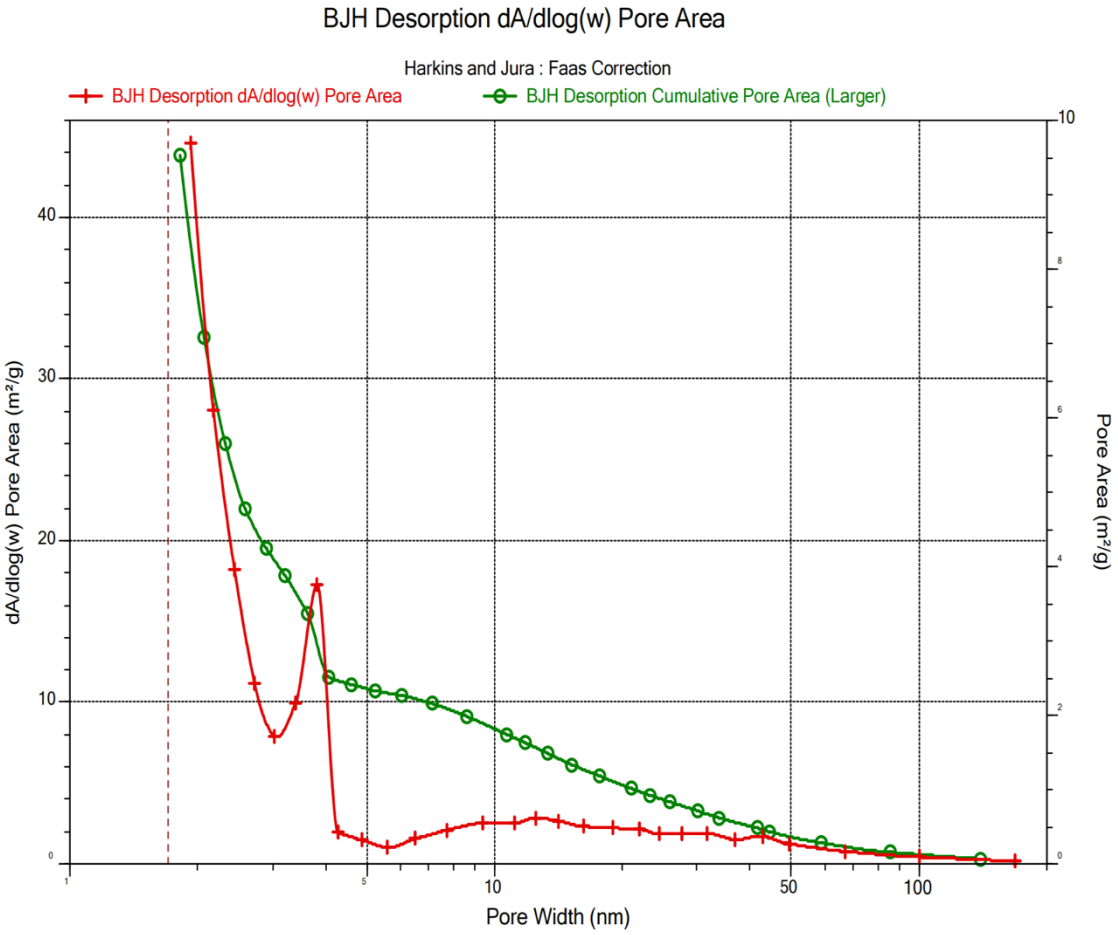


Figure D-4.6: MBc BJH Adsorption dA/dlog (w) Pore Area

APPENDIX E

BIOCHAR KINECTICS

In general, the linear forms of a pseudo-first and second order models, and an Intraparticle diffusion can be expressed using equations 5.1 (Georgin et al., 2018). Where, k_1 and k_2 are the rate constants of pseudo first and second order respectively, q_e and q_t are amounts of metal ions biosorbed in mg g^{-1} at equilibrium and at time t (min) respectively. The rate constants, K_1 were calculated from the plots of log ($q_e - q_t$) against time t for different concentrations of metal ion (Figures 5.5, 5.6 and 5.7). The kinetic parameters (q_e, k_1, and k_2) and the statistical information (coefficient of determination R^2, table 5.3 a, b, c). Furthermore, the intra particle diffusion equation was used to investigate the behaviour of intra particle diffusion as the rate limiting step in the biosorption process. R is the percent metal ions biosorbed, K_d (mg g^{-1} $min^{-1/2}$) is the intra particle diffusion rate constant, t is the contact time, while b is the gradient of the linear plot. In the linear form, equation (5.3) turns to equation (5.4). The intra particle kinetic plot is also presented in Figure E 1.0 and 5.10 for Pb while the kinetic parameters are presented in Table E 1.0 to Table E 1.4.

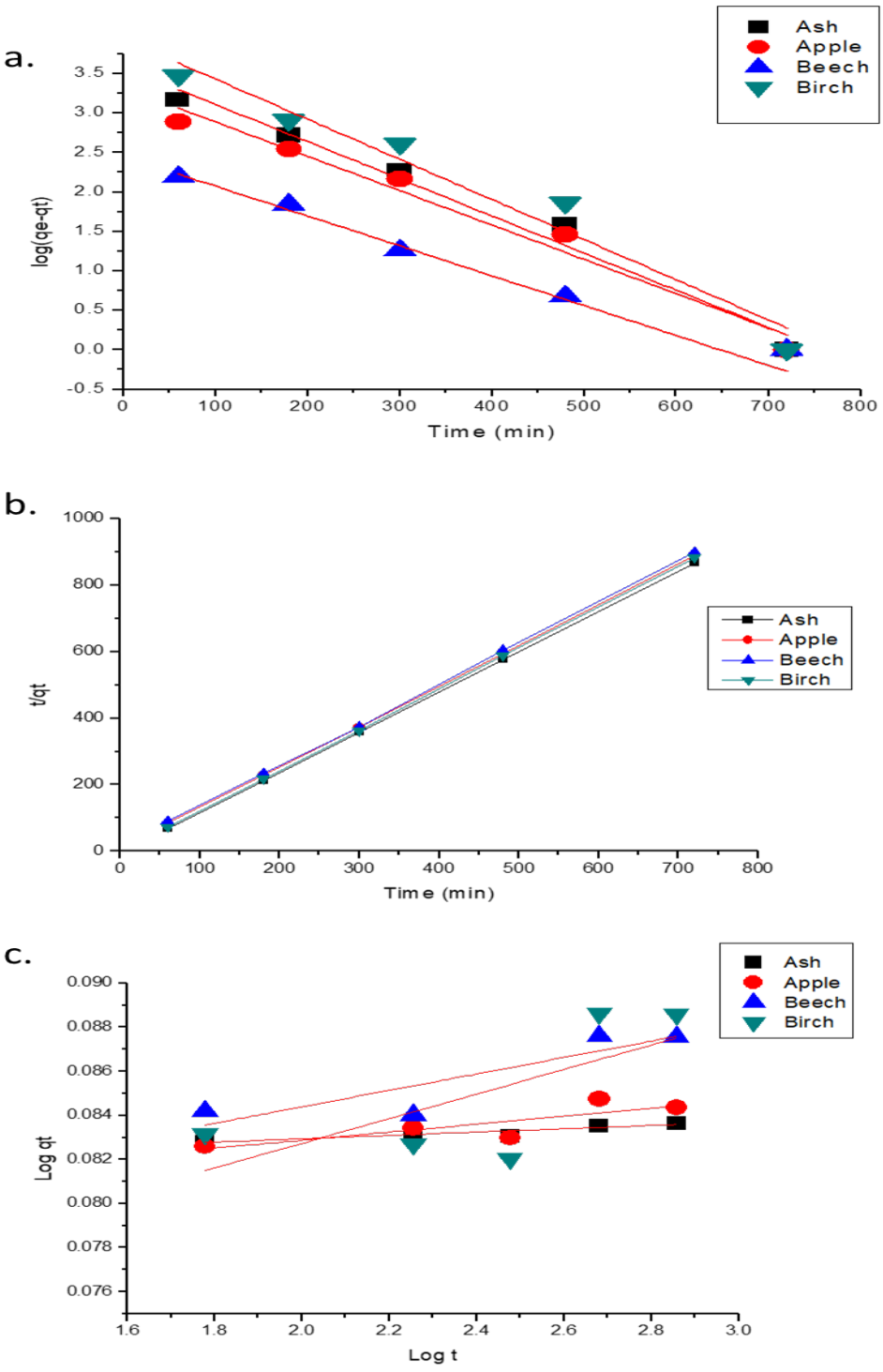


Figure E 1.0: (a,b,c): Pseudo first order of Ni^{2+} at 0.3 g adsorbent. b. Pseudo second order Ni^{2+} at 0.3 g adsorbent. c. Intraparticle diffusion of Ni^{2+} at 0.3 g adsorbent.

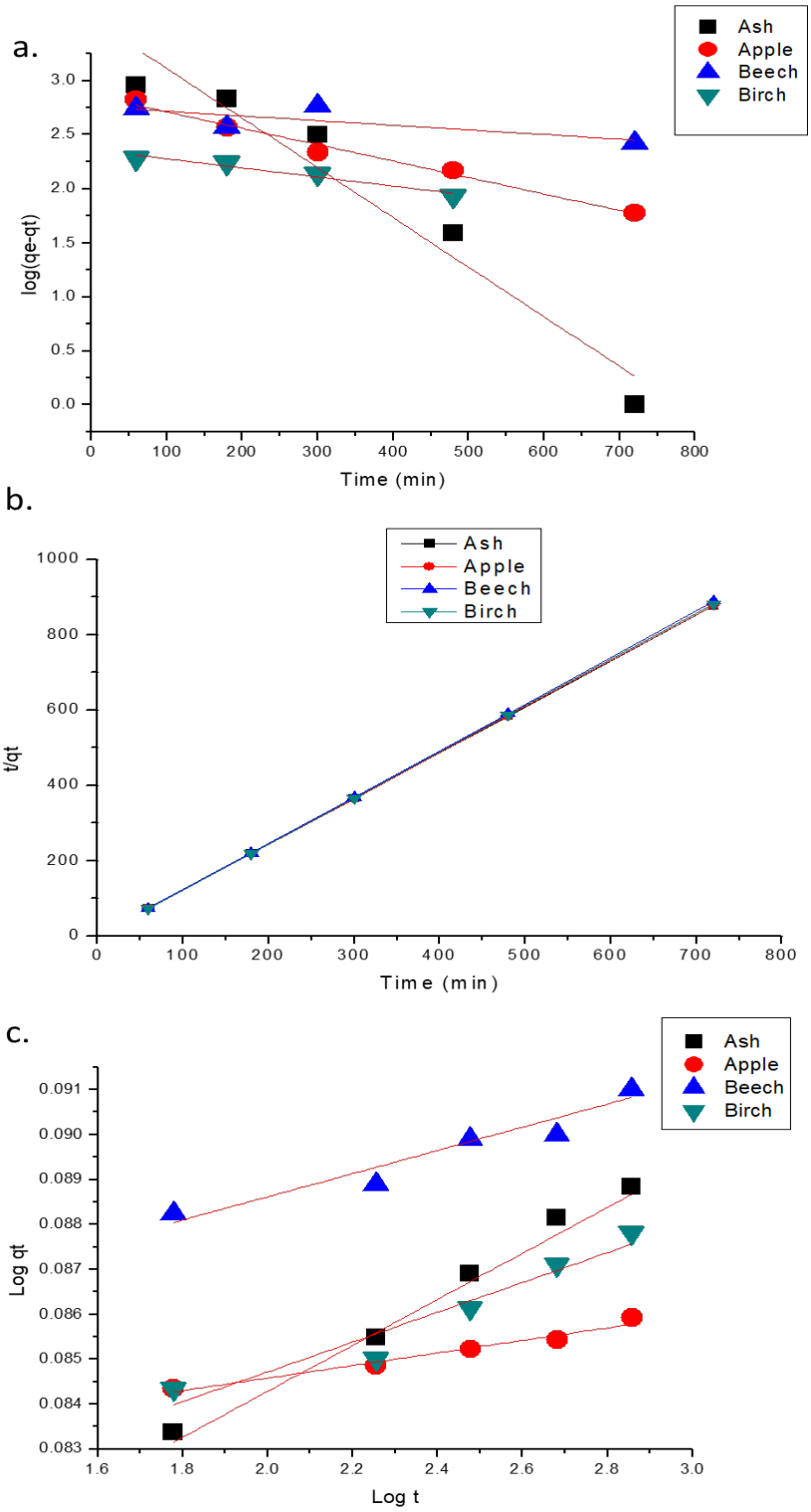


Figure E1.1: (a,b,c): Pseudo first order of Ni^{2+} at 0.5 g adsorbent. b. Pseudo second order Ni^{2+} at 0.5 g adsorbent. c. Intraparticle diffusion of Ni^{2+} at 0.5 g adsorbent.

Table E 1.0: Kinetic parameters for the biosorption of Ni^{2+} onto 0.3 g adsorbents showing q_e k_1 and R^2 values insinuating sorption mechanism.

Kinetic Model	**Parameter**	**Bc-Ash**	**Bc-Apple**	**Bc-Beech**	**Bc-Birch**
Pseudo-first order	qe(mgg-1)	0.5539	0.5213	0.3892	0.5955
	K1(min-1)	1.0 x 10-2	9.99 x 10-2	8.7 x 10-3	1.177 x 10-2
	R2	0.97153	0.9649	0.8195	0.94772
Pseudo-second order	qe (mg g-1)	0.8243	0.82	0.8141	0.813
	K2(g mg-1 min-1)	3.0 x 10-2	9.84 x 10-4	5.62 x 10-3	9.76 x 10-2
	R2	0.9999	0.9998	0.99976	0.99994
Intraparticle diffusion	Kd (mgg-1 min-1/2)	3.1243	1.1011	2.14283	1.1452
	B	0.08144	0.07925	0.00373	0.00558
	R2	0.7829	0.5925	0.67994	0.33504

Table E1.1: Kinetic parameters for the biosorption of Ni^{2+} onto 0.5 g adsorbents showing q_e k_1 and R^2 values insinuating sorption mechanism.

Kinetic Model	Parameter	Bc-Ash	Bc-Apple	Bc-Beech	Bc-Birch
Pseudo-first order	qe(mgg-1)	0.4532	0.4505	0.4411	0.3732
	K1 (min-1)	1.0 57x 10-2	3.5 x 10-3	9.94 x 10-4	1.937 x 10-3
	R2	0.92593	0.9802	0.93764	0.93809
Pseudo-second order	qe (mg g-1)	0.8203	0.80906	0.80906	0.81632
	K2(g mg-1 min-1)	1.0 x 103	4.84 x 10-3	3.22 x 10-3	3.76 x 10-2
	R2	0.9999	0.9999	0.99996	1
Intraparticle diffusion	Kd (mgg-1 min-1/2)	1.0809	1.0874	1.07856	1.1075
	B	0.00156	0.0014	0.00258	0.00332
	R2	0.99968	0.95672	0.88865	0.91164

Table E 1.2: Kinetic parameters for the biosorption of Ni^{2+} onto 1.5 g adsorbents showing q_e k_1 and R^2 values insinuating sorption mechanism.

Kinetic Model	Parameter	Ash	Apple	Beech	Birch
Pseudo-first order	qe(mgg-1)	0.32864	0.19154	0.17302	0.2786
	K1(min-1)	1.00 x 10-2	1.4 x 10-2	1.69 x 10-2	1.56 x 10-2
	R2	0.93119	0.97633	0.90992	0.9265
Pseudo-second order	qe (mg g-1)	0.81037	0.80775	0.79176	0.81103
	K2 (g mg-1 min-1)	2.093 x 10-2	2.483 x 10-2	1.4365x10-2	3.80952 x 10-2
	R2	0.99994	0.97666	1	1
Intraparticle diffusion	Kd (mgg-1 min-1/2)	1.2898	1.0013	1.07856	1.1035
	B	0.00681	0.00228	0.00258	0.00243
	R2	0.99968	0.91291	0.98865	0.81432

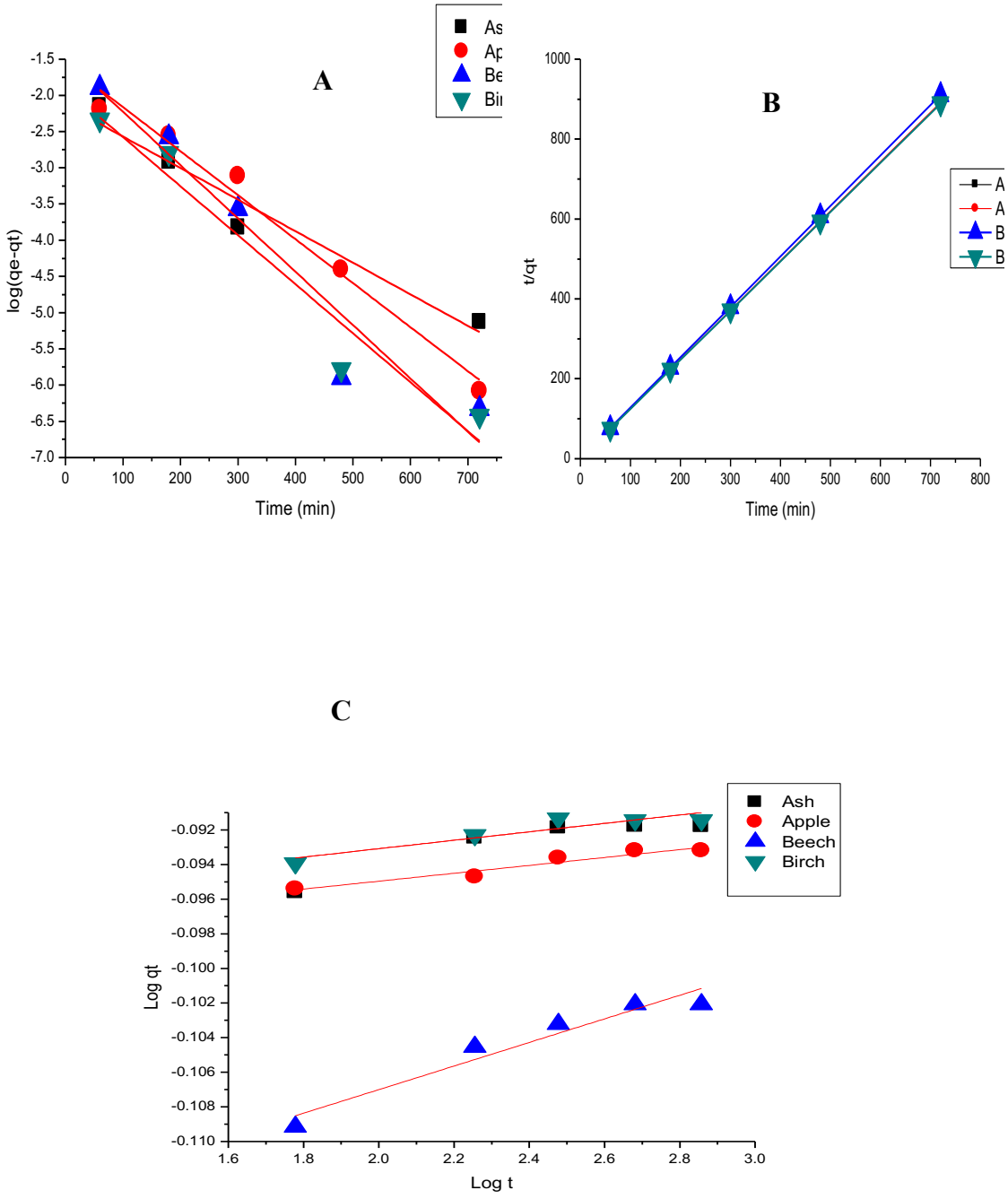


Figure E 1.2 (a, b, c): Pseudo first order Ni^{2+} at 1.5 g adsorbent. b. Pseudo second order Ni^{2+} at 1.5 g adsorbent.

1.1: Discussion

The adsorption mechanisms observed by the adsorbents on adsorbate (Ni^{2+} and Pb^{2+}) were evaluated through adsorption kinetics studies. Three kinetics models were investigated, a Pseudo-first order, Pseudo-second order and Intra particle diffusion model. These linear regression coefficients (R^2) and q_e-cal values are normally used to assess the goodness of fit of kinetics models and thy give insight of sorption phenomenon. These parameters gotten (from the models) at various adsorbent dosage are shown in Table E 1.1 and Table E 1.2. It can be seen that the pseudo first order model fit well to the experimental data (data from Figure E 1.0 and 1.2) for all the adsorbents at 0.3 g. This finding was proven by the q_e- cal values (0.3892–0.5955 mg/g) which were observed to be equivalent to the experimental values (qe 0.826 mg/g), and good linear regression coefficient values (R^2 = 0.8195– 0.97153) which implies that fit is less good than those obtained from the pseudo second order model (R^2 = 0.9897–0.97153). similarly, It can be seen that pseudo second order model fit well to the experimental data (Table E1.2). In contrast, the R^2 values of Intraparticle diffusion were lower than those of the Pseudo first order model and Pseudo second order, indicating the sorption process is not limited through diffusion. Table E1.2 Shows the Kinetic parameters for the biosorption of Ni^{2+} onto 1.5 g Adsorbents. It can be seen that the three models fit well to the experimental data due to the R^2 values. Similarly, figures E 1.0, 1.1 and 1.2 shows the adsorption of Pb^{2+} unto Ash, Apple, Beech and Birch at different contact times (60– 720 min) and also at 0.3, 0.5 and 1.5 g respectively. For all the sorption processes, the adsorption efficiency increases with increase in contact time, after which it is more or less constant. The higher and rapid biosorption at the initial contact time was observed and related to the driving

force of Pb^{2+}into the surfaces of adsorbents (Ash, Apple, Beech, and Birch) and the abundance of active sites on the adsorbent(Jawed et al., 2020). Basically, most sorption occurred during the first hour followed by a slowly attained equilibrium state.

Table E 1.3: Kinetic parameters for the biosorption of Pb^{2+} onto 0.3 g (a.) and 0.5 g (b.) adsorbents showing q_e k_1 and R^2 values insinuating sorption mechanism.

Kinetic Model	**Parameter**	**Ash**	**Apple**	**Beech**	**Birch**
Pseudo-first order	qe(mgg-1)	0.49864	0.99154	0.37302	0.5786
	K1(min-1)	1.50 x 10-2	1.49 x 10-2	1.89 x 10-2	1.56 x 10-2
	R2	0.99119	0.99633	0.98992	0.9865
Pseudo-second order	qe (mg g-1)	0.91037	0.89775	0.99176	0.81103
	K2(g mg-1 min-1)	2.8736	2.42483	1.49365	3.80952
	R2	1	1	1	1
Intraparticle diffusion	Kd (mgg-1 min-1/2)	1.2898	1.0013	1.07856	1.1035
	B	0.00681	0.00228	0.00258	0.00243
	R2	0.99968	0.91291	0.98865	0.81432

Table E1.4: Kinetic parameters for the biosorption of Pb^{2+} onto 0.5 g adsorbents showing q_e k_1 and R^2 values insinuating sorption mechanism.

Kinetic Model	**Parameter**	**Ash**	**Apple**	**Beech**	**Birch**
Pseudo-first order	Qe (mgg-1)	0.79564	1.89154	1.47302	2.5786
	K1(min-1)	1.89.50 x 10-2	1.79 x 10-2	2.49 x 10-2	4.56 x 10-2
	R2	0.99119	0.99633	0.98992	0.9865
Pseudo-second order	qe (mg g-1)	0.65037	0.97775	1.99176	2.81103
	K2(g mg-1 min-1)	5.8736	10.96483	11.79365	8.80952
	R2	0.9997	0.9999	0.9999	0.9998
Intraparticle diffusion	Kd (mgg-1 min-1/2)	5.8898	7.8013	5.87896	9.8035
	B	0.00981	0.01228	0.06258	0.007243
	R2	0.51123	0.91291	0.2981	0.56709

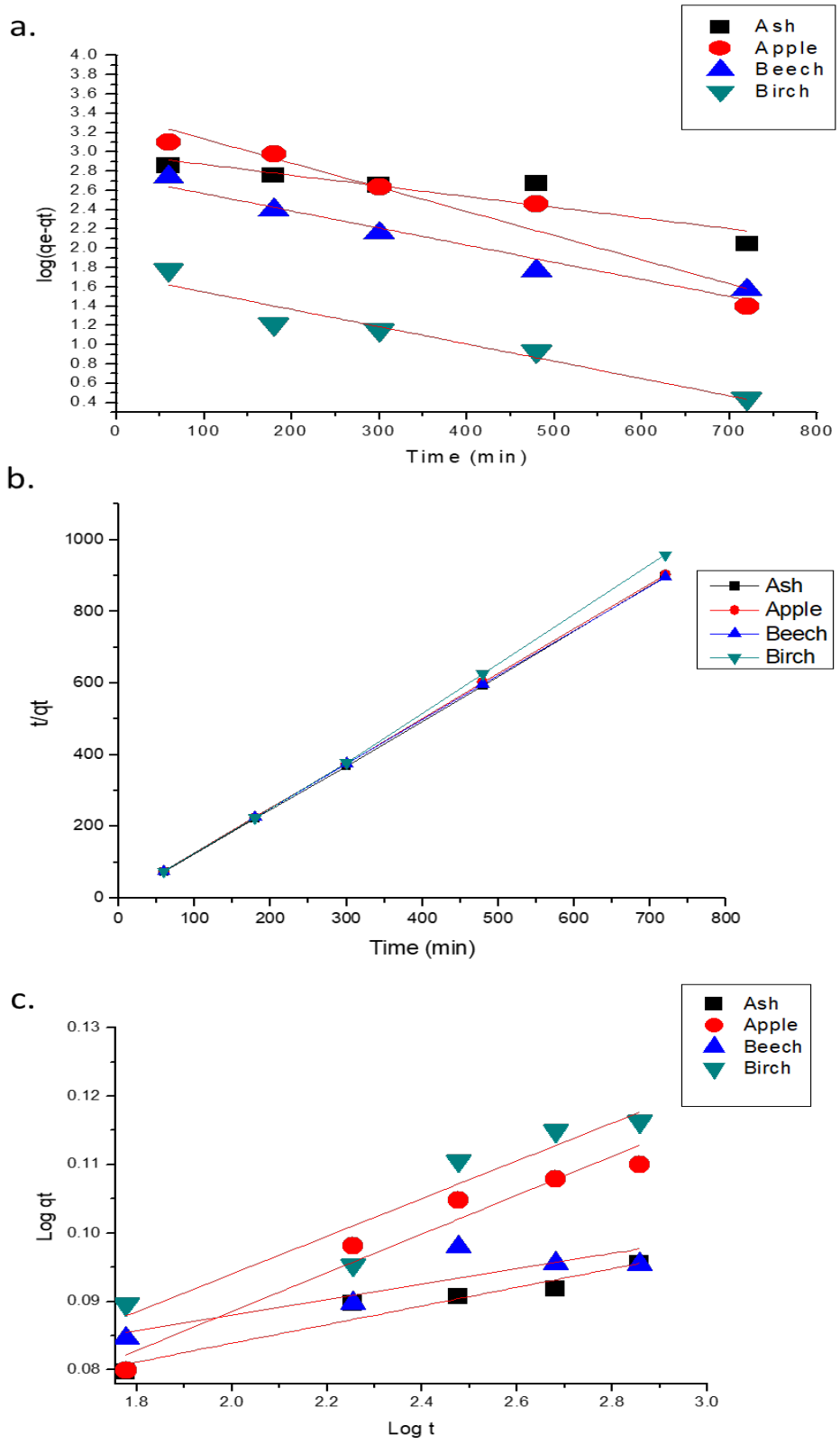


Figure E 1.3: (a, b, c): Pseudo first order of Pb^{2+} at 0.3 g adsorbent. b. Pseudo second order of Pb^{2+} at 0.3 g adsorbent. c. Intraparticle diffusion of Pb^{2+} at 0.3 g adsorbent

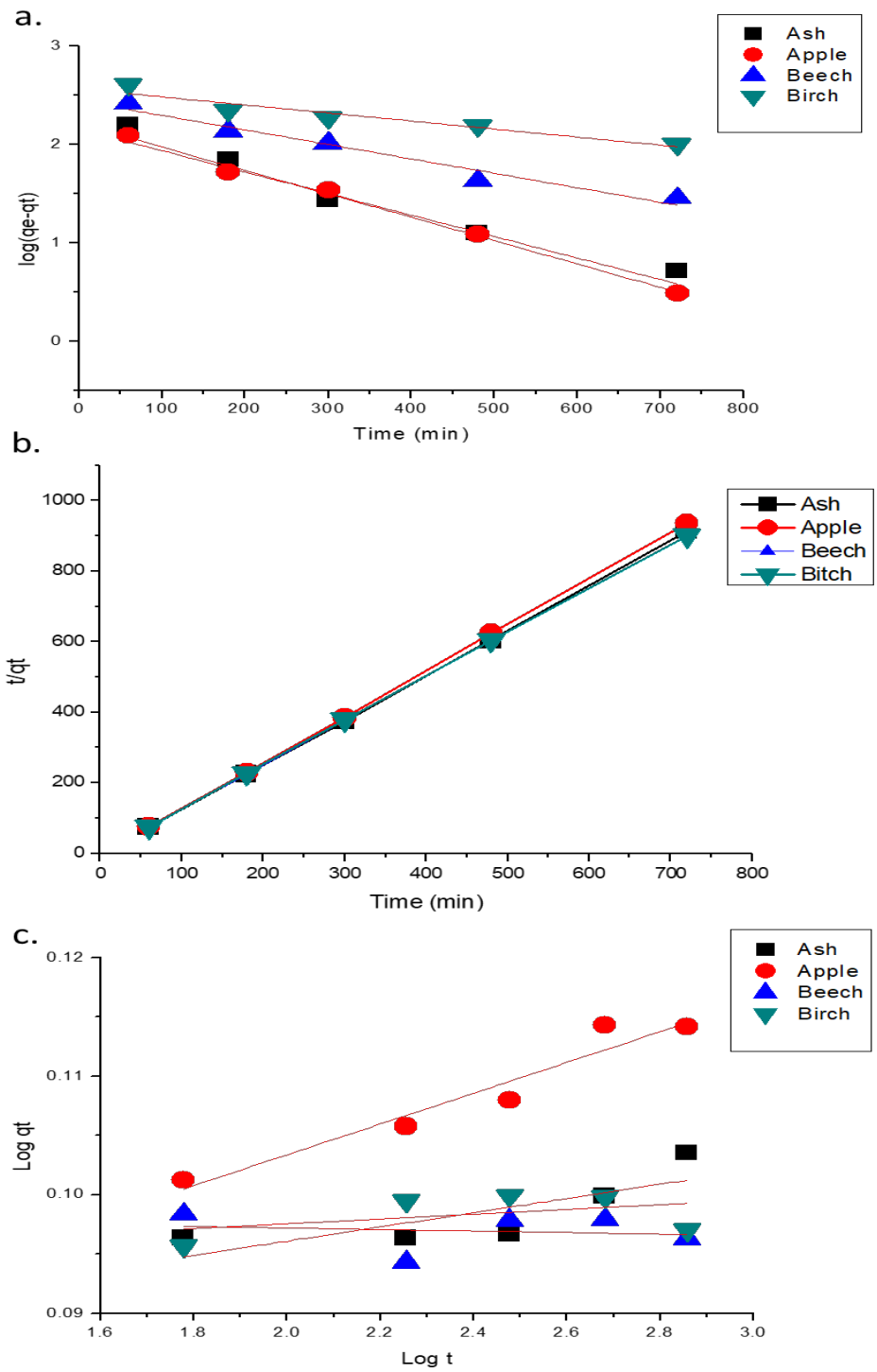


Figure E 1.4: a, b, c:. Pseudo first order of Pb^{2+} at 0.5 g adsorbent. b. Pseudo second order of Pb^{2+} at 0.5 g adsorbent. c. Intraparticle diffusion of Pb^{2+} at 0.5 g adsorbent